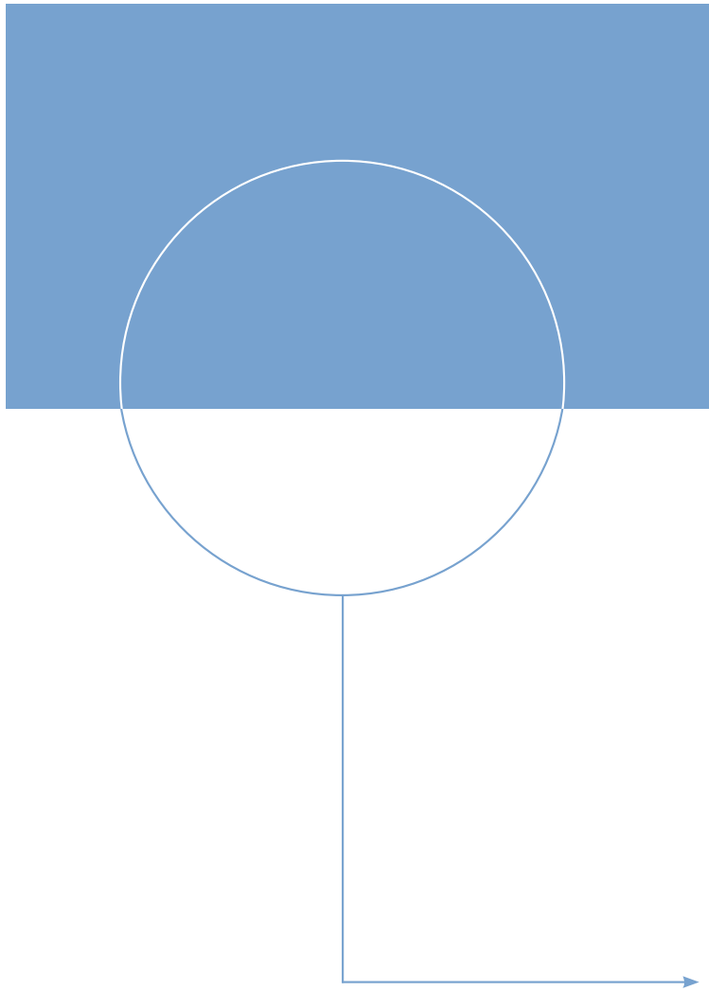

Master's thesis

2019

Per-Anders Mortensen

NTNU
Norwegian University of
Science and Technology
Faculty of Engineering
Department of Civil and Environmental Engineering

Per-Anders Mortensen

Pore pressure build-up due to pile driving in clay

June 2019

NTNU
Norwegian University of
Science and Technology

NTNU
Norwegian University of
Science and Technology

NTNU
Norwegian University of
Science and Technology

Pore pressure build-up due to pile driving in clay

Per-Anders Mortensen

Civil and Environmental Engineering
Submission date: June 2019
Supervisor: Steinar Nordal
Co-supervisor: Yeganeh Attari

Norwegian University of Science and Technology
Department of Civil and Environmental Engineering

Preface

This document contains a literature study into some of the currently available methods of predicting the excess pore pressure developed due to pile driving in clay, and correspondence of the predictions to measurements. The results produced by the Cavity Expansion Method coupled with the Modified Cam Clay and the Tresca material models have been studied and empirical data gathered in the literature study has been used to do regression analyses. The study is performed as a master thesis in geotechnics as part of the Master of Science in Civil and Environmental Engineering at the Norwegian University of Technology and Science (NTNU). It is part of the course TBA4900 lead by the Department of Civil and Transport Engineering and was written during the spring semester of 2019.

The main supervisor of the study has been Prof. Steinar Nordal at NTNU, while the co-supervisor has been Ph.D. student Yeganeh Attari. I express my gratitude to them both for the guidance and help I have received.

The study is connected to the research and development project REMEDY by the Norwegian Geotechnical Institute (NGI). The aim of the REMEDY project is to reduce the risk of damage in connection to groundwork during and after execution of a building project. One of the activities in REMEDY is to study the effects that pile driving have on slope stability. This is the scope of Yeganeh Attari's PhD. The aim of the study reported here is to contribute to this activity in REMEDY, by looking into analytical, numerical and empirical methods of estimating the pore pressure build-up due to pile driving in clay.

Trondheim, 05/06/2019

Per-Anders Mortensen

Summary

The study presents some general information on the effects of pile driving based on measurements and the current understanding of the problem. Some basic geotechnical background on how excess pore pressure is generated is gone through. Then two ways of modelling the installation of piles, namely the Strain Path Method (SPM) and the Cavity Expansion Method (CEM), are discussed. These methods are coupled with different material models. The material models that are mainly discussed is the elastic-perfectly plastic material model with a Tresca yield criterion (EP), the Modified Cam Clay model (MCC), and other types of Critical State Soil models that include the anisotropy of the material through a rotated yield ellipse, and the structure of the material by adding a notional intrinsic yield ellipse (i.e. S-CLAY1, S-CLAY1S, MIT-E1,-E2 and -E3). The MCC, S-CLAY1 and S-CLAY1S models are gone through in detail so that the discussion and evaluation of the results produced when using these, or similar, material models can be as precise as possible. Some empirical prediction methods are introduced and most of the presented prediction methods are compared to measurements.

A numerical model of CEM is presented, and the results produced when using the MCC and the EP material models is studied closer. The effects of introducing an inner remoulded zone with a lower undrained shear strength is studied with the CEM-EP model. 12 sites where the pore pressure was measured at the pile shaft, directly after pile driving, is presented with soil conditions and other relevant information. This data is further used in regression analyses, and to assess some of the presented prediction methods.

The measurements of the excess pore pressure at the pile shaft display a large scatter for the heavily overconsolidated clays. For the slightly over- and normally consolidated clays the scatter is much smaller. SPM is believed to give the most correct stress state compared to CEM. CEM is shown to grossly over-predict the radial effective stress, however the recorded excess pore pressure sometimes correspond better to CEM, and sometimes it fits best with the SPM prediction. The radial extent of the excess pore pressure seems to correspond relatively good with what CEM-EP predicts.

The measurements show that the main parameters influencing the excess pore pressure are the undrained shear strength (s_u), the undrained shear modulus (G_u), the overconsolidation ratio (OCR) and whether the pile is open- or closed-ended. In addition, the plasticity index (I_P),

sensitivity (S_t), and coefficient of lateral earth pressure (K_0) is shown to have an effect in some of the numerical studies, but a trend in the measured data with I_P and K_0 is not found. The sensitivity of the soil is in the presented dataset very correlated to the OCR, and therefore the magnitude and effect of S_t is uncertain.

When driving piles in a group, the effect seems to be that a somewhat constant maximum excess pore pressure level is reached. This harmonizes with the critical state soil theory, which say that the inner remoulded zone of an already installed pile is unaffected by the driving of a new pile as the soil is already at critical state. However, the extent of the excess pore pressure is shown to increase somewhat compared to what CEM-EP predicts.

The effect on slope stability is only briefly discussed. The pile is shown to have a stabilizing effect if it is driven through the critical slip surface. The main negative effects of pile driving in a slope is a decrease in strength due to remoulding, and due to a reduction of the vertical effective stress. However, CEM only predicts decreasing vertical effective stress when the material contracts. Johansson and Jendeby (1998) found that the radial total stress decrease faster than the excess pore pressure due to stress relaxation. It could be that the increase in vertical total stress found when using CEM also reduce faster than the excess pore pressure. Karlsrud, Kalsnes et al. (1993) reports vertical silo effects occurring in lean clays during the reconsolidation phase, which causes lower vertical effective stress close to the pile. If this is the case then introducing the full excess pore pressure without increasing the total vertical stress may be necessary in order to avoid failure.

Table of Contents

List of Figures

List of Tables

List of Symbols and Abbreviations

Some symbols are only used once or twice and is then not included in the list. However, they should be presented both by symbol and name as they appear.

Greek letters

Δ	Change of the parameter to the right (mostly used as the difference between the initial value and the value found directly after pile driving)
α_i	Parameter i used in a regression
γ	Shear strain also used as the total unit weight of the soil (see context)
γ_f	Shear strain at which the maximum undrained shear strength is observed
γ_r	Shear strain at which the undrained shear strength has reduced to its remoulded value (i.e. s_{ur})
ε	Total strain
ε^p	Plastic strain
ε^e	Elastic strain
ε_θ	Strain in the circumferential direction
ε_r	Strain in the radial direction
ε_{vol}	Volumetric strain
ε_z	Strain in the vertical direction
κ	Compression index (relates p' to e in the OC region in MCC)
λ	Swelling index (relates p' to e in the NC region in MCC)
λ_i	Inclination of the intrinsic normal compression line in S-CLAY1S
ν	Drained Poisson's ratio

ν_{ur}	Poisson's ratio for unloading/reloading
ν_u	Undrained Poisson's ratio ($= 0{,}5$)
ρ	Density of the material
σ_{axial}	Axial stress in a triaxial test
σ_{cell}	Cell pressure in a triaxial test
$\sigma_{v0}, \sigma'_{v0}$	Initial vertical stress (total, effective)
$\sigma_\theta, \sigma'_\theta$	Circumferential stress (total, effective)
σ_r, σ'_r	Radial stress (total, effective)
σ_z, σ'_z	Vertical stress (total, effective, v is also used as subindex)
σ_1, σ'_1	Major principal stress (total, effective)
σ_2, σ'_2	Intermediate principal stress (total, effective)
σ_3, σ'_3	Minor principal stress (total, effective)
τ	Shear stress
τ_f	Shear stress at failure
τ_{mob}	Mobilized shear strength
φ	Friction angle

Upper case Latin letters

A	Skempton's pore pressure parameter
A_f	Skempton's pore pressure parameter at failure
B	Skempton's saturation parameter
B_b	Bishop's pore pressure parameter
C_s	Compressibility of the solid material
C_w	Compressibility of the fluids inside the soil (water and air)
D	Janbu's pore pressure parameter referred to as the Dilatancy parameter also used as the pile diameter (see context)
E_u, E'	Young's modulus (undrained/drained)
F	Safety factor
G_u, G'	Shear modulus (undrained/drained)
G_u^{50}	Undrained shear modulus taken at 50% mobilization of the shear strength, often called the undrained average shear modulus
I_L	Liquidity index
I_P	Plasticity index
K	Bulk modulus
K_0	Coefficient of earth pressure at rest, also called the coefficient of lateral earth pressure
K_0^{NC}	Coefficient lateral stress at rest in normal consolidation
K_i	Radial effective stress ratio at end of pile installation
L	Embedded length of pile

M	Slope of the Coulomb line in the $q - p'$ plane or oedometer modulus (see context)
R_{eq}	Equivalent pile radius
$R^2, \bar{R}^2$	Coefficient of determination, Adjusted coefficient of determination
S_t	Sensitivity

Lower case Latin letters

e	Void ratio
e_0	Initial void ratio
m_0/m_{NC}	Modulus number for virgin loading (above p_c')
m_{OC}	Modulus number for reloading (below p_c')
n	Porosity of the soil, used as number of data points in Chapter 14
g	The gravitational constant
k	Permeability of the soil
p'	Effective mean stress
p_p	Isotropic preconsolidation pressure
p_c'	Vertical preconsolidation pressure
p_0	External pressure (i.e. in-situ horizontal stress in the ground)
p_{eq}	Equivalent isotropic stress
p	Total mean stress (also used as internal pressure in Chapter 4 & 5, and as number of parameters used in a regression in Chapter 14)
q	Deviatoric stress

r	Radial distance from center of pile (a few times it is the radial distance from pile wall, but then it is stated explicitly)
r_0	Pile radius
r_p	Radius of plastic zone around pile
r_r	Radius of remoulded zone around pile
s_{uf}	Undrained peak shear strength
s_{ur}	Remoulded undrained shear strength
s_u	Undrained shear strength (can be assumed equal to the direct unless otherwise stated)
s_{uC}/s_{uA}	Undrained shear strength from triaxial compression test
s_{uD}	Undrained shear strength from direct simple shear test
s_{uE}/s_{uP}	Undrained shear strength from triaxial extension test
t	Time or thickness of pile (see context)
u	Total pore water pressure (also used as displacement)
u_0	Initial pore water pressure
Δu	Excess pore water pressure
Δu_{max}	Excess pore pressure at the pile shaft
v	Specific volume also used as velocity (see context)
w	Natural water content
w_L	Liquid limit
w_P	Plastic limit
x_i	Regressor or input variable i used in regression

$y_i, \hat{y}_i$	Measured and predicted dependent variable of a regression
z	Depth (the measurement depth of the pore pressure in Chapter 13 & 14)
z_{tip}	Depth of the pile tip

Abbreviations

BBC	Boston Blue Clay
CEM	Cavity Expansion Method
CPT	Cone Penetration Test
CSL	Critical State Line
CSSM	Critical State Soil Mechanics
ESP	Effective Stress Path
EP	Linear Elastic-Perfectly Plastic material with a Tresca yield criterion
FEM	Finite Element Method
iso-ncl	Isotropic normal compression line in the MCC model
MCC	Modified Cam Clay
MIT	Massachusetts Institute of Technology
MIT-E1/2/3	Effective stress based critical state soil model developed at MIT
NGI	Norwegian Geotechnical Institute
NC	Normally consolidated
OC	Overconsolidated
OCR	Overconsolidation Ratio
OMS	Ordinary Method of Slices

PLB	Prévost-Levadoux-Baligh total stress based material model developed at MIT
RSS	Residual Sum of Squares
S-CLAY1(S)	Effective stress based critical state soil model including anisotropy (and destructuration)
SPM	Strain Path Method
TSP	Total Stress Path
TSS	Total Sum of Squares
url	unloading/reloading line in the MCC model

1 Introduction

1.1 Background

Installation of a pile causes large strains and remoulding of the soil around the pile. Large strains leads to large changes in the total stress state. The effective stress principle gives the total stress as the sum of the pore pressure and the total stress. Clay have a low permeability, this causes the large change in total stress to initially be carried by the pore water. As the excess pore pressure dissipates the soil skeleton will gradually increase the effective stresses between the grains.

Driven piles are often used in geotechnical engineering to transfer loads to deeper layers. Due to urbanization and the following densification, more buildings are being built in slopes than before. The stabilizing and destabilizing effects piles have on slope stability is therefore an important issue. In addition to the soil remoulding and disturbance, there is a destabilizing effect due to the excess pore pressure. The exact influence that excess pore pressure has on slope stability is however somewhat unclear.

Piles are almost always driven in groups. The combined effect of a pile group is therefore important. Understanding the soil behavior of a single pile is in the author's view fundamental in order to further evaluate the combined effect of a pile group, and the effect on slope stability. The excess pore pressure is also important for understanding how the pile bearing capacity increases with time. In fact, most of the reports cited are interested in the exact prediction of the excess pore pressure solely for this reason. The effects of pile driving are also closely related to other deep penetration problems such as the Cone Penetration Test (CPT). This report will focus on pile driving, but hopefully it will also be useful in other settings and give the reader some insight to some of the currently available methods for predicting the stresses, and the difficulties that are faced, in deep penetration problems.

1.2 Objective

The main objective of this study is:

- To present and evaluate analytical, empirical and numerical methods of predicting the pore pressure build-up due to the driving of a single pile in clay.

Secondary objectives are:

- Getting a better understanding of the effects that causes the pore pressure build-up.
- Evaluate the prediction of the final stress state produced by the prediction method. Specifically the radial and vertical effective stresses, in addition to the excess pore pressure.
- To assess the prediction methods based on our understanding of the soil's behavior during and after pile driving, in addition to its correspondence to measurements.
- The effect on slope stability due to the driving of piles.
- Prediction of the excess pore pressure due to the driving of multiple piles in a group.

1.3 Approach

This report contains a literature study on the stress condition after the driving of a pile in clay. The first ten chapters are mainly based on data found in the literature, and most of the figures have been collected from other authors. If something is unclear or seems wrong I encourage you to check the original source. Analytical and numerical solutions have been given the most weight as they give a better understanding of the mechanisms causing pore pressure build-up.

The effect on slope stability are only shortly discussed, however the main goal of predicting the excess pore pressure correctly is to be able to look further into this. The prediction methods and material models presented are gone through in detail. This is done so that the reader is given the required background information that is needed to understand the discussion of the faults and imperfections in the methods and material models. A study of the Cavity Expansion Method (CEM) in a Modified Cam Clay (MCC) and a linear elastic-perfectly plastic (EP) material is performed. In addition, softening is studied by introducing a remoulded zone with lower undrained shear strength in the CEM-EP model. Measurements of the excess pore pressure at the pile shaft from 12 sites are used in the evaluation of some of

the prediction methods. This data is also used to study whether trends can be found with respect to different soil parameters, and to present some new empirical prediction methods.

1.4 Limitations

This report only considers saturated clay loaded under undrained conditions. The predicted excess pore pressure is the main focus, but the pore pressure is part of the stress state in the soil so a discussion of the principal or Cartesian stresses is also included. For slope stability the vertical stress is of interest, and for pile bearing capacity the radial stress is of importance.

Many aspects of the soil behavior are discussed closely, including the assumed impact it will have on the prediction of the excess pore pressure. Not all topics are discussed in detail, and I refer to the original source for more information on a specific topic. Whenever triaxial testing is mentioned, it may be assumed that the test has been conducted under undrained conditions in the conventional way unless otherwise stated.

The figures are gathered from multiple sources, so the use of symbols is not consistent. I apologize for this, however the figure text should clarify when different symbols are used. This is done in the end of the figure text by setting the symbol used in the graph equal to the symbol used in this study. There are other ways to model this problem, and there are prediction methods that have not been included. This study should therefore not be considered as a complete list of methods for predicting the excess pore pressure due to pile driving.

1.5 Structure of Report

This report consists of a literature study, numerical simulations and empirical data. Chapter 1 to 10 is mainly based on findings from the literature, but is occasionally supplemented with results from the numerical and empirical work presented in the later chapters. The numerical simulations are presented in Chapter 11 and 12, while the empirical work is presented in Chapter 13 and 14.

The study presents some general information on the effects of pile driving based on measurements and the current understanding of the problem in Chapter 2. In addition, some of the effects of installing a pile group, and the effects on slope stability when installing piles, are shortly discussed. Chapter 2 requires some understanding of the methods and contains

therefore some reference to later chapters. Some basic geotechnical background on how excess pore pressure is generated is gone through in Chapter 3.

In Chapter 4 and 5, the Cavity Expansion Method (CEM) is presented. Chapter 4 presents the derivation of an analytical solution using CEM and an elastic material, while Chapter 5 looks at the analytical elastic-perfectly plastic solution with the Tresca yield criterion (EP). Chapter 5 also contains a discussion about the input parameters, and a short description of how to model open-ended piles.

The Modified Cam Clay (MCC), the S-CLAY1 and the S-CLAY1S models are described in Chapter 6. Some numerical predictions using these material models with CEM is presented. In addition, the mesh dependency introduced when using a softening material model is shortly explained. Chapter 7 presents the Strain Path Method (SPM) and the difference between CEM and SPM are discussed.

Chapter 8 contains some of the empirical prediction methods that exist, together with a short description. Comparison of results obtained by the discussed prediction methods and measurements is presented in Chapter 9. In Chapter 10 the results gathered in the literature study is discussed and summarized.

A Plaxis model of CEM is presented and checked against results presented by other authors in Chapter 11. The same model is used in Chapter 12, in order to study the stresses predicted when using a linear elastic-perfectly plastic (EP) material model with a Tresca failure criterion, as well as the Modified Cam Clay (MCC) material model. Differences in the obtained results between the two material models are discussed, and especially the overconsolidation ratio (OCR) and the coefficient of lateral earth pressure (K_0) is studied closely. The chapter is concluded by investigating strain softening. This is modeled by introducing an inner remoulded zone with lower undrained shear strength in the CEM-EP model, and the result is compared to more complex Critical State Soil models that include softening.

Chapter 13 presents the soil conditions at the 12 sites where pore pressure has been measured at the pile shaft. This chapter is mainly based on the data gathered by Karlsrud (2012), but the soil parameters have been cross-checked and additional soil parameters such as the sensitivity (S_t) and the undrained shear modulus (G_u) has been gathered/derived to supplement the

dataset. This data is further used in Chapter 14 to evaluate the CEM-EP solution, two expressions based on the study of the CEM-MCC model, and a trend line suggested by Karlsrud (2012). In addition, the data is used in a couple of multivariate linear regressions.

The report is ended with a conclusion, and proposals for specific topics which need further work. Lastly, the Appendix contains plots which are not essential for the discussion, but either proves a statement or shows something in a different way than the plots included in the text.

2 Effects of pile installation

2.1 Pile installation

Piles are most commonly used when either one or more of the points below are problematic:

- The top layer has insufficient bearing capacity and replacement of the masses are not economically doable. This is often the case in Norway due to large instances of sensitive clays.
- When differential settlements exceed a tolerable limit. This is often the case in slopes or for unfavorable layering.
- When there are large horizontal loads on the fundament. Piles can either take these forces as bending moment, or the piles can be installed with an angle and take the forces as axial loads.
- When there is tension or uplift forces, which often is the case for slim structures. Piles can carry the load by side friction.
- When a fundament is installed in water that is flowing. Piles are then favorable as one can dimension with respect to erosion.

When using piles, the loads from the structure are distributed to deeper soil layers. Piles carry the load through side friction and tip resistance, where one effect often is dominant. Piles can be made of steel, concrete, timber and plastic. The choice of pile material is determined by load size, and economic and environmental considerations. (Group 2016)

Piles are most commonly categorized based on the installation process or the load transferring method. Two main categories based on the installation process are driven and bored piles. The driving of piles creates excessive noise and ground vibration which can damage structures in the vicinity. Bored piles create less noise, but are more costly. The driving of piles will also create larger excess pore pressure than bored piles. The choice of installation method is therefore based on whether the above presented problems can be tolerated, and are of course weighted against the economic costs.

The driven piles can be further divided into displacement and non-displacement piles. Displacement piles displaces a large volume of soil, which is the case for closed-ended piles.

Non-displacement piles displace less than ten percent of the external pile volume, which often is the case for open-ended piles. This study looks at excess pore pressure generated by the driving of a pile. Bored piles are normally installed by first drilling a hole in the soil and then the pile is either casted in or lowered into the hole. Excess pore pressure will then mainly be produced due to the drilling process. To calculate this one must use a fundamentally different model, and the pore pressure build-up that is created will be of a much lower magnitude than for a driven pile. The installation process is therefore crucial to the pore pressure build-up that is generated. Closed-ended piles will be the focus as they displace more soil and thus create larger pore pressure build-up. In Chapter 5.4 the modifications of the Cavity Expansion Method (CEM) to model open-ended piles is briefly discussed as later chapters show results for both open- and closed-ended piles. (Budhu 2008)

2.2 General effect on soil

When a pile is penetrating the soil it punches a hole forcing the soil to flow both downwards and radially outwards. The pressure required to do this produce large increases in total stresses both under the tip and alongside the pile wall. The clay reacts to the pile volume by shearing to large strains. As the pile tip advance to greater depths the soil alongside the pile wall is unloaded in shear and the mean effective stress developed may decrease due to the effect of driving or jacking load cycles. One could say that the stresses required to form a cylindrical cavity are smaller than the stresses required to keep the cavity open. A network of shear surfaces form and become a permanent feature of the soil. This allows the pile to further advance without causing large distortion to the soil above the shear surface. These shear surfaces depend on soil type, rate of installation, and the piles surface roughness. (Bond and Jardine 1991)

Clay has a very low permeability, and the time used to drive a pile is in relation to the permeability short. The pile driving should therefore be considered as rapid loading, and undrained conditions are assumed. Under undrained conditions, excess pore pressure will occur due to change in total stresses. This is further explained in the beginning of Chapter 3. Unless the pile is pushed down into the soil at a steady rate, pile driving will cause repeated unloading and reloading cycles. This will generate positive cyclic pore pressure within the unloading/reloading cycles that the models presented in this study do not account for.

The expansion of a cylindrical cavity causes large radial strains, but the effect of the downward drag when installing a pile will cause very large vertical shear strains close to the pile wall. These vertical shear strains will be of a much larger magnitude than the radial strains close to the pile wall according to Baligh (1985). The large deformations also cause extensive remoulding and disturbance around the pile. (Karlsrud 2012)

When the shear stresses surpass the undrained shear strength of an intact clay, failure will occur and lead to deformations. These deformations will lead to a lower shear strength called the remoulded shear strength (s_{ur}). Karlsrud and Haugen (1984) defined three zones close to the pile wall. From results of falling cone tests, water content and x-ray photographs from the Haga test site they describe the zones. Figure 2.1 illustrates the results.

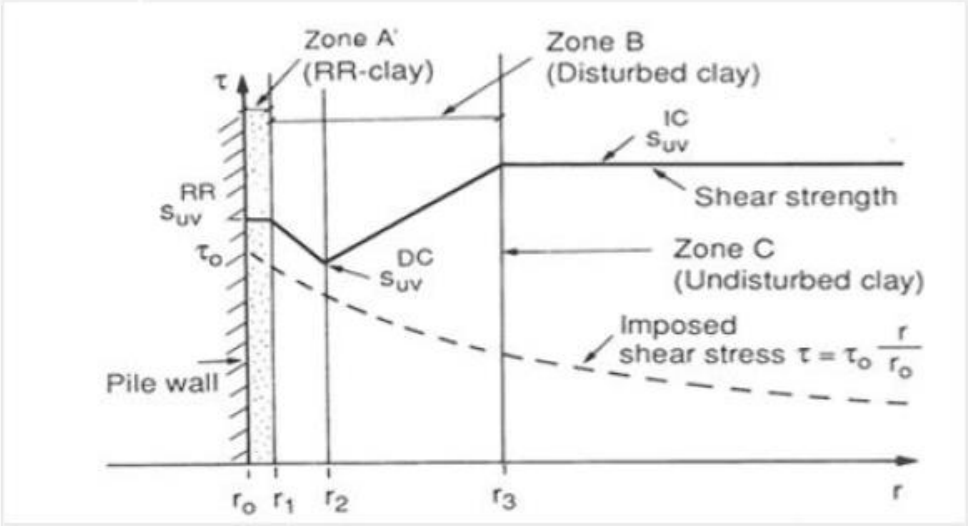

Figure 2.1: Impact of pile installation on the undrained shear strength (s_u) as a function of the radial extent from the pile wall (r). (Karlsrud and Nadim 1990)

In Zone A there is RR-clay which stands for remoulded and reconstituted clay. This zone extend to about $0{,}22\,{}^{r}/_{r_0}$ from the pile wall, and has gone through severe remoulding. The clay has lost all memory of aging effects and preconsolidation stress. The reconsolidation causes a reduction in water content and corresponding volume change, which also leads to a higher undrained shear strength determined from the falling cone test.

Zone B appears to have undergone a more uniform shear distortion. The water content gradually goes back to its initial values at the transition between Zone B and C. However,

falling cone tests show a reduction in undrained shear strength from $0{,}22\,{}^{r}/_{r_0}$ to about $0{,}9\,{}^{r}/_{r_0}$, and then an increase to the initial values in Zone C.

Zone C is intact clay which shows no impact of the pile driving in the x-ray photos, water content and undrained shear strength. The interface between Zone B and C is about $3{,}6\,{}^{r}/_{r_0}$ from the pile wall. The distances described are only results from the Haga test site and does not hold for other sites. Figure 2.2 shows the results that these descriptions are based on.

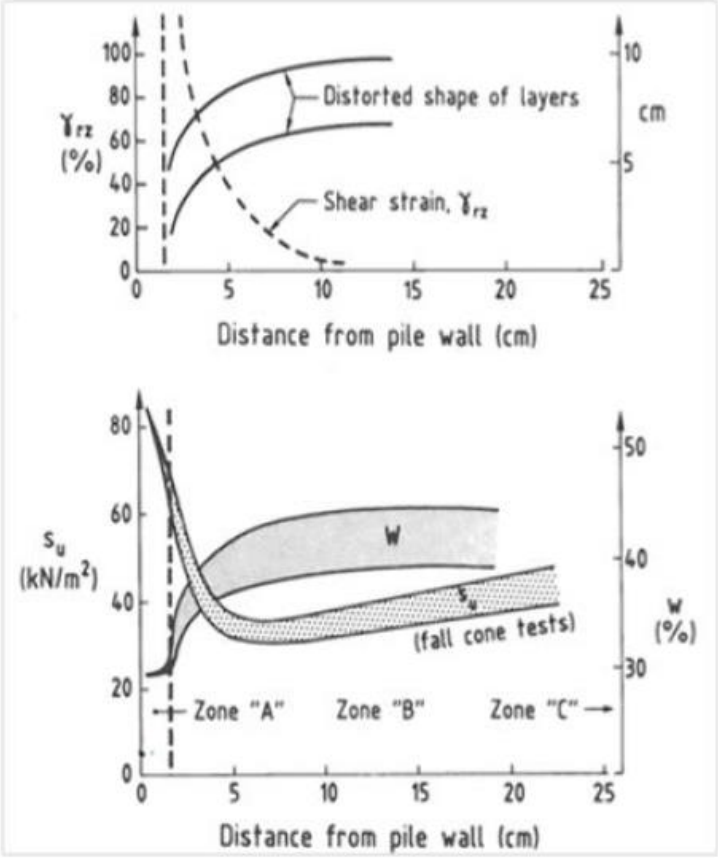

Figure 2.2: Measured shear strain (γ_{rz}), water content (w) and undrained shear strength (s_u) from falling cone tests as function of the radial distance from the pile wall. Based on data from the Haga test site. (Karlsrud and Haugen 1985)

Karlsrud, Kalsnes et al. (1993) suggest that vertical silo effects and cylindrical arching may occur in lean clays in the reconsolidation phase. As the pile is driven a remoulded zone is created close to the pile (i.e. zone A). The remoulded zone have a decreased stiffness which increase the volumetric compressibility. The circumferential stress will increase at the edge between the inner remoulded zone and the outer plasticized zone due to the difference in stiffness. Since the inner remoulded zone have a low stiffness the stiffer outer zone attracts the stresses and create an arching effect around the remoulded zone. The inner remoulded

zone is then experiencing lower pressure due to the large circumferential stress around the inner zone. Vertical silo effect is when the vertical effective stress is relieved due to friction on the “silo” wall. The “silo” wall is located at the transition between the inner remoulded and the outer plasticized zone. This could cause even lower vertical effective stress than what is predicted with SPM-MITE3 according to Karlsrud (2012).

With time the excess pore pressure will dissipate causing an increase of the effective stresses. This increase the friction against the pile wall, thereby further increasing the piles bearing capacity. The decay of the excess pore pressure depends on the relative size of the zone A and the zone B, the magnitude of the excess pore pressure in each zone, and the permeability and compressibility of the soil. According to Bond and Jardine (1991) and Karlsrud (2012), among others, simple linear radial consolidation theory can be used to estimate the magnitude of the pore pressures in the soil as it decay with time. The consolidation process is not discussed in detail in this study.

2.3 Effect of overconsolidation

Field measurements of the excess pore pressure have shown that for heavily overconsolidated clays, suction may develop. This is due to strong dilation of heavily overconsolidated clays when sheared. Dilation means that the volume of the material expands, and that the excess pore pressure reduces, when sheared. Heavily overconsolidated clays have experienced a higher mean stress causing the soil to compact plastically. When the soil is then unloaded it will unload elastically, but it will not go back to its original state due to the plastic deformations. If we then shear the soil it will expand in volume, just as sand grains in a compacted state would climb over each other thus expanding the volume. Under the pile tip, the mean stress dominates the excess pore pressure. However, for points above the pile tip shear induced pore pressure is large and often negative for heavily overconsolidated clays. (Bond and Jardine 1991)

Coop and Wroth (1989) found that for normally consolidated clays the CEM-EP model gives reasonable results. For heavily overconsolidated clays however, the measured normal stress is almost half of what is calculated as the cylindrical limit pressure. Karlsrud (2012) found that the measured excess pore pressure at the pile shaft for heavily overconsolidated clays shows a very large scatter. This could be due to the presence of sand seams, desaturation of the pore

pressure measurement equipement or other unknown effects. The result is anyway that predictions obtained for heavily overconsolidated clays are very uncertain.

2.4 Effect of soil structure

Soil structure refers to bonding between particles, which can arise from many causes. It is a general term for soil behavior that cannot be explained by stress history or initial porosity. Leroueil and Vaughan (1990) say that the soil structure can arise from "cold welding at interparticle contacts under high pressure, from the deposition of carbonates, hydroxides and organic matter from solution, from recrystallization of minerals during weathering, and from the modification of the adsorbed water layer and interparticle attractive forces in clayey soils." The processes in themselves can be rather complex, however the conclusion is the same: soil particles are bonded together through chemical processes over time. This creates structure in the clay with planes of weakness and planes of strength. This soil structure is the reason clay behavior is anisotropic. When a clay has been loaded in a certain direction over many years bonding between the particles can occur. The clay has a higher strength and stiffness when loaded in the same direction as previously loaded, than if the clay is loaded in a new direction.

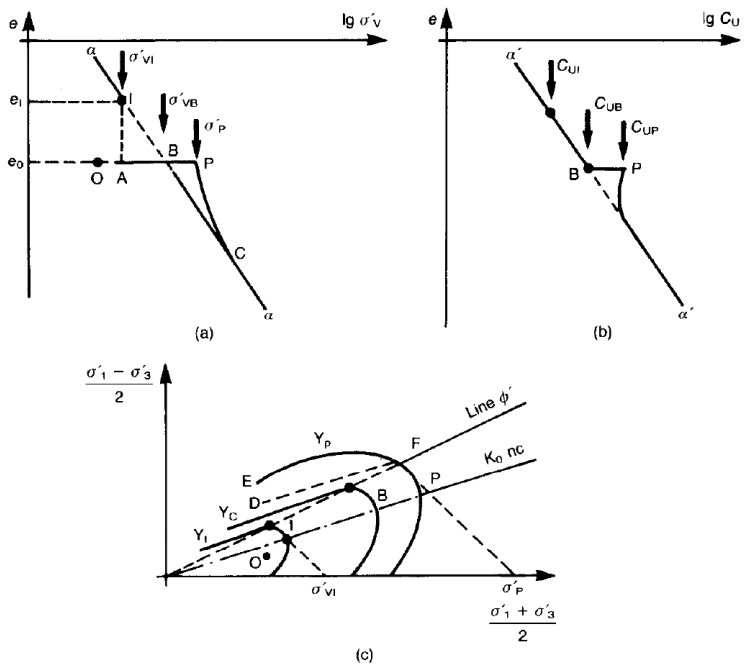

Figure 2.3: The effects of secondary compression and structure on (a) void ratio, (b) undrained strength and (c) yield. (Leroueil and Vaughan 1990)

Figure 2.3 (a) shows this increased stiffness when loaded in the vertical direction. If the soil is previously loaded to point B, then unloaded to A, reloading should take us back to point B and then straight to point C. However, the soil structure gives us an increased strength as seen in Figure 2.3 (b) (point P). The structure gives an apparent preconsolidation pressure coinciding with point P. When sufficient volume deformation has occurred, the soil will again follow the normal compression line (after point C). When the soil has been loaded to point C we say that it is destructurated.

A destructurated state is produced when the soil structure is partially broken by volume or shear deformations. In a remoulded sample all soil structure is lost and the strength of the clay is reduced to a minimum. When doing sampling some disturbance will always occur and the true soil structure is hard to determine.

Terzaghi (1944) defined sensitivity (S_t) as the ratio between the undrained strength of undisturbed clay (s_u) and the undrained strength of the remoulded clay (s_{ur}) at the same water content. The sensitivity is generally regarded as the parameter embodying the differences of the microstructures of the natural and the remoulded clay. The softening of a clay is thus governed by the sensitivity. There are material models that include strain softening. The Modified Cam Clay model introduce some softening when the overconsolidation ratio is higher than two. This softening can however not be controlled so that both the peak undrained shear strength equals s_u and the undrained shear strength at large strains equals s_{ur}.

The effects of using a strain softening material model is discussed in Chapter 12.8. The conclusion is that the excess pore pressure increases when including strain softening. However, if the radial extent of the remoulded zone is chosen to be very large, a decrease in excess pore pressure can be produced when using simple Tresca based material models. If one uses a critical state soil model then softening will give some contraction of the soil. This causes the effective mean stress to decrease, which will give an additional increase in excess pore pressure.

2.5 Pile groups

This study mainly focuses on the excess pore pressure produced due to a single driven pile. However, in practical problems a single pile is seldom driven alone. Therefore the effect of multiple driven piles in a pile group is of great practical importance. To understand how the soil reacts to a pile group one must understand how a single pile influences the soil. This is the reason single piles are the focus of this study. Some general behavior of pile groups, as described in the literature, will however be rendered in this chapter due to the importance of the combined effect in practical engineering.

Figure 2.4 shows how the pore pressure increased as each pile in a pile group was driven. The excess pore pressure peaks were reduced by $20 - 40\%$ in some few hours after the pile driving. After this the excess pore pressure decreased much slower.

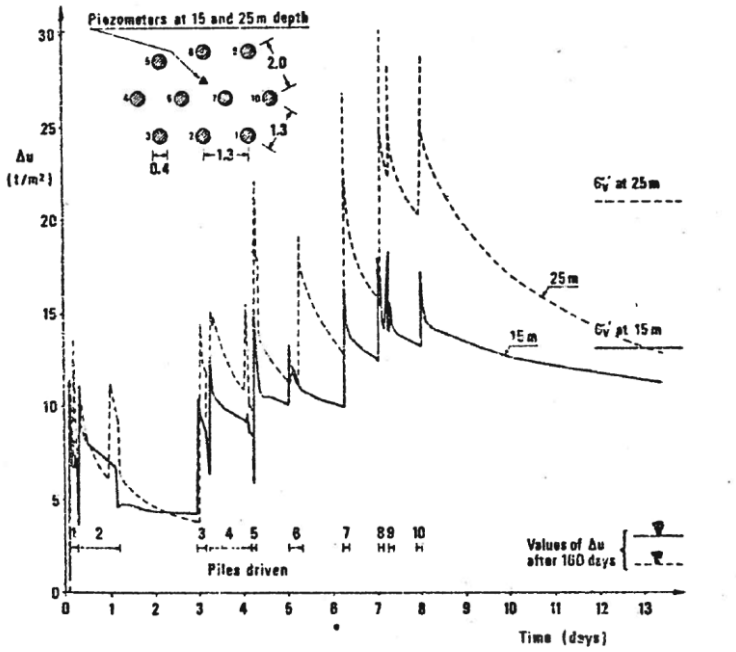

Figure 2.4: Excess pore pressure plotted against time when driving multiple piles measured at two depths (15m and 25m). (Croce, Calabresi et al. 1973)

Figure 2.5 shows a principal sketch of how the pore pressure builds up after each new pile installed. The decrease is similar for each new pile added, however the excess pore pressure goes towards an upper boundary. This means that the excess pore pressure calculated for a single pile cannot simply be multiplied with the number of piles in the pile group.

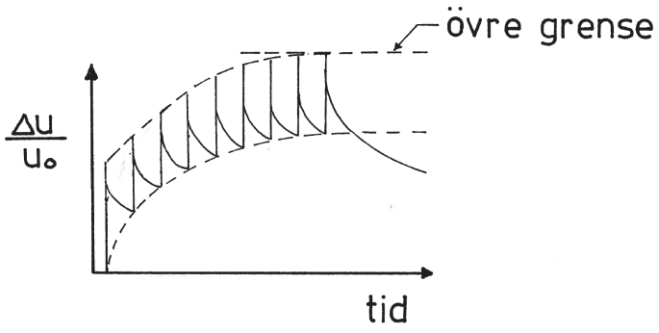

Figure 2.5: Principal sketch of excess pore pressure normalized with the initial pore pressure against time, when driving multiple piles with equal length of time between the driving of each pile. (övre grense=upper boundary) (Hoem 1975)

Poulos (1994) finds that the installation of a pile adjacent to an already installed pile will give axial forces and bending moments in the pile that have already been installed. This is due to the horizontal and vertical displacements that are developed in the soil when a pile is driven. Possible consequences in the already installed pile are structural damage or cracking, tensile failure or that the pile tip lifts off the bearing stratum.

However, the impact on the excess pore pressure at the pile wall seems to be small. Bozozuk, Fellenius et al. (1978) presented data for a pile group containing 116 piles. They found that the excess pore pressure was relatively constant in the pile group and that the radial extent was only slightly higher than that predicted for a single pile.

McCabe and Lehane (2006) make the same observation and explain that the soil close to an already driven pile is at the critical state condition. This means that the maximum pore pressure is reached for a single pile at the pile surface and installing further piles will not increase the pore pressure at the pile shaft of the already installed pile. If a pile group is installed sufficiently close, so that the remoulded zone of each pile overlap, then the excess pore pressure would be constant between the piles if McCabe and Lehane (2006) are right. The installation of a new pile will then only cause accumulation of the excess pore pressure beyond the plastic zone. However, some decrease in excess pore pressure between the piles is to be expected as the radial extent of the soil which is in critical state condition is quite small.

Figure 2.6 shows measured pore pressure from Bozozuk, Fellenius et al. (1978) at three different locations. The scatter before the maximum pore pressure is reached is due to the installation time of different piles and their distance to the piezometer. The main result is that there seem to be a peak value that is reached at the different piezometers. This is also shown in Figure 2.5, this upper boundary is believed to be reached for a single pile if the piezometer

is located at the pile shaft. The only reason Figure 2.5 shows an increase for each new pile installed is then believed to be because the piezometer is often placed between the piles where the soil is not at critical state. As more piles are installed the soil between the piles become more plasticized and the upper boundary is reached. Since the soil between the piles is not at critical state, this upper boundary will probably not equal the maximum excess pore pressure at the pile shaft for a single pile, but should in theory be somewhat lower. The same applies for Figure 2.6 as the piezometers are placed between or outside the pile group.

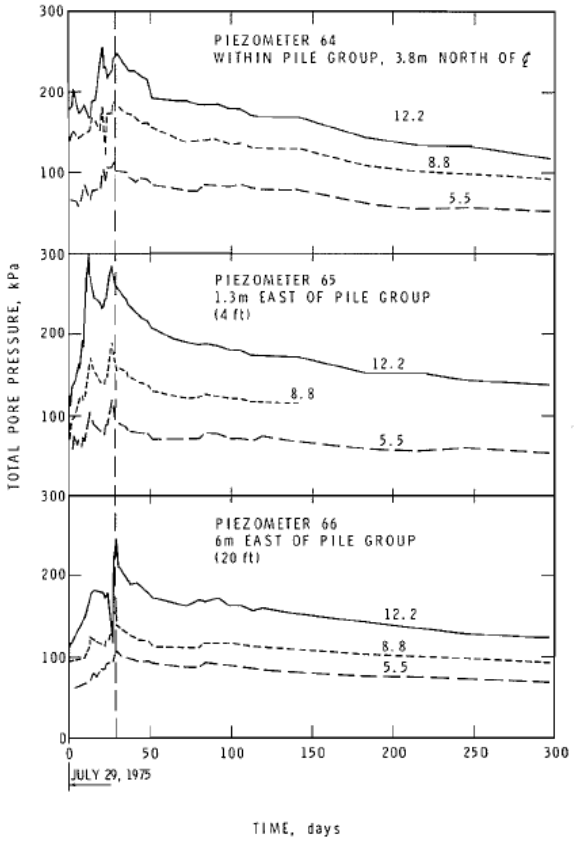

Figure 2.6: Measured total pore pressure (u) against time at three different locations close to the pile group. (Bozozuk, Fellenius et al. 1978)

2.6 Effect on slope stability

Pile installation causes remoulding and generates excess pore pressure, which leads to a reduction in the factor of safety of a slope. If the end of the pile is driven past the critical slip surface then the pile also have a stabilizing effect, increasing the factor of safety. As seen in Figure 2.7, the driving force of the upper sliding soil mass is transmitted to the underlying stable soil through the pile, giving a stabilizing effect.

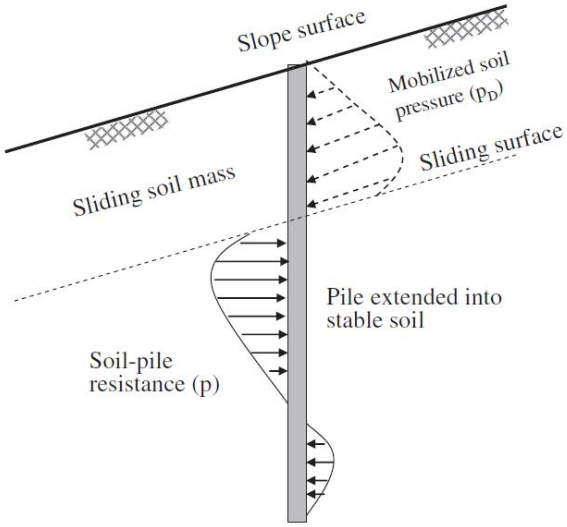

Figure 2.7: Stabilizing effect of a pile, where the sliding soil mass is stopped due to the transmission of the driving force through the pile to underlying stable soil. (Ashour and Ardalan 2012)

The effect of excess pore pressure on slope stability is difficult to include in the calculations, and the overall effect is discussable. If one looks at the simple Ordinary Method of Slices (OMS) then the factor of safety is given by:

$$F = \frac{R \int \tau_f dL}{W * X + Q * e} \tag{2.1}$$

which is found by applying moment equilibrium around the circular slip surface's center as seen in Figure 2.8. F is the safety factor, W is the weight of the soil prism, R is the radius of the slip surface, X is the horizontal distance between the soil prisms center of gravity and the circle center, Q is the external force, e is the momentum arm between the force Q and the circle center, L is the length of the slip surface, and τ_f is the shear strength where failure occurs.

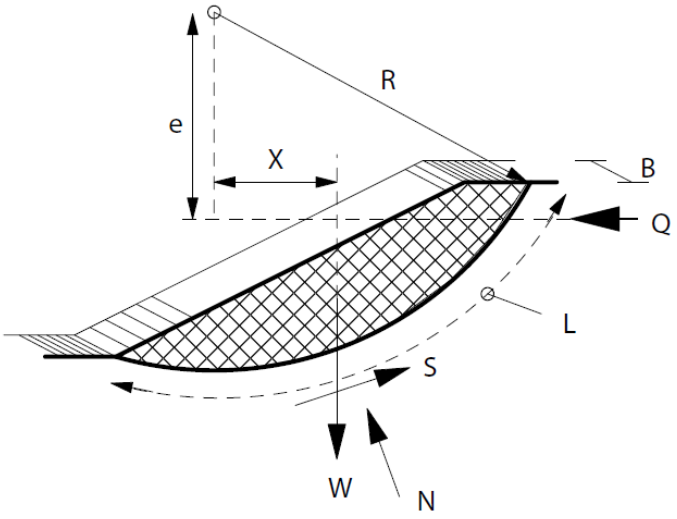

Figure 2.8: Slope equilibrium of a circular slip surface. Where B is the width of the slope, S is the force resultant of the shear stresses along the slip surface and N is the resultant force of the normal stresses between the soil prism and the underlying soil and the rest of the parameters are described above. (Group 2016)

For an undrained analysis the excess pore pressure is not included and the soil's shear strength at failure (τ_f) is taken as the constant undrained shear strength (s_u). The installation of a pile causes remoulding of the inner zone and disturbance of the plastic zone, which will decrease the undrained shear strength as seen in Figure 2.1. If an effective stress based model is used then the effect of excess pore pressure can be included. Using the Mohr-Coulomb failure criterion, the shear strength is given as:

$$\tau_f = (\sigma'_N + a)\tan\varphi = \frac{(\sigma'_v + a)\tan\varphi}{1 + \frac{1}{F}\tan\varphi\tan\alpha} \tag{2.2}$$

where the symbols are explained in Figure 2.9, and the second equality comes from vertical equilibrium as shown in Figure 2.9, where $\tau = {}^{\tau_f}/_{F}$ is the mobilized shear friction. This makes the equation iterative as the safety factor (F) is on both sides of the equation. Notice also that we neglect the vertical shear forces between the slices. This means that we assume the vertical shear forces (T) to be equal between all the slices ($\Delta T = 0$), which is often assumed for circular failure surfaces.

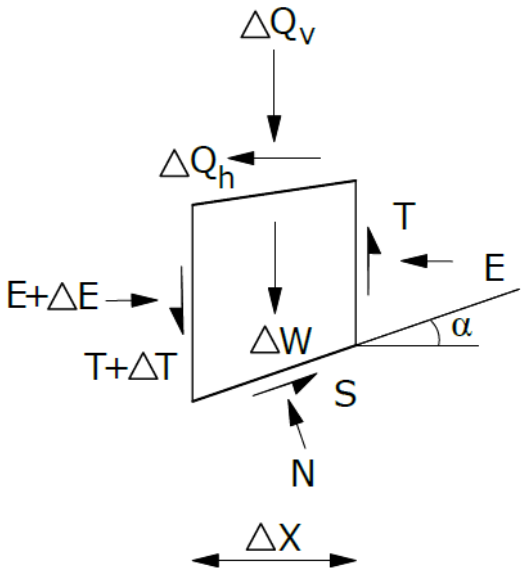

$$\sigma_N = \frac{N}{\Delta L} \quad \sigma_v = \frac{\Delta W + \Delta Q_v}{\Delta X}$$

$$\tau = \frac{S}{\Delta L} \quad t = \frac{\Delta T}{\Delta X}$$

$$\Delta X = \Delta L \cos \alpha$$

Figure 2.9: Equilibrium of a single slice. Where ΔW is the weight of the slice, ΔQ_v and ΔQ_h is the external vertical and horizontal forces on the slice respectively, T is the force resultant of the vertical shear stresses (t) between the slices and ΔT is the change in the vertical shear force, E is the normal force between the slices and ΔE is the change in the normal force, S is the force resultant of the shear stresses (τ) working along the slip surface of the slice, N is the force resultant of the normal stresses (σ_N) working on the slip surface from the underlying soil, ΔX is the horizontal length of the slice, α is the angle between the slip surface of the slice and the horizontal axis, σ_v is the total vertical stress, ΔL is the length of the slip surface of the slice. (Group 2016)

The effect of excess pore pressure is not directly seen in the effective stress approach either, but it is there. It is accounted for through the effective vertical stress (σ_v'). The effective stress principle gives us: $\sigma_v' = \sigma_v - u$, where $u = u_0 + \Delta u$ is the total pore pressure, equal to the sum of the initial pore pressure (u_0) and the excess pore pressure (Δu). The excess pore pressure is due to two effects: an increase in total mean stress and dilation or contraction due to shear. This is further explained in Chapter 3.

According to Johansson and Jendeby (1998) reduction in slope stability due to pile driving can in an undrained analysis be checked by including strength reduction due to remoulding, as previously mentioned, but one must also include a reduction in strength due to high pore pressure.

Ladd (1977) have shown that the undrained shear strength reduce if the vertical effective stress is reduced following a trend line described by:

$$\tau_r = s_u * \left(\frac{\sigma'_{v0}}{\sigma'_{v1}}\right)^{-0,25} \quad (2.3)$$

where τ_r is the reduced shear strength due to reduction of vertical effective stress, σ'_{v0} is the vertical effective stress before pile driving, and σ'_{v1} is the final vertical effective stress after pile driving. Equation 2.3 is only valid when $\sigma'_{v0} \leq \sigma'_{v1}$. The Mohr-Coulomb strength can also be used to describe a reduction in shear strength due to a reduction in vertical effective stress (here assuming $\sigma'_N = \sigma'_{v1}$):

$$\tau_r = (a + \sigma'_{v1}) * \tan(\varphi') < s_u \quad (2.4)$$

For comparison between Equation 2.3 and Equation 2.4, Johansson and Jendeby (1998) used the empirical relation proposed by Hansbo (1954) based on a Swedish high plasticity clay:

$$s_u = 0,45 * \sigma'_{v0} * w_L \quad (2.5)$$

Figure 2.10 shows the reduction in shear strength normalized with the initial shear strength against the initial vertical effective stress over the final vertical effective stress, based on Equation 2.3, and the combination of Equation 2.4 and 2.5.

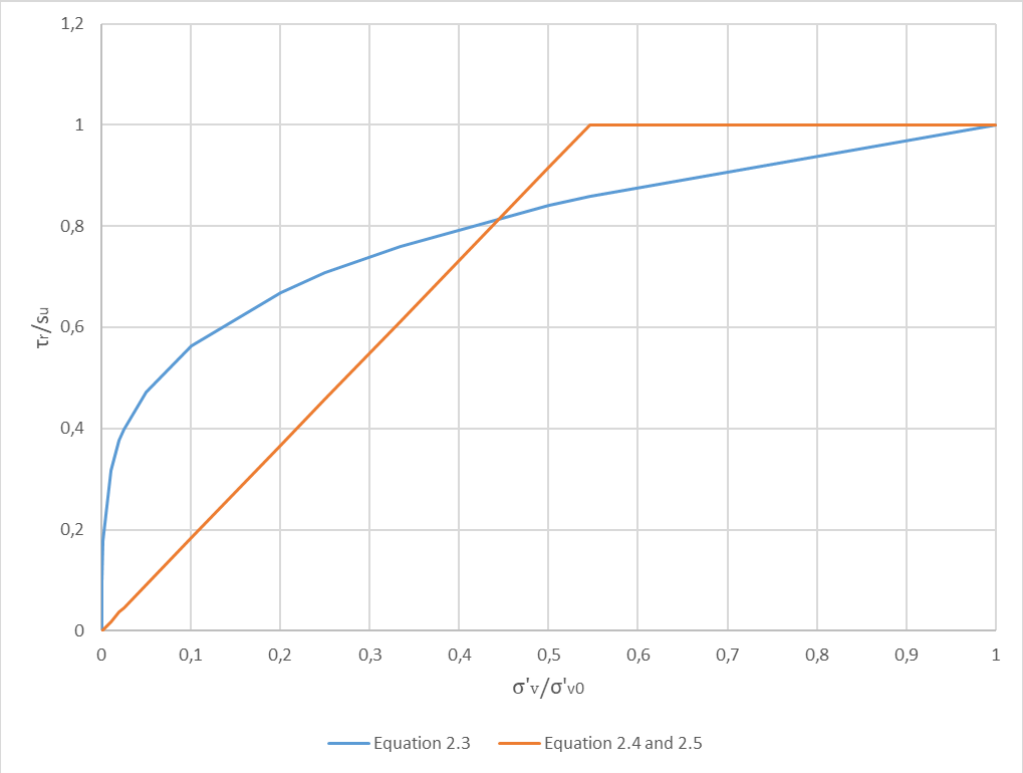

Figure 2.10: Reduced over initial shear strength versus final over initial vertical effective stress based on Equation 2.3 and the combination of Equation 2.4 and 2.5 with $w_L = 70\%$, $a = 0$ and $\varphi' = 30°$. Based on an older figure by Johansson and Jendeby (1998).

In a drained analysis failure cannot really happen due to excess pore pressure in theory. However, permeable layers may lose it strength according to Johansson and Jendeby (1998).

If the vertical and radial total stress is assumed to be unchanged while the excess pore pressure increases, failure, according to the Mohr-Coulomb failure criterion, will occur when:

$$\frac{\Delta u}{\sigma'_{v0}} = \frac{1}{2} * \left(1 - \frac{1}{\sin(\varphi')} + K_0 \left(1 + \frac{1}{\sin(\varphi')}\right)\right) \tag{2.6}$$

where K_0 is the coefficient of lateral earth pressure. This is derived from the Mohr circle seen in Figure 2.11.

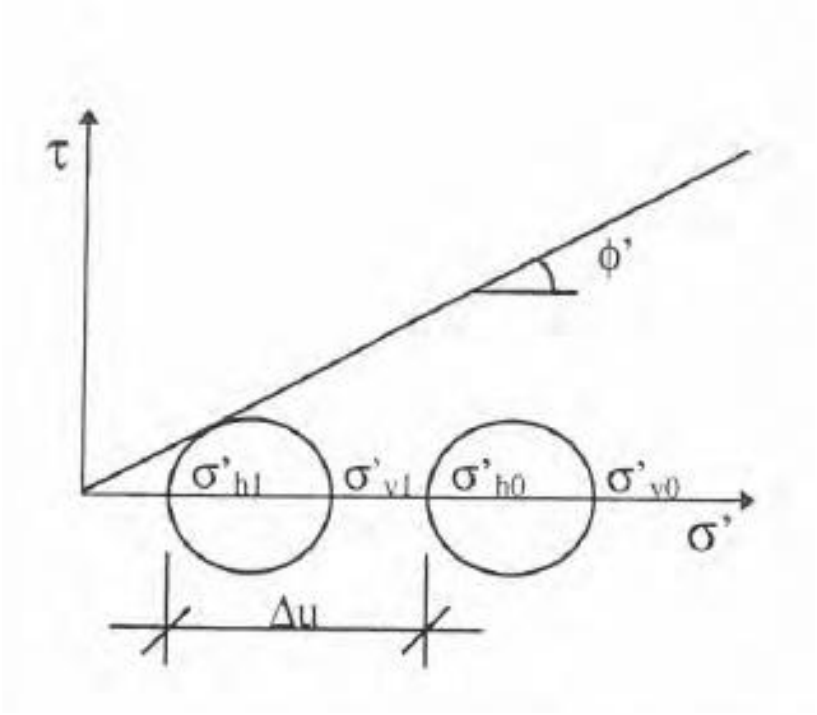

Figure 2.11: Plot of Mohr's circle with no change in vertical and horizontal total stress (i.e. $\Delta\sigma_h = \Delta\sigma_v = 0$ and $\Delta\sigma'_h = \Delta\sigma'_v = \Delta u$). The subindex h and v indicates horizontal and vertical stress respectively. While 1 and 0 indicates after and before pile driving respectively. (Johansson and Jendeby 1998)

We do however know that pile driving causes the radial total stress to increase. If the vertical total stress is assumed to be unchanged while the radial total stress increase, failure will occur when:

$$\frac{\Delta u}{\sigma'_{v0}} = \frac{A * \left(1 + \frac{1}{\sin(\varphi')} + K_0\left(1 - \frac{1}{\sin(\varphi')}\right)\right)}{2A - \frac{1}{\sin(\varphi')}} \tag{2.7}$$

according to the Mohr Coulomb failure criterion, given that the radial stress becomes larger than the vertical stress. Where A is Skempton's pore pressure parameter (see Chapter 3.2). This is illustrated in Figure 2.12.

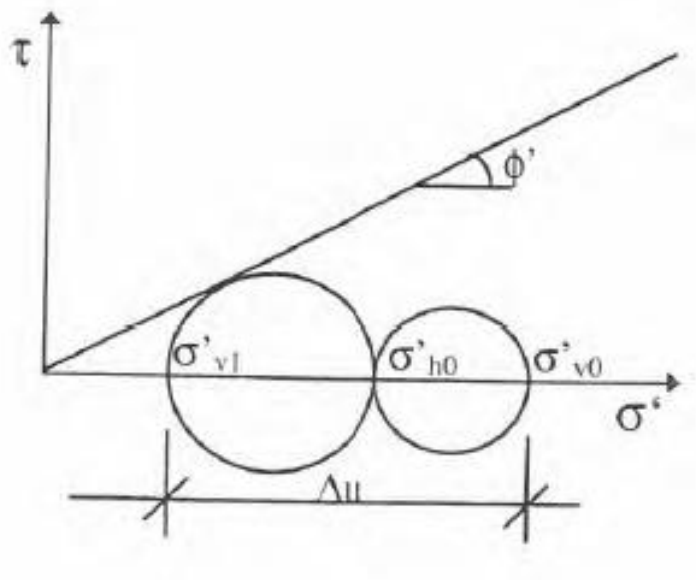

Figure 2.12: Plot of Mohr's circle with no change in vertical total stress (i.e. $\Delta\sigma_v = 0$ and $\Delta\sigma'_v = \Delta u$), while the total horizontal stress increase equally much as the excess pore pressure (i.e. $\Delta\sigma_h = \Delta u$ and $\Delta\sigma'_h = 0$). The subindex h and v indicates horizontal and vertical stress respectively. While 1 and 0 indicates after and before pile driving respectively. (Johansson and Jendeby 1998)

The easiest and most common assumption used in practice, is to assume no change in Cartesian total stresses and then introduce the excess pore pressure in a slope stability calculation with the Mohr-Coulomb failure criterion. This does however seem overly conservative based on the fact that the total stresses will increase.

There are different ways of modeling the pile driving. The installation of the pile gives large radial deformations, which again causes a large radial total stress increase. This means that the total mean stress increases and thus creates a positive excess pore pressure. However, the total vertical stress also increase when using the Cavity Expansion Method (CEM) to model the pile driving. Using CEM will therefore give no decrease or increase in vertical effective stress due to the increase in total mean stress.

The second part of the excess pore pressure is due to shearing. A clay can either dilate or contract. Normally consolidated clays are known to contract, while overconsolidated clays are known to dilate. If the clay contracts then we will get an additional increase of the pore pressure, causing a decrease in the effective vertical stress and then the safety factor will decrease as well. If the clay dilates then the excess pore pressure decreases and the factor of

safety goes up. If the clay is heavily overconsolidated then suction or negative excess pore pressure may occur. This will then, in theory, increase the factor of safety of the slope.

The different prediction methods explained in the following chapters produce different effective vertical stresses. However, the Cavity Expansion Method coupled with the Tresca material model never predicts any change in vertical effective stress when plane strain is assumed (i.e. $\Delta\varepsilon_v = 0 \rightarrow \Delta\sigma_v' = 0$). Close to the terrain, CEM can cause some heave and then also a reduction in vertical effective stress. However, plane strain is usually assumed when CEM is used and the results herhein are gathered from models that assumes plane strain or from sufficient depth so that $\Delta\varepsilon_v \approx 0$. If softening is included in the Tresca material model as done in Chapter 12.7, there is still no change in effective vertical stress. If the Modified Cam Clay (MCC) model is used with CEM then a reduction in vertical effective stress is only predicted when the material is contracting ($OCR < 2$ in MCC). If the material dilates ($OCR > 2$ in MCC) then CEM actually predicts an increase in vertical effective stress (see Chapter 12), and thus an increase in the safety of the slope.

Figure 2.13 shows the vertical effective stress produced with CEM and the Strain Path Method (SPM) and different material models (PLB, MIT-E1 and MCC, see Chapter 6 and 7). The soil parameters are based on Boston Blue Clay (BBC) with an overconsolidation ratio (OCR) of one (i.e. a contracting material). The SPM method predicts a decrease in stresses as the pile tip has passed (see Figure 7.2). The major difference between CEM and SPM, is that SPM introduce the downward motion induced by the pile installation giving vertical deformations. While CEM introduce no vertical deformations. Differences between these two models are discussed in Chapter 7.3. Based on Figure 2.13 we see that CEM coupled with a critical state soil (CSS) model that includes strain softening (MIT-E1 and PLB) gives no further decrease in vertical effective stress than what the CEM-MCC produce due to contraction.

In the results produced with SPM we see a larger decrease in vertical effective stress for the strain softening material models (MIT-E1 and PLB). However, if SPM is used together with the MCC material model we see an increase in vertical effective stress compared to CEM-MCC. This leads to the conclusion that SPM predicts larger decrease in effective vertical stress than CEM when a CSS model which includes softening is used.

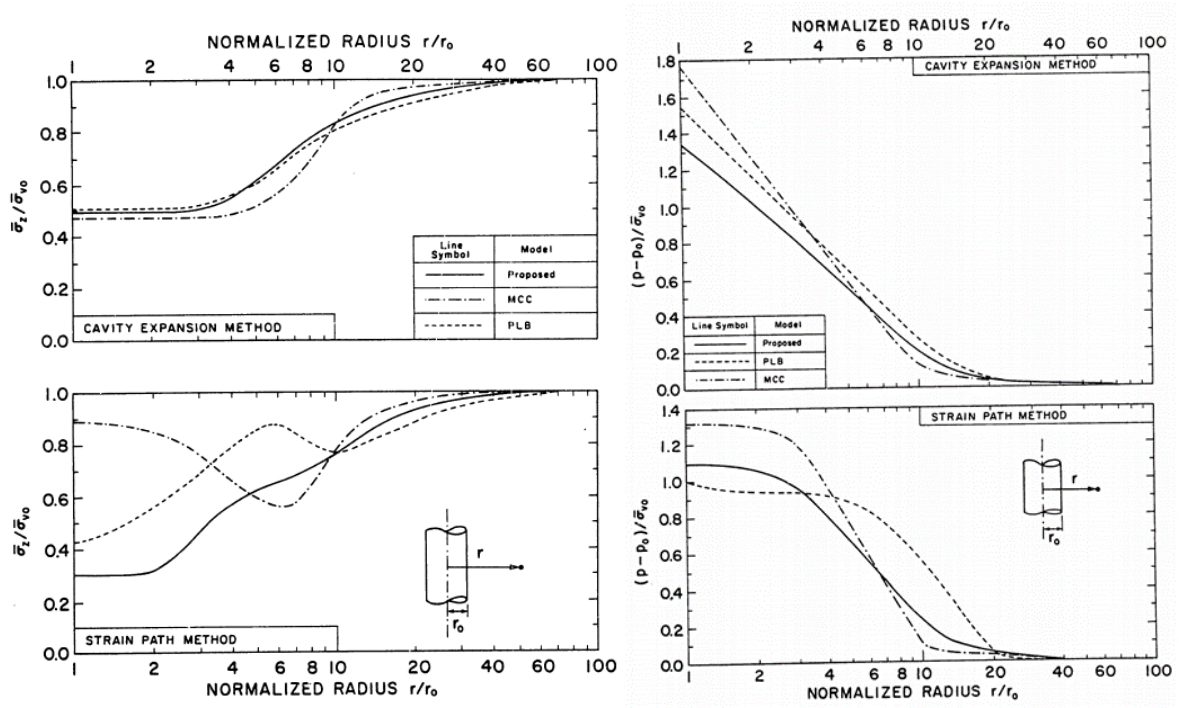

Figure 2.13: Normalized effective vertical stress and excess pore pressure predicted by CEM (upper graph) and SPM (lower graph) coupled with the MIT-E1 (solid line), PLB (dotted line) and MCC (dash-dot line) material models. Predictions are based on Boston Blue Clay (BBC) soil parameters with an overconsolidation ratio (OCR) of one. Where $\bar{\sigma}_z = \sigma'_v$, $\bar{\sigma}_{v0} = \sigma'_{v0}$ and $p - p_0 = \Delta u$. (Kavvadas 1982)

The excess pore pressure could also dissipate to other, more critical, parts of the slope. We will then have a reduction in effective stress in this initially unaffected area combined with the effect of remoulding of the area close to the pile. In addition, the shear strength will increase in the remoulded area with time giving an increase in safety. Combining all these effects is quite difficult.

In a slope calculation, piles can be introduced by cavity expansion in a 3D model. However, the largest decrease in vertical effective stress is found when using SPM and a CSS model that includes strain softening. We see that when using CEM the vertical effective stress is only reduced due to contraction. No empirical data on the vertical effective stress after pile driving has been found. It is therefore difficult to say which method predicts the most correct vertical effective stress. However, if the method predicts the correct excess pore pressure, which is more easily measured, it could be an indication that the method also produce the best prediction of the other stress components after pile driving.

Johansson and Jendeby (1998) finds that the radial total stress decrease much more rapidly than the excess pore pressure with time. This was observed at Tibble Ängar where there is a dry crust of $0{,}5 - 1m$ thickness and then a muddy clay down to $5m$ depth. Below this is a

homogenous clay down to bedrock at $20m$ depth. Figure 2.14 shows the U-shaped stress path found when combining the radial total stress and the pore pressure measurements. They assume that this is because of relaxation of the soil skeleton, while the excess pore pressure prevails due to the low permeability of the clay.

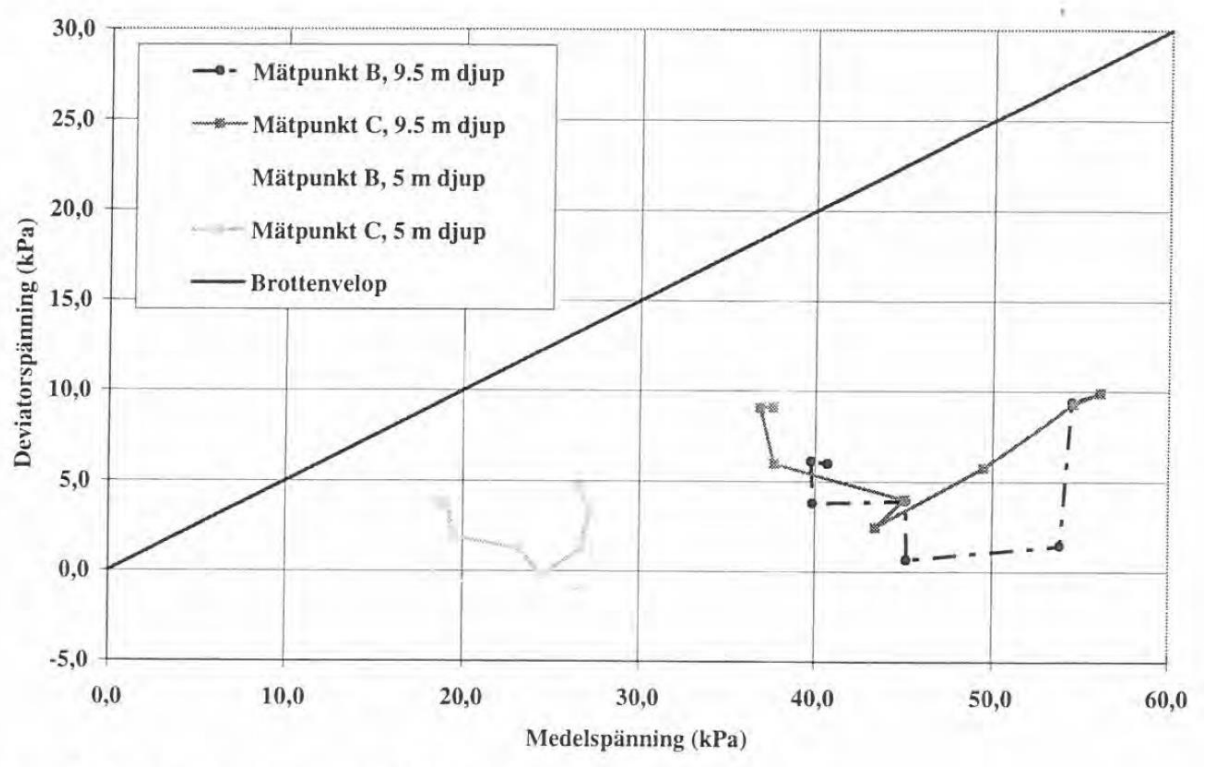

Figure 2.14: Stress path from Johansson and Jendeby (1998) found by combining measurements of horizontal total stress and pore pressure. The x-axis shows the mean effective stress (p') found by assuming $\Delta\sigma_v = 0$ against the deviatoric stress (q) on the y-axis. The darker lines are from measurements at $9{,}5m$ depth, while the barely visible lines are from measurements done at $5m$ depth. (Johansson and Jendeby 1998)

To verify this result Johansson and Jendeby (1998) performed undrained triaxial tests on the same clay. The tests were ran in the conventional way, except the tests were stopped at 2% vertical strain by locking the loading device. Then the vertical total stress and excess pore pressure were measured with time before the loading continued. The same tendency was observed, the total vertical stress reduced quicker than the pore pressure, causing the effective stress to reduce with time. This is not seen in the CEM-MCC model. Appendix C.2 contains plots of the dissipation process with time. Figure C.2.1, C.2.2 and C.2.3 shows the excess pore pressure, total and effective radial stress respectively. From these we see that the reduction in excess pore pressure happens simoultaneously as the total radial stress decrease and the radial effective stress increase.

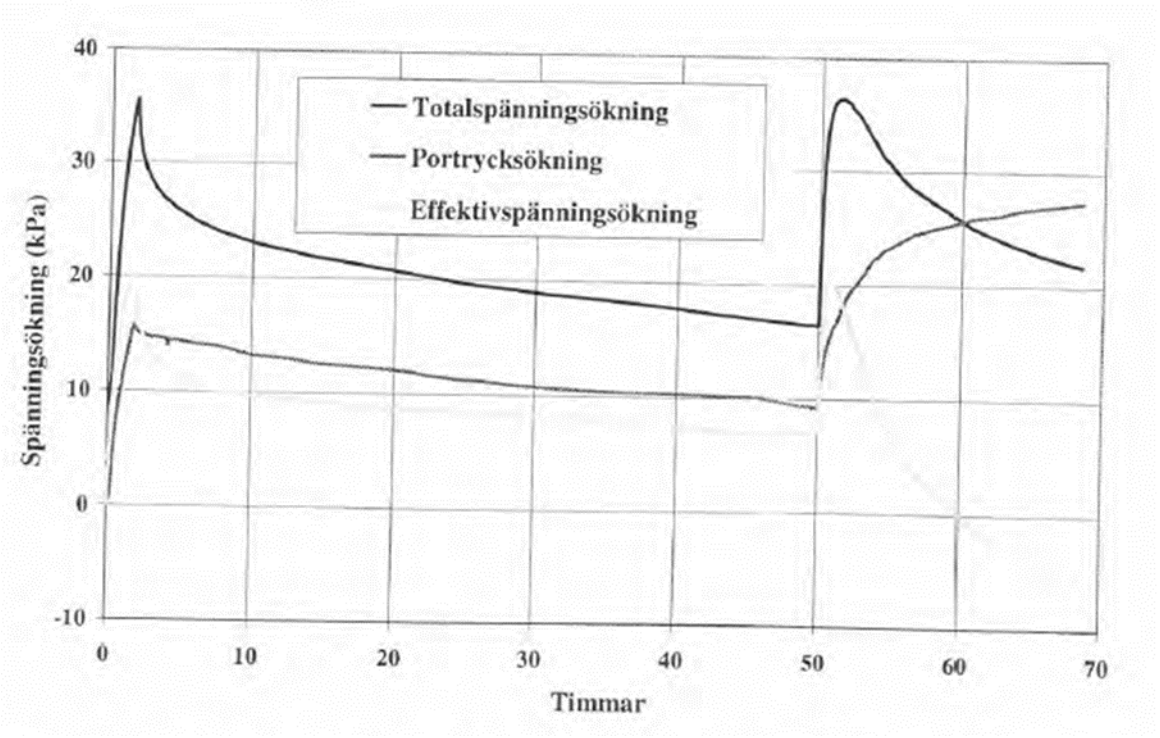

Figure 2.15: Results from one of the four triaxial tests performed. Showing the change in stress on the y-axis and the time on the x-axis, where the black line is the change in total stress, the grey line is the change in pore pressure and the barely visible line is the change in effective stress. The first peak is when 2% vertical deformation is reached and the second peak shows the reloading to 10% vertical strain. (Johansson and Jendeby 1998)

It could be that the stress relaxation observed in the radial total stress also happens to the vertical total stress after driving a pile. Karlsrud (2012) mention vertical silo effects occurring in the reconsolidation phase in lean clays (explained in Chapter 2.2), which would reduce the vertical effective stress. Whether it is stress relaxation causing the total stress to decrease faster than the excess pore pressure or if it is vertical silo effects, the conclusion is that even the largest reduction in vertical effective stress found, when using SPM and a CSS model that includes softening, could in fact be too small.

As a conservative estimate it may then be necessary to introduce the excess pore pressure without any increase in vertical total stress. We will in the following chapters look more into the stresses produced with different installation and material models. The excess pore pressure produced due to pile driving will be the main focus as this can readily be checked with measurements.

3 Pore pressure equations

3.1 General

For completely saturated soil, rapid loading leads to a build-up of the pore pressure. The water, located in the pores of the clay, is trapped under rapid loading due to low permeability. If assuming water is incompressible, then applying a uniform pressure rapidly will cause the pore pressure to increase, causing no change in effective stresses. Excess pore pressure is then the only result. This excess pore pressure will dissipate with time leading to an increase in the effective mean stress. Under undrained conditions we assume that the dissipation of the excess pore pressure has not yet started (i.e. we assume the pore water to be completely trapped). This means that a uniform stress increase will be accompanied by an equivalent increase in excess pore pressure. Similarly, reducing the pressure in the soil uniformly leads to a reduction in pore pressure, and maybe even suction. When increasing or reducing the shear stresses in the soil, experiments have shown that the excess pore pressure produced changes as well. So the excess pore pressure is related to changes in both the total mean pressure and the shear stress. The following chapter present different suggestions on the relation between stress change and excess pore pressure under undrained conditions. (Emdal 2014, Nordal 2018)

3.2 Skempton's pore pressure equation

Skempton (1954) found from triaxial testing that the change in pore pressure was related to the change in the minor principle stress ($\Delta\sigma_3$) and the deviatoric stress ($\Delta q = \Delta\sigma_1 - \Delta\sigma_3$).

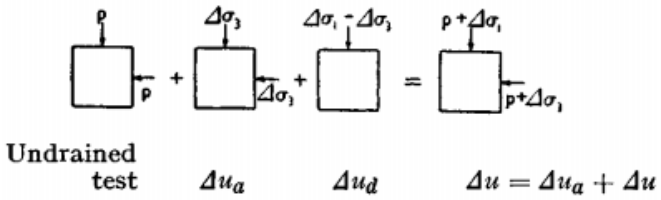

Figure 3.1: Excess pore pressure (Δu) divided into two separate parts; Δu_a and Δu_d. Related respectively to the change in the minor principle stress ($\Delta\sigma_3$) and the change in deviatoric stress (Δq). (Skempton 1954)

He defined B as the saturation parameter given by:

$$B = \frac{\Delta u_a}{\Delta \sigma_3} = \frac{1}{1 + \frac{nC_w}{C_s}} \tag{3.1}$$

where C_w is the compressibility of the fluids (water and air), C_s is the compressibility of the solid material and n is the porosity of the soil.

For a fully saturated soil there are zero air voids. This means C_w is the compressibility of water. ${C_w}/{C_s}$ is then approximately zero since the compressibility of water is negligible compared to the compressibility of the soil, so $B = 1$. For an unsaturated clay, C_w equals the compressibility of air which is far greater than the compressibility of the soil. ${C_w}/{C_s}$ is then approaching infinity and $B = 0$.

Using isotropic elasticity theory Skempton found that:

$$\Delta u_d = \frac{B}{3}(\Delta \sigma_1 - \Delta \sigma_3) \tag{3.2}$$

The behavior of soil is however generally not in accordance with isotropic elasticity and Skempton proposed:

$$\Delta u_d = A * B(\Delta \sigma_1 - \Delta \sigma_3) \tag{3.3}$$

where A is Skempton's pore pressure parameter which can be found experimentally. Using this, the final form of Skempton's pore pressure equation becomes:

$$\Delta u = B\big(\Delta \sigma_3 + A(\Delta \sigma_1 - \Delta \sigma_3)\big) \tag{3.4}$$

(Skempton 1954)

A is found from a conventional undrained triaxial test, but depends on the way the test is conducted. Conventional undrained active triaxial testing means that the cell pressure is held

constant during the shearing process (i.e. $\Delta\sigma_3 = 0$). If the sample is fully saturated then $B = 1$ and Equation 3.4 reduces to:

$$\Delta u = A_a \Delta\sigma_1 \tag{3.5}$$

where the subindex a is used to specify that this is Skempton's pore pressure parameter found from an active triaxial test. The excess pore pressure is the difference between the total stress path (TSP) and the effective stress path (ESP). In Figure 3.2, the TSP goes straight up, and is determined by the test conducter. While the ESP is based on the test result, and is determined by the soil reaction.

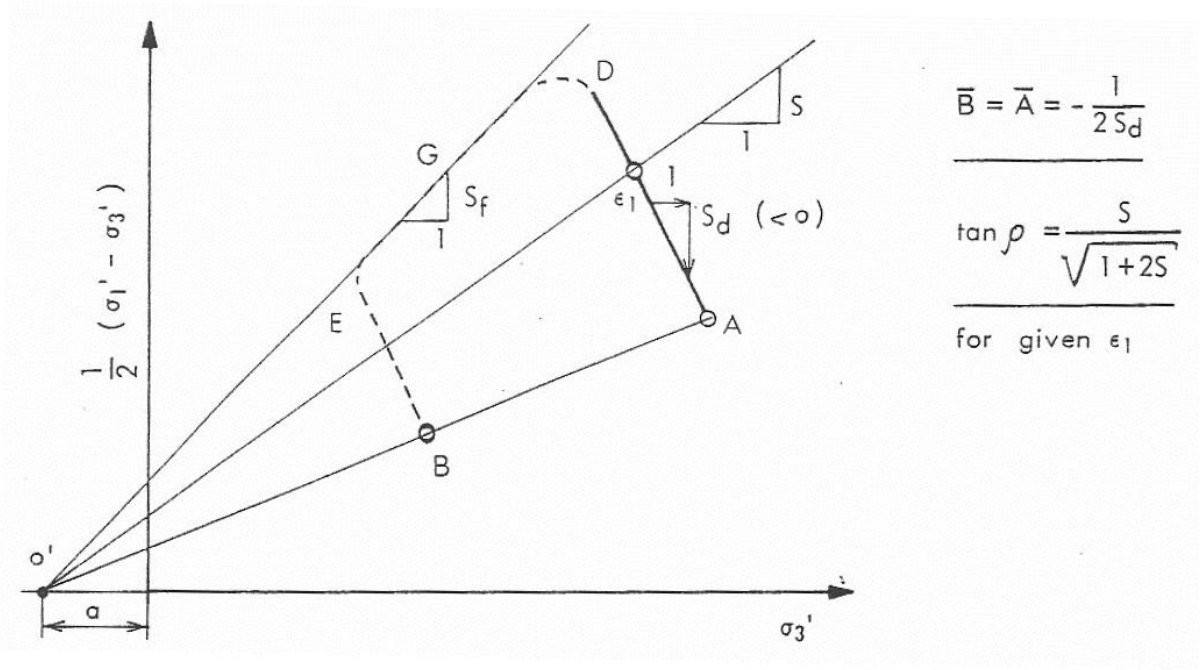

Figure 3.2: Determination of the classical pore pressure parameters, $A = \bar{A}$ (Skempton) and $B_b = \bar{B}$ (Bishop). (Sandven, Senneset et al. 2017)

From the geometry seen in Figure 3.2, use of the effective stress principle ($\sigma = \sigma' + u$), and knowing that the excess pore pressure equals the difference between the TSP and ESP, Equation 3.5 can be rewritten into:

$$A_a = \frac{\Delta u}{\Delta\sigma_1} = \frac{\Delta\sigma_3 - \Delta\sigma_3'}{\Delta\sigma_1' + \Delta u} = \frac{\Delta\sigma_3 - \Delta\sigma_3'}{\Delta\sigma_1' + \Delta\sigma_3 - \Delta\sigma_3'} = \frac{-\Delta\sigma_3'}{\Delta\sigma_1' - \Delta\sigma_3'} \tag{3.6}$$

The first equality is the simplest to use as we measure the pore pressure and the vertical additional load, while the cell pressure is known and constant. For a passive undrained triaxial test the axial load is held constant while the cell pressure is increased. This means $\sigma_1 = \sigma_2 = \sigma_{cell}$ and $\Delta\sigma_3 = \Delta\sigma_{axial} = 0$. Since Equation 3.4 does not depend on σ_2, Equation 3.5 and 3.6 are unchanged for a passive triaxial test.

However, the soil behavior is not the same. A determined from an active triaxial test will not be equal to A determined from a passive triaxial test (i.e. $A_a \neq A_p$). This is due to the anisotropy of the material. A normal Norwegian clay will show a smaller undrained shear strength from a passive triaxial test than from an active triaxial test ($s_{uA} > s_{uP}$). The same anisotropy can be explained by the angle between the horizontal axis and the failure line being smaller in a passive triaxial test, which gives a smaller slope than in the active test ($S_{f,a} > S_{f,p}$). Anisotropy is larger in lean clays, which is normal in Norway, and some further explanation is given Chapter 5.3. Figure 3.3 shows an illustrative example of what we can observe in a passive and an active triaxial test on an anisotropic clay.

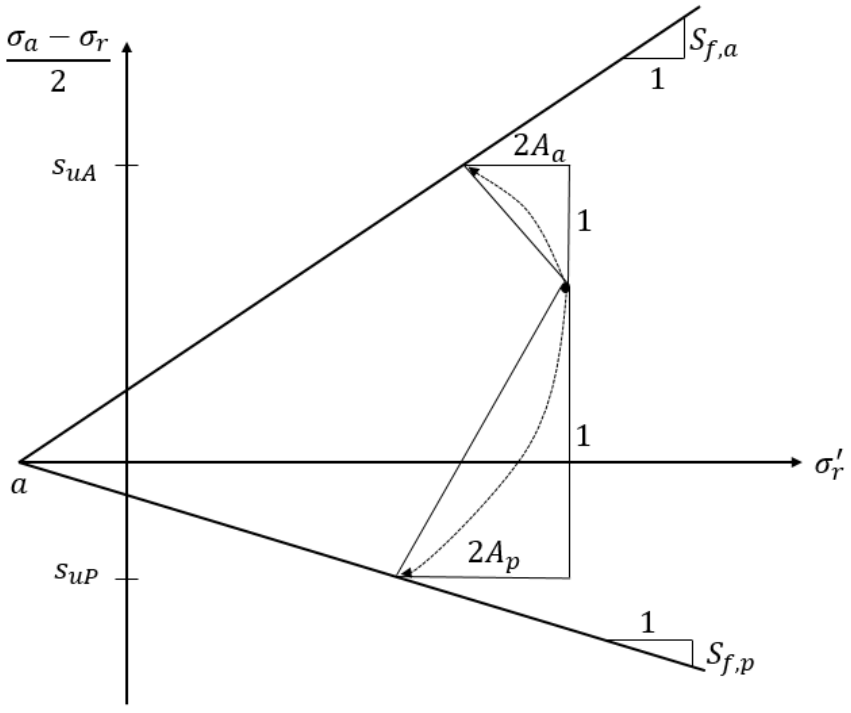

Figure 3.3: Pore pressure parameter from passive and active triaxial testing. Example of the Effective Stress Path drawn as a stippled line.

Figure 3.3 shows that the secant values of the pore pressure parameter. That is when A is determined by the start point and the point where the effective stress path hits the failure line.

The pore pressure parameter can also be determined for small increments along the effective stress path. This is called the tangential value of A. Figure 3.3 shows that the tangential value of A depends on the degree of mobilization. A starts as a small value and increases as the mobilization increases.

Typical values of A at failure are given by Massarsch (1976) and are listed in Table 3.1.

Table 3.1: Typical values of Skempton's pore pressure parameter A at failure according to Massarsch (1976)

Sensitive clay	$1{,}5 - 2{,}5$
Normally consolidated clay	$0{,}7 - 1{,}3$
Lightly overconsolidated clay	$0{,}3 - 0{,}7$
Heavily overconsolidated clay	$-0{,}5 - 0$

Similar result is obtained by Bishop and Henkel (1957), but not showing the same range as Massarsch (1976) found. Skempton's pore pressure parameter shows a clear relation to the overconsolidation ratio at failure, as seen in Figure 3.4.

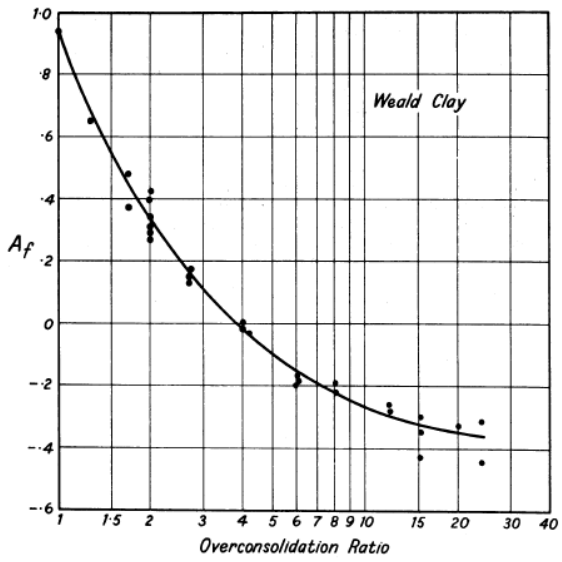

Figure 3.4: The variation of the pore pressure parameter A at failure (A_f) with overconsolidation ratio for Weald clay. (Bishop and Henkel 1957)

3.3 Bishop's pore pressure equation

In the same journal as Skempton presented his solution, Bishop (1954) presented practical applications of the solution. Bishop (1954) looked at the effective stresses in an earth dam during construction and during rapid draw down. Due to the complexity, accurate determination of $\Delta\sigma_3$ required a detailed analysis. Bishop (1954) conveniently expressed the excess pore pressure as an equation of $\Delta\sigma_1$, and looked at the influence of variations in the principle stress ratio.

$$\Delta u = B * \Delta\sigma_1 \left(1 - (1 - A)\left(1 - \frac{\Delta\sigma_3}{\Delta\sigma_1}\right)\right) \approx B_b * \Delta\sigma_1 \tag{3.7}$$

where B_b is the overall pore pressure coefficient, later named Bishop's pore pressure parameter. Bishop (1954) found that the principle stress ratio had an influence. This means that the approximately equal sign is of importance. We see that Equation 3.7 is the same as Skempton proposed for a conventional undrained triaxial compression test where the cell pressure is kept constant and the sample is fully saturated. Then $\Delta\sigma_3 = 0$ and $B = 1$, so $B_b = A$. Since the principle stress ratio is of importance, Equation 3.7 is not normally used for other stress states than that of the triaxial test.

3.4 Janbu's pore pressure equation

Because Skempton's pore pressure equation does not depend on $\Delta\sigma_2$, Skempton's pore pressure parameter A will depend on the type of test conducted. The same applies for Bishop's pore pressure parameter. Janbu (1976) and Henkel (1960) therefore suggested an alternative formulation based on the three dimensional stress state, to make a more consistent and generally applicable expression for the excess pore pressure. The solution by Janbu (1976) and Henkel (1960) is practically equal. The one difference is that Henkel (1960) used the octahedral shear stress defined by:

$$\Delta\tau_{oct} = \frac{1}{3}\sqrt{(\Delta\sigma_1 - \Delta\sigma_3)^2 + (\Delta\sigma_2 - \Delta\sigma_3)^2 + (\Delta\sigma_1 - \Delta\sigma_2)^2} \tag{3.8}$$

Janbu (1976) instead used the deviatoric stress, which in a triaxial test is equal to the double of the maximum shear stress. The octahedral shear stress in both passive and active triaxial testing is equal to the deviatoric stress, but with a factor of $\sqrt{2}/3$ in front. This means that the pore pressure parameter determined from triaxial tests are proportional to each other by a factor of $\sqrt{2}/3$. This also holds for plane strain conditions under undrained loading. This can easily be checked by inserting Equation 4.5 into Equation 3.8 with Poisson's ratio equal to $0{,}5$. In conclusion, there is a difference when we do not have plane strain or triaxial conditions. The details of this difference are not discussed further in this study. From here on out, only Janbu's equation will be discussed as it is more commonly used in Norway.

In isotropic elasticity there is no coupling between change of size and change of shape. This means that for an undrained triaxial test we will have a pure change of shape as $\Delta p' = 0$. This is generally not the result found from actual triaxial tests. Janbu (1976) used that in anisotropic elasticity the volumetric strain is related to both the deviatoric and the mean stress through:

$$\Delta\varepsilon_v = \frac{1}{K}\Delta p' + \frac{1}{H}\Delta q \tag{3.9}$$

where K is the bulk modulus, H is a temporary variable called the dilatancy modulus, p and q denotes the mean and the deviatoric stress respectively, defined by:

$$p = \frac{1}{3}(\sigma_1 + \sigma_2 + \sigma_3) \tag{3.10}$$

$$q = \sigma_1 - \sigma_3 \tag{3.11}$$

For undrained conditions it is generally assumed that $\Delta\varepsilon_v = 0$. Equation 3.9 then gives:

$$\Delta p' = -\frac{K}{H}\Delta q = D\Delta q \rightarrow D = \frac{\Delta p'}{\Delta q} \tag{3.12}$$

where D is Janbu's pore pressure parameter, often simply called the Dilatancy parameter. Utilizing the effective stress principle ($\sigma = \sigma' + u$), Equation 3.12 can be rewritten into:

$$\Delta u = \Delta p - D\Delta q \tag{3.13}$$

Equation 3.13 is known as Janbu's pore pressure equation. Notice that when assuming the change of the volumetric strain to be equal to zero, one assumes that the material is completely saturated.

The upper and lower limits of the Dilatancy parameter, based on experience, are as shown in Table 3.2. From Equation 3.12 it can be seen that the material dilates, this means that the volume expands, when D is positive. This again causes the excess pore pressure to be smaller, as seen in Equation 3.13. This effect can be observed in dense sand and overconsolidated clay. When D is negative, the material contracts. This means that the volume reduces, and that the excess pore pressure increases. This effect can be seen in loose sand and normally consolidated clay. When $D = 0$, the material follows elastic isotropy and we have no volume change.

Table 3.2: Definition, limits and effect on volume change of the Dilatancy parameter (Nordal 2018)

Contracting material	$-0{,}5 < D < 0$	Volume reduction
Dilatancy neutral material (isotropic elastic material)	$D = 0$	No volume change
Dilating material	$0 < D < 0{,}5$	Volume expansion

The Dilatancy parameter is normally determined by triaxial testing. In an active triaxial test $\sigma_2 = \sigma_3$, and under shearing $\Delta\sigma_3 = 0$. Inserting this into Equation 3.13 and solving for D gives:

$$D - \frac{1}{3} = \frac{\Delta\sigma_3'}{\Delta\sigma_1' - \Delta\sigma_3'} \tag{3.14}$$

We can see the similarities to Skempton's pore pressure parameter. Utilizing Equation 3.6, the relationship between the parameters found from active triaxial testing is given by:

$$D_a = \frac{1}{3} - A_a \tag{3.15}$$

Doing the same for a passive undrained triaxial test ($\sigma_1 = \sigma_2 = \sigma_{cell}$ and $\Delta\sigma_3 = \Delta\sigma_{axial} = 0$) gives:

$$D - \frac{2}{3} = \frac{\Delta\sigma_3'}{\Delta\sigma_1' - \Delta\sigma_3'} \tag{3.16}$$

Equation 3.6 then gives the relationship to Skempton's pore pressure parameter as:

$$D_p = \frac{2}{3} - A_p \tag{3.17}$$

When the stress changes are arbitrary in three directions there are no one-to-one relation between the two equations. So the above relations only holds for triaxial testing.

In the above equations the subindex a and p has been used to mark the active and the passive triaxial test. The reason for this is that both Skempton's and Janbu's pore pressure parameter changes depending on the type of test conducted. This is shown in Figure 3.3. The pore pressure parameters also change depending on the degree of mobilization. Figure 3.5 shows that the value of the Dilatancy parameter is smaller for passive triaxial tests compared to active for different values of the consolidation stress. This means that A_a must be smaller than $A_p - {}^1/_3$, utilizing Equation 3.15 and 3.17. From Figure 3.3 we see that A_a is smaller than A_p, but how much is not shown.

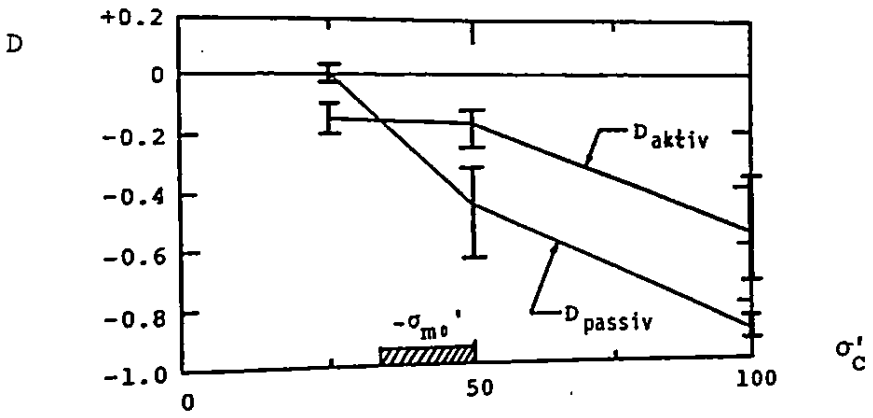

Figure 3.5: Tangential values of the Dilatancy parameter from active and passive triaxial testing for different values of the consolidation stress. (Svanø 1981)

Svanø (1981) used tangential values when comparing D_a and D_p. The difference will become smaller if the secant value is used, but the true material behavior is best described by the tangential values. The conclusion is however that some difference in D_a and D_p is to be expected, especially if tangential values are used.

3.5 Excess pore pressure in finite element codes

In finite element codes, the dilatancy angle ψ is commonly used. The dilatancy angle describes the volume expansion during plastic yielding. In Plaxis 2D the excess pore pressure is calculated by:

$$\dot{\Delta u} = \frac{\alpha \dot{\varepsilon_v}}{nC_w + (\alpha - n)C_s} \tag{3.18}$$

where α is Biot's pore pressure coefficient, C_w is the compressibility of water, C_s is the compressibility of the solid material and n is the soil porosity. Biot's pore pressure coefficient is a value between zero and one, describing the compressibility of the soil skeleton. Usually it can be set equal to one, however at very large pressure the stiffness of the soil matrix comes close to the stiffness of the solid material, and the compressibility of the grains must be taken into account. Notice that $\dot{\Delta u}$ is the rate of the excess pore pressure and $\dot{\varepsilon_v}$ is the rate of the volumetric strain. The dilatancy angle, which describes the volume expansion during plastic yielding, is therefore very important in determining the excess pore pressure. (Brinkgreve, Kumarswamy et al. 2018)

The Dilatancy parameter describes the dilatancy up until failure, while for an elastic-perfectly plastic material the dilatancy angle is only connected to the plastic failure. For a more complex elasto-plastic material model, plastic strains occur before failure. The dilatancy angle is therefore relevant before failure and can be related to the Dilatancy parameter. This relation will involve the materials volumetric stiffness and is therefore not one-to-one. (Nordal 2018)

For the critical state soil models (i.e. MCC, S-CLAY1/1S and MIT-E1/2/3) the volume expansion during plastic yielding is given by associated flow. The dilatancy of the material is then given by the yield surface of the material model. In Chapter 6.2 determination of the excess pore pressure in the MCC material model is explained. The S-CLAY1/1S and MIT-E1/2/3 follows the basic principle explained there as well.

4 Cavity expansion in an elastic material

4.1 General

Chapter 4 presents the fundamental solution of the Cavity Expansion Method (CEM) in an elastic material. CEM is widely applied in geotechnics, for example in assessing in-situ soil tests, deep foundations, tunnels, underground excavations and pile driving. In the literature we can find many reports comparing measured field data with predicted results from the Cavity Expansion Method coupled with different material models. Some of the results from such reports are presented in Chapter 9, while in this chapter only the method itself will be presented. Chapter 9 shows that the theory gives relatively good results when modeling Zone B in Figure 4.1 as a cylindrical expansion. CEM does however not fully model the behavior in Zone A and Zone C. Clark and Meyerhof (1972) finds that for Zone C, the displacement pattern is somewhere between what is found by the expansion of a cylindrical cavity and the expansion of a spherical cavity.

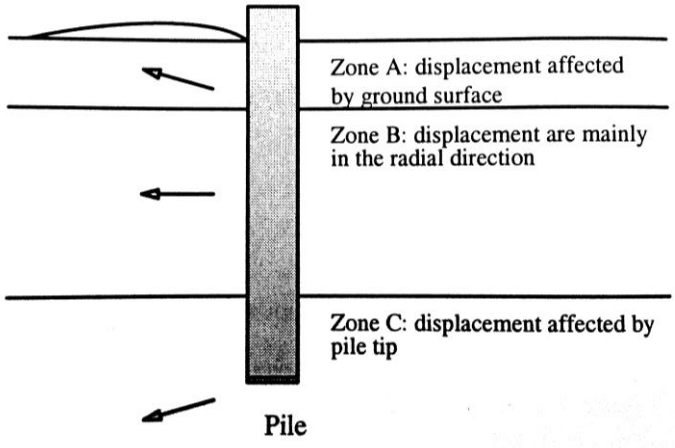

Figure 4.1: Different zones characterized by what affects the displacement due to pile installation. (Yu 2000)

The biggest fault of the cavity expansion method, when applying it to the installation of piles, is that we do not include the downward motion of pile installation. CEM is expanding a cylinder from an initial (in pile driving zero) radius to a given radius. However, pile driving is pushing a pile into the soil, not expanding a pile from zero radius. The model has in other words some fundamental flaws. However, field measurements of the pore pressure show that for Zone B one can obtain reasonable answers using CEM. Similar solutions as those presented here can also be found for a spherical cavity expansion.

The expansion of a cavity is a one-dimensional boundary value problem, solved by using continuum mechanics and a mathematical material model relating the stresses to the strains. This means that cavity expansion can be described by an ordinary differential equation of the unknown function of either the circumferential or the radial stress. The radial stress is used in this derivation. Described by one variable, here the distance from the cavity center r, and the boundary conditions of the stress when r is at its maxima and minima. Solving this differential equation will give us the radial stress as a function of r. Continuum mechanics will then give the relations between the different stresses and the relation between different strains and displacements. While the material model relates the stresses to the strains. (Yu 2000)

This elastic solution is a necessary introduction to the development of the solution for an elasto-plastic material presented in Chapter 5. Only the isotropic case with uniform external pressure and both uniform internal and external pressure is presented. In 1898, Kirsch found the general solution for an isotropic far field stress, which is used throughout this chapter.

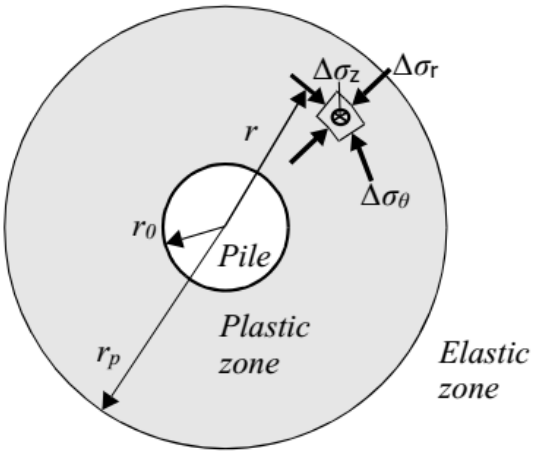

Figure 4.2: Definition of parameters used in the presentation of the Cavity Expansion Method. From Nordal (2018) slightly edited by the author.

In the following chapters the definitions from Figure 4.2 is used. Where r_p is the plastic radius, r_0 is the radius of the cavity/pile, r is the distance from the cavity center out to the considered soil element, $\Delta\sigma_r$ is the change of the radial total stress, $\Delta\sigma_\theta$ is the change of the circumferential total stress, and $\Delta\sigma_z$ is the change of the vertical total stress. Other parameters will be defined as they are presented.

The solutions presented all have an outer radius of the material going towards infinite. This is just a choice, and the solutions can be presented with a finite outer radius. In geotechnics letting the outer radius go to infinite is a common assumption. This is a fair assumption for the pile driving problem as long as multiple piles are not installed closely in a group. We would then need to consider the combined effect of the pile group as explained in Chapter 2.5.

Cavity expansion in an elastic material have been solved for biaxial external pressure, cross-anisotropic material and so on. For the pile driving problem biaxial external pressure is not very relevant as we often assume equal horizontal pressure in all directions at a given depth. Cross-anisotropic material is more relevant, but pile driving causes large strains and plasticity is therefore a necessity. As the analytical plastic solution is not solved for cross-anisotropy, the analytical elastic solution for this is not rendered here. The solution for biaxial external pressure was found by Kirsch and is rendered in Terzaghi and Richart (1952). The solution for a cross-anisotropic material is found in Lekhnitskii (1963). Pile driving is, as mentioned, a large strain problem. For soils, the displacements are dominated by plasticity. However, the elastic solution is important for correctly representing the stresses and thus in establishing the elasto-plastic solution. (Yu 2000)

4.2 Cylindrical expansion with uniform external pressure

Kirsch looked at an elastic, infinitely long, thick-walled cylinder, where the outer diameter of the cylinder is approaching infinity. For simplicity isotropic external pressure is used, and it is assumed that the external pressure is applied from initial values equal to zero. The current stress is then equal to the change of the stress. Delta (Δ), from Figure 4.2, is therefore skipped in the derivation of the elastic solution.

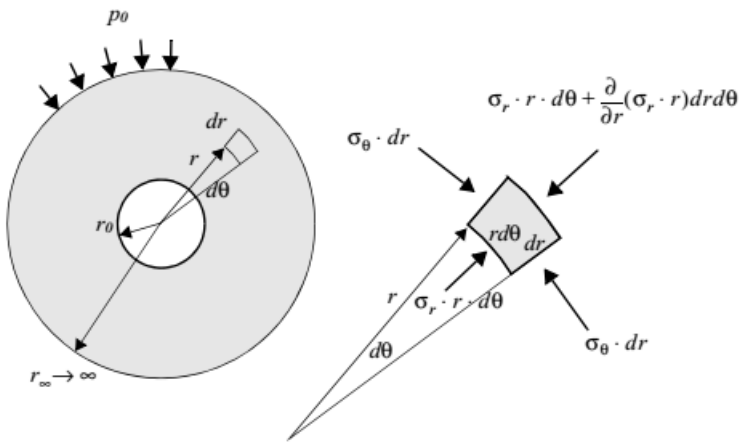

Figure 4.3: Equilibrium of an infinitesimal element in a thick-walled pipe. (Nordal 2018)

Equilibrium of Figure 4.3 gives:

$$r\frac{\partial \sigma_r}{\partial r} + \sigma_r - \sigma_\theta = 0 \tag{4.1}$$

Isotropic elasticity yields:

$$\varepsilon_r = \frac{1}{E}(\sigma_r - \nu\sigma_\theta - \nu\sigma_z) \tag{4.2}$$

$$\varepsilon_\theta = \frac{1}{E}(-\nu\sigma_r + \sigma_\theta - \nu\sigma_z) \tag{4.3}$$

$$\varepsilon_z = \frac{1}{E}(-\nu\sigma_r - \nu\sigma_\theta + \sigma_z) \tag{4.4}$$

where E is Young's modulus, ν is Poisson's ratio, and ε is the strain in the radial, circumferential and vertical direction depending on the subtext.

Due to the infinite length of the pipe, plane strain conditions are assumed (i.e. $\varepsilon_z = 0$). Equation 4.4 then gives:

$$\sigma_z = \nu(\sigma_r + \sigma_\theta) \tag{4.5}$$

By inserting Equation 4.5 back into Equation 4.2 and 4.3, can σ_z be eliminated. The strains are then given by:

$$\varepsilon_r = \frac{1-\nu^2}{E}(\sigma_r - \frac{\nu}{1-\nu}\sigma_\theta) \tag{4.6}$$

$$\varepsilon_\theta = \frac{1-\nu^2}{E}(-\frac{\nu}{1-\nu}\sigma_r + \sigma_\theta) \tag{4.7}$$

Compatibility requirements are given by:

$$\varepsilon_r = -\frac{\partial u}{\partial r} \tag{4.8}$$

$$\varepsilon_\theta = -\frac{u}{r} \tag{4.9}$$

where the circumferential strain is found by considering Figure 4.4:

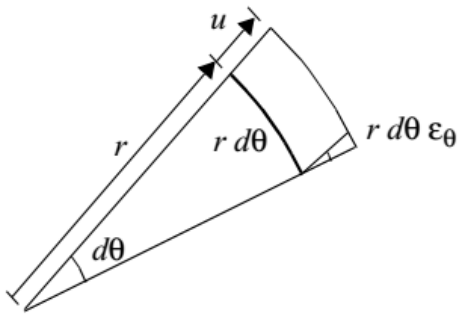

$$\frac{r d\theta \varepsilon_\theta}{u} = \frac{r d\theta}{r}$$

$$\Downarrow$$

$$\varepsilon_\theta = -\left(\frac{u}{r}\right)$$

Figure 4.4: Strains in the circumferential direction are given by u/r, where u is the radial displacement which vary along the radial extent from the pile center, r. (Nordal 2018)

Equation 4.8 and 4.9 can be combined to eliminate u:

$$\varepsilon_r = \frac{\partial}{\partial r}(r\varepsilon_\theta) \tag{4.10}$$

By using Equation 4.6, 4.9 and 4.10, can the circumferential stress be eliminated, and a differential equation for the radial stress can be established as:

$$r\frac{\partial^2\sigma_r}{\partial r^2} + 3\frac{\partial\sigma_r}{\partial r} = 0 \tag{4.11}$$

The solution of this differential equation is known as Kirsch solution for isotropic far-field stress:

$$\sigma_r = C_1 + \frac{C_2}{r^2} \tag{4.12}$$

where C_1 and C_2 are constants that are determined by the boundary conditions.

Inserting 4.12 into 4.1 gives the circumferential stress as:

$$\sigma_\theta = C_1 - \frac{C_2}{r^2} \tag{4.13}$$

For the boundary conditions of Figure 4.3 we have:

$$\sigma_r|_{r\to\infty} = p_0 \;\rightarrow\; C_1 = p_0 \tag{4.14}$$

$$\sigma_r|_{r\to r_0} = 0 \;\rightarrow\; C_2 = -p_0{r_0}^2 \tag{4.15}$$

where p_0 is the uniform external pressure. Utilizing these boundary conditions gives:

$$\sigma_r = p_0\left(1 - \left(\frac{r_0}{r}\right)^2\right) \tag{4.16}$$

$$\sigma_\theta = p_0\left(1 + \left(\frac{r_0}{r}\right)^2\right) \tag{4.17}$$

From Equation 4.5 we find the vertical stress, and the second equality comes from assuming undrained conditions (i.e. $\nu = 0{,}5$):

$$\sigma_z = 2\nu p_0 = p_0 \tag{4.18}$$

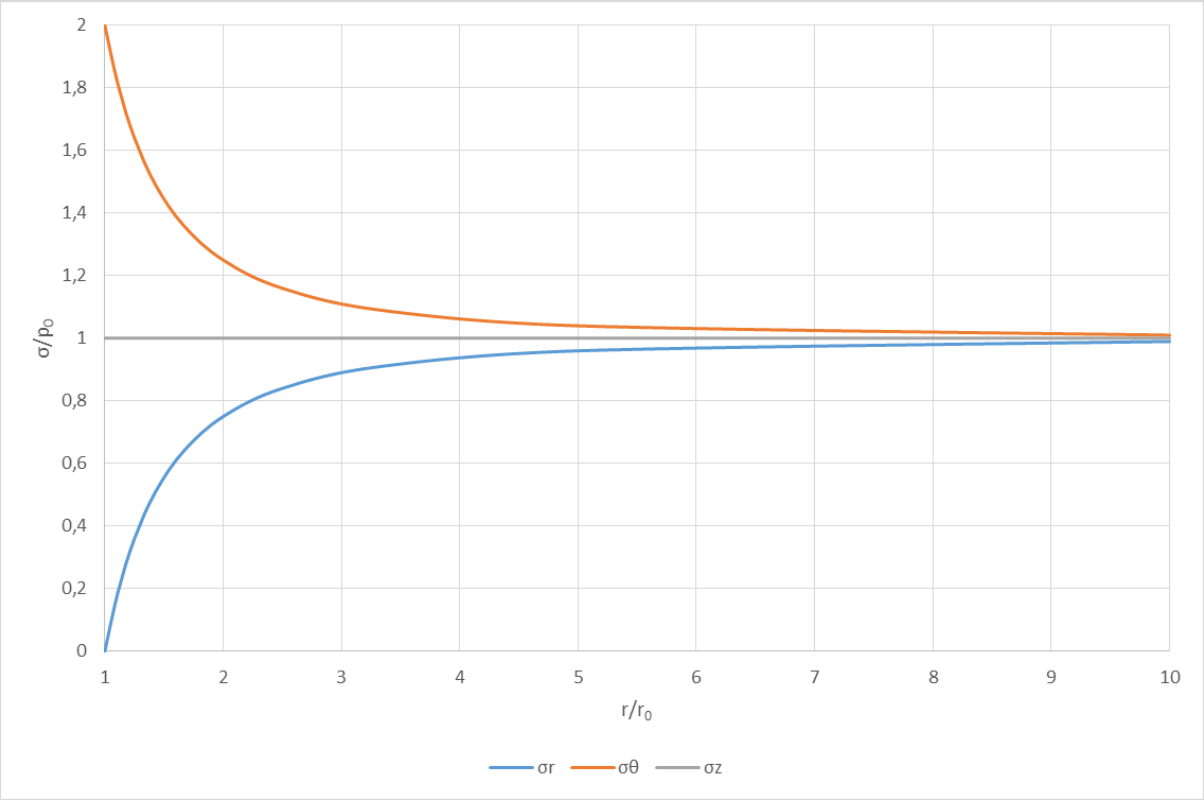

Figure 4.5: Kirsch solution for the total stresses against the radial extent from the pile center normalized with the pile radius given that only an isotropic external pressure is applied. Made by the author utilizing Equation 4.16, 4.17 and 4.18.

From Figure 4.5 we can see that at the cavity surface, the circumferential stress is equal to $2p_0$. It can be seen from Figure 4.5 or from Equation 4.16, 4.17 and 4.18 that $\sigma_1 = \sigma_\theta$, $\sigma_2 = \sigma_z$, and $\sigma_3 = \sigma_r$. The maximum shear stress is then $\tau_{max} = \frac{\sigma_1 - \sigma_3}{2} = p_o$. If we apply the Tresca yield criterion and use a yield stress equal to $2s_u$, where s_u is the undrained shear strength of the material, then initial yielding will occur at the cavity surface when $p_0 = s_u$. (Yu 2000, Nordal 2018)

4.3 Cylindrical expansion with isotropic internal and external pressure

When using CEM to model pile installation an internal pressure, that increase until the cavity expand, is applied. Kirsch solution for a far field stress can also give us the solution for both external and internal pressure by using the boundary conditions of Figure 4.6.

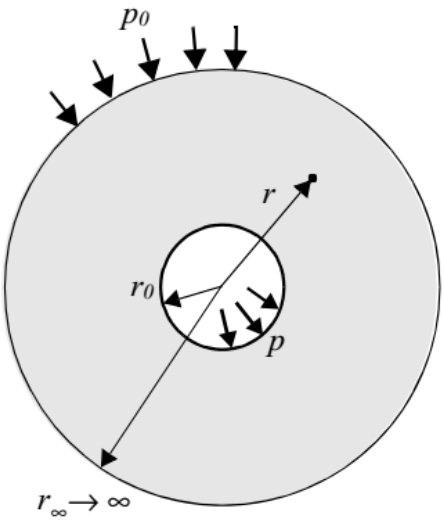

Figure 4.6: Cavity with radius r_0 under uniform internal (p) and external pressure (p_0). From Nordal (2018) slightly edited by the author.

$$\sigma_r|_{r\to\infty} = p_0 \;\rightarrow\; C_1 = p_0 \tag{4.19}$$

$$\sigma_r|_{r\to r_0} = p \;\rightarrow\; C_2 = (p - p_0){r_0}^2 \tag{4.20}$$

which gives the stresses:

$$\sigma_r = p_0 + (p - p_0)\left(\frac{r_0}{r}\right)^2 \tag{4.21}$$

$$\sigma_\theta = p_0 - (p - p_0)\left(\frac{r_0}{r}\right)^2 \tag{4.22}$$

As before we have from Equation 4.5:

$$\sigma_z = 2\nu p_0 = p_0 \tag{4.23}$$

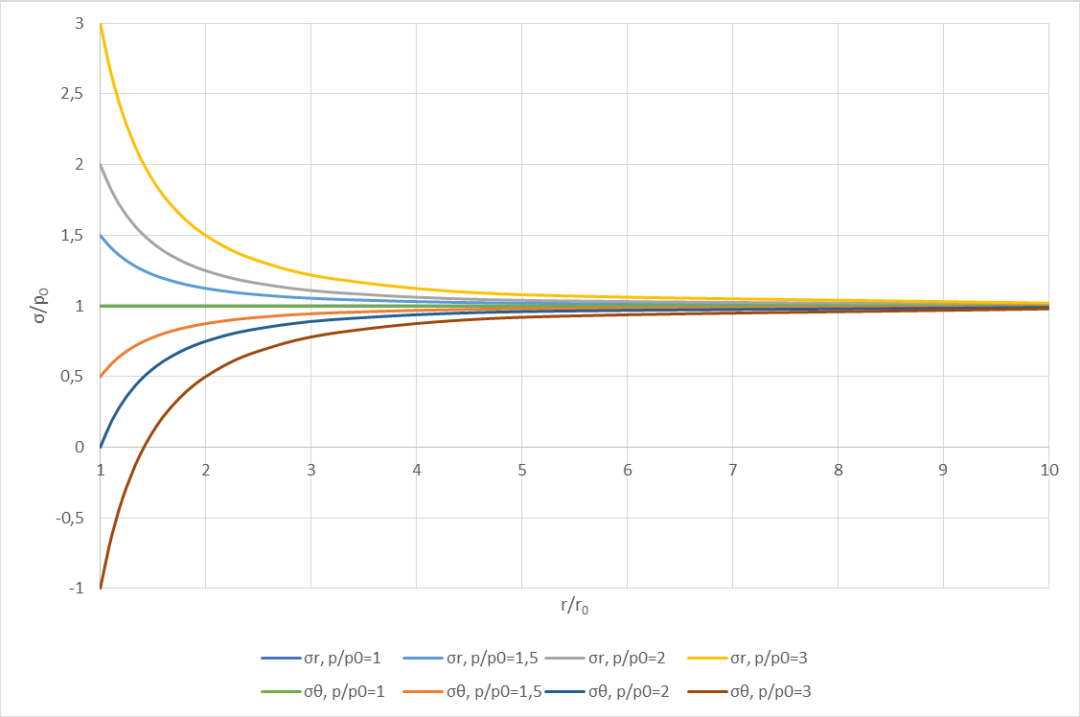

Figure 4.7: Kirsch solution for the total stresses against the radial extent from the pile center normalized with the pile radius when both an external (p_0) and an internal (p) pressure is applied. Four different values of $^{p}/_{p_0}$ is used, all assuming $p \geq p_0$. Made by the author utilizing Equation 4.21 and 4.22.

From Figure 4.7 we can see similarities to the solution presented in Figure 4.5. The main difference is that in Figure 4.5 we had no internal pressure. This caused the radial stress to be equal to zero at the cavity surface, due to equilibrium of stresses. In Figure 4.7 we have an internal pressure and it is assumed larger or equal to p_0. This causes a change in the major and minor principle stress. As in Figure 4.5, we can see that initial yielding is occurring at the cavity wall. Because of the internal pressure we now have $\sigma_1 = \sigma_r$ and $\sigma_3 = \sigma_\theta$, knowing that $\sigma_2 = \sigma_z = p_0$ for undrained conditions. Initial yielding will then occur when:

$$Y = 2s_u = \sigma_1 - \sigma_3 = \sigma_r - \sigma_\theta = 2(p - p_0)\left(\frac{r_0}{r}\right)^2_{max} \rightarrow s_u = p - p_0 \tag{4.24}$$

The different ratios of p/p_0 in Figure 4.7 can therefore be viewed as steadily increasing the internal pressure from an initial value of p_0. At some point, we will get yielding because of the difference in radial and circumferential stress at the cavity wall, or internal and external pressure, as Equation 4.24 indicates. (Yu 2000)

5 Cavity expansion in an elastic-perfectly plastic material

5.1 General

Bishop, Hill et al. (1945) researched the indentation of work-hardened and annealed copper by penetration of a conical punch with a cut-back shank. Assuming plane strain and no volume change, they found a solution for a frictionless medium using the Tresca yield criterion. Hill (1950) present a complete solution for large strains, but only for a case with external pressure equal to zero. This solution also contained some simplifying assumptions for a cylindrical cavity expanding from zero initial radius. Gibson and Anderson (1961) found a large strain solution for a cylindrical cavity in an infinite, incompressible undrained clay. A large strain solution uses the true or logarithmic strains, and not the engineering strains. This solution is also known from Vesic (1972). In Yu (2000) a solution for any value of Poisson's ratio is given. Notice also that the elastic solution derived in the previous chapter was found using the small strain definition (i.e. engineering strains).

Some of the solutions mentioned above use the von Mises yield criterion. For a spherical cavity the Tresca and the von Mises yield criterions produce the same solution. For a cylindrical cavity, the von Mises criterion can be approximated by increasing the yield stress in the Tresca criterion by 15% according to Hill (1950). The analytical solution for a Mohr-Coulomb criterion with non-associated flow in an infinite medium was found by Yu and Houlsby (1991), but only the solution for the Tresca criterion will be presented in this study. This is because the Tresca criterion, with an yield stress of $Y = 2s_u$, is more relevant for clay experiencing undrained loading. (Yu 2000)

5.2 Solution with the Tresca yield criterion

We will here present the large strain solution of the undrained case with Poisson's ratio equal to 0,5, found by Gibson and Anderson (1961), as this is the most relevant case for modelling pile driving in clay.

Knowing that at the cavity surface the major principle stress is equal to the radial stress ($\sigma_1 = \sigma_r$), and that the minor principle stress is equal to the radial stress ($\sigma_3 = \sigma_\theta$), we assume that the internal pressure (p) is increased monotonically from its initial value (p_0).

The material will then behave elastic until the internal pressure causes yielding, as discussed in Chapter 4.3. Further increase of the internal pressure after initial yielding causes a plastic region to spread. In this study, only the solution is presented, as the derivation of the expressions are quite long and are mostly a mathematical exercise. However, the derivation can be followed in Yu (2000). The solution presented is for a cylindrical cavity expansion from zero initial radius in an infinite medium using the Tresca yield criterion $Y = \sigma_1 - \sigma_3$, with an yield stress of $Y = 2s_u$. When assuming an initial radius of zero, the stresses become a function of the ratio between the point r over the current cavity size. This causes the ratio of the plastic region over the current cavity radius to be constant. We therefore assume a constant internal pressure of such a size that the final radius of the cavity equals the radius of the pile:

$$p_{lim} = s_u \left(1 + \ln\left(\frac{G}{s_u}\right)\right) + p_0 \tag{5.1}$$

The plastic boundary is then given by:

$$\frac{r_p}{r_0} = \sqrt{\frac{E}{2(1+\nu)s_u}} = \sqrt{\frac{G}{s_u}} \tag{5.2}$$

Stresses in the elastic zone are given by:

$$\frac{\Delta\sigma_r}{s_u} = \left(\frac{r_p}{r}\right)^2 \tag{5.3}$$

$$\frac{\Delta\sigma_\theta}{s_u} = -\left(\frac{r_p}{r}\right)^2 \tag{5.4}$$

$$\Delta\sigma_z = 0 \tag{5.5}$$

While stresses in the plastic zone are given by:

$$\frac{\Delta\sigma_r}{s_u} = 2\ln\left(\frac{r_p}{r}\right) + 1 \tag{5.6}$$

$$\frac{\Delta\sigma_\theta}{s_u} = 2\ln\left(\frac{r_p}{r}\right) - 1 \tag{5.7}$$

$$\frac{\Delta\sigma_z}{s_u} = 2\ln\left(\frac{r_p}{r}\right) \tag{5.8}$$

(Yu 2000)

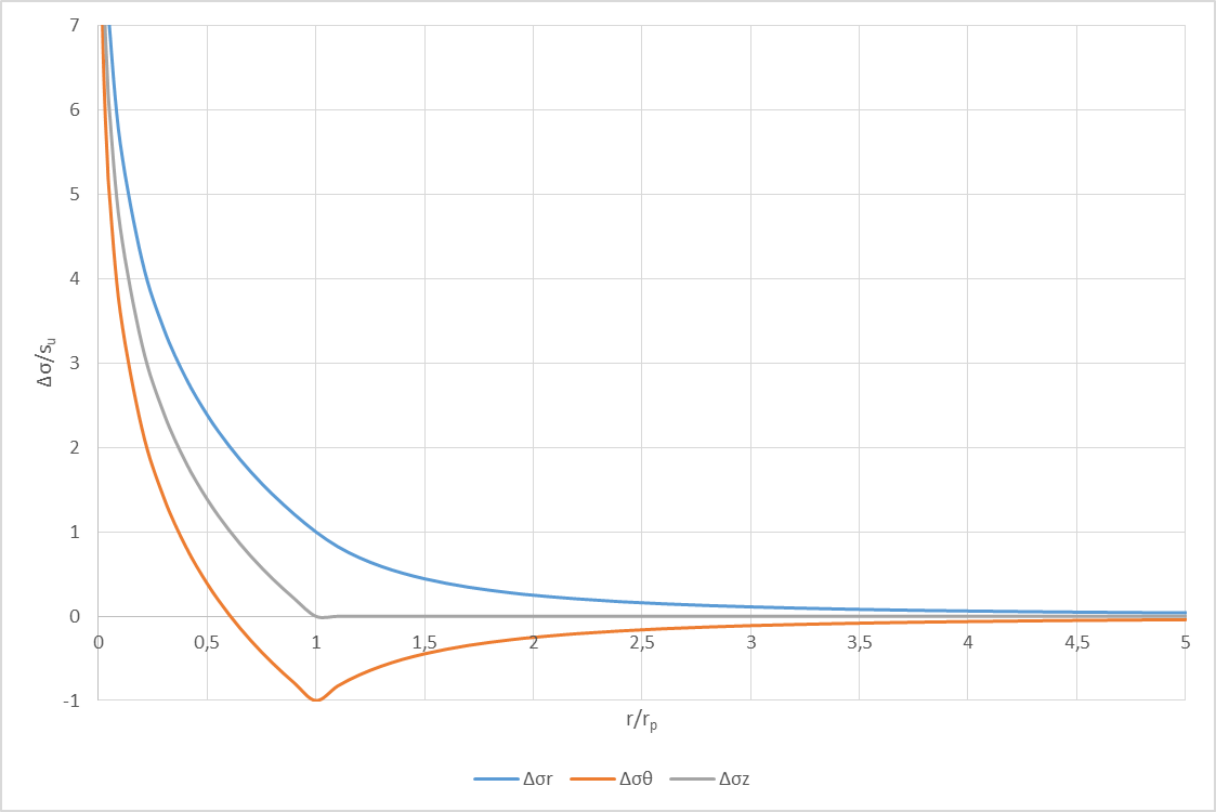

Figure 5.1: The analytical solution of Gibson and Anderson (1961) for the change in total stresses against the radial extent from the pile center normalized with the plastic radius for cavity expansion in an undrained Tresca material. Made by the author utilizing Equation 5.6, 5.7 and 5.8.

Figure 5.1 shows the linear elastic-perfectly plastic solution for the stress changes in an undrained Tresca material (EP). When r/r_p goes towards zero, the stress changes go towards infinity. A lower limit of r/r_p is given by Equation 5.2, and gives a non-infinite maximum stress change at the pile surface. Notice that the difference between the change of the radial

total stress ($\Delta\sigma_r$) and the circumferential total stress ($\Delta\sigma_\theta$) is constant for $^r/_{r_p} \leq 1$, and equals 2. This means that the entire region where $^r/_{r_p} \leq 1$ is fulfilling the Tresca yield criterion (i.e. $\sigma_r - \sigma_\theta = 2s_u$) as one would expect from a perfectly plastic soil model.

From Figure 5.1 it is easily verified that: $\Delta\sigma_r = \Delta\sigma_1, \Delta\sigma_z = \Delta\sigma_2, \Delta\sigma_\theta = \Delta\sigma_3$, both in the elastic and the plastic zone, when the initial soil stress is isotropic (p_0). Using Janbu's pore pressure equation and the expressions in Chapter 3.4, we can estimate the pore pressure build-up as:

For the plastic zone $r \leq r_p$:

$$\frac{\Delta u}{s_u} = 2\ln\left(\frac{r_p}{r}\right) - 2D \tag{5.9}$$

For the elastic zone $r \geq r_p$:

$$\frac{\Delta u}{s_u} = -2D * \left(\frac{r_p}{r}\right)^2 \tag{5.10}$$

The maximum excess pore pressure is obtained at the pile shaft (i.e. $r = r_0$), and if Equation 5.2 is inserted with $r = r_0$ into Equation 5.9 we get:

$$\frac{\Delta u_{max}}{s_u} = \ln\left(\frac{G}{s_u}\right) - 2D \tag{5.11}$$

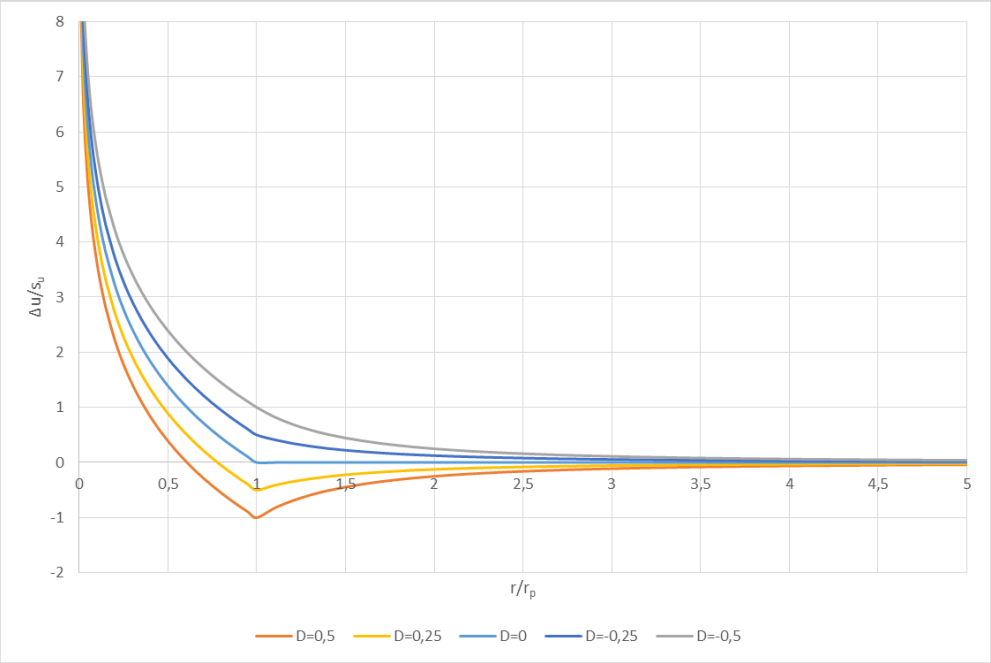

Figure 5.2: Normalized excess pore pressure estimated by using Janbu's pore pressure equation with the stress changes found by Gibson and Anderson (1961) for five different values of the Dilatancy parameter (D) against the radial extent from the pile center normalized with the plastic radius. Made by the author utilizing Equation 5.9 and 5.10.

Figure 5.2 shows the excess pore pressure predicted by CEM-EP over the undrained shear strength against r/r_p for different values of the Dilatancy parameter (D) between the limits presented in Table 3.2. As for Figure 5.1 the excess pore pressure goes towards infinity as r/r_p goes towards zero. The minimum value of r is the pile radius r_0, and thus the maximum excess pore pressure is found at the pile surface. Janbu's pore pressure equation is normally not used (and not Henkel's either) in the literature when using CEM-EP. The change in excess pore pressure is usually set equal to the change of the total mean stress. This is the same as setting $D = 0$ in Equation 5.9 and 5.10, which gives the following:

For the plastic zone $r \leq r_p$:

$$\frac{\Delta u}{s_u} = 2 \ln\left(\frac{r_p}{r}\right) \tag{5.12}$$

For the elastic zone $r \geq r_p$:

$$\frac{\Delta u}{s_u} = 0 \tag{5.13}$$

Notice that this assumption will give zero excess pore pressure in the elastic region. The maximum excess pore pressure is still at the pile shaft, and using Equation 5.2 with $r = r_0$ we get:

$$\frac{\Delta u_{max}}{s_u} = \ln\left(\frac{G}{s_u}\right) \tag{5.14}$$

The results presented in Chapter 9 shows that for heavily overconsolidated clays, negative excess pore pressure can occur. As described in Chapter 3.4 the Dilatancy is often positive for overconsolidated clays. From Figure 5.2 we see that for positive Dilatancy, negative excess pore pressure is indeed produced. The accuracy of this prediction was not found as Dilatancy equal to zero is usually used. In Figure 5.3 the same results are presented as in Figure 5.2, but with the radial extent from the pile center in a logarithmic scale. It is then clear that for the plastic region the solution gives a linear decrease of the excess pore pressure with the logarithm of r.

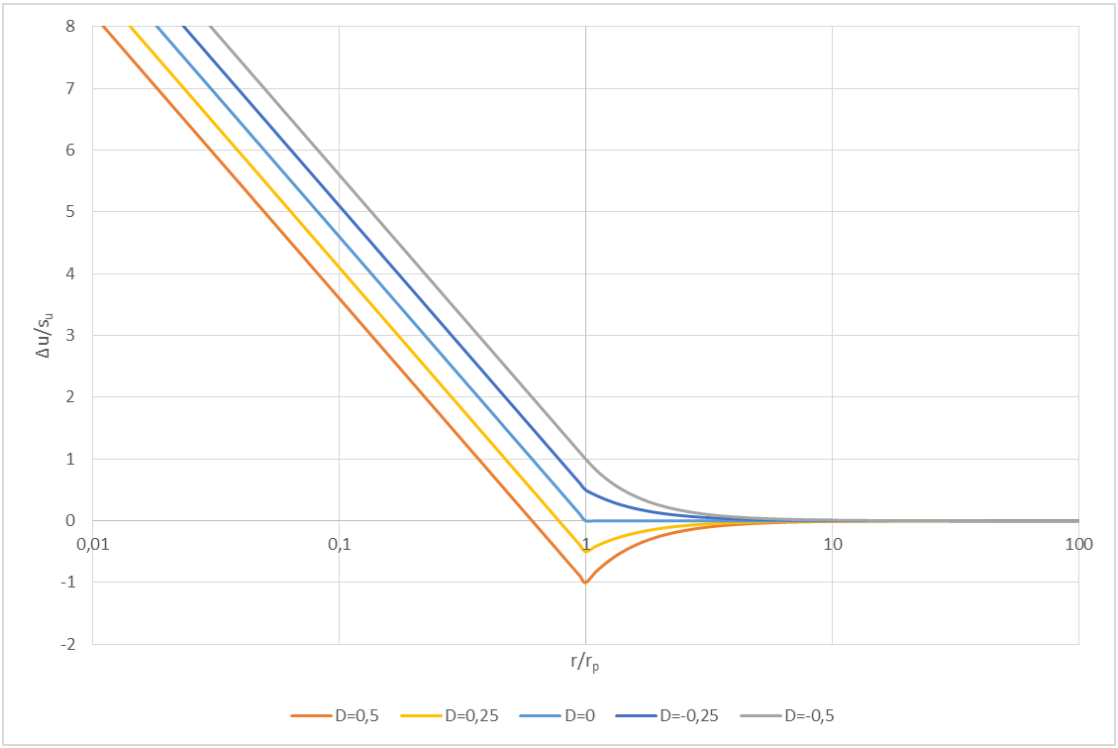

Figure 5.3: Normalized excess pore pressure estimated by using Janbu's pore pressure equation with the stress changes found by Gibson and Anderson (1961) for five different values of the Dilatancy parameter (D) against the radial extent from the pile center normalized with the plastic radius in a logarithmic scale. Made by the author utilizing Equation 5.9 and 5.10.

5.3 Choice of input parameters and effect of *OCR*

In the analytical solution of CEM, with an elastic-perfectly plastic Tresca material (CEM-EP), there is only three soil parameters needed: the shear modulus (G), the undrained shear strength, (s_u) and the Dilatancy parameter (D) (which can be neglected).

In isotropic elasticity it can readily be shown that the drained shear modulus equals the undrained shear modulus (i.e. $G' = G_u$). However, for clays, the shear modulus found from drained triaxial testing does not equal that which is found from undrained testing. This is discussed more in Chapter 13.2, as we there try to find the undrained shear modulus from the modulus number (m_0), found from oedometer testing. Since the CEM-EP solution assumes undrained loading it is natural to use the undrained shear modulus (G_u) in the above equations.

Generally we have a non-linear relationship between the shear strain and the shear stress. This means that the shear modulus is not constant. A much used method for approximating a decreasing shear modulus with increasing strains and stresses, is to use the shear modulus at 50% mobilization of the undrained shear strength (G_u^{50}). Figure 5.4 shows the principal for determining G_u^{50} from an undrained triaxial test. This is the most commonly used method when fitting a linear-elastic perfectly plastic soil model to the non-linear soil behavior, and we often call G_u^{50} the undrained average shear modulus.

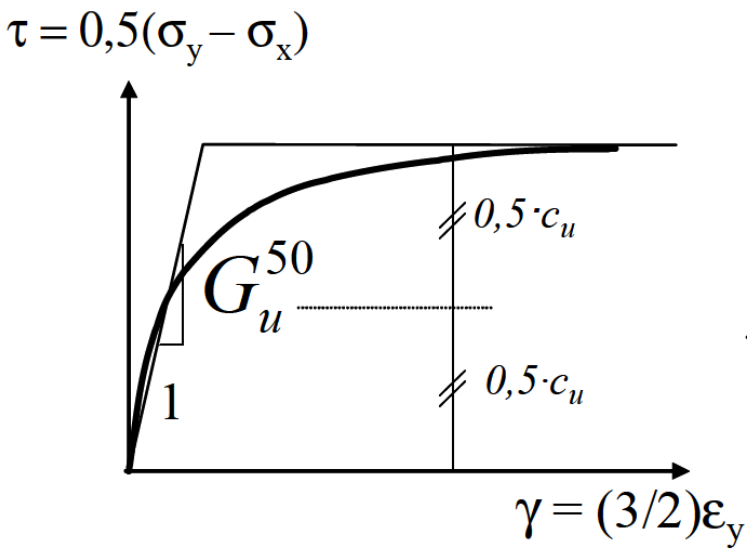

Figure 5.4: Undrained shear modulus taken at 50% mobilization of the undrained shear strength from an undrained triaxial test. (Nordal 2018)

The undrained shear strength of the soil may also vary depending on the test used. In general clays show anisotropy, and the undrained shear strength of the clay varies depending on the loading direction. One way of describing this anisotropy is to divide the undrained shear strength into three categories: the undrained active/compression shear strength (s_{uA} or s_{uC}), the direct undrained shear strength (s_{uD}) and the undrained passive/extension shear strength, (s_{uP} or s_{uE}). The undrained compression shear strength is commonly determined by an undrained triaxial compression test, the direct undrained shear strength is determined by a direct simple shear test, and the undrained extension shear strength is determined by an undrained triaxial extension test.

When modeling this numerically one can for example use the NGI-ADP soil model or another model including anisotropy. However, for the analytical CEM-EP solution one can only insert a constant undrained shear strength. Figure 5.5 shows how the different shear strengths depend on the plasticity index (I_P). We see that the anisotropy is larger for lean clays than fat clays. The discussion of which undrained shear strength to use is therefore mainly a problem in lean clays. The green line in Figure 5.5 shows the typical range of the plasticity index found in Norwegian clays.

In international practice one often use the direct undrained shear strength and simply call it s_u. All the tests of the CEM-EP model done internationally is therefore assumed, unless otherwise stated, to have used the direct undrained shear strength. This is something to be aware of when reading the literature.

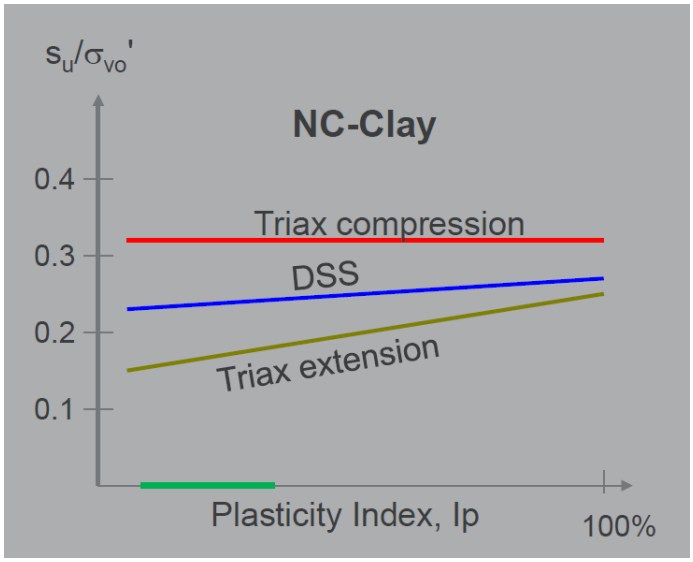

Figure 5.5: Normalized undrained shear strength found from different test as a function of the plasticity index. The green line shows typical values of the plasticity index for Norwegian clays. (Jostad 2018)

In CEM we see that the radial stress increase while the circumferential stress decrease, and the vertical stress is constant before failure. This compares to the shearing process seen in the direct simple shear test (DSS), and one should therefore use the direct undrained shear strength (s_{uD}) in CEM-EP. In Chapter 14.3 we have looked at the empirical data and used both the s_{uD}, s_{uC} and s_{uE}. Due to the scatter of the high OCR clays s_{uE} gives the lowest sum of errors. However, the data shows that s_{uD} gives the best approximation for most of the sites, when ignoring the outliers.

To summarize, the recommendation is to use the direct undrained shear strength (s_{uD}) and the undrained average shear modulus (G_u^{50}) in CEM-EP. This means that Equation 5.14 can be written more specifically as:

$$\frac{\Delta u_{max}}{s_{uD}} = \ln\left(\frac{G_u^{50}}{s_{uD}}\right) \tag{5.15}$$

In the following chapters G_u can be assumed to be equal to G_u^{50} unless otherwise stated. Increasing the overconsolidation ratio (OCR) leads to an increase of the undrained shear strength, and an increase of the undrained shear modulus. Figure 5.6 shows the undrained average shear modulus normalized with the undrained compression shear strength against OCR. The data has been obtained using conventional undrained triaxial compression test on high quality block samples. The lower range is for more plastic clays, while the upper range is observed in marine clays with a low plasticity index in the range of $12 - 20\%$.

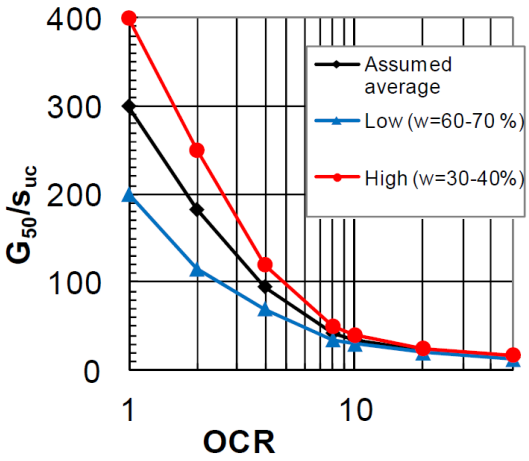

Figure 5.6: Typical range of the undrained shear modulus taken at 50% mobilization of the undrained shear strength normalized with the undrained compression shear strength against the overconsolidation ratio in a logarithmic scale. Values obtained from CAUC triaxial tests on high quality block samples (based on data from Karlsrud and Hernandez (2011) made by Karlsrud (2012))

From Equation 5.11 the effects of OCR become quite obvious: as OCR increase G_u^{50}, s_{uD}, and D also increase (see Chapter 3.4, Figure 5.6 and Figure 5.7). Figure 5.7 shows the dependency between the undrained compression shear strength normalized with the initial vertical effective stress and OCR, and we see that the undrained shear strength indeed do increase with OCR. s_{uC} increase more rapidly with OCR than G_u^{50} meaning G_u^{50}/s_{uC} decrease with OCR. Since an increase in s_{uC} also means an increase in s_{uD} according to Figure 5.5, $\Delta u_{max}/s_{uD}$ will decrease as G_u^{50}/s_{uD} decrease, and D increase.

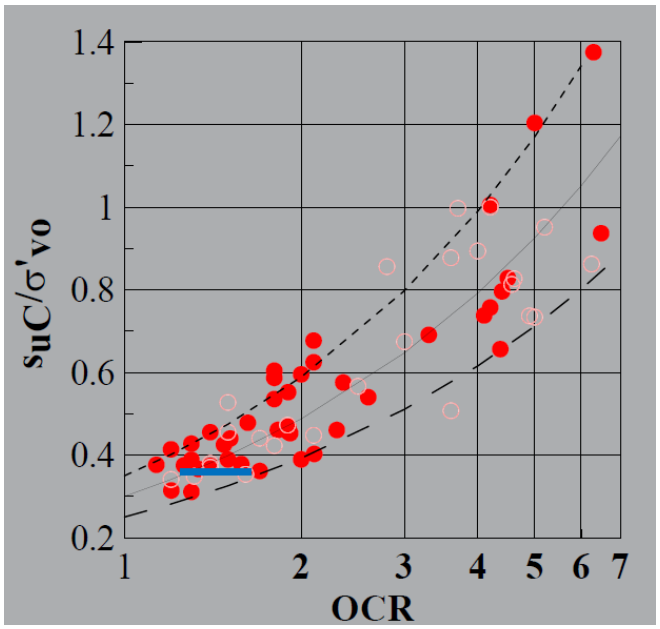

Figure 5.7: Normalized undrained compression shear strength against the overconsolidation ratio in a logarithmic scale. Based on measurements from Norwegian clays. (Jostad 2018)

Figure 5.8 shows the effect of G_u^{50}/s_{uD} decreasing using the data from Figure 5.6 and the CEM-EP model. However, Figure 5.8 sets the excess pore pressure equal to the change in mean stress and does not include the added effect that the Dilatancy parameter would give.

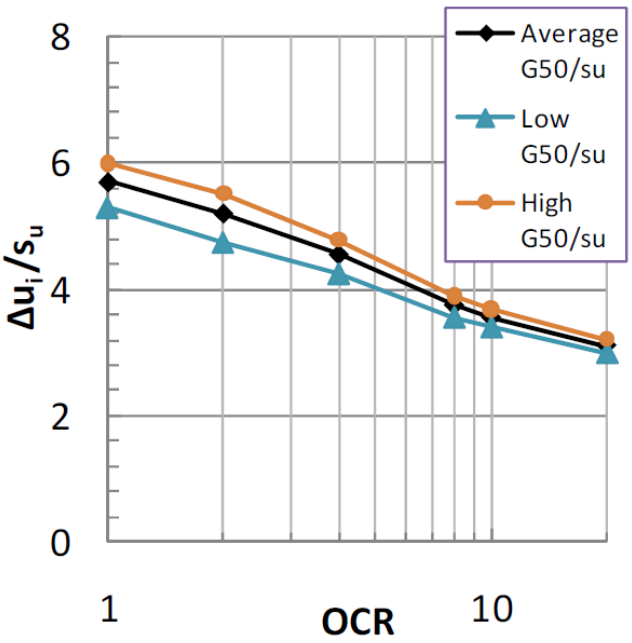

Figure 5.8: Typical normalized excess pore pressure at the pile shaft against the overconsolidation ratio based on predictions of the CEM-EP model with data from Figure 5.6. Where $\Delta u_i = \Delta u_{max}$. (Karlsrud 2012)

In addition to this, we have some change with depth as neither the shear modulus, OCR nor the undrained shear strength is constant with depth.

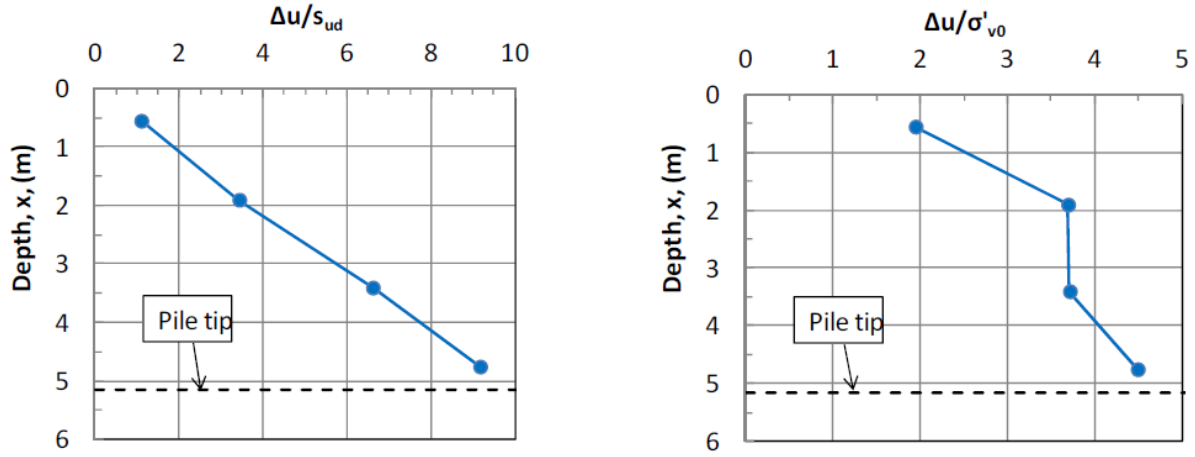

Figure 5.9: Measured excess pore pressure (Δu) normalized with the direct undrained shear strength (s_{uD}) and the initial effective vertical stress (σ'_{v0}) against depth at the Haga site. (Karlsrud 2012)

Figure 5.9 shows an increase of the measured normalized excess pore pressure with depth. This increase is close to linear when the measured excess pore pressure is normalized with the direct undrained shear strength. Neglecting the dry crust, clay often show an increase of the undrained shear strength and shear modulus with depth due to the increase in vertical stress, while the OCR normally decrease with depth.

According to Figure 5.6, decreasing OCR with depth means increasing G_u^{50}/s_{uC}, which again yields increasing $\Delta u_{max}/s_{uD}$. This can be seen directly from Figure 5.8, and gives us the general trend we see in the measured results.

It is useful to remember these results as things tend to become more complicated when using more advanced soil model. The CEM-EP model display similar behavior as the more advanced models, even though it only needs two/three input parameters for the soil (G_u^{50}, s_{uD} (and D)). As shown, all three parameters depend on the clay type and the strain history, and the model behave according to the general trends that we see in measurements. However, the accuracy in the predictions is yet to be shown, and the CEM-EP solution does not include the sensitivity of the material.

5.4 Open-ended piles

When using CEM, the pile radius is the only input in the model of the pile. When a closed-ended pile is used, then the pile radius is quite obviously the outer radius of the pile, but when an open-ended pile is used then the input pile radius cannot be taken as the outer radius. The most intuitive approach is to expand the cylinder from the inner radius to the outer. The displaced volume is then the same as for a closed-ended pile with radius given by:

$$r_0 = \sqrt{r_{outer}^2 - r_{ie}^2} \tag{5.16}$$

where r_{ie} is the equivalent inner radius. For an idealized open-ended pile, the equivalent inner radius equals the inner radius. However, open-ended piles are usually only partially plugged, that means that the inner volume of the pile is not completely filled with soil. The equivalent inner radius can then be found from the following expression:

$$\frac{\Delta V}{V_0} = \frac{r_{outer}^2 - r_{ie}^2}{r_{ie}^2} \tag{5.17}$$

where ΔV is the actual volume of the pile minus the volume of the plug, and V_0 is the inner volume of the pile. Establishing an input radius for CEM therefore require that the volume of the plug or the volume of soil going into the pile is estimated.

6 Cavity expansion in a Critical State Soil

6.1 General

In perfect plasticity, the strength remains constant during loading and unloading. In clay, the strength of the soil may vary considerably due to the deformation history of the material. For normally consolidated and lightly overconsolidated clays the linear elastic-perfectly plastic model (EP) may give reasonable results. For heavily overconsolidated clays, the stress history of the material causes the stress estimates to be larger than what we measure (Karlsrud 2012). These effects may be included using a strain-hardening/softening plasticity model. Many of such models, and perhaps the most widely used, are based on the Critical State Soil Mechanics (CSSM) developed at the University of Cambridge by Schofield and Wroth (1968), and Roscoe and Burland (1968). (Yu 2000)

In this chapter the Modified Cam Clay (MCC) model will be explained, and the results from a semi-analytical exact solution is presented. A more complete description of the MCC material model is given by Wood (1990). Lastly, a short description and some numerical results of the material models S-CLAY1 and S-CLAY1S will be presented. These are critical state material models which include anisotropy, and both anisotropy and destructuration of the material, respectively.

Some criticism has been directed at the MCC model. The essence of that criticism is that for heavily overconsolidated clays the MCC may give unrealistically large ratios of shear stress over mean stress. Randolph, Carter et al. (1979) argues that if the excess pore pressure is normalized by the initial undrained shear strength, and not the overburden pressure, then this difficulty is avoided. The MCC model is interesting since it does include some of the main features of a heavily overconsolidated clay: A large pseudo-elastic region, and the increase of the mean stress if the soil under undrained conditions is sheared to failure.

6.2 Critical State Soil Mechanics and the Modified Cam Clay model

The hardening process of a material is most commonly controlled by either the development of plastic shear strains or volumetric deformation. In principle, this is not important as the shear and volume strains are related. However, when measuring the hardening of a soil it is favorable to have large response in the parameter measured. The MCC model is mainly a clay model, and clay has large volumetric deformations. The MCC is therefore based on volumetric hardening. The preconsolidation stress is used as the hardening parameter in MCC.

The principle of the CSSM is based on experimental results from Roscoe, Schofield et al. (1958) on small steel balls and Weald clay.

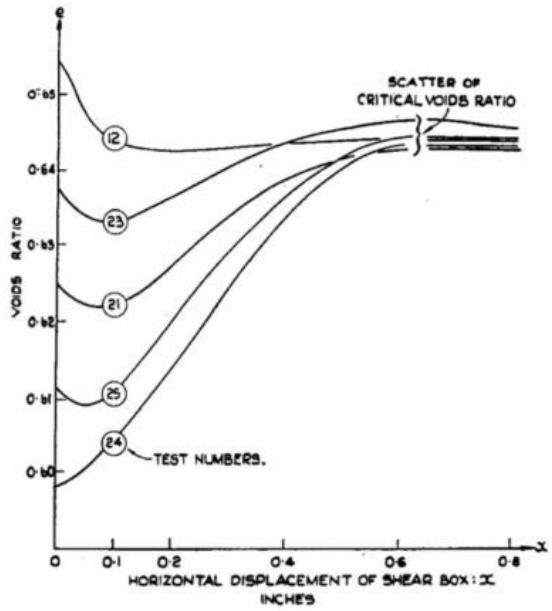

Figure 6.1: Measured void ratio (e) against the horizontal displacement of the shear box, where the results are obtained from shear box tests on 1mm steel balls with a normal stress of 20 lb./sq.in. (Roscoe, Schofield et al. 1958)

Figure 6.1 shows that initial void ratio (e_0) is insignificant when a certain level of shear strain is reached. This then also holds for the porosity ($n = \frac{e}{1+e}$) and the specific volume ($v = 1 + e$). The void ratio (e) goes, independent of initial void ratio, towards a critical state void ratio. Experimental data on sand and clay, both remolded and reconstituted, show the same tendency. So for a given normal stress there is a unique critical void ratio, which is reached at large strains. The definition is: "A critical state is a state where unlimited shear strains may occur without any change in effective stress, volume or shear stress."

In the MCC model a linear dependency between the specific volume and the natural logarithm of the mean stress (p) is assumed. If the clay is loaded in the normally consolidated (NC) range the inclination λ (i.e. the swelling index) is used, and if the clay is loaded in the overconsolidated (OC) range the inclination κ (i.e. the compression index) is used. The curves these assumptions construct are shown in Figure 6.2.

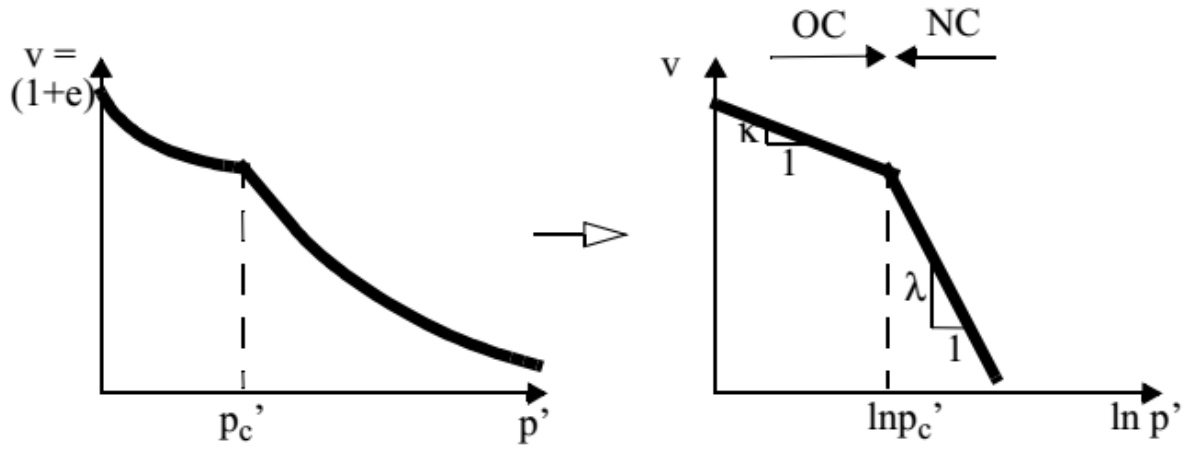

Figure 6.2: Specific volume (v) against effective mean stress (p') using the flexibility parameter λ in the normally consolidated area ($p' < p'_c$) and κ in the overconsolidated area ($p' > p'_c$), where $p'_c = p_p$ is the isotropic preconsolidation pressure. (Nordal 2018)

In the MCC model an elliptic yield surface in the $q - p'$-plane is used. (The shape of the yield surface is the main difference between the Original Cam Clay (OCC) model and the MCC model). The yield surface of the MCC model is given by:

$$F = q^2 - M^2\left[p'\left(p_p - p'\right)\right] \tag{6.1}$$

where p' is the effective mean stress, p_p is the isotropic preconsolidation pressure, and M is the slope of the Coulomb line in the $q - p'$-plane, given by:

$$M = \frac{6\sin\varphi}{3 \pm sin\varphi} \tag{6.2}$$

(minus for triaxial compression, plus for triaxial extension). The ellipse will differ about the p'-axis since M differ.

Lastly q is the deviatoric stress defined by:

$$q = \sqrt{\frac{1}{2}[(\sigma_1' - \sigma_2')^2 + (\sigma_2' - \sigma_3')^2 + (\sigma_1' - \sigma_3')^2]} \tag{6.3}$$

As discussed in Chapter 3, Equation 6.3 will give the same results as Equation 3.9 under triaxial conditions.

Figure 6.3 shows experimental data that substantiates a sort of elliptic yield surface in the $q - p'$-plane.

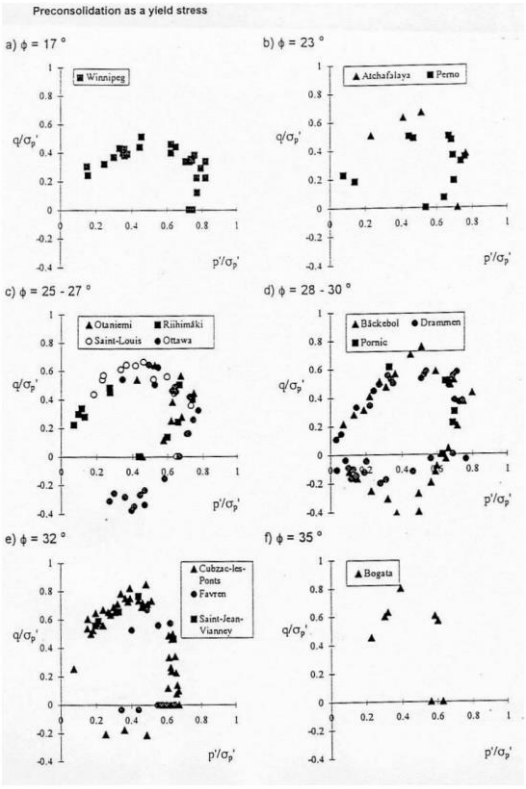

Figure 6.3: Cam clay type of yield surfaces found from experimental studies (data from Leroueil (1990), (1994), made by Lansivaara (1996), obtained from Nordal (2018))

Figure 6.3 also shows that the ellipse seems to be somewhat tilted. This will be introduced in the S-CLAY1 material model, but for now, we assume an ellipse with center on the p'-axis.

In the MCC model associated flow is assumed. This means that the gradient of the plastic flow is perpendicular to the elliptic yield surface.

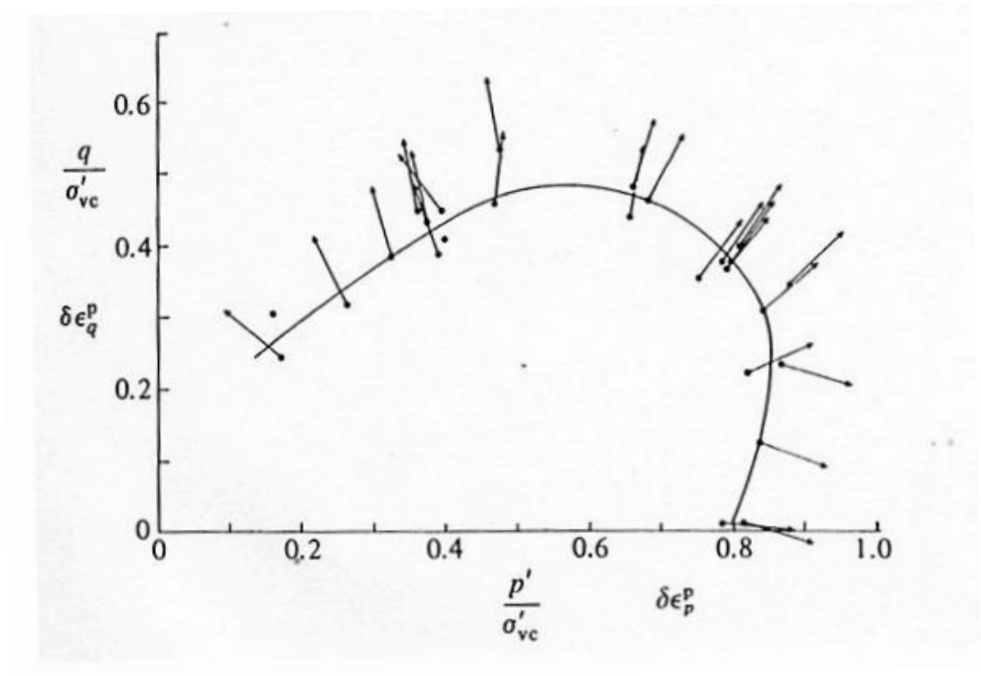

Figure 6.4: Vectors of plastic strain increments plotted at yield points deduced from triaxial tests on undisturbed Winnipeg clay (data from Graham, Noonan, and Lew (1983), made by Wood (1990), obtained from Nordal (2018))

Figure 6.4 shows experimental data of the plastic strain increment, which substantiate the assumption of associated plastic flow.

The Mohr-Coulomb line is used to define the Critical State Line (CSL) and is defined by:

$$q = Mp' \tag{6.4}$$

When we are on the CSL we have no change in effective stresses, shear stress nor volume, while unlimited shear strains can develope. The stiffness of the soil is in the MCC model represented by the bulk modulus (K) and the shear modulus (G), given by:

$$K = \frac{(1+e) * p'}{\kappa} \tag{6.5}$$

$$G = \frac{3(1-2\nu_{ur})}{2(1+\nu_{ur})} K \tag{6.6}$$

where ν_{ur} is the Poisson's ratio for unloading and reloading (Chen and Abousleiman 2012).

The most important input parameters in the MCC model is hence: $\lambda, \kappa, M, e_0, OCR$ and ν_{ur}. All other parameters can be determined or estimated from these parameters.

To summarize the method we have Figure 6.5 and Figure 6.6, which give a graphical explanation of a strain softening ($OCR > 2$) and a strain hardening ($OCR < 2$) material in a conventional undrained triaxial compression test.

For undrained loading it is assumed that the volumetric strains are zero. This also means that the specific volume is unchanged. For a triaxial compression test done with constant cell pressure the change in deviatoric stress is $\Delta q = \Delta\sigma_1$, and the change in total mean stress is $\Delta p = {\Delta\sigma_1}/{3}$. This then defines the total stress path (TSP). In the MCC model the elastic volumetric strains are defined by:

$$\Delta\varepsilon_{vol}^{e} = \frac{\Delta p'}{K} \tag{6.7}$$

This means that for undrained conditions, the change in effective mean stress is equal to zero within the elastic region. Meaning that within the ellipse, the effective stress path (ESP) goes straight up in the $q - p'$-plane, with only the deviatoric stress changing. This can be seen in Figure 6.5 from point A to B and in Figure 6.6 from point P to Q. In point B, the yield function is fulfilled and plastic strains will develop. MCC assumes associated flow which means that the strain increment is perpendicular to the yield surface. The hardening rule relates the isotropic preconsolidation pressure to the volumetric strain on incremental form through:

$$\Delta\varepsilon_{vol}^{p} = \frac{\lambda - \kappa}{\nu} \ln\left(\frac{p_p + \Delta p_p}{p_p}\right) \tag{6.8}$$

The strain increment can be decomposed into a volumetric strain increment and a deviatoric strain increment that corresponds to the effective mean stress axis and the deviatoric stress axis respectively. In point B, the volumetric strain increment is positive and thus the yield ellipse must expand according to Equation 6.8. The sum of elastic and plastic volumetric strain must be equal to zero, so an increase in isotropic overconsolidation pressure must be matched by a decrease in the effective mean stress. Geometrically this is shown in Figure 6.5,

when the yield ellipse expands one needs to move upwards on the isotropic normal compression line (iso-ncl), but the specific volume must be constant. This means one moves back to the constant specific volume on the unloading reloading line (url). As the mean stress decrease one moves towards the critical state and the plastic volumetric strain increment decreases monotonically. In point F we are on the critical state line and the plastic strain increment is vertical, meaning there is only plastic deviatoric strain and no plastic volumetric strain developing. When the plastic volumetric strain increment is zero there is no hardening, and then also no change in effective stress. We are stuck in point F while plastic deviatoric strains can develop towards infinity, without change in effective stress, shear stress nor volume.

The deviatoric strain is linked to the volumetric strain through the flow condition:

$$d\varepsilon_q^p = \frac{2q}{M^2(2p' - p_p)} d\varepsilon_{vol}^p \tag{6.9}$$

The pore pressure is the difference between the ESP and the TSP. Based on this one can make the plots presented in Figure 6.5 (d) and Figure 6.6 (d).

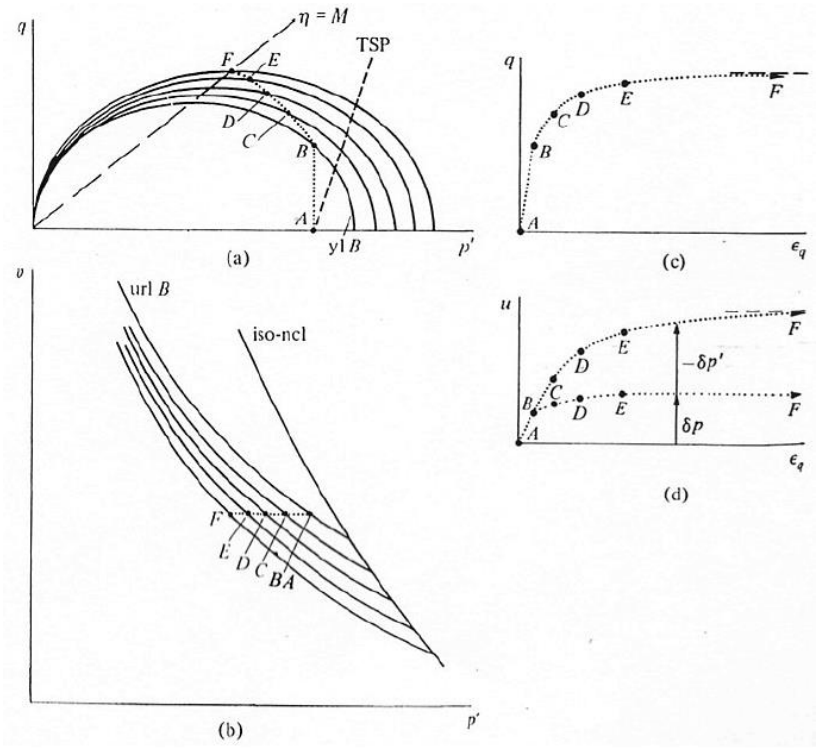

Figure 6.5: Conventional undrained triaxial compression test on lightly overconsolidated soil: (a) p': q effective stress plane; (b) v: p'compression plane; (c) q: ε_q stress strain plot; (d) u: ε_q pore pressure strain plot. (Wood 1990)

Figure 6.6 shows an undrained triaxial compression test of a high OCR clay and it shows some interesting effects. When the yield criterion is fulfilled (point Q), associated flow gives a plastic volumetric strain increment in negative direction. This means that the yield ellipse will decrease according to Equation 6.8. The sum of the volumetric strain still needs to be zero, so the effective mean stress increase until the critical state line is met. From point P to Q the pore pressure will build up, but as the effective mean stress increase the ESP goes towards the TSP, and the pore pressure becomes negative when the ESP crosses the TSP. Accordingly, in point T, one has suction in the test sample. This is the effect that is seen in the measured excess pore pressure in heavily overconsolidated clays after pile driving. For undrained loading we see that the TSP goes straight up in the elastic area. This means that for OCR less than two the material will contract, and something similar to what we see in Figure 6.5 will happen. While the material will dilate for OCR above two, and something similar to what we see in Figure 6.6 will happen. For OCR equal to two neither dilation nor contraction will happen, the ESP will go straight up until it meets the critical state (i.e. elastic-perfectly plastic).

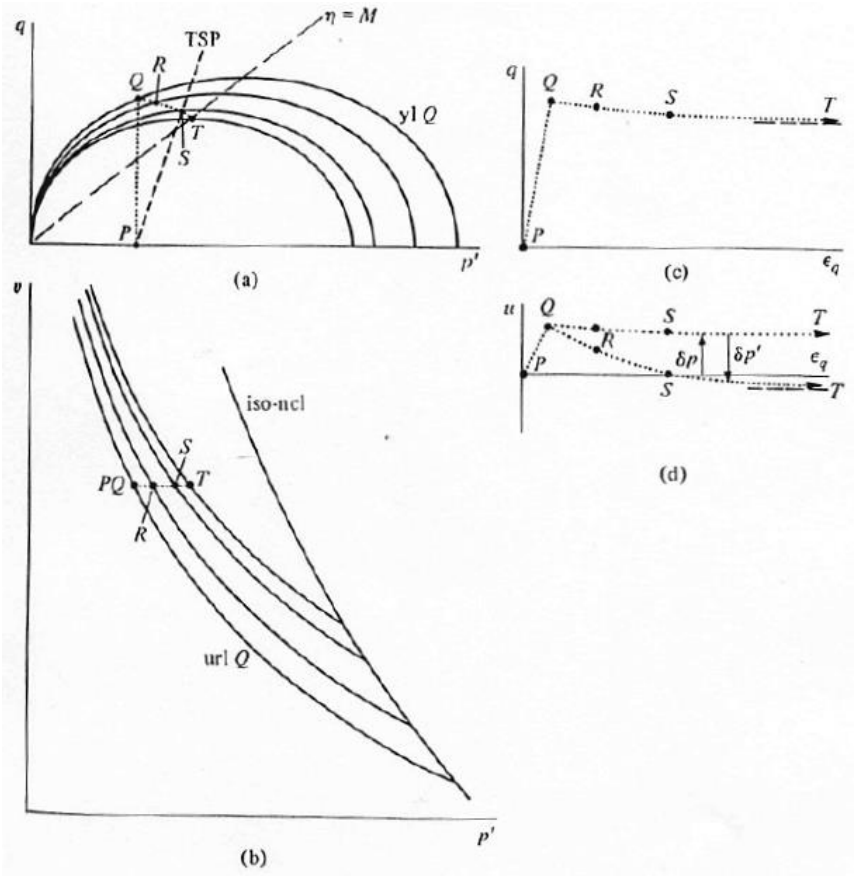

Figure 6.6: Conventional undrained triaxial compression test on heavily overconsolidated soil: (a) p': q effective stress plane; (b) v: p' compression plane; (c) q: ε_q stress strain plot; (d) u: ε_q pore pressure strain plot. (Wood 1990)

The MCC model has some deficiencies. When determining the slope of the critical state line (M) based on the friction angle one also determines the stress ratio in the normally consolidated state (K_0^{NC}). This is problematic as experiments show that M based on the friction angle gives too high K_0^{NC}, and thus also too high horizontal stresses. The softening behavior in Figure 6.6 is also problematic. Point Q has been shown to be too high in some cases, which means one overestimates the peak undrained shear strength. In addition, the softening from the peak is not always a good fit to experimental data. The problem is simply that the softening is based on M and cannot be controlled. In addition there is no strain softening in the NC range although this may very well happen in a real clay.

6.3 Semi-analytical solution of MCC in CEM

In this section we will look at the solution presented by Chen and Abousleiman (2012). Semi-analytical is referring to the fact that the solution is presented as a one-dimensional boundary value problem, which can be solved by for example an ordinary differential equation system solver. Collins and Yu (1996) presented a simpler semi-analytical solution. Cao, Teh et al. (2001) followed a similar procedure to make an approximate closed form solution. The assumption made by Collins and Yu (1996), and Cao, Teh et al. (2001) is that the effective mean stress equals: $p' = \frac{1}{2}(\sigma_r' + \sigma_\theta')$, and that the deviatoric stress equals: $q = \sigma_r' - \sigma_\theta'$, instead of the full 3D definitions previously presented. In addition, they used constant shear modulus rather than one which varies in proportion to the mean stress. Chen and Abousleiman (2012) finds that for the special case of isotropic initial stresses the solution in Cao, Teh et al. (2001) happens to be correct.

A general assumption used in all the above solutions is that the small strain formulation (i.e. engineering strains) is applicable for the elastic strains, and that the large strain formulation (i.e. logarithmic strains) is applicable for the plastic strains. Chen and Abousleiman (2012) finds that the overconsolidation ratio (OCR) has a large influence on the results. The equations used to establish the one-dimensional boundary value problem is not repeated in this study, but can readily be found in Chen and Abousleiman (2012).

In contrast to the analytical elastic-perfectly plastic solution, an initial cavity radius of zero is problematic when solving CEM numerically. Carter, Randolph et al. (1979) says that for numerical simulations there is need of a non-zero initial radius to avoid infinite

circumferential strains. Carter, Randolph et al. (1979) argues that for an outer region the stresses and strains of the deforming soil body has no connection to the inner material other than the total radial pressure transmitted. So instead of using 0 to r_0, we can use a_0 to a as long as the same amount of volume is displaced. Carter, Randolph et al. (1979) recommend using a_0 to $2a_0$. a_0 is then found by:

$$\Delta V = \pi(r_0^2 - 0^2) * L = \pi((2a_0)^2 - a_0^2) * L \rightarrow a_0 = \frac{r_0}{\sqrt{3}} \tag{6.10}$$

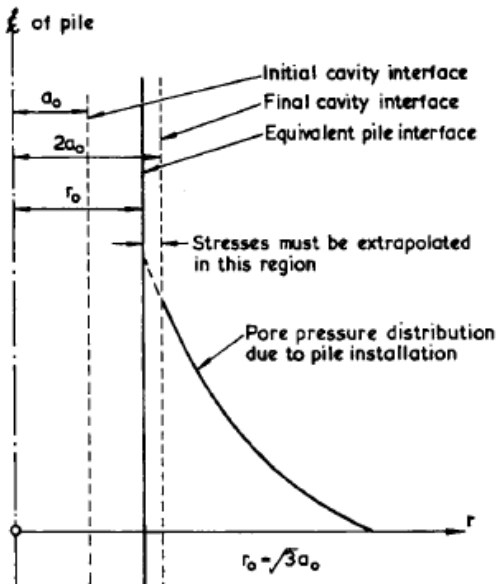

Figure 6.7: Change of cavity expansion from 0 to the pile radius (r_0), into cavity expansion from a_0 to $2a_0$.(Carter, Randolph et al. 1979)

Figure 6.7 shows the principle, and that this way of avoiding numerical troubles have some drawback. From r_0 to $2a_0 = \frac{2}{\sqrt{3}} r_0 \approx 1.15 r_0$, we have no information on the stress components or the excess pore pressure. These values will have to be extrapolated from the values we do know.

Some of the results obtained by Chen and Abousleiman (2012) is presented in Figure 6.8 to Figure 6.11.

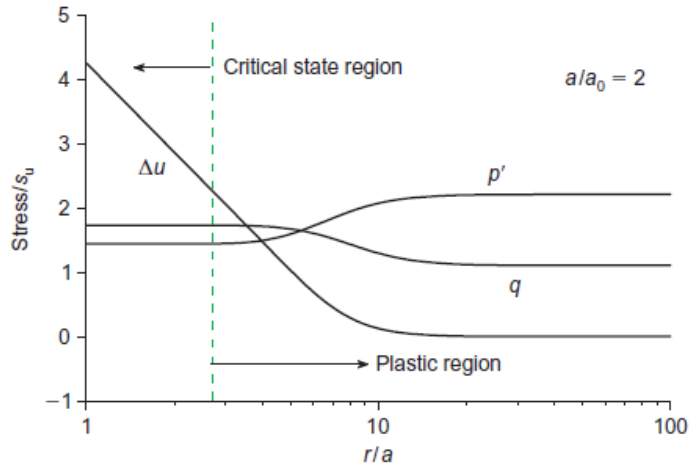

Figure 6.8: Effective mean stress (p'), deviatoric stress (q) and excess pore pressure (Δu) predicted by CEM-MCC for a normally consolidated soil, $OCR = 1$. (Chen and Abousleiman 2012)

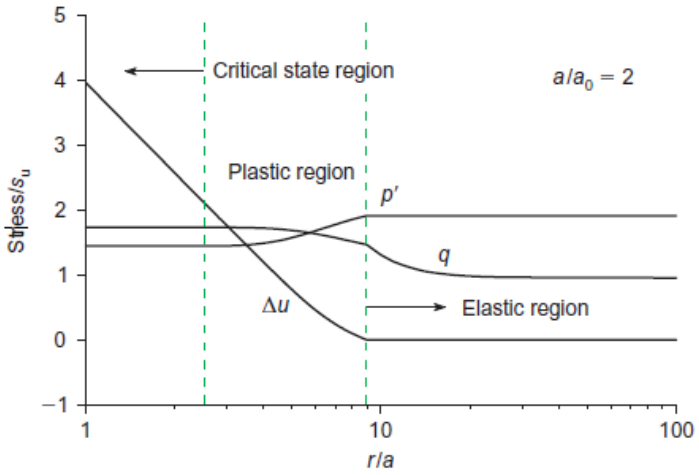

Figure 6.9: Effective mean stress (p'), deviatoric stress (q) and excess pore pressure (Δu) predicted by CEM-MCC for a lightly overconsolidated soil, $OCR = 2$. (Chen and Abousleiman 2012)

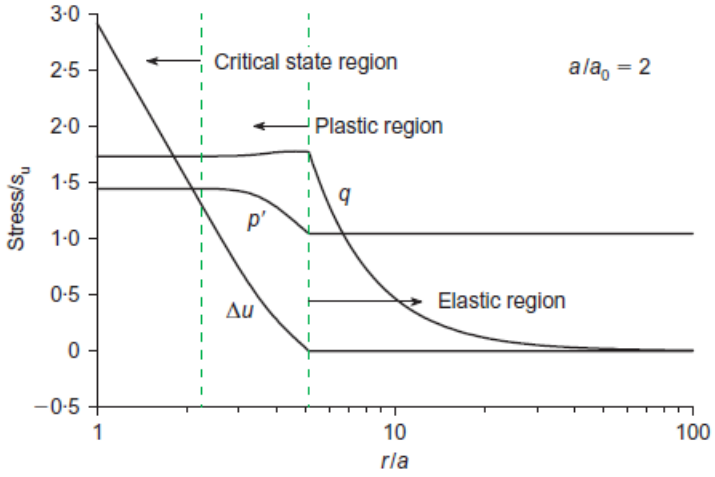

Figure 6.10: Effective mean stress (p'), deviatoric stress (q) and excess pore pressure (Δu) predicted by CEM-MCC for a moderately overconsolidated soil, $OCR = 3$. (Chen and Abousleiman 2012)

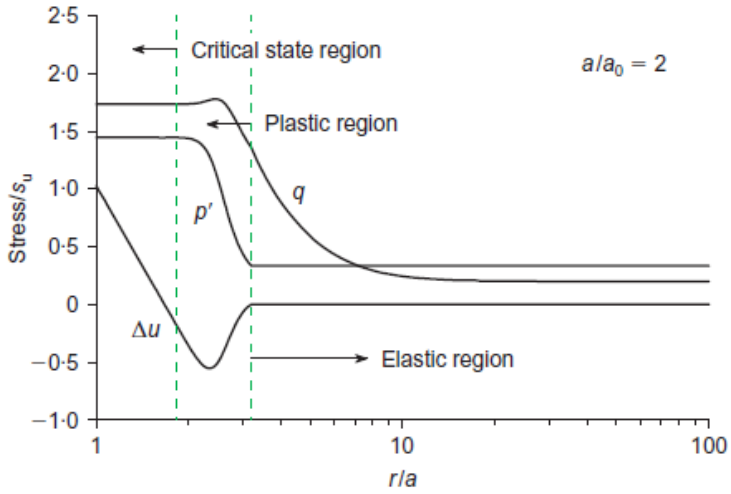

Figure 6.11: Effective mean stress (p'), deviatoric stress (q) and excess pore pressure (Δu) predicted by CEM-MCC for a heavily overconsolidated soil, $OCR = 10$. (Chen and Abousleiman 2012)

In the critical state region the effective stresses are constant and on the CSL. In the plastic region, the stresses are outside the initial yield surface, while in the elastic region the stresses are inside the initial yield surface.

From Figure 6.8 to Figure 6.11 it is seen that the excess pore pressure decreases linearly with the logarithm of r in the critical state region. In the elastic region, there is no change in pore pressure due to constant total and effective mean stress. We see that an increase of the OCR leads to a decrease of the maximum excess pore pressure and that the critical state, and plastic region shrinks, while the elastic region expands. For the heavily overconsolidated case, we

see that negative excess pore pressure is generated. This was also found by Collins and Yu (1996). Notice also that for $OCR = 1$ we have no elastic region as the initial stress condition is at the yield surface, and loading will then give plastic strains from the start. Chen and Abousleiman (2012) also found that the vertical stress in the critical state region is equal to the mean of the radial and circumferential stress. This means that the excess pore pressure change due to the coefficient of lateral earth pressure (K_0) as seen in Chapter 12.5.

Randolph, Carter et al. (1979) did a parametric study of OCR. Figure 6.12 shows the log-linear decrease of the excess pore pressure normalized with the undrained shear strength with increasing OCR found by Randolph, Carter et al. (1979) using CEM-MCC. Randolph, Carter et al. (1979) chose the input parameters so that the initial plane strain undrained shear strength is constant with OCR. G/s_u increase with OCR since s_u is constant giving a larger excess pore pressure. For $OCR > 2$ the soil dilates giving lower excess pore pressure. These two effects seem to almost cancel each other out, giving only a slight reduction in the normalized excess pore pressure with increasing OCR.

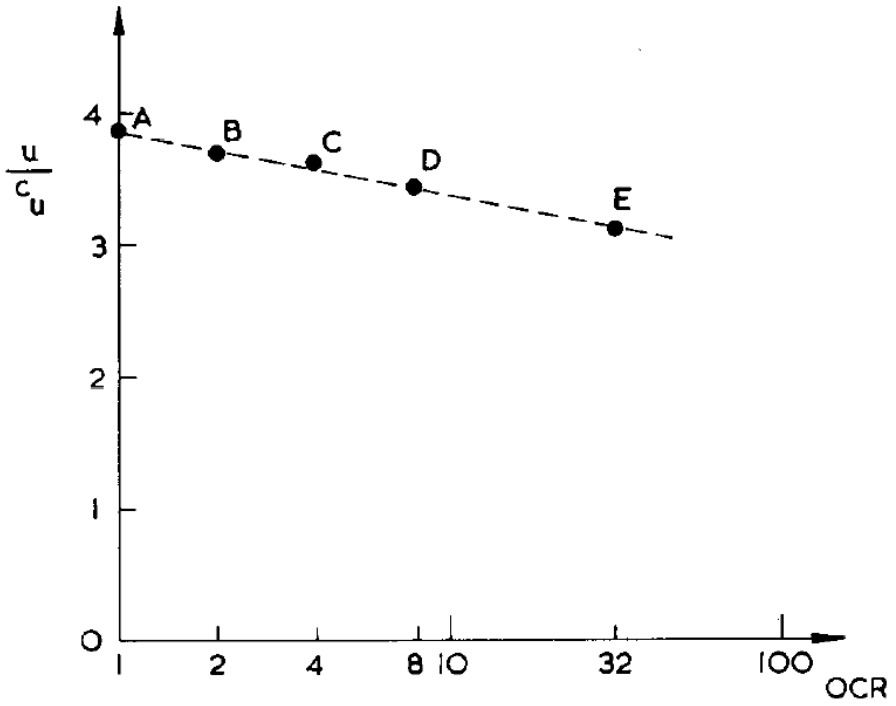

Figure 6.12: Excess pore pressure ($u = \Delta u$) near the pile surface ($r = 1{,}15r_0$) normalized to (a) the undrained shear strength ($c_u = s_u$) and (b) the initial vertical effective stress ($\sigma_z'(0) = \sigma_{v0}'$) as a function of the overconsolidation ratio (OCR) computed with CEM-MCC. (Randolph, Carter et al. 1979)

Randolph, Carter et al. (1979) uses the results of Figure 6.12 to argue that if the excess pore pressure is normalized with the undrained shear strength of the material then the effect of

increasing OCR only give a very slight reduction in excess pore pressure. The stiffness was chosen based on typical trends with OCR similar to that of Figure 5.6. However, the empirical data shows a much larger decrease with OCR than what Figure 6.12 suggests, as seen in Figure 6.13. Figure 6.13 is based on the empirical data found in Table 13.6. The reason CEM-MCC predicts too high excess pore pressure for the high OCR sites might be due to the unrealistically large ratios of shear stress over mean stress for $OCR > 2$, as previously mentioned.

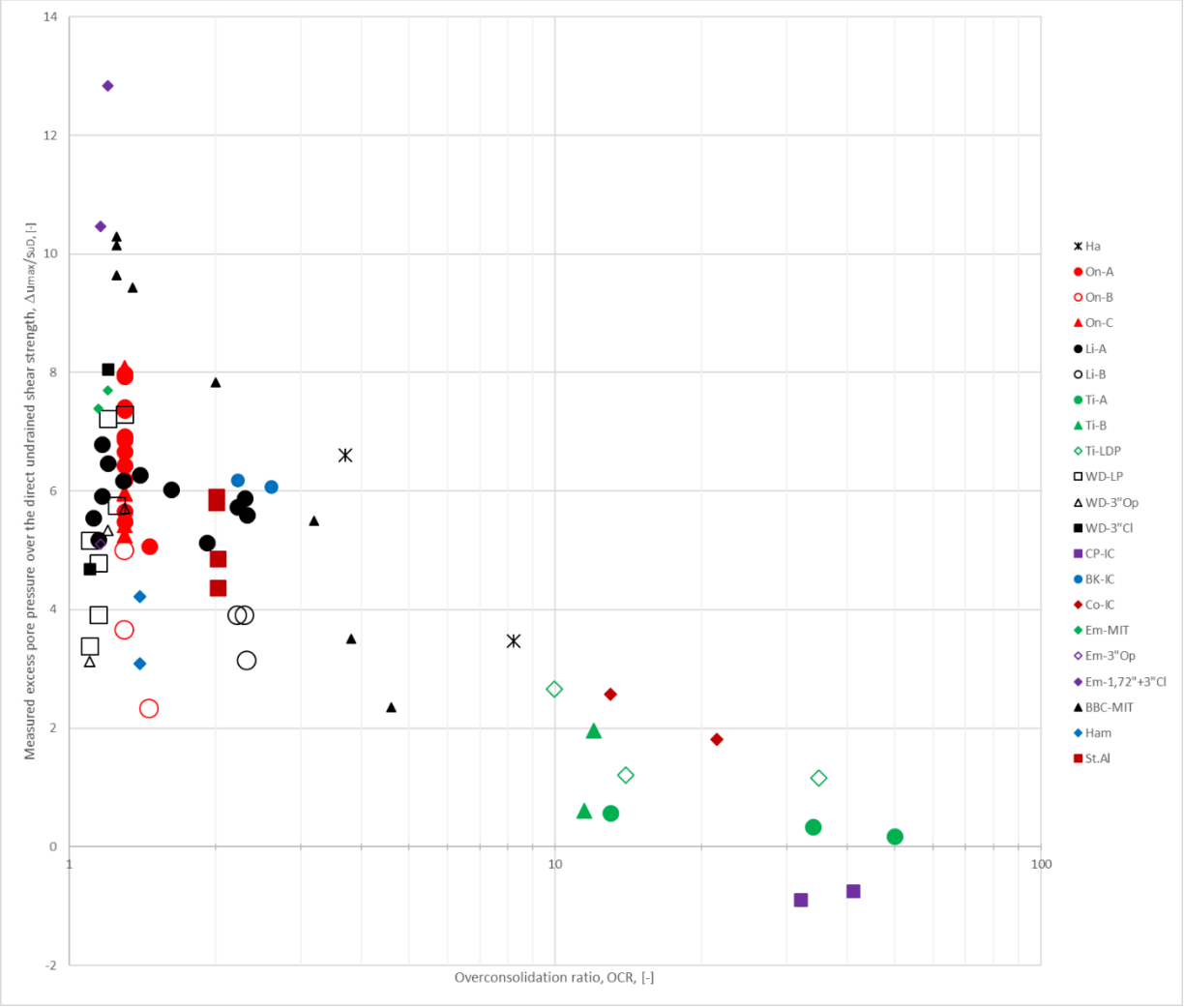

Figure 6.13: Measured excess pore pressure normalized over the direct undrained shear strength against the overconsolidation ratio in a logarithmic scale using the data from Table 13.6.

6.4 Numerical solution of S-CLAY1 and S-CLAY1S in CEM

S-CLAY1 is a critical state soil model that is based on many of the same assumptions as the MCC model. The difference between the MCC model and the S-CLAY1 model is mainly that the yield ellipse in the S-CLAY1 model is tilted to account for the anisotropy of the material. This also calls for a rotational hardening law, which gives the change of the parameter α, in addition to the hardening law describing the change of the size of the yield ellipse. Figure 6.3 shows the background for using a rotated ellipse as yield surface. The model is based on triaxial results of Otaniemi clay from Finland, which is a soft clay.

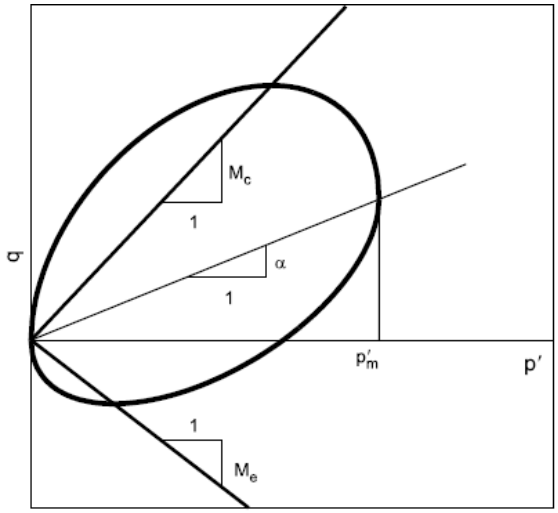

Figure 6.14: The tilted yield surface of the S-CLAY1 model. (Wheeler, Näätänen et al. 2003)

Figure 6.14 shows the tilted yield surface of the S-CLAY1. If $\alpha = 0$ we have the MCC yield surface. In the simplified stress space of the triaxial test, Equation 6.11 can be used with degree of the plastic anisotropy (α) as the only new variable. This yield surface was proposed by Dafalias (1987) and Korhonen and Lojander (1987) as:

$$F = (q - \alpha p')^2 - (M^2 - \alpha^2)(p'_m - p')p' = 0 \qquad (6.11)$$

When switching the M, depending on the sign of $\eta - \alpha$, as we go from triaxial compression to extension, we will get a discontinuity in the yield surface. Here η is the stress ratio equal to $\eta = \frac{q}{p'}$. This problemed is solved by Wheeler, Näätänen et al. (2003) through making M a function of the lode angle $\theta_{\sigma\alpha}$ of the deviatoric tensor. The general formulation used in the S-CLAY1 model, which gives the yield surface in Figure 6.14, can be found in Wheeler,

Näätänen et al. (2003). Wheeler, Näätänen et al. (2003) say that the S-CLAY1 model is not intended to be used if the majority of the soil is on the dry side of critical state, and the results will be inaccurate in this region. They have however ensured that the model stays stable if local regions yield on the dry side of the critical state line. While ensuring this they have made α so that when the soil goes towards critical state, α also goes towards a critical state value. α is then a constant for a definite stress state and is independent of the initial conditions. If α and μ is set equal to zero then the S-CLAY1 model reduces to the MCC model. Where μ is a constant that is used in the rotational hardening law and describes the absolute rate at which α heads toward its current target value. (Karstunen, Krenn et al. 2005)

The S-CLAY1S model is presented by Koskinen, Karstunen et al. (2002) and is made so that one can account for bonding and destructuration of the soil. The way these effects are introduced is through a notional yield surface, called the intrinsic yield surface, and an additional hardening law describing the degradation of the bonding. The intrinsic yield surface represents how the yield surface of the material would have been without the bonding effect. Figure 6.15 shows the principle. Where p'_m defines the real yield surface, including the bonding effect, and p'_{mi} defines the intrinsic yield surface.

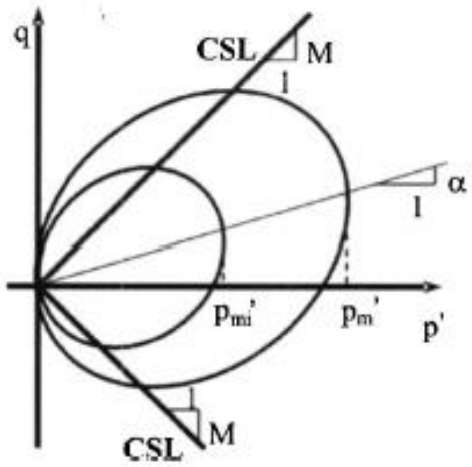

Figure 6.15: S-CLAY1S yield surface in triaxial stress space. (Koskinen, Karstunen et al. 2002)

p'_m is related to p'_{mi} through:

$$p'_m = (1 - x)p'_{mi} \tag{6.12}$$

where x is the amount of bonding, going towards zero as plastic strains increase. In addition, λ_i is needed for the hardening law describing the change of the size of the intrinsic yield surface, which again through Equation 6.12 describes the actual yield surface. In contrast, the MCC and the S-CLAY1 model uses the same hardening law, but with λ as described for the MCC model. λ_i is the inclination of the intrinsic normal compression line in the $v - \ln p'$-plane. λ_i can be determined from an oedometer test on a reconstituted sample. The initial amount of bonding x_0 can be estimated by the sensitivity as described by Koskinen, Karstunen et al. (2002). If x_0 is set equal to zero, and the apparent value λ, based on natural clay, is used instead of the intrinsic (λ_i), based on reconstituted clay, then S-CLAY1S reduces to S-CLAY1.

To summarize, in addition to the soil parameters needed in the MCC model, the S-CLAY1 needs the initial value of the degree of plastic anisotropy (α_0), and the material constants β and μ for the rotational hardening law determining the change of α. The S-CLAY1S also needs the initial value of the amount of bonding (x_0) and the material constants a and b for the hardening law describing the degradation of the bonding as well as λ_i. So in short, an extensive laboratory program needs to be implemented to use these material models.

Castro and Karstunen (2010) looked at the installation effects of stone columns in a natural soft clay. They modelled the problem as an undrained expansion of a cylindrical cavity (CEM) using two soil models: the S-CLAY1 and S-CLAY1S. They looked at installation of a single column and used an axisymmetric model with a large displacement formulation.

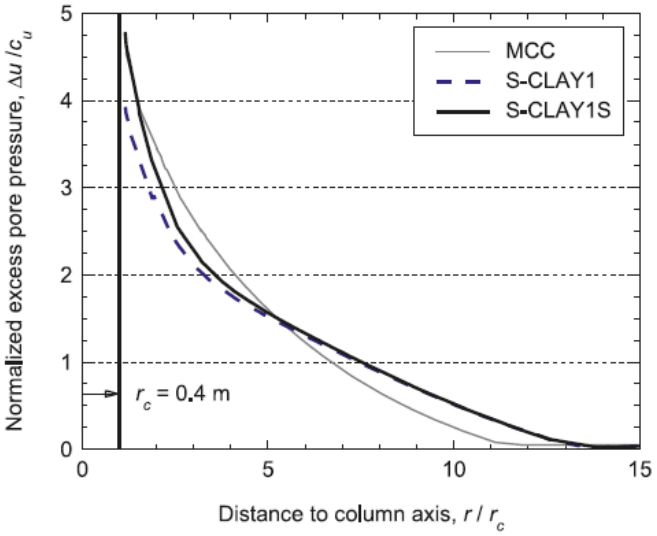

Figure 6.16: Normalized excess pore pressure computed with CEM coupled with MCC (grey solid line), S-CLAY1 (blue dotted line), and S-CLAY1S (black solid line). Where $c_u = s_u$ and $r_c = r_0$. (Castro and Karstunen 2010)

Figure 6.16 shows the excess pore pressure modelled by the MCC, S-CLAY1 and S-CLAY1S material models. The difference in the predicted excess pore pressure is quite small. For the S-CLAY1S model the excess pore pressure close to the column surface is slightly larger. This is then due to the destructuration, or remoulding, of the soil close to the column.

Unfortunately, measurements of the excess pore pressure was not presented, but lateral earth pressure coefficient and destructuration (ratio between undrained shear strength after and undrained shear strength before installation) are presented in Figure 6.17 and Figure 6.18 respectively.

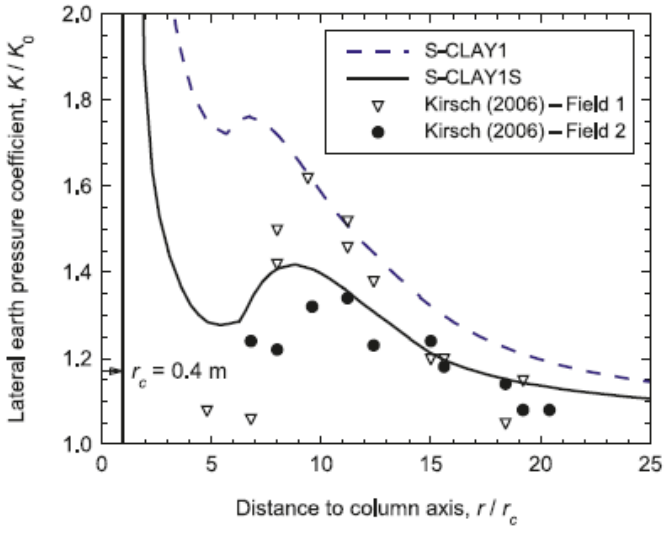

Figure 6.17: Comparison of lateral earth pressure coefficient after column installation (K) normalized with its initial value (K_0) computed numerically with CEM and the discussed material models. Compared to measurements. Where $r_c = r_0$ and $K = K_i$. (Castro and Karstunen 2010)

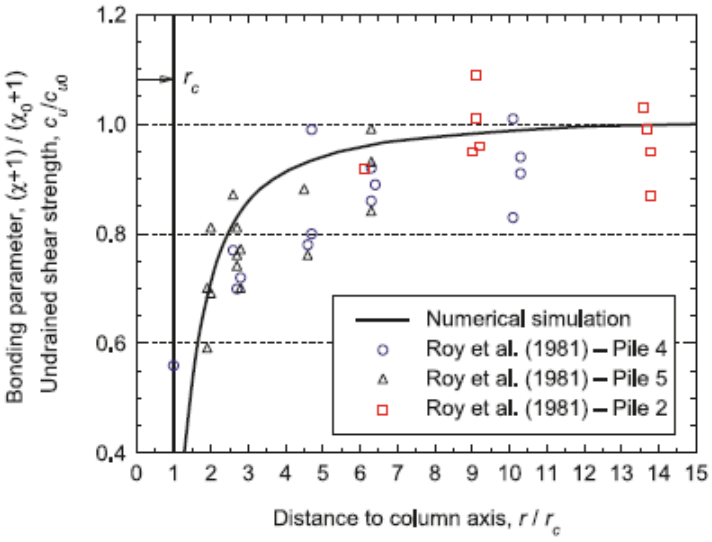

Figure 6.18: Destructuration computed numerically using the S-CLAY1S model, compared with field measurements after pile driving. Where $c_u = s_u$ and $r_c = r_0$. (Castro and Karstunen 2010)

From Figure 6.17 we can see that the S-CLAY1S model gives a slightly better fit to the final radial effective stress. However, there are no measurements close to the pile wall. Figure 6.18 shows that the S-CLAY1S model captures the destructuration pretty well. Destructuration is not included in any of the other material models mentioned up until now in this study, and from Figure 6.16 we can see that the destructuration/remoulding leads to an increase of the excess pore pressure for this specific case. A discussion on strain softening of the soil, and different ways of modeling this, can be found in Chapter 12.8.

6.5 Mesh dependency

The material models MCC, S-CLAY1 and S-CLAY1S all have a dry side to the left of the Coulomb line or the Critical state line. This means that the material models can give softening due to high OCR (S-CLAY1S gives softening due to destructuration as well), however softening generally leads to mesh dependency. This is an important side effect of using these material models, and it means that the solution depend on the mesh and that there is no unique solution found from finite element method (FEM). The reason for the mesh dependency comes from the fact that a thinner shear band dissipates less energy. Thus, the FEM solution will try to make the shear band as thin as possible. The thickness of the shear band then depends on the mesh, and with a finer mesh, the shear band becomes thinner and the failure load or safety decrease.

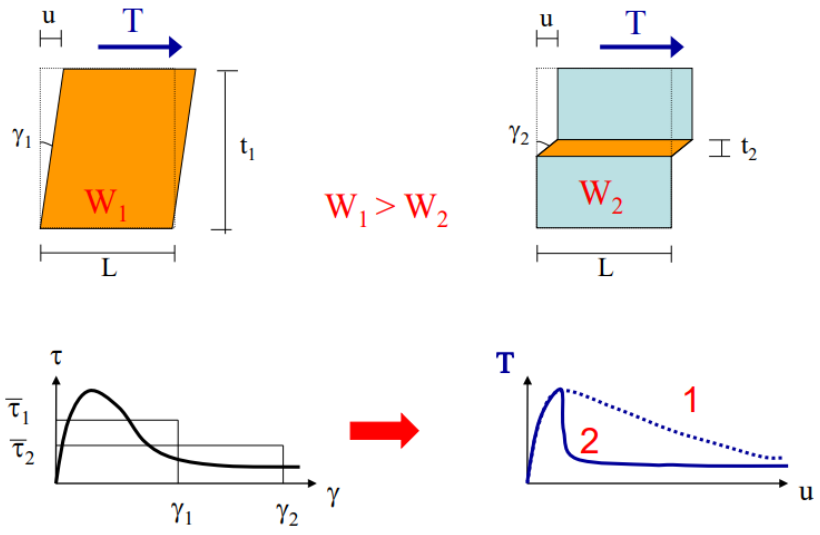

Figure 6.19: Effect of softening on shear band thickness and corresponding work. Where 1 represents a thicker shear band than 2. (Nordal 2018)

Figure 6.19 gives a graphical explanation of how the thinner shear band does less work and thus dissipates less energy. A thinner shear band (t) give the same deformation (u) as reaction to the shear force (T) by a larger shear strain (γ). In the bottom left plot we can see that for larger shear strains the material has less shear strength (τ) due to the softening effect. Therefore, by creating a thinner shear band with larger shear strain the material gives the same deformation, but does less work (W, (area in bottom right plot)). The shear band will therefore become infinitely thin due to the fact that the solution that requires the minimum amount of work always is chosen. In numerical software, the shear band becomes thinner with a finer mesh, and the solution will not converge. In nature, this is not the case. The real soil manages to take some advantage of the peak strength, and the shear band does not become infinitely thin. There are some different modeling solutions existing where you decide the minimum thickness of the shear band so that the solution converge, however there is no consensus in the geotechnical society on how thick this shear band should be.

7 The Strain Path Method

7.1 General

The Strain Path Method (SPM) was presented by Baligh (1985), and is an approximate analytical method to determine displacements when installing rigid objects in the ground. It was developed to solve deep penetration problems with the assumption that the shearing resistance has no influence due to the severe kinematic constrains in such problems. This means that the problem is strain controlled, and the error by estimating deformations using relatively "simple" soil properties is expected to be small.

Similarly, shallow problems are stress controlled and estimating the stress increments with simple soil models leads to small errors neglected by engineers, especially since there are major uncertainties regarding the in situ soil behavior. The deformations and strains are determined based on kinematic considerations and boundary conditions. Stresses and pore pressure is then approximated by the strains through a soil model which uses more "advanced" soil properties. The stresses would be exact if the problem is fully strain controlled, or if the "simple" soil properties give the exact displacement pattern of the actual problem.

Use of SPM for modelling driven piles in clay assumes undrained conditions, and that the strains can be determined based on the steady irrotational flow of an incompressible inviscid fluid. Inviscid means that the viscosity of the fluid is equal to zero, in other words the fluid has no shear resistance. Irrotational means that there is no swirls in the flow. This happens when the cross gradient of the velocity (i.e. shear strength) is zero. If inertial effects are neglected and assuming steady state, meaning for an observer moving with the penetrating object strains do not vary, then the penetration problem reduces to a flow problem where soil particles move along streamlines around a fixed rigid body. (Baligh 1985)

Table 7.1 compares the stress path method (i.e. stress controlled problems) and the strain path method (i.e. strain controlled problems).

Table 7.1: Comparison of the Stress Path Method and the Strain Path Method. (Baligh 1985)

Stress path method	Strain path method
a. APPLICATIONS	
Shallow Problems: Depth of soil of interest is relatively small compared to its lateral extent.	*Deep Problems*: Soil of interest is relatively deep below ground surface compared to its lateral extent.
b. STEPS	
1. Estimate initial stresses. 2. Estimate incremental *stresses*. 3. Perform stress path tests on samples (or use adequate soil model) to obtain strains at selected locations. 4. Estimate deformations by integrating strains.	1. Estimate initial stresses. 2. Estimate incremental *strains*. 3. Perform strain path tests on samples (or use adequate soil model) to obtain effective stresses at selected locations. 4. Estimate pore pressures by integrating equilibrium equations.
c. APPROXIMATIONS	
In Step 2 stresses are approximate thus leading to path-dependent deformations in Step 4, i.e., strains violate some compatibility requirements.	In Step 2 strains are approximate thus leading to either: (1) Path dependent pore pressures in Step 4, i.e., total stresses violate some equilibrium requirements; or (2) effective stresses that violate some constitutive relations.
d. ITERATION (IMPROVEMENT OF SOLUTION)	
Use results of Step 3 to improve estimates in Step 2.	Use results in Step 3 to improve estimates in Step 2.

In Step 2 in Table 7.1, one must estimate a velocity field that satisfy the conservation of volume requirement and the boundary conditions. From this, the soil deformations can be computed by integration along streamlines. Strain rates can then be computed along the streamlines by differentiating the velocities with respect to the spatial coordinates. Integrating the strain rates along the streamlines then gives the strain path of a soil element.

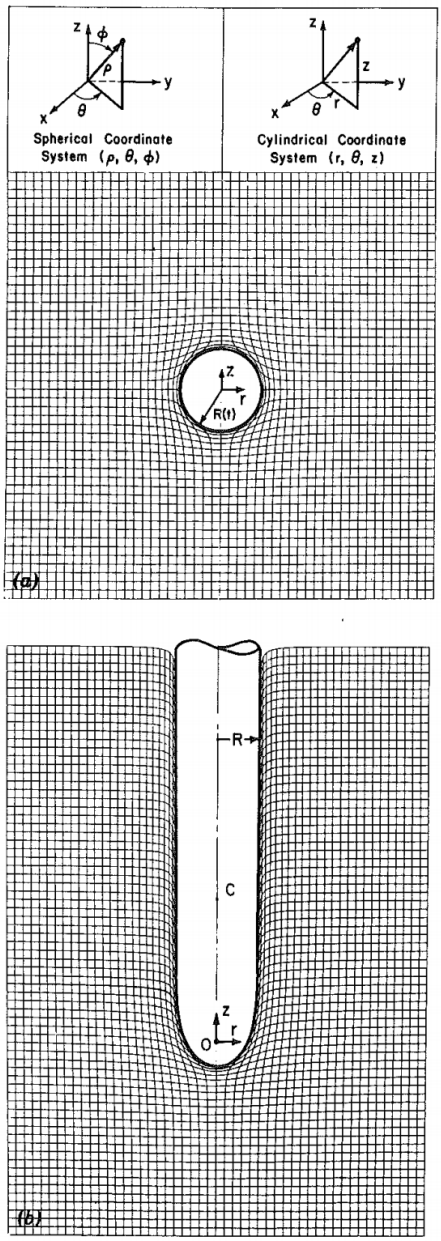

Figure 7.1: Deformation of a Square Grid in Saturated Clays: (a) During Deep Spherical Cavity Expansion (or Single Source); (b) During Penetration of "Simple Pile". (Baligh 1975)

When obtaining the solution presented in Figure 7.1 a), Baligh (1985) looked at a spherical cavity expanding in an infinite, incompressible (i.e. undrained), isotropic and homogeneous material with isotropic initial stresses. The velocity field is then given by:

$$v_r = \frac{V}{4\pi}\frac{r}{(r^2+z^2)^{3/2}}, v_\theta = 0 \; and \; v_z = \frac{V}{4\pi}\frac{z}{(r^2+z^2)^{3/2}} \tag{7.1}$$

where v is the velocity in the radial, circumferential and vertical direction based on the subindex, V is the volume of the pile, and r, θ and z is the cylindrical coordinates of the soil element investigated. In Figure 7.1 b) Baligh (1985) uses Equation 7.1, and assumes an constant uniform flow with velocity U giving:

$$v_r = \frac{V}{4\pi}\frac{r}{(r^2+z^2)^{3/2}}, v_\theta = 0 \; and \; v_z = \frac{V}{4\pi}\frac{z}{(r^2+z^2)^{3/2}} + U \tag{7.2}$$

So quite simple assumptions involving the velocity fields are done, and these can be used to solve for different shapes of the tip. It is also worth noting that the SPM method includes the downward motion induced by the pile installation giving vertical deformations, which are not included when CEM is used. (Baligh 1985)

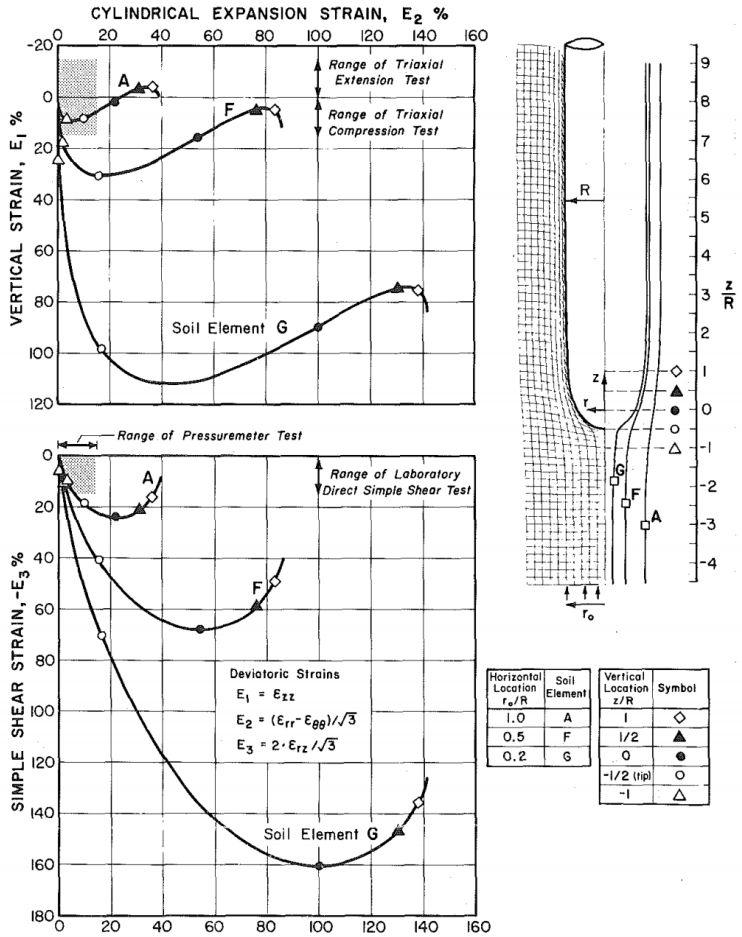

Figure 7.2: Deviatoric strain paths during penetration of a "Simple Pile". (Baligh 1985)

Figure 7.2 shows the deviatoric strains $E_{1,2,3}$ defined in the figure for different soil elements, and at different depths during penetration of a "simple pile". The "simple pile" has rounded tip to ensure smooth laminar flow around the tip, avoiding singularities and enabling a mathematical formulation of the displacements.

E_1 is imposed in a conventional triaxial test, E_2 is imposed when using a pressure meter or for a cylindrical cavity expansion, and E_3 is imposed in the direct simple shear test. The figure also shows the corresponding maximum strain these tests normally impose. Figure 7.2 shows us that the strain levels encountered in pile installation are much larger than what we apply in the laboratory. The post peak behavior of the clay can therefore be expected to have large influence on the resulting stresses and pore pressure.

Soil elements A, F and G represents different streamlines where the horizontal distance to the pile differ. The different symbols represents different vertical positions on the streamlines. The different vertical positions give an aspect of what happens with time. The soil element goes from the triangle with no fill to the tilted square with no fill as the pile is penetrated. We see from the figure a reversal of the strain as the tip has passed. This is an unloading procedure that could have a large influence on the final stresses. Figure 7.2 indicate that the soil will fail due to vertical compression mainly (i.e. E_1 strain).

In SPM the strains does not need to be monotonic. From Figure 7.2 one can see reversals of strains E_1 and E_3. E_2 does not reverse, but that is due to the tip geometry according to Baligh (1985). Strain reversal is very important when estimating the stresses and the pore pressure, some have neglected it due to the fact that if the last strain increment is of a certain magnitude then the history of the material is "erased". Baligh (1985) does however empathize the importance of strain history even for large deformation problems. The shaded area in Figure 7.2 shows the soil that experience a strain rate higher than 14000 times that applied in a conventional undrained triaxial test. High strain rate has shown to increase the peak strength, reduce the strain to peak and increase the softening behavior. (Baligh 1985)

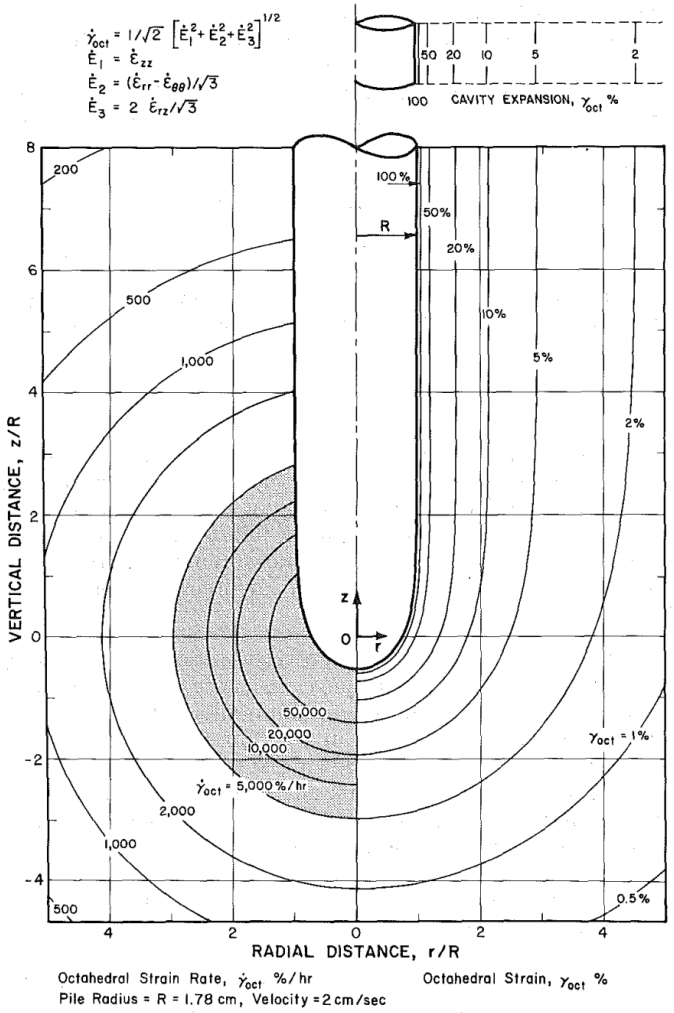

Figure 7.3: Strain and Strain Rate Contours during penetration of a "Simple Pile". (Baligh 1985)

Figure 7.3 indicate that the strains far behind the tip correspond to that of the cylindrical cavity expansion method. Baligh (1985) concretizes that this does not mean the same solution for stresses and pore pressure is obtained, as previously discussed. In addition, the vertical deformations that are neglected in CEM has an effect on the octahedral strains close to the pile wall. Figure 7.3 has been constructed using the von Mises yield criterion, which yields for two percent octahedral shear strain. The shape of the inner plastic zone (i.e. from $2\%\gamma_{oct}$ and inwards) will change somewhat using a different yield criterion. (Baligh 1985)

7.2 The MIT-E3 model

CEM has been combined with anisotropic, non-linear, strain softening material models. The same has also been done with SPM, but since the method was developed at MIT most results obtained by using SPM is coupled with the MIT-E1/2/3 material models. A few years before Baligh (1985) presented SPM, Baligh and Levadoux (1980) presented a total stress based material model called Prévost-Levadoux-Baligh (PLB), based on the model presented by Prévost (1977). Two years after this Kavvadas (1982) presented an effective stress based material model called MIT-E1, which could reasonably well simulate results from triaxial extension and compression test as well as the direct simple shear tests for lightly overconsolidated clays. Baligh (1985) further refined the effective stress based model to better fit results for overconsolidated clays. This model was named the MIT-E2 model. Lastly, Whittle (1987), (1992) presented the MIT-E3 model, which was a modification of the MIT-E2 model to enhance the fit to triaxial compression, direct simple shear tests and unloading/reloading in oedometer tests. The MIT-E3 model is quite similar to the S-CLAY1S model. The principles of the models are the same, but the formulation differ. The rotational hardening law is for example slightly different in the two models. We will not go into detail of the differences in the models, as it is quite theoretical and not that relevant for this study.

7.3 Comparison between CEM and SPM

In the following are predictions obtained with CEM and SPM, coupled with various material models presented. Figure 7.4 shows the predictions produced by CEM in the top two plots and by SPM in the two plots below. The predictions have been produced using MCC (dash-dot line), MIT-E1 (solid line) and PLB (dotted line), as material models for normally consolidated Boston Blue Clay (BBC). Comparing SPM to CEM, we see that SPM predicts much lower radial stress and excess pore pressure at the pile shaft than CEM does using the same material model. This is due to the unloading as the pile tip has passed, which can be seen in Figure 7.2, while CEM only apply increasing radial and circumferential strain. At a normalized radius of approximately ten, the results using SPM and CEM follow each other quite closely. The effect of using SPM is thus a reduction of stresses at the pile surface and in the close vicinity of the pile. Comparing MCC to the MIT-E1 model we see that the predicted excess pore pressure is approximately 30% lower for the MIT-E1 model than for the MCC

model. The MIT-E1 model also predicts lower radial stress than the MCC model, more or less equal to the initial condition at the pile shaft.

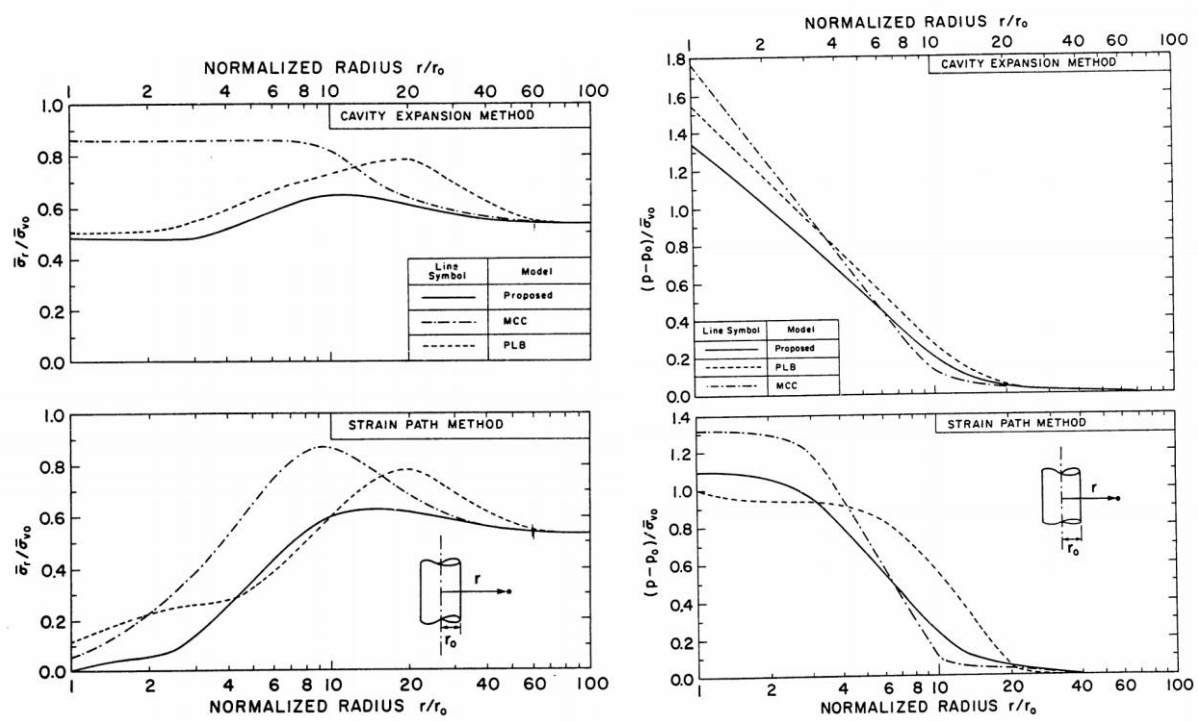

Figure 7.4: Comparison of effects of soil models (MIT-E1 solid line, PLB dotted line and MCC dash-dot line) and installation models (Cavity Expansion Method top two plots, Strain Path Method bottom two plots) on radial stresses (plots to the left) and excess pore pressures (plots to the right) surrounding a closed-ended pile. Input parameters are based on Boston Blue Clay (BBC) with $OCR = 1$. Where $\bar{\sigma}_r = \sigma'_r$, $\bar{\sigma}_{vo} = \sigma'_{vo}$ and $(p - p_0) = \Delta u$. (Kavvadas 1982)

The effect of reduced stresses using the MIT-E1 model is most likely due to strain softening according to Karlsrud (2012). However, Figure 7.5 shows that the parameters of the MCC model is chosen so that higher shear stresses are allowed, compared to that of the PLB and MIT-E1. The decrease in excess pore pressure compared to what CEM-MCC predicts can then solely be due to lower shear stresses and not softening. The effect of softening when included in CEM is discussed in more detail in Chapter 12.8. The conclusion is that softening causes higher excess pore pressure when included in CEM, not a decrease. Due to the difference in allowed shear stress, Figure 7.4 must mainly be used to compare CEM and SPM for the same soil model.

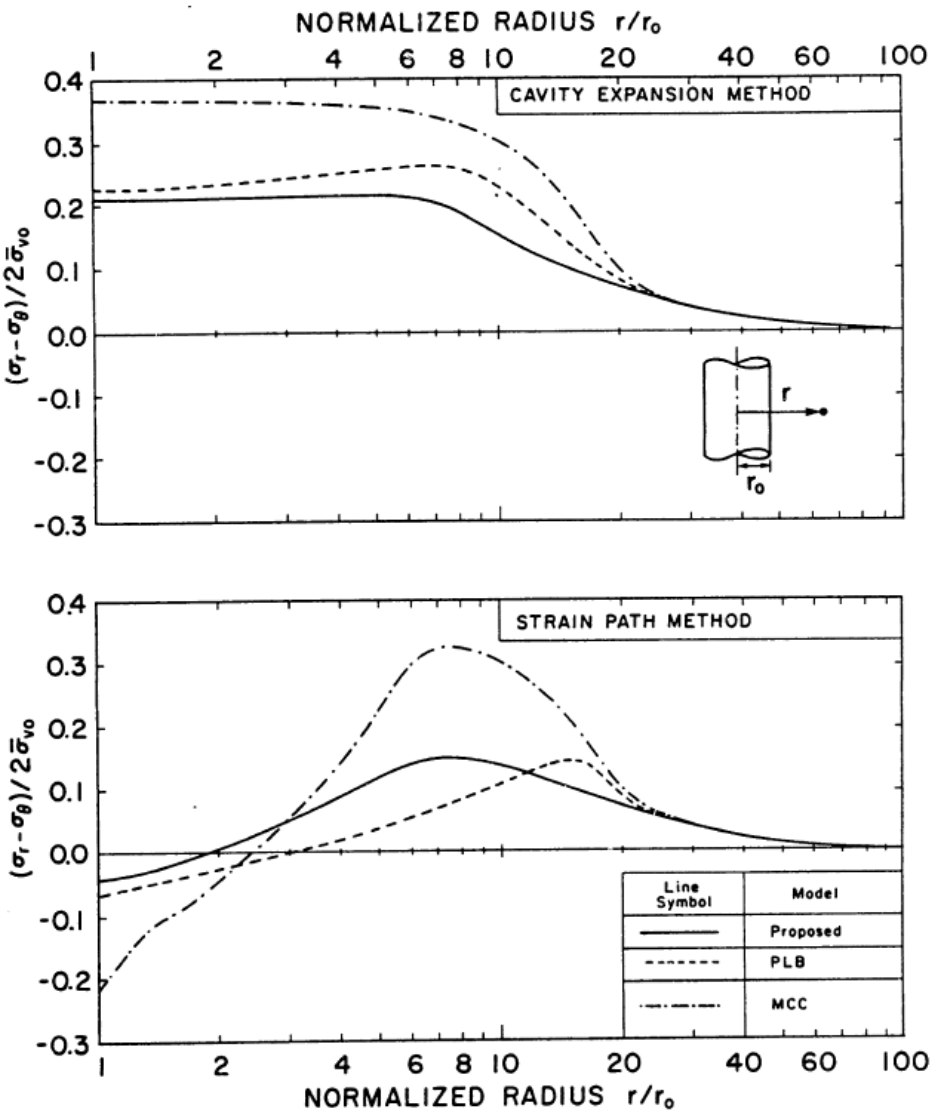

Figure 7.5: Comparison of effects of soil models (MIT-E1 solid line, PLB dotted line and MCC dash-dot line) and installation models (Cavity Expansion Method top two plots, Strain Path Method bottom two plots) on radial stresses (plots to the left) and excess pore pressures (plots to the right) surrounding a closed-ended pile. Input parameters are based on Boston Blue Clay (BBC) with $OCR = 1$. Where $\bar{\sigma}_{vo} = \sigma'_{vo}$. (Kavvadas 1982)

Figure 7.6 shows the predicted stresses by SPM and CEM in the same plot. Input parameters are based on a normally consolidated Boston Blue Clay (BBC). We see the same tendency as in Figure 7.4, SPM gives lower predictions than CEM at the pile surface and at a radial distance of ten times the pile radius the solutions give approximately the same answer.

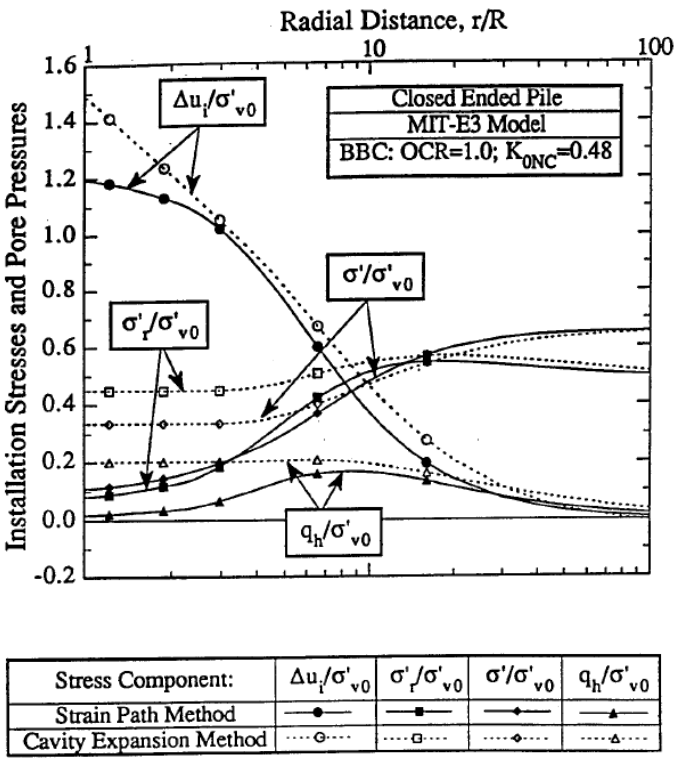

Figure 7.6: Comparison between stresses predicted with the Cavity Expansion Method and the Strain Path Method coupled with the MIT-E3 material model for Boston Blue Clay (BBC). Where $\Delta u_i = \Delta u_{max}, q_h = q, \sigma' = p'$. (Whittle 1992)

Table 7.2 summarizes some key parameters gathered from different sources. This gives an easy comparison of SPM and CEM for different clays, OCR, and the resulting effect on the predicted excess pore pressure at the pile shaft. The data from Table 7.2 has also been used by Karlsrud (2012) to create plots showing the effect of OCR on predicted excess pore pressure (Figure 7.7) and radial stress (Figure 7.8), with different material models and modeling methods. Table 7.2 shows that SPM leads to lower excess pore pressure and effective stresses than CEM in all the cases. We also see that MIT-E3 gives somewhat higher stresses than the previous versions of the model. Based on Figure 7.5, one should however be careful comparing different material models to each other as the allowed maximum shear stress is not constant.

Table 7.2: Predictions of normalized stresses against the pile shaft predicted with different installation models (i.e. modeling methods) and material models for different types of clays and OCR. Where $K_i = {\sigma'_{ri}}/{\sigma'_{z0}}$ and $K_c = {\sigma'_{rc}}/{\sigma'_{z0}}$ (i.e. the radial effective stress directly after installation and after consolidation respectively, over the initial vertical effective stress. (Karlsrud 2012)

Clay type	OCR	Inst. model	Soil model	$\Delta u_i / \sigma'_{vo}$	K_i	K_c	Reference
BBC	1.0	CEM	MCC	1.77	0.86	1.54	Kavvadas (1982)
		CEM	MITE1	1.34	0.50	0.88	
		SPM	MCC	1.32	0.06	1.30	
		SPM	MITE1	1.1	0.00	0.40	
BBC	1.2	SPM	MITE1	1.19	0.02	0.56	
BBC	1.35	SPM	MITE1	1.32	0.04	0.80	
Empire	1.5	CEM	MCC	2.31	1.14	1.67	Baligh (1985b)
		SPM	MCC	1.31	0.34	1.34	
		SPM	MITE2	1.36	0.19	0.72	
Empire	2.0	CEM	MCC	2.76	1.43	2.11	
		SPM	MCC	1.56	0.44	1.79	
		SPM	MITE2	1.56	0.29	1.30	
BBC	1.0	CEM	MITE3	1.49	0.45	-	Whittle (1987)
	1.5	CEM	MITE3	2.08	0.70	-	
	2.0	CEM	MITE3	2.42	0.85	-	
	4.0	CEM	MITE3	3.65	1.44	-	
BBC	1.0	SPM	MITE3	1.20	0.08	0.40	
	1.5	SPM	MITE3	1.49	0.17	0.60	
	2.0	SPM	MITE3	1.68	0.20	0.70	
	4.0	SPM	MITE3	2.50	0.28	1.13	

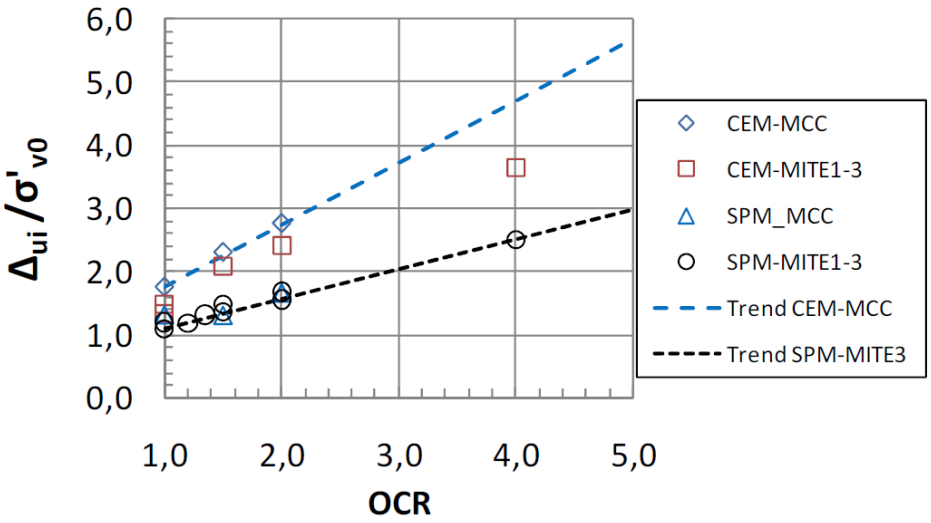

Figure 7.7: Comparison of normalized excess pore pressure at the pile shaft versus OCR for CEM and SPM with different material models based on the data from Table 7.2. Where $\Delta_{ui} = \Delta u_{max}$. (Karlsrud 2012)

Figure 7.7 shows that the ratio between the predicted excess pore pressures found by CEM and SPM are increasing with OCR when normalized with the initial effective vertical stress. SPM gives a lower estimate of the excess pore pressure independent of the material model compared to CEM, and the difference increase with OCR.

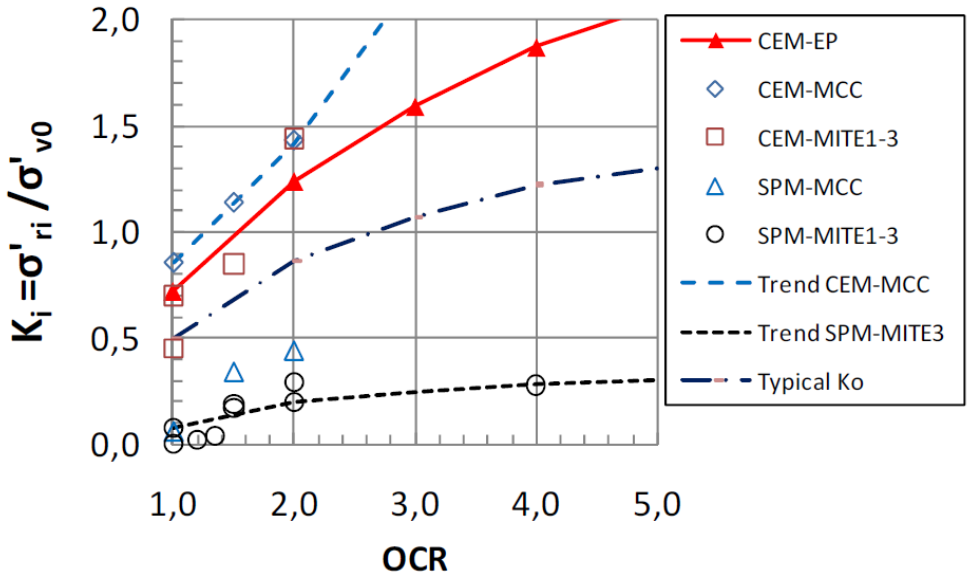

Figure 7.8: Comparison of normalized radial effective stresses at the pile shaft versus OCR for CEM and SPM with different material models based on the data from Table 7.2. (Karlsrud 2012)

Figure 7.8 shows the quite large difference in normalized radial stress after pile driving produced by SPM and CEM. The difference between the predictions is also here increasing with OCR, and SPM produces lower radial effective stress compared to CEM, independent of the material model.

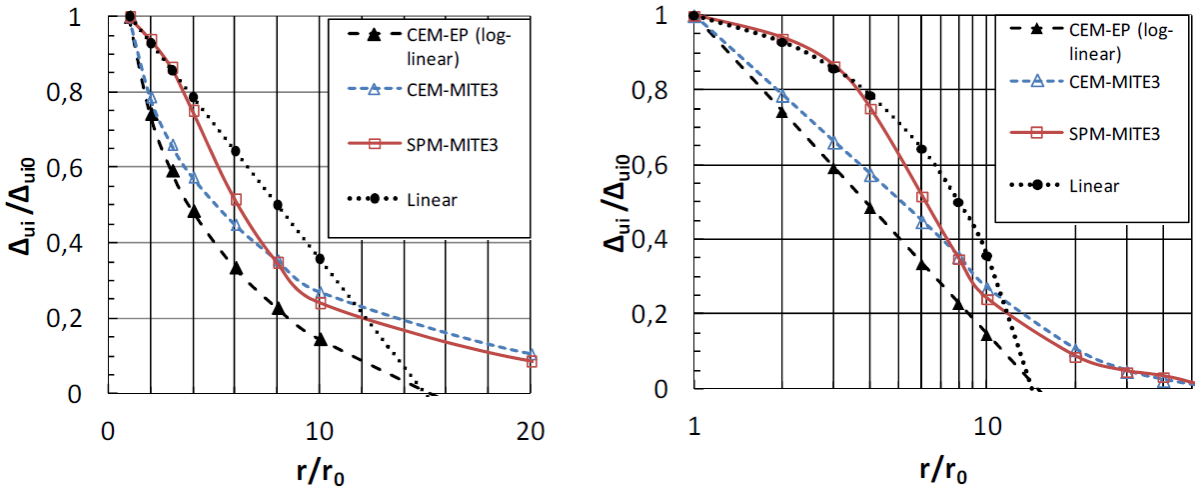

Figure 7.9: Distribution of excess pore pressure predicted by CEM and SPM for BBC with $OCR = 1{,}5$. Where $\Delta_{ui} = \Delta u$ and $\Delta_{ui0} = \Delta u_{max}$. Based on results from Whittle (1987), plotted by Karlsrud (2012).

Figure 7.9 shows the difference in the predicted radial distribution of the excess pore pressure with $OCR = 1{,}5$. The excess pore pressure is normalized to the prediction at the pile surface, thus giving the maximum value one, at the pile shaft. The elastic-perfectly plastic (EP) Tresca solution gives a shorter tail, meaning that the excess pore pressure has a shorter radial extent.

CEM coupled with MIT-E3 give almost a log-linear decrease, but curves slightly in the end. SPM together with MIT-E3 has an entirely different appearance. It is quite similar to CEM after about ten times the pile radius as previously mentioned, but before that the excess pore pressure is at a higher level than for CEM. Comparing Figure 7.9 to Figure 7.6 we see that the SPM predicts a lower value of the excess pore pressure at the pile shaft, but then it decreases much more slowly close to the pile than what CEM predicts. After about three times the pile radius, the decrease speeds up until eight times the pile radius, where the results of SPM and CEM become quite similar.

The conclusion is therefore that CEM and SPM predicts quite similar radial strains, but SPM also introduce vertical strains. This causes an unloading procedure as the pile tip passes. This unloading procedure do not affect the stresses far away from the pile, but close to the pile the stresses obtained with SPM are of a lower magnitude than CEM. The radial distribution is then also different, where SPM predicts a close to constant level, while CEM predicts a decrease close to the pile. Far away from the pile the distributions, as well as the predicted stresses, become quite similar.

8 Empirical and semi-empirical methods

8.1 General

In this chapter, some empirical and semi-empirical methods are presented and discussed briefly. Most of the methods are quite old, more recent estimates seem to be based on measurements from similar places instead of an empirical formula. Most of the methods presented are based on an assumption of no change in vertical pressure. Some of the methods are modifications of the analytical elastic-perfectly plastic (EP) solution presented by Gibson and Anderson (1961) to a more realistic stress state.

8.2 Nishida (1963)

Nishida (1963) used the CEM-EP solution presented in Chapter 5. However, the solution assumes plane strain, and introducing a different initial pressure in the vertical direction is impossible in the analytical solution. It has been solved for different stresses in the plane, but out of the plane stress is not considered when assuming plane strain, other than through Equation 4.5 where the change is set equal to the sum of the in plane stress multiplied with poisons ratio, as continuum mechanics dictate. Nishida (1963) assumed no change in the vertical stress, and changed the initial stresses to a more relevant case as seen in Figure 8.2. He further assumed the change of the in plane stresses to be equal to the change found in the analytical solution, and also kept the plastic radius equal. He set the excess pore pressure equal to zero in the elastic zone and equal to the change in mean stress in the plastic zone (i.e. $D = 0$).

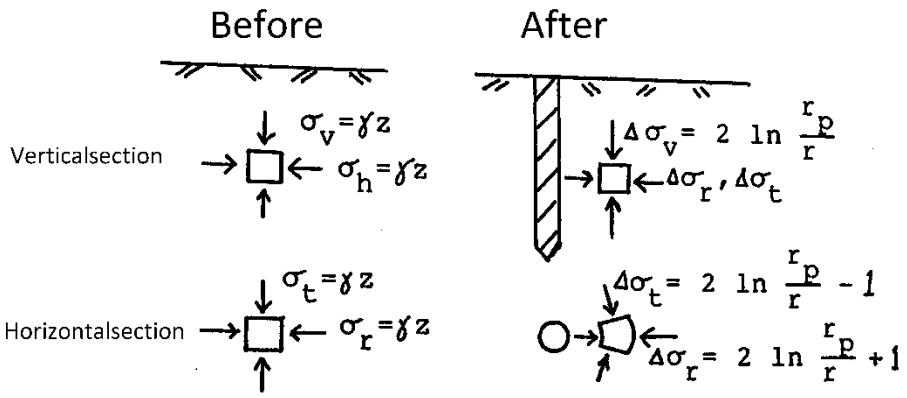

Figure 8.1: Stress conditions from the analytical solution of a cavity expansion in an elastic-perfectly plastic Tresca material (CEM-EP). Initial stress conditions to the left and the stress changes after pile driving to the right. Where $\sigma_t = \sigma_\theta$. (Berg-Knutsen 1986)

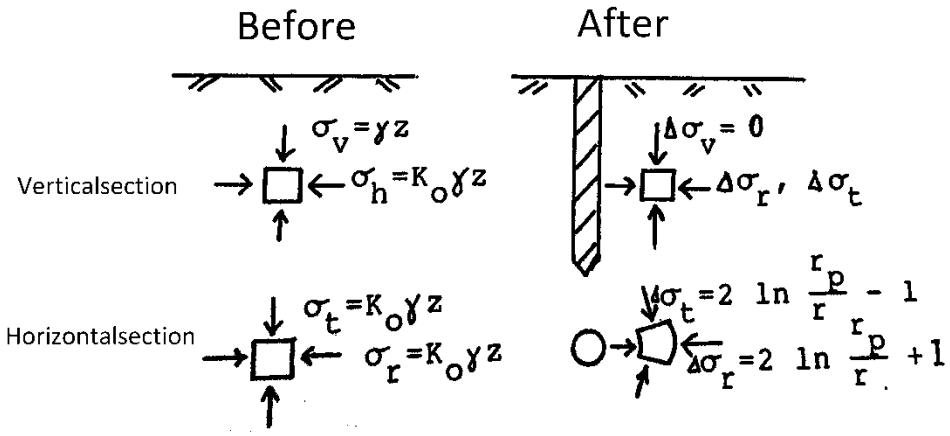

Figure 8.2: Stress conditions assumed by Nishida (1963). Initial stress conditions to the left and changes of stress after pile driving to the right. Where $\sigma_t = \sigma_\theta$ and $\gamma z = \sigma_{v0}$. (Berg-Knutsen 1986)

The excess pore pressure is set equal to the change of the mean stress in the plastic zone. Using the stresses seen in Figure 8.2 this gives:

$$\frac{\Delta u}{s_u} = \frac{4}{3} ln \frac{r_p}{r} \tag{8.1}$$

If Janbu's pore pressure equation (Chapter 3.4, Equation 3.13) is used then the excess pore pressure is given by:

$$\frac{\Delta u}{s_u} = \frac{4}{3} ln \frac{r_p}{r} - D(2 - \frac{\sigma_{v0}}{s_u}(1 - K_0)) \tag{8.2}$$

In the elastic zone, the excess pore pressure is assumed equal to zero. Inserting Equation 5.2 and $r = r_0$ into Equation 8.1, gives a maximum excess pore pressure equal to:

$$\frac{\Delta u}{s_u} = \frac{2}{3} ln \frac{G_u}{s_u} \tag{8.3}$$

This means that the method of Nishida (1963) is simply reducing the maximum excess pore pressure by 33%, if the excess pore pressure is assumed equal to the change in total mean stress. Appendix B.1 shows residual plots of the prediction based on Equation 8.3 compared to the measured data presented in Chapter 13 and Table 13.6.

Comparing the residual plot obtained by using the method of Nishida (1963) (i.e. Figure B.1.1 and B.1.2) to the residual plot obtained when using CEM-EP (i.e. Equation 14.6, Figure 14.1 and Figure 14.2) we see that CEM-EP have a better fit for the low OCR clays. The high OCR clays are not captured by any of the methods, but due to dilation, the excess pore pressure is low and hence the method of Nishida (1963) fits better as he reduce the predicted excess pore pressure of CEM-EP by 33%.

Using CEM and numerical software makes it possible to introduce the initial stress condition that Nishida (1963) describes. This will then be solved for the given material model and the assumptions Nishida (1963) makes become unnecessary. However, it shows the implicit assumptions that Gibson and Anderson (1961) makes in order to develop the analytical solution of a Tresca material (i.e. plane strain $\varepsilon_z = 0$ and $\Delta\sigma_v = 0{,}5(\Delta\sigma_r + \Delta\sigma_\theta)$ in the plastic zone).

8.3 Lo and Stermac (1965)

Lo and Stermac (1965) proposed a semi-empirical expression for the maximum pore pressure at the pile shaft. The initial conditions are assumed equal to the ones described by Nishida (1963) in Figure 8.2. When the pile is driven, the direction of the maximum strain is assumed to be radial. The vertical stress is after piling assumed as the minor principal stress, while the radial becomes the major. The excess pore pressure is assumed to be composed of two parts. The first part is a result of an increase of the total ambient pressure ($\Delta\sigma_3$). The second part is a result of the shearing.

$$\Delta u_a = \Delta\sigma_3 = (1 - K_0)\sigma'_{v0} \tag{8.4}$$

where the second equality assumes that the vertical total stress is unchanged after pile driving. The proposed solution can be written as:

$$\Delta u_{max} = \Delta u_a + \Delta u_s = ((1 - K_0) + \left(\frac{\Delta u}{\sigma'_c}\right)_{max})\sigma'_{v0} \tag{8.5}$$

where $\left(\frac{\Delta u}{\sigma'_c}\right)_{max}$ is the maximum pore pressure ratio that is measured in a conventional undrained triaxial test, and σ'_c is the consolidation pressure used in the test. The pore pressure ratio is increasing with the applied stress until it reaches its maximum and remains constant after a certain strain is achieved. Lo and Stermac (1965) argues that the pore pressure ratio is independent of the direction of the stress path, time of the sustained load, and the consolidation pressure for normally consolidated clays. This is also the reason for using the pore pressure ratio. The proposed formula was checked with measurements, as seen in Figure 8.3. In Figure 8.3 the estimations are the dotted lines close to the vertical axis, and show a reasonable estimate given the data. However, there were no measurements on the pile shaft, and an empirical method to estimate the pore pressure at the pile surface should include, and be compared to, measurements at the pile wall.

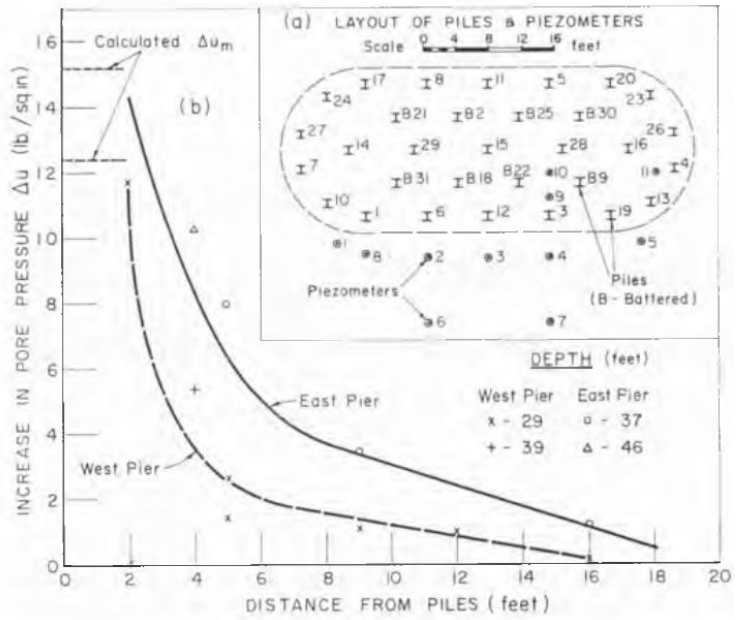

Figure 8.3: (a) Layout of piles and piezometers; (b) distribution of excess pore pressures, Wabi river. (Lo and Stermac 1965)

8.4 Blanchet (1976)

Blanchet (1976) did some modifications to the solution presented by Lo and Stermac (1965). He found that the pore pressure ratio became constant when the consolidation pressure in the triaxial test was equal to the preconsolidation pressure (p_c') of the soil. Blanchet (1976) then proposed the modification:

$$\Delta u_{max} = (1 - K_0)\sigma_{v0}' + \left(\frac{\Delta u}{\sigma_c'}\right)_{max} p_c' \tag{8.6}$$

(Bozozuk, Fellenius et al. 1978). The method of Blanchet (1976) and Lo and Stermac (1965) have not been checked against the empirical data presented in Table 13.6, as we do not have data on the ratio $\left(\frac{\Delta u}{\sigma_c'}\right)_{max}$. However, Berg-Knutsen (1986) have included these two methods in a comparison with CEM-EP, the expansion of a spherical cavity, and the methods of Nishida (1963) and Svanø (1978), as seen in Figure 9.2 and Figure 9.3. From these figures we see that the method of Lo and Stermac (1965) gives a lower estimate of the excess pore pressure than the method of Blanchet (1976). Both methods are however below the prediction obtained by using the method of Nishida (1963), which is shown to under-predict the data presented in Table 13.6.

8.5 Svanø (1978)

Svanø (1978) argued that the modifications applied by Nishida (1963) is not correct since the minor principle stress is equal to the vertical stress after pile driving close to the pile surface. Svanø (1978) assumes that the passive earth pressure model for undrained analysis can be applied. If the roughness ratio (r) is assumed equal to zero, then the increase of the horizontal stresses become $2s_u$. Figure 8.4 shows the initial stress condition to the left, and the stress conditions after pile driving given the assumptions above.

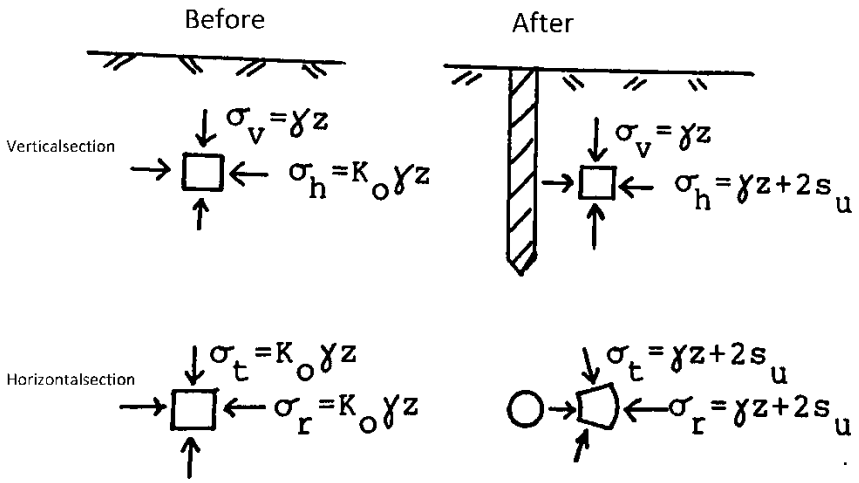

Figure 8.4: Stress conditions assumed by Svanø (1978). Initial stress conditions to the left and changes of stress after pile driving to the right. Where $\sigma_t = \sigma_\theta$ and $\gamma z = \sigma_{v0}$. (Berg-Knutsen 1986)

If Janbu's pore pressure equation (Chapter 3.4, Equation 3.13) is used together with the stress condition shown in Figure 8.4, then the maximum excess pore pressure at the pile surface is given by:

$$\frac{\Delta u_{max}}{s_u} = 2\left(\frac{2}{3} - D\right) + \frac{\sigma_{v0}}{s_u}\left(\frac{2}{3} + D\right)(1 - K_0) \tag{8.7}$$

(Berg-Knutsen 1986). If one assumes the excess pore pressure to be equal to the change in total mean stress then Figure 8.4 gives:

$$\frac{\Delta u_{max}}{s_u} = \frac{2}{3}\left((1 - K_0) * \frac{\sigma_{v0}}{s_u} + 2\right) \tag{8.8}$$

Equation 8.8 has been checked against the data of Table 13.6, and residual plots are presented in Appendix B.2. Figure B.2.1 and B.2.2 shows an interesting fit to the data. The adjusted coefficient of determination is $\bar{R}^2 = 0{,}285$, which is higher than what CEM-EP predicts (i.e. $\bar{R}^2 = -4{,}21$ see Chapter 14.3). However, if only the data with $OCR \leq 2$ is included CEM-EP gives $\bar{R}^2 = 0{,}689$ while Equation 8.8 gives $\bar{R}^2 = 0{,}225$. As discussed in Chapter 14.3 CEM-EP gives a relatively good fit to the low OCR data, but over-predicts the high OCR clays grossly. Equation 8.8 gives a better fit when including the high OCR clays than CEM-EP, but the fit is not satisfactory, including or excluding the high OCR clays.

8.6 Hagerty and Garlanger (1972)

Hagerty and Garlanger (1972) used the geometry of the total stress path of an earth element close to the pile wall to estimate the maximal pore pressure. If the vertical pressure is assumed constant, then the pile driving only leads to an increase of the horizontal pressure. A passive triaxial test is conducted in a similar manner. The axial stress (σ_{axial}) is kept constant, while the cell pressure (σ_{cell}) is increased. The difference between the total stress path and the effective stress path then gives the excess pore pressure, and the maximum is reached at failure. Figure 8.5 shows the principle of the passive triaxial test, and using the figure one can find the expression of the maximum excess pore pressure as:

$$\frac{\Delta u_{max}}{\sigma'_{v0}} = 1 - \left(\frac{1 - \sin(\varphi_p)}{\sin(\varphi_p)}\right)\left(\frac{s_u}{\sigma'_{v0}}\right)_p \tag{8.9}$$

where the parameters should all be determined from a passive undrained triaxial test, hence the subtext p. The parameters needed to use Equation 8.9 is not included in the dataset of Table 13.6, therefore the fit of this approximation have not been checked. (Berg-Knutsen 1986)

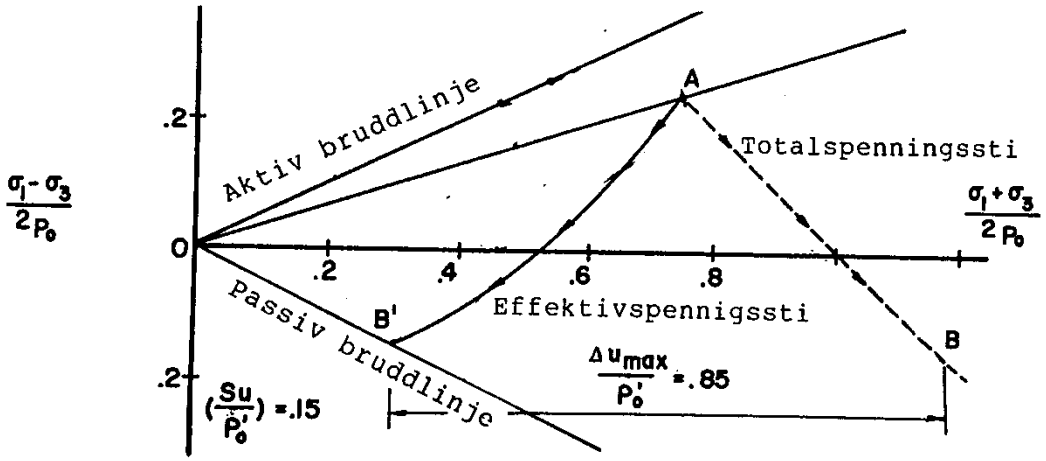

Figure 8.5: Maximal pore pressure ratio in a passive triaxial test. Where; Aktiv bruddlinje = Active failure line, Passiv bruddlinje = Passive failure line, Effektivspenningssti = Effective stress path, Totalspenningssti = Total stress path and $p_0 = \sigma_{v0}$. (Berg-Knutsen 1986)

8.7 Broms and Massarch (1979)

Broms and Massarch proposed an estimation close to the pile wall in normally consolidated clay based on empirical data. The formula is rendered by Berg-Knutsen (1986) as:

$$\frac{\Delta u_{max}}{s_u} = 2ln\sqrt{\frac{E_u}{4{,}5s_u}} + 0{,}8 \tag{8.10}$$

The prediction obtained by using Equation 8.10 is checked against the empirical data presented in Chapter 13 and Table 13.6, and the resulting residual plots are presented in Appendix B.3. Looking at the residual plots (i.e. Figure B.3.1 and B.3.2) we see that Equation 8.10 over-predicts the excess pore pressure grossly for all but one measurement done at the Empire site.

9 Comparison of prediction methods to measurements

From the previous chapters it has been shown that the solution for the excess pore pressure found by the Cavity Expansion Method (CEM) is close to a linear curve in the $\Delta u - \ln(r)$ plane regardless of the material model. This linear relationship occurs in the plastic zone for the elastic-perfectly plastic Tresca material (EP), and in the critical state region for the Modified Cam Clay (MCC) model. In other words, the excess pore pressure is assumed to be decaying logarithmic with r close to the pile wall. Figure 9.1 shows field measurements on low OCR clays together with a least square fit line based on the assumption of a linear decay of the excess pore pressure with a slope of $2s_u$ against $\ln(r)$. This decrease of $2s_u$ with $\ln(r)$, is found when using the CEM-EP model as seen in Chapter 5. However, the maximum pore pressure at the pile shaft is not found with CEM-EP, but have been calibrated to fit the data.

Figure 9.1 shows that the radial extent of the pore pressure field is captured with a simple model such as CEM-EP given that the maximum excess pore pressure at the pile shaft is known. The pore pressure distribution in the two upper graphs seems to correspond well to a linear decrease with the logarithm of r. The bottom graph does however seem to be closer to the shape obtained with the Strain Path Method (SPM), seen in Figure 9.6.

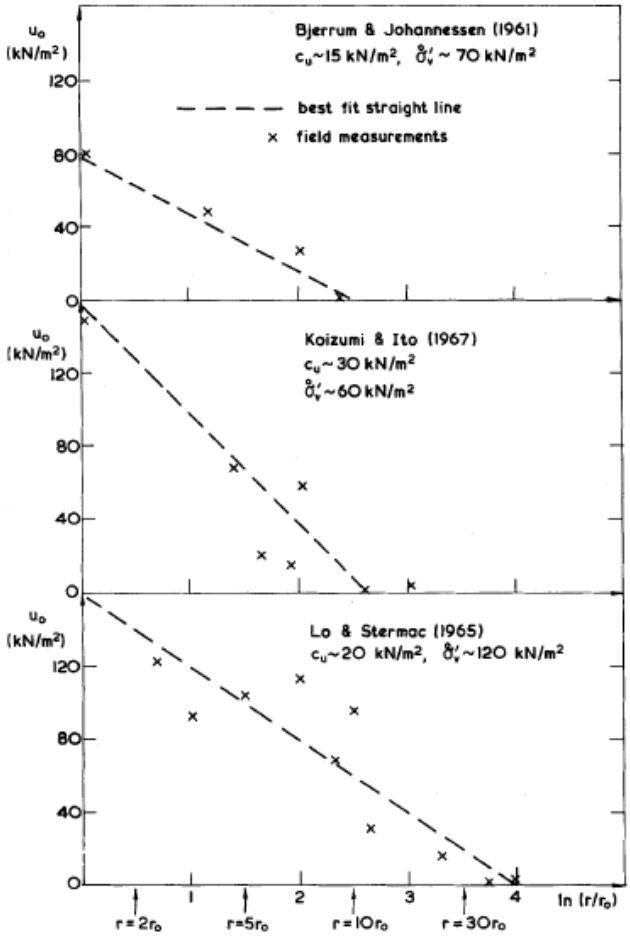

Figure 9.1: Field measurements of excess pore pressures resulting from pile driving. Broken line is the best fit straight line with a slope of $2s_u$. Where $u_0 = u$. (Randolph and Wroth 1979)

Figure 9.2 and Figure 9.3 show data obtained by Roy, Blanchet et al. (1981). They conducted full scale tests on instrumented piles in St. Alban clay. Berg-Knutsen (1986) compared the measured excess pore pressure to predictions obtained by CEM-EP (called Vesic, syl.), spherical cavity expansion in an elastic-perfectly plastic material (called Vesic, sf.), and some of the empirical methods presented in Chapter 8. “Passivt j.” refers to the method of Svanø (1978) from Chapter 8.5. The other methods are referring to the name of the engineer/scientist that proposed the solution (see Chapter 8). From Figure 9.2 we see that CEM-EP over-predicts the excess pore pressure at the pile surface, but the radial extent of the pore pressure field is predicted correctly.

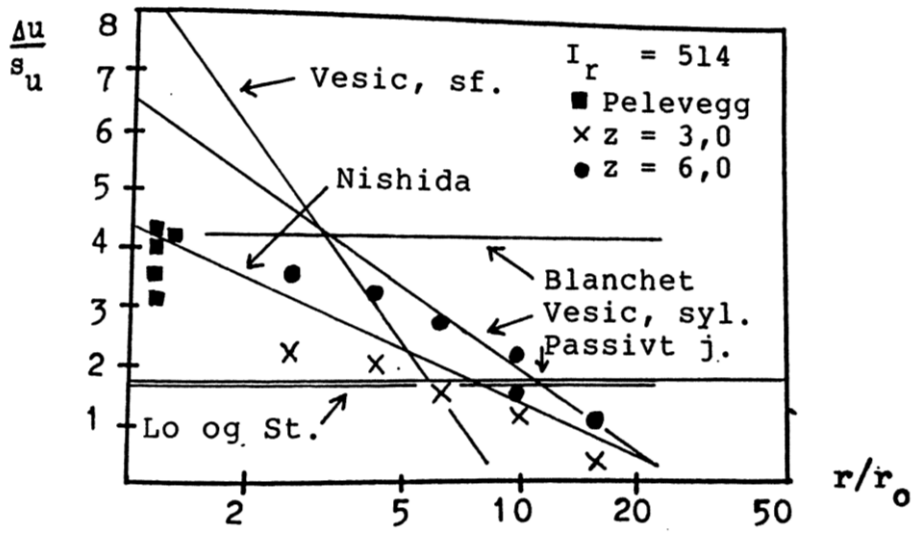

Figure 9.2: Excess pore pressure measured at 3m, 6m depth and at the pile wall (=pelevegg) from Roy, Blanchet et al. (1981). Compared to CEM-EP and some of the empirical methods presented in Chapter 9. (Berg-Knutsen 1986)

Figure 9.3 shows us that the measurements at the pile tip is somewhere between the cylindrical and the spherical cavity expansion as proposed by Clark and Meyerhof (1972), and previously discussed in Chapter 4.1. The CEM-EP grossly over-predicts the excess pore pressure at the pile shaft, while the method of Nishida (1963) and Blanchet (1976) give a much better correspondence to the data. Berg-Knutsen (1986) found, from the data on low OCR clays, that CEM-EP was an upper limit to the measured data and the minimum value obtained when using both the method of Svanø (1978) and Nishida (1963) was a lower limit to the measured data. After looking at the empirical data from 12 different sites we know now that these bounds do not hold. CEM-EP is not an upper boundary as seen in Chapter 14.3 and Figure 14.2.

For the high OCR clays we see very low excess pore pressure compared to the stiffness and strength of the soil, most likely due to dilation, and these pore pressures are lower than what the method of Nishida (1963) predicts. Based on the empirical data in Table 13.6 the CEM-EP method is the best fit to the data with $OCR \leq 2$. For the data with $OCR > 2$, none of the methods presented in Chapter 8 seems to predict low enough pore pressures. However, the method of Lo and Stermac (1965) and Blanchet (1976) has not been checked against the data in Table 13.6 itself, as the ratio $\left(\frac{\Delta u}{\sigma_c'}\right)_{max}$ is not determined for each site specifically. The above conclusion is then only based on Figure 9.2 and Figure 9.3 for these methods.

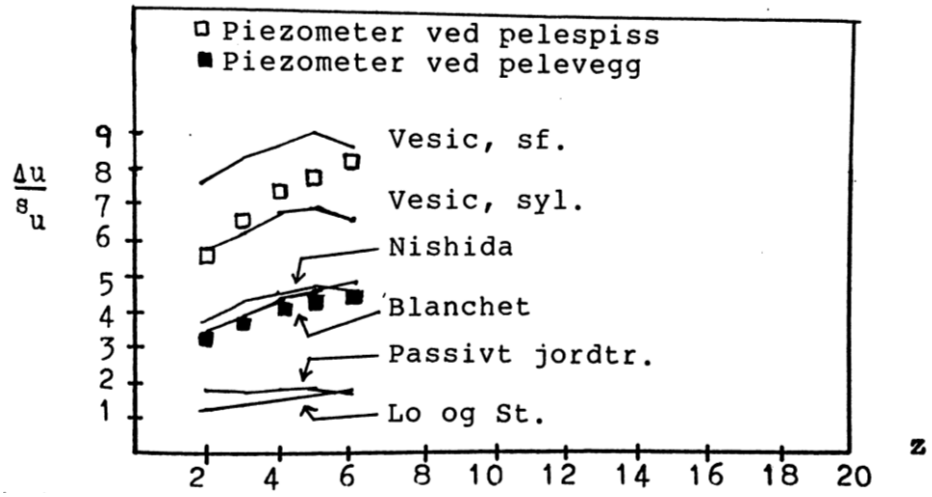

Figure 9.3: Measurements of pore pressure at the pile tip (=pelespiss) and the pile wall (=pelevegg) from Roy, Blanchet et al. (1981). Compared to CEM-EP and some of the empirical methods presented in Chapter 9. (Berg-Knutsen 1986)

Randolph, Carter et al. (1979) used the CEM-MCC model and compared the radial displacement at the midpoint of the pile with field measurements done by Cooke and Price (1973) as well as from model test done by Randolph, Steenfeld et al. (1979). Randolph, Carter et al. (1979) used the assumption of plane strain under constant volume in their model. The result is presented in Figure 9.4, and show great correspondence between the model and field measurements. As discussed in Chapter 7.1, SPM and CEM predicts the same radial strain far behind the tip.

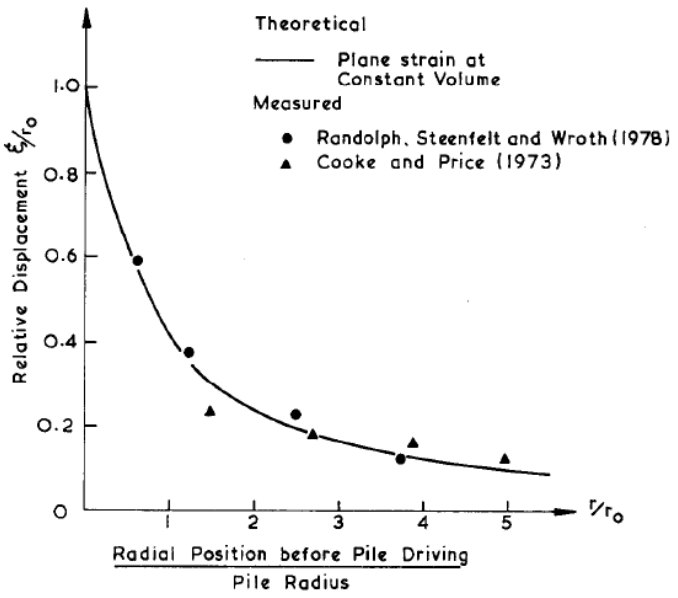

Figure 9.4: Comparison of measured and theoretical soil displacement in the radial direction. (Randolph, Carter et al. 1979)

However, Baligh and Levadoux (1980) argue that Randolph, Carter et al. (1979) neglect the importance of the strain path followed by the soil element to reach the final strain. Figure 7.2 shows that even though soil particles move monotonically away from the pile, the radial strain decrease slightly behind the tip. An unloading procedure such as this can have a large influence on the change of the stresses.

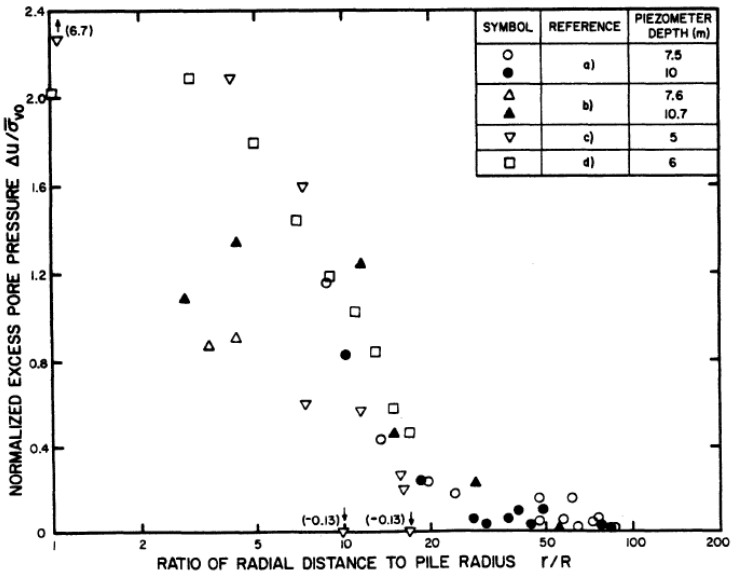

Figure 9.5: Measurements of excess pore pressure due to pile driving from four studies; a) Bjerrum and Johannessen (1960) NC marine clay, b) Lo and Stermac (1965) NC soft to firm silty clay, c) Koizumi and Ito (1967) OCR=3-4 very sensitive slightly organic silty clay, d) Roy et al (1979) OCR=2-2.3 very sensitive marine soft silty clay. Where $R = r_0$ and $\bar{\sigma}_{v0} = \sigma'_{v0}$. (Baligh and Levadoux 1980)

Figure 9.5 shows measurements from four different sites. The measurements seems to agree somewhat regardless of the fact that the clays differ in type (I_P) and stress history (OCR). We also see that the excess pore pressure at the pile shaft is much lower than what a linear trend of the data suggests.

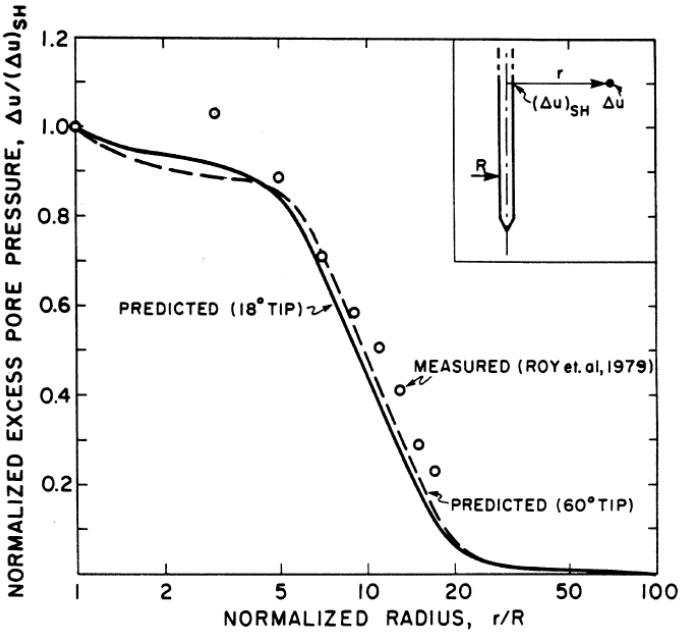

Figure 9.6: Predictions from SPM coupled with the PLB material model for normally consolidated BBC. Using two different cones and data from a distance of 14 times the pile radius behind the tip. Compared to measurements of cone penetration in Champlain clay (OCR=2). Where $(\Delta u)_{SH} = \Delta u_{max}$ and $R = r_0$. (Baligh and Levadoux 1980)

Figure 9.6 shows predictions for a BBC clay with OCR equal to one using the SPM-PLB model. The predictions are compared to measurements from a Champlain clay with an OCR of two, and shows a very good fit to the measurements. Baligh and Levadoux (1980) uses this result, together with the measurements from Figure 9.5 to argue that the normalized excess pore pressure due to pile driving is not very sensitive to soil type or stress history.

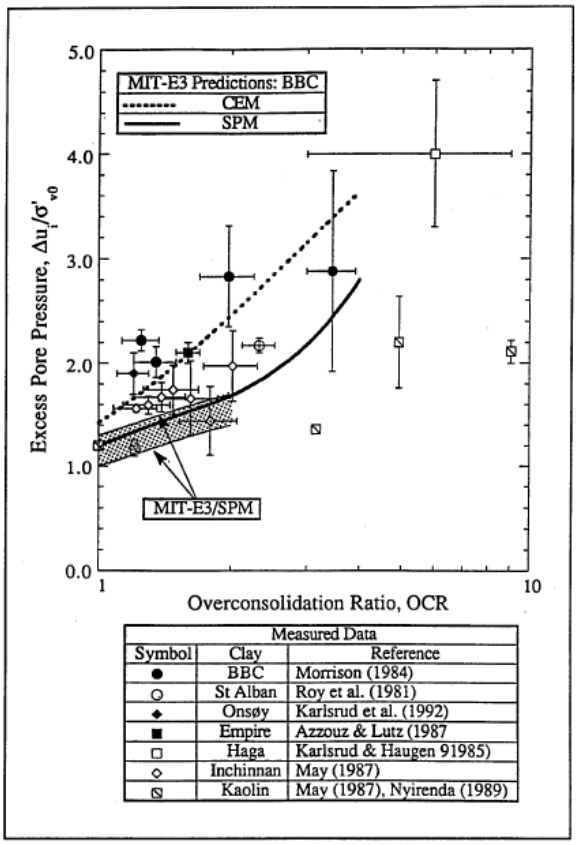

Figure 9.7: Measurements of excess pore pressure at the pile shaft and predictions from both CEM and SPM using the MIT-E3 material model with BBC parameters. Where $\Delta u_i = \Delta u_{max}$. (Whittle 1992)

Figure 9.7 shows predictions obtained with CEM and SPM coupled with the material model MIT-E3 using BBC input parameters, and measurements at the pile shaft from different studies. The measured data is very consistent at low OCR, but for the more heavily overconsolidated clays, it shows more scatter. This is deemed to probably be due to the presence of sand seams. SPM and CEM both underestimates the measured data from the BBC clay, however CEM shows a slightly better fit to the measured pore pressure at the pile shaft than SPM.

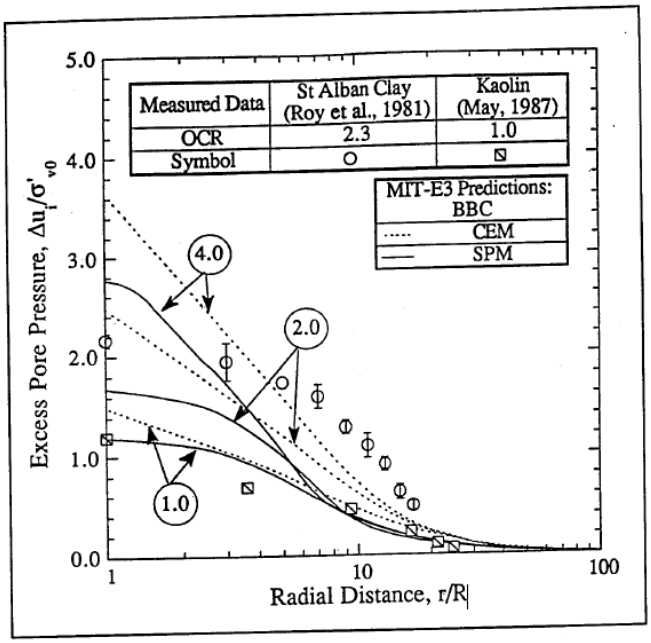

Figure 9.8: Predictions with both CEM and SPM with MIT-E3 as material model and BBC parameters and different OCR's. Compared to measured data from two sites. Where $\Delta u_i = \Delta u_{max}$ and $R = r_0$. (Whittle 1992)

Figure 9.8 is similar to Figure 9.7, but Figure 9.8 only looks at two of the sites and include the radial distribution. SPM with OCR equal to one compares well to measurements of Kaolin clay. However, the predictions from SPM at OCR equal to two underestimates both the magnitude and the radial extent of the excess pore pressure when compared to the measurements done in St. Alban Clay. Whittle (1992) uses the results from Figure 9.8 to argue that the CEM analysis does not describe the shape of the excess pore pressure accurately, thus overestimating the maximum excess pore pressure at the pile shaft, while under-predicting the pore pressure measured in the far field. Whittle (1992) further interprets the results and argue that the main source of discrepancy in the SPM solution is due to the effective stresses in the far field, which are affected by small strain properties of the clay. If this is the case then it can be fixed through further refinement of the material model.

Figure 9.9 shows the fit between the measured data and the predictions obtained by SPM and CEM when normalized to the maximum excess pore pressure at the pile shaft. The figure shows a great fit between the SPM predicted radial distribution and the measured radial distribution of the excess pore pressure. Karlsrud (2012) find that the numerical solutions often give a fair assessment of the radial extent of the excess pore pressure field. However, the exact shape of the excess pore pressure field does not always agree. The SPM method seems to fit in some cases, and CEM in other cases. There seems to be more cases where the SPM method fit than CEM however.

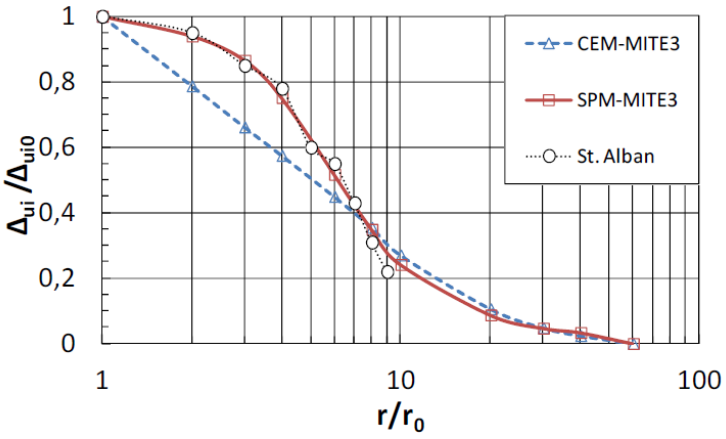

Figure 9.9: Measured excess pore pressure field at St. Alban compared to CEM-and SPM-MITE3 predictions, when normalized to the maximum excess pore pressure at the pile shaft. Where $\Delta_{ui} = \Delta u$ and $\Delta_{ui0} = \Delta u_{max}$. (Karlsrud 2012)

Karlsrud (2012) studied twelve sites in his PhD-thesis where pore pressure was measured at the pile shaft. These measurements was used to propose the α- and β- methods for determining the pile bearing capacity. Figure 9.10 and Figure 9.11 shows measurements of the pore pressure at the pile shaft against OCR. The pore pressure is normalized with the initial vertical effective stress in Figure 9.10 and with the direct undrained shear strength in Figure 9.11. Figure 9.10 and Figure 9.11, made by Karlsrud (2012), only include clays where undrained conditions can be assumed and exclude measurements done closer than about four pile diameters to the tip due to possible effects of geometry.

The dataset gathered by Karlsrud (2012) is used in Chapter 13 and 14, with some minor modifications. We will there use similar plots so a detailed description of the plot is presented here. The filled symbols represent the closed-ended piles, while the non-filled symbols represent the open-ended piles. The size of the symbol represents the size of the pile diameter. Ha represents the measurements from Haga, On from Onsøy, Li from Lierstranda, Ti from Tilbrook Grange, WD from West Delta, CP from Canons Park, BK from Bothkennar, Co from Cowden, Em from Empire, BBC from Saugus, Ham from Hamilton and St.Al from St.Alban. The name/letter behind the hyphen represents the type of pile used. The sites, with soil conditions and information on the piles used, is presented in Chapter 13.1.

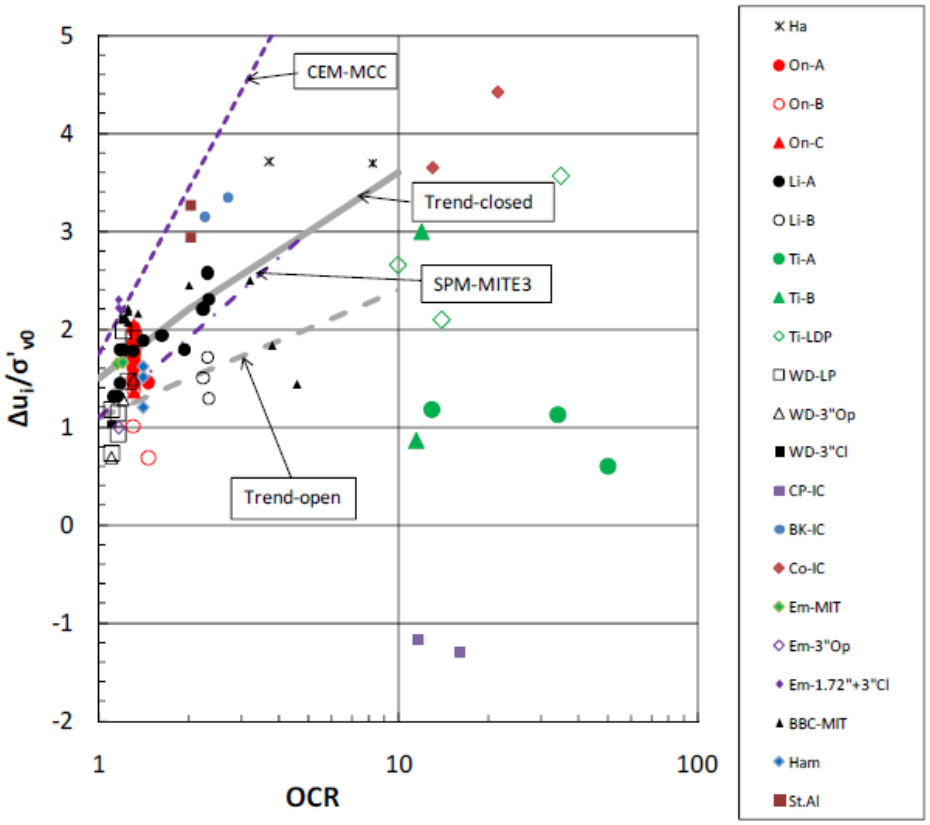

Figure 9.10: Measured normalized excess pore pressure against the pile shaft versus OCR. Where $\Delta u_i = \Delta u_{max}$. (Karlsrud 2012)

Figure 9.10 is as mentioned normalized according to the initial vertical effective pressure. The measurements are plotted together with predictions from CEM coupled with the MCC material model (CEM-MCC) and SPM coupled with the MIT-E3 material model (SPM-MITE3), the parameter input are based on idealized BBC, and is not site specific. The CEM-MCC line lies on the high side of the measured values, while the SPM-MITE3 lies on the low side. Use of site specific data would slightly improve the comparison to the corresponding measurements, but will not change the broad picture according to Karlsrud (2012). The trend lines are stopped at OCR larger than ten as the scatter in the data becomes quite large. The trend lines are a least square fit of a linear line in a logarithmic scale of OCR.

In Figure 9.11, the data is normalized with the direct undrained shear strength. The plot also contains predictions made by CEM with an elastic-perfectly plastic Tresca material model (CEM-EP). The input parameters in the CEM-EP model has been chosen as the average of the data from all the sites. For both the closed- and open-ended piles the CEM-EP appears to be under-predicting the excess pore pressure at the pile surface for low OCR and over-predicting for high OCR.

The data from Figure 9.11 shows a clear trend of decreasing normalized excess pore pressure at the pile shaft with increasing OCR according to Karlsrud (2012). Baligh and Levadoux (1980) found that there is no well-defined correlation between excess pore pressure at the shaft and clay type, stress history, undrained shear strength or sensitivity. However, Baligh and Levadoux (1980) only looked at data from four sites with OCR less than four.

Notice that the excess pore pressure at the pile shaft normalized with the initial vertical effective stress increase with increasing OCR. This is because as OCR increase, G_u and s_u increase. However, G_u/s_u decrease, meaning s_u increase faster with OCR than G_u. σ'_{v0} is constant so that from CEM-EP we have $\Delta u_{max} = s_u ln \frac{G_u}{s_u}$ increasing. This correspond to the general trend found in CEM-MCC as well.

For OCR less than three it seems that the measurements of the open-ended piles lies about 25% lower than the closed-ended piles. For higher degrees of OCR, no such relationship can be argued. All the small-scale model piles/probes, except Cannons Park (CP-IC), seems to give larger excess pore pressure than the full-scale piles. This could be because small-scale model piles are driven at a faster rate than the real size piles. However, the consolidation time is proportional to the square of the pile radius, and this should counteract such an effect to some extent according to Karlsrud (2012). The MIT probe in BBC clay (BBC-MIT) measured pore pressure while driving the probe, whereas the other data was collected after installation. This could explain the high values of the normalized excess pore pressure at the pile shaft reported from the BBC-MIT experiment.

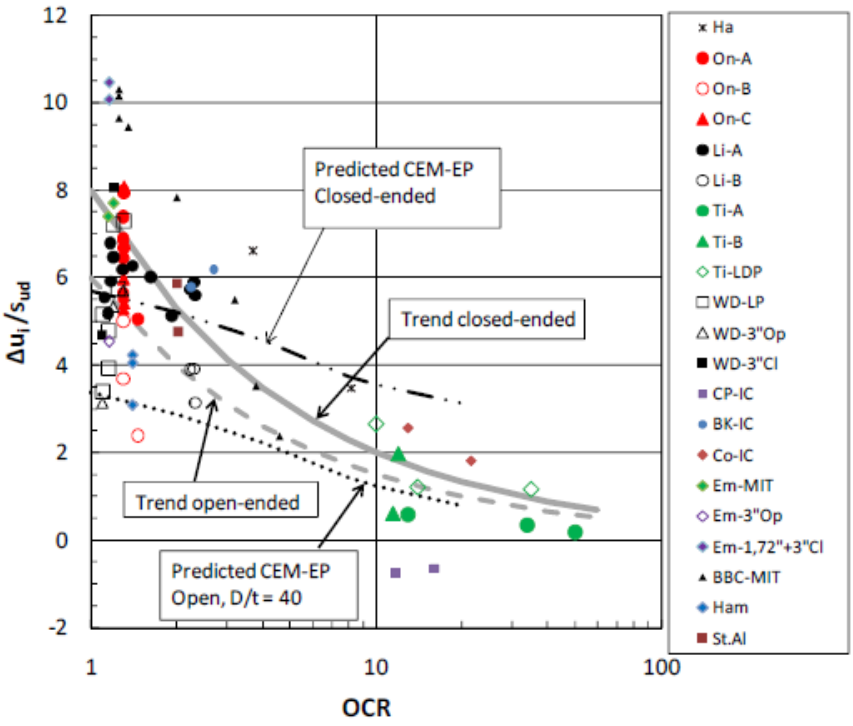

Figure 9.11: Measured normalized excess pore pressure against the pile shaft versus OCR. Where $\Delta u_i = \Delta u_{max}$. (Karlsrud 2012)

According to Karlsrud (2012), the scatter of the data seen in Figure 9.10 and Figure 9.11, is most likely due to the difference in pile size, pile type, time used for installation and inaccuracy in the instrumentation system used. Some of the scatter is probably due to the different stress-strain behavior of the clays, including the post-peak large strain behavior. Karlsrud (2012) believes that very little of the scatter comes from the assessment of the direct undrained shear strength and OCR, as the uncertainty in these values are approximately $10-15\%$ and $20-30\%$, respectively.

Trustworthy measurements of pore pressure requires that the piezometer filter is de-aired and fully saturated, before they enter the ground. In heavily overconsolidated clays negative pore pressure or suction may develop. This can de-saturate the piezometer even if the piezometer filter was carefully prepped before entering the ground. This would lead to too low pore pressure measurements shortly after pile installation, and cause an increase in readings with time. This was observed at the Hamilton site (Ham), and could be an influencing factor at other sites as well.

In Figure 7.8 we see that CEM predicts much higher normalized effective stress ratio ($K_i = \sigma'_r/\sigma'_{v0}$) at the end of pile installation than SPM. Figure 9.12 shows measurements of K_i plotted against OCR. Since the generated total radial earth pressure and pore pressure is

relatively large compared to the initial stress state, small errors in total earth pressure or pore pressure can give a large error in effective stress. Figure 9.12 shows therefore an even larger scatter than the previous plots. Negative values of K_i is incorrect since tension in the radial effective stress is very unlikely. If the results from Figure 7.8 is compared to the data in Figure 9.12, we see that SPM-MITE3 seems to correctly assess the low radial effective stresses after installation for low OCR clays. While CEM-EP and CEM-MCC over-predicts K_i quite substantially for low OCR clays. The lower estimate produced by SPM is due to the unloading procedure as the pile tip passes, as discussed in Chapter 7.1. For high OCR clays K_i seems to approach K_0, but the scatter is quite large and no definitive conclusion can be drawn.

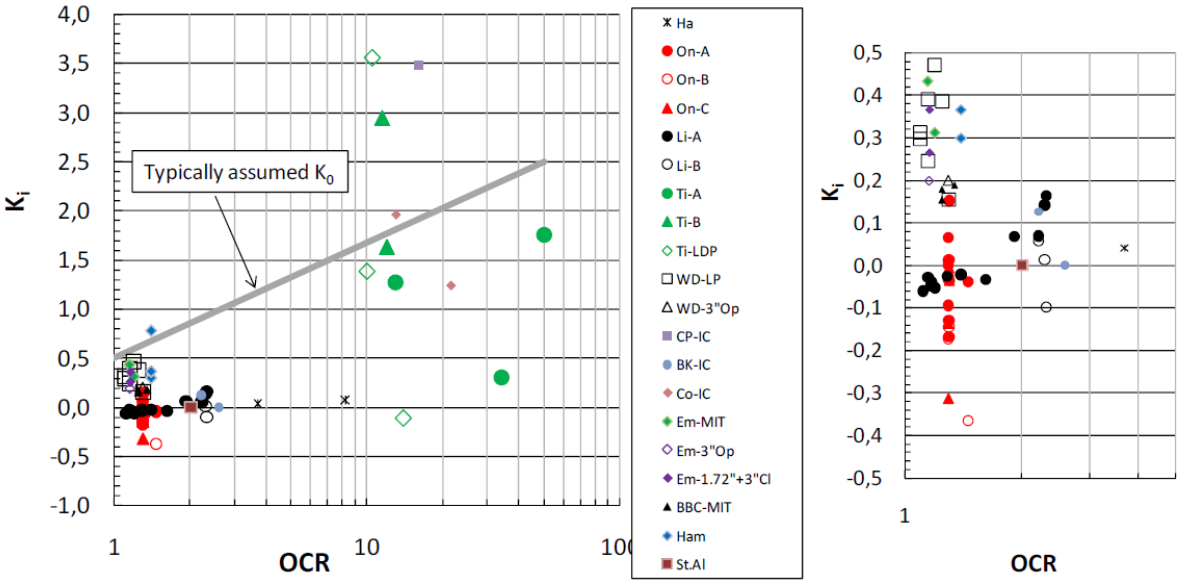

Figure 9.12: Normalized effective stress ratio, $K_i = \sigma'_r/\sigma'_{v0}$, at end of installation against OCR. (Karlsrud 2012)

Figure 9.13 shows the measured results of excess pore pressure at the pile shaft normalized with the direct undrained shear strength against the plasticity index, at the sites with OCR less than two. If the measurements on full scale, closed-ended piles (large filled symbols) are looked at separately then the data suggest an increase of normalized excess pore pressure at the pile shaft with increasing plasticity index. The same tendency is observed if only looking at the full scale open-ended piles (large non-filled symbols). This is interesting since Figure 5.6 shows that if the plasticity index increase, then the ratio between the shear modulus over the undrained shear strength decrease. This means that the measurements do not show the same tendency as the CEM-EP model for an increasing plasticity index.

$G_u^{50}/_{s_{uC}}$ decrease with increasing plasticity index according to triaxial tests done on block samples. CEM-EP only depends on $G_u/_{s_{uD}}$ (if the Dilatancy is neglected), and the normalized excess pore pressure decrease if $G_u/_{s_{uD}}$ decrease.

Bergset (2015) looked at the CEM-MCC model and found in his parametric study that the normalized excess pore pressure at the pile shaft decrease with increasing plasticity index for this model as well. However, the increase in normalized excess pore pressure with plasticity index seen in Figure 9.13 is very small. The uncertainties in the measurements combined with the influence of other material parameters makes this small increase with plasticity index very uncertain.

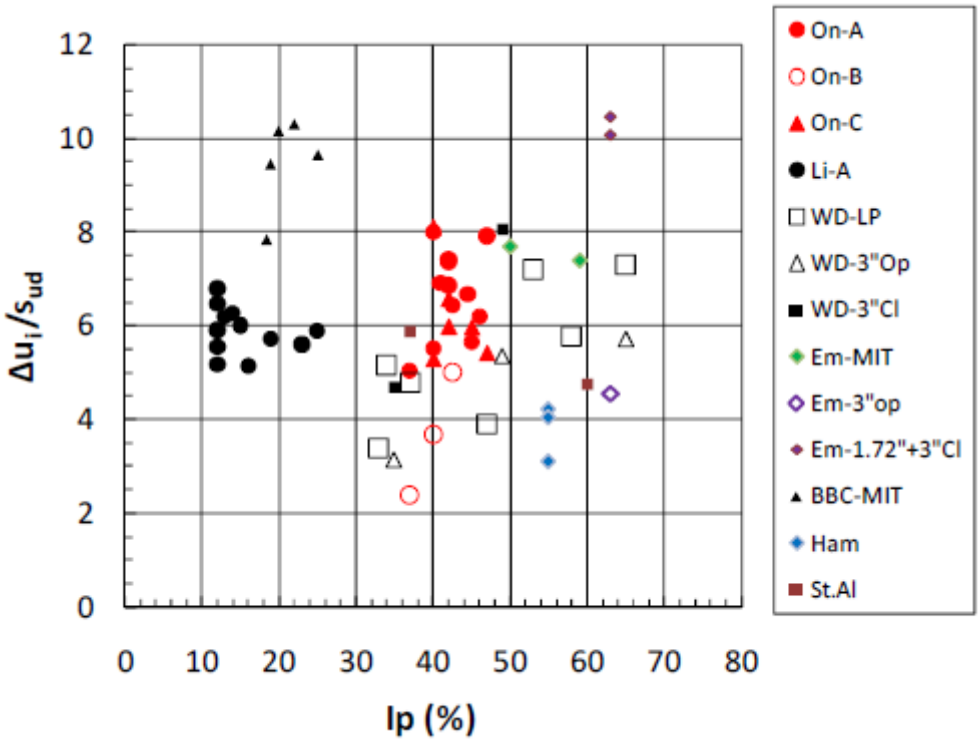

Figure 9.13: Measured normalized excess pore pressure against the pile shaft versus plasticity index (I_p) for $OCR < 2$. Where $\Delta u_i = \Delta u_{max}$. (Karlsrud 2012)

Karlsrud (2012) concludes that no single numerical or analytical solution fully capture the trends found in the measured data, and that the trend curves may be the most reliable approach for estimating the excess pore pressure at the pile shaft.

Figure 9.14 is a proposed empirical way of estimating the excess pore pressure against the pile shaft based on trend curves seen in Figure 9.11. For heavily overconsolidated clays, the

trend curves are very uncertain since the amount of reliable data is small, and the scatter in the data that exist is quite large. Karlsrud (2012) propose to use these trend curves and get the radial extent using the CEM-EP model, and check the value of G_u/s_{uD} with Figure 5.6. If the shape of the distribution is of importance, SPM-MITE3 has shown better correspondence to the measured results than CEM, in most of the cases. However, there is no guarantee that this will be a good fit for a single randomly chosen case.

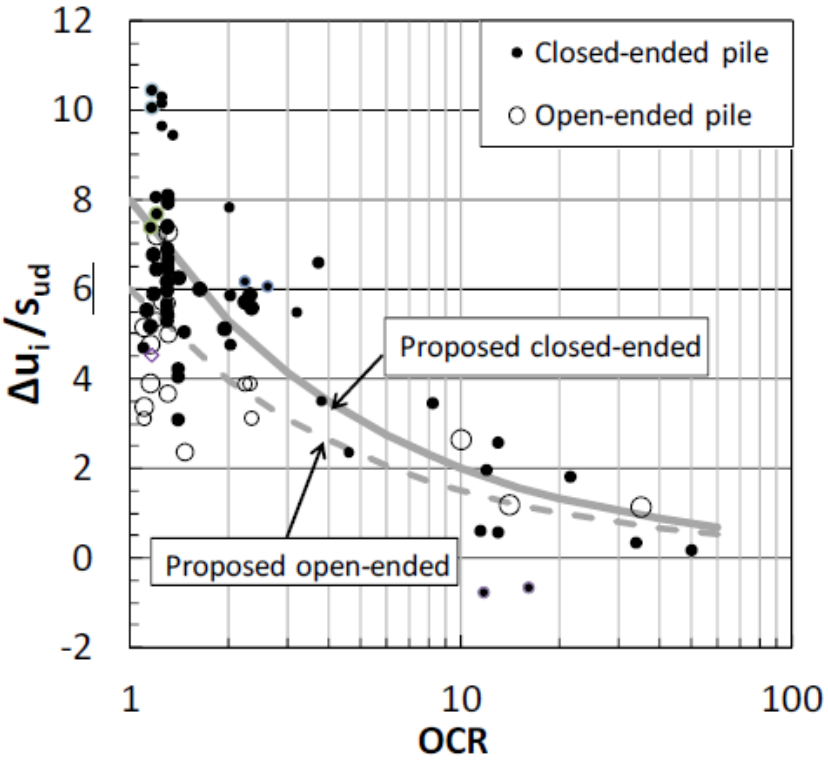

Figure 9.14: Proposed empirical correlation for predicting excess pore pressure against the pile shaft at end of pile installation by Karlsrud (2012). Where $\Delta u_i = \Delta u_{max}$. (Karlsrud 2012)

10 Conclusions from the literature study

Based on the predictions and measurements presented up until now we will draw some conclusions. In the remaining chapters we will mainly look closer at the Cavity Expansion Method (CEM) coupled with a linear elastic-perfectly plastic (EP) material model, and the Modified Cam Clay (MCC) material model. We will also study the effect of including strain softening, and compare some of the prediction methods to measurements done at the pile shaft (i.e. Table 13.6).

The radial extent of the excess pore pressure field is seen to be predicted quite well (Figure 9.2 and Figure 9.8) by both CEM and SPM. The differences between CEM and SPM, coupled with different material models, are quite small far away from the pile, as seen in Figure 7.4, 7.9 and 9.9. Using the analytical CEM-EP solution (i.e. Equation 5.2) with the direct undrained shear strength (s_{uD}) and the undrained shear modulus (G_u^{50}), taken at 50% of the mobilized shear strength as input parameters, is therefore a good approximation. This is supported by Karlsrud (2012), but is something that could be looked further into.

The empirical and semi-empirical methods presented in Chapter 8 is seen to give a worse fit to the measured data presented in Chapter 13 than CEM-EP (see Appendix B, Figure 9.2, Figure 9.3 and Figure 12.2). These methods will therefore not be discussed further. The trend lines proposed by Karlsrud (2012) in Figure 9.14 will be looked further into as they are based on a quite large amount of empirical data, and is seen to give a relatively good estimate of the excess pore pressure at the pile shaft.

Based on what we see in Figure 9.11, we conclude that OCR have an important role in the resulting excess pore pressure, contrary to what some authors conclude. The excess pore pressure is decreasing with OCR more rapidly than what CEM-EP suggests, probably due to dilation. This will be looked further into in Chapter 12, where CEM-EP and CEM-MCC is compared, and in Chapter 14 where predicton methods are compared to measurements.

CEM have been shown to grossly over-predict the effective radial stress after installation (see Figure 9.12 and Figure 7.8). This is due to the unloading of the radial stress after the pile tip has passed. Since the Strain Path Method (SPM) include the downward motion of installing a

pile it captures this unloading procedure. Comparing Figure 7.8 and Figure 9.12, we see that the radial effective stress is much better predicted by SPM than CEM. SPM is shown not only to give lower radial stress, but lower excess pore pressure as well. However, Figure 9.8 shows that the SPM prediction is lower than what is measured in a clay with $OCR = 2$, and that the CEM prediction is more correct in this case. It is difficult to say whether CEM or SPM gives the most correct prediction of the excess pore pressure. The prediction also varies with the soil model chosen.

In Chapter 14.3, we see that CEM-EP does not grossly over-predict the excess pore pressure at the pile shaft for the clays with $OCR \leq 2$, but rather under-predicts this, for these sites, on average. Based on this observation, SPM would give too low excess pore pressure for the sites with $OCR \leq 2$. However, SPM is not modeled in this study with site specific data, this conclusion is therefore purely based on the fact that SPM is shown to give lower excess pore pressure than CEM, when compared.

Johansson and Jendeby (1998) find that the radial total stress relaxes, and that this happens faster than the excess pore pressure dissipates (see Figure 2.14). This could very well be the reason as to why the measured radial effective stress is very low as seen in Figure 9.12, and it also explains why the pore pressure predicted by SPM could be somewhat low.

The difference in the predictions obtained by SPM and measurements, can come from errors in the measurements (described in Chapter 9), but are just as likely to come from the estimated deformation field or the material model. However, errors from the latter are believed to be of a smaller magnitude. The strain rate found by Baligh (1985) is shown to be higher than 14000 times that applied in an conventional undrained triaxial test, close to the pile (Figure 7.2). A high strain rate has been shown to increase the peak strength, reduce the strain to peak, and increase the softening behavior. This means that the input parameters determined from triaxial testing will not be accurate, and that the material model will therefore be unable to reproduce the exact stresses measured. This would affect the results of both CEM and SPM. In addition, SPM is much more complex to implement than CEM making it less available.

The shape of the radial distribution is shown to be sometimes close to a log-linear decrease of $2s_u$ (Figure 9.1). However, there are limited measurements close to the pile shaft. The Strain Path Method (SPM) coupled with the strain softening MIT-E3 model gives a more constant

value in the closest remoulded zone and then a log-linear decrease. In Figure 9.2, 9.5, 9.6, 9.8 and 9.9, this kind of distribution has been measured. All the measurements are done at sites with $OCR \leq 4$ so the distribution when the clay has an OCR higher than this is unknown.

The vertical effective stress is found to only increase or decrease due to contraction and dilation respectively in CEM. SPM gives a lower estimate of the vertical effective stress if a strain softening material model is used (see Figure 2.13). The vertical effective stress is rarely measured, and it is therefore hard to draw definitive conclusions. Karlsrud (2012) mention vertical silo effects occurring in the reconsolidation phase in lean clays (explained in Chapter 2.2), which would reduce the vertical effective stress. In addition, the stress relaxation observed in the radial total stress by Johansson and Jendeby (1998) could very well occur in the vertical total stress as well. Due to this, it might be necessary to assume no change in vertical total stress when checking the stability of a slope to avoid failure.

11 Cavity Expansion Method in Plaxis

11.1 The Model

The Cavity Expansion Method (CEM) is modeled in Plaxis 2D 2018, using an axisymmetric model and 15-noded triangular elements. The model is created following the descriptions of the model used by Bergset (2015). He did a parametric study of the effect of overconsolidation ratio (OCR) and plasticity index (I_P) on stresses, directly after expansion and after dissipation of the excess pore pressure, utilizing the Cavity Expansion Method (CEM) coupled with the Modified Cam Clay (MCC) material model. Figure 11.1 shows the model in the initial phase with boundary conditions. The model is ten by ten meters in size and is normally fixed at $x = 0{,}029m$, $x = 10m$ and $y = -10m$. The global ground water table is located at the terrain level. Figure 11.2 shows the flow conditions, and the model is closed for groundwater flow at $y = -10m \; and \; x = 0{,}029m$.

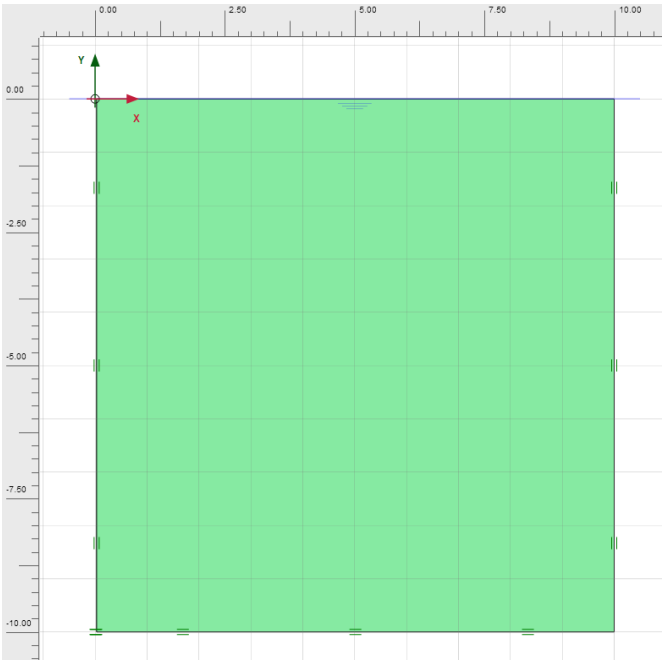

Figure 11.1: Boundary conditions in the initial phase.

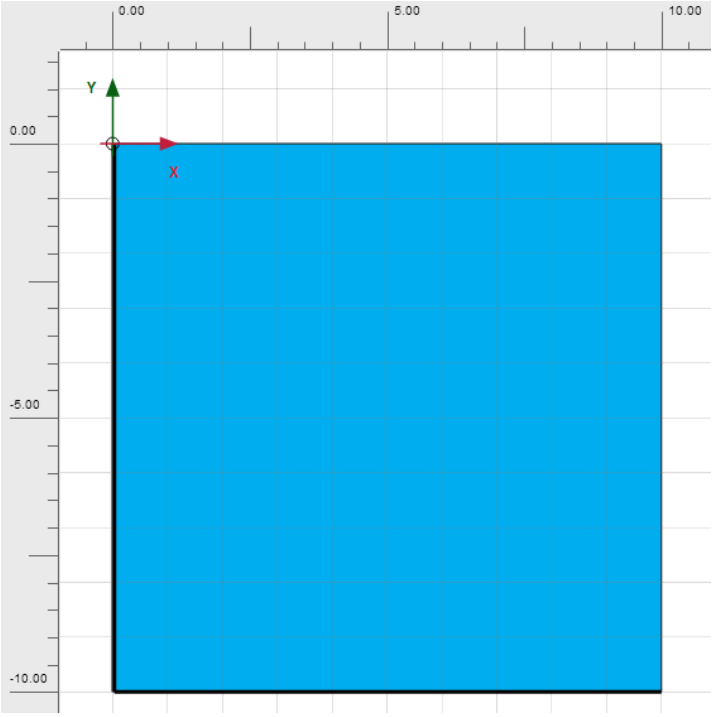

Figure 11.2: Groundwater flow boundary conditions during all phases.

As discussed in Chapter 6.3 one have need of a non-zero initial radius when modelling CEM numerically. So instead of using 0 to r_0, we use a_0 to $2a_0$, as explained by Carter, Randolph et al. (1979). Bergset (2015) used a pile with radius equal to $50{,}5mm$, Equation 6.10 then gives:

$$a_0 = \frac{r_0}{\sqrt{3}} = \frac{50{,}5mm}{\sqrt{3}} = 29mm \tag{11.1}$$

Notice that from r_0 to $2a_0 = \frac{2}{\sqrt{3}} r_0 \approx 1.15 r_0$, we have no information of the stress components or the excess pore pressure. Figure 11.3 shows the initial cavity radius, and this is then also the reason for the model being normally fixed and closed for groundwater flow at $x = 0{,}029m$.

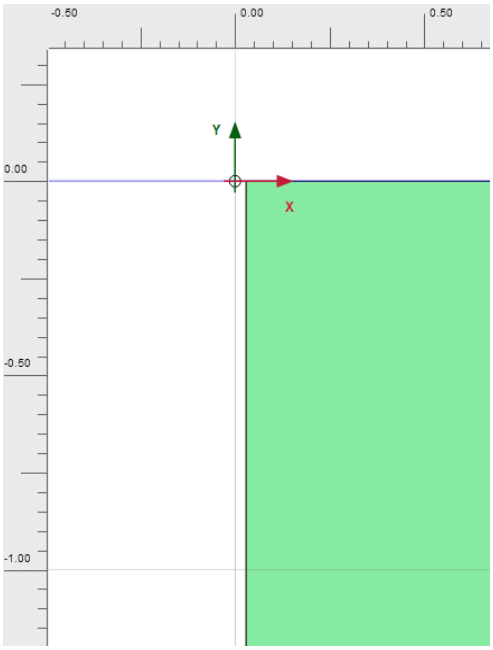

Figure 11.3: Initial cavity radius of $a_0 = 29mm$.

After the initial phase utilizing the K0 procedure, an expansion phase is added. This is a plastic staged construction phase where a prescribed displacement is applied. Figure 11.4 shows the boundary conditions of the expansion phase. The prescribed displacement is $a_0 = 29mm$ since $a_f = 2a_0$. The default numerical control parameters is used, however the "updated mesh" future, under "deformation control parameters", is utilized. This is done due to the fact that the Cavity Expansion Method generates large strains, and it is therefore necessary to account for large displacements. The "updated mesh" future takes the influence of changes in mesh geometry on the equilibrium equations into account.

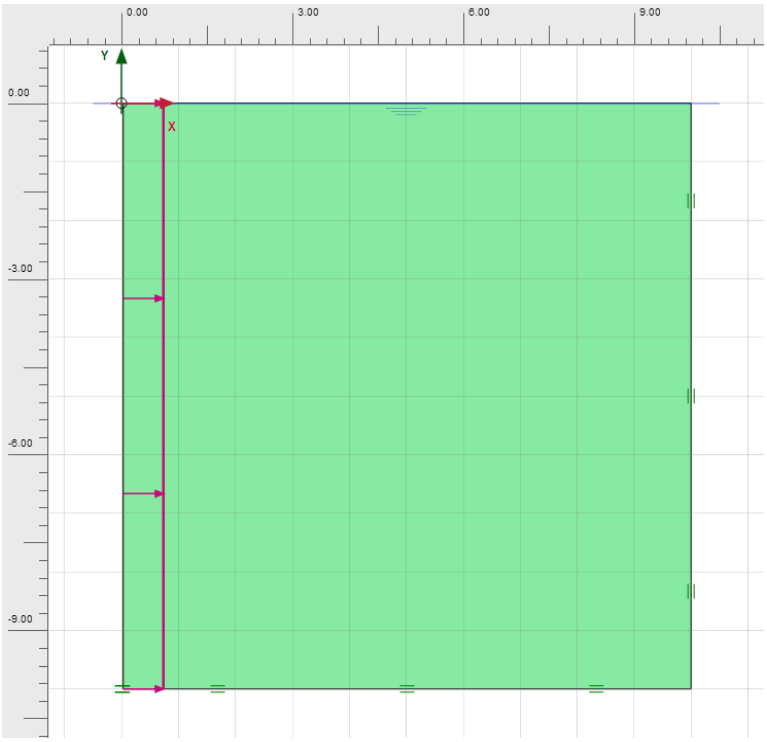

Figure 11.4: Boundary conditions and prescribed displacement of $a_f - a_0 = 29mm$ in the expansion phase.

The modeled is meshed using the automatic meshing future in Plaxis with a very fine element distribution and a constant coarseness factor of one over the entire model, except for a coarseness factor of 0,1 between $x = 0$ and $x = 0{,}2m$ (see Figure 11.5). The reason for this choice of coarseness factor is explained later. This generates the mesh viewed in Figure 11.6.

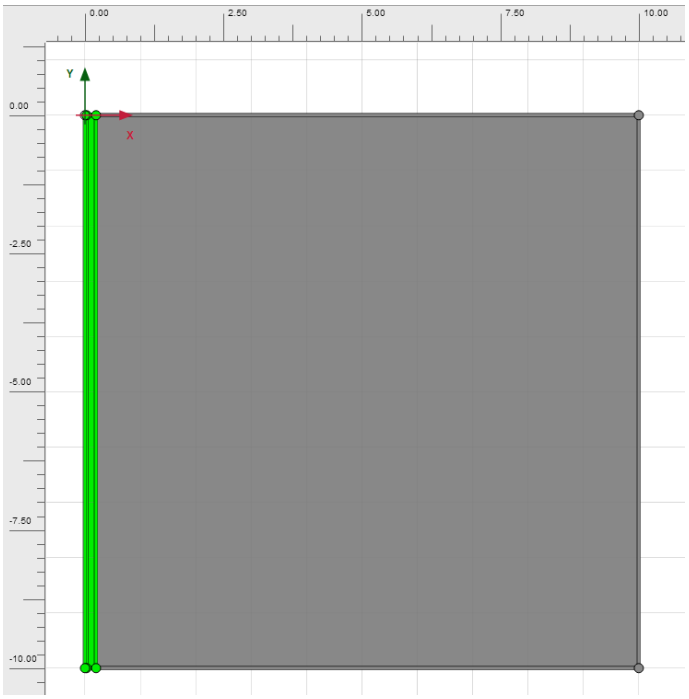

Figure 11.5: Plot of coarseness factor chosen to generate the mesh in Figure 11.6.

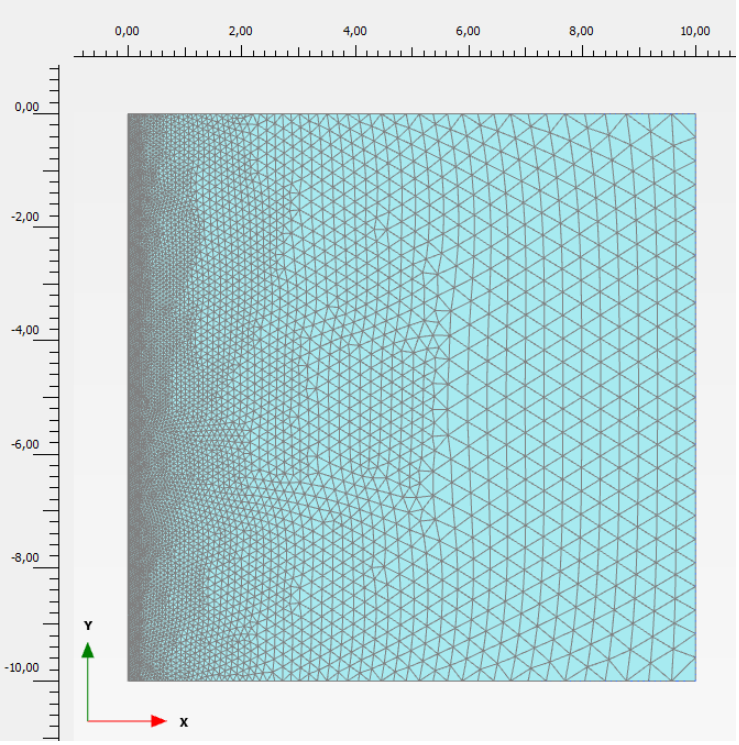

Figure 11.6: View of the mesh used in the Plaxis2D calculations. Number of soil elements: 11360. Number of nodes: 91657. Average element size: 0,1103m. Maximum element size: 0,593m. Minimum element size: 0,0248m.

11.2 Verification of the Model

In order to validate the model, the results produced and presented in Bergset (2015), and Randolph, Carter et al. (1979) are reproduced. The data is extracted at the bottom of the model along $y = -10m$ from $x = 0{,}058m$ to $x = 10m$. Table 11.1 shows the material properties used by Randolph, Carter et al. (1979) for their Case A. Figure 11.7 shows the stresses produced by the model presented above, and Figure 11.8 shows the results presented by Randolph, Carter et al. (1979).

Table 11.1: Material properties used to reproduce results obtained by Randolph, Carter et al. (1979) Case A.

Material Model	Modified Cam-Clay
Drainage type	Undrained (A)
Unit weight, γ, $\left[{}^{kN}/_{m^3}\right]$	18
Compression index, λ, [-]	0,15
Swelling index, κ, [-]	0,03
Unloading/reloading Poisson's ratio, ν'_{ur}, [-]	0,2
Initial void ratio, e_0, [-]	1,2
Strength (inclination of CSL), M, [-]	1,2
Coefficient of lateral earth pressure, K_0, [-]	0,55
Overconsolidation ratio, OCR, [-]	1
Undrained shear strength, s_u, [kPa]	27,8

The undrained shear strength is based on the maximum shear stress obtained in the model (that is at the pile shaft unless one have a very large OCR). In Plaxis 2D this is found as the mobilized shear strength (τ_{mob}) defined as the maximum value of shear stress (i.e. the radius of the Mohr stress circle $\left({}^{1}/_{2}\,(\sigma_1 - \sigma_3)\right)$). Bergset (2015) and Randolph, Carter et al. (1979) seems to have used this mobilized shear strength as the undrained shear strength when normalizing their results. The undrained shear strength, found from an undrained compression triaxial test performed from the in-situ stress conditions, is with the material properties from

Randolph, Carter et al. (1979) (given in Table 11.1) equal to $29{,}55kPa$. With the material properties from Bergset (2015), given in Table 11.2, the undrained shear strength from conventional undrained triaxial testing is $27{,}4kPa$. Using these gives too low and too high stress over undrained shear strength, respectively, when compared to the results presented by Randolph, Carter et al. (1979) and Bergset (2015). The presented model gives however a very good fit in both cases, if the mobilized shear strength is used to normalize the results.

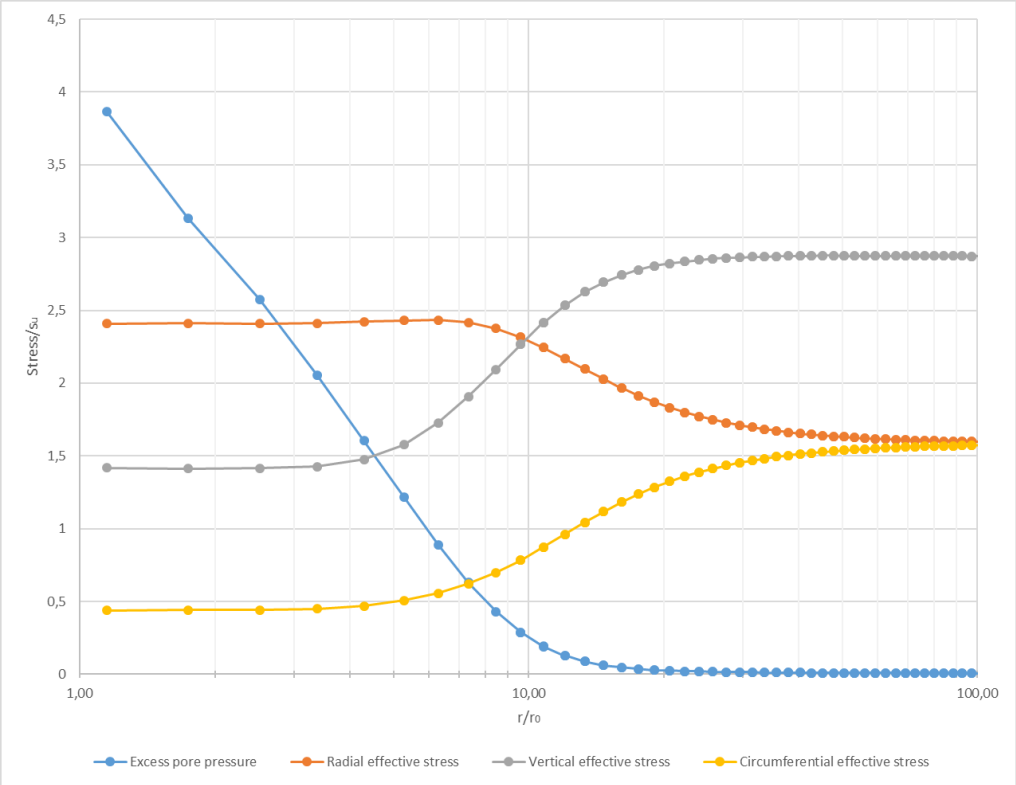

Figure 11.7: Stresses after expansion normalized with the undrained shear strength against distance from pile center normalized with the pile radius in a logarithmic scale. Found by using the material set given in Table 11.1 and the model described above.

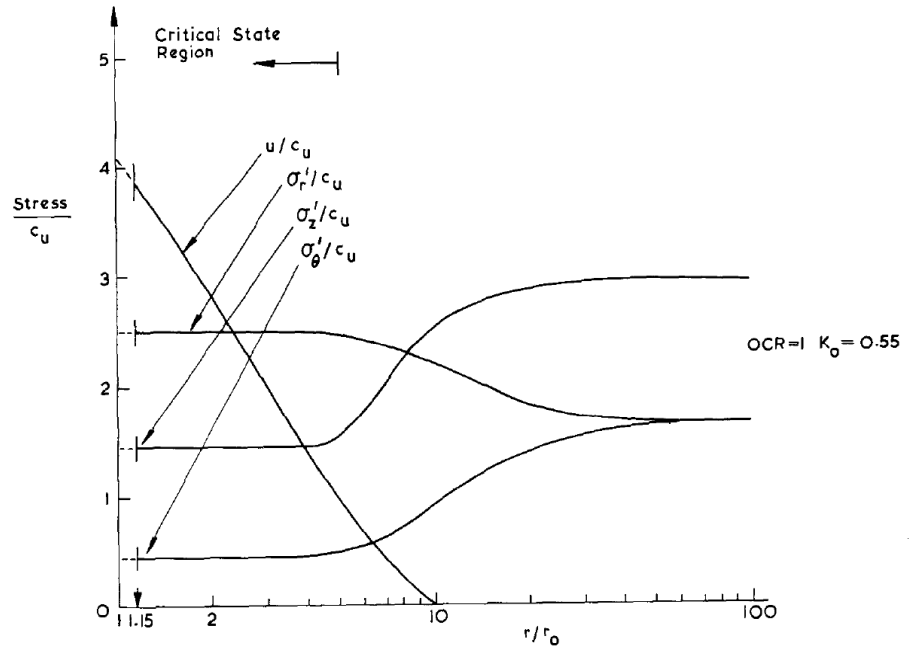

Figure 11.8: Stresses after expansion normalized with the undrained shear strength against distance from the pile center normalized with the pile radius in a logarithmic scale. From Randolph, Carter et al. (1979) and their case A.

From Figure 11.7 and Figure 11.8, we see that the presented model reproduces the results of Randolph, Carter et al. (1979) to a reasonable degree of accuracy when stresses are normalized with the mobilized shear strength.

In addition to the results presented by Randolph, Carter et al. (1979), the model have been checked with results presented by Bergset (2015). Table 11.2 presents the material properties used by Bergset (2015) for his case a).

Table 11.2: Material properties used to reproduce results obtained by Bergset (2015) case a).

Material Model	Modified Cam-Clay
Drainage type	Undrained (A)
Unit weight, γ, $\left[{}^{kN}/_{m^3}\right]$	20
Compression index, λ, [-]	0,0875
Swelling index, κ, [-]	0,0087
Unloading/reloading Poisson's ratio, ν'_{ur}, [-]	0,2
Initial void ratio, e_0, [-]	1,2
Strength (inclination of CSL), M, [-]	1,2
Permeability, k, $\left[{}^{m}/_{day}\right]$	$8{,}64 * 10^{-6}$
Change of permeability, c_k, [-]	0,6
Coefficient of lateral earth pressure, K_0, [-]	0,656
Overconsolidation ratio, OCR, [-]	1
Undrained shear strength, s_u, [kPa]	32,3

The undrained shear strength is as before based on the mobilized shear strength ($\tau_{mob} = {}^{1}/_{2}\,(\sigma_1 - \sigma_3)$) found when running the model. Figure 11.9 shows the results generated and Figure 11.10 shows the results presented by Bergset (2015).

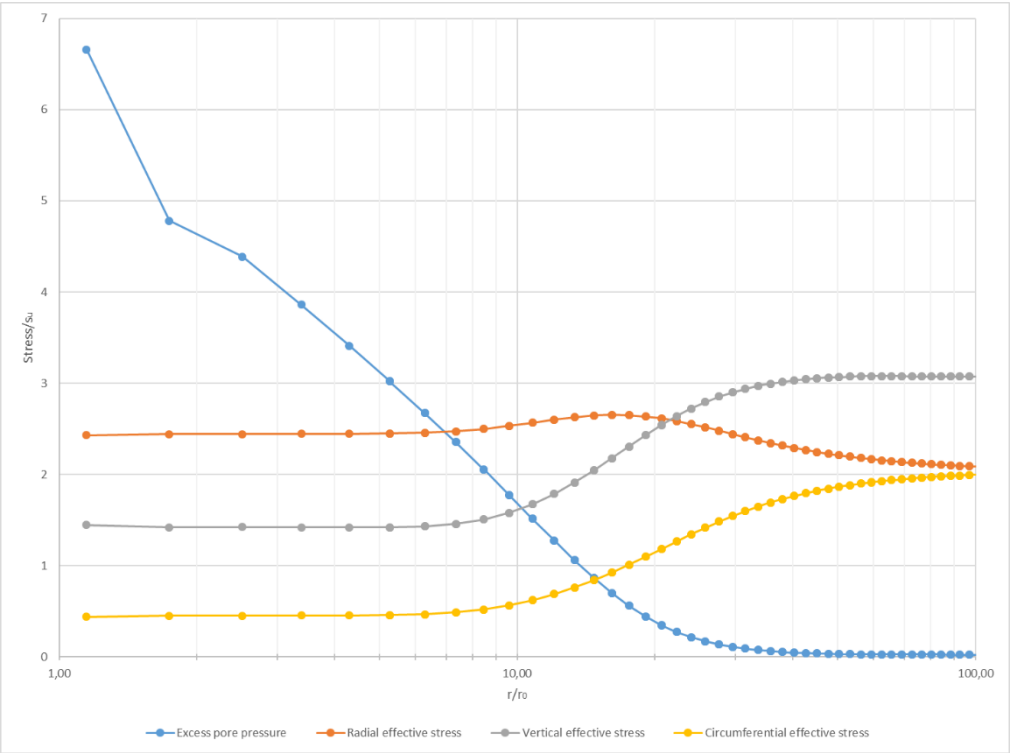

Figure 11.9: Stresses after expansion normalized with the undrained shear strength against distance from pile center normalized with the pile radius in a logarithmic scale. Found by using the material set given in Table 11.2 and the model described above but with a mesh generated using a constant coarseness factor of one over the entire model.

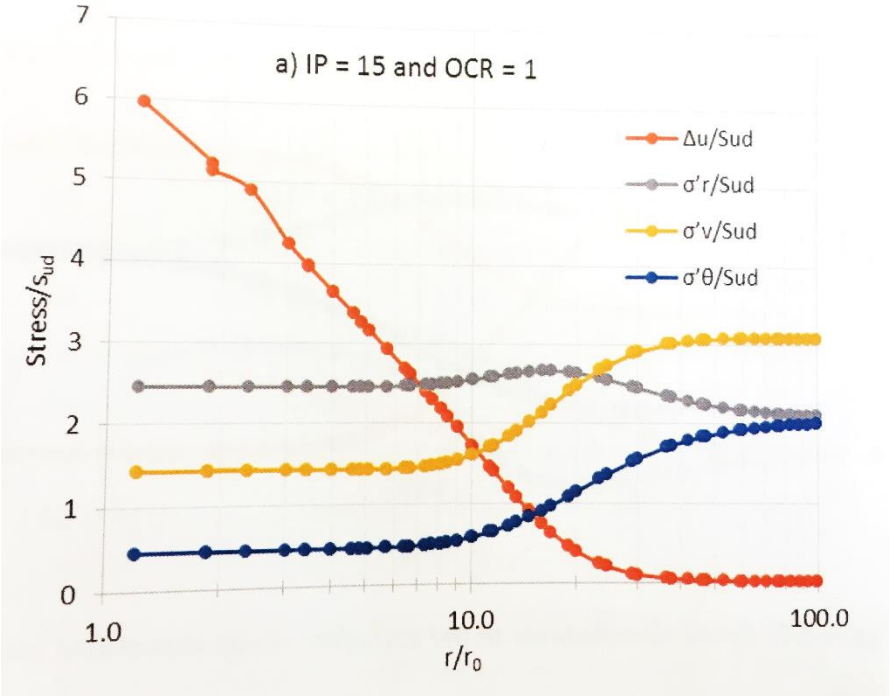

Figure 11.10: Stresses after expansion normalized with the undrained shear strength against distance from the pile center normalized with the pile radius in a logarithmic scale. From Bergset (2015) for his case a).

We see that the stress point closest to the pile shows slightly higher excess pore pressure than what Bergset (2015) reports. This is studied closer in Chapter 11.3, but is probably due to the combined effect of the geometry of the mesh, and numerical uncertainties because of the singularity of the closest stress point.

In addition to checking results obtained by using the Modified Cam Clay (MCC) material model, the results from using a linear elastic-perfectly plastic Tresca material model has been compared to the analytical solution presented in Chapter 5. Table 11.3 shows the input material data used in the Plaxis simulation. The analytical solution (Equation 5.2-5.10) uses Janbu's Dilatancy parameter equal to zero, as well as the undrained shear strength and the undrained shear modulus reported in the table as input. Figure 11.11 shows the results where the Plaxis results are represented by dots and the analytical solution is represented by solid lines.

Table 11.3: Material properties used to check with the analytical solution of a linear elastic-perfectly plastic Tresca material presented in Chapter 5.

Material Model	Mohr-Coulomb
Drainage type	Undrained (B)
Unit weight, γ, $\left[{}^{kN}/_{m^3}\right]$	20
Undrained shear modulus, G_u, [kPa]	6000
Drained Poisson's ratio, ν', [-]	0,33
Coefficient of lateral earth pressure, K_0, [-]	1
Undrained shear strength, s_u, [kPa]	20

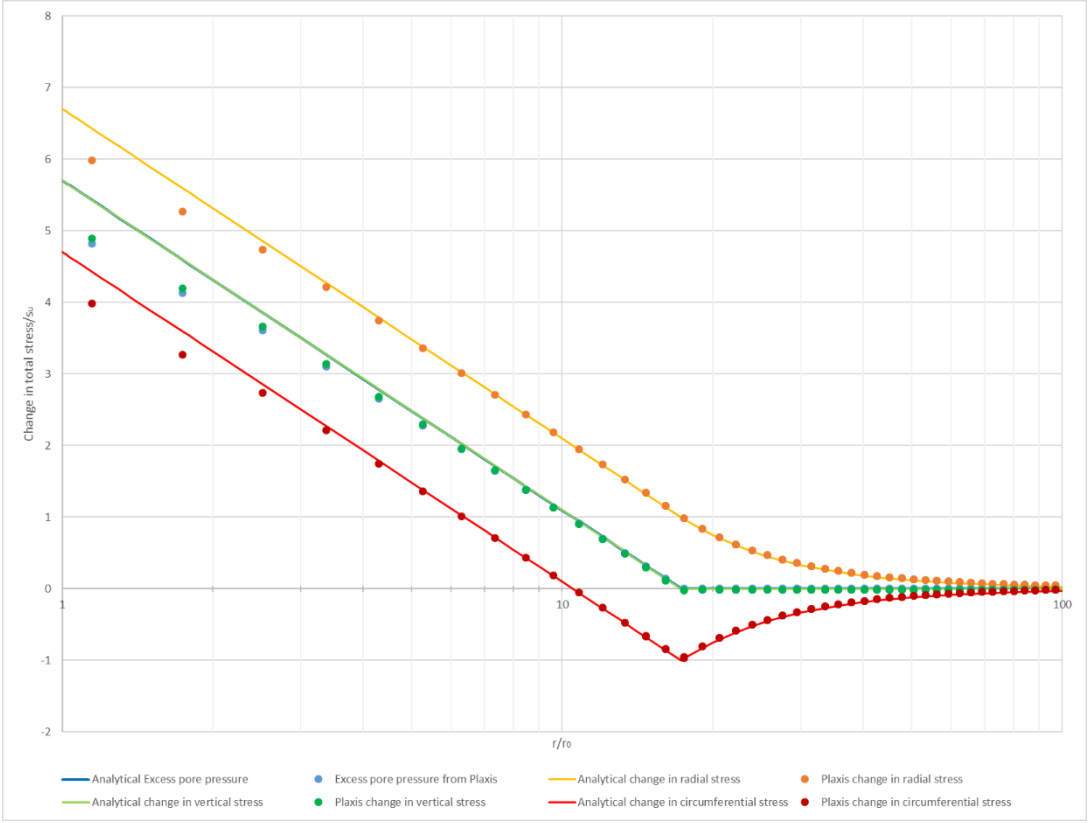

Figure 11.11: Results from Plaxis using the material properties from Table 11.3 compared to the analytical solution presented in Chapter 5 for a linear elastic-perfectly plastic Tresca material.

Figure 11.11 shows a good fit between the analytical solution and the numerical simulation. The three stress points closest to the pile wall are slightly lower than the analytical solution. There could be many reasons for the reduction, one is that the numerical model is free to displace vertically again causing a reduction in stiffness due to the reduced vertical support. This also fits the fact that the vertical displacement is largest close to the pile, and quite rapidly decrease following a sort of logarithmic decay as seen in Figure 11.12. Other factors influencing the results could be the “updated mesh” future and numerical uncertainties due to the large strains close to the pile wall.

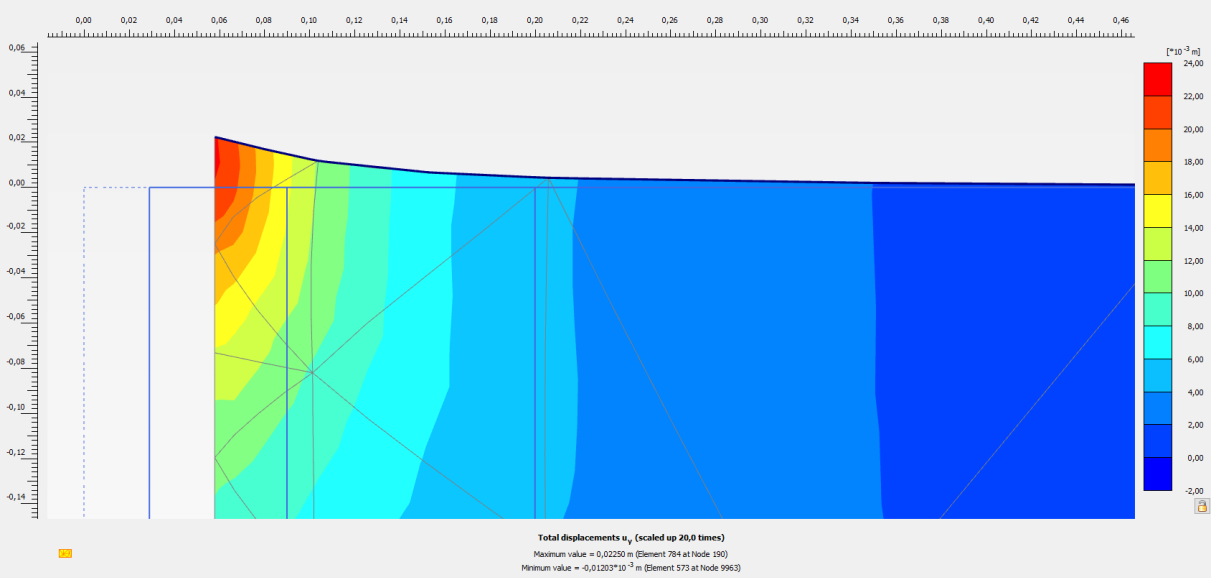

Figure 11.12: Vertical displacement after expansion in a Tresca material with soil properties as described in Table 11.3.

11.3 Some testing of the boundary conditions

In addition to verifying that the model functions by reproducing results, different boundary conditions have been tested. The boundary conditions chosen in Chapter 11.1 are in accordance with what the physical problem implies. If the terrain is fixed so that it cannot displace vertically the results from the expansion phase are close to unchanged in many cases, but for some cases there seem to be slightly more numerical disturbance when having the terrain free. In reality the terrain is free, however the results obtained by having the terrain free seems to sometimes cause the stress points nearest the pile wall to deviate from what we expect. Figure 11.13 shows the normalized stresses after expansion for Randolph, Carter et al. (1979) case A, with both the terrain fixed and the terrain free to displace vertically.

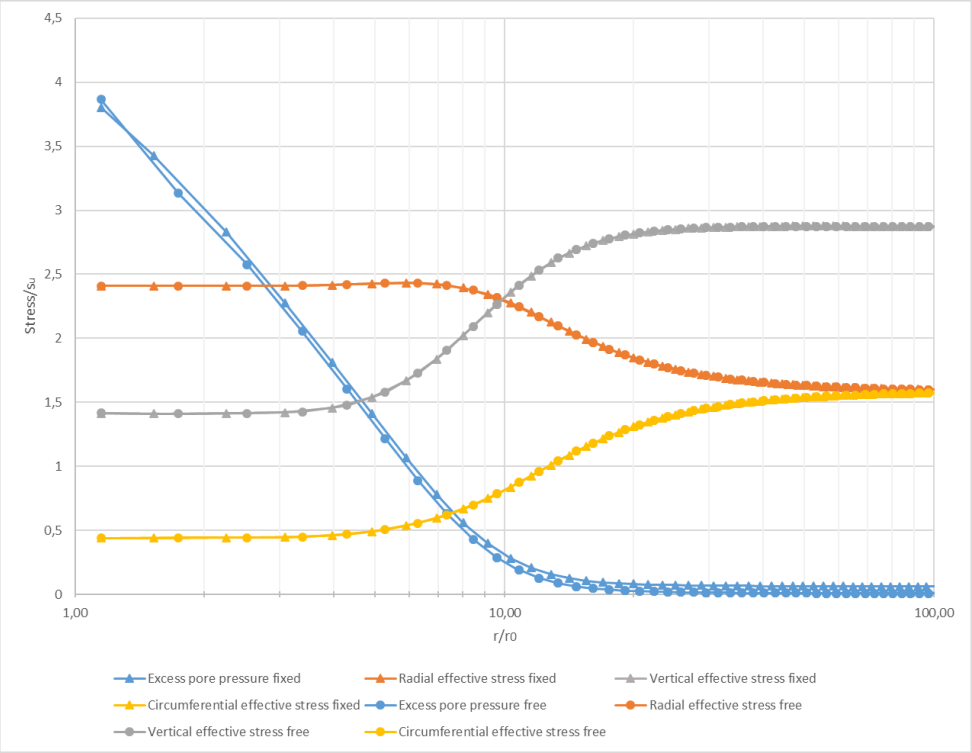

Figure 11.13: Stresses after expansion normalized with the undrained shear strength against distance from pile center normalized with the pile radius in a logarithmic scale. Found by using the material set given in Table 11.1 and the model described above with the terrain both fixed and free to displace vertically ($y = 0m$).

Figure 11.13 shows that the Cartesian effective stresses are unchanged. However, the excess pore pressure changes slightly. With the terrain fixed the excess pore pressure does not go towards zero but 0,06 $\Delta u_{max}/s_u$. This is because when the terrain is fixed the soil have nowhere to displace causing an increase in excess pore pressure in the entire model. This is not in accordance with the elastic analytical solution saying that the excess pore pressure should be zero in the elastic range.

Figure 11.14 shows similar results but for Bergset (2015) case a). Here we also see that the closest stress points are slightly more disturbed with the terrain free. The difference in the excess pore pressure from having the terrain fixed and free are close to constant if the stress points close to the pile are neglected. One way of avoiding numerical uncertainties due to the singular point between the terrain and the pile could then be to fix the terrain and subtract a constant value equal to the value of the excess pore pressure far away from the pile, where it should be zero. Fixing only a meter or two from the pile (instead of the full length of the model) causes the excess pore pressure difference to be smaller. This procedure have however not been tested and is solely based on Figure 11.13 and Figure 11.14.

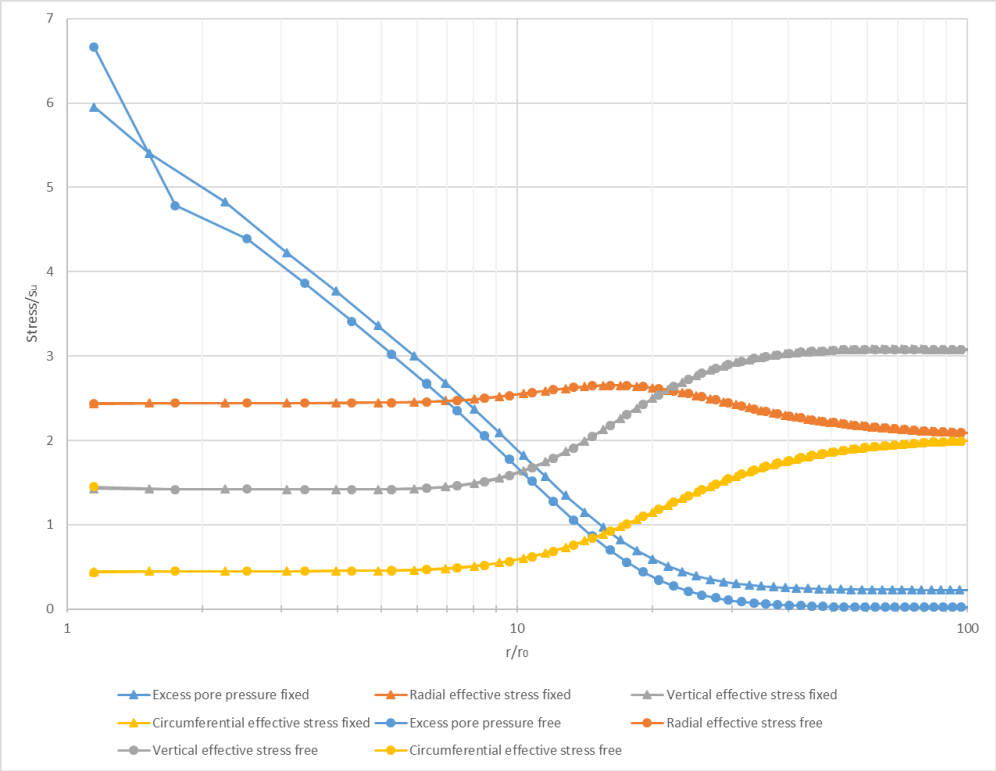

Figure 11.14: Stresses after expansion normalized with the undrained shear strength against distance from pile center normalized with the pile radius in a logarithmic scale. Found by using the material set given in Table 11.2 and the model described above with the terrain both fixed and free to displace vertically ($y = 0m$).

Due to the disturbance of the results from the closest stress points, and the differences between what Bergset (2015) reports and what the model presented here gives, the effect of mesh geometry has been studied.

Figure 11.15 shows the excess pore pressure produced after the expansion phase using the material properties from Table 11.2 together with three different meshes. The blue line have a constant coarseness factor of one, while the green and orange line use a coarseness factor of 0,25 and 0,1 respectively, from $x = 0$ to $x = 0{,}2m$.

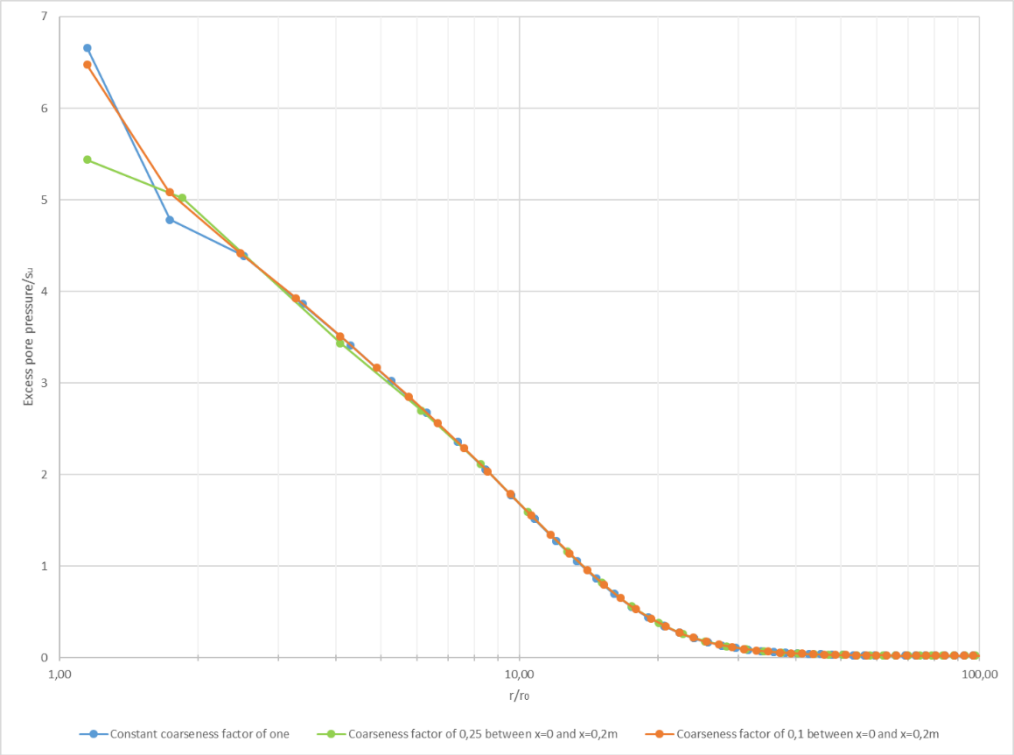

Figure 11.15: Influence of mesh on excess pore pressure using the material properties from Table 11.2.

Figure 11.15 shows that the differences in excess pore pressure in the two stress points closest to the pile wall may very well come from the mesh geometry. From Chapter 6.3 and the semi-analytical solution of CEM-MCC of Chen and Abousleiman (2012) we know that in the critical state region, the excess pore pressure is a straight line in a log-plot. Knowing this the best results seem to be obtained by using a coarseness factor of 0,1 between $x = 0$ and $x = 0{,}2m$. However, the results using a coarseness factor of 0,25 between $x = 0$ and $x = 0{,}2m$ are worse than using a constant coarseness factor of 1. This is believed to be caused by the irregularity of the mesh as seen in Figure 11.16. Due to these results, it is recommended to view the mesh and to try to achieve as regular a mesh as possible close to the pile.

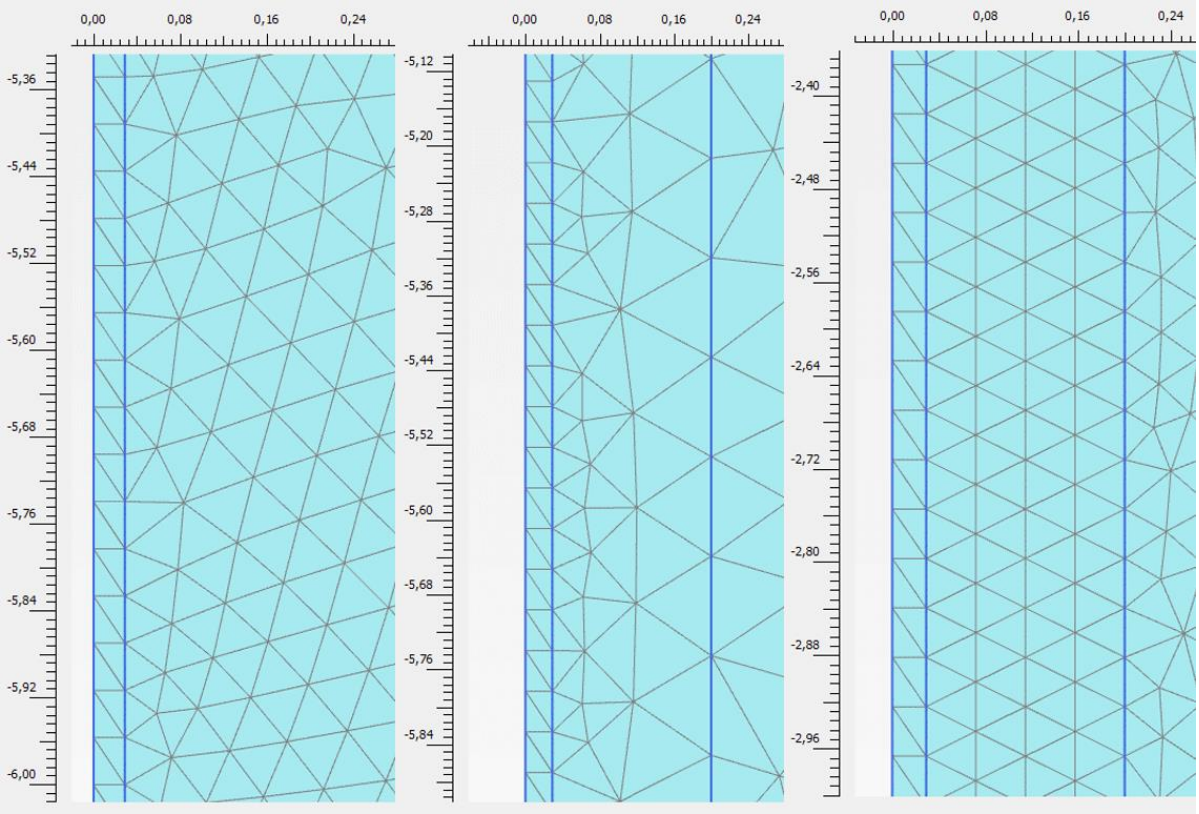

Figure 11.16: Different meshes, from the left: constant coarseness factor of 1*, coarseness factor of* 0,25 *from* $x = 0$ *to* $x = 0{,}2m$ *and coarseness factor of* 0,1 *from* $x = 0$ *to* $x = 0{,}2m$*.*

The groundwater flow boundary condition at terrain (i.e. $y = 0m$) have also been tested. The boundary have been both closed and open for groundwater flow. This did nothing to change the excess pore pressure after expansion. The groundwater flow boundary has therefore been left open as this is what the real physical problem implies. Setting the vertical permeability equal to zero have also been tested. This was done since both Bond and Jardine (1991) and Karlsrud (2012) find that a one dimensional radial consolidation process fit experimental data quite well. The difference in the obtained stresses directly after expansion are as expected unchanged by this. The time to reach a minimum excess pore pressure of $1kPa$ was also checked. When the vertical permeability is zero the time increase by 7% compared to having the vertical permeability equal to the horizontal, when using the material properties in Table 11.2. The dissipation is mainly radial even when the vertical permeability equals the horizontal, and the change in time is so small that the fit to experimental data is probably still quite good. Whether this improves or weakens the fit of the consolidation time to experimental data has not been checked.

12 Study of the Cavity Expansion Method

12.1 General

In this chapter we will look closer at the results generated with the Cavity Expansion Method (CEM), and explain the produced results with respect to the material models. The intention is to better understand what may be lacking in the material models or in the modelling procedure (i.e. CEM). The model presented in Chapter 11 is used, and the results are not normalized with the undrained shear strength as often done in the literature. This was chosen since it may confuse the reader when normalizing the stresses. As seen in Figure 7.5 the undrained shear strength is not always chosen to be equal, and the results presented in Figure 7.4 is then easily misinterpreted. We will however choose the input parameters so that the maximum mobilized shear strength of the model always equal $37kPa$. It may therefore be noteworthy that the initial stresses are: $\sigma_{v0} = 200kPa, u_0 = 100kPa$ and $\sigma'_{v0} = 100kPa$.

12.2 Tresca material model

Table 12.1 shows the chosen parameters for the linear elastic-perfectly plastic Tresca (EP) material. These parameters are chosen so that they fit the parameters in Table 12.2 for the Modified Cam Clay (MCC) material. Figure 12.1 shows a deviatoric stress-strain plot generated in Plaxis SoilTest using the material parameters in Table 12.1 and 12.2. The plot shows the results from an undrained triaxial compression test isotropically consolidated to $100kPa$, and the parameters in Table 12.1 were adjusted to give a reasonable fit. Later it was found that the results from CEM-MCC are equivalent to CEM-EP, if the slope of the critical state line (M) in the MCC model is modified until the maximum mobilized shear strength (τ_{mob}) obtained from the model equals the undrained shear strength (s_u) of the Tresca material (i.e. $37kPa$), given that the overconsolidation ratio (OCR) equals two.

Table 12.1: Material properties of the linear elastic-perfectly plastic Tresca material used to look at differences in produced results when using different material models.

Material Model	Mohr-Coulomb
Drainage type	Undrained (B)
Unit weight, γ, $\left[{}^{kN}/_{m^3}\right]$	20
Shear modulus, G_u, [kPa]	7500
Drained Poisson's ratio, ν', [-]	0,30
Coefficient of lateral earth pressure, K_0, [-]	1 (unless otherwise stated)
Undrained shear strength, s_u, [kPa]	37 (unless otherwise stated)

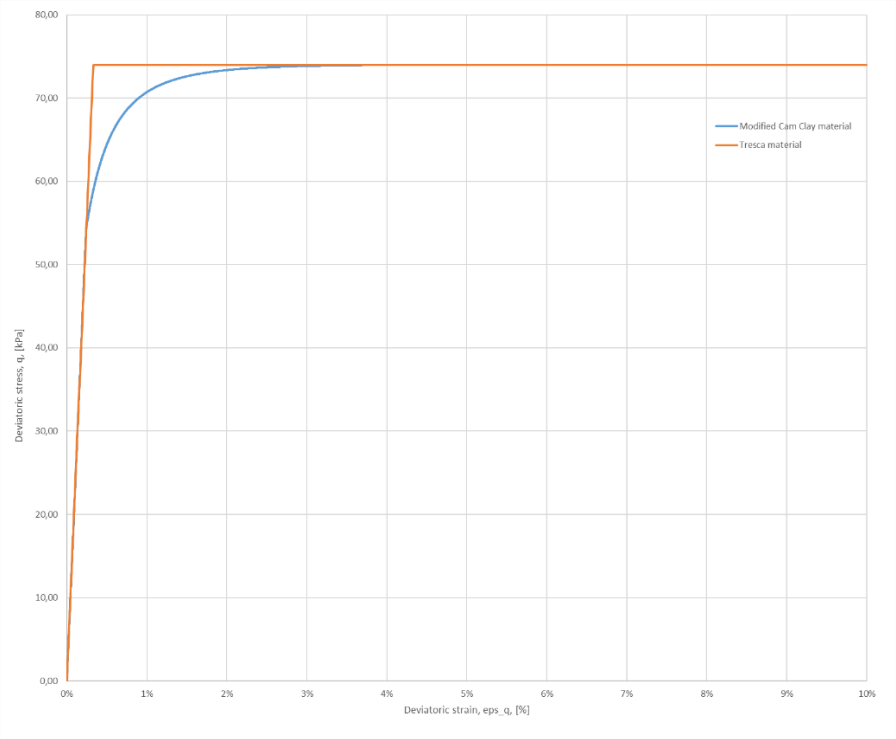

Figure 12.1: Plot of deviatoric stress and strain to show the fit of the stiffness and strength between the Modified Cam Clay and the Tresca material. Results from an undrained triaxial compression test isotropically consolidated to $100kPa$ in Plaxis SoilTest.

Figure 12.2 shows the stresses after the cavity expansion phase in a Tresca material with the properties from Table 12.1 and coefficient of lateral earth pressure (K_0) equal to one.

Similar plots have been shown previously, but in the following many plots similar to that of Figure 12.2 will be presented so some extra description is included here. On the x-axis is the distance from the center of the pile (r) normalized with the pile radius (r_0) in a logarithmic scale. At the pile wall we then have $^{r}/_{r_0} = 1$ and the plot is limited to $^{r}/_{r_0} = 100$. Figure 12.3 shows the same results with a linear scale, and it becomes clear why a logarithmic scale is used. The data close to the pile wall, which is the data we are mostly interested in, becomes easier to interpret. It is however important not to forget the real scale of things.

On the y-axis the stress is presented in kilopascals (kPa) in a linear scale. The legend shows which line that corresponds to which stress component. The plot shows the Cartesian total and effective stresses together with the total and effective mean stress, deviatoric stress, and mobilized shear strength directly after the prescribed displacement has developed completely (i.e. without any dissipation). The vertical red line shows the location of the plastic limit. The plastic limit, described in Chapter 5, shows where the excess pore pressure will start to develop when using the Tresca and Modified Cam Clay (MCC) material models. To the left of this limit the yield criterion of the soil model is fulfilled and plastic strains develop, while to the right of the limit, the yield criterion is not fulfilled, and only elastic strains have developed.

The results shown in Figure 12.2 compare to the analytical solution (given in Chapter 5) giving a maximum excess pore pressure of $\Delta u_{max} = s_u \ln\left(^{G_u}/_{s_u}\right) = 196kPa$. Which shows that the numerical results are slightly lower than the analytical as discussed for Figure 11.11. The plastic limit is found by examining the plastic points, called failure points in Plaxis for the Tresca material model (see Figure 12.4). Analytically the limit is found by: $^{r_p}/_{r_0} = \sqrt{^{G}/_{s_u}} = 14{,}24$. Which coincides very well with the numerical results.

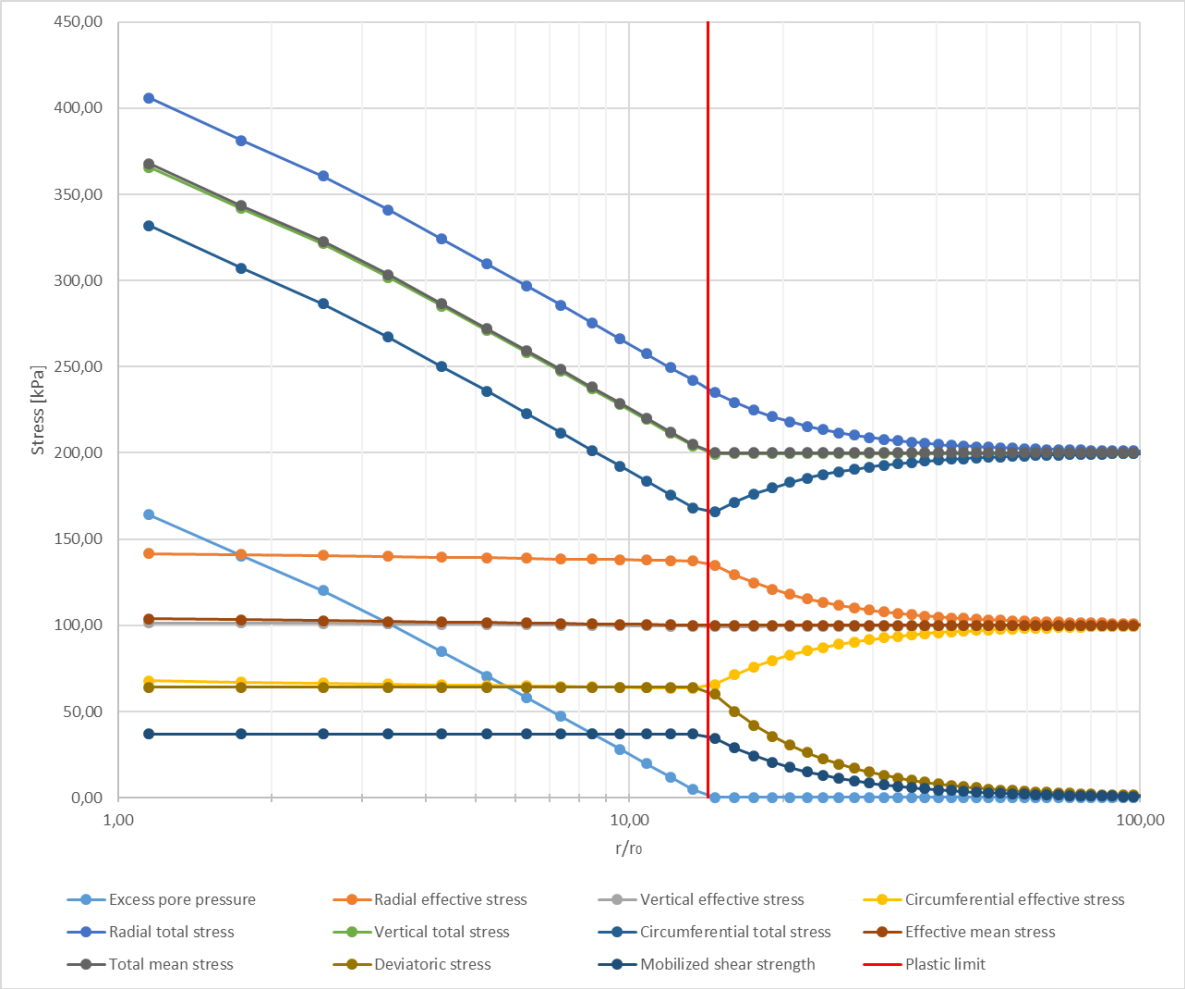

Figure 12.2: Stresses after the cavity expansion phase against the logarithm of the normalized distance from the pile center in a Tresca material with parameters as in Table 12.1.

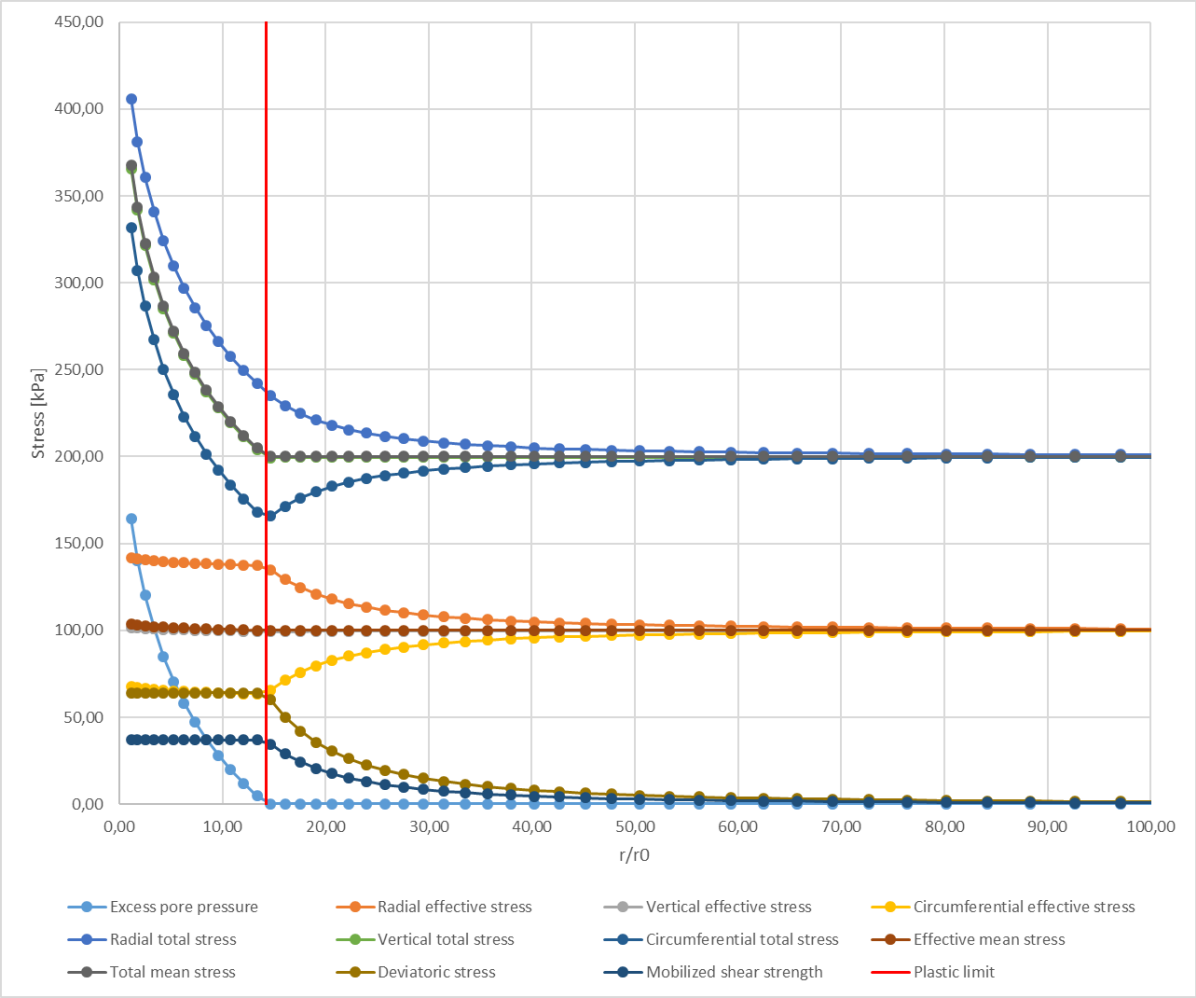

Figure 12.3: Stresses after the cavity expansion phase against the normalized distance from the pile center in a linear scale in a Tresca material with parameters as in Table 12.1.

To the right of the plastic limit is the elastic range. The analytical solution for this was presented in Chapter. 4. A less formal description is given below. In the elastic range Hooke's law applies, and under undrained conditions the volume change is assumed to be zero.

$$\Delta\varepsilon_{vol} = \frac{\Delta p'}{K} = 0 \tag{12.1}$$

Equation 12.1 then yields that the change in effective mean stress must be zero in the elastic range. CEM is applying a radial displacement, which again means applying positive radial strains and negative circumferential strains (see Figure 4.4). The vertical displacement is zero, and the radial stresses increase due to the applied radial displacement. Circumferential stress decrease due to the negative circumferential strains. Radial stresses increase equally much as

the circumferential stresses decrease because the vertical strain, and then also the stress is unchanged, and the effective mean stress must be constant (following Equation 12.1).

The shear stress equals the difference between the radial (major) and the circumferential (minor) stress, and increase until the yield criterion is fulfilled. For a Tresca material this is: $2s_u = \sigma_1 - \sigma_3$. This means that the plastic limit (i.e. red line) is located where the difference between the radial and circumferential stress (both effective (orange and yellow) and total (blue and dark blue)) is $2s_u = 74kPa$. Within the plastic region, the yield criterion is fulfilled. That means the difference between radial and circumferential stress is constant and equal to $2s_u$ left of the plastic limit. Within the plastic region the radial displacement is still increasing. This causes the total radial stress to increase, but the difference between the total radial stress and the total circumferential stress must be constantly equal to $2s_u$, meaning the total circumferential stress also must increase. This increase in total stress cannot be compensated for by increasing the effective stresses, as the change in mean effective stress must be zero. The excess pore pressure is therefore increasing equally much as the total stress. In other words, the radial total stress must increase to compensate increasing radial displacement. The radial effective stress cannot change since $2s_u = \sigma_1' - \sigma_3'$ and $\Delta p' = 0$. The excess pore pressure must hence increase to account for the increase in total radial stress, while the vertical total stress will increase as the excess pore pressure increase.

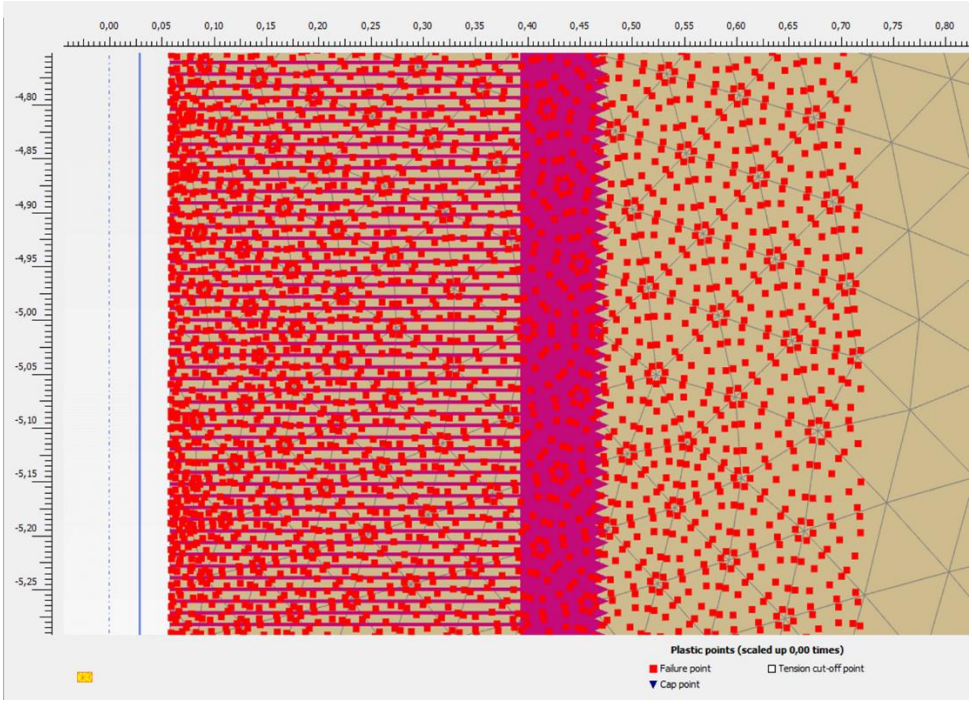

Figure 12.4: Plastic points after cavity expansion in a Tresca material with parameters as in Table 12.1.

12.3 Modified Cam Clay material model and effect of *OCR*

In addition to the Tresca material model, the Modified Cam Clay (MCC) material model have been studied. As mentioned previously the Tresca material parameters were chosen so that it gave a reasonable fit to the MCC material properties. The MCC material properties are listed in Table 12.2, and were chosen so that they represent a medium stiff Norwegian clay as presented by Nordal (2018). Later it was decided to change the slope of the critical state line (M) so that the obtained maximum mobilized shear strength (τ_{mob}) equals the undrained shear strength of $37kPa$.

Table 12.2: Material properties of the Modified Cam Clay material used to look at differences in produced results when using different material models.

Material Model	Modified Cam-Clay
Drainage type	Undrained (A)
Unit weight, γ, $\left[{}^{kN}/_{m^3}\right]$	20
Compression index, λ, [-]	0,1
Swelling index, κ, [-]	0,02
Unloading/reloading Poisson's ratio, ν'_{ur}, [-]	0,2
Initial void ratio, e_0, [-]	1
Strength (inclination of CSL), M, [-]	Changed so that $s_u = \tau_{mob} = 37kPa$
Coefficient of lateral earth pressure, K_0, [-]	1 (unless otherwise stated)
Overconsolidation ratio, OCR, [-]	1,4 (unless otherwise stated)

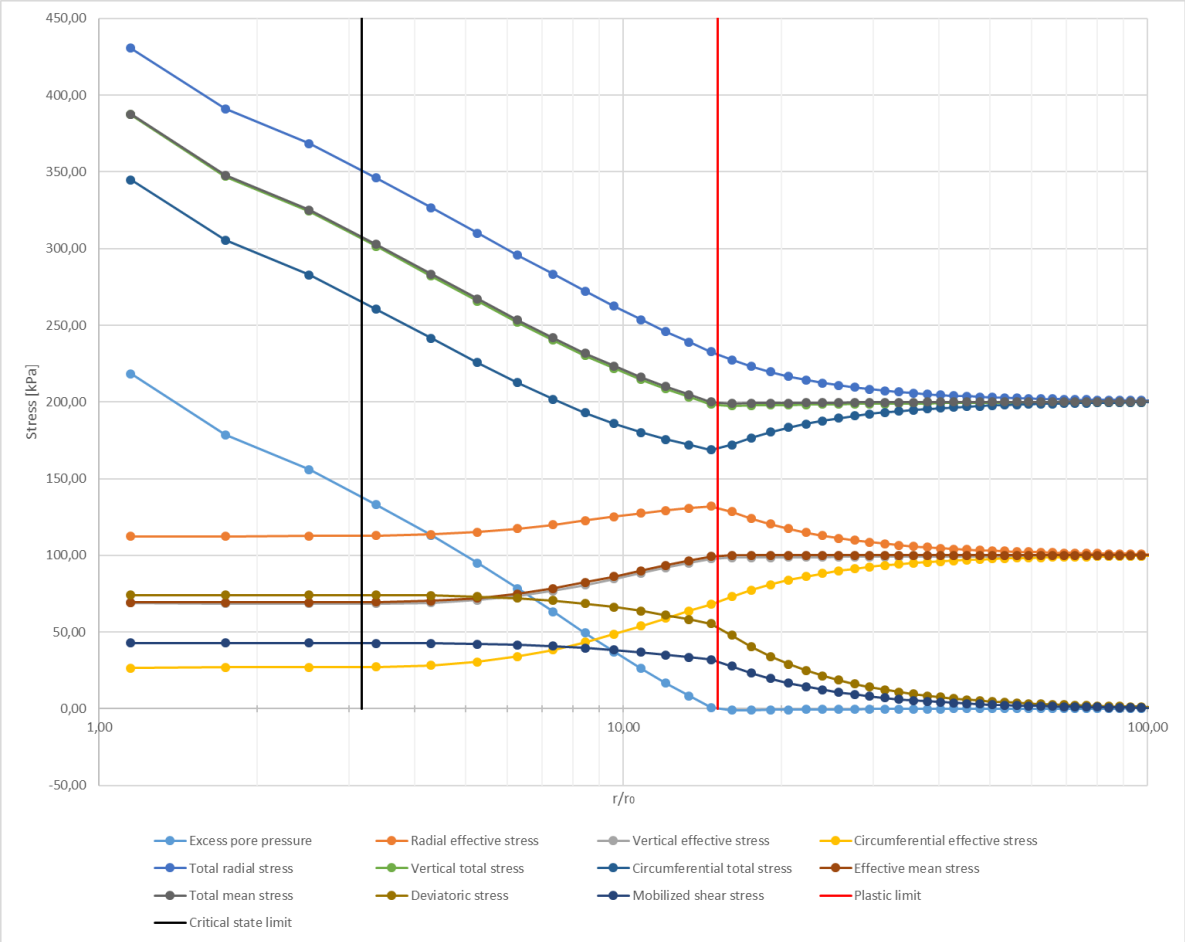

Figure 12.5: Stresses after the cavity expansion phase against the logarithm of the normalized distance from the pile center in a Modified Cam Clay material with parameters as in Table 12.2 and $M = 1{,}07$.

Figure 12.5 shows the stresses after expanding the cavity using the material properties listed in Table 12.2, and the initial choice of $M = 1{,}07$. Figure 12.5 include one more line, namely the critical state limit. To the left of this line, the soil is in critical state, as discussed in Chapter 6, and unlimited shear strains can develop without any change in effective stress, volume or shear stress. Between the critical state limit and the plastic limit, the soil develops plastic strains. While to the left of the plastic limit the soil only develop elastic strains as previously explained.

Comparing Figure 12.5 to Figure 12.2 we can see some of the differences between using the MCC and the EP material models. Firstly we see that the mobilized shear strength is about $43kPa$. This causes the total stresses to also be slightly higher than observed in Figure 12.2.

The best fit between MCC and EP is obtained when matching the resulting mobilized shear strength from the MCC model to the undrained shear strength used in the Tresca model. This was checked by changing the slope of the critical state line until the obtained mobilized shear

strength equaled $37kPa$. Figure 12.6 shows that if the maximum mobilized shear strength is matched between the MCC and the EP material models then the total stresses are principally equal.

To the right of the plastic limit we have the elastic range and the results are quite similar regardless of the material model. Since the overconsolidation ratio (OCR) is less than two, the effective mean stress will reduce when expanding the ellipse of the MCC model until critical state is reached, as described in Chapter 6. In other words, the effective mean stress will be reduced in the plastic range (i.e. between the plastic limit and the critical state limit), and be constant within the critical state region and the elastic region. The reduction in effective stresses is accompanied by an increase in excess pore pressure so that the total stresses are left unchanged. The MCC model then only introduce a reduction in effective stresses (due to $OCR < 2$), which again results in an increase in excess pore pressure.

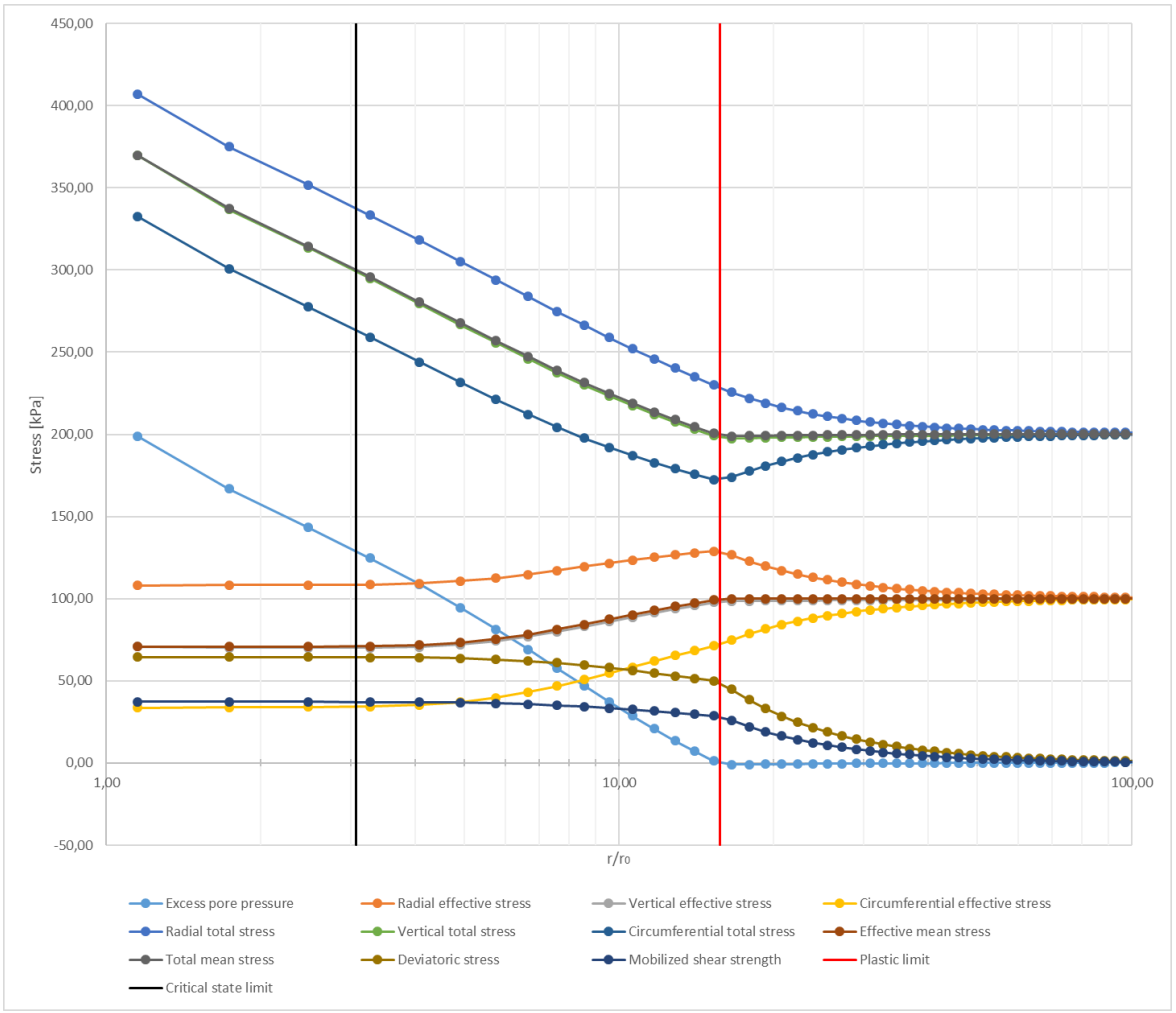

Figure 12.6: Stresses after the cavity expansion phase against the logarithm of the normalized distance from the pile center in a Modified Cam Clay material with parameters as in Table 12.2 but with $M = 0{,}91$ so that $\tau_{mob} = s_u = 37kPa$.

If the overconsolidation ratio (OCR) is higher than two then the mean effective stress will increase as plastic strains develops. Figure 12.7 shows the results from the cavity expansion using the material parameters from Table 12.2, but now with OCR equal to three. In order to obtain a maximum mobilized shear strength of $37kPa$ the inclination of the critical state line is reduced to $M = 0{,}46$, which again compares to a frictional angle of 12,3°. This is unnaturally low and not very realistic. However, the response of the material model is the same regardless of M being small, and for comparison it is favorable that the maximum mobilized shear strength is constant.

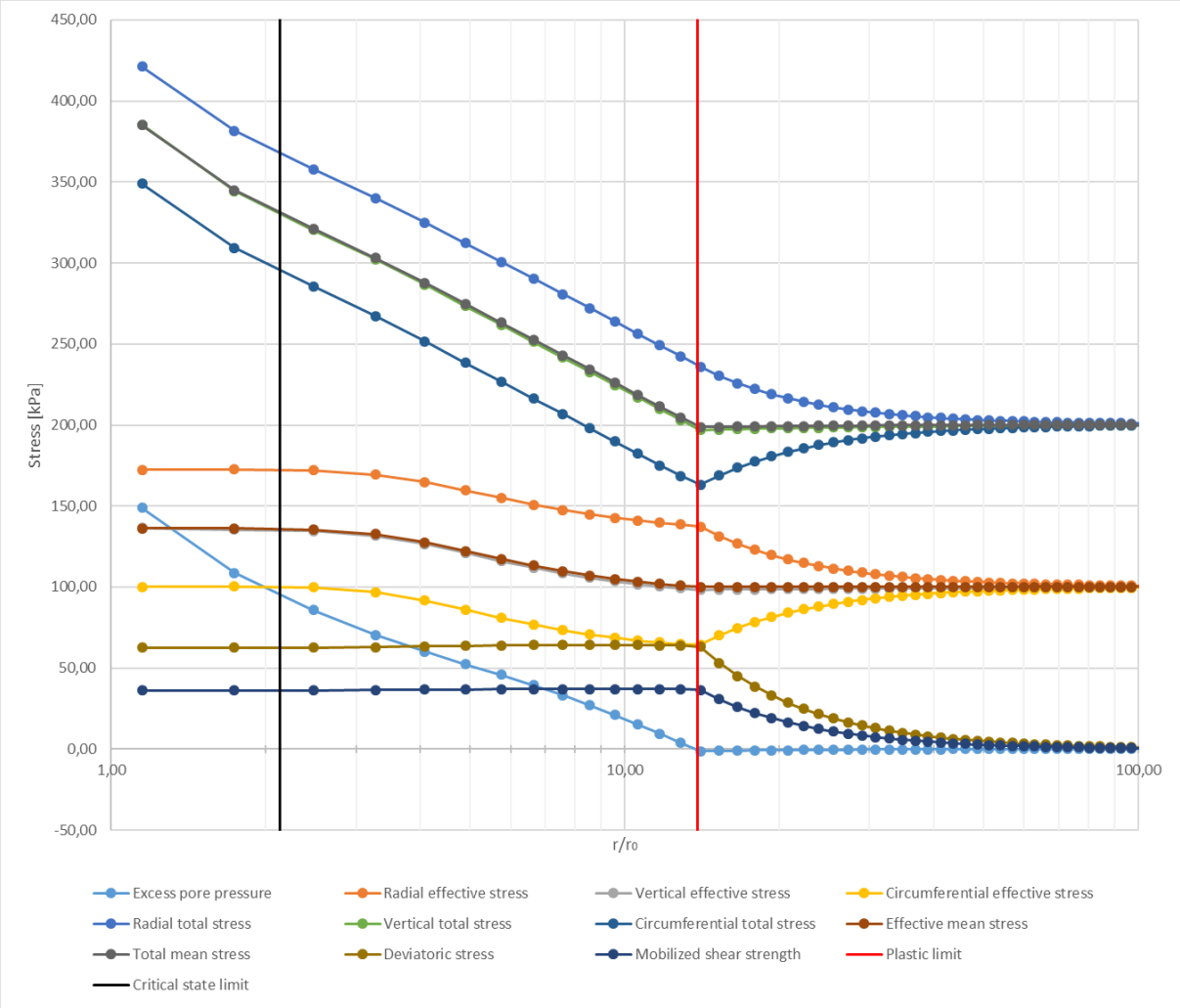

Figure 12.7: Stresses after the cavity expansion phase against the logarithm of the normalized distance from the pile center in a Modified Cam Clay material with parameters as in Table 12.2 but with $OCR = 3$ and $M = 0{,}46$ so that $\tau_{mob} = s_u = 37kPa$.

Figure 12.6 and Figure 12.7 shows us that the MCC model mainly differ from the EP model due to the dilation/contraction of the material. When the material dilates (i.e. $OCR > 2$ in the MCC material model) then the excess pore pressure decrease, while the effective stresses

increase. If the material contracts (i.e. $OCR < 2$ in the MCC model) then the excess pore pressure increase, while the effective stresses decrease. For the chosen material properties, the excess pore pressure equals 1,21 times the Tresca solution when $OCR = 1{,}4$, and the excess pore pressure equals 0,91 times the Tresca solution when $OCR = 3$.

In Appendix A.1 figures showing the stress paths, both effective and total, of CEM-MCC with OCR equal to 1, 2 and 10 are presented. Appendix A.2 shows stress paths of CEM-EP with changing coefficient of lateral earth pressure (K_0). While Appendix C.1 shows the stresses as the displacement evolve in CEM-MCC, and C.2 shows them during the dissipation process as time evolve. The results are not presented here as they are not nessecary for the discussion, but has been included in the Appendix so that they can be checked.

This dilation, when the clay is overconsolidated, and contraction, when the clay is normally consolidated, could also be modelled using the analytical solution presented in Chapter 5 with Janbu's Dilatancy parameter (D) to produce similar results at the pile shaft as the ones obtained using the MCC model.

If there is no dilation nor contraction then the MCC model is equivalent to a linear elastic-perfectly plastic model (i.e. equal to the analytical solution with $D = 0$). Meaning that the CEM-MCC model reproduces the stresses found by using the analytical solution quite precisely given $OCR = 2$ and $K_0 = 1$. Figure 12.8 shows both the stresses produced by the CEM-MCC model with $OCR = 2$ and $K_0 = 1$, and the analytical solution with $G_u = 7500kPa$ and $s_u = 37kPa$. The correspondence is just as good, or even better than when using the Tresca material (see Figure 11.11).

This is not surprising as the MCC material model becomes linear elastic-perfectly plastic when the isotropic preconsolidation pressure (p_p) equals two times the effective mean stress (i.e. $p_p = 2p'$). Also CEM monotonically increases the radial strain, giving monotonically increasing total stress. This means that we do not have any unloading, and if then the flexibility parameters of the MCC model (κ and λ) is fitted, as described in Chapter 11, to the shear modulus (G_u), and the slope of the critical state line (M) is fitted so that the maximal mobilized shear strength (τ_{mob}) equals the undrained shear strength (s_u) used in the analytical solution, then it is seen that the CEM-MCC model equals the analytical solution given $OCR = 2$ and $K_0 = 1$.

Because the input in Plaxis is the vertical overconsolidation ratio, and the isotropic preconsolidation pressure does not equal the vertical overconsolidation ratio times the initial effective stress ($p_p \neq OCR * p'$), it is a little problematic to get no dilation/contraction in the Plaxis model. The next chapter discuss this further, and shows that it is not as simple as to say $OCR = 2$ (even with $K_0 = 1$) in the Plaxis input to get $p_p = 2p'$.

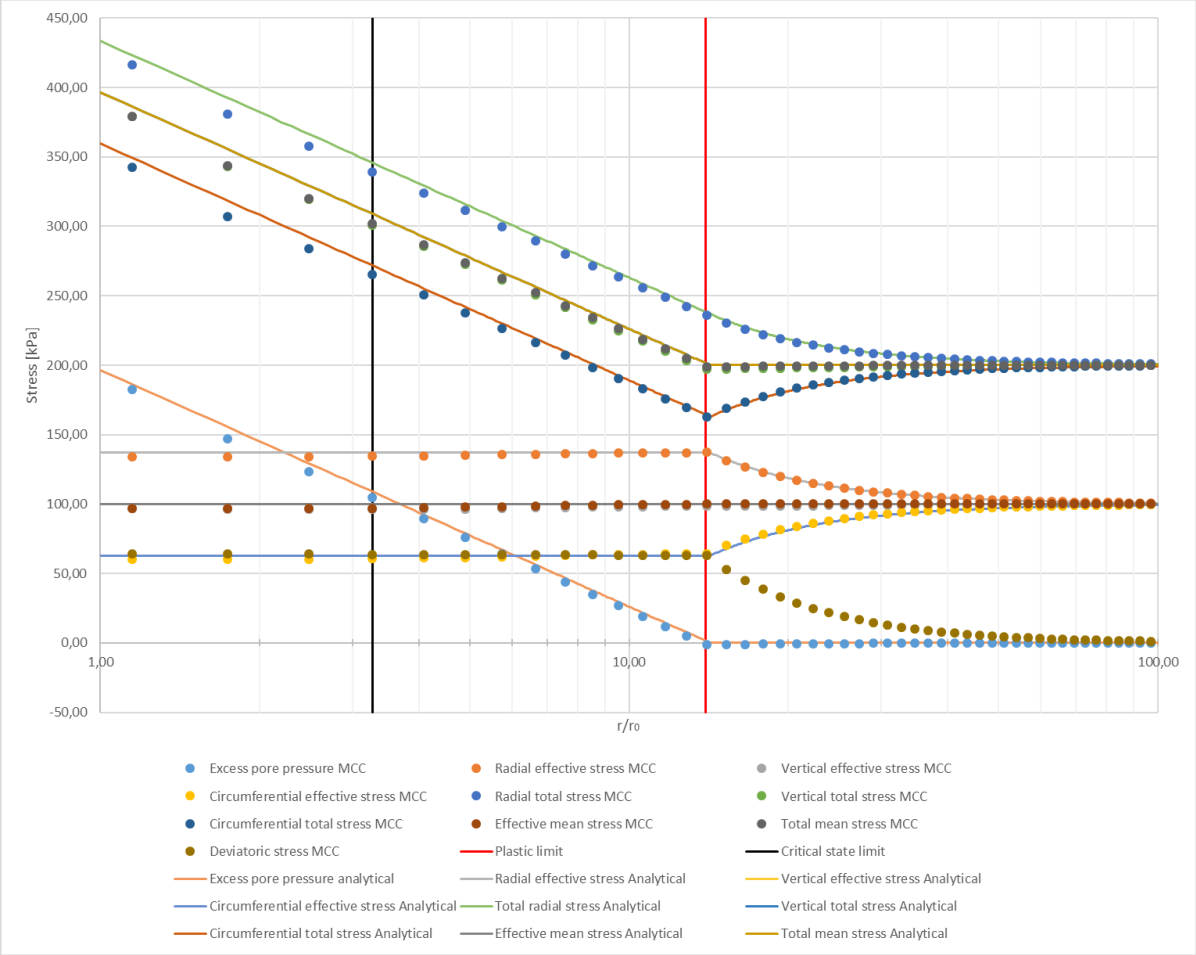

Figure 12.8: Stresses after the cavity expansion phase against the logarithm of the normalized distance from the pile center. The dots are stresses found by using the Modified Cam Clay material with parameters as in Table 12.2 but with $OCR = 2$ and $M = 0{,}66$ so that $\tau_{mob} = s_u = 37kPa$. The lines are the analytical solution found in Chapter 5 using Janbu's pore pressure parameter $D = 0$.

12.4 Isotropic *OCR* and vertical *OCR* in Plaxis

Included here is an explanation of the isotropic overconsolidation ratio versus the vertical overconsolidation ratio. We often determine the vertical overconsolidation ratio from testing, but when doing a parametric study of OCR in CEM-MCC we want to control the isotropic overconsolidation ratio. The Plaxis material manual by Brinkgreve, Kumarswamy et al. (2018) is the source of the explanation presented here. In Plaxis, the inputted OCR defines the vertical overconsolidation ratio. This is given by:

$$OCR = \frac{\sigma_p}{\sigma'_{v0}} \tag{12.2}$$

where OCR is the vertical overconsolidation ratio, σ_p is the vertical preconsolidation stress and σ'_{v0} is the initial vertical effective stress. The MCC model does however use the isotropic preconsolidation stress (p_p). The effective mean stress and deviatoric stress once were:

$$q_c = (1 - K_0^{NC}) * OCR * \sigma'_{v0} \; and \; p'_c = \frac{1 + 2K_0^{NC}}{3} * OCR * \sigma'_{v0} \tag{12.3}$$

In the MCC model the coefficient of lateral stress at rest in normal consolidation (K_0^{NC}) is determined based on the slope of the critical state line (M), the unloading/reloading Poisson's ratio (ν_{ur}), and the flexibility parameters (λ, κ) through:

$$M = 3\sqrt{\frac{(1 - K_0^{NC})^2}{(1 + 2K_0^{NC})^2} + \frac{(1 - K_0^{NC})(1 - 2\nu_{ur})(\lambda/\kappa - 1)}{(1 + 2K_0^{NC})(1 - 2\nu_{ur})\,\lambda/\kappa - (1 - K_0^{NC})(1 + \nu_{ur})}} \tag{12.4}$$

Lastly the initial isotropic preconsolidation pressure may be found using the relationship:

$$p_p = p'_c + \frac{q_c^2}{M^2 * p'_c} \tag{12.5}$$

Plaxis operates with an isotropic overconsolidation ratio which is defined as:

$$OCR_i = \frac{p_p}{p_{eq}} \; where \; p_{eq} = p' + \frac{q^2}{M^2 * p'} \tag{12.6}$$

where p_{eq} is the equivalent isotropic stress, and OCR_i is the isotropic overconsolidation ratio. The vertical overconsolidation ratio needed to get no dilation/contraction ($\Delta p' = 0$) is quite hard to find if at the same time the slope of the critical state line (M) is to be so that the mobilized shear strength equals the undrained shear strength ($\tau_{mob} = s_u$). Already the modeling is an iterative procedure where one guesses a M, check the τ_{mob}, and choose either a lower or higher M, so that one gets $\tau_{mob} = s_u$. If we then want no dilation/contraction then the vertical overconsolidation ratio OCR must be so that $p_p = 2p'$. This can be solved for OCR using the equations above, but the OCR would become a function of M. This makes the iterative procedure even more cumbersome as the vertical overconsolidation ratio very much influence τ_{mob}.

12.5 Changing the coefficient of lateral earth pressure

By changing the coefficient of lateral earth pressure another difference between the Tresca and the MCC material models is revealed. Figure 12.9, 12.10 and 12.11 shows the stresses after the cavity expansion phase in a Tresca material with properties as in Table 12.1, and coefficient of lateral earth pressure (K_0) equal to 0,4, 1,4 and 0,6 respectively. Comparing Figure 12.2 to Figure 12.9, 12.10 and 12.11 we see the effect of changing the K_0.

When K_0 is less than one then the vertical stress is the major principle stress initially. If K_0 is bigger than one then the vertical stress is the minor principle stress initially. As described for Figure 12.2 the radial stress will increase in the elastic range, while the circumferential will decrease. Failure occurs in a Tresca material when $2s_u = \sigma_1 - \sigma_3$. Depending on the undrained shear strength (s_u), initial vertical effective stress (σ'_{v0}) and K_0, failure will occur either between the vertical and the circumferential stress (K_0 less than one and relatively low s_u, as seen in Figure 12.9 and barely in Figure 12.11), between the radial and the circumferential stress (relatively high s_u so that the radial and circumferential stress increase, and decrease, are dimensioning or for $K_0 = 1$, Figure 12.2) or between the radial and the vertical stress (K_0 bigger than one and relatively low s_u, Figure 12.10).

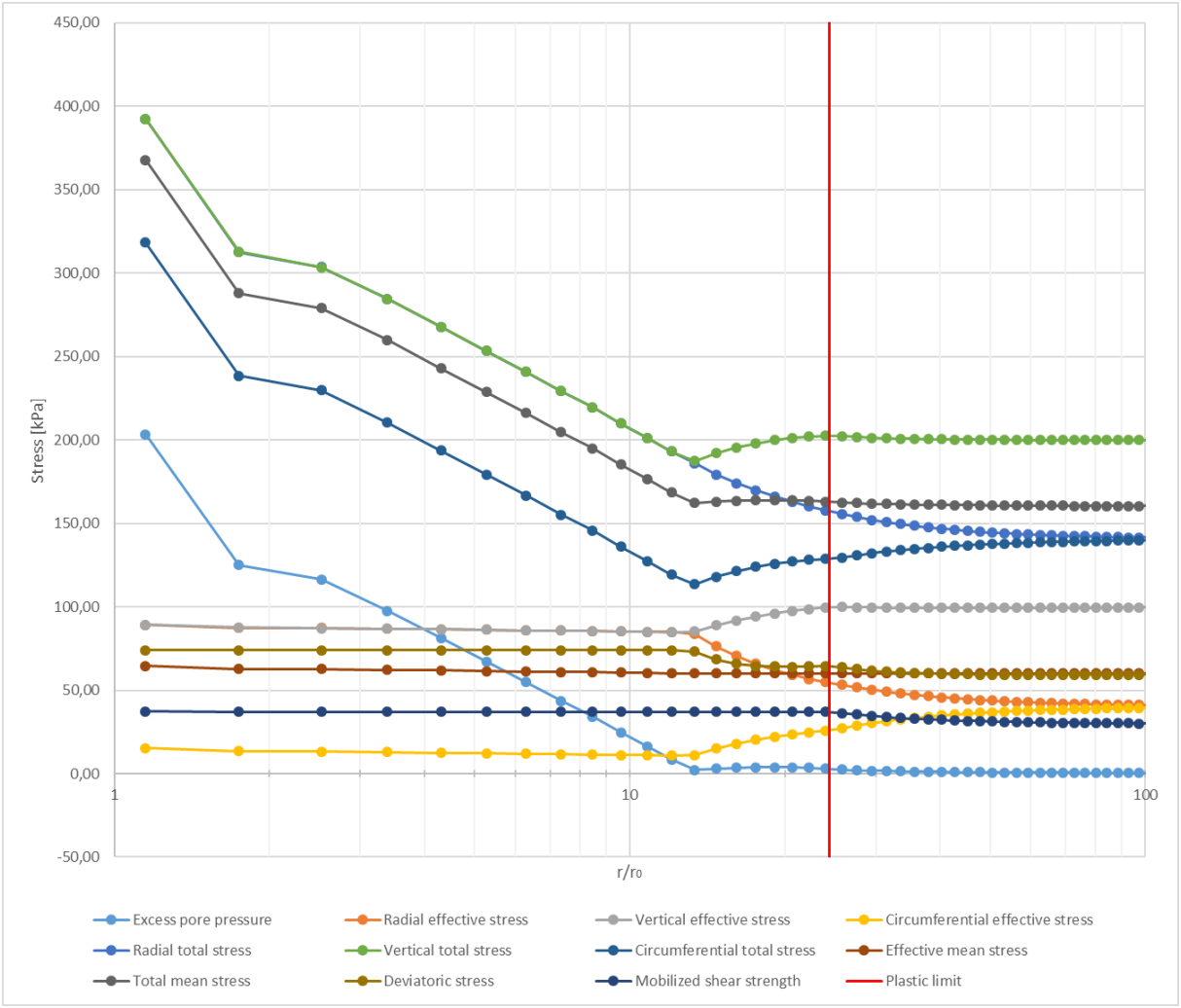

Figure 12.9: Stresses after the cavity expansion phase against the logarithm of the normalized distance from the pile center in a Tresca material with parameters as in Table 12.1 but with $K_0 = 0{,}4$.

To the left of the plastic limit the radial total stress will keep increasing as explained before. If possible, the circumferential total stress will decrease so that the increase in radial total stress leads to no excess pore pressure, and no change in mean stress. See Figure 12.9 where we have failure between the vertical and the circumferential stresses. Directly to the left of the plastic limit the vertical and circumferential stresses will decrease to account for the increasing radial stress. This increase and decrease, continues until failure between the radial and circumferential stresses occurs, at which point the graph follow the behavior explained previously for Figure 12.2.

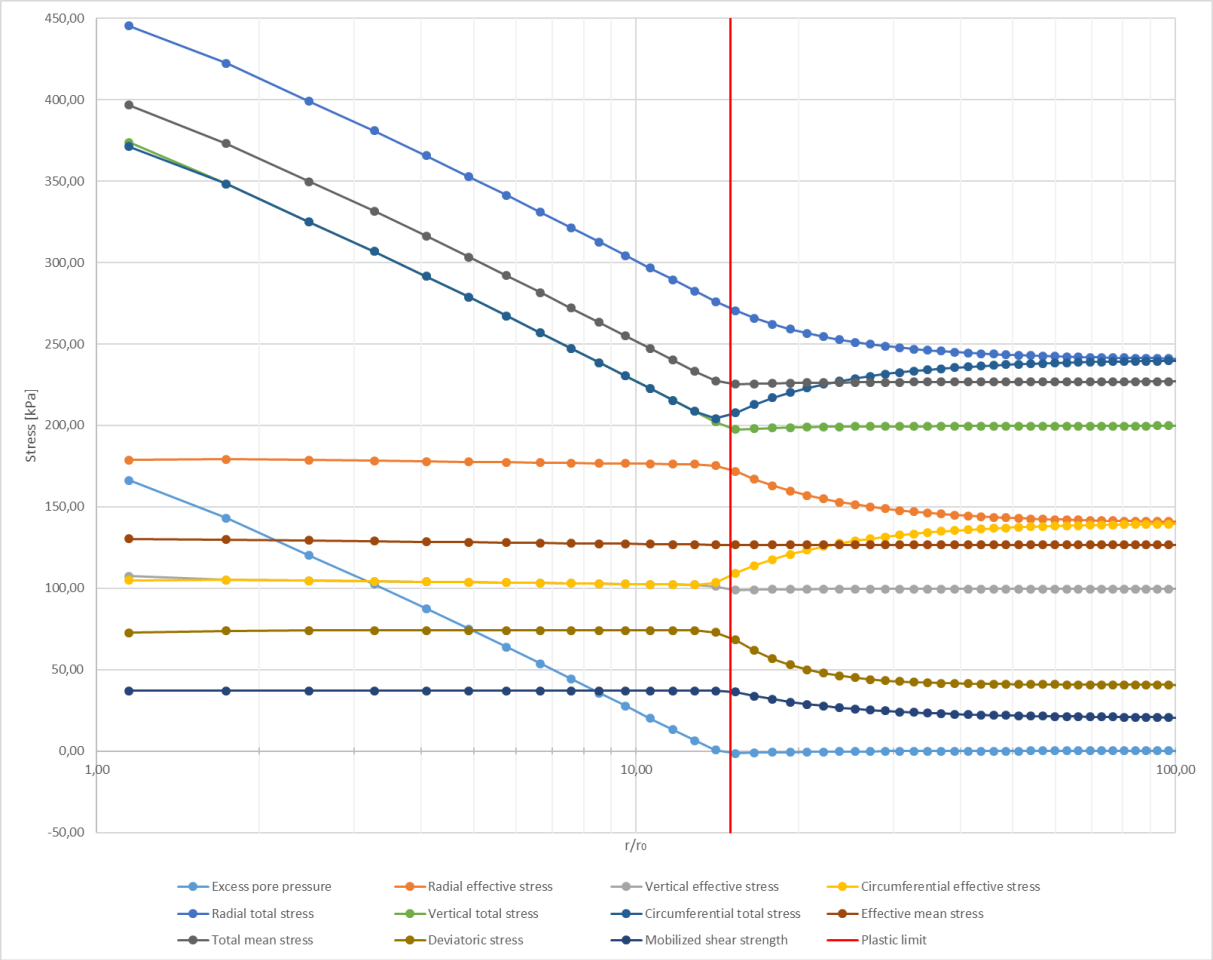

Figure 12.10: Stresses after the cavity expansion phase against the logarithm of the normalized distance from the pile center in a Tresca material with parameters as in Table 12.1 but with $K_0 = 1{,}4$.

Figure 12.10 shows the situation where the initial minor principle stress is the vertical stress. As before the radial stress will increase and the circumferential stress will decrease in the elastic range (i.e. to the right of the plastic limit). Failure will occur between the radial (major) stress and the vertical (minor) stress due to K_0 and relatively low s_u. The circumferential stress is then free to decrease after failure between the vertical and radial stresses, until failure occurs between the radial and circumferential stresses as well.

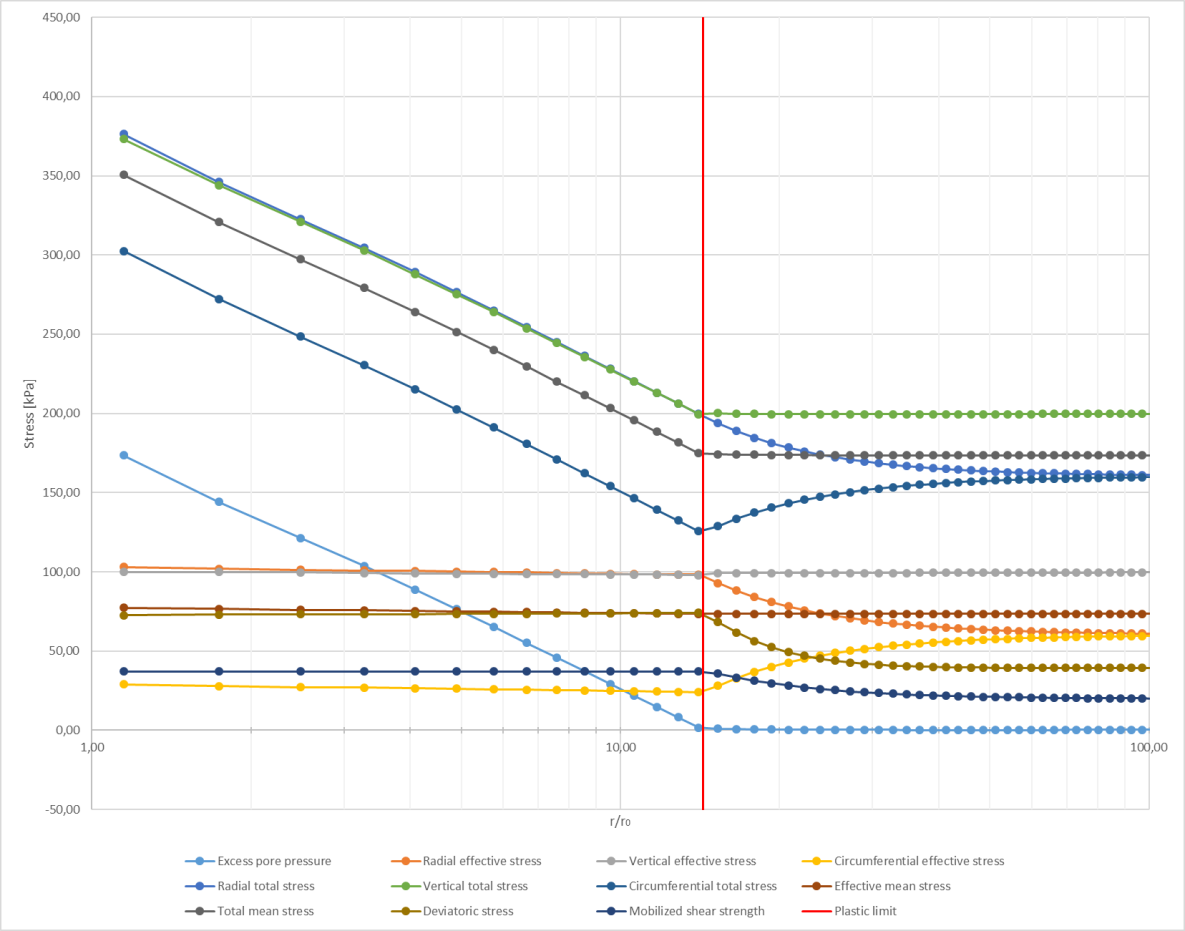

Figure 12.11: Stresses after the cavity expansion phase against the logarithm of the normalized distance from the pile center in a Tresca material with parameters as in Table 12.1 but with $K_0 = 0{,}6$.

In Figure 12.11 we see that if the s_u was slightly higher, then failure would be between the radial and the circumferential stresses. The initial mobilized shear stress can be found as $\tau_{mob,0} = {}^1/_2\left(\sigma_{1,0} - \sigma_{3,0}\right) = 0{,}5 * (200 - 160) = 20kPa$. In Figure 12.8 the initial shear stress in the soil is $\tau_{mob,0} = 0{,}5 * (240 - 200) = 20kPa$, and in Figure 12.9; $\tau_{mob,0} = 0{,}5 * (200 - 140) = 30kPa$. Since s_u is constant and equals $37kPa$, Figure 12.9 which have $\tau_{mob,0} = 30kPa$ is already quite close to failure and therefore it fails before the radial and circumferential stresses increase and decrease sufficiently. In Figure 12.11 this only barely happens due to $\tau_{mob,0} = 20kPa$. If $\tau_{mob,0}$ was slightly lower (that means either K_0 was slightly higher or σ'_{v0} was slightly lower), or if s_u was slightly higher, then failure would not occur between the vertical and circumferential stresses, but between the radial and circumferential stresses.

When assessing the excess pore pressure obtained in Figure 12.2, 12.9, 12.10 and 12.11, it is seen that if the data is extrapolated to the pile shaft (i.e. ${}^r/_{r_0} = 1$) then the excess pore

pressure is in the magnitude of $175kPa$ in all cases. In other words, the excess pore pressure seems relatively unaffected by changing the coefficient of lateral earth pressure when modeled with the EP material model, and all other parameters are unchanged.

The excess pore pressure does not start to rise before failure between the radial and circumferential stresses occurs. This is because if the failure is initiated by the vertical stress as the major or minor principal stress, then the circumferential stress still can decrease to compensate for the radial stress increase, rendering the excess pore pressure and mean stress virtually unaffected as if in the elastic range. The initial vertical stress is equal in all cases, causing the stress states to be quite different when changing the K_0 value. So even though the excess pore pressure is constant when changing K_0, the Cartesian stresses are quite substantially changed.

Figure 12.12 and Figure 12.13 shows similar results for $K_0 = 0{,}6$ and $1{,}4$ respectively, but have been produced using the MCC material model. The inclination of the critical state line (M) have been modified so that the maximum mobilized shear strength equals the undrained shear strength of the Tresca material ($37kPa$), to ease the comparison between the material models. At the same time OCR have been modified so that there is no dilation/contraction (i.e. $\Delta p' = 0$).

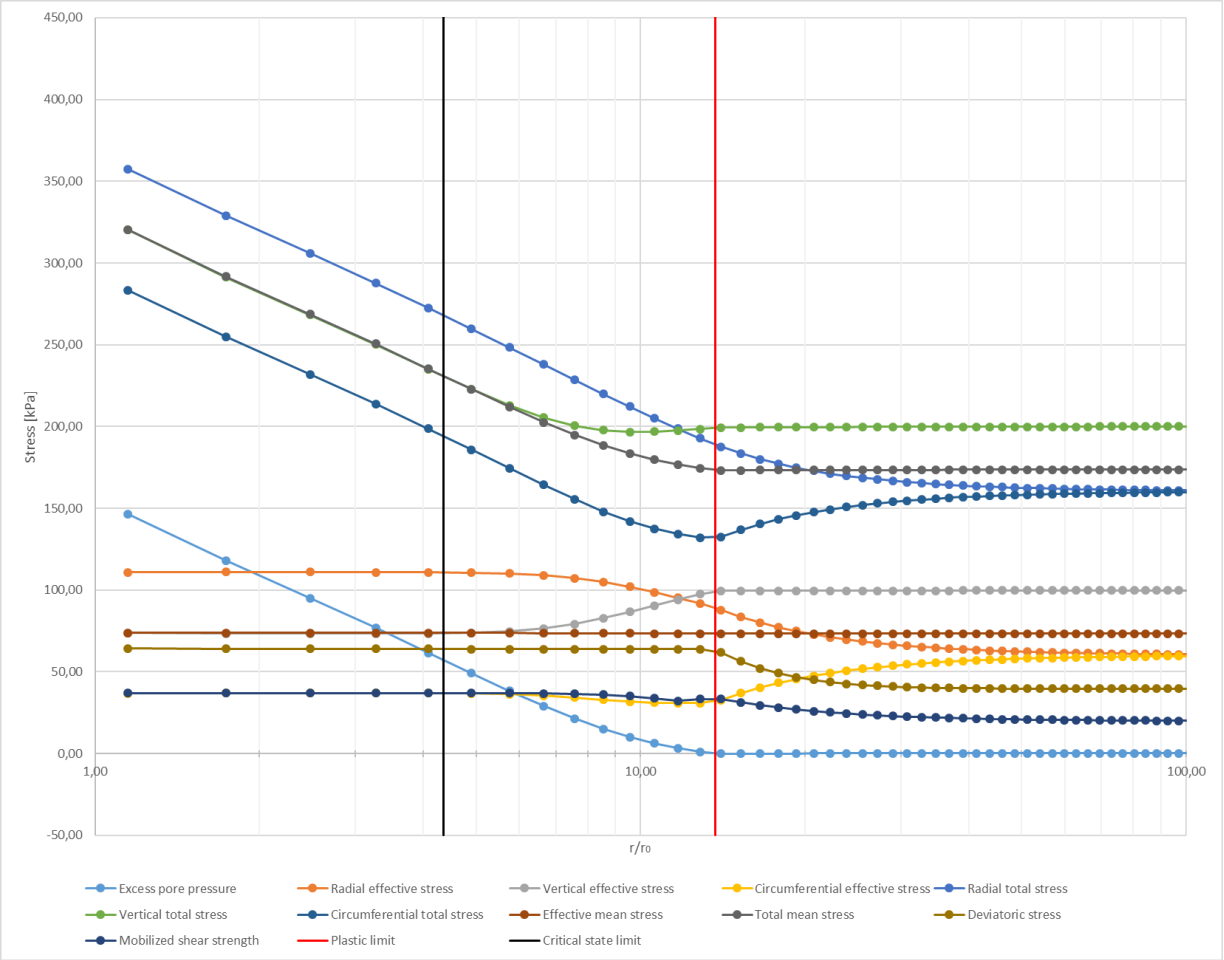

Figure 12.12: Stresses after the cavity expansion phase against the logarithm of the normalized distance from the pile center in a Modified Cam Clay material with parameters as in Table 12.2 but with $K_0 = 0{,}6$, $OCR = 1{,}58$ and $M = 0{,}87$ so that $\tau_{mob} = s_u = 37kPa$ and $\Delta p' = 0$.

Comparing Figure 12.11 and Figure 12.12 (which both have $K_0 = 0{,}6$) we see a lot of similarities, and also some differences obtained when changing the material model. To the right of the plastic limit (i.e. the elastic range) the plots are nearly identical. Between the critical state limit and the plastic limit (i.e. the plastic range) the MCC model gives a more curved change in stresses due to the gradual change in stiffness.

Using the MCC model we also see that the vertical stress (both total and effective) goes towards the mean stress as one goes towards the critical state limit. Another way of seeing it is that the vertical stress equals the mean of the radial and circumferential stress. This was also found by Chen and Abousleiman (2012), as mentioned in Chapter 6.3. This is believed to be related to the shape of the yield surface and normality of the flow in the MCC model. To the right of about $r/r_0 = 10$, the radial stress will increase and the circumferential will decrease equally much until about $r/r_0 = 10$, where the difference becomes $2s_u$. Then further

decrease in the circumferential stress is prohibited, however the vertical effective stress keeps decreasing. The radial and the circumferential effective stress will then have to increase as the vertical effective stress decrease, to keep the mean effective stress constant. Higher radial effective stress means that the excess pore pressure can be lower while the radial total stress is close to unchanged.

This causes the MCC model to predict ca. $25kPa$ lower excess pore pressure than the EP model. The small difference in radial total stress is probably due to the fact that the stiffness decrease gradually in MCC so that the final radial total stress can be somewhat lower. The main difference is anyway that the MCC model predicts the vertical effective and total stresses to reduce when $K_0 < 1$.

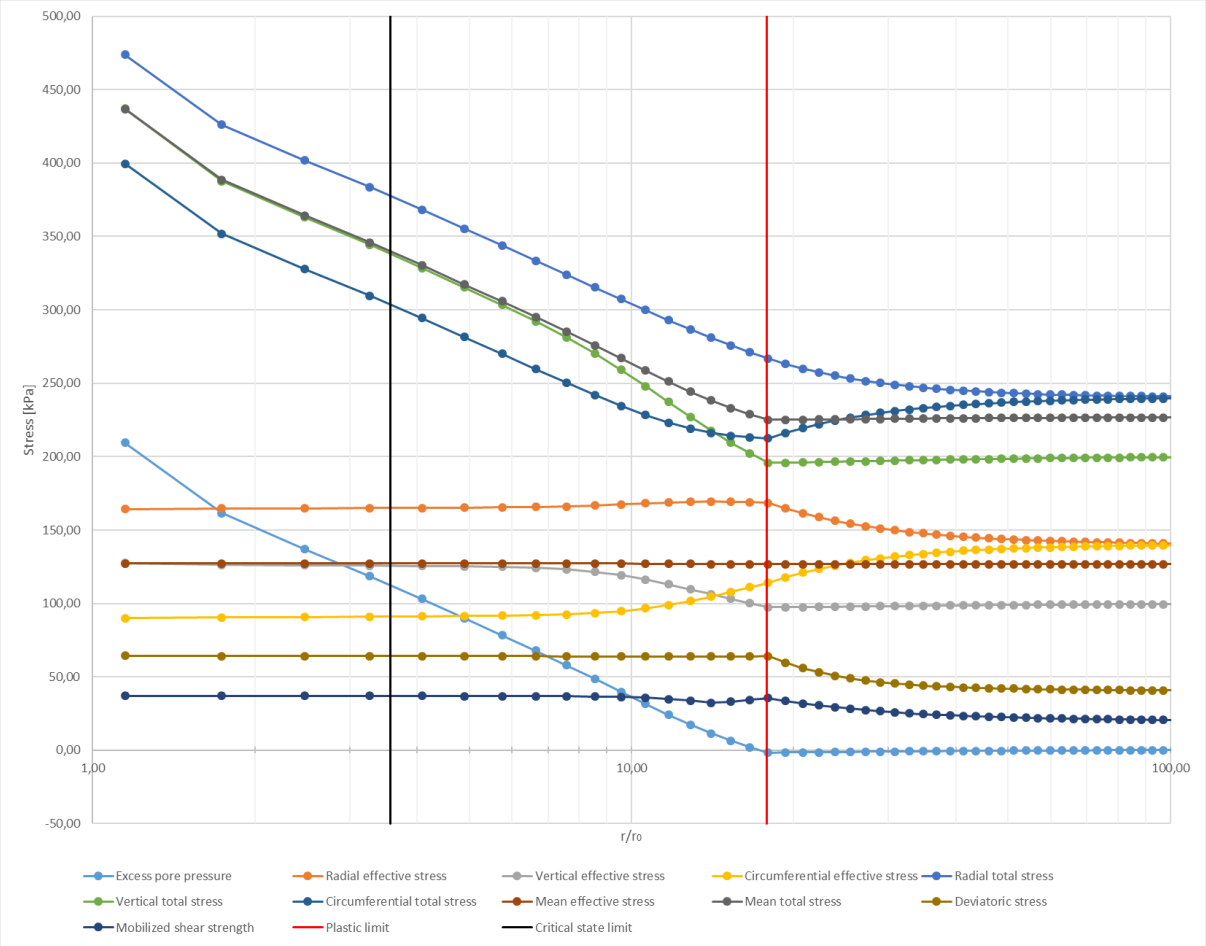

Figure 12.13: Stresses after the cavity expansion phase against the logarithm of the normalized distance from the pile center in a Modified Cam Clay material with parameters as in Table 12.2 but with $K_0 = 1{,}4$, $OCR = 2{,}6$ and $M = 0{,}505$ so that $\tau_{mob} = s_u = 37kPa$ and $\Delta p' = 0$.

Figure 12.13 and Figure 12.10 shows the obtained stresses when using $K_0 = 1{,}4$ in the MCC and the EP material models respectively. Figure 12.10 and Figure 12.13 shows the same tendencies and differences as Figure 12.9 and Figure 12.12 did, but having the opposite effect.

In Figure 12.13 the vertical stress will increase in order to follow the mean stress. This causes a reduction in the other effective stresses. The excess pore pressure must then increase in order for the radial total stress to be sufficiently large relative to the prescribed radial displacement.

When using the MCC model, the vertical stress goes towards the mean stress. This causes the vertical total stress to increase when K_0 is high (Figure 12.13), and to decrease when K_0 is low (Figure 12.12). As the excess pore pressure equals the difference between the total mean stress and the effective mean stress, this affect the excess pore pressure generated. When using the EP material model the change in effective mean stress equals zero (following Equation 12.1) so that the excess pore pressure equals the change in total mean stress. As seen from Figure 12.9 and Figure 12.10 changing the K_0 does not influence the change in total mean stress, which again means changing K_0 does not change the excess pore pressure when using the Tresca material model. However, when using the MCC material model we see from Figure 12.12 and Figure 12.13 that the change in total mean stress is affected by changing the K_0, again causing a change in excess pore pressure.

Appendix A.2 and A.3 shows stress paths from the simulations of CEM-EP and CEM-MCC respectively, with different coefficients of lateral earth pressure (K_0). The results are not presented here as they do not contribute to the discussion, but are included in Appendix so that they may be readily checked if wanted.

Whether this extra increase or decrease in excess pore pressure due to high or low K_0, respectively, is realistic is another question. K_0 is very dependent on OCR so it is hard to check this against empirical data as the two effects merge. However, we have now shown that the MCC model gives this result and whether the empirical data suggests any relation between excess pore pressure and K_0 is tested in Chapter 14.

12.6 Trends found from the CEM model

Looking at the results produced by the Cavity Expansion Method (CEM) we expect the maximum excess pore pressure from the CEM-MCC model to be equal to the analytical solution presented in Chapter 5 when $OCR = 2$ and $K_0 = 1$. Below is the variation in excess pore pressure found when changing the coefficient of lateral earth pressure (K_0) in the CEM-MCC model shown.

Figure 12.14 has been produced by using the parameters in Table 12.2 and changing the K_0 and M. Table 12.3 shows the values of M in order to get $\tau_{mob} = s_u = 37kPa$ for the different values of K_0.

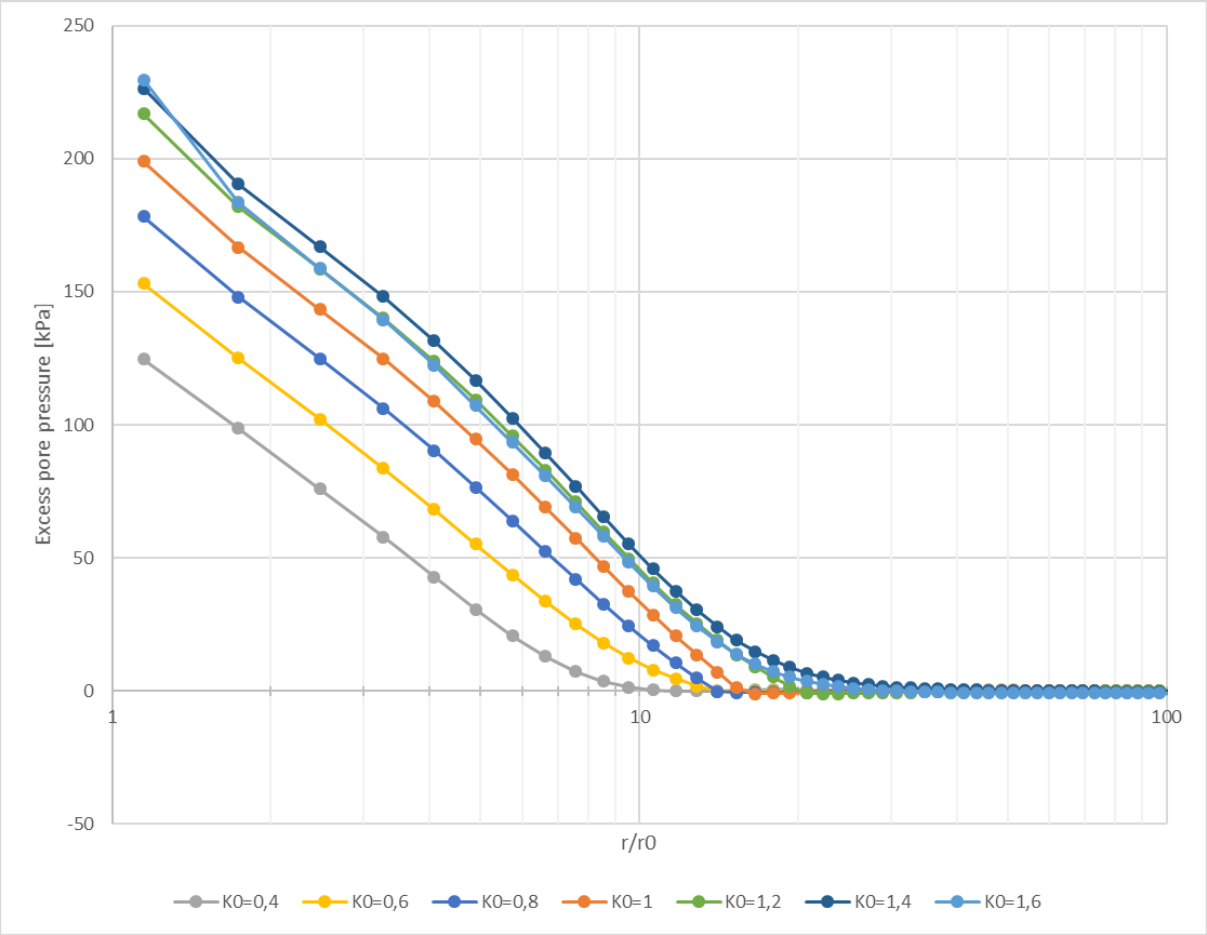

Figure 12.14: Excess pore pressure against normalized distance from pile center in a logarithmic scale for different values of the coefficient of lateral earth pressure.

Table 12.3: Coefficient of lateral earth pressure and corresponding slope of the critical state line in order for the mobilized shear strength to equal the undrained shear strength of $37kPa$.

Coefficient of lateral earth pressure, K_0	Slope of the critical state line, M
0,4	1,05
0,6	0,98
0,8	0,95
1,0	0,91
1,2	0,88
1,4	0,78
1,6	0,53

Since the initial shear stress is given by $\tau_{mob,0} = {}^{1}/_{2}\,(1 - K_0) * \sigma'_{v0}$ when $K_0 \leq 1$, which must be less than the undrained shear strength of $s_u = 37kPa$, the lowest limit of K_0 is 0,26. However, $K_0 = 0{,}3$ gave some numerical disturbance due to the small difference between initial shear stress and shear strength. Therefore was $K_0 = 0{,}4$ chosen as the lower boundary. Similarly, the initial shear stress is given by $\tau_{mob,0} = {}^{1}/_{2}\,(K_0 - 1) * \sigma'_{v0}$ when $K_0 \geq 1$. The upper limit given by $s_u = 37kPa$ then becomes 1,74. $K_0 = 1{,}6$ was chosen as the upper limit due to numerical disturbance when higher values were chosen. Figure 12.15 was made by plotting the results gathered at ${}^{r}/_{r_0} = 1{,}15$ (i.e. the closest stress point) and using simple regression tools in Excel.

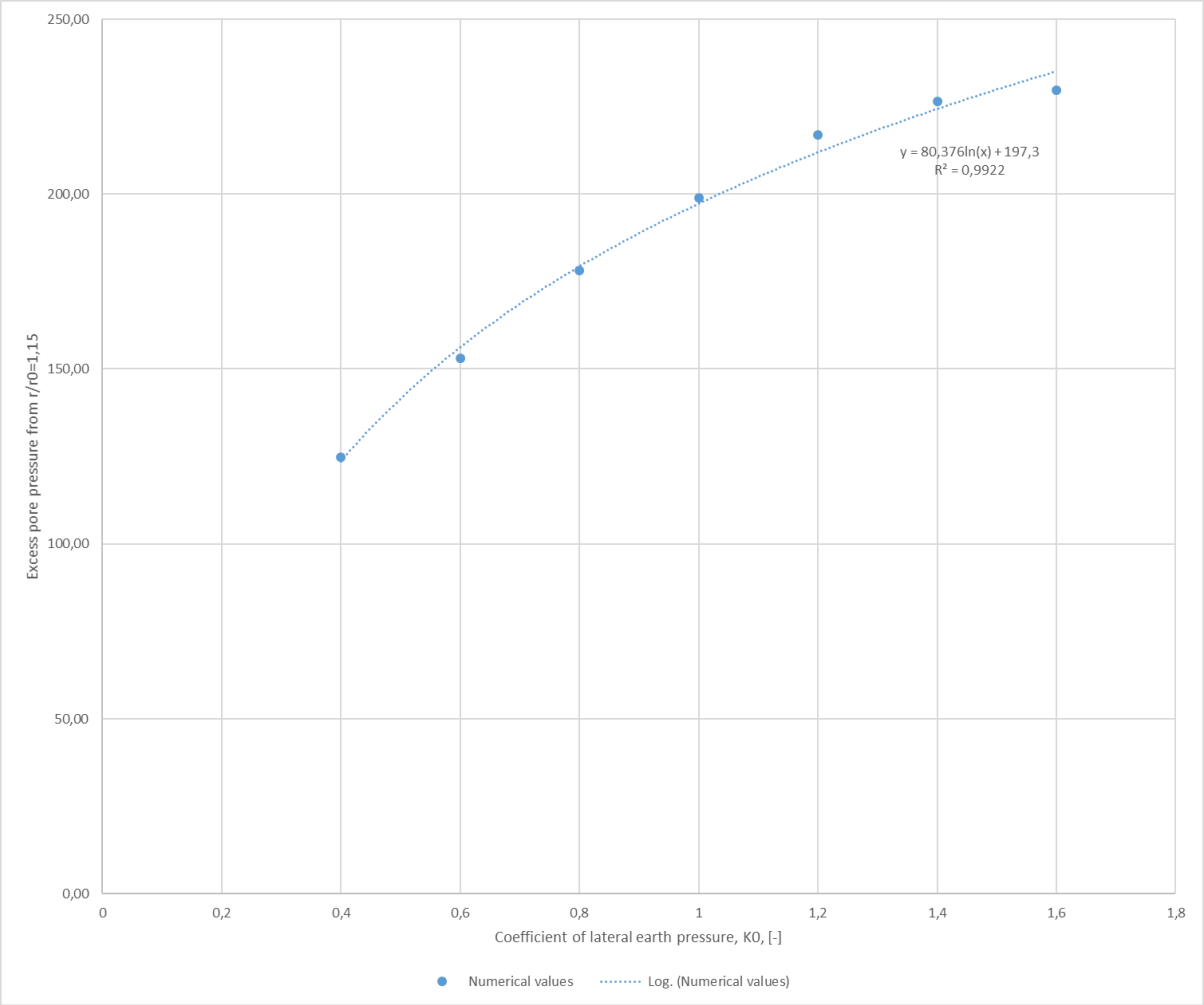

Figure 12.15: Excess pore pressure from $^{r}/_{r_0} = 1{,}15$ using CEM-MCC with the parameters listed in Table 12.2 and Table 12.3 against the coefficient of lateral earth pressure. Together with a logarithmic regression line with the coefficient of determination, $R^2 = 0{,}9922$.

The best fit to the data was found to be a logarithmic regression line. The exact values of the parameters in this regression line is however probably related to the stiffness and strength chosen so that the regression line must not be used for any random value of the undrained shear modulus (G_u) and the undrained shear strength (s_u). The meaning of this regression is simply to find that the excess pore pressure varies logarithmically to the coefficient of lateral earth pressure in CEM-MCC given that all other parameters are unchanged.

The procedure was repeated, but now with OCR and M changing, while K_0 is constant and equal to 1. Table 12.4 shows the values of M in order to get $\tau_{mob} = s_u = 37kPa$ for each different value of OCR. The data from Table 12.2 and Table 12.4 have then been used to produce the results presented in Figure 12.16 and Figure 12.17.

Table 12.4: Overconsolidation ratio and corresponding slope of the critical state line in order for the mobilized shear strength to equal the undrained shear strength of $37kPa$.

Overconsolidation ratio, OCR	Slope of the critical state line, M
1	1,12
1,4	0,91
2	0,66
3	0,46
4	0,375
10	0,18
15	0,13
32	0,07
50	0,07

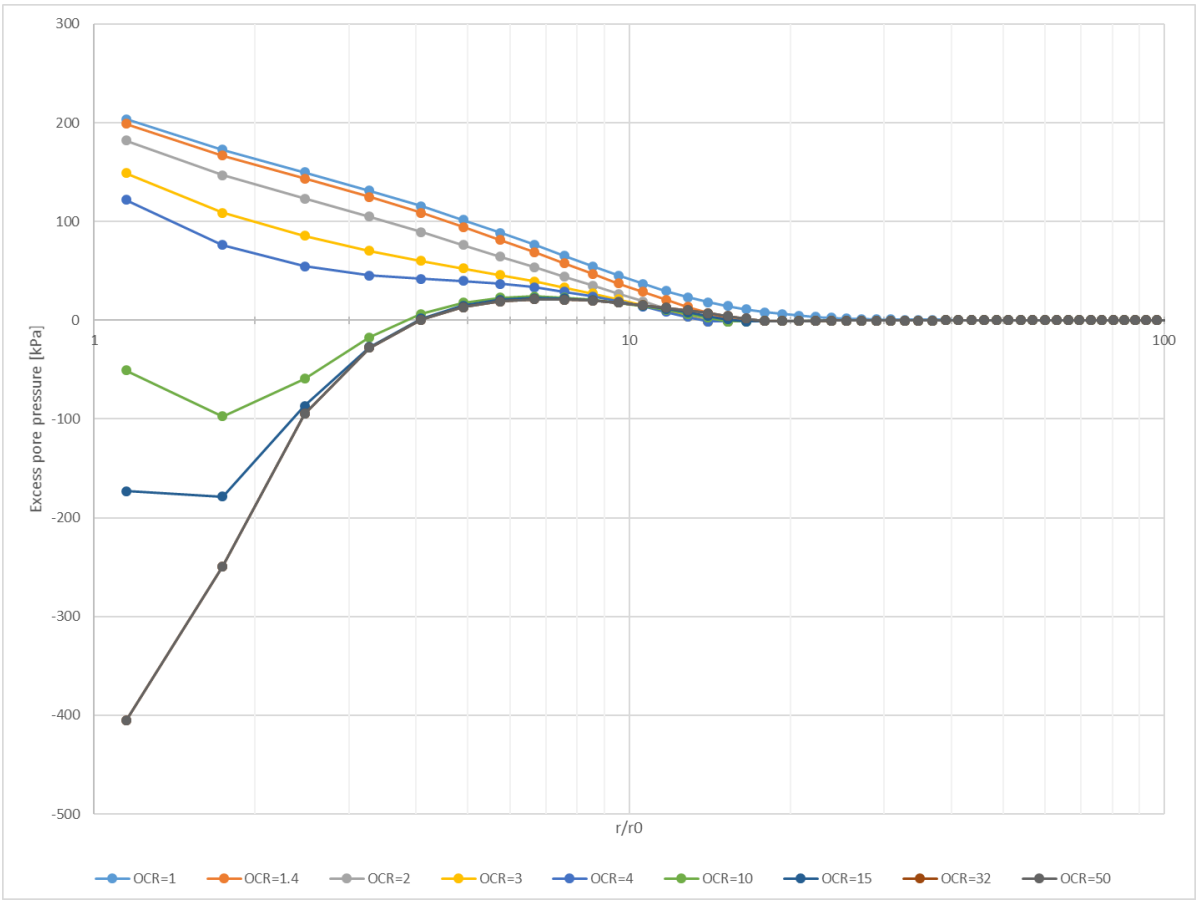

Figure 12.16: Excess pore pressure against normalized distance from pile center in a logarithmic scale for different values of the consolidation ratio (OCR).

For large values of OCR the excess pore pressure becomes negative due to dilation as previously explained. This seems to also be quite challenging numerically, based on the observation that the stress points near the pile wall seem more disturbed for higher values of OCR, and the discussion on mesh dependency due to softening in Chapter 6.5. This may also come from the fact that the slope of the critical state line (M) becomes very small for high OCR in order for the undrained shear strength to only be $37kPa$ at ten meters depth (i.e. $\sigma'_{v0} = 100kPa$). The shape of the distribution of excess pore pressure against OCR looks logarithmic, and even more so if the stress point at $^{r}/_{r_0} = 2{,}48$, which is less disturbed, is looked at. Figure 12.17 shows the data from $^{r}/_{r_0} = 1{,}15$, and the logarithmic trend line fitted to the data. As for K_0, a linear logarithmic regression gave the best fit to the data.

This also fits what Randolph, Carter et al. (1979) found which is presented in Figure 6.12, however they increased the stiffness as the OCR increased, giving a much smaller decrease in excess pore pressure with OCR than what Figure 12.17 shows.

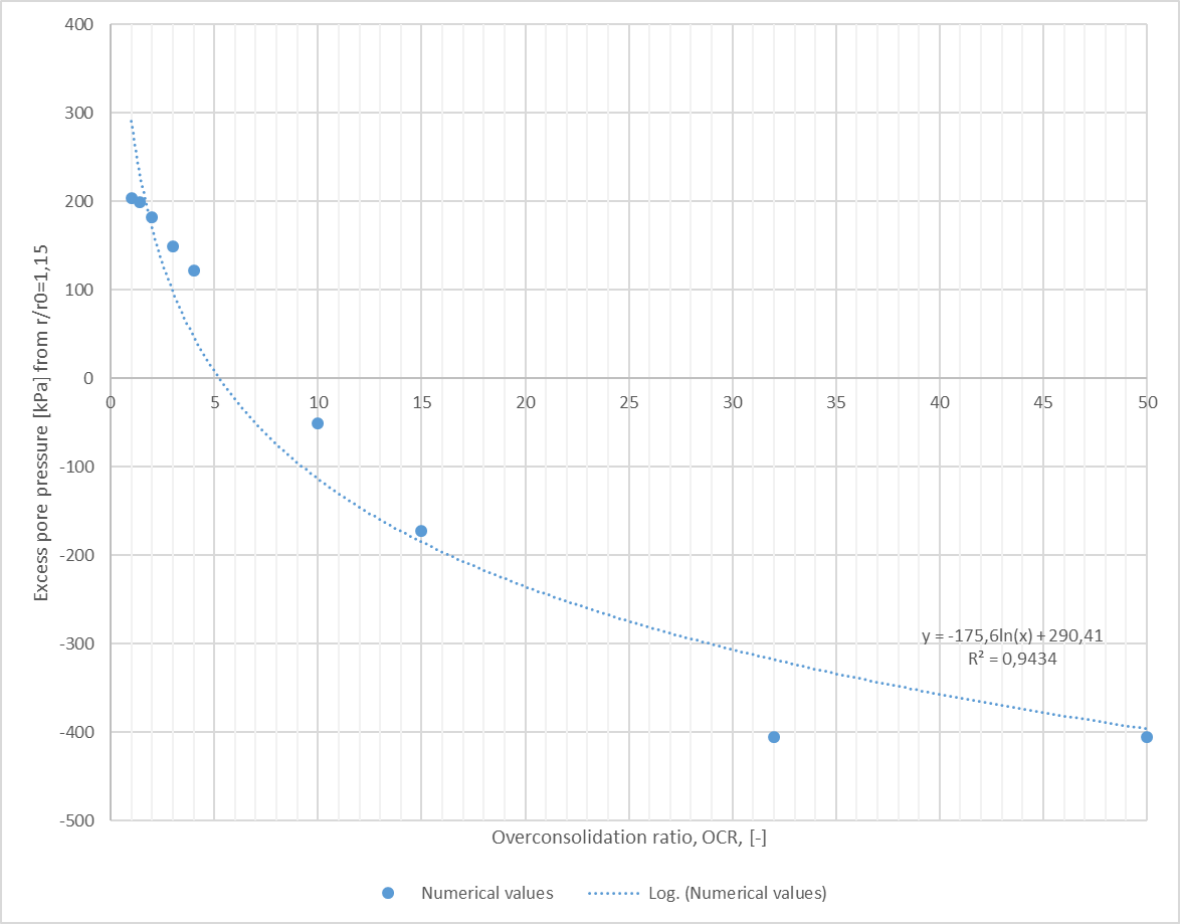

Figure 12.17: Excess pore pressure from $^{r}/_{r_0} = 1{,}15$ *using CEM-MCC with the parameters listed in Table 12.2 and Table 12.4 against the overconsolidation ratio. Together with a logarithmic regression line with the coefficient of determination,* $R^2 = 0{,}9434$.

Combining these results one gets:

$$\Delta u_{max} = 196{,}53 - 175{,}6 * \ln\left({}^{OCR}/_{2}\right) + 80{,}376 * \ln(K_0) \qquad (12.7)$$

where the first value is found by using the analytical solution from Chapter 5 (Equation 5.15). This was included because when $OCR = 2$ and $K_0 = 1$, we have seen that the CEM-MCC model predicts the same excess pore pressure as the analytical solution. The numbers in front of the logarithmic terms are found from the regressions shown in Figure 12.15 and Figure 12.17. However, the effect of changing the OCR or the K_0 together have not been checked. We know that due to the definition of OCR in Plaxis (see Chapter 12.4), the regression is not precise since we would have some dilation/contraction for $OCR = 2$ when $K_0 \neq 1$.

This means Equation 12.7 actually needs some modification to take the covariance of K_0 and OCR into account. However, the meaning of Equation 12.7 is simply to show that the numerical results found from CEM-MCC can be estimated by using the analytical solution and some terms containing the logarithm of OCR and K_0.

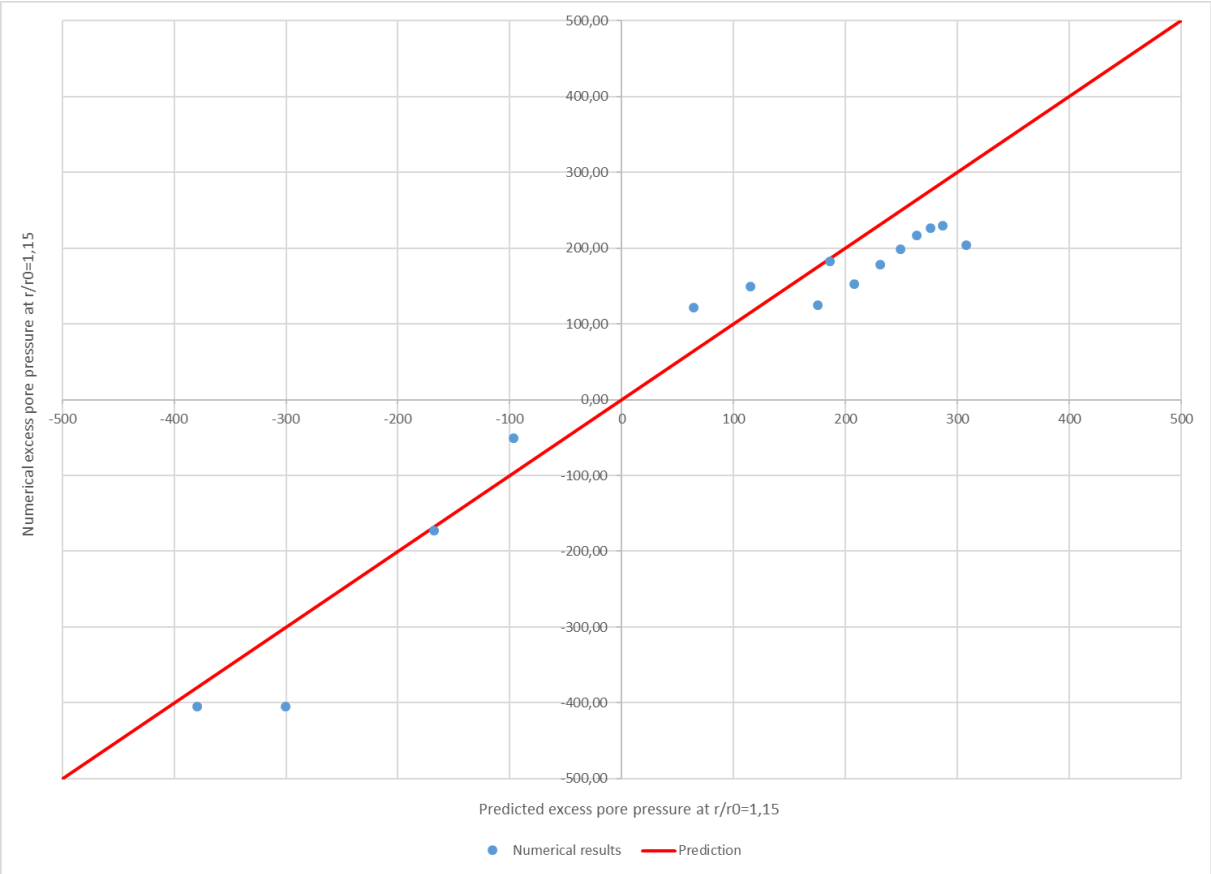

Figure 12.18: Predicted excess pore pressure at $^{r}/_{r_0} = 1{,}15$ using Equation 12.7 against the numerical values found using the CEM-MCC model. Coefficient of determination, R^2=0,9333.

Figure 12.18 shows the excess pore pressure found by the numerical analysis on the y-axis, and the excess pore pressure predicted by Equation 12.7 on the x-axis. If the prediction equals the numerical results then the dot lies on the $x = y$-line. We see that Equation 12.7 is not a perfect fit, but gives a coefficient of determination of $R^2 = 0{,}9333$ (explained in Chapter 14.1). This is high enough for us to say that the CEM-MCC predicts something similar to what Equation 12.7 suggests. This result will be used in Chapter 14 when looking for trends in the empirical data.

12.7 Effect of softening using the Tresca material model in CEM

As a simple test the model described in Chapter 11 have been used to look into the effects of softening. Instead of using a material model that includes softening, an inner zone have been replaced with a material with lower undrained shear strength representing the remoulded soil. The remoulded zone was chosen to stop at $^{r}/_{r_0} = 9{,}9$ together with a sensitivity (S_t) of 2 when modeling this. This bypasses the problems of material softening discussed in Chapter 6.5. However, the extent of the remoulded zone is then purely chosen by the user and not by the imposed strain, and one gets a quite abrupt change in stresses instead of a more realistic smooth transition.

The inner remoulded zone then has a shear strength of $s_{ur} = {}^{s_u}/_{S_t} = {}^{37}/_{2} = 18{,}5kPa$.

Except for changing the undrained shear strength of the inner zone all the other parameters are unchanged and can be found in Table 12.1.

Figure 12.19 shows the analytical solution (solid lines) found for a linear elastic-perfectly plastic (EP) material with parameters as in Table 12.1, while the dots are from the Plaxis model using the same parameters. The figure is included merely to simplify the comparison to the results of the model with an inner remoulded zone shown in Figure 12.20.

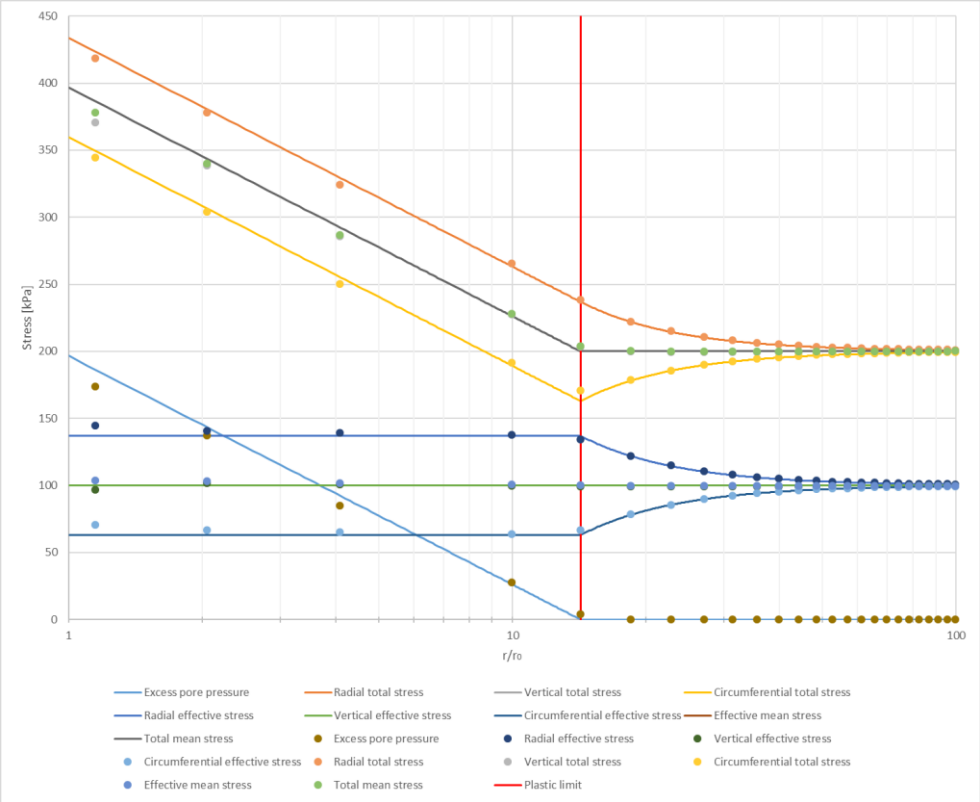

Figure 12.19: Stresses after the cavity expansion phase against the logarithm of the normalized distance from the pile center in a Tresca material with parameters as in Table 12.1. The dots are from a Plaxis analysis while the solid lines are given by the analytical solution presented in Chapter 5.

The dots in Figure 12.20 are from the Plaxis model with an inner remoulded zone, while the solid lines are from the analytical solution with both $s_u = 37kPa$ and $s_u = 18{,}5kPa$. The solution of the inner remoulded zone with $s_u = 18{,}5kPa$ have been shifted so that the total radial stress in continuous over the remoulded limit (black line not to be confused with the critical state line shown in previous plots).

It is important to notice that the solid lines does not represent an analytical solution for a linear elastic-perfectly plastic softening material, but merely is a combination of the analytical solution with $s_u = 37kPa$ and $s_u = 18{,}5kPa$. Comparing Figure 12.19 to Figure 12.20 we see that the remoulding causes the excess pore pressure and the total stresses to decrease. The vertical and mean effective stresses are unchanged, while the radial effective stress decrease and the circumferential effective stress increase.

The linear elastic-perfectly plastic material model need the change in effective mean stress to be zero for undrained loading, as mentioned before. Since the undrained shear strength reduces to the remoulded shear strength ($s_{ur} = 18{,}5kPa$) in the remoulded zone, the difference between the radial effective stress and the circumferential effective stress reduce

from $2s_u = 74kPa$ to $2s_{ur} = 37kPa$. In order for the effective mean stress to be unchanged, the radial effective stress must be reduced by $18{,}5kPa$, while the circumferential effective stress must increase by $18{,}5kPa$.

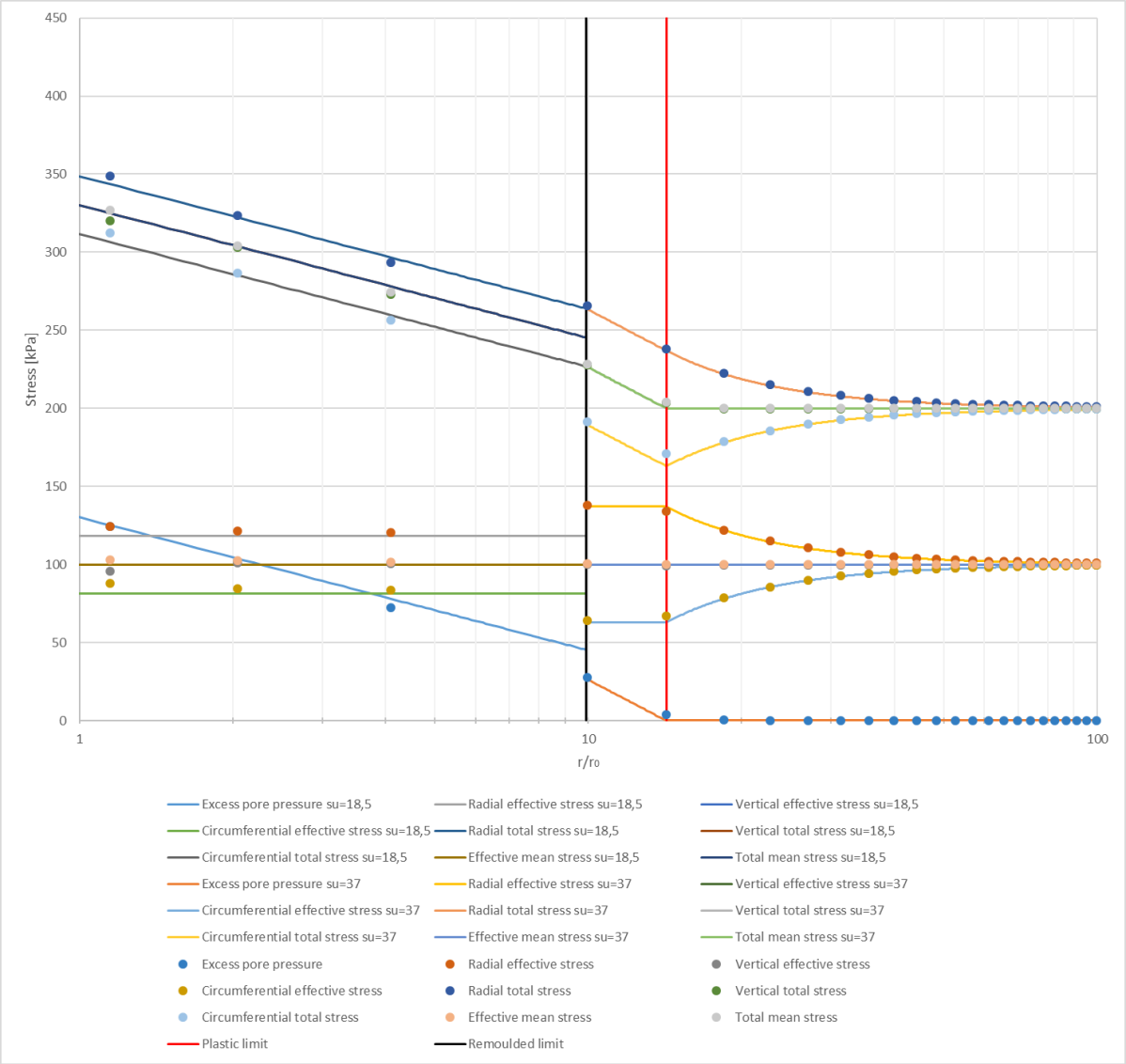

Figure 12.20: Stresses after the cavity expansion phase against the logarithm of the normalized distance from the pile center in a Tresca material with parameters as in Table 12.1 to the right of the remoulded limit (black line) at $r_r/r_0 = 9{,}9$, and with $s_u = 18{,}5kPa$ to the left of the remoulded limit. The dots are from a Plaxis analysis while the solid lines are given by the analytical solution presented in Chapter 5, shifted to fit when having a remoulded inner zone.

From the analytical solution presented in Chapter 5 we find by derivation of Equation 5.6, 5.7, 5.8 and 5.9 that the total stresses (in all directions), and excess pore pressure in the plastic zone have a log-linear slope given by:

$$\frac{d\sigma}{d\left(ln\frac{r}{r_0}\right)} = -2s_u \tag{12.8}$$

The radial total stress must be continuous due to equilibrium considerations, but because of the remoulding: the total radial stress needed to produce the radial displacement decrease. In other words between the plastic limit (red) and the remoulded limit (black), we have the total stresses (and excess pore pressure) increasing by $2s_u = 74kPa$. When we pass the remoulded limit, the slope of the increase reduce to $2s_{ur} = 37kPa$. As the radial effective stress decrease with $18{,}5kPa$, the excess pore pressure must increase by $18{,}5kPa$ for the radial total stress to be continuous. The vertical and mean effective stresses are unchanged, thus making the total vertical and mean stresses increase as the excess pore pressure increase. The circumferential effective stress is increasing by $18{,}5kPa$, as previously mentioned. The total circumferential stress is thus increasing by $37kPa$.

Having an inner remoulded zone will therefore give an abrupt change in stress (equal to $s_u - s_{ur}$, (times two for the cirumferential total stress)), and a change in the slope of the total stresses and the excess pore pressure, from $2s_u$ to $2s_{ur}$.

The strain is not given by a material model when using an inner remoulded zone. The strain is indirectly chosen when the user decides the remoulded limit. Based on the results in Figure 12.20, it is quite easy to set up an equation for the maximum excess pore pressure at the pile shaft as a function of sensitivity (S_t), undrained shear strength of the intact material (s_u), undrained shear modulus (G_u), and the so called remoulded limit (r_r).

$$\Delta u_{max} = 2s_u\left(\ln\left(\sqrt{\frac{G_u}{s_u}}\right) - \ln\left(\frac{r_r}{r_0}\right)\right) + \frac{s_u}{S_t}\left(S_t - 1 + 2\ln\left(\frac{r_r}{r_0}\right)\right) \tag{12.9}$$

A boundary of this equation is that $\frac{r_r}{r_0} \leq \sqrt{\frac{G_u}{s_u}}$, which means the remoulded limit cannot be in the elastic region. If there is no remoulding then $r_r = r_0$ and $S_t = 1$, giving $\Delta u_{max} = 2s_u \ln\left(\sqrt{\frac{G_u}{s_u}}\right)$. If the remoulded clay becomes completely like water (i.e. the remoulded shear strength goes towards zero and the sensitivity goes towards infinity) we see that the maximum excess pore pressure becomes; $\Delta u_{max} = 2s_u\left(\ln\left(\sqrt{\frac{G_u}{s_u}}\right) - \ln\left(\frac{r_r}{r_0}\right)\right) + s_u$. The resulting stresses are then as presented in Figure 12.21. The remoulded soil have no shear strength so there cannot be any increase in stresses. In order for the radial total stress to be continuous the excess pore pressure must increase equally much as the decrease in effective radial stress which is $s_u - s_{ur} = s_{ur}$.

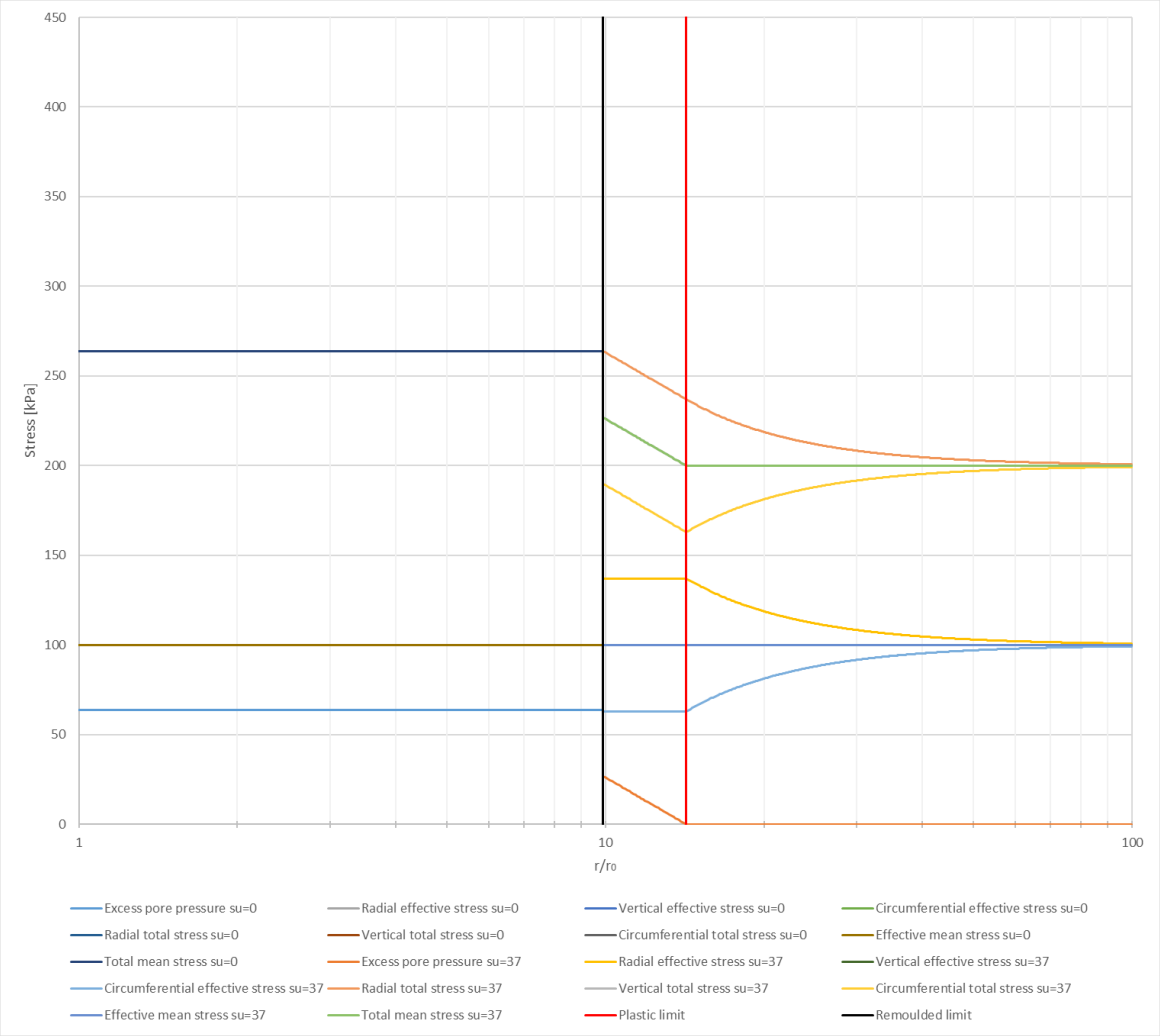

Figure 12.21: Stresses after cavity expansion against the logarithm of the normalized distance from the pile center in a Tresca material with parameters as in Table 12.1 to the right of the remoulded limit (black line) at $r_r/r_0 = 9{,}9$, and with $s_u = 0kPa$ to the left of the remoulded limit.

Trying to model a completely remoulded inner zone with $s_{ur} = 0$ in Plaxis is problematic. We can however decrease the remoulded strength, and look at the general trend. The remoulded strength have been reduced to $s_{ur} = 10kPa$ and $s_{ur} = 1kPa$, and the corresponding results support Equation 12.9. Figure 12.22 and Figure 12.23 show the results obtained.

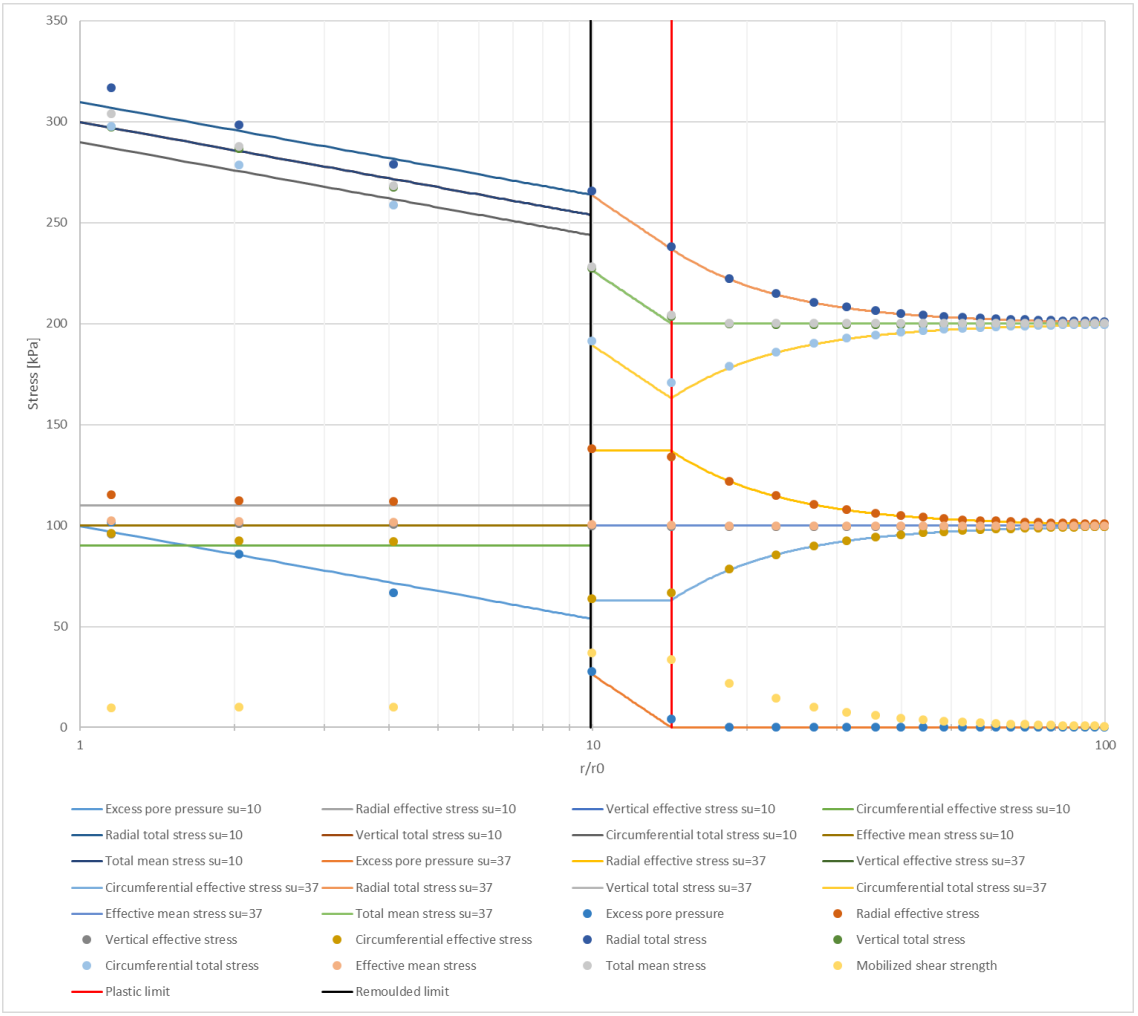

Figure 12.22: Stresses after the cavity expansion phase against the logarithm of the normalized distance from the pile center in a Tresca material with parameters as in Table 12.1 to the right of the remoulded limit (black line) at $r_r/r_0 = 9{,}9$, and with $s_u = 10kPa$ to the left of the remoulded limit. The dots are from a Plaxis analysis while the solid lines are given by the analytical solution presented in Chapter 5, shifted to fit when having a remoulded inner zone.

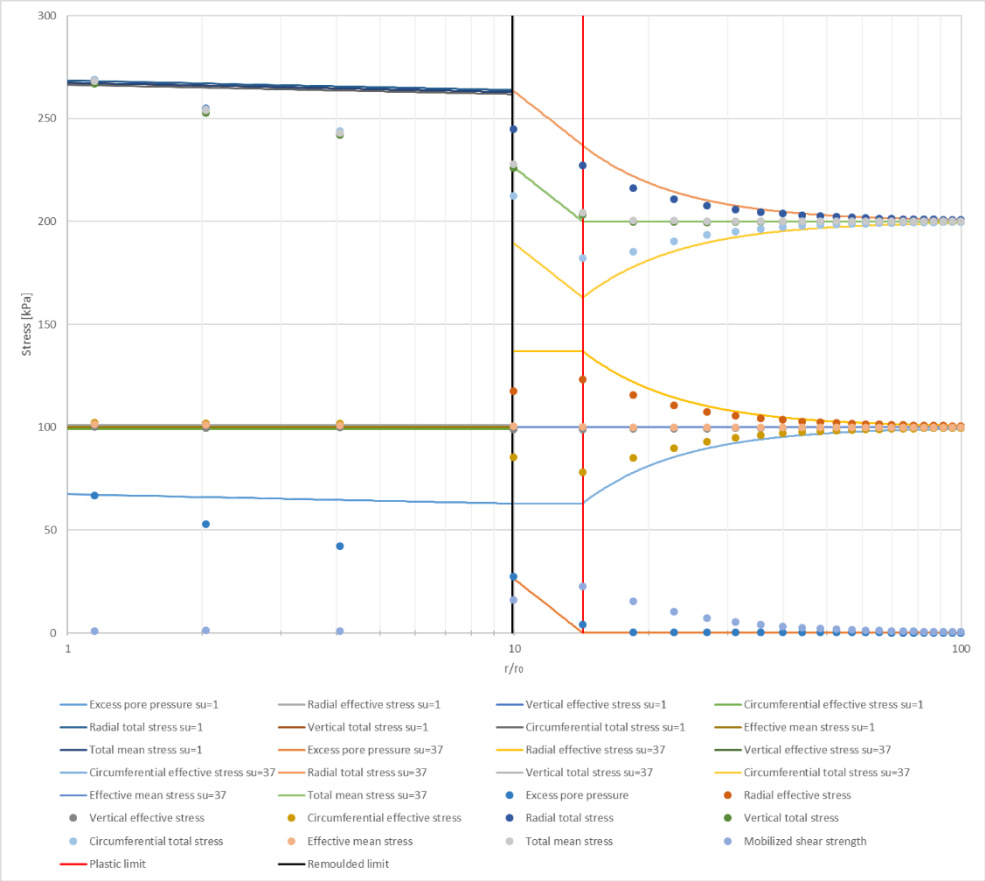

Figure 12.23: Stresses after the cavity expansion phase against the logarithm of the normalized distance from the pile center in a Tresca material with parameters as in Table 12.1 to the right of the remoulded limit (black line) at $r_r/r_0 = 9{,}9$, and with $s_u = 1kPa$ to the left of the remoulded limit. The dots are from a Plaxis analysis while the solid lines are given by the analytical solution presented in Chapter 5, shifted to fit when having a remoulded inner zone.

We see that having the remoulded shear strength as low as $1kPa$ causes the Plaxis analysis to give results that do not correspond to the other results, and the discussion we have had up until now. At the plastic limit, the mobilized shear strength does not equal the undrained shear strength of $37kPa$ as we have seen in the other figures, and instead of being constant up to the remoulded limit it reduces as well. This causes the slope of the stresses to be higher than $2s_{ur}$ in the remoulded zone. We see that the stress point closest to the pile shaft is in agreement with Equation 12.9, and our understanding of the problem. It is my belief that having the shear strength as low as $1kPa$ causes some numerical disturbance as the difference between s_{ur} and s_u becomes quite large, and an abrupt change in strength is known to be problematic.

As one can see from Equation 12.9, a decrease in shear modulus in the remoulded region has no effect on the resulting stresses. This is because the soil is already plasticized (i.e. in the flat plateau seen in Figure 12.29 for the perfectly plastic model), and the Plaxis model also gave this conclusion.

Rewriting Equation 12.9 we can obtain:

$$\frac{\Delta u_{max}}{s_u} = \ln\left(\frac{G_u}{s_u}\right) - \left(1 - \frac{1}{S_t}\right) * \left(2ln\left(\frac{r_r}{r_0}\right) - 1\right) \tag{12.10}$$

From this we see that the first term is simply the analytical EP solution. After that we have a term that includes $\left(1 - \frac{1}{S_t}\right)$. This gives zero contribution if $S_t = 1$. If the sensitivity (S_t) is not equal to one, we see that the maximum excess pore pressure only decrease given that:

$$2ln\left(\frac{r_r}{r_0}\right) - 1 > 0 \rightarrow \frac{r_r}{r_0} > e^{1/2} \approx 1{,}649 \tag{12.11}$$

So if $r_r = r_0 e^{1/2}$ then $\Delta u_{max} = s_u * \ln\left(\frac{G_u}{s_u}\right)$ regardless of the sensitivity (S_t). If the sensitivity is larger than one, and we have a thin inner remoulded zone ($r_r < r_0 e^{1/2}$) then Equation 12.9 (and 12.10) give an increase in excess pore pressure.

The Plaxis model support this observation as well. Using the parameters from Table 12.1 as before, and having a sensitivity of $S_t = 2$, meaning $s_{ur} = 18{,}5kPa$. Figure 12.24 show that when the remoulded limit is placed at $^{r_r}/_{r_0} = 1{,}584 < 1{,}649$, we do indeed see an increase in excess pore pressure compared to having no remoulding (i.e. Figure 12.19). The closest stress point to the pile surface, located at $^{r}/_{r_0} = 1{,}15$, show $\Delta u = 173{,}96kPa$ when having no remoulded zone as in Figure 12.19. While in Figure 12.24 the closest stress point (still located at $^{r}/_{r_0} = 1{,}15$) show $\Delta u = 185{,}75kPa$. This shows an increase of 6,3%, while at the pile surface (i.e. $^{r}/_{r_0} = 1$) we expect according to Equation 12.10; $\Delta u_{max} = 198{,}01kPa$ when having a remoulded zone of $^{r_r}/_{r_0} = 1{,}584$, and $\Delta u_{max} = 196{,}53kPa$ when having no remoulding.

This increase can be explained by the model, and the fact that the excess pore pressure increase abruptly by $s_u - s_{ur}$ at the remoulded limit. This is a consequence of the fall in radial effective stress and the fact that the total radial stress must be continuous.

Since the remoulded limit is so close to the pile shaft, the decrease of the slope of the excess pore pressure from $2s_u$ to $2s_{ur}$ does not matter. When looking at Equation 12.10 we can see

that the second term contains $1 - \frac{1}{S_t}$ which is similar to $s_u - s_{ur}$, multiplied with the term $2ln\left(\frac{r_r}{r_0}\right) - 1$. Where the first part is the decrease of the slope, while the -1 represent the abrupt jump at the remoulded limit. An increasing excess pore pressure due to softening then means in simple terms that the abrupt jump in excess pore pressure is larger than the decrease of the slope.

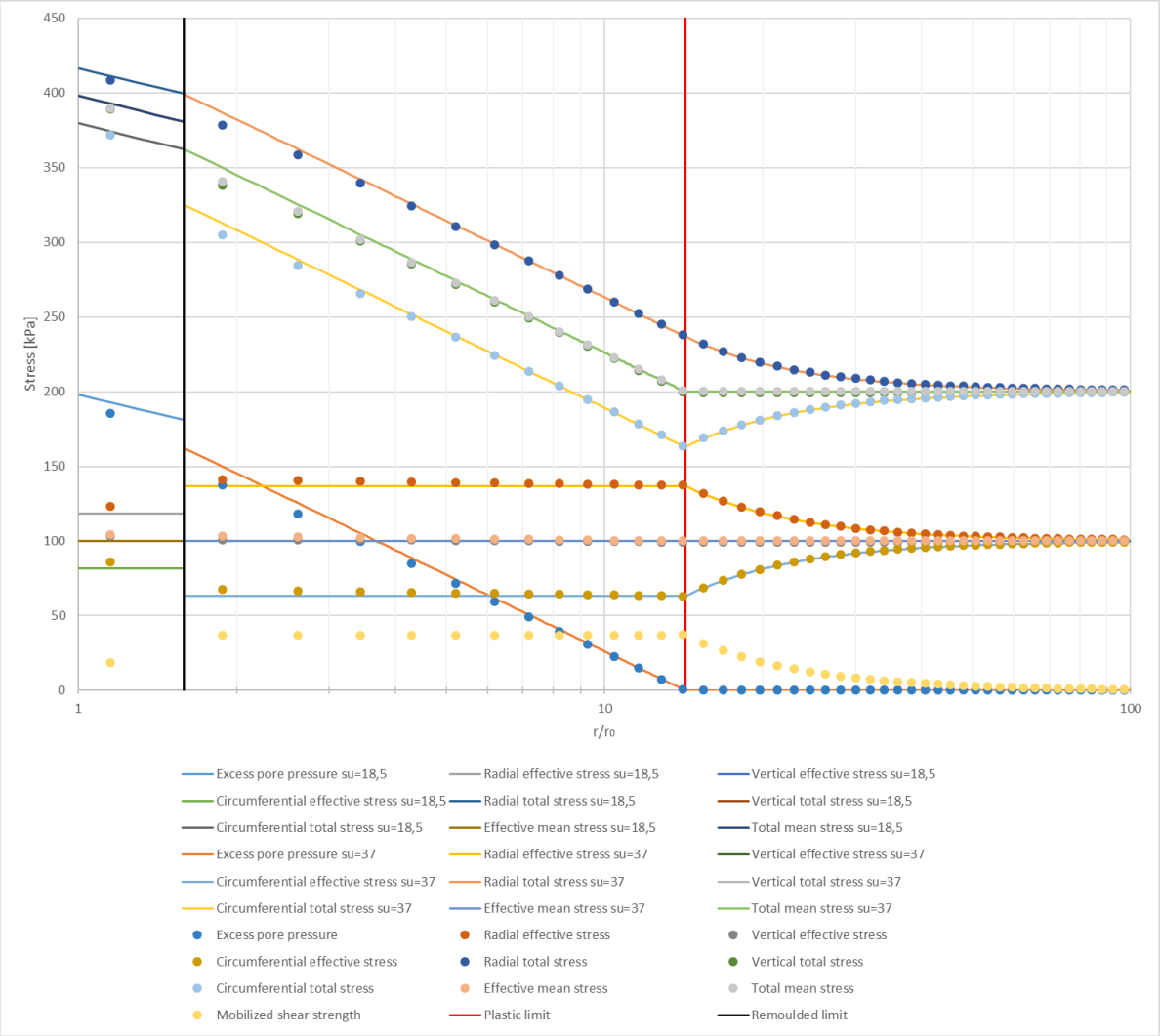

Figure 12.24: Stresses after the cavity expansion phase against the logarithm of the normalized distance from the pile center in a Tresca material with parameters as in Table 12.1 to the right of the remoulded limit (black line) and with $s_u = 18{,}5kPa$ to the left of the remoulded limit. The dots are from a Plaxis analysis while the solid lines are given by the analytical solution presented in Chapter 5, shifted to fit when having a remoulded inner zone.

For a given r_r/r_0 we see that the maximum excess pore pressure can be written as the linear line:

$$\frac{\Delta u_{max}}{s_u} = \ln\left(\frac{G_u}{s_u}\right) - \beta * \left(1 - \frac{1}{S_t}\right) \tag{12.12}$$

where β is a factor which depend on the remoulded limit, and the relation is given by:

$$\beta = 2ln\left(\frac{r_r}{r_0}\right) - 1 \rightarrow \frac{r_r}{r_0} = e^{\frac{\beta+1}{2}} \tag{12.13}$$

Figure 12.25 displays this graphically for $\ln\left(\frac{G_u}{s_u}\right) = \ln\left(\frac{7500}{37}\right) = 5{,}312$ and $\frac{r_r}{r_0} = 6$, giving $\beta = 2\ln(6) - 1 \approx 2{,}584$. Equation 12.12 will become useful when looking for trends in the empirical data as we have little information about the extent of the remoulded region.

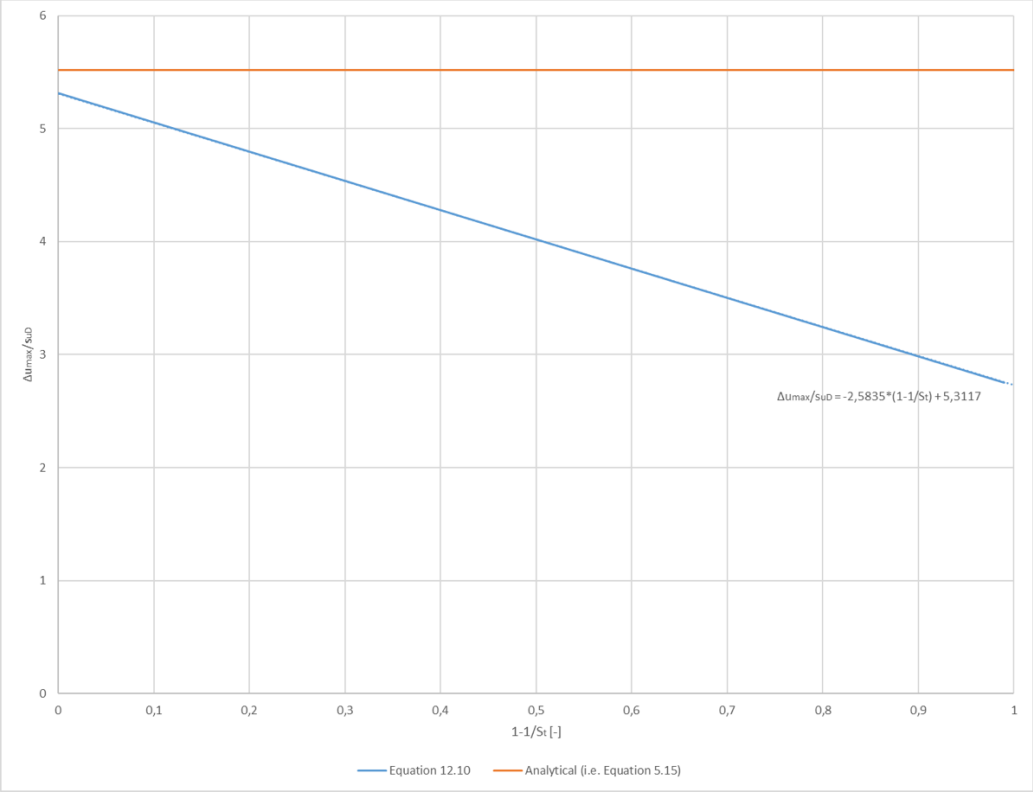

Figure 12.25: Maximum excess pore pressure normalized with the undrained shear strength against $1 - 1/S_t$ on the horizontal axis, where S_t is the sensitivity. The orange line represents the analytical linear elastic-perfectly plastic (EP) solution that does not take softening into account, while the blue line represents Equation 12.10 with $ln\left(\frac{G_u}{s_u}\right) = ln\left(\frac{7500}{37}\right) = 5{,}3117$ and $\frac{r_r}{r_0} = 6$.

12.8 Comparison between different ways of modeling the softening

The softening effect that is explained below is not to be confused with the softening one can find in the Modified Cam Clay (MCC) (and the other Critical State Soil (CSS) models) when one loads into the dry side of the Critical State Line/Coulomb line. In MCC one can have softening due to high overconsolidation ratio (OCR) since the material dilates. Softening due to OCR/dilation gives lower excess pore pressure as explained in Chapter 6.2 and 12.3. The softening effect explained below is softening due to remoulding, and sensitivity of the material, and the CSS models does not generally include this.

Figure 12.26 is from Randolph, Carter et al. (1979), they did not use the S-CLAY1S model but a MCC model with softening (no anisotropy). The softening behavior is however based on similar assumptions.

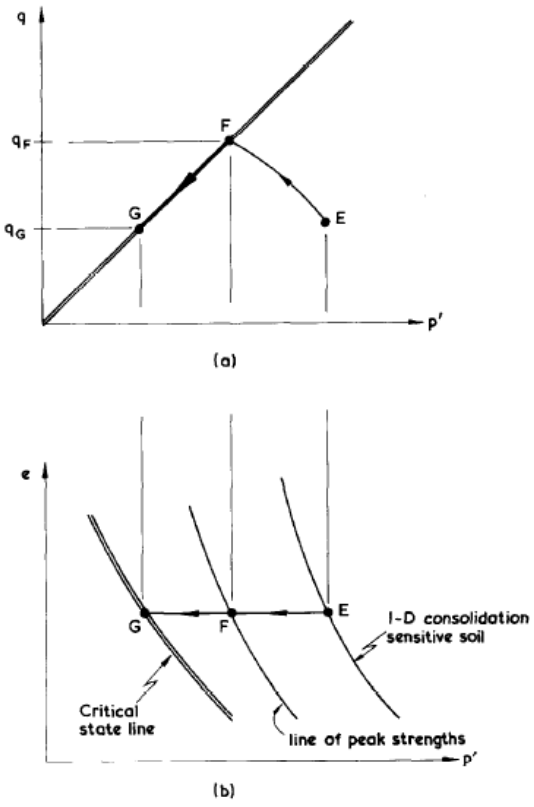

Figure 12.26: (a) Undrained effective stress path in (a) $q - p'$space and (b) $e - p'$space for a sensitive soil. (Randolph, Carter et al. 1979)

Figure 12.26 (a) shows that the difference from the MCC model is that the critical state is governed by an intrinsic yield ellipse. This causes the critical state point to change from F to

point G. This means that the deviatoric stress (q) is allowed to slide on the Coulomb line and decrease from q_F (related to the peak shear strength s_u) to q_G (related to the remoulded shear strength s_{ur}). In Figure 12.26 (b) we see how this relates to the void ratio, where the critical state line have a slope λ_i, and the lines that point E and F lie on have a slope of λ, using the S-CLAY1S model's terminology.

The excess pore pressure is the difference between the total stress path (TSP) and the effective stress path (ESP). However, the TSP is not drawn in the figure so it is hard to draw conclusions from this. Figure 12.27 shows the assumed variation of shear strength against the normalized distance from the pile, and corresponding shear stress-strain plot. We see that they assume that for $^{r}/_{r_0}$ larger than six, the shear strength is undisturbed, and that at the pile shaft one has full remoulding with a sensitivity of five. Randolph, Carter et al. (1979) report an increase in excess pore pressure for this specific case of softening.

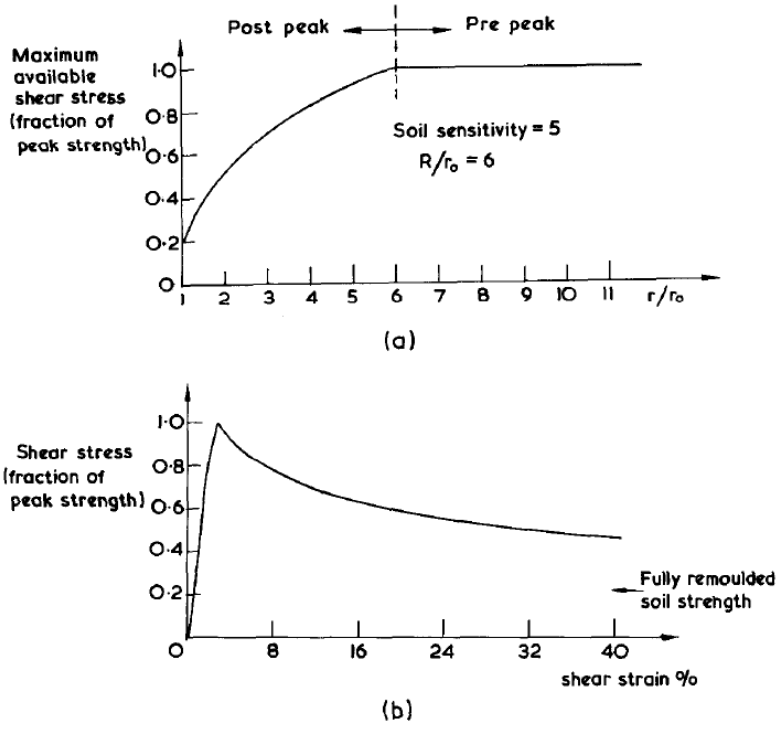

Figure 12.27: Randolph, Carter et al. (1979) assumed variation of the shear strength with $^{r}/_{r_0}$ (a) and corresponding shear stress versus shear strain (b). We see that they assume a soil sensitivity of $S_t = 5$ and that this increases gradually to the full shear strength at $^{r}/_{r_0} = 6$. (Randolph, Carter et al. 1979)

Ladanyi (1963) used a simpler strain softening material model. Figure 12.28 shows the maximum excess pore pressure against the stiffness, both normalized with the undrained shear strength, for $^{\gamma_r}/_{\gamma_f} = 5$ and the inverse of the sensitivity (i.e. $^{\tau_r}/_{\tau_f} = {}^{s_{ur}}/_{s_u}$) ranging from 1

to 0. The soil softening is, as shown in Figure 12.28, defined by a linear increase defined by the undrained shear modulus (G_u), up to a peak strength (s_u) defined at shear strain γ_f, and a linear decrease to a residual or remoulded shear strength (s_{ur}) defined at shear strain γ_r.

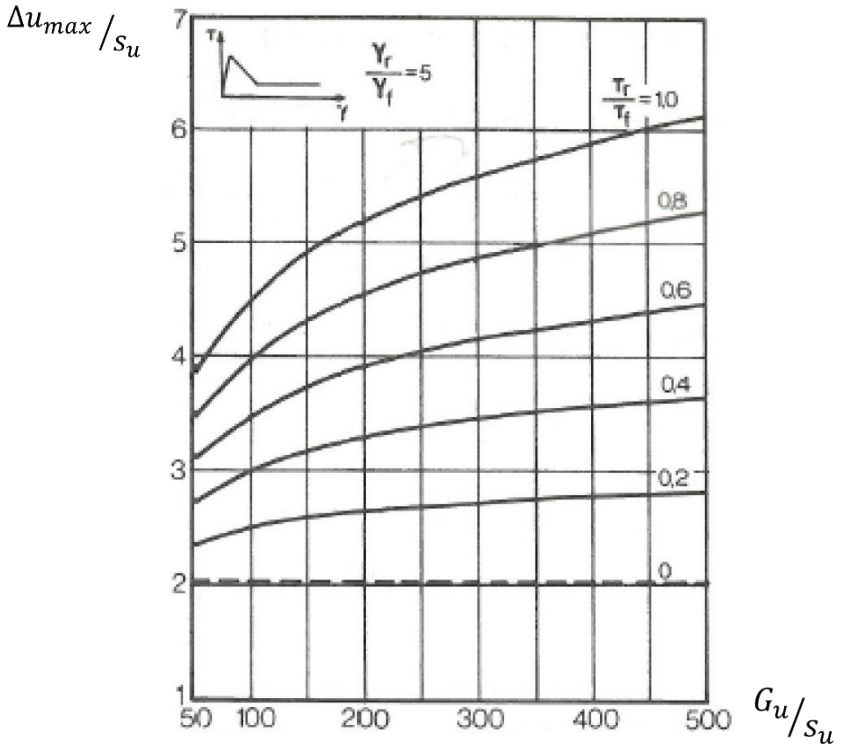

Figure 12.28: Normalized excess pore pressure at the pile shaft against normalized stiffness produced with CEM including the effect of softening. Where $\tau_f = s_u$ and $\tau_r = s_{ur}$. (Ladanyi 1963)

Figure 12.28 shows a decrease of the excess pore pressure at the pile shaft for increasing sensitivity (i.e. decreasing $s_{ur}/_{s_u}$). That is, a decrease in excess pore pressure compared to using an elastic-perfectly plastic model with a shear strength of s_u. These results contradict the results presented by Randolph, Carter et al. (1979) and Castro and Karstunen (2010) (see Chapter 6.4, Figure 6.16 and Figure 6.18) which show an increase in excess pore pressure. They have however used critical state soil models that include softening.

In Chapter 12.7 we model softening in CEM by introducing an inner remoulded zone with lower shear strength and an outer zone with the full shear strength. Both zones uses the EP material model with the same parameters except for the undrained shear strength. This gives the softening behavior illustrated in Figure 12.29.

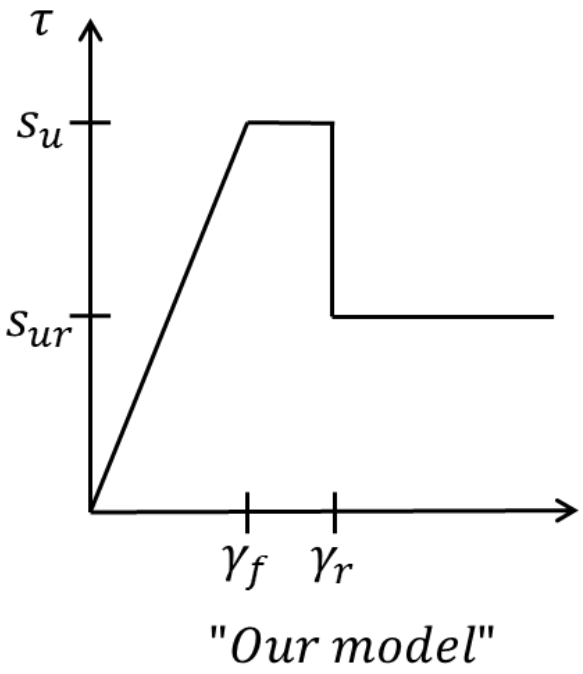

Figure 12.29: Our way of modeling the soil softening, where we have a linear increase defined by the shear modulus (G_u), up to a peak strength (s_u) defined at shear strain (γ_f) and a vertical decrease to a residual or remoulded shear strength (s_{ur}) defined at shear strain (γ_r). However, γ_f and γ_r is not chosen explicitly, but defined implicitly by choosing the size of the remoulded zone $^{r_r}/_{r_0}$.

In Appendix A.4 stress paths, both total and effective, are shown for different sizes of the inner remoulded zone. Based on these results a principal sketch of the stress paths is made, as shown in Figure 12.30.

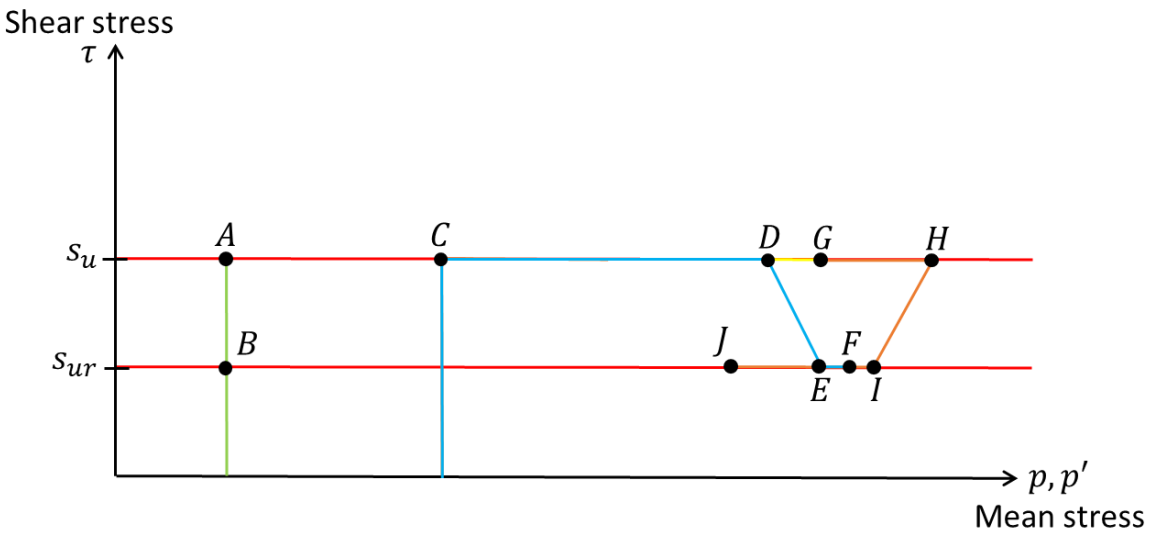

Figure 12.30: Principal sketch of the stress paths presented in Appendix A.4 based on results obtained when introducing an inner remoulded zone with a shear strength of s_{ur}. This gives a soil softening behavior as shown in Figure 12.29. The blue line represents the total stress path (TSP) when the remoulded zone $^{r_r}/_{r_0} = 1{,}58$. The orange line respresents the TSP when $^{r_r}/_{r_0} = 9{,}90$, while the yellow line represents the TSP when there is no remoulded zone. The green line represents the ESP for all cases.

The green line is the ESP which goes from $\tau = 0$ to $\tau = s_u$ (i.e. point A) and down to $\tau = s_{ur}$ (i.e. point B). The ESP is unaffected by the size of the inner remoulded zone $^{r_r}/_{r_0}$ where r_r is the radial extent of the remoulded zone from the pile center. The TSP on the other hand, differ depending on the size of the inner remoulded zone. The TSP with $^{r_r}/_{r_0} = 1{,}58$ is represented by the blue line and goes from $\tau = 0$ through the points C, D, E and F. The orange line represents the TSP when $^{r_r}/_{r_0} = 9{,}90$, and goes through the points $\tau = 0$, C, H, I and J. Lastly, the yellow line is when there is no remoulded zone at all. The TSP then goes from $\tau = 0$ up to point C and then to point G.

Based on these results we see that depending on the size of the remoulded zone the excess pore pressure can either increase or decrease. $^{r_r}/_{r_0} > e^{1/2} \approx 1{,}65$ gives a decrease, while $^{r_r}/_{r_0} < e^{1/2}$ gives an increase. This is based on Equation 12.10, which is derived based on the numerical results presented in Chapter 12.7. A discussion as to how these limits are obtained, and why the TSP change with $^{r_r}/_{r_0}$ are included there. These limits does however only hold for that specific way of modeling the soil behavior.

Our model uses the radius of the remoulded zone (r_r), while Ladanyi (1963) uses the remoulded shear strain (γ_r). These can be related to each other if one uses the analytical solution presented by Gibson and Anderson (1961). The maximum shear strain is given by Equation 12.14, the derivation of this expression can be found in Yu (2000).

$$\gamma_{max} = \varepsilon_1 - \varepsilon_3 = \varepsilon_\theta - \varepsilon_r = \left(\frac{m}{1-m} + \frac{m}{1-2\nu}\right) * \left(\frac{r}{r_p}\right)^{2m-2} \tag{12.14}$$

where m is defined as:

$$m = \frac{2(1+\nu)(1-2\nu)}{3G_u} s_u \tag{12.15}$$

Looking at the shear strain $\gamma_r = 5\gamma_f$ where $\gamma_f = {s_u}/{G_u}$, and using ${G_u}/{s_u} = 200$ as an example, we can see that this gives $\gamma_f = 0{,}005$ again giving $\gamma_r = 0{,}025$. Equation 12.14 and 12.15 with ${G_u}/{s_u} = 200$ gives ${r_r}/{r_0} = 6{,}879$ in order for $\gamma_{max} = \gamma_r$.

Using Equation 12.10, the above information, and ${s_{ur}}/{s_u} = 0{,}6 \rightarrow S_t = {1}/{0{,}6} \approx 1{,}67$ we get ${\Delta u_{max}}/{s_u} = 4{,}156$, which is slightly higher than the results presented in Figure 12.28 by Ladanyi (1963). However, we assume that for ${r}/{r_0} > 6{,}88$ the shear strength is undisturbed. Ladanyi (1963) gets slightly lower excess pore pressure because of the linear increase from s_{ur} back to s_u behind ${r}/{r_0} = 6{,}88$. The reason Ladanyi (1963) gets a decrease is assumed to be due to the large extent of the fully remoulded zone.

To summarize we see that Ladanyi (1963) gets a decrease in excess pore pressure for $\gamma_r = 5\gamma_f$ for all $S_t > 1$. Randolph, Carter et al. (1979) gets an increase in excess pore pressure for $S_t = 4$ with a decrease in strength up to ${\mathrm{r}}/{\mathrm{r}_0} = 6$. Castro and Karstunen (2010) let the shear strength go towards zero as seen in Figure 6.18, and the shear strength is unaffected past ${\mathrm{r}}/{\mathrm{r}_0} \approx 12$. This gave them an increase in excess pore pressure compared to not including the softening. Introduzing an inner remoulded zone with lower shear strength gives a decrease in excess pore pressure when ${r_r}/{r_0} > e^{1/2} \approx 1{,}65$ and an increase when ${r_r}/{r_0} < e^{1/2}$ for all $S_t > 1$.

These results do not easily compare as the softening behavior in each of these models are quite different. Randolph, Carter et al. (1979) and Castro and Karstunen (2010) have a much larger extent of the affected zone than what our model say are the limits for an increasing excess pore pressure. However, they have a much slower reduction in shear strength which means the limits produced by our model are irrelevant. In addition, the critical state soil models used includes contraction of the material when softening (i.e. $\Delta p' < 0$). Contraction is shown to give further increase in excess pore pressure than when using a linear-elastic perfectly plastic material model.

Measurements of the pore pressure at the pile shaft presented in Chapter 13 suggests an increase in excess pore pressure due to sensitivity (as seen in Chapter 13.4). However, the sensitivity is very correlated to the OCR for our dataset. This means that the increase in excess pore pressure could very well be due to OCR solely, and be unrelated to the sensitivity. The

empirical data does however disprove a decrease of the excess pore pressure with increasing sensitivity.

Castro and Karstunen (2010) shows the fit of their model to measurements done by Roy et al. (1981) in Figure 6.18. We see that the prediction fits the measurements quite well, however the shear strength does not go towards zero, but stops at $S_t \approx 1{,}8$. Based on these results and the discussion above, is seems that softening causes a reduction in shear strength with a gradual decrease towards the pile surface. The extent of the zone with a lower shear strength can be quite large. However, the excess pore pressure should increase due to softening, as seen in the empirical data. If the material model do not include contraction as the soil soften, we see that a decrease in excess pore pressure is produced if the remoulded zone is relatively large.

If one use an inner remoulded zone, following the method of Chapter 12.7, then the extent of this zone should be chosen with care. If one choose a large extent with only a small reduction (i.e. averaging the decrease in strength) one would get a decrease in excess pore pressure. Based on the above information this would give the wrong result. Using a small inner remoulded zone with a larger reduction in shear strength would give a more correct result. However, the model does not include the added effect of contraction, and deciding the size of the remoulded zone becomes very difficult. Using a gradual decreasing shear strength and a CSS strain softening material model will probably give a better prediction, but is more cumbersome to implement.

13 Measured excess pore pressure from 12 different sites

Karlsrud (2012) have gathered empirical data from multiple sources for twelve different sites, listing the radius and thickness of the piles, water content, plasticity index, in-situ stress conditions, modulus number and undrained shear strength of the soil, together with the measured excess pore pressure at the pile shaft and the depth that this was measured, and more.

Karlsrud (2012) only included clays where undrained conditions can be assumed, and excluded measurements done closer than about four pile diameters to the tip, due to possible effects of geometry. This data have been checked and supplemented, the result being Table 13.6. In Chapter 13.1 the data gathered from Karlsrud (2012) have been checked with other sources, and in a few cases changes have been made compared to what Karlsrud (2012) propose.

The dataset have been supplemented with the undrained shear modulus (G_u) and the sensitivity (S_t) of the soil at the different sites. The undrained shear modulus is determined in Chapter 13.2, the estimates are mainly based on the modulus number (m_0) gathered by Karlsrud (2012). The sensitivity of the soil at the different sites is gathered from multiple sources. Some discussion on the determination of the specific sensitivity for each site is found in Chapter 13.3. Chapter 13.4 shows the sensitivity from all the sites together, and we look into whether a trend can be found in the empirical data or not. Chapter 13.5 checks if a trend can be found in the excess pore pressure with respect to the coefficient of lateral earth pressure. Lastly, Table 13.6 in Chapter 13.6, shows all the final soil parameters for each site, which will later be used in Chapter 14.

13.1 The sites with index parameters and general info on the piles

Karlsrud (2012) include a quite detailed description of each site with regard to soil conditions, the test piles used, and also other information. We will only give a brief description of each site to give some very basic insight, for a more complete picture of the pile driving procedure and more, I refer you to Karlsrud (2012).

13.1.1 Haga

The Haga site is located in Norway, $60km$ north-east of Oslo. The original terrain had a slope of $1{:}\,20$ towards Glomma, but about $5m$ have been excavated only a few years before the testing due to tile production and plate loading tests, and the terrain have been flattened.

The data included from the Haga site is from what they have referred to as B-piles. This test pile is a closed-ended fully instrumented pile with a diameter of $154mm$, a wall thickness of $4{,}5mm$ and an embedded length of $4{,}85m$. Pore pressure cells where mounted at 4 levels, and the same pile was jacked into the ground and extracted to do multiple tests. The included measurements are from $1{,}9m$ and $3{,}4m$ depth.

At the site there is marine clay which is very homogeneous to a depth of about $4{,}5m$ with a water content of $w = 38\%$, a plasticity index of $I_P = 15$ %, a clay content of $40 - 60\%$, and a direct undrained shear strength of about $s_{uD} = 40kPa$. As seen in Figure 13.1, there is from 4,5 to $5{,}5m$ a more plastic clay layer with water content reaching 55%, I_P and s_{uD} reaching 30% and $55kPa$ respectively. Below $5{,}5m$ depth, the clay gradually becomes siltier. At a depth of about $8m$, there is a transition to layered fine grained sands with some interbedded silty clay layers, reaching down to bedrock at a depth of about $13m$.

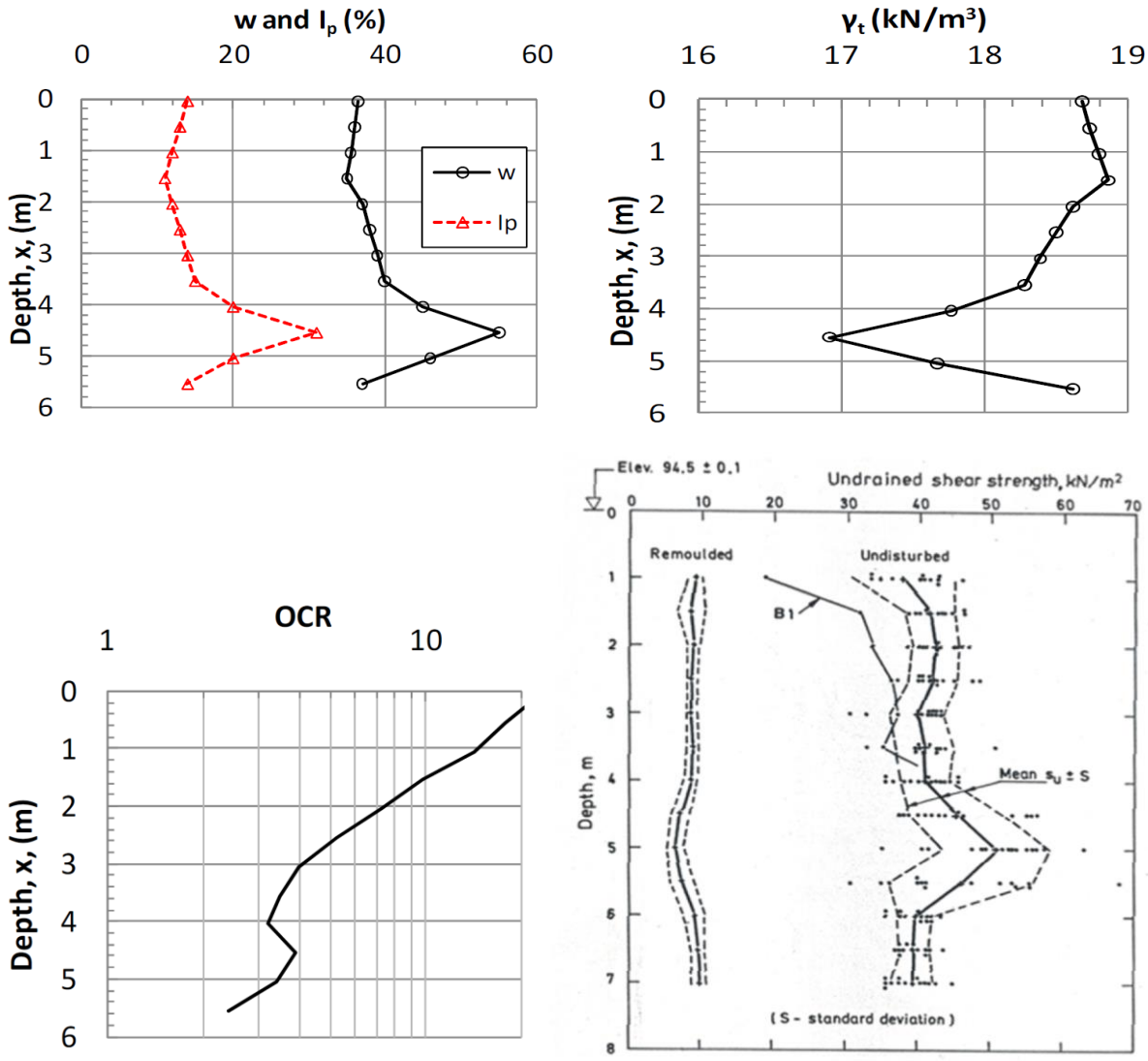

Figure 13.1: Index parameters of the Haga test site and strength from in-situ remote vane borings. (Karlsrud 2012)

The direct undrained shear strength profile is chosen as the mean of the in-situ remote vane borings as multiple direct shear strength (DSS) tests show close agreement with the vane borings.

The marine clay at the site is leeched showing a salt content of less than $1 g/l$. The sensitivity is however still moderate and range from $S_t = 4 - 6$ according to fall cone tests and in-situ vane borings.

Due to the sandy layers below $8m$ depth the clay drain rather freely towards Glomma. This leads to very low pore pressures throughout the clay profile as shown by Figure 13.2.

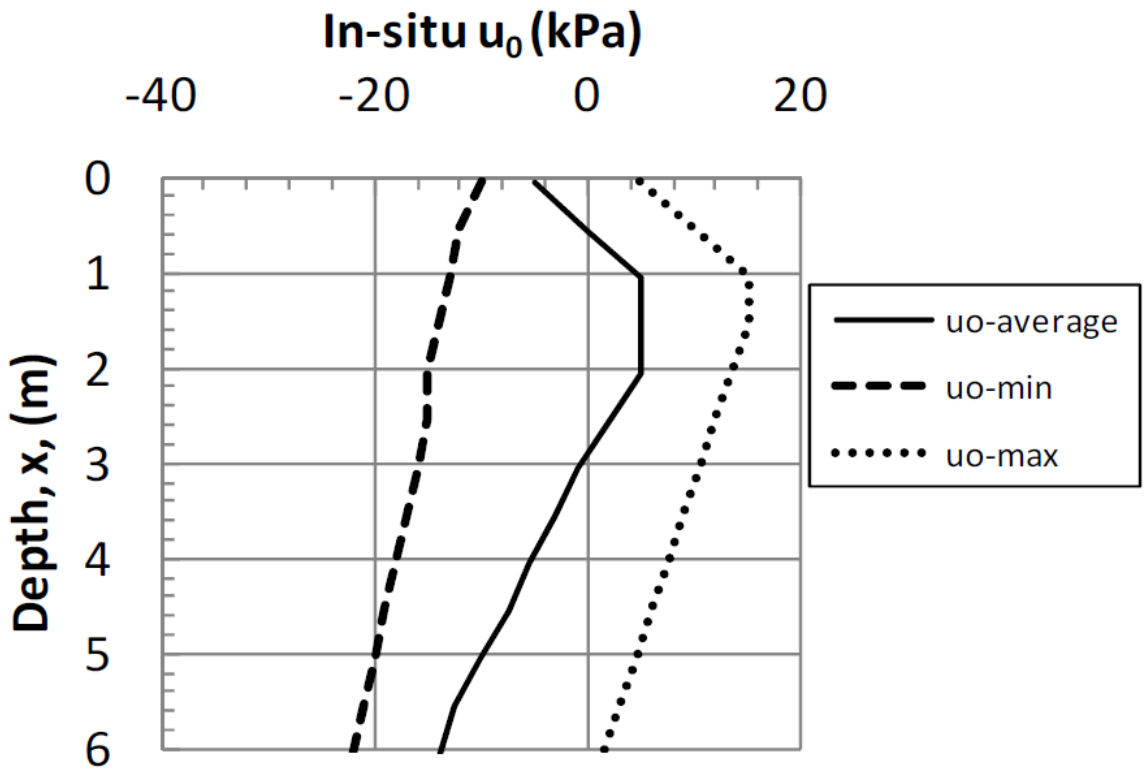

Figure 13.2: In-situ pore pressure with variations observed between 1981 and 1982 when also the pile testing took place. (Karlsrud 2012)

13.1.2 Onsøy

The Onsøy site is located in Norway, about $3km$ north-west of Fredrikstad. Two types of piles where used at both the Onsøy and Lierstranda sites. One is referred to as type A pile, and the other is called type B pile. The type A pile is a closed-ended fully instrumented pile with a diameter of $219mm$, a wall thickness of $8{,}2mm$ and an embedded length of $10m$. These piles were driven through cased boreholes to reach the wanted depth, using a $1-3$ ton drop hammer. For the Onsøy site the measurement depths included range from $7{,}5-35m$ for the type A pile.

The type B pile is an open-ended fully instrumented pile with a diameter of $809mm$, a wall thickness of $9{,}5mm$, also with an embedded length of $10m$ and was driven through a casing as for the type A pile. Measurements included where recorded at 7,5 to $12{,}5m$ depth for the type B pile.

For both the type A and the type B piles, pore pressure were measured at $2{,}5m$, $5m$ and $7{,}5m$ from the tip of the pile.

In addition to the type A and type B piles, type C piles where used at the Onsøy site (these where not used at the Lierstranda site). The type C pile is equivalent to the type A pile except instead of being $10m$ long, the C1 pile was $30m$ long and had 6 positions, $5m$ apart, where pore pressure was recorded.

At the site there is a $1-1{,}5m$ thick dry crust, followed by a normally consolidated soft plastic marine clay with water content between $50-70\%$, plasticity index from $35-50\%$ and clay content from $40-60\%$. The clay contains traces of iron oxide specifically in the top part, and organic matter and shell fragments. As seen in Figure 13.3, the water content peaks at about $10m$ depth, while the plasticity index have its maximum at about $15-25m$ depth. From the highest level there is a clear decreasing trend. The deepest sample is from $32{,}5m$ depth and data further down is extrapolated. At $2m$ depth the salt content is found to be 8%, and it increases to 30% at $8m$ depth and below.

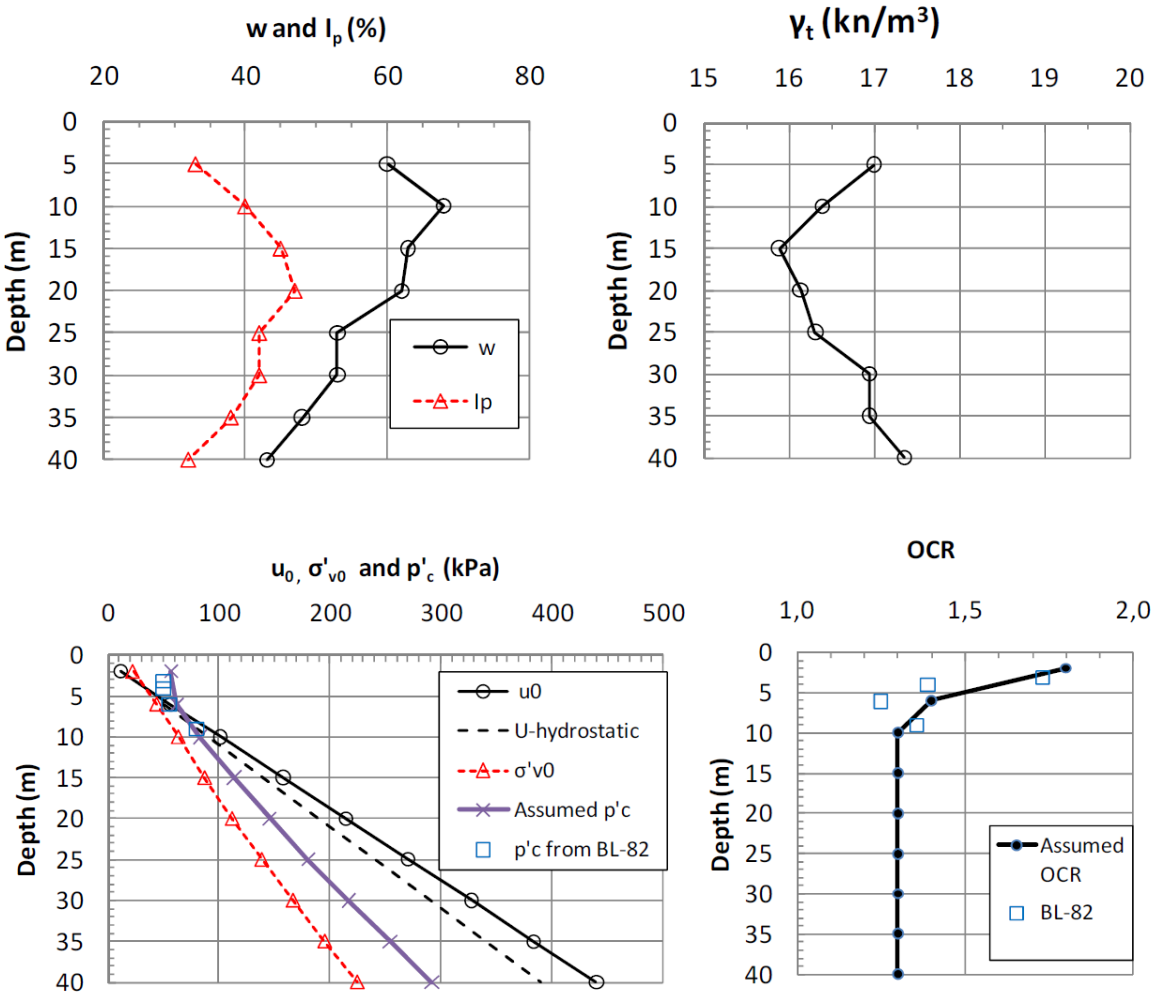

Figure 13.3: Index data of the soil at the Onsøy site, together with the in-situ stress conditions. (Karlsrud 2012)

The in-situ pore pressure shows a slight artesian overpressure, 11,3% above hydrostatic values. Geologically the site is normally consolidated, however it is still assumed to have an apparent pre-consolidation pressure due to creep or ageing effects corresponding to $OCR = 1{,}3$ which is a low (conservative) estimate. Due to desiccation and chemical weathering the top part down to about $5m$ depth shows a higher OCR.

The undrained shear strength is determined based on vane borings, CPTU data and block samples, as Figure 13.4 indicate. The direct undrained shear strength is about $10kPa$ at $2m$ depth and increase by approximately $1{,}21\ {}^{kPa}/_{m}$.

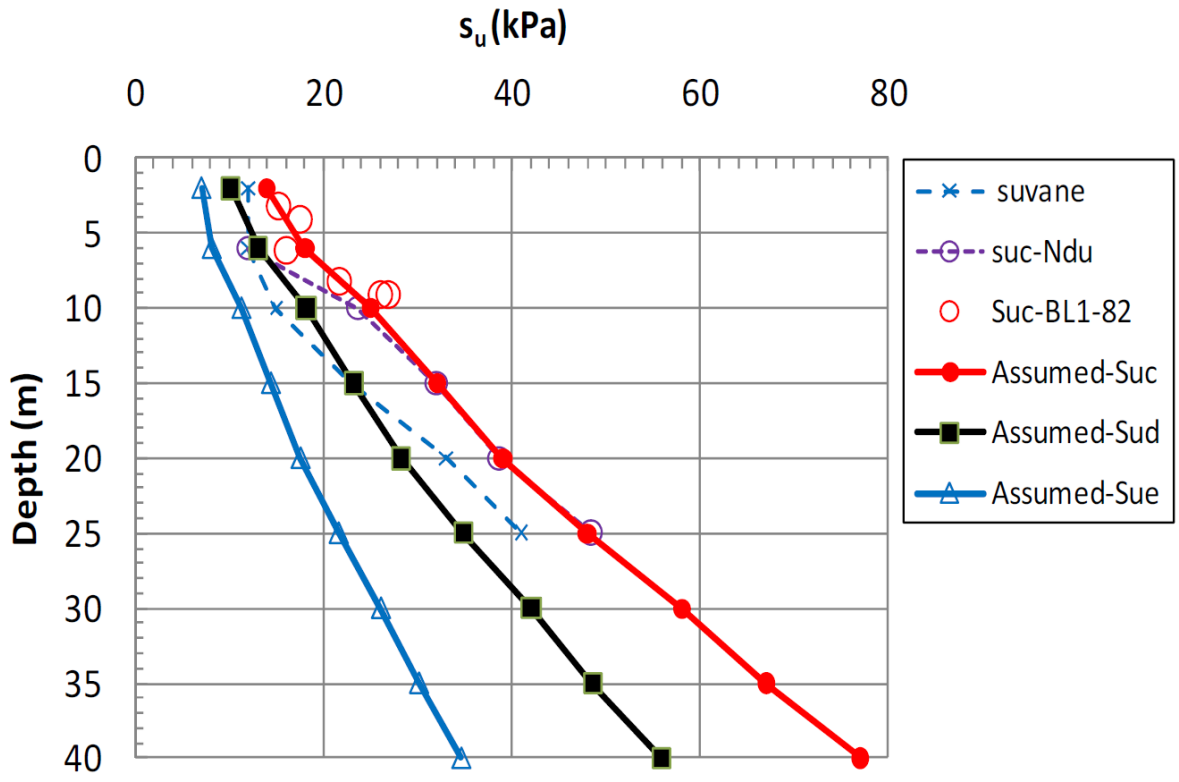

Figure 13.4: The undrained shear strength at the Onsøy site, showing results from vane borings, CPTU and block samples together with the chosen/assumed strength profiles. (Karlsrud 2012)

13.1.3 Lierstranda

The Lierstranda site, located in Norway, lies near the shoreline of Drammensfjorden. It is about $1{,}2km$ east of the outlet of the Drammen river and $1{,}5km$ west of the outlet of the Lier river. About 15 years before the pile tests were conducted the ground was raised by about $2m$. In addition to land reclamation being conducted on a tidal flat with water depths of less than $3m$, $300-500m$ south of the testing area.

The test piles used at Lierstranda is of the same type as those used at the Onsøy site, but only type A and type B piles were used at Lierstranda. Measurements that have been included range from $7{,}5-35m$ depth.

At the site there is the recent fill which is $1{,}5-2m$ thick, followed by more than $50m$ of normally consolidated clay. Below the fill and to about 12m depth, there is a medium plastic clay with water content of $40-42\%$, plasticity index of $20-25\%$ and a clay content of $32-28\%$. From Figure 13.5 we see that below $12m$ depth there is a gradual transition to a silty low plastic clay layer with a water content below 30%, plasticity index of 12% and clay content decreasing to about 20%. Figure 13.5 also shows the unit weight increasing with decreasing water content as one would expect. The salt content is about $32\,{}^{g}/_{l}$ meaning the clay has not been leached. The clay has low organic content and a sensitivity of $3{,}5$ (range $3-6$) according to in-situ vane borings. However, the fall cone test suggest a sensitivity of 11 (range $7-14$).

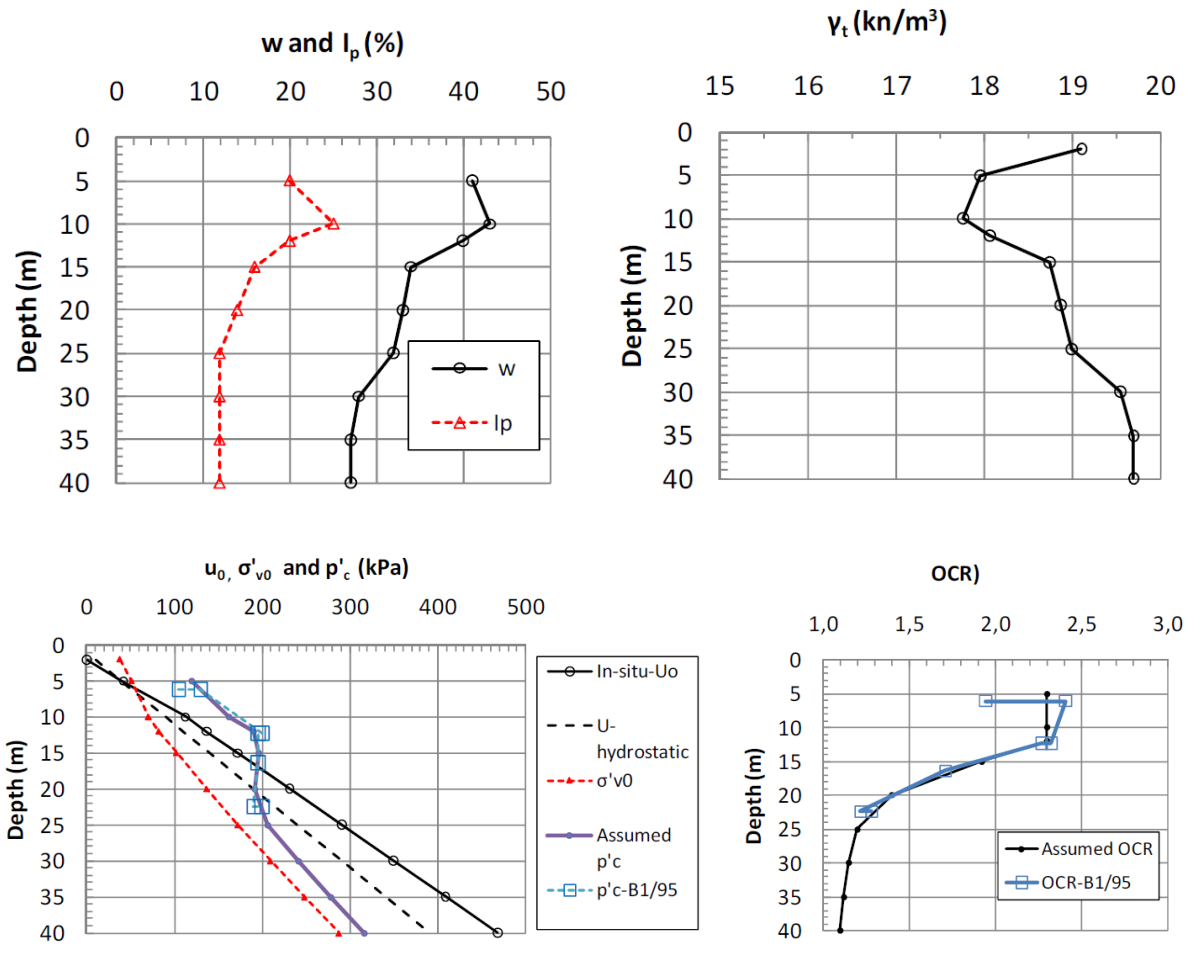

Figure 13.5: Index data of the soil at the Lierstranda site, together with the in-situ stress conditions. (Karlsrud 2012)

There is also here a slight artesian overpressure, about 20% above hydrostatic values. The overconsolidation ratio (OCR) is determined based on results from block samples. The high OCR in the medium plastic clay is hard to explain from a geological view, but it may be partly an effect of creep and also maybe due to some overburden. Below the lowest block sample the OCR trend is speculative. The chosen direct undrained shear strength profile is viewed in Figure 13.6. It is $20kPa$ at $5m$ depth and increase approximately with $1{,}26\ {}^{kPa}/_{m}$. The profile is based on vane borings, CPTU data, and lab results from both block and piston samples.

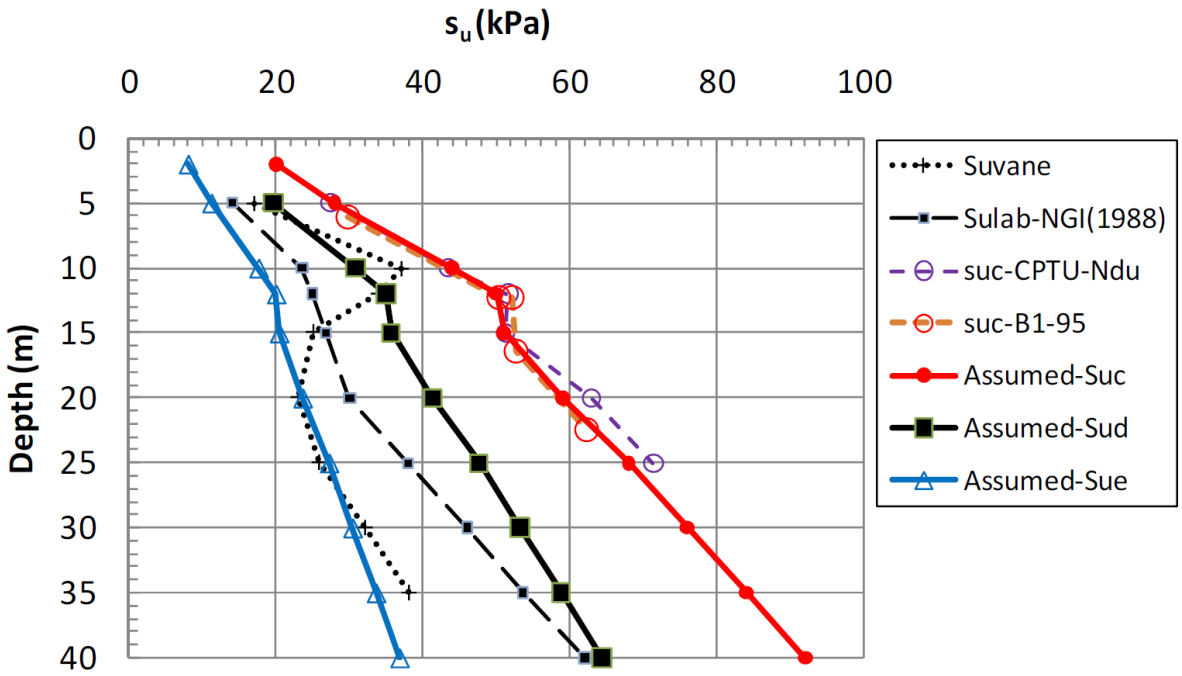

Figure 13.6: The undrained shear strength at the Lierstranda site, showing results from vane borings, CPTU data, and block and piston samples together with the chosen/assumed strength profiles. (Karlsrud 2012)

13.1.4 Tilbrook Grange

The Tilbrook Grange site is in the United Kingdom, and lies about $20km$ north-northeast of Bedford. The clay at the site is highly overconsolidated and very stiff, resembling conditions often met in the parts of the North Sea that have been overlain by glaciers according to Karlsrud (2012).

Data from three different types of test piles are included for the Tilbrook Grange site, namely the NGI pile A, the NGI pile B and the LDPT-McClelland compression pile.

The NGI pile A, which is a closed-ended fully instrumented pile with a diameter of $219mm$, thickness of $16mm$ and embedded length of $9{,}5m$, is similar to the type A piles used at

Onsøy and Lierstranda. Pore pressure was measured at 3 levels: $5{,}1m$, $7{,}6m$ and $10{,}1m$ depth, and the pile was driven through a $3m$ deep casing.

The NGI pile B is exactly as the NGI pile A except it only had 2 levels where the pore pressure was measured. It is $10m$ long and the casing was $17{,}5m$ long, measurements were then done at $22{,}5$ and $25m$ depth.

The LDPT-McClelland compression pile is an open-ended fully instrumented pile with an outer diameter of $762mm$, and a wall thickness decreasing from $40mm$ for the upper part to $32mm$ for the lower part. The pile was driven using a 40t BSP HA40 hydraulic hammer with a rated energy of $470kNm$. The pile was partially plugged with the top of the plug recorded at $16{,}9m$ depth. The pile is $30{,}5m$ long with 4 levels of pore pressure measurement equipment. Only readings from $8m$, $14{,}3m$ and $26{,}2m$ depth are included.

At the site there is an upper layer of Lowstoft till to about $17{,}1 - 18{,}6m$ depth. McClelland (1998) describe this layer as very stiff, dark grey silty clay with scattered sand to gravel size fragments of flint, chalk and mudstone within the clay matrix. Below this is a very stiff dark grey fissured clay, defined as Middle Oxford clay, with scattered silt and sand pockets extending to bedrock at about $40m$ depth. Figure 13.7 shows the index data of the soil. The water content is about 15%, and the plasticity index is about 25% in the Lowstoft till, increasing respectively to about 18% and 35% in the Oxford clay. The clay content increase from $35 - 50\%$ in the Lowstoft till to $45 - 60\%$ in the Oxford clay.

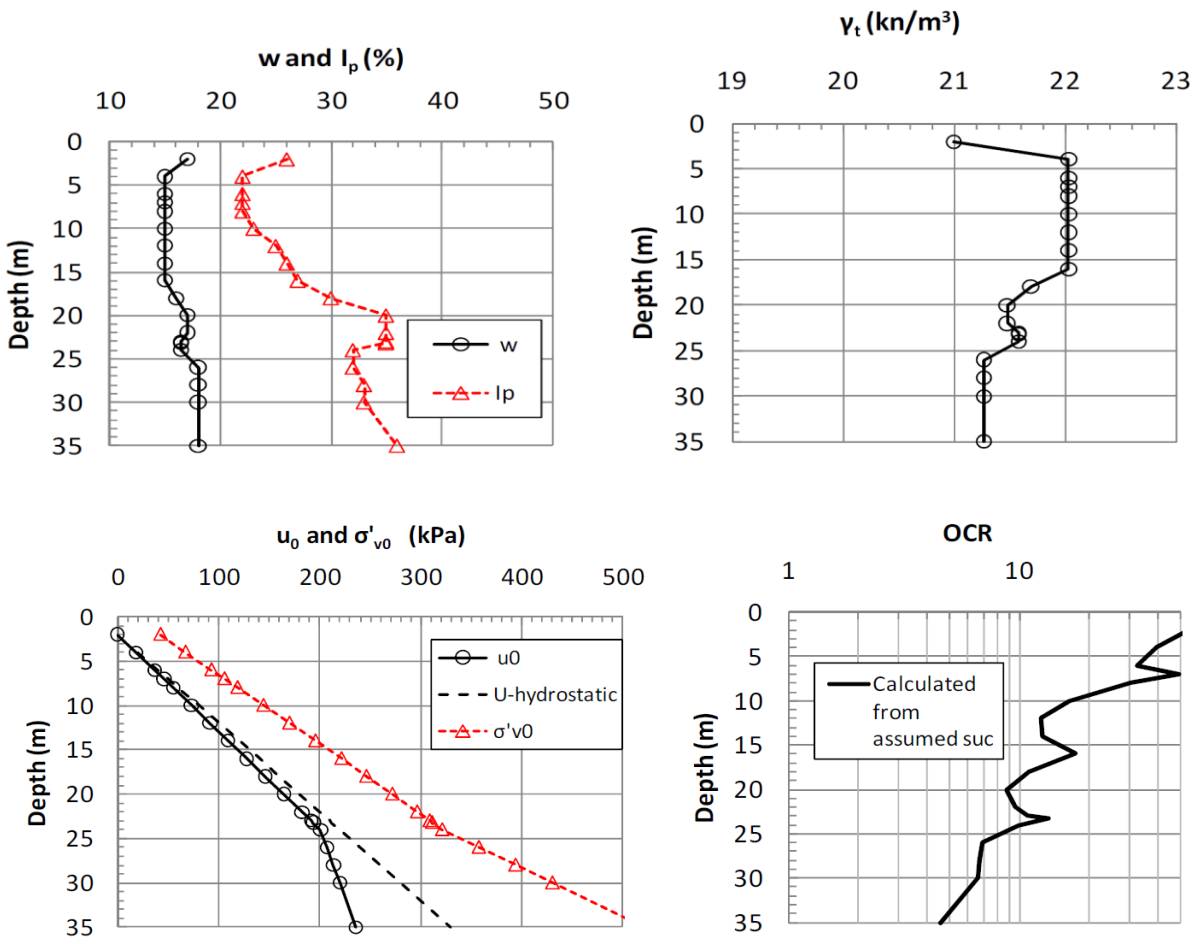

Figure 13.7: Index data of the soil at the Tilbrook Grange site, together with the in-situ stress conditions. (Karlsrud 2012)

The in-situ pore pressure measurements suggest hydrostatic conditions within the Lowstoft till with a water table at $2m$ depth. In the Oxford clay there is an under pressure measured compared to hydrostatic conditions. According to Lambson et al (1993) the Oxford clay has a very low permeability and they reported that it took 5 months after the piezometers were installed for the pore pressures to come to an equilibrium level.

Little data have been found in available literature on the anisotropy of the undrained strength of such stiff and highly overconsolidated clays. Based on results of the Drammen clay by Andersen (2004), and the Haga clay by Lacasse (1979), Karlsrud (2012) assumes that $s_{uD} = 0{,}6 s_{uC}$ in the Lowstoft till and $s_{uD} = 0{,}7 s_{uC}$ in the Oxford clay. The chosen s_{uC}-profile is based on Unconsolidated Undrained (UU) triaxial tests and CPTU data ($s_{uC} - N_{kt}$). The other data was disregarded due to possible error in the tests, the reasoning behind this can be found

on page 115-116 in Karlsrud (2012).

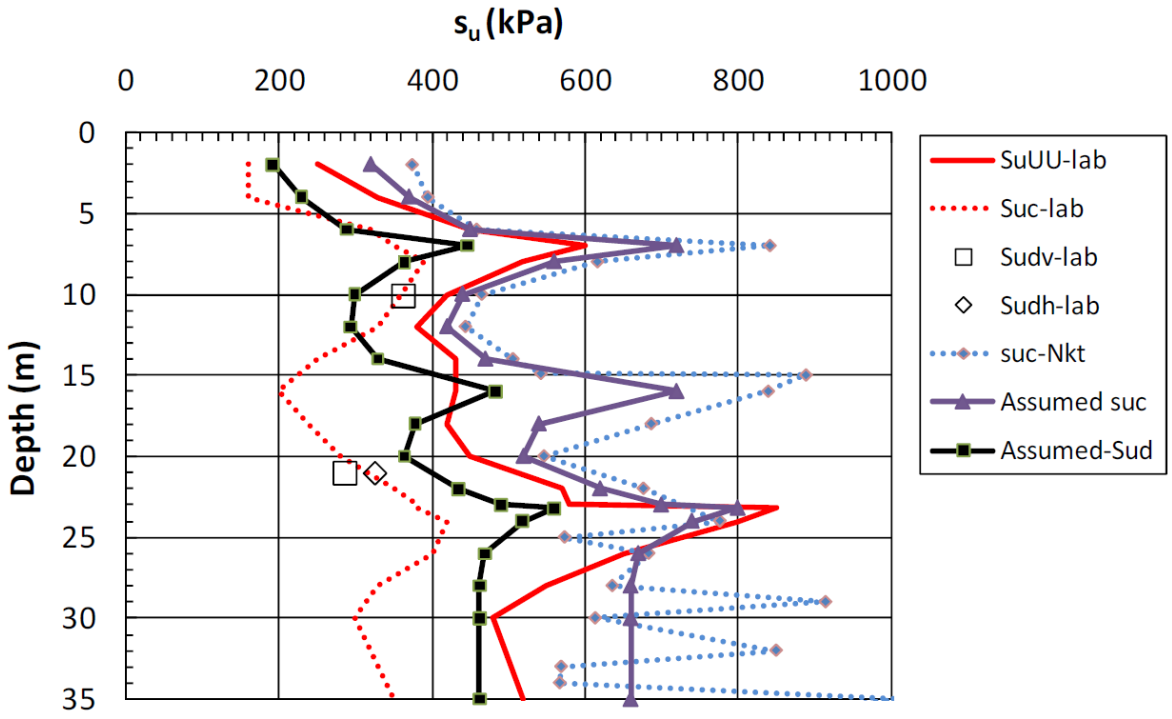

Figure 13.8: The undrained shear strength at the Tilbrook Grange site, showing results from CPTU data, different lab tests on piston samples together with the chosen/assumed strength profiles. SuUU-lab is results from unconsolidated undrained triaxial tests, while Suc-lab is results from CIUC/CAUC triaxial tests. Sudv-lab and Sudh-lab are DSS test, vertically and horizontally trimmed, respectively. Lastly suc-Nkt are the CPTU data interpreted by using Nkt values based on the correlation proposed by Karlsrud et al (2005). (Karlsrud 2012)

13.1.5 Bothkennar

The Bothkennar site is located in the United Kingdom, about $35km$ west-northwest of Edinburgh. Nash, Powell et al. (1992) say that the soft silty clay at the site is quite homogeneous compared to other UK clays, and according to Karlsrud (2012) the clay is believed to have been deposited in a marine/estuarine environment.

At the Bothkennar, Cowden and the Canons Park sites, the IC (Imperial College) pile was used. The IC-pile has undergone improvements over the years, but details of this will not be included. The pile is closed-ended with a diameter of $101{,}6mm$. Pore pressure was recorded at 3 levels, but only the recordings from the top two sensors are included. At the Bothkennar site the test pile was $4{,}8m$ long and was jacked through a $1{,}2m$ deep preinstalled casing. Measuring was then done at $3{,}5m$ and $4{,}7m$ depth.

There are some minor discrepancies regarding the plasticity index of the clay at Bothkennar. According to Karlsrud (2012): “The natural water content increases gradually from about

40% at $1m$ depth to 73% at $6m$ depth. The plasticity index correspondingly increases from about 40% to 70%." (page. 138). Karlsrud (2012) refer to Lehane and Jardine (1994) and Jardine and Lehane (1993), "Research into the behavior of offshore piles: Field experiments in soft clay". The latter paper was not available. Hight, Paul et al. (2003) say that the plasticity index increase from about 35% at $2{,}5m$ to 55% at $6-8m$, and reduce below $8m$ to 30%. This is seen to correspond with Figure 13.9 from Nash, Powell et al. (1992). Lehane and Jardine (1994) state that the plasticity index is about 25% at $1{,}5m$ increasing to about 50% at $4-6m$ depth. According to Hight, Paul et al. (2003):

> "The clay has anomalously high and variable plasticity, which results from its particular organic content, and which gives rise to misleading values of apparent activity and poor correlation of parameters with plasticity index. After removal of the organic content, the plasticity index lies between 18% and 22% and the activity is approximately 0,5. These values provide a truer reflection of the illite, quartz and rock flour mineralogy, and improve correlations with engineering properties." (page. 594)

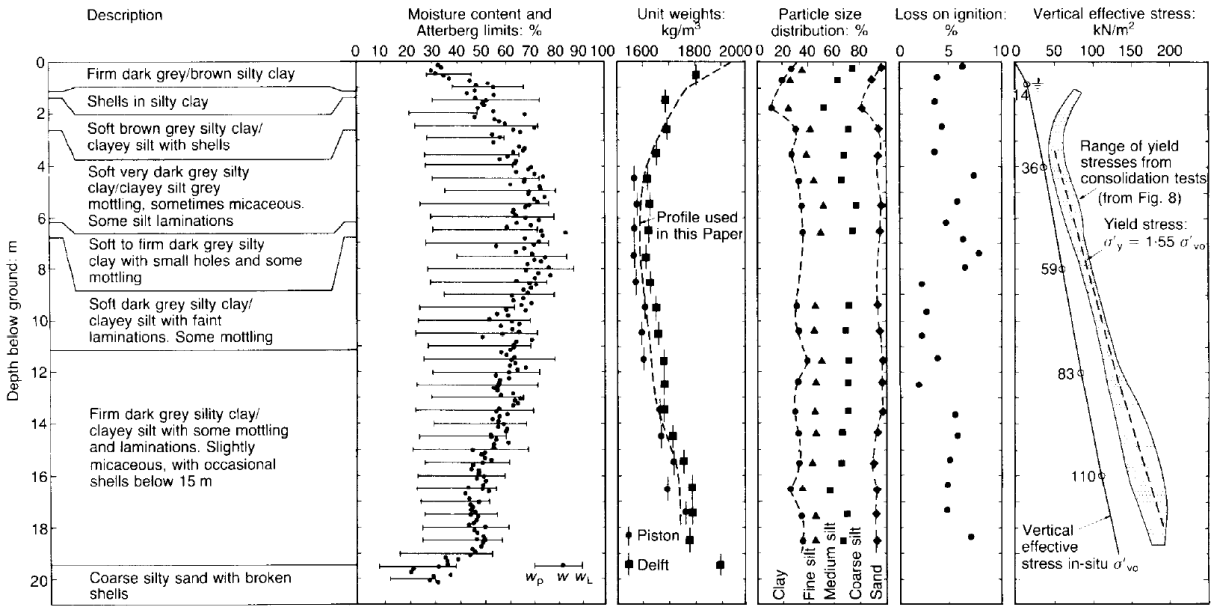

Figure 13.9: Index data of the soil at the Bothkennar site, together with the in-situ vertical effective stress. (Nash, Powell et al. 1992)

Lehane and Jardine (1994) also mentions this, and report a plasticity index reducing to about $20-25\%$ when the moderate proportion ($\sim 3\%$) of organic residues are extracted. Figure 13.9, by Hight, Paul et al. (2003), shows the plastic limit and the liquid limit measured from natural water content, after air drying, and after treatment with hydrogen peroxide. The clay content is according to Lehane and Jardine (1994) increasing from 15% at $2m$ to 40% at $6m$ depth. This is supported by Hight, Paul et al. (2003).

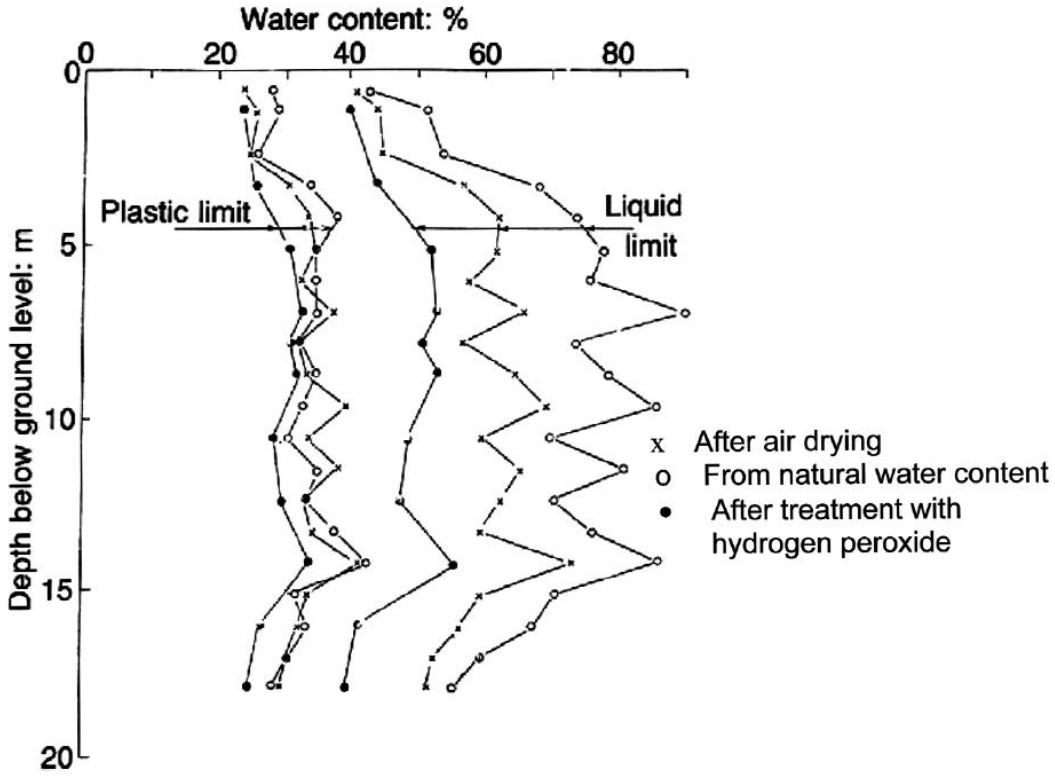

Figure 13.10: Plastic limit and Liquid limit measured from natural water content, after air drying and after treatment with hydrogen peroxide for the Bothkennar site. (Hight, Paul et al. 2003)

Since this data is to be used in a regression analysis, correlation with engineering properties, and true reflection of the soil characteristics is important. The R^2-value of the regression proposed in Chapter 14.6 is seen to increase with $0{,}23\%$ when using the plasticity index proposed by Hight, Paul et al. (2003). The apparent improvement of the regression is however so small and the scatter so large that it is not a trustworthy way of determining which value that is correct. One should be careful not to change the value of a parameter just in order to try to improve some kind of regression. Here I believe there is some cause and reasoning behind changing the variable. However, if one is to use the regression based equations and the clay show very high and variable plasticity index due to the organic content, then the plasticity

index should be chosen so that it reflects the clay and its properties, similar to what Hight, Paul et al. (2003) have done.

According to Nash, Powell et al. (1992) the water table is located at about $1m$ depth and the pressure is assumed to be hydrostatic with depth. Figure 13.9 shows the effective vertical stress profile, and the unit weight used to make the profile. Karlsrud (2012) gives that at $3{,}5m$ and $4{,}7m$ depth, the initial pore pressure is $27kPa$ and $38{,}5kPa$ respectively. While the vertical effective pressure is listed to be $32{,}9kPa$ and $39{,}7kPa$ at the two depths mentioned. This seems to coincide quite well and the initial stresses proposed by Karlsrud (2012) is adopted.

Figure 13.11 shows the undrained strength profile suggested by Hight et al (1992), results from block samples and interpretation on CPTU data. Hight et al (1992) based their trend line on multiple test conducted on piston samples. Karlsrud (2012) used the trend line suggested by Hight et al (1992) as the results seems to agree quite well, except for the CPTU u_2-based strength coming out a little high. The OCR-profile suggested by Nash et al (1992) was adopted by Karlsrud (2012) and is also used herein.

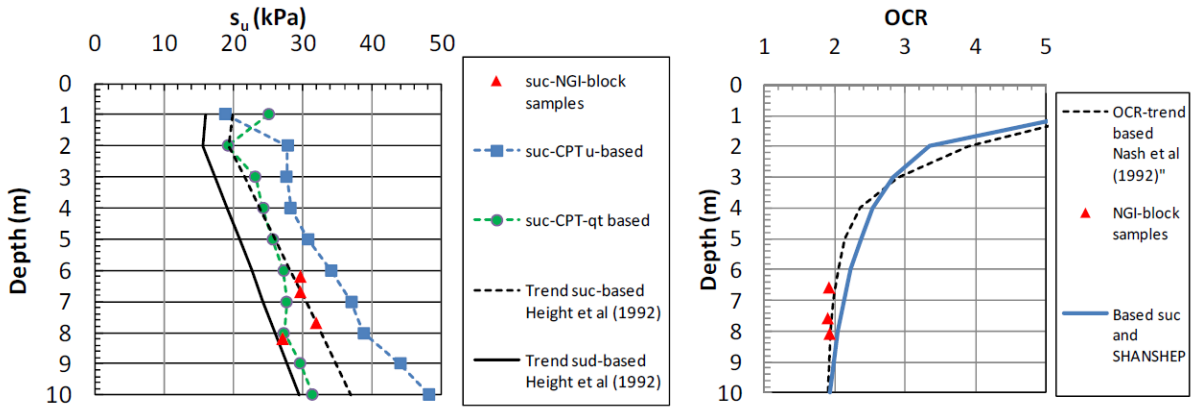

Figure 13.11: The undrained shear strength and the overconsolidation ratio (OCR) at the Bothkennar site. Where the plot to the left shows the undrained shear strength found from tests on block samples, interpretation on CPTU data from Jakobs and Coutts (1992), and trend lines suggested by Hight et al (1992) based on tests conducted on piston samples. The plot to the right shows the OCR profile suggested by Nash et al (1992), results from tests on block samples and results from interpretation of the CPTU data. (Karlsrud 2012)

13.1.6 Cowden

The Cowden site is located in the United Kingdom, about 17km north-east of Kingston upon Hull. The IC-pile described previously, was used at the Cowden site as well. The pile was jacked through a $2{,}5m$ deep preinstalled casing to a depth of $6{,}2m$, and measuring was then done at $3{,}8m$ and $4{,}9m$ depth.

At the site there is a glacial till clay, which has a water content of about $16-18\%$ and a plasticity index of approximately 20%. The clay content is about 27% and increase slightly with depth, there are also some fragments of chalk and flint observed.

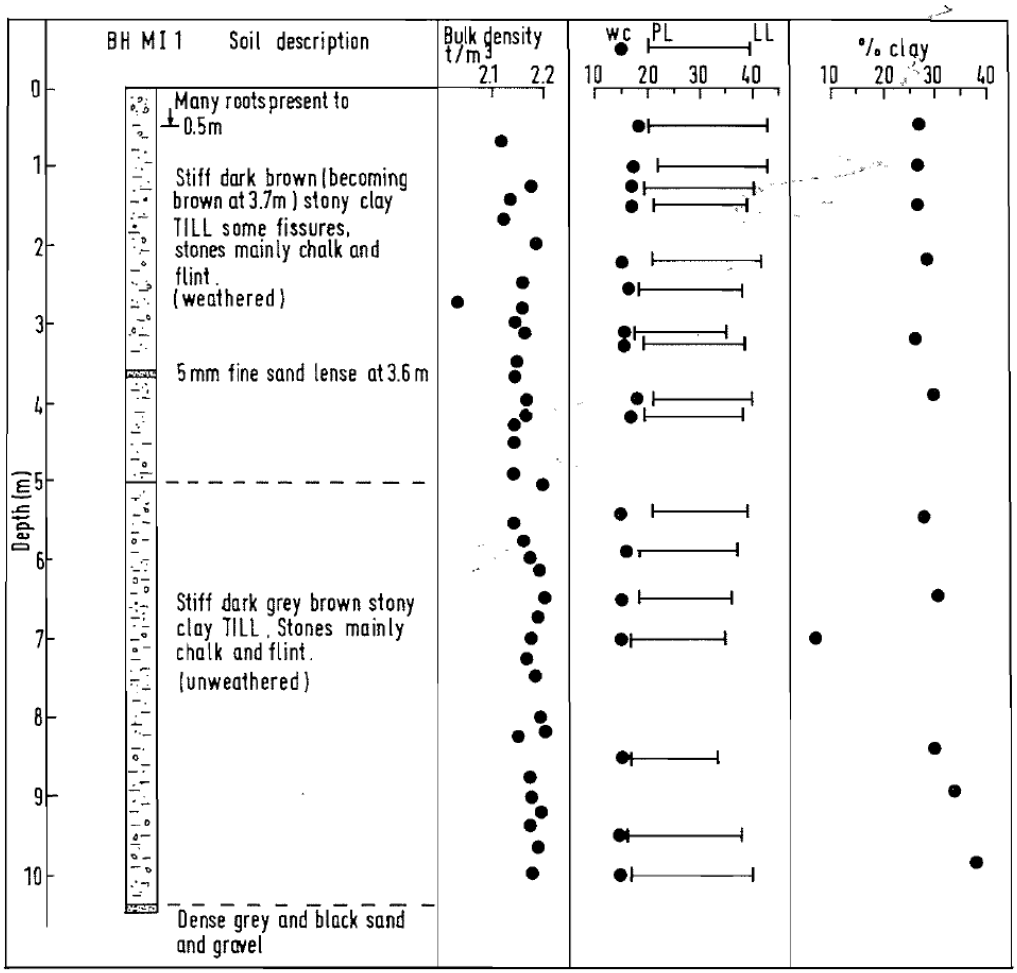

Figure 13.12: Index data of the soil at the Cowden site. (Lehane and Jardine 1994)

Lehane and Jardine (1994) report close to hydrostatical pore pressure with depth. This, combined with the bulk densities from Figure 13.12, coincides well with the in-situ pore pressure and vertical effective stress reported by Karlsrud (2012), given a groundwater table at about $1{,}3m$ depth.

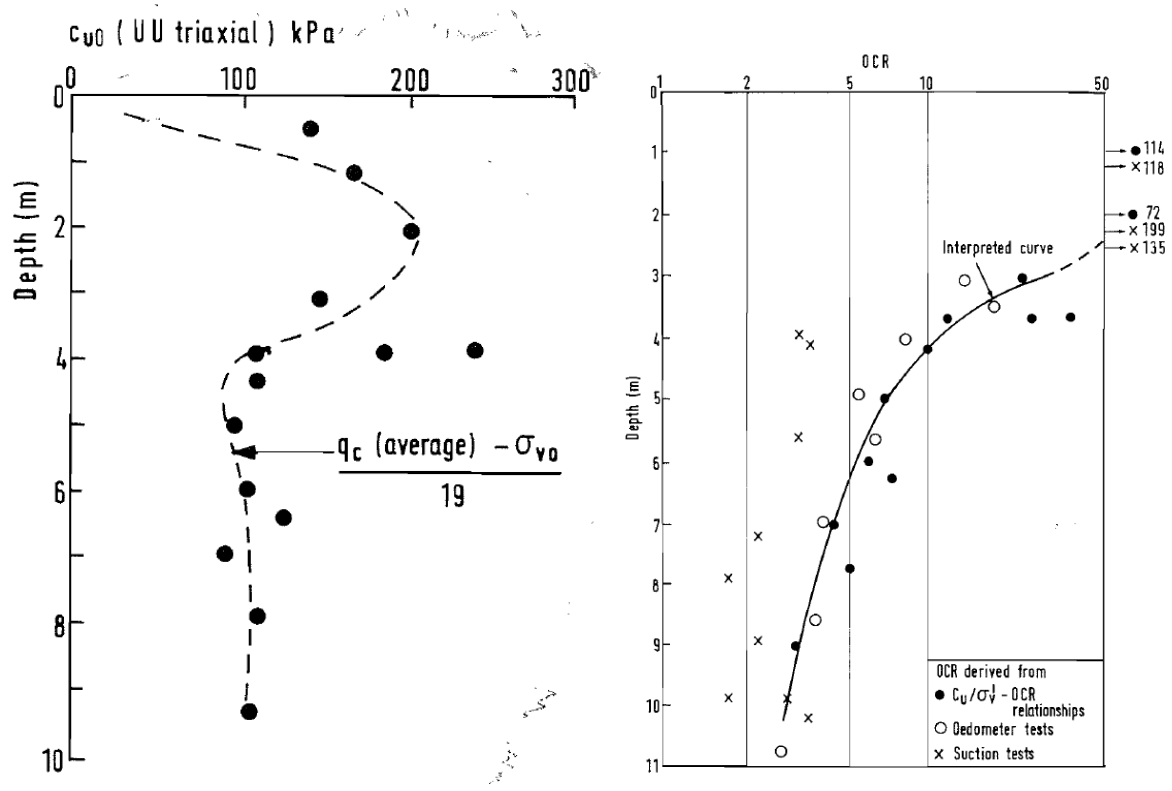

Figure 13.13: Undrained shear strength and overconsolidation ratio from tests and CPTU interpretation according to Lehane and Jardine (1994) for the Cowden site.

Figure 13.13 and Figure 13.14 shows the undrained shear strength and overconsolidation ratio profiles proposed by Lehane and Jardine (1994) and Karlsrud (2012) respectively. The undrained shear strength profile agrees quite well and parameters proposed by Karlsrud (2012) are used. The OCR profile suggested by Karlsrud (2012) is based on CPTU data and the SHANSEP procedure. The SHANSEP procedure was presented by Ladd and Foott (1974) and suggest the following relationship:

$$\frac{s_u}{\sigma'_{v0}} = S * OCR^m \tag{13.1}$$

where S represents the normalized strength for a sample consolidated well beyond the preconsolidation pressure, and m is a power chosen based on empirical data, often related to the plasticity index. Karlsrud (2012) used this procedure with $S = 0{,}28$ and $m = 0{,}8$ due to the low plasticity of the clay. The cone factor depends on OCR, which Bond & Jardine (1990) suggested could vary within wide limits. Karlsrud (2012) therefore used an iterative procedure

until the assumed UU triaxial test based s_{uC}-profile agree with the CPTU calculated s_{uC}-profile, which depend on the OCR-profile due to the cone factor. The CPTU calculated s_{uC}-profile uses the CPTU tip resistance as basis, and the CPTU correlations between q_t and s_{uC} proposed by Karlsrud et al (2005). The ratio between the direct and active undrained shear strength (i.e. the anisotropy ratio) was taken as $s_{uD} = 0{,}7 s_{uC}$.

The OCR values this procedure obtains are higher than what Lehane and Jardine (1994) suggests below $3m$ depth. The pore pressure measurements are done at $3{,}8m$ and $4{,}9m$ depth, as previously mentioned. Karlsrud (2012) have used an OCR of 21,5 and 13, respectively. The data from Lehane and Jardine (1994) suggests an OCR of 13 and 7,5, respectively. The difference is as one can see, quite substantial.

There is very little reasoning provided as to why Karlsrud (2012) trusts the SHANSEP procedure and the CPTU data to be more correct than the oedometer results presented by Lehane and Jardine (1994). The oedometer test results are not presented, only the interpreted values of OCR, and so it is hard to tell if the test results or samples have been of an adequate quality. However, Lehane and Jardine (1994) do not mention that the tests seem faulty, and oedometer tests are generally accepted as a more trustworthy method of determining the OCR. So the values proposed by Lehane and Jardine (1994) was adopted.

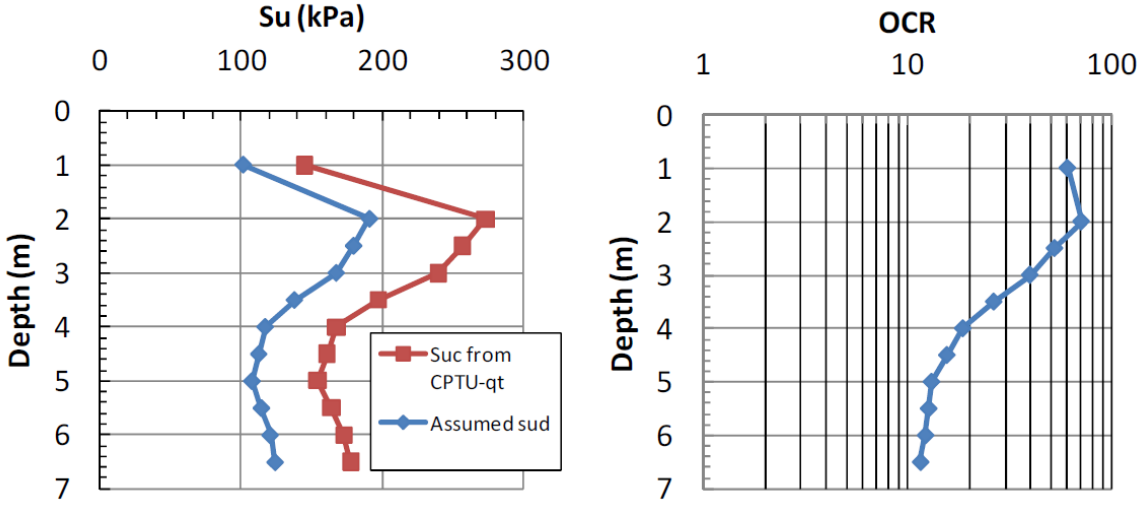

Figure 13.14: Undrained shear strength and overconsolidation ratio interpreted from CPTU data and used by Karlsrud (2012) for the Cowden site.

The pore pressure did at this site decrease during the jacking, but within some minutes after the end of jacking the pore pressure increased above the in-situ levels, and then tapered off with time. In Table 13.6, the maximum values observed some minutes after jacking is listed.

13.1.7 Canons Park

The Canons Park site is located in the United Kingdom, about $16km$ north-west of London. The IC-pile described previously, was also used at the Canons Park site. The pile was jacked through a $2m$ deep preinstalled casing to a depth of $6m$, and measuring was then done at $3{,}2m$ and $4{,}0m$ depth.

At the site there is so called London clay from $2{,}5m$ to $25m$ depth. Above this there are superficial deposits of topsoil, gravel and silty clay. The London clay can be categorized into three zones as seen in Figure 13.15. From $2{,}5m$ to $4{,}1m$ depth, there is a so called disturbed London clay. The disturbed London clay is a stiff brown silty fissured clay with plasticity index going from 60% to 40% with depth.

This weathered clay shows signs of mechanical disturbance possibly due to glacial process or mass movement, according to Bond and Jardine (1991). From $4{,}1m$ to $7m$ depth, there is an intact brown London clay. This is a stiff, light brown, silty fissured clay with a plasticity index of about 30%. Below this there is blue London clay, which is a stiff grey-brown, silty fissured clay of intermediate plasticity. From Figure 13.15, we see a sharp drop in liquid limit (w_L), and corresponding increase in undrained shear strength, marking the transition between the disturbed and intact clay. The water content is quite constant with depth and equals about 30%.

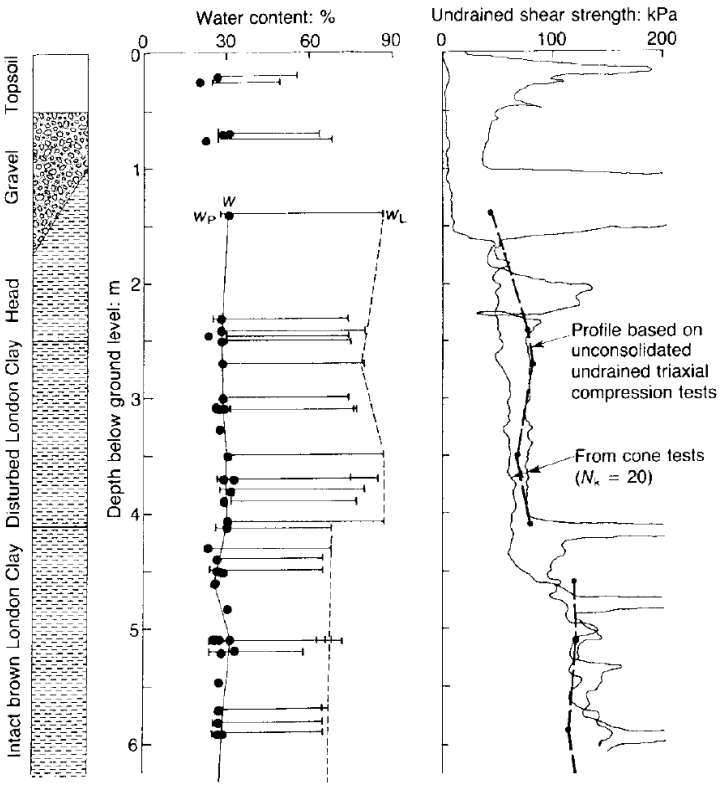

Figure 13.15: Index properties and undrained shear strength from Bond and Jardine (1991) for the Canons Park site..

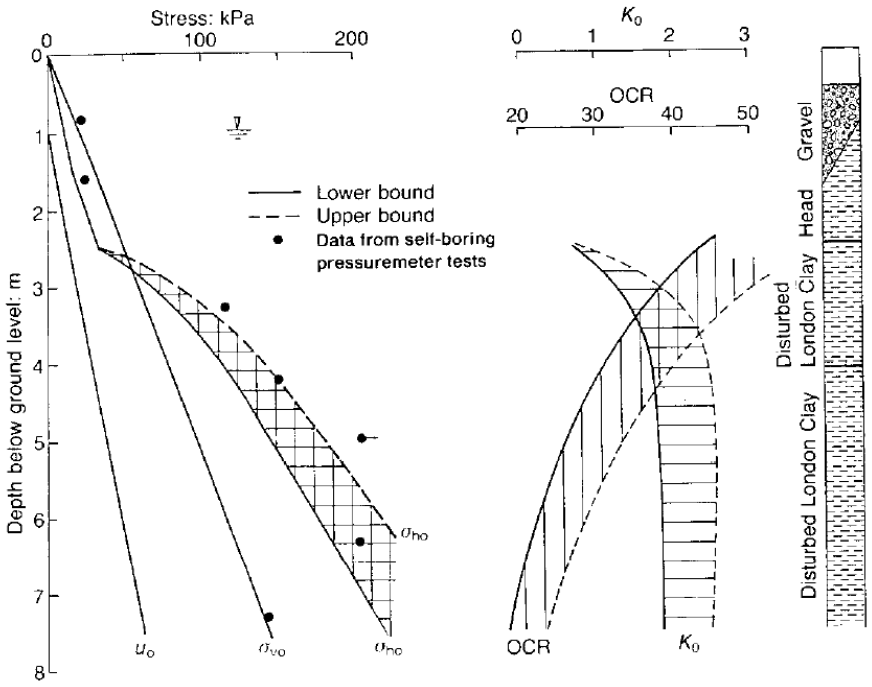

Figure 13.16: In-situ stress conditions, coefficient of lateral earth pressure and overconsolidation ratio from Bond and Jardine (1991) at the Canons Park site.

Figure 13.17 shows the undrained shear strength and OCR-profile used by Karlsrud (2012). The CPTU data was used in an iterative procedure with the SHANSEP method (as explained for the Cowden site). Since this is a high plastic clay, Karlsrud (2012) assumed that $s_{uD} = 0{,}75 s_{uC}$, $S = 0{,}3$ and $m = 0{,}85$. The direct undrained shear strength profile is about $15 - 20\%$ higher than what Bond and Jardine (1991) propose, and the OCR-profile is a factor of 2 or more lower. This is stated by Karlsrud (2012) himself, but similarly as for the Cowden site there is not much explanation as to why one have this discrepancy.

Bond and Jardine (1991) states that it is difficult to find the exact overconsolidation ratio of the London clay due to several loading and unloading cycles and glacial processes, chemical bonding and ageing. However, the bond suggested in Figure 13.16 is based on oedometer results and using the same argumentation as for the Cowden site we choose to trust these results. Since the values of Karlsrud (2012) is lower than what Figure 13.16 suggests, we chose a low estimate following the solid black line.

The in-situ pore pressure and effective vertical stress reported by Karlsrud (2012) differ somewhat from what Bond and Jardine (1991) report. Karlsrud (2012) list that at $2{,}8m$ and $4m$ depth, the initial pore pressure is $u_0 = 25kPa$ and $40kPa$, while the effective vertical stress is $\sigma'_{v0} = 46kPa$ and $60kPa$, respectively. Bond and Jardine (1991), as seen in Figure 13.16, assume a hydrostatic pore pressure distribution with a groundwater table at $1m$ depth, and a unit weight of $\gamma = 20\ {}^{kN}/_{m^3}$. This gives $u_0 = 18kPa$ and $30kPa$, $\sigma'_{v0} = 38kPa$ and $50kPa$, at $2{,}8m$ and $4m$ depth, respectively.

The data chosen by Karlsrud (2012) suggests a unit weight of $24\ {}^{kN}/_{m^3}$ as $\sigma_{v0} = \gamma * z = \sigma'_{v0} - u_0$. This is quite high and Karlsrud (2012) does not mention the in-situ stress conditions specifically when describing the site. Only a table similar to Table 13.6 gives the in-situ stresses of the Canons Park site. We choose the stress conditions proposed by Bond and Jardine (1991), and also the undrained shear strength and OCR are determined based on results from their report.

This is then the one site where parameters deviate substantially from what Karlsrud (2012) have suggested. Having a single person choose soil parameters is an advantage as this means the same procedure and method have been used for all the sites. This could very well lead to better correspondence between the measured values and soil conditions, and then a better regression analysis can be performed. The same procedure can then readily be followed for a

new site, which leads to some continuity and also maybe better predictions. However, at this site the parameters proposed by Karlsrud (2012) seemed faulty, and parameters from Bond and Jardine (1991) were chosen.

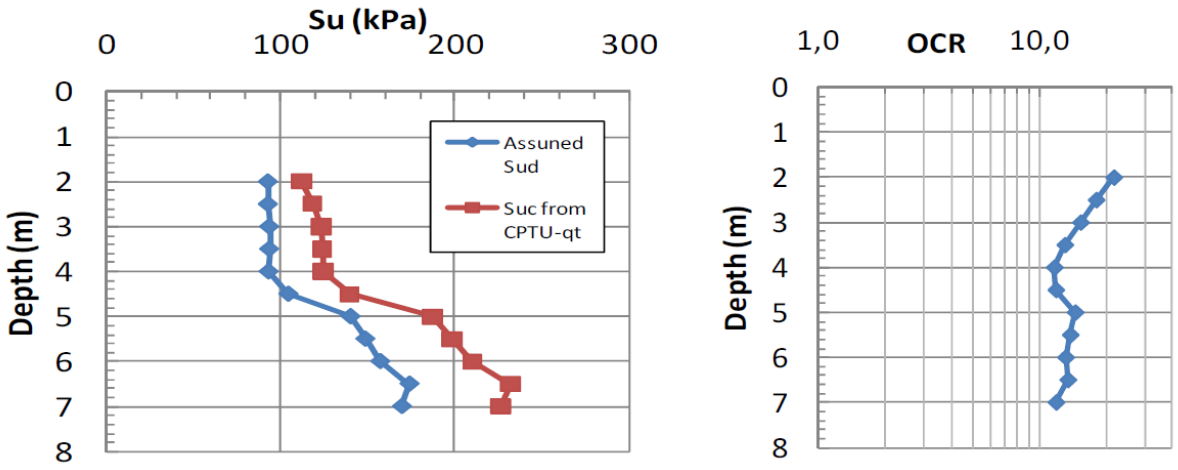

Figure 13.17: Undrained shear strength and overconsolidation ratio interpreted from CPTU data and used by Karlsrud (2012) for the Canons Park site.

13.1.8 Empire

The Empire site is located in the USA in the Gulf of Mexico. It is about $78km$ south-east of New Orleans in Louisiana. The site is a few feet above the sea level with a water table close to the surface.

Measurements from four different types of small scale model piles, or probes, have been included. The piezo-lateral stress (PLS) cell is a probe developed by the Massachusetts Institute of Technology (MIT). The probe is $1{,}2m$ long with a diameter of $38mm$. The pore pressure is measured at $1{,}8m$ from the tip and for the Empire site measurements from $44{,}7m$ and $73{,}6m$ depth are included.

In addition to the PLS probe, a 3" probe with an open- and closed-ended mode, plus a 1,72" closed probe (x-probe), have been used. The 3" probe has an instrumented tip of $4{,}28m$ length and a diameter of $3" = 76{,}2mm$. For the open-ended mode a thickness of $3mm$ is assumed by Karlsrud (2012). Measurements were done at $43m$ and $48{,}8m$ depth. The x-probe has a diameter of $1{,}72" = 43{,}6mm$, and measurements were done at $36{,}6m$ depth after pushing the probe $3m$ into the soil. These probes are pushed from the end of a cased borehole so that the embedded length is much shorter than the measurement depth.

At the site there is fine sand, with some clay and organic seams, down to $23m$ depth. Below this there is mainly clay all the way down to $135m$ depth, but with seams of silts and fine sands. The clay is a soft overconsolidated clay, with a water content of about 40%, and a plasticity index close to $50-60\%$.

Table 13.1: Index properties at the Empire site from Cox et al. (1979). (Karlsrud 2012)

Zone	Approximate Depth range (m)	w_n (%)	w_L (%)	w_P (%)	I_P (%)	Liquidity index I_L
1	35-50	46	90	27	63	0,3
2	63-78	36	75	22	53	0,26
3	82-95	36	70	20	50	0,32
4	99-111	38	78	21	57	0,30

The measured in-situ pore pressure show a slight artesian overpressure of about $40kPa$ according to Azzouz and Lutz (1986). This correspond very well with what Karlsrud (2012) reports, as seen in Figure 13.18.

According to Karlsrud (2012) the in-situ total vertical stress is uncertain. Figure 13.18 shows the total unit weight used by MIT, which is an average from several boreholes. However, there were only a few samples all from the upper $20m$. Karlsrud (2012) state that it seems that they have selected values from local layers with high water and organic content, which does not fit the description from the bore logs. Karlsrud (2012) has calculated a unit weight based on the water content and the results fit with results presented by Kraft et al (1981). The difference in effective vertical stress is about $80kPa$, which is quite substantial. Azzouz and Lutz (1986) report what Karlsrud (2012) calls the MIT results. We will use the soil weight proposed by Karlsrud (2012).

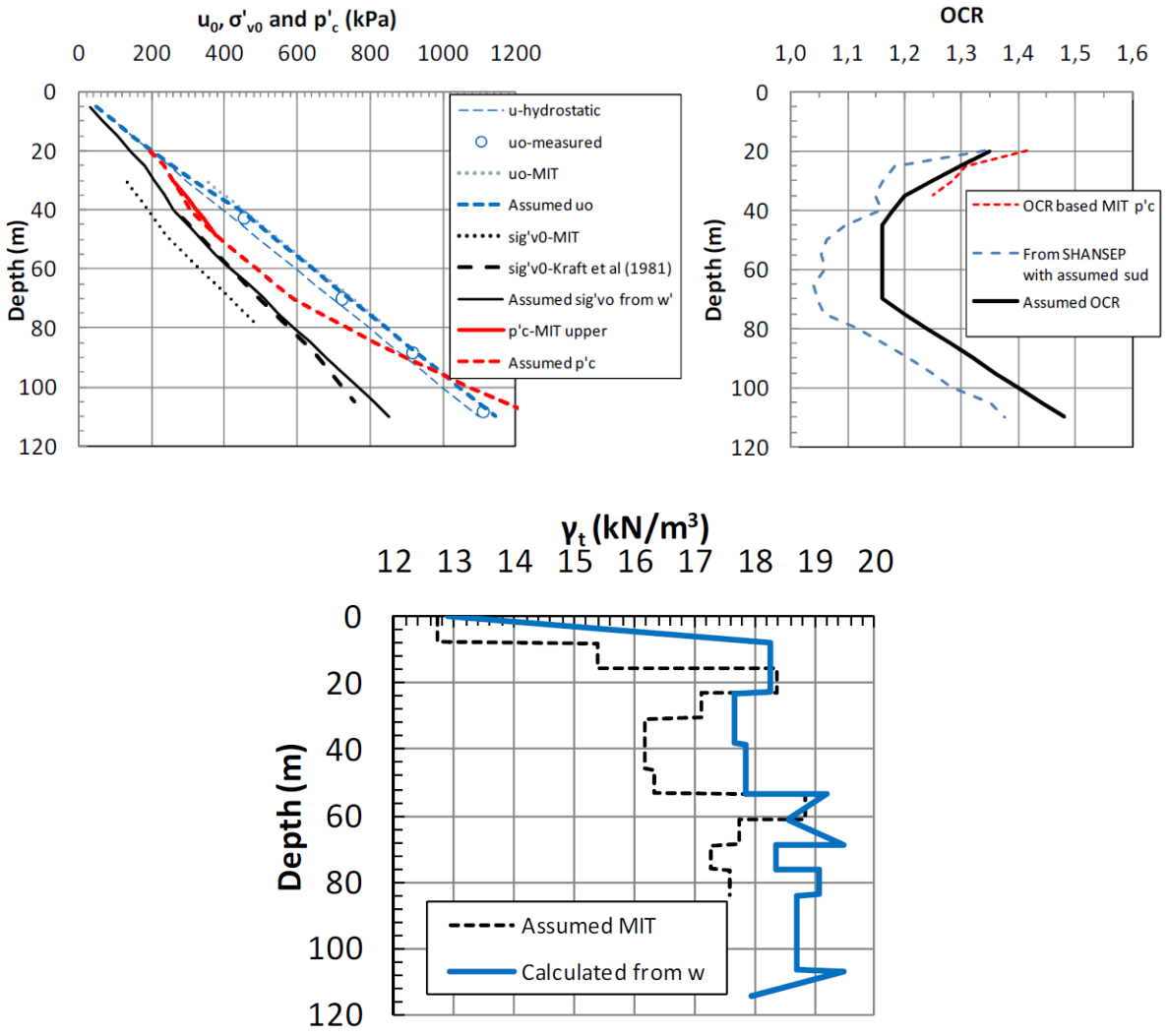

Figure 13.18: In-situ stress conditions, overconsolidation ratio and total unit weight at the Empire site. (Karlsrud 2012)

OCR values well above 2 would not be unlikely for $I_L = 0{,}3$. It is therefore possible that the OCR assumed herein could be too low. Alternatively, if MIT's σ'_{v0}-profile is closer to the truth than the one assumed herein, the OCR values back-calculated would become significantly larger according to Karlsrud (2012).

The undrained shear strength profile chosen is shown in Figure 13.19, and is mainly based on CPTU data, as there were only lab data from the upper zone. The same SHANSEP parameters found for zone 1 were adopted for the deeper layers, which of course implicates some uncertainty.

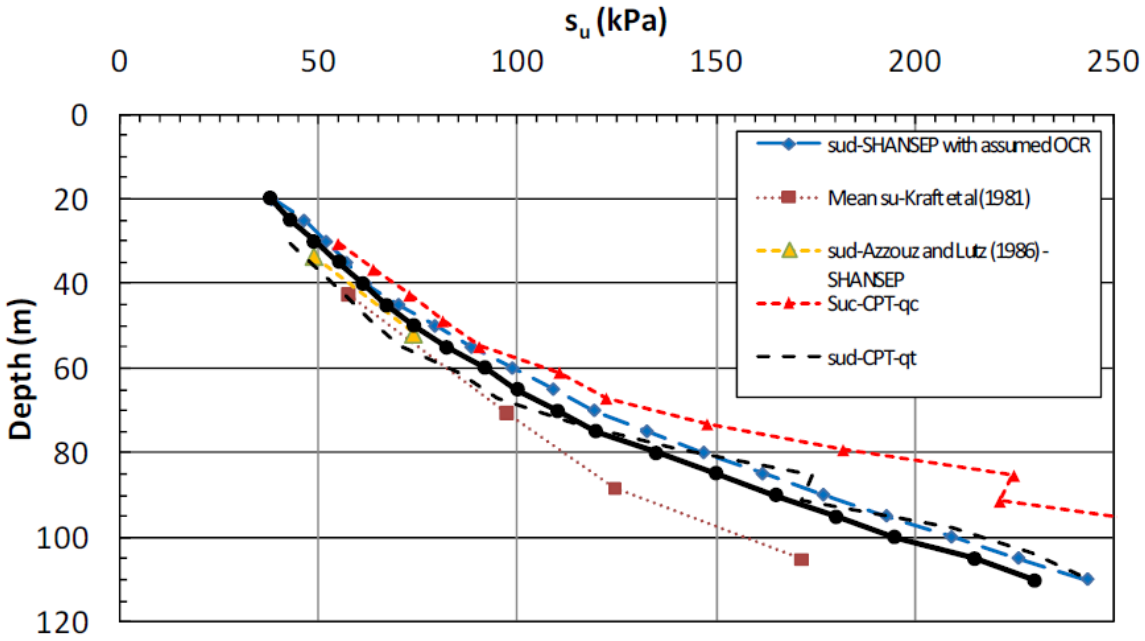

Figure 13.19: Undrained shear strength interpreted from CPTU data, together with the chosen profile in thick black dotted line at the Empire site. (Karlsrud 2012)

13.1.9 Saugus

The Saugus site is located in Massachusetts USA, about $10km$ north-east of Boston. The measurements are from the PLS probe described earlier, which was also used at the Empire site. The probe was pushed continuously (i.e. steady penetration), but some of the tests had stops in penetration, and then also allowed some dissipation. The resulting measurements showed an increase in pressure during subsequent penetration than what the steady penetration test showed. In Table 13.6 only pore pressure from steady penetration is included. The measurements were done from 10,5 to $35{,}8m$ depth and this is the only site included where measurements were recorded continuously.

At the site there is so called Boston Blue Clay (BBC), which is a lean normally consolidated clay with a water content of $40-45\%$, and a plasticity index of $19-26\%$. According to Morrison (1984) the Saugus site consist of $2{,}5m$ of sand and peat then sand from $2{,}5-5$m depth. From $5-9m$ depth there is a transition from sand to sandy clay. Below this is a medium BBC down to $20m$, followed by soft BBC down to $40m$, and glacial till below this. This is illustrated in Figure 13.20.

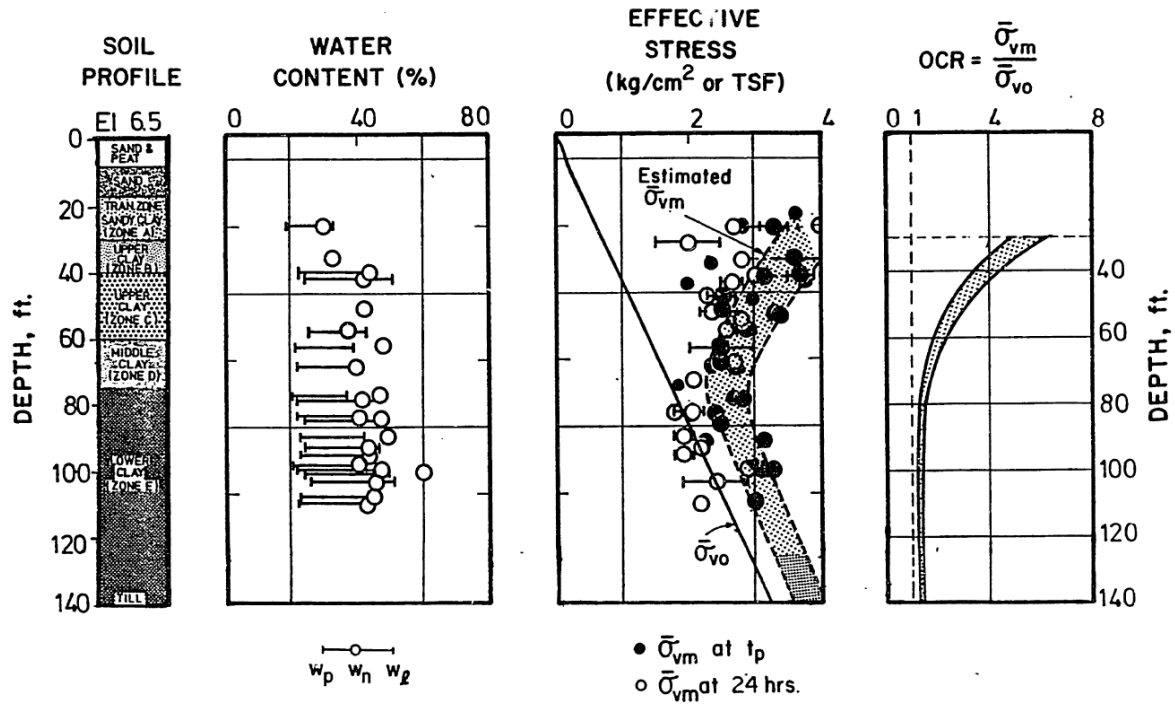

Figure 13.20: Index properties, vertical effective stress and overconsolidation ratio at the Saugus site. Notice that the depth scale is in feet. (Morrison 1984)

In geological terms the clay is normally consolidated, but have a high OCR in the top part probably due to chemical weathering. Below this, the OCR goes toward 1,25 due to creep. The in-situ pore pressure is close to hydrostatic, with a groundwater table at about $1{,}5m$ depth. The total unit weight is on average $\gamma = 17{,}5\,{}^{kN}/_{m^3}$. The in-situ stress conditions reported by Morrison (1984) agree with what Karlsrud (2012) have used, as seen in Figure 13.21.

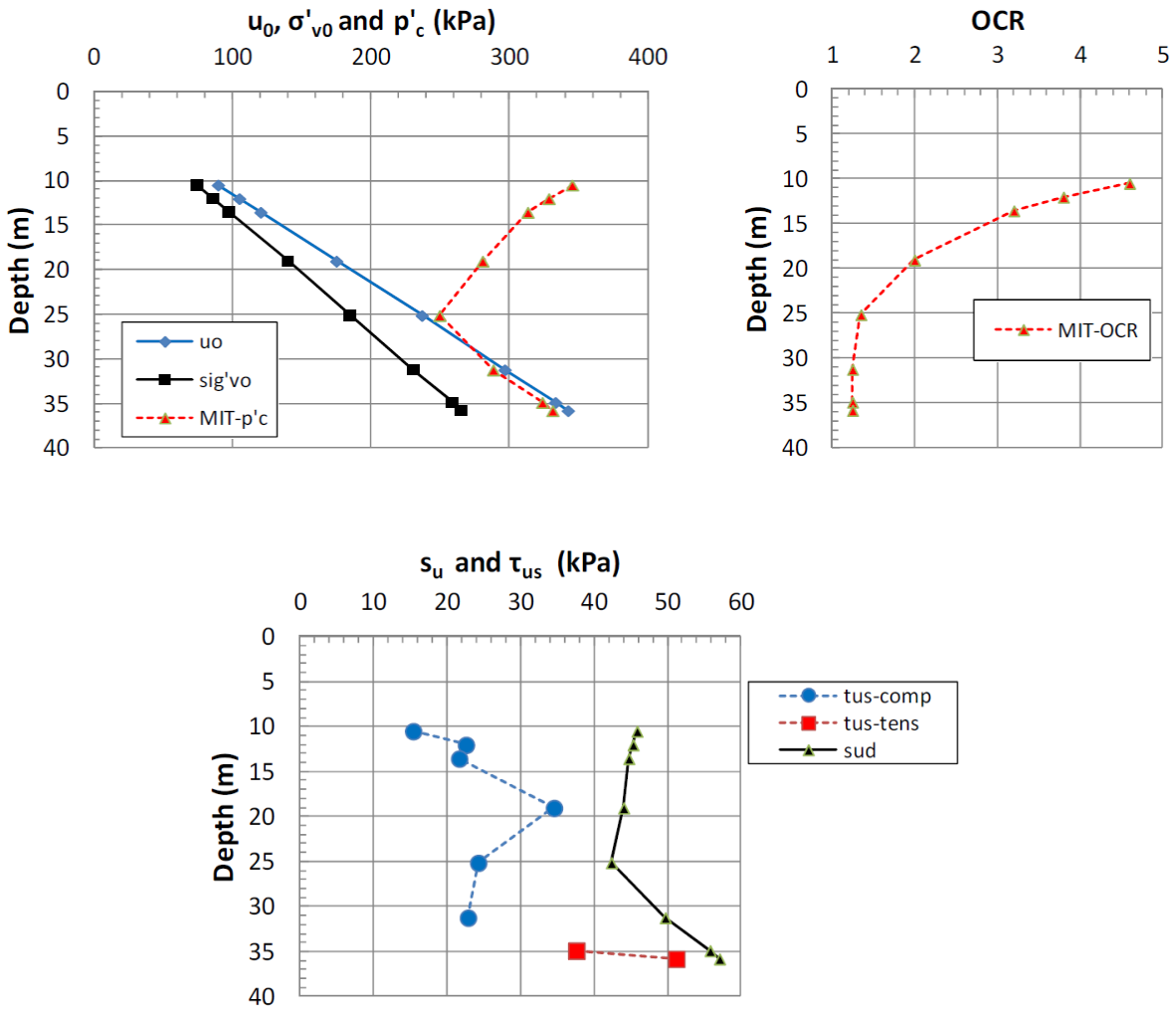

Figure 13.21: Stress condition, overconsolidation ratio and undrained shear strength at the Saugus site. (Karlsrud 2012)

The undrained shear strength is based on the SHANSEP method, using the OCR profile and in-situ vertical effective stress from Figure 13.21, with $S = 0{,}18$ and $m = 0{,}8$ as this is the best fit to the data presented by Morrison (1984) according to Karlsrud (2012). It should however be mentioned that the results presented by Ladd and Foott (1974) for idealized BBC, suggest $S = 0{,}20$ and $m = 0{,}8$, which would lead to an 11% increase in shear strength according to Karlsrud (2012).

13.1.10 West Delta

The West Delta site is located in the Gulf of Mexico. It is about $15 - 20$ miles south-west of Venice in Louisiana USA. The soil is under about $16m$ of water, and the area is characterized by deep sediments of soft clays and fairly high sedimentation rates arising from the Mississippi river outlet according to Karlsrud (2012).

The same kind of small scale model sized piles or probes used at the Empire site has also been used at the West Delta site. In addition, large scale fully instrumented pipe piles have been installed. These are open-ended piles with a diameter of $762mm$, a wall thickness of $19{,}1mm$ and an embedded length of $71{,}3m$. Measuring was done at seven different depths ranging from $14m$ to $68m$ depth.

Figure 13.22 suggests that the clay is more plastic in the top and bottom part, than in the middle part. The middle part extends from approximately $25 - 45m$ depth and have a water content of about 40%, plasticity index of $30 - 35\%$ and clay content of $30 - 38\%$. Below $60m$ depth the water content, plasticity index and clay content rise to approximately 55%, 65% and 60% respectively.

The total unit weight have been computed by Karlsrud (2012) based on the water contents. This has been done since the clay contained saturated gas, which expanded the volume of the samples when exposed to atmospheric pressure. This led the measured total unit weights to be about 10% lower than what the water content suggests. The sensitivity of the clay has been determined by various tests and is low ($S_t = 1{,}5 - 2$).

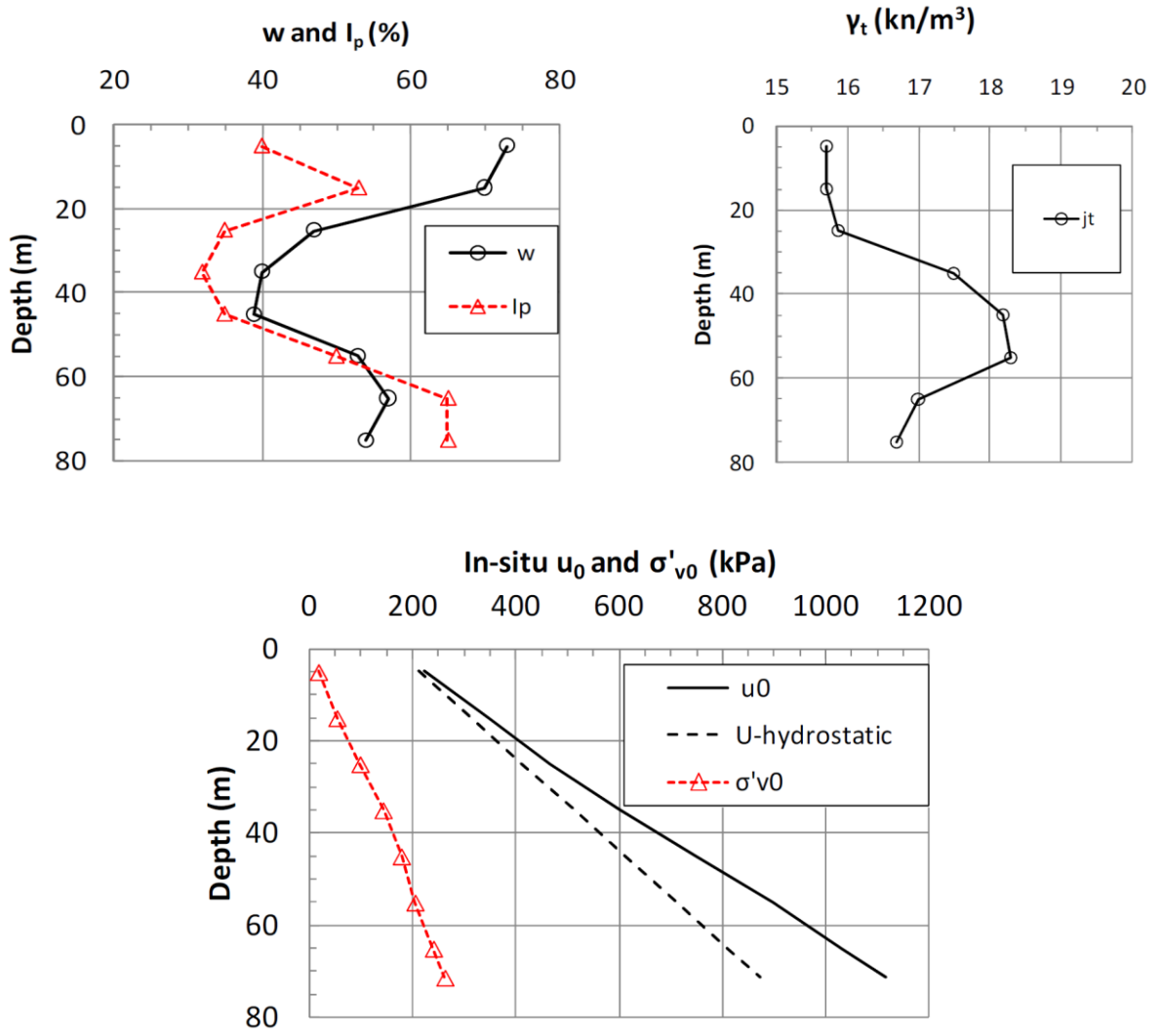

Figure 13.22: Index data of the soil at the West Delta site, together with the in-situ stress conditions. (Karlsrud 2012)

Measurements of the in-situ pore pressure showed a considerable artesian overpressure. The deepest piezometer was installed at $68{,}7m$ depth, and showed an excess pore pressure of about $200kPa$ compared to hydrostatic conditions. This artesian overpressure combined with the low unit weights implies very low effective stresses. The clay is normally consolidated, but the sample quality was according to Karlsrud (2012) insufficient to verify the exact apparent overconsolidation ratio (OCR). An OCR from 1,2 to 1 has been assumed.

The undrained shear strength has been determined based on a number of different tests, as seen in Figure 13.23. The main basis of the chosen direct undrained shear strength (s_{uD}) profile is the unconsolidated undrained triaxial tests (UU), and the direct simple shear (DSS) tests conducted. The results are shown in Table 13.2, and show a strength of $10kPa$ at $5m$ depth increasing by approximately $0{,}873\ {}^{kPa}/_{m}$.

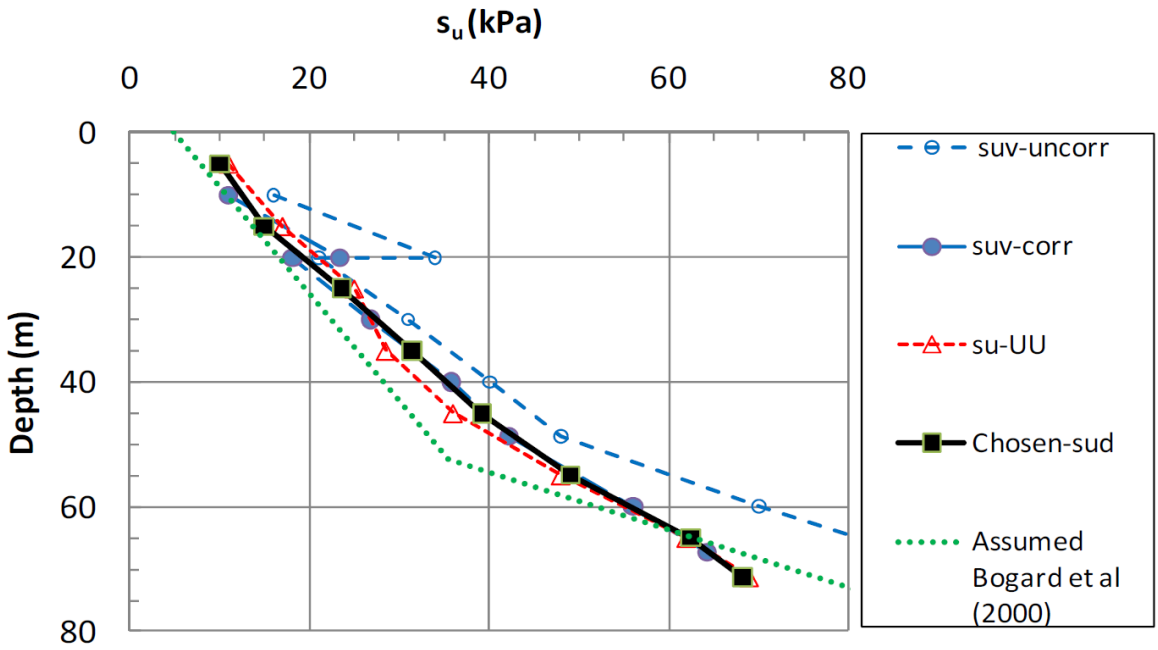

Figure 13.23: The undrained shear strength at the West Delta site, showing results from vane borings and unconsolidated undrained (UU) triaxial tests. Together with the chosen/assumed strength profile of Karlsrud (2012) and Bogard et al (2000). (Karlsrud 2012)

Table 13.2: Results of unconsolidated undrained (UU) triaxial tests and direct simple shear (DSS) tests combined to give the direct undrained shear strength for the West Delta site. (Karlsrud 2012)

Depth (m)	σ'_{v0} (kPa)	$s_{u\text{-}UU}$ (kPa)	DSS s_{ud}/σ'_{ac}	s_{ud} (kPa)
0	0	5	0,28	8,0
5	18	11	0,28	10,0
15	53	17	0,28	14,9
25	98	25	0,24	23,5
35	143	28,5	0,22	31,4
45	178	36	0,22	39,2
55	204	48	0,24	49,1
65	240	62	0,26	62,4
75	277	69	0,26	68,2

13.1.11 Hamilton Air Force base

The decommissioned Hamilton Air Force base is located in California USA near the town Novato, about $30km$ north-northwest of San Francisco. The site is protected by a dike to avoid flooding since it is located $1{,}3m$ below sea level.

Four different types of piles were installed at the Hamilton Air Force base site. Only the TP1 and TP3 piles were instrumented with pore pressure measuring equipment. Both of these piles are closed-ended piles with a pile diameter of $111{,}9mm$, and an embedded length of $12{,}2m$. Both piles measured the pore pressure at three depths, where only one depth is included in Table 13.6, namely $6{,}3m$ for the TP1 pile, and $6{,}2m$ for the TP3 pile. The difference is due to the fact that the TP1 pile was jacked, while the TP3 pile was driven conventionally, leading to a minor difference in height of the measuring equipment.

At the site there is about $4m$ of weathered dry crust followed by a soft San Francisco Bay mud, which is a normally consolidated clay with a water content of about 95%, and a plasticity index of 55%.

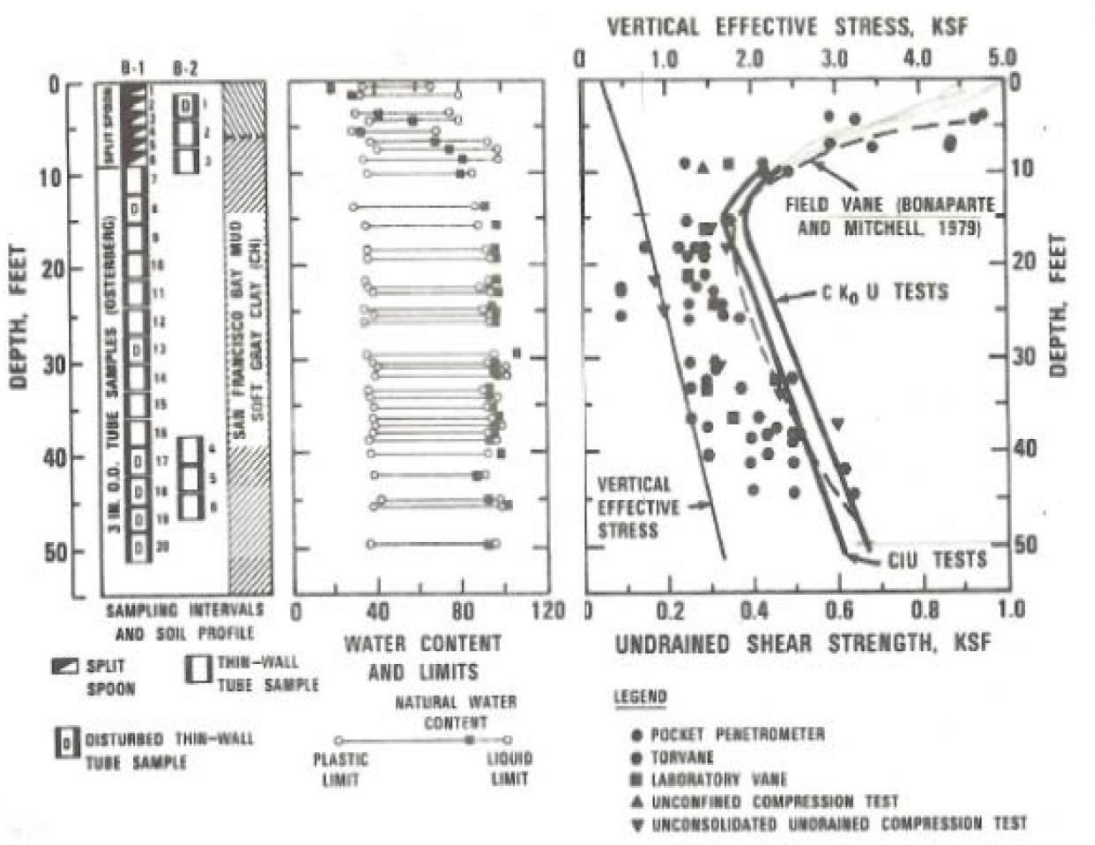

Figure 13.24: Index parameters, vertical effective stress and undrained shear strength from Kraft et al. (1980) for the Hamilton site. (Karlsrud 2012)

The in-situ pore pressure is measured to be slightly higher than under hydrostatic conditions (about 12%). With a groundwater table that varies seasonally, but deemed to be at about $1{,}5m$ depth during the pile testing. Karlsrud (2012) increased the pre-consolidation pressure with about 10% to $OCR = 1{,}4$, due to the results of five incremental oedometer tests done on samples of seemingly good quality.

The in-situ stress conditions and OCR-profil is shown in Figure 13.25. The s_{uC}-profil was established by using the SHANSEP method with $S = 0{,}355$ and $m = 0{,}86$. These parameters were based on a series of CAUC triaxial tests. The s_{uD}-profile is found by $s_{uD} = 0{,}8 s_{uC}$, assumed due to the high plasticity of the clay. The s_{uC}-profil proposed by Karlsrud (2012) is seen to be about $10 - 15\%$ higher than what Kraft et al. propose. We will use the values Karlsrud (2012) propose.

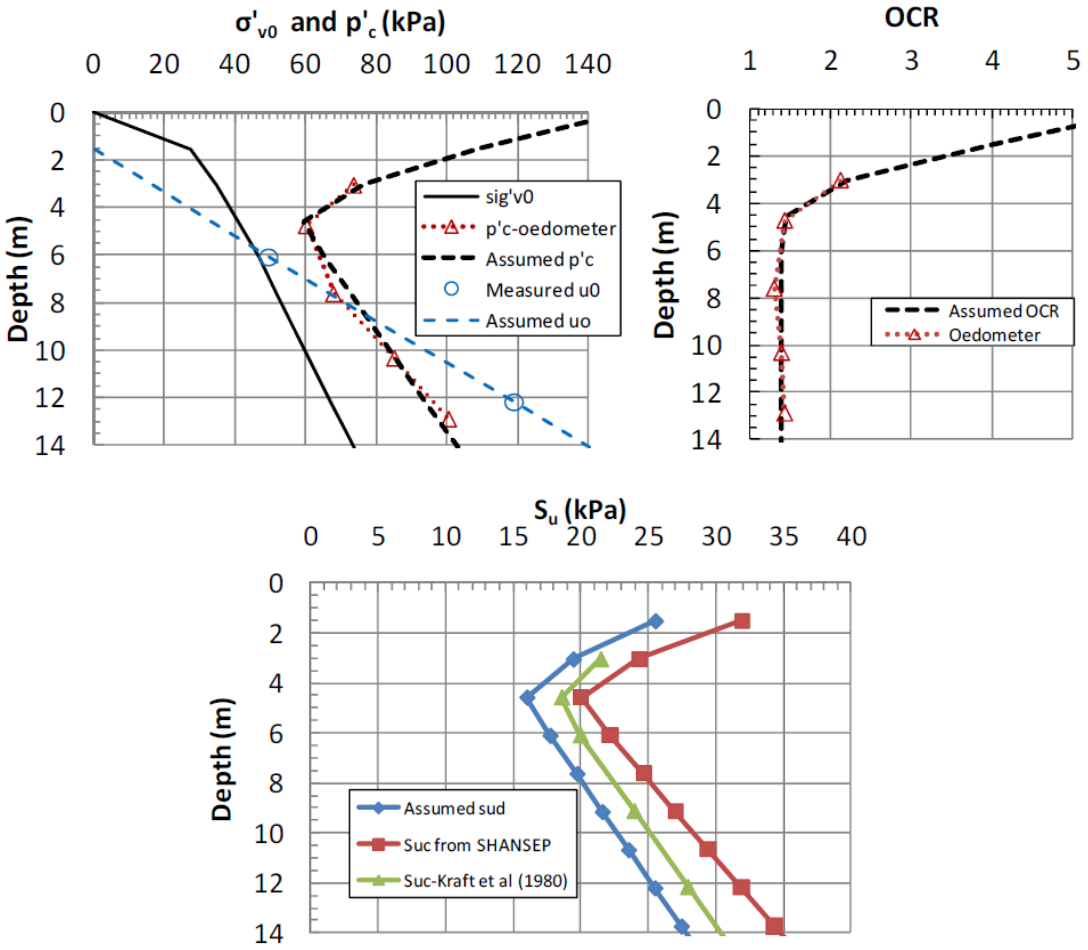

Figure 13.25: In-situ stress conditions, overconsolidation ratio and undrained shear strength used for the Hamilton site. (Karlsrud 2012)

According to Karlsrud (2012), the normalized excess pore pressure ($\Delta u_{max}/s_{uD}$) is on the low side, compared to data from other sites with soft clay. The pore pressure increased the first two minutes after installation, suggesting that the piezometer filters might have not been fully saturated. This would explain the relative low excess pore pressure observed.

13.1.12 St. Alban

The St. Alban site is located in Canada, about $67km$ west-southwest of Québec city. The piles used at the site were closed-ended with a diameter of $219mm$, a thickness of $8mm$ and an embedded length of $6{,}1m$. The top $1{,}5m$ were pre-augured so that the tip penetrated to $7{,}6m$ depth. The test piles had pore pressure sensors at four levels along the shaft, along with 35 piezometers installed prior to the pile jacking capturing the shape of the excess pore pressure distribution around the pile.

The top $1{,}5m$ consist of a weathered clay crust. Below this is a highly sensitive, structured Champlain Sea clay deposit with increasing amount of silt with depth, as seen in Figure 13.26. The water content increase from 20% from the water table located at $0{,}8m$ depth, up to as much as 100% at $2m$ depth, before it goes down to about 60% at $4m$ depth. According to Karlsrud (2012) the high sensitivity ($S_t \approx 20$) causes the liquid limit (w_L) to be lower than normal, again causing the plasticity index to be low compared to the water content. The plasticity index (I_P) then gives a false impression of the clay characteristics.

The clay is in geological terms normally consolidated, which according to Karlsrud (2012) should give a water content close to the liquid limit, if it was not for the high sensitivity. Karlsrud (2012) therefore use an I_P of 80% at $2m$ depth decreasing to 40% from $4m$ depth and below, instead of the values indicated by Figure 13.26 of $I_P = w_L - w_P \approx 20\%$. We will use the values proposed by Karlsrud (2012) as an empirical relation is based on the soil characteristic and misleading properties might give a more unreliable relation.

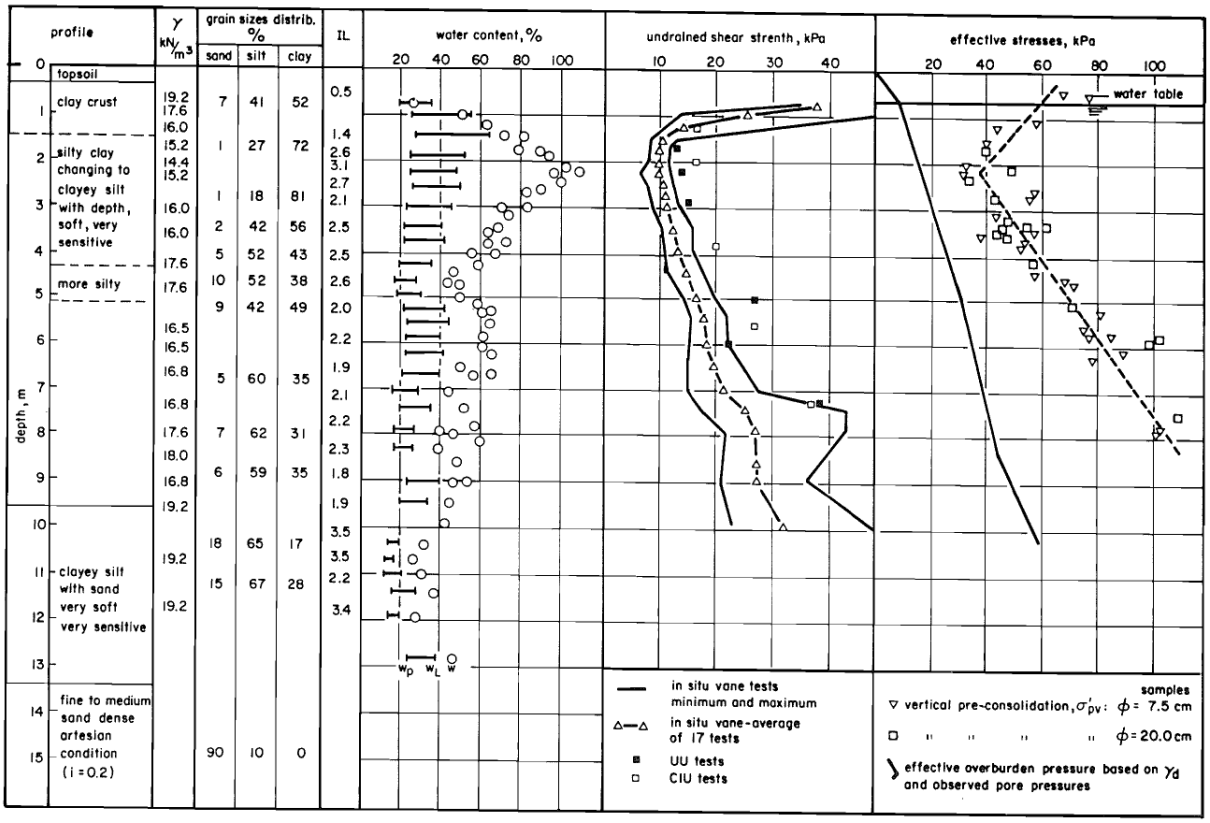

Figure 13.26: Index properties, shear strength and effective stress at the St. Alban site. (Roy, Blanchet et al. 1981)

Figure 13.26 shows the initial vertical effective stress found by Roy, Blanchet et al. (1981). Karlsrud (2012) have recalculated the in-situ vertical effective stress and got $10 - 15\%$ higher values than what Roy, Blanchet et al. (1981) propose. Karlsrud (2012) used the reported total unit weights and also checked the values against the water content. Comparing the results, we see that Roy, Blanchet et al. (1981) have used roughly averaged values, and that the values chosen by Karlsrud (2012) agrees more with the total unit weights found in Figure 13.26. The values proposed by Karlsrud (2012) was therefore chosen.

In Figure 13.27 we see the chosen in-situ stress conditions and the overconsolidation ratio, showing a weathered top part before reaching $OCR \approx 2$. Results of CIUC triaxial tests correspond to the active undrained shear strength (s_{uC}) profile given in both Figure 13.26 and Figure 13.27. The direct undrained shear (s_{uD}) strength was assumed by Karlsrud (2012) to correspond to $s_{uD} = 0{,}8 s_{uC}$.

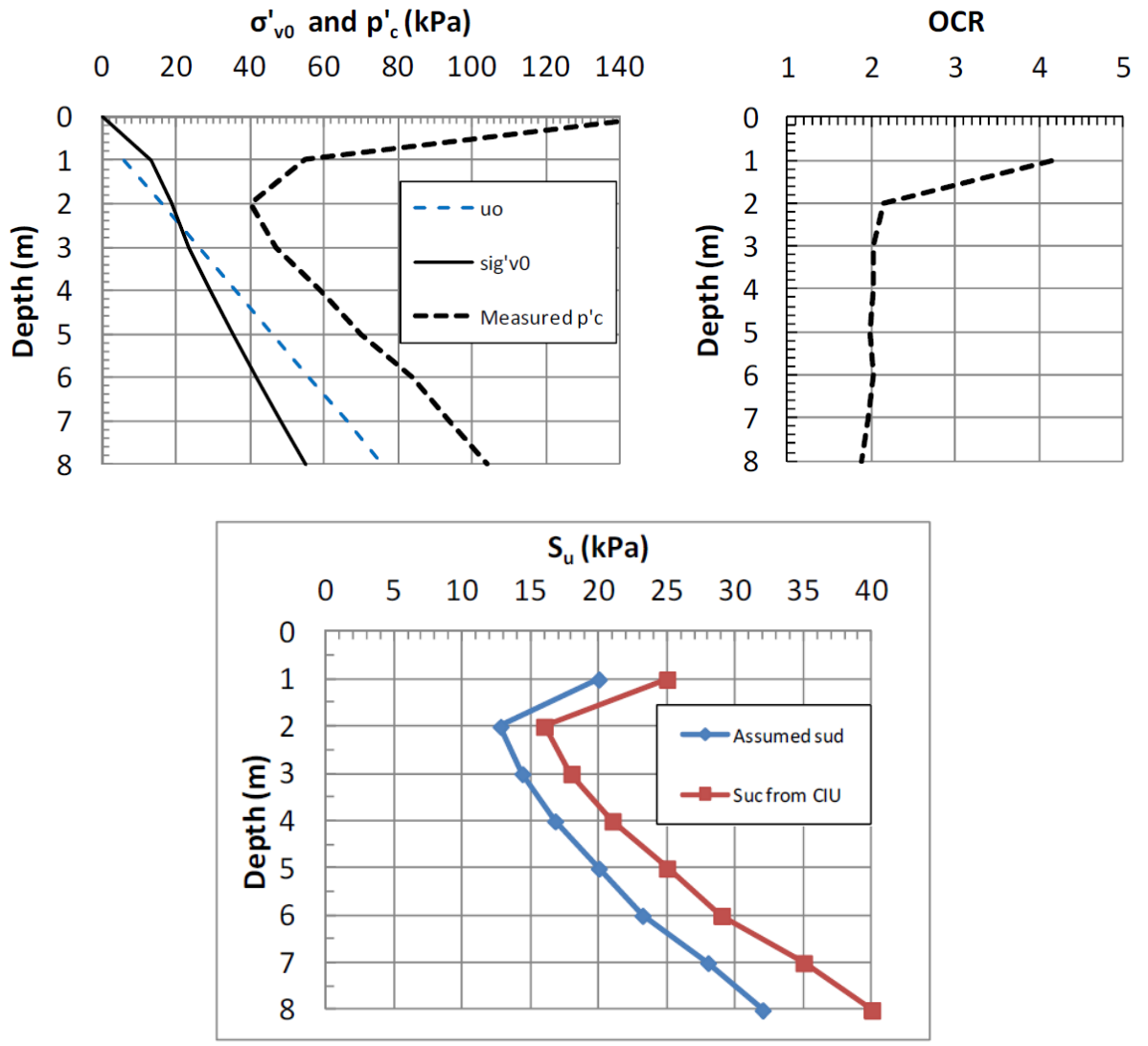

Figure 13.27: In-situ stress conditions, overconsolidation ratio and undrained shear strength of the St. Alban site. (Karlsrud 2012)

13.2 The undrained shear modulus

Two ways of determining the undrained shear modulus of the soil have been used. Firstly, the stiffness of the soil at the different sites have been estimated by using the empirical relationship indicated by Figure 5.6, and secondly an assumed relation (Equation 13.8) to the modulus number (m_0) have been used.

The stiffness to strength ratio (G_u^{50}/s_{uC}) in Figure 5.6 are obtained by CAUC triaxial tests on high quality block samples presented by Karlsrud and Hernandez (2011). Figure 13.28 shows how the data from the sites have been fitted based on the trend lines, OCR and five levels/ranges of natural water content. The five ranges are: Fitted Very High ($w < 30\%$), High ($w = 30 - 40\%$), Middle ($w = 40 - 60\%$), Low ($w = 60 - 70\%$), and Very Low ($w > 70\%$). The trend lines are based on samples with a water content below 70% and above 30%. The stiffness is still estimated with these trend lines even when the water content is outside of these limits.

The Hamilton Air Force Base and the top few meters at the St. Alban site have a water content above 70%. While the Tilbrook Grange, Cowden, Canons Park and below $30m$ depth at the Lierstranda site show a water content below 30%. Since an empirical relation is used to estimate the stiffness, the uncertainty in the determined undrained shear modulus is much higher than the other soil parameters presented in Chapter 13.1.

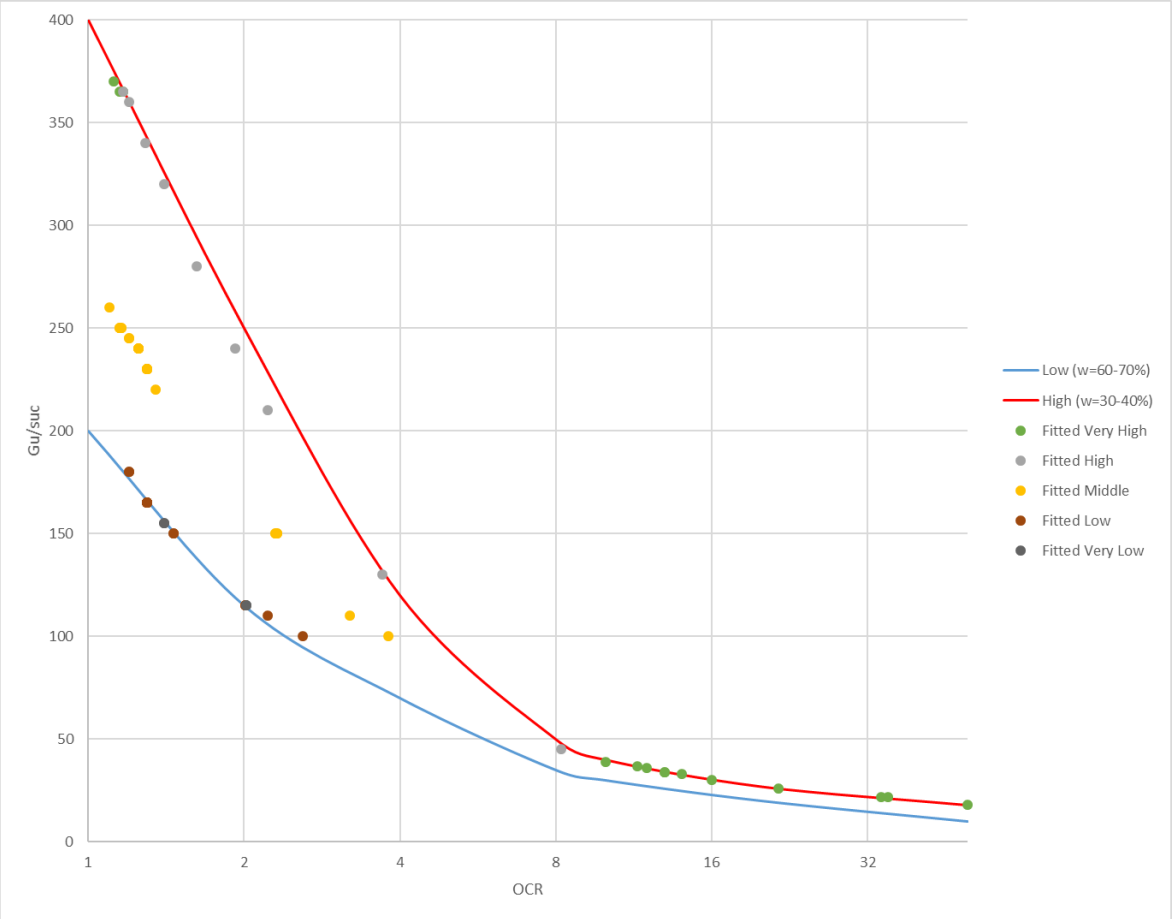

Figure 13.28: Trend lines for the stiffness and strength ratio (G_u^{50}/s_{uc}) against OCR for different levels of natural water content after Karlsrud and Hernandez (2011) and Karlsrud (2012). The data from the different sites is fitted based on the water content, OCR and the trend lines.

Karlsrud (2012) have determined the modulus number with depth, for all the sites except the Canons Park site. For the Cowden site Karlsrud (2012) assumes a modulus number of 30. The other modulus numbers have been determined based on oedometer tests and are presented in Table 13.6.

The modulus number is as defined in Figure 13.29 equal to $m = \frac{d^2\varepsilon}{d\sigma^2}$. However, an average value is assumed for the normally consolidated (NC) range and for the overconsolidated (OC) range going through the origin.

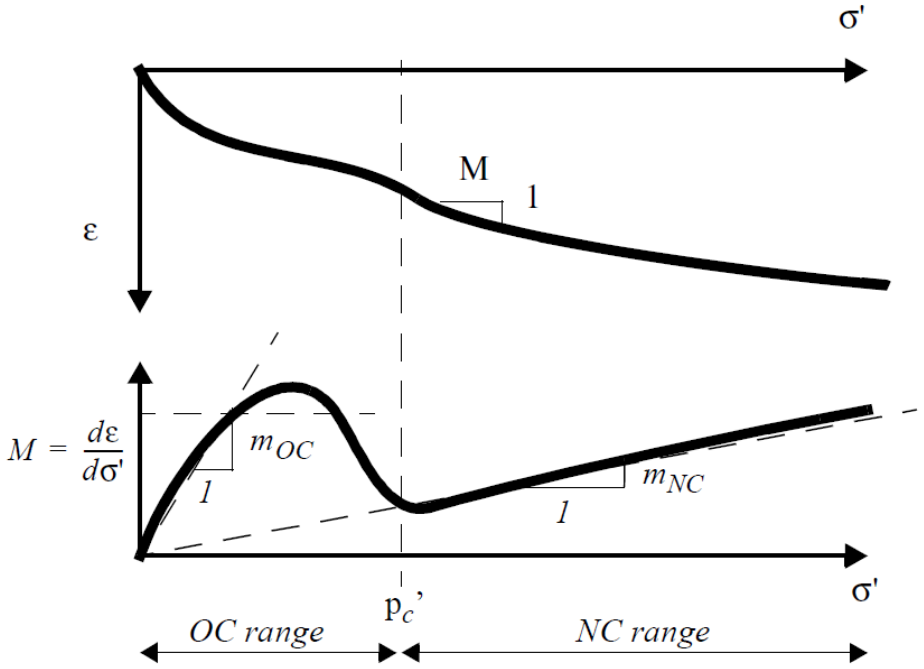

Figure 13.29: The oedometer modulus (M) and modulus number (m) for the overconsolidated (OC) and normally consolidated (NC) range as defined by Janbu (1963). (Nordal 2018)

The modulus numbers (m_0) determined by Karlsrud (2012), are equal to m_{NC} in Figure 13.29. In Figure 13.29 the oedometer modulus (M) and modulus number (m) relate by a linear relationship through the origin for both the OC and NC range defined by:

$$M = m\sigma'_v \tag{13.2}$$

Using isotropic elastic theory and assuming $\nu' = {}^1/_3$ gives:

$$E' = \frac{(1+\nu)(1-2\nu)}{1-\nu} M = \frac{2}{3} m\sigma'_v \tag{13.3}$$

The shear modulus relate according to elastic theory to the Young's modulus (given $\nu' = {}^{1}/_{3}$ and $\nu_u = {}^{1}/_{2}$) by:

$$G = \frac{E}{2(1+\nu)} \rightarrow G_u = \frac{E_u}{3} \; and \; G' = \frac{3E'}{8} \tag{13.4}$$

Elastic theory therefore yields $G_u = G'$ and then $E_u = {}^{9}/_{8}\, E'$ assuming $\nu' = {}^{1}/_{3}$. However, experiments have shown that for clays, these last two equations do not fit with what is observed. The factor ${}^{9}/_{8}$ are often found to be more in the order of 10. As a crude assumption we use $E_u = 10E'$. The undrained stiffness of the clay should however be determined from an undrained triaxial test, but given the drained stiffness an assumption must be made. This gives:

$$G_u = \frac{E_u}{3} = \frac{10}{3} E' = \frac{10}{3} * \frac{2}{3} m\sigma'_v = \frac{20}{9} m\sigma'_v \tag{13.5}$$

Going back to Figure 13.29 we see that m_0 (called m_{NC}) is determined based on the stress-strain relationship experienced for stress levels above the preconsolidation pressure. This is called virgin compression, as the soil has never been compressed under such high pressure before. In Nordal (2018), the modulus number in the OC range is shown as a function of the m_{NC}:

$$m_{OC} = n * m_{NC} \tag{13.6}$$

where n typically is in the range of $2 - 5$. The undrained shear modulus determined from undrained triaxial tests, which is what we want to estimate, is most often defined at 50% mobilization of the undrained shear strength, as discussed in Chapter 5.3. The question then is which effective vertical stress to use in Equation 13.5, and is it below the preconsolidation stress or above.

The oedometer stiffness in the overconsolidated area is also often assumed to be constant. One could then write:

$$M_{OC} = m_{OC} p_c' = n * m_{NC} p_c' \tag{13.7}$$

An undrained triaxial test is often either anisotropically consolidated to the believed stress level or isotropically consolidated to the believed horizontal stress level. The deviatoric stress is then either $q_0 = \sigma_{v0}' - \sigma_{h0}'$ or equal to zero. In a triaxial test the deviatoric stress is equal to two times the undrained shear strength at failure ($q_f = 2s_u$). Halfway to failure we then have $q_{50} = s_u$, and for a test that has been ran conventionally: $\Delta q = \Delta\sigma_v = \Delta\sigma_v' - \Delta\sigma_h'$. If one disregard dilation/contraction then $\Delta p' = \frac{1}{3}(\Delta\sigma_v' + 2\Delta\sigma_h') = 0$. Finally giving $\Delta q = \frac{3}{2}\Delta\sigma_v'$, which at 50% mobilization of the undrained shear strength yields: $\Delta q = q_{50} - q_0 = \frac{3}{2}\Delta\sigma_v' \rightarrow \Delta\sigma_v' = \frac{2}{3}(s_u - q_0)$.

The undrained shear modulus was estimated by inserting m_{NC} and m_{OC} for m, and σ_{v0}' and p_c' for σ_v', in Equation 13.5. n was changed from 2 to 5, and adding the change in vertical effective stress to σ_{v0}' was also tested (i.e. $\sigma_v' = \sigma_{v0}' + \frac{2}{3}(s_u - q_0)$). Using $\sigma_v' = \sigma_{v0}'$ if $s_u - q_0 < 0$, and only including q_0 if it was larger than zero, was also checked.

All these different estimates were measured against the empirical estimated stiffness from Figure 13.28. The sum of the differences between what Equation 13.5 and what Figure 13.28 predicted were minimal when $\sigma_v' = \sigma_{v0}'$ and $m = m_{OC}$, estimated with $n = 3{,}6$, were used in Equation 13.5. This value was found by using Excel solver and minimizing the sum of the differences between the predictions.

The Canons Park site did not have a modulus number, but Jardine, Fourie et al. (1985) presents the undrained Young's modulus found from UU triaxial tests, as seen in Figure 13.30, together with other tests and empirical relations. The UU triaxial test results were given the most weight, and the undrained shear modulus ($G_u = {}^{E_u}/_{3}$) was found to be $31667kPa$ at $2{,}8m$ depth and $23333kPa$ at $4{,}0m$ depth.

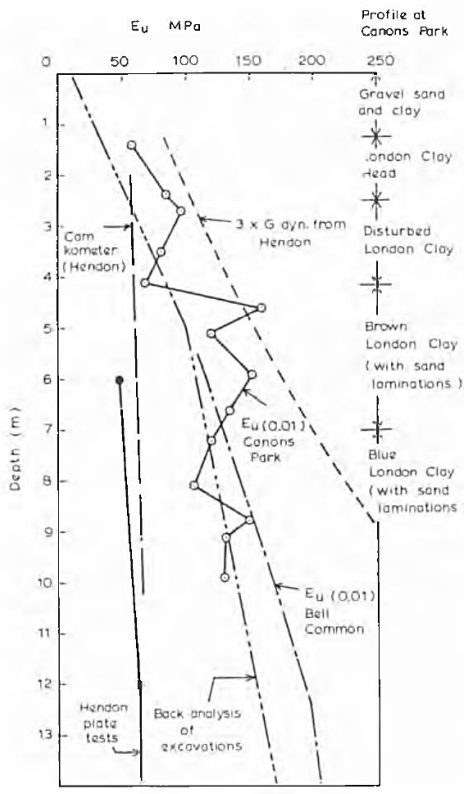

Figure 13.30: Undrained Young's modulus against depth for the Canons Park site. (Jardine, Fourie et al. 1985)

At three sites the difference between the two prediction methods was quite high. This was the Cowden, Canons Park and Tilbrook Grange sites. At the Canons Park site, the stiffness was determined by testing and not Equation 13.5, so the prediction made by using Figure 13.28 is probably inaccurate. Cowden is the one site that Karlsrud (2012) has assumed a modulus number, in contrast to finding the value from oedometer testing.

What these sites have in common is a high OCR (above 10), a very low water content (below 30%), and high stiffness ($m_0 > 24$). In Chapter 13.3 it is shown that all these sites also are insensitive (i.e. $S_t = 1$). If these sites are excluded the smallest sum of differences is obtained for $\sigma_v' = \sigma_{v0}'$ with m_{OC} estimated with $n = 4{,}5$. $n = 4{,}5$ is quite high in the expected range, this might have something to do with using σ_{v0}' and not some slightly higher value. However, using these values minimized the difference between the two predication methods. If this makes the prediction more correct or reliable is however discussable.

The undrained shear modulus used in Chapter 14 has thus been based on:

$$G_u = 4{,}5 * \frac{20}{9} m_0 \sigma'_{v0} = 10 m_0 \sigma'_{v0} \tag{13.8}$$

The Haga test site also had a plot of the undrained shear modulus at the site, as seen in Figure 13.31, but against OCR and not depth. This was used and gave a shear modulus of $G_u = 1522kPa$ at $1{,}9m$ depth, and $G_u = 4100kPa$ at $3{,}4m$ depth. This is slightly lower than what Equation 13.8 and Figure 13.28 suggest. The above values, found from undrained triaxial testing, is used in Chapter 14.

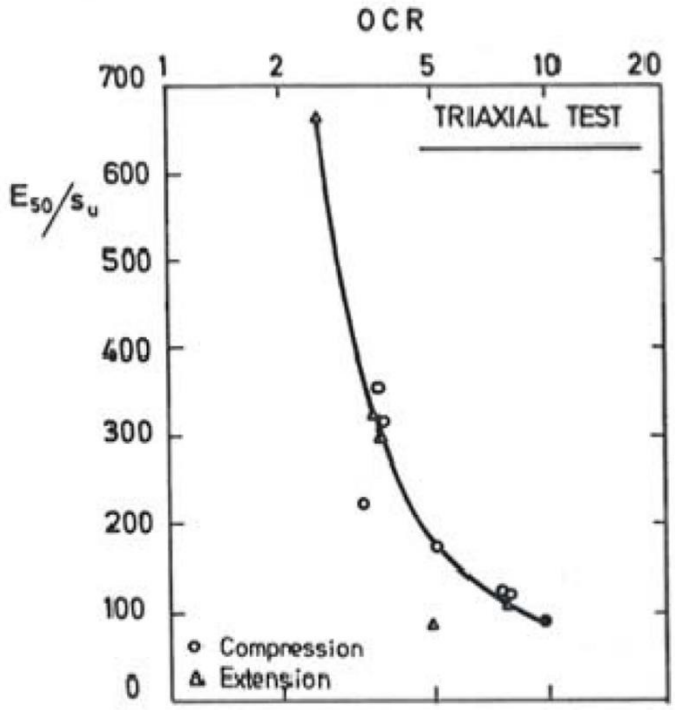

Figure 13.31: Undrained Young's modulus normalized with the undrained shear strength, found from undrained triaxial testing, plotted against the overconsolidation ratio (OCR) for the Haga site. (Karlsrud 2012)

Figure 13.32 shows the values obtained by using Equation 13.8 together with the trend lines of Figure 5.6.

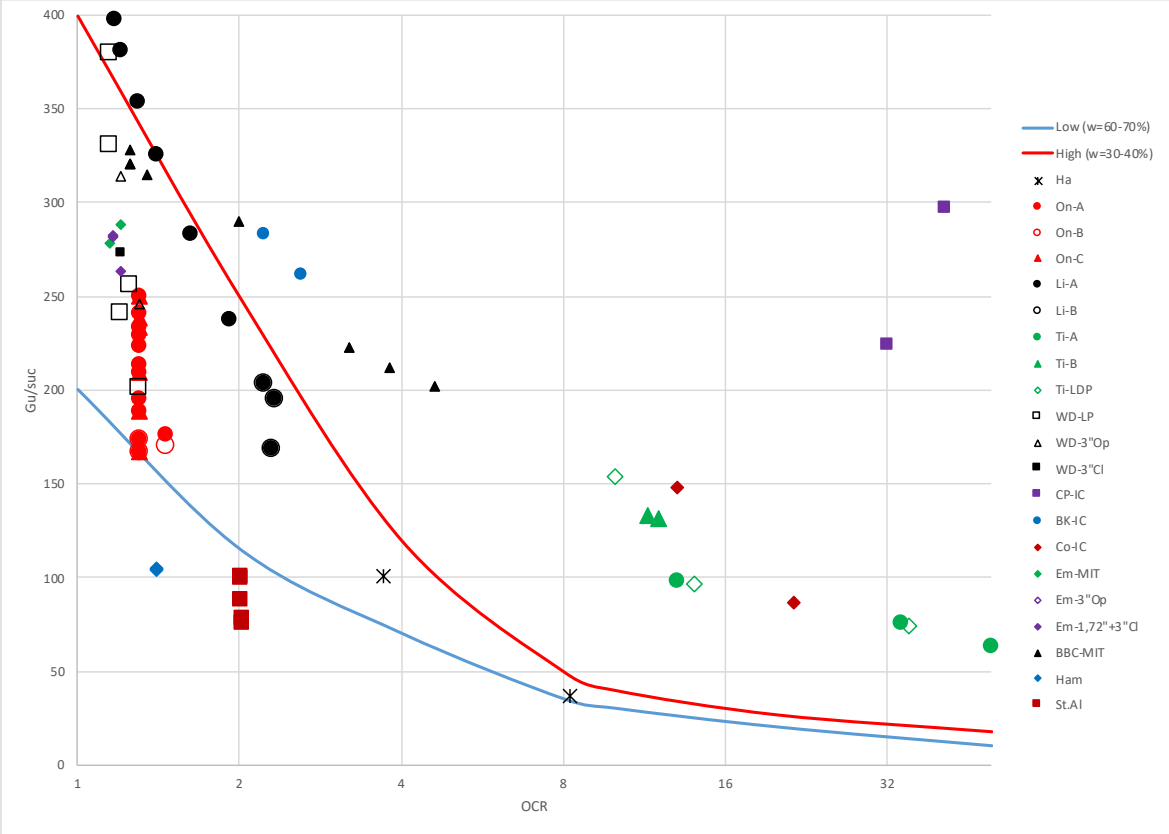

Figure 13.32: Normalized undrained shear modulus obtained by Equation 13.8. Plotted together with the trend lines from Figure 5.6 obtained by CAUC triaxial tests on block samples of Norwegian clays by Karlsrud and Hernandez (2011). The Haga (Ha) and the Canons Park (CP-IC) are plotted with the stiffness found from triaxial testing and not Equation 13.8 as explained. Further description of the legend can be found above Figure 9.10.

The predictions obtained by Equation 13.8 seems to fit relatively well to the trend lines from Figure 5.6 in the low OCR range ($OCR < 8$). In the high OCR range ($OCR > 8$) the data from the Cowden and Tilbrook Grange sites is estimated with Equation 13.8, while The Haga site and the Canons Park site are illustrated with the values found from undrained triaxial testing.

The trend lines from Figure 5.4 indicate much lower values than what Equation 13.8 suggests for the Cowden and Tilbrook Grange sites. It could be that Equation 13.8 is giving too high stiffness over strength ratio for these two sites. Equation 13.8 assumes the same relation to apply for all the sites regardless of OCR. However, the relation between the undrained stiffness and the modulus number is probably a function of OCR. The Haga site fits the trend lines, but Canons Park, which has comparable soil conditions as the Cowden and Tilbrook Grange sites, have much higher stiffness to strength ratio than what the trend lines suggests. The shear modulus found for the Canons Park site, is assumed to be more or less correct as it

is determined by triaxial testing, and suggest that the trend lines in Figure 5.6 underestimates the stiffness of the heavily overconsolidated stiff British clays.

We therefore choose to use Equation 13.8 to estimate the undrained shear modulus. This could be the wrong choice. Figure 13.32 indicates that we might have removed the reduction in G_u/s_{uC} that should occure when OCR increase, by assuming an equal expression regardless of OCR. However, an assumption had to be made and comparison between the Canons Park, Cowden and Tilbrook Grange sites outweighed the trend lines of Figure 5.4.

Other sites that do not completely follow the trend lines from Figure 5.4 are the St.Alban site (St.Al). Here the stiffness is lower than what the trend lines suggest. This could very well be due to the high sensitivity of the clay ($S_t \approx 18$), and also the water content is as high as 90%, which is outside of the range that Figure 5.4 is based on.

The Saugus site (BBC-MIT) shows higher stiffness than what the trend lines suggests, but not much, and the water content is around 40%. Bothkennar (BK-IC) have a high water content (above 60%), yet it is above the highest trend line (associated with a low water content). This is also a British clay, and a similar explanation as for the Cowden and Tilbrook Grange might apply. However, the clay at Bothkennar is not heavily overconsolidated nor does it have the very high shear strength seen in the other British clays.

To summarize, the undrained shear modulus chosen for the Canons Park and the Haga sites are those obtained from undrained triaxial tests. For the other sites Equation 13.8 have been used as an estimation. Most of these sites have undrained triaxial results available, and a much better estimate of the undrained shear modulus can be made. Unfortunately I did not have time to do this. Doing this would change the regression lines and maybe show a more uniform trend.

13.3 The sensitivity

The dataset gathered from Karlsrud (2012) does not include the sensitivity (S_t) of the soil at the different sites. In the site descriptions written by Karlsrud (2012), sensitivity is mentioned occasionally, but mostly as a range or an average value, rarely plotted with depth. The literature has been searched for plots of measured sensitivity with depth and other mentions of sensitivity for the different sites listed in Chapter 13.1. The result of this search is gathered in this chapter.

Many of the British and American sites have very little mention of sensitivity. At the Tilbrook Grange, Cowden, Canons Park, Empire, Saugus and Hamilton Air Force Base sites, the sensitivity is barely, if at all, mentioned and empirical relationships with the liquidity index (I_L) have been used to estimate the sensitivity.

Bjerrum (1954) propose a log-linear relationship between the liquidity index and the sensitivity of the soil as seen in Figure 13.33. Similar relationships can be found in Carter and Bentley (1990), Wood (1990) and Skempton and Northey (1952). The liquidity index is defined as:

$$I_L = \frac{w - w_P}{w_L - w_P} \tag{13.9}$$

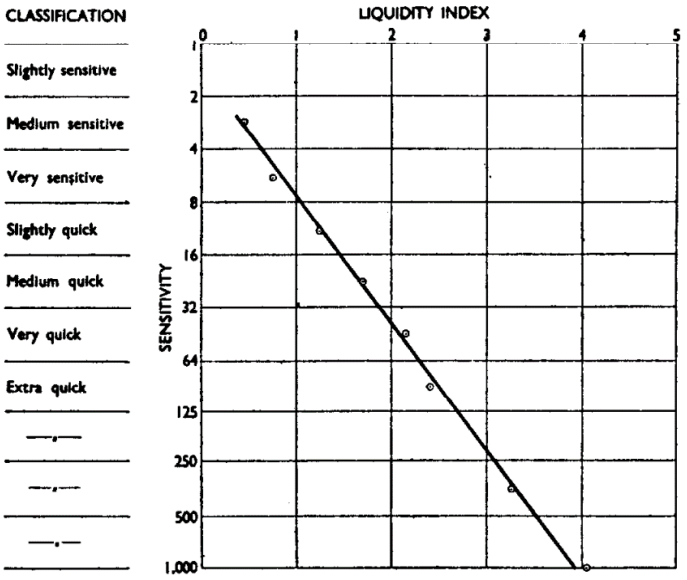

Figure 13.33: Log-linear relationship between the liquidity index and the sensitivity of the soil proposed by Bjerrum (1954) based on Norwegian marine clays.

The data utilized by Bjerrum (1954), was based on Norwegian marine clays with a sensitivity of 3 or more. Figure 13.34 shows the relationship proposed by Skempton and Northey (1952). As seen in the figure, only data with a liquidity index below 1,2 is included. All proposed relationships, including does not shown here by Carter and Bentley (1990) and Wood (1990), have been checked and most often give a similar conclusion. The relationship by Skempton and Northey (1952) (i.e. Figure 13.34) has been the decisive estimation method. This is because most of the sites mentioned (i.e. where the sensitivity is estimated based on I_L) have a low liquidity index and Figure 13.34 includes more data on clays with a low liquidity index.

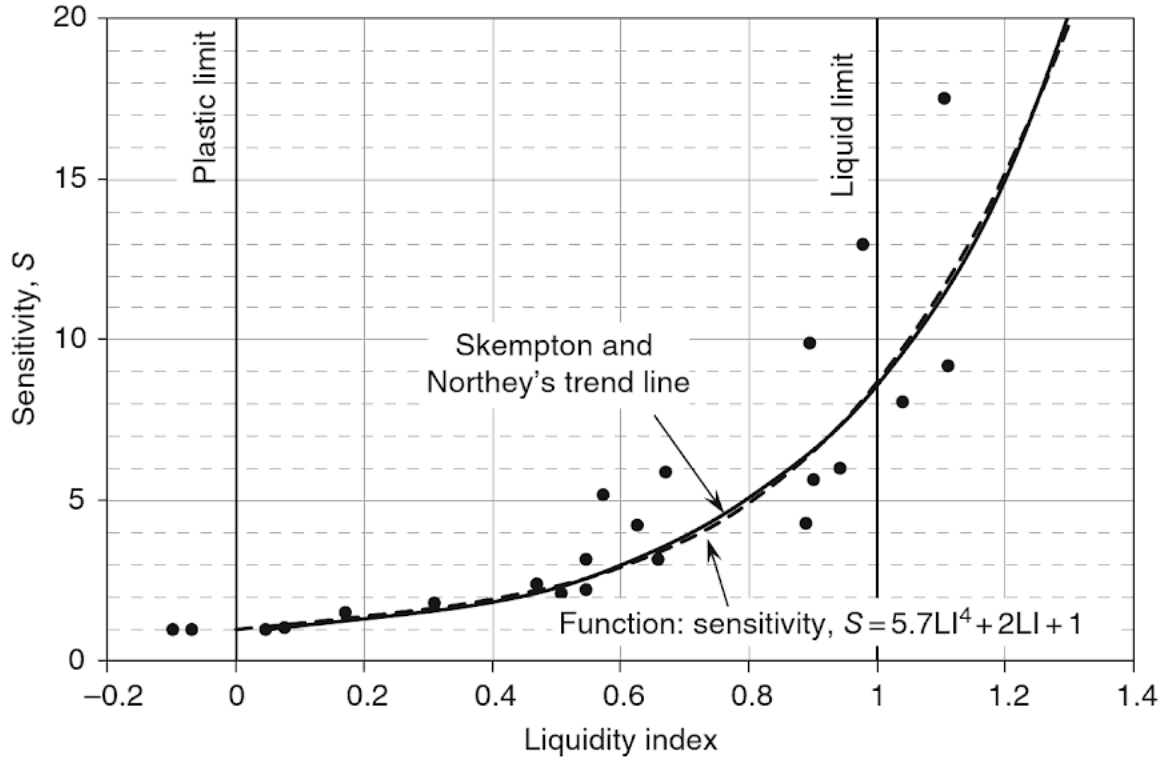

Figure 13.34: Relation between sensitivity and liquidity index proposed by Skempton and Northey (1952). (Carter and Bentley 2016)

13.3.1 Haga

According Karlsrud (2012) fall cone tests and in-situ vane borings show that the sensitivity (S_t) range from $4-6$. Results from the falling cone tests have not been found, but Figure 13.35 shows the results from the in-situ vane borings. This figure have been used to determine a sensitivity of 4,8 at $1{,}9m$ depth and 4,6 at $3{,}4m$ depth.

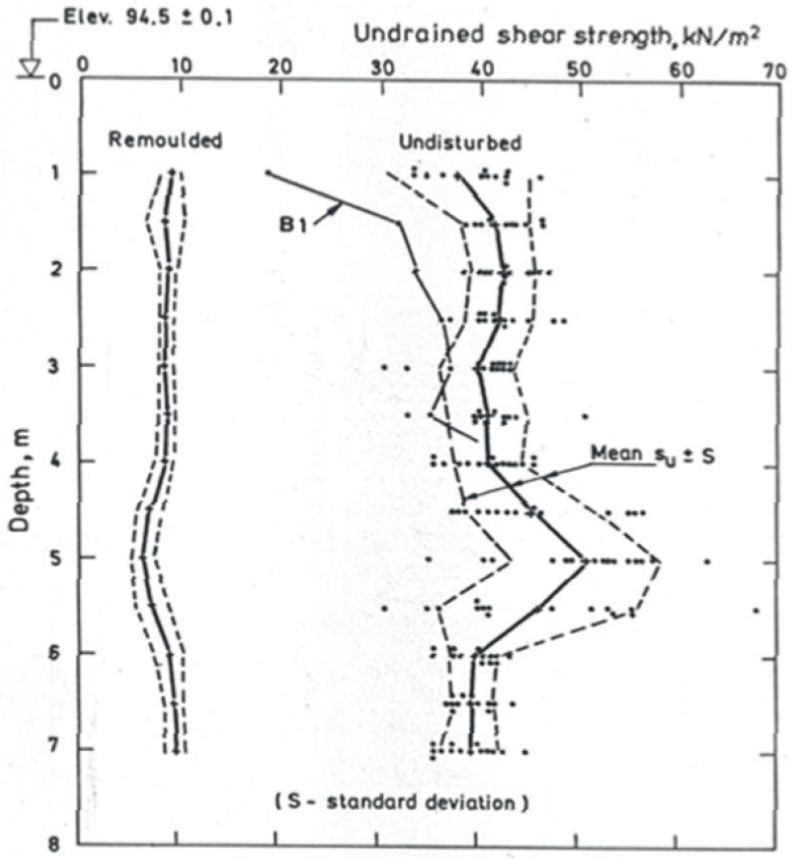

Figure 13.35: In-situ vane strength, both remoulded and undisturbed, from Karlsrud and Haugen (1984) used to determine the sensitivity of the clay at the Haga site.

13.3.2 Onsøy

At the Onsøy site Karlsrud (2012) does not mention the sensitivity of the clay. Berre (2013) report the results of falling cone tests on piston samples as seen in Figure 13.36, together with sensitivities from in-situ vane borings reported by Lunne, Long et al. (2003). In addition, Lunne, Berre et al. (2006) report sensitivities found from falling cone tests on block samples as listed in Table 13.3. The reported sensitivities from the different sources are shown in Figure 13.37 together with the chosen sensitivity profile. The measurements at Onsøy are from $7{,}5 - 35m$ depth, and the results from Lunne, Berre et al. (2006) (i.e. the block samples) are given the most weight when choosing the sensitivity profile.

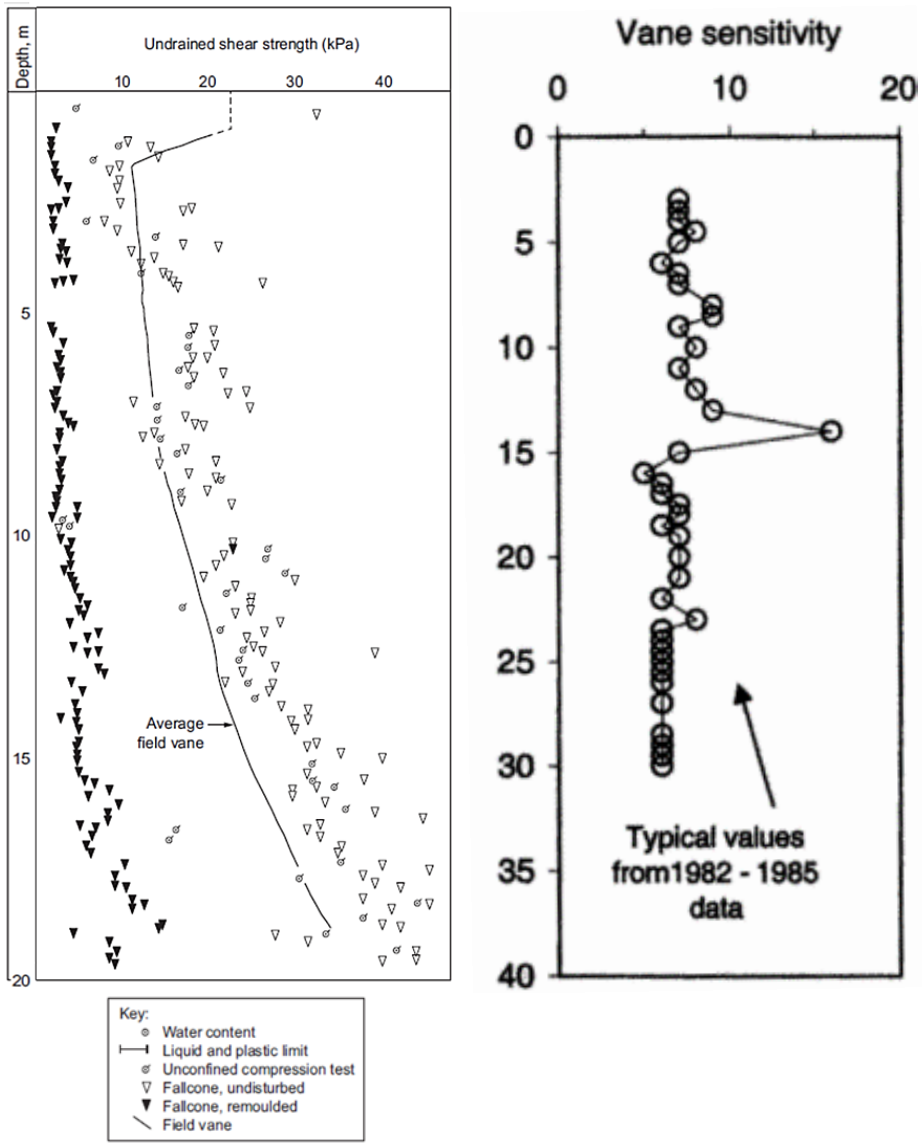

Figure 13.36: To the left, results from falling cone tests on piston samples, both disturbed and undisturbed, against depth from Berre (2013). To the right, sensitivity with depth found from in-situ vane borings reported by Lunne, Long et al. (2003) for the Onsøy site.

Table 13.3: Sensitivity from falling cone tests conducted on block samples with depth for the Onsøy site reported by Lunne, Berre et al. (2006).

Depth [m]	Falling cone sensitivity from block samples
7,2	4,6
12,1	5,9
12,7	4,8
14,7	4,5
18,9	11

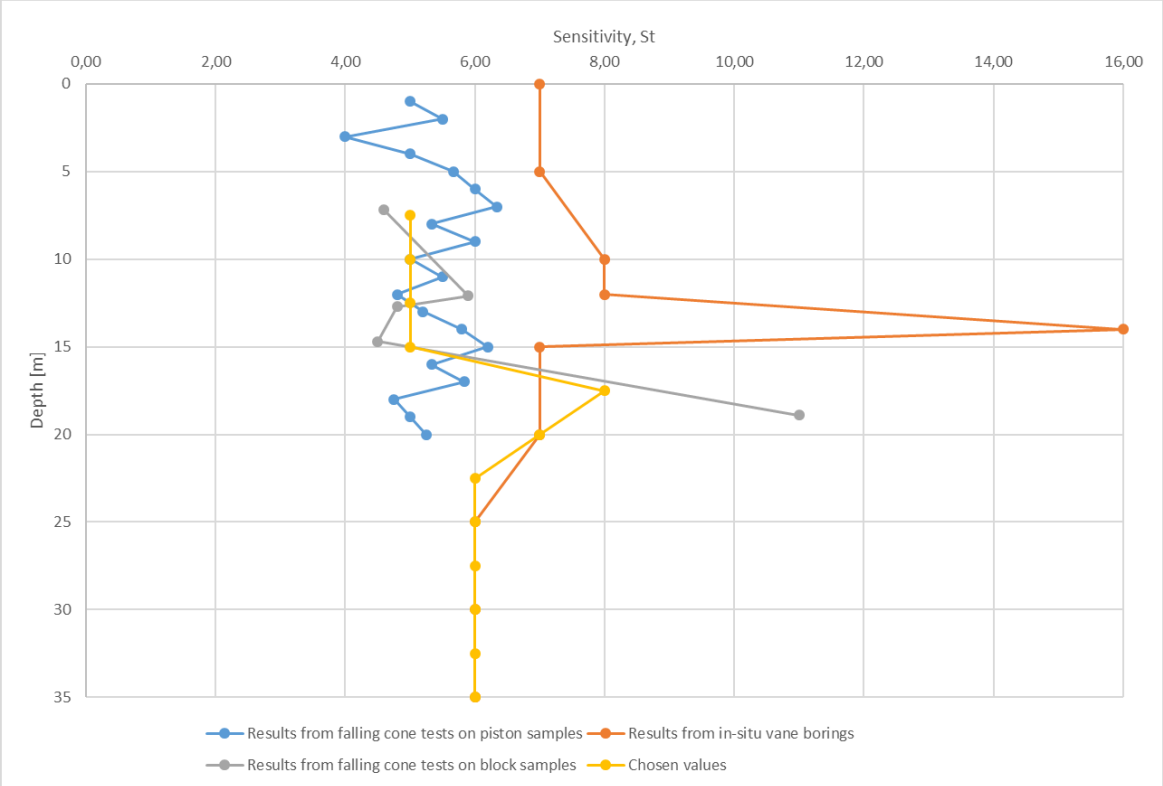

Figure 13.37: Results from the different sources (somewhat simplified) together with the chosen sensitivity profile for the Onsøy site.

13.3.3 Lierstranda

Karlsrud (2012) report that for the Lierstranda site, the sensitivity of the clay range from $3-6$, when determined from in-situ vane borings. On the other hand, the range is from $7-14$ according to falling cone tests. Table 13.4 shows the sensitivities determined by falling cone tests on block samples reported by Lunne, Berre et al. (2006). The results from the in-situ vane borings where not found. The pore pressure measurements are from $7{,}5-35m$ depth, and a sensitivity of 8 was chosen for the top $7{,}5-12{,}5m$, while a value of 12 was chosen for the remaining measurements. The sensitivities found from the block samples was given the most weight, but the fact that the vane sensitivity was reported to be lower influenced the choice and the values chosen are slightly lower than what the falling cone tests might suggest alone.

Table 13.4: Sensitivity from falling cone tests conducted on block samples with depth for the Lierstranda site reported by Lunne, Berre et al. (2006).

Depth [m]	Falling cone sensitivity from block samples
6,0	7,7
6,0	7,1
6,4	11
12,2	8,1
16,3	12
16,3	14
22,3	8,4
22,3	15

13.3.4 Tilbrook Grange

Figure 13.38 shows the Atterberg limits and the natural water content of the clay at the Tilbrook Grange site. Since the natural water content is either equal or even lower than the plastic limit, the liquidity index becomes zero or negative. This is indicating that the soil is insensitive according to Figure 13.34, and a constant sensitivity of one was chosen for the Tilbrook Grange site.

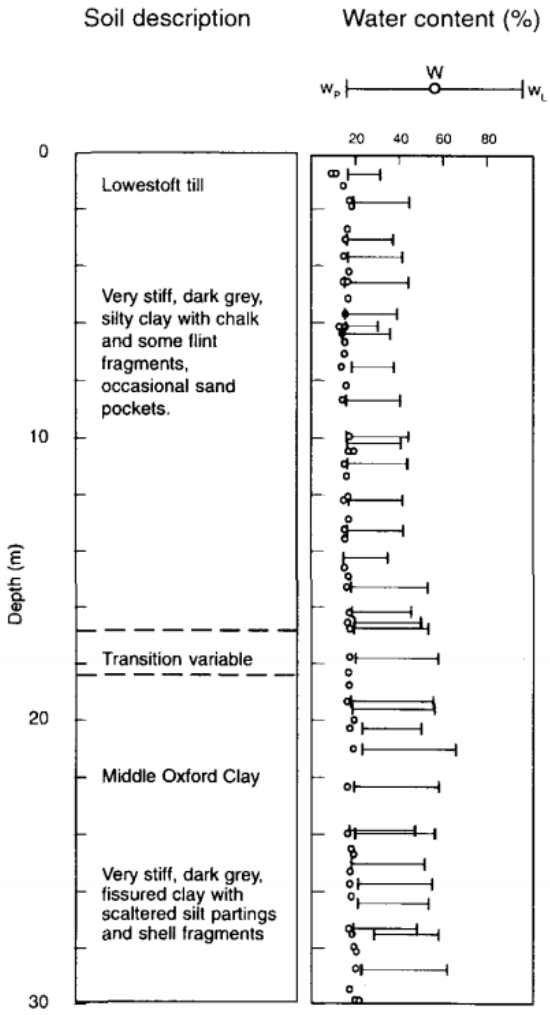

Figure 13.38: Soil description and water content of the soil at the Tilbrook Grange site after McClelland (1988).

13.3.5 Bothkennar

The sensitivity of the clay at the Bothkennar site is determined based on the results presented by Hight, Paul et al. (2003). Figure 13.39 illustrates the sensitivity found from in-situ vane borings reported by Nash, Powell et al. (1992), together with falling cone tests conducted in the laboratory. The excess pore pressure due to pile driving was measured at 3,5 and 4,7m depth, and the sensitivity at these depths were chosen as 5,6 and 6,6 respectively.

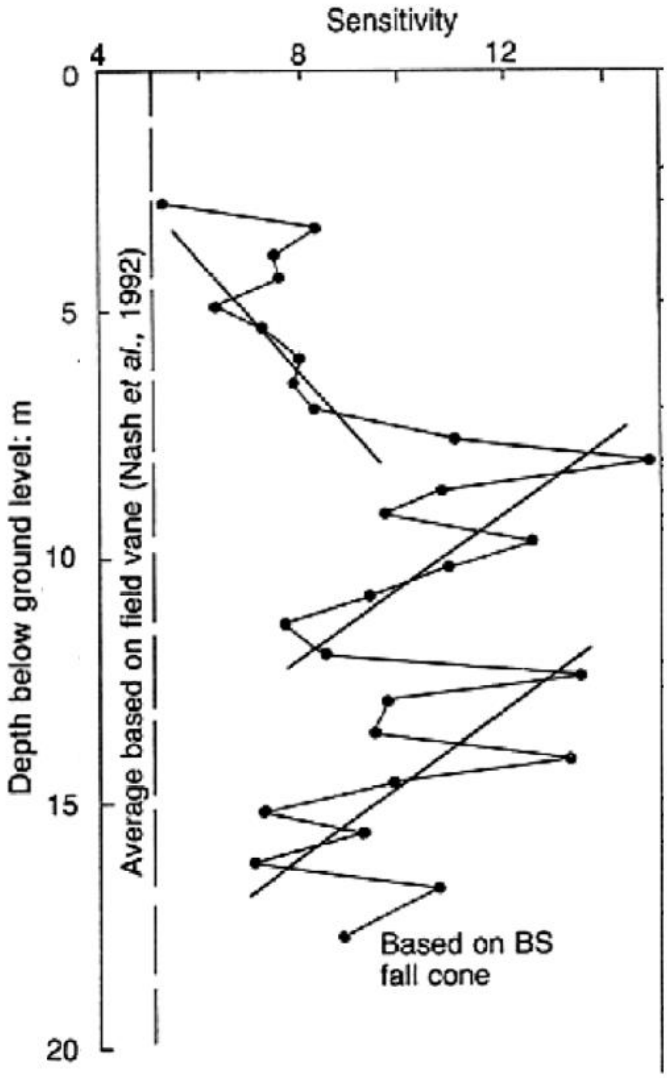

Figure 13.39: Sensitivity at the Bothkennar site determined from in-situ vane borings and falling cone tests. (Hight, Paul et al. 2003)

13.3.6 Cowden

Figure 13.12 displays the index parameters of the glacial till clay found at the Cowden site. Since the natural water content is less than the plastic limit, the liquidity index becomes negative as for the Tilbrook Grange site, indicating that the soil is insensitive. Lehane and Jardine (1994) supports this conclusion as they call the Cowden till insensitive in their report. This is the only mention of sensitivity, in the reports about the Cowden site, red by the author and so a sensitivity of one is chosen.

13.3.7 Canons Park

Also for the Canons Park site very little information was found regarding the sensitivity of the clay. Bond and Jardine (1991) report the water content, plastic limit and liquid limit for the Canons Park site, as seen in Figure 13.15. Using Equation 13.9 the liquidity index was found to be $I_L = 0{,}02$ and $0{,}035$, at the relevant depths: $2{,}8m$ and $4{,}0m$ respectively. Figure 13.34 gives a sensitivity very close to one, which is then the assumed sensitivity for both the measurement depths at the Canons Park site.

13.3.8 Empire

Table 13.1 give a liquidity index of 0,3 for the upper $35 - 50m$ (zone 1), and 0,26 from $63 - 78m$ (zone 2), which is the relevant range of depth. Looking more closely at the specific depths, Figure 13.40 supports a liquidity index of about 0,3 for the relevant depths. Using the relationship from Figure 13.34, proposed by Skempton and Northey (1952), gives a sensitivity of 1,65 given a liquidity index of 0,3, which is then chosen for the measurement depths.

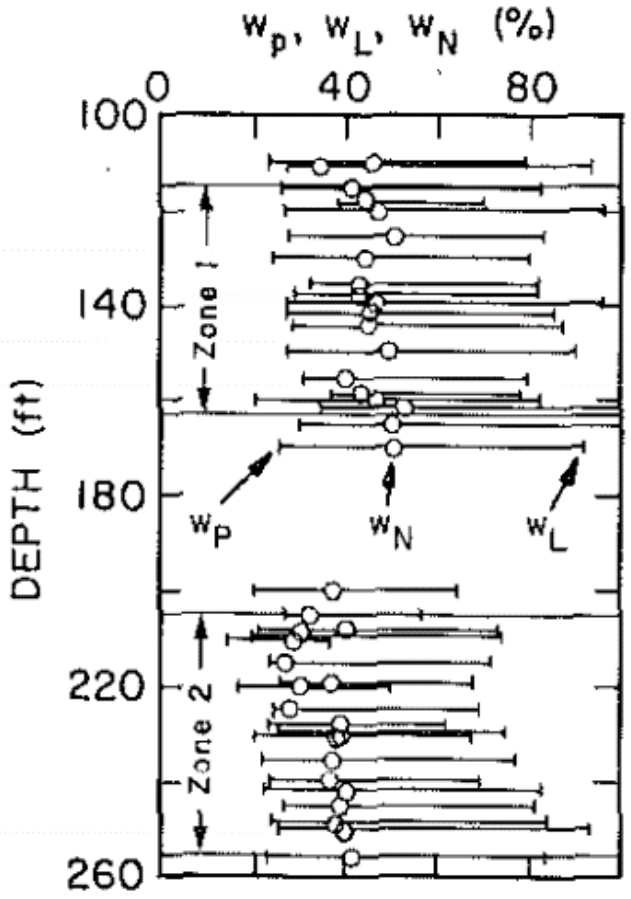

Figure 13.40: Natural water content, plastic limit and liquid limit against depth (in feet) for the Empire site. (Azzouz and Lutz 1986)

13.3.9 Saugus

Baligh, Vivatrat et al. (1979) reports an average sensitivity of 6 for the Saugus site, but no plot nor information on how this value was found is included. By calculating the liquidity index using the data from Morrison (1984), shown in Figure 13.41, and the relationship proposed by Skempton and Northey (1952) (i.e. Figure 13.34) for the relevant depths an average sensitivity of 5,76 was found. Based on this estimate, the information given by Baligh, Vivatrat et al. (1979) was deemed to be correct, and a sensitivity of 6 was chosen for the relevant depths.

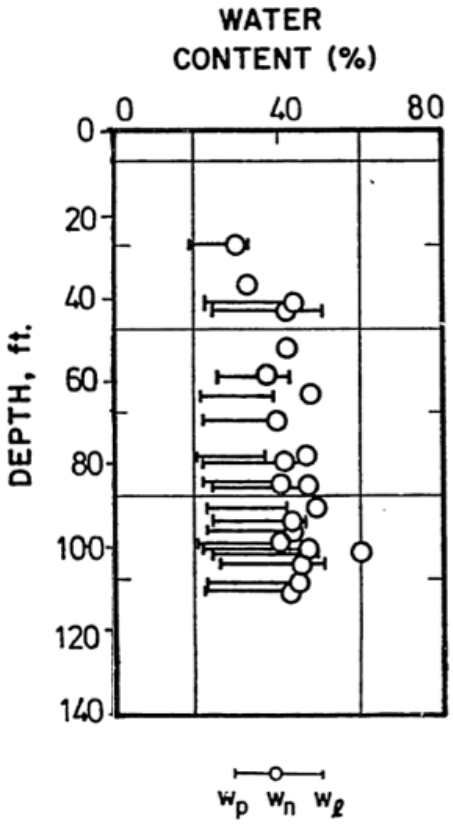

Figure 13.41: Natural water content, plastic limit and liquid limit against depth (in feet) for the Saugus site. (Morrison 1984)

13.3.10 West Delta

Karlsrud (2012) report that various tests conducted to determine the remoulded shear strength gave a sensitivity between $S_t = 1{,}5 - 2{,}0$. The inverse of the normalized shaft friction ($^{t_{si}}/_{s_{uD}}$) should according to Karlsrud (2012) reflect the sensitivity. Immediately after pile driving, $^{t_{si}}/_{s_{uD}}$ was measured in the range $0{,}2 - 0{,}35$. The inverse of this gives: $S_t = 2{,}85 - 5{,}0$. This is a about a factor of 2 larger than the sensitivity measured in the laboratory.

Audibert and Hamilton (1998) reported the sensitivities found from undrained compression strength tests as seen in Figure 13.42. This figure have been used when determining the sensitivity of the clay at the depths where the excess pore pressure due to the pile driving was measured (i.e. from a depth of $14 - 68m$). The sensitivities chosen range from 1,4 to 1,7, and are purely based on the laboratory results. The apparent sensitivity (i.e. inverse of $^{t_{si}}/_{s_{uD}}$) mentioned by Karlsrud (2012), have not influenced the chosen sensitivities.

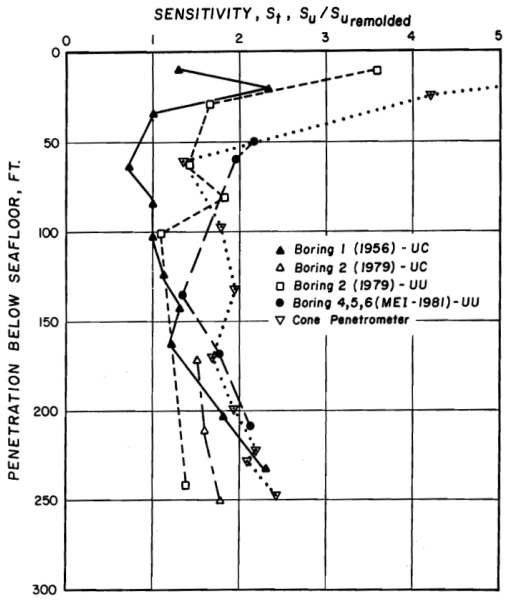

Figure 13.42: Sensitivity against depth in feet reported by Audibert and Hamilton (1998) for the West Delta site.

13.3.11 Hamilton Air Force Base

The index data from the Hamilton site, shown in Figure 13.24, indicate a liquidity index of 0,93 at about $6m$ depth, which is the approximate depth that the pore pressure was measured. This gives a sensitivity of 7,0 and 7,2, using the relationship proposed by Bjerrum (1954) and Skempton and Northey (1952) respectively. A sensitivity of 7 was chosen for the Hamilton Air Force Base site at the relevant depths.

13.3.12 St. Alban

Rochelle, Trak et al. (1974) report the sensitivity, measured at five depths, in the St. Alban clay. Tavenas and Leroueil (1977), Tavenas, Leroueil et al. (1978) and Konrad and Roy (1987) report a sensitivity measured by field vane of 14 and 22, at $3m$ and $5{,}7m$ depth respectively. Roy and Lemieux (1986) report a sensitivity also measured by field vane of 12 at $2{,}3m$ depth, and 17 at $5m$ depth. Figure 13.43 shows the chosen values at the relevant depths, together with the measured sensitivites mentioned above.

Table 13.5: Index properties and especially sensitivity of the clay at the St. Alban site. (Rochelle, Trak et al. 1974)

Depth (ft)	Consistency W_L	Consistency I_P	Consistency I_L	Clay content (%)	Sensitivity	Salt content[1] (g/l)
5	67	37	1.4	—	8	—
6	55	28	2.4	72	—	0.9
9	51	24	2.7	81	14	—
12	41	18	2.5	56	—	0.5
13	37	15	2.0	43	16	—
18	31	12	2.7	49	—	0.3
21	40	19	1.9	—	22	—
27	26	9	2.3	31	—	0.3
29	40	17	1.8	35	12	—

[1]Salt content given in grams per liter equivalent to concentration of NaCl.

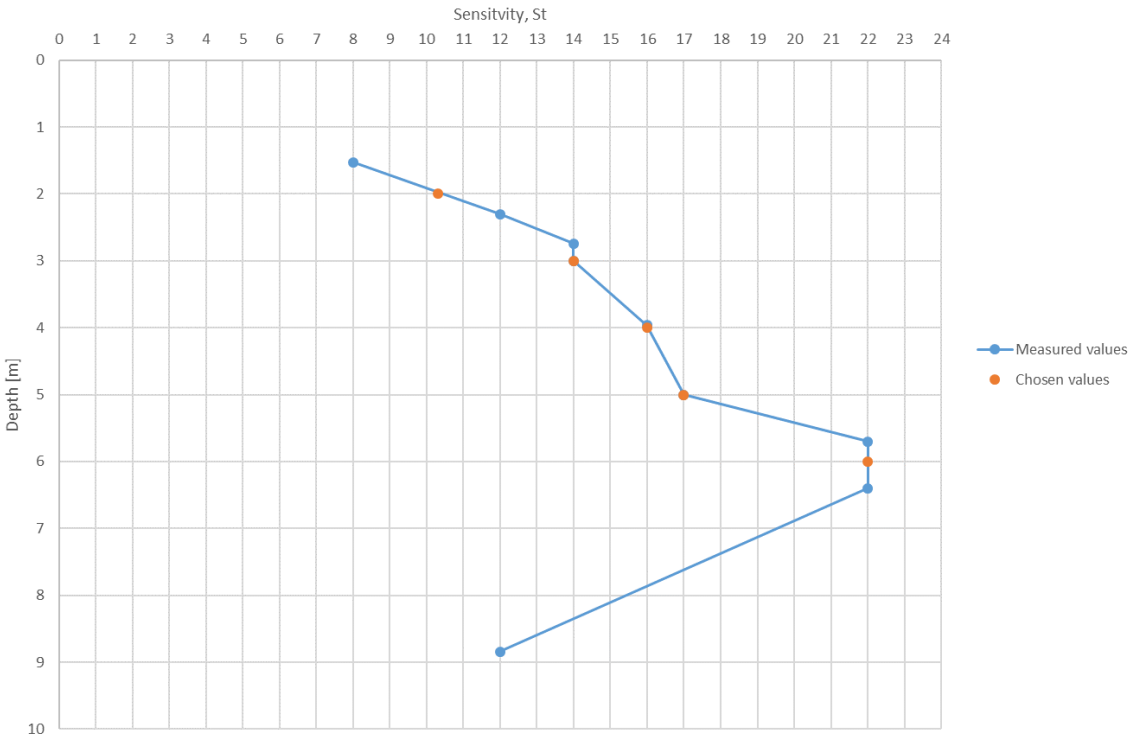

Figure 13.43: Sensitivity of Champlain clay at the St. Alban site. Chosen values in orange and measured values in blue gathered from Rochelle, Trak et al. (1974), Tavenas and Leroueil (1977), Tavenas, Leroueil et al. (1978), Roy and Lemieux (1986) and Konrad and Roy (1987).

13.4 Sensitivity of all the sites

Combining all the information presented in Chapter 13.3 with the measured pore pressure, we will look for trends in the excess pore pressure with the sensitivity. Karlsrud (2012) presents plots of overconsolidation ratio (OCR, Figure 9.11), and plasticity index (I_P, Figure 9.13) against measured excess pore pressure normalized with the direct undrained shear strength ($\Delta u_{max}/s_{uD}$).

Figure 13.44 and Figure 13.45 shows the same kind of plot, but with sensitivity (S_t) along the x-axis in a linear and logarithmic scale, respectively. In addition to the measured data, five trend lines are plotted. In Figure 13.44 these lines are linear with respect to S_t, while in Figure 13.45 these lines are log-linear.

As the legend indicates: the red trend line is for all the data combined, the orange is only based on the closed-ended piles, the yellow is based on the open-ended piles, the blue is based on the full sized piles, and the green is only based on the model sized piles. The equation of these trend lines are depicted in the figure in the same order as the legend suggests.

In both plots we see that the model sized piles indicate a larger increase in excess pore pressure with sensitivity than the other data, while the open-ended piles show a very small decrease. The spread of the data is much larger for the clays with low sensitivity. This is partly because we have more data in that range, but also because the sites with the highest OCR (Tilbrook Grange (Ti), Canons Park (CP-IC) and Cowden (Co-IC)) are sites where the soil is deemed insensitive.

The sites with high OCR show a lot more scatter, and they are also grossly over-predicted by the CEM-EP solution. This will be explained more thoroughly in Chapter 14.9, however these sites are the main reason we see an increase in excess pore pressure with increasing sensitivity. If these sites are removed from the data the slope reduce quite significantly.

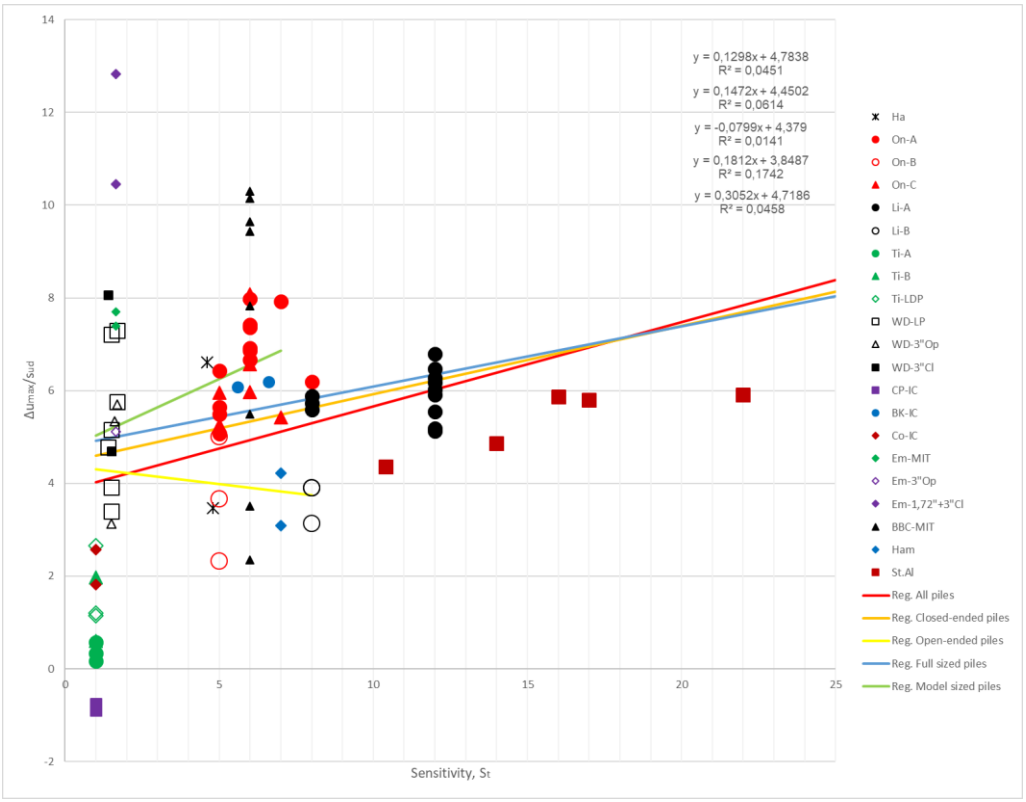

Figure 13.44: Normalized excess pore pressure ($\Delta u_{max}/s_{ud}$) versus sensitivity (S_t) in a linear scale for all sites together with different trend lines. Further description of the legend can be found above Figure 9.10.

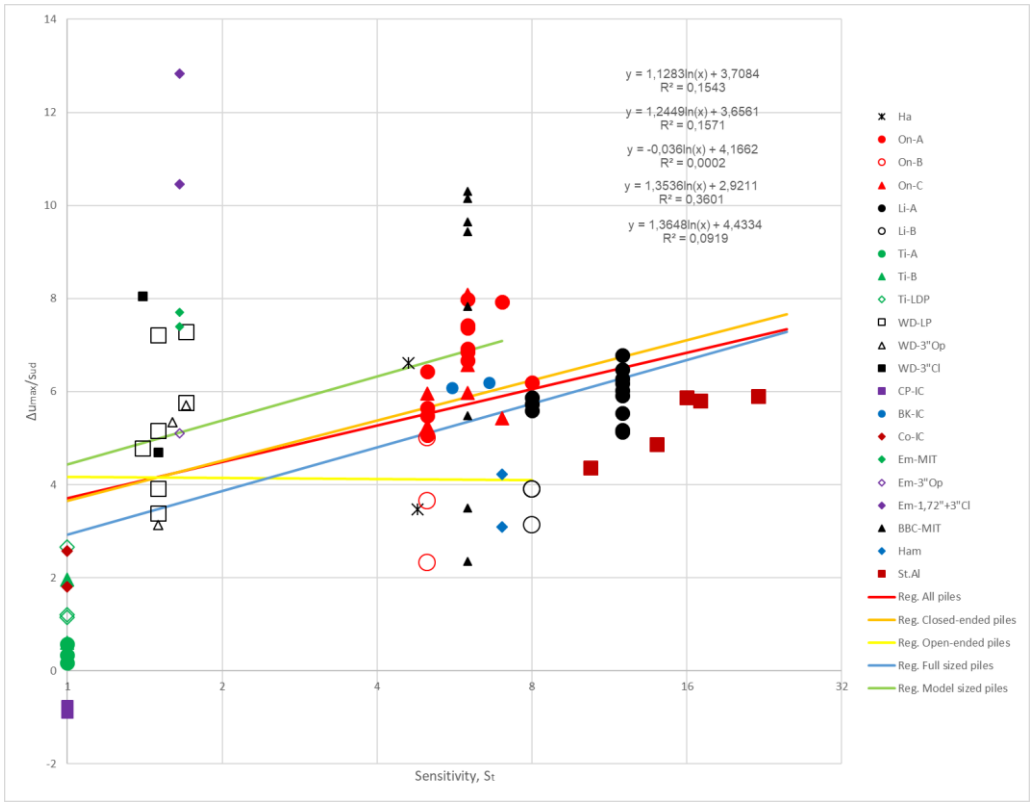

Figure 13.45: Normalized excess pore pressure ($\Delta u_{max}/s_{ud}$) versus sensitivity (S_t) in a logarithmic scale for all sites together with different trend lines. Further description of the legend can be found above Figure 9.10.

The coefficient of determination (explained in Chapter 14.1) is very low in the linear plot, only $R^2 = 0{,}045$ for the regression based on all the piles. If the sensitivity is plotted in a logarithmic scale (i.e. Figure 13.45) this increase to $R^2 = 0{,}154$. This is because we have more data with a low sensitivity. Using a logarithmic axis then makes it possible to improve the fit in the low range compared to using a linear axis.

In Chapter 12.7 we found a linear expression (Equation 12.12) where the normalized excess pore pressure minus the CEM-EP solution $\left({}^{\Delta u_{max}}/_{s_{ud}} - \ln\left({}^{G_u}/_{s_{ud}}\right)\right)$ equals a factor $\beta(1 - {}^{1}/_{S_t})$. Figure 13.46 shows the normalized excess pore pressure against the factor $1 - {}^{1}/_{S_t}$. All the trend lines do now show an increasing excess pore pressure with increasing sensitivity. The coefficient of determination for the trend line based on all the piles has gone up to $R^2 = 0{,}266$. This is however still quite low.

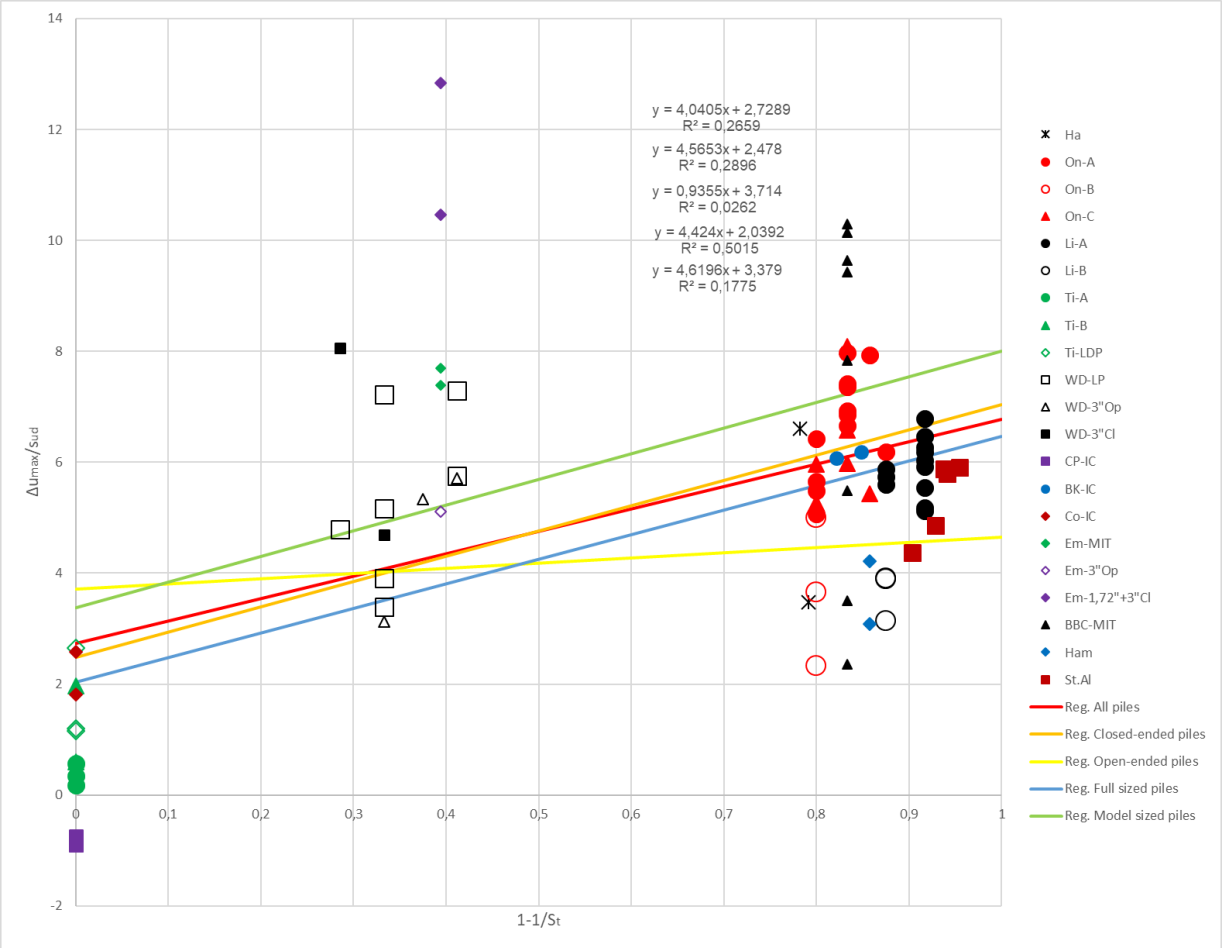

Figure 13.46: Normalized excess pore pressure (${}^{\Delta u_{max}}/_{s_{ud}}$) versus $1 - {}^{1}/_{S_t}$ for all sites together with different trend lines. Further description of the legend can be found above Figure 9.10.

Equation 12.12 actually suggests that the analytical linear elastic-perfectly plastic cavity expansion solution (CEM-EP), should be subtracted from the normalized excess pore pressure. This makes a lot of sense as we then will have removed the part of the measured pore pressure that can be described by the analytical solution. The part that is left must then be explained by other factors.

This is illustrated in Figure 13.47, and we see that the result is quite similar to that of Figure 13.46. However, the factor in front of x in the regression lines is now directly comparable to the β factor seen in Equation 12.12 (only β is defined to be negative, so that $\beta = -3{,}838$ for the Reg. All piles trend line). The coefficient of determination does not change significantly but increase to $R^2 = 0{,}274$ for the trend line based on all the piles.

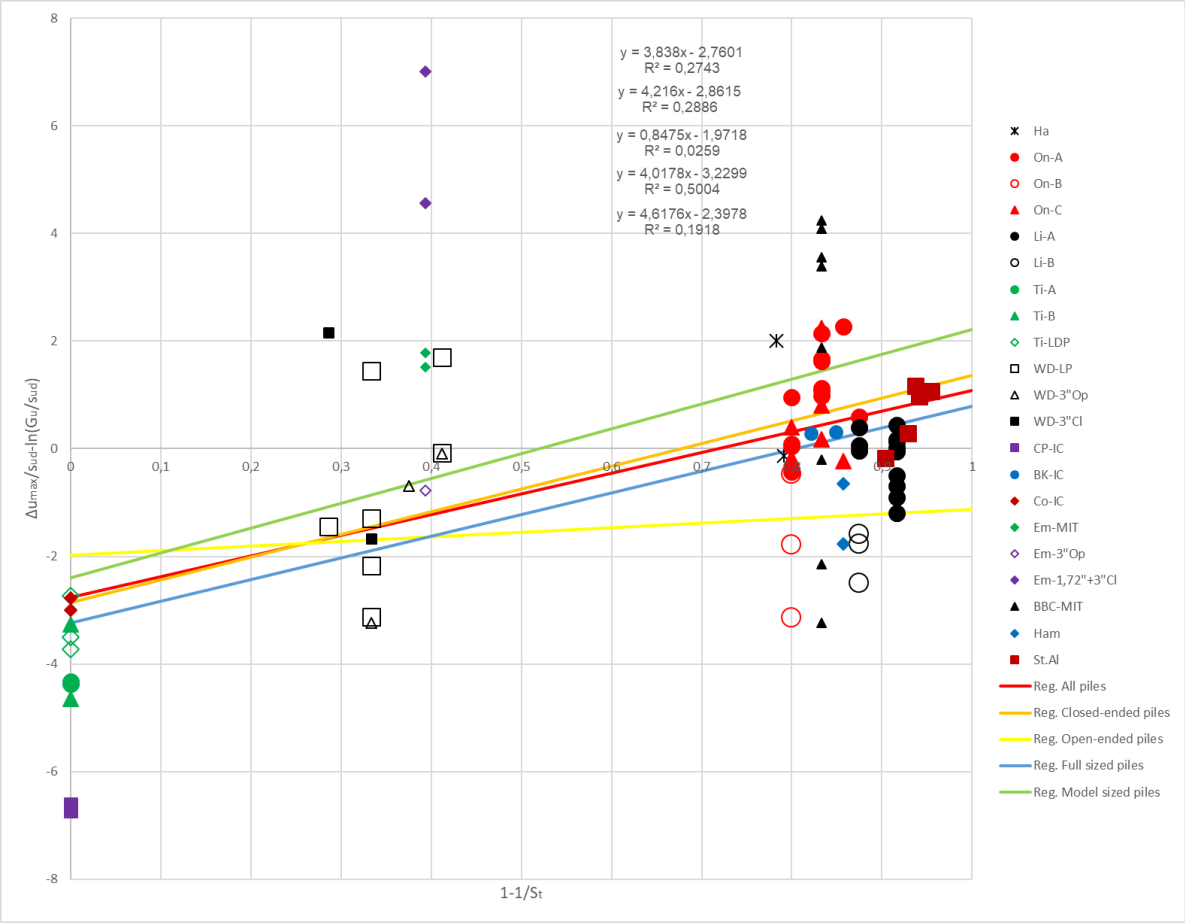

Figure 13.47: Residual between the measured normalized excess pore pressure and the analytical linear elastic-perfectly plastic cavity expansion method solution (CEM-EP) (i.e. $\frac{\Delta u_{max}}{s_{ud}} - ln\left(\frac{G_u}{s_{ud}}\right)$*) against the factor* $1 - \frac{1}{S_t}$ *found in Chapter 12.7. Including the data from all sites and different trend lines. Further description of the legend can be found above Figure 9.10.*

The β can be related to the remoulded limit by Equation 12.13. The regression line in Figure 13.47, based on the data from all the piles, then suggests a remoulded limit of ${}^{r_r}/_{r_0} = 0{,}242$.

Similarly to Figure 12.25 showing a decreasing excess pore pressure due to increasing sensitivity for ${}^{r_r}/_{r_0} = 6$ and $\ln\left(\frac{G_u}{s_u}\right) = \ln\left(\frac{7500}{37}\right) = 5{,}312$, Figure 13.48 shows an increasing excess pore pressure with increasing sensitivity when ${}^{r_r}/_{r_0} = 0{,}242$ and $\ln\left(\frac{G_u}{s_u}\right) = \ln\left(\frac{18394}{73{,}7}\right) = 5{,}520$. These values of G_u and s_{uD} is, as seen in Table 14.1, the average values of the dataset presented in Table 13.6. As discussed in Chapter 12.7 the excess pore pressure will increase due to softening if $\frac{r_r}{r_0} < e^{1/2} \approx 1{,}649$ as seen in Equation 12.11.

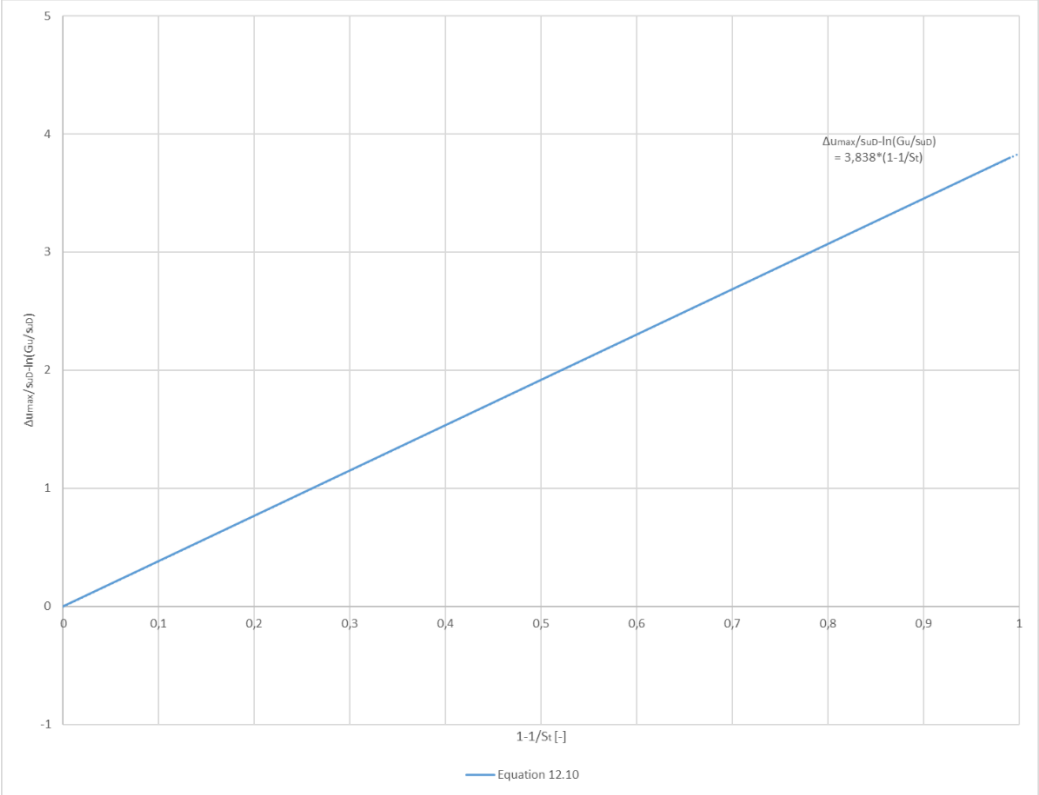

Figure 13.48: Normalized excess pore pressure $({}^{\Delta u_{max}}/_{s_{uD}})$ *minus the CEM-EP solution* $\left(ln\left(\frac{G}{s_{uD}}\right)\right)$ *versus* $1 - {}^{1}/_{S_t}$. *The blue line represents Equation 12.10 with* $ln\left(\frac{G}{s_{uD}}\right) = ln\left(\frac{18394}{73{,}7}\right) = 5{,}5198$ *and* $\frac{r_r}{r_0} = 0{,}242 \rightarrow \beta = -3{,}838$

However, Figure 13.47 shows that many of the sites, especially the insensitive sites, have a lower excess pore pressure than what the CEM-EP solution predicts. It is seen that using $\beta = -3{,}838$ in Equation 12.12, does not give the same results as the trend lines in Figure 13.47, due to this.

Karlsrud (2012), among many others, have shown that the overconsolidation ratio (OCR) (i.e. dilation/contraction) influence the excess pore pressure generated due to pile driving. As already discussed the sites with very high OCR are all insensitive (i.e. plottet at $1 - \frac{1}{S_t} = 0$ in Figure 13.47). This means the effect of OCR affect and disturbs the picture drawn by Figure 13.47. In the same way, Figure 9.11 only showing OCR against excess pore pressure is probably disturbed by other factors such as sensitivity. If only the sites with $OCR \leq 2$ is included then the trend line from Figure 13.47 becomes completely straight as seen in Figure 13.49. This has also been checked directly against sensitivity (S_t) on the x-axis, giving the same result as Figure 13.49 indicates.

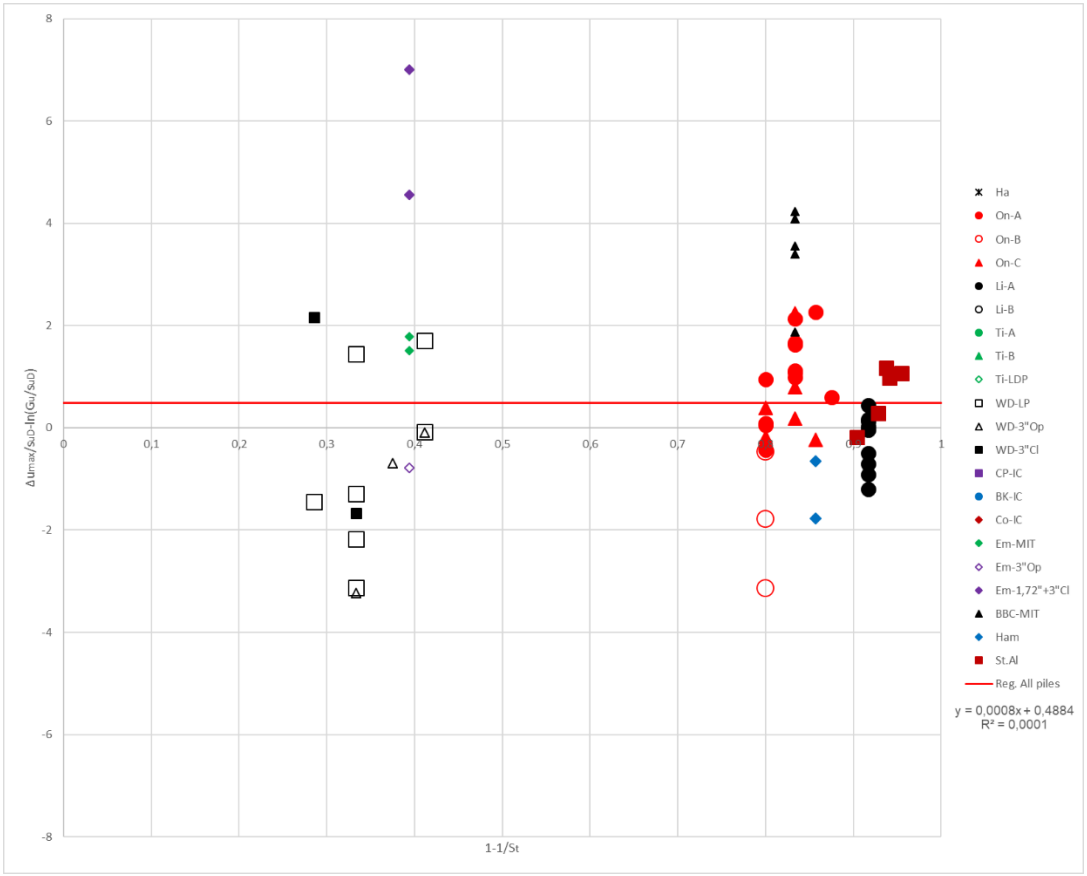

Figure 13.49: Residual between the measured normalized excess pore pressure and the analytical linear elastic-perfectly plastic cavity expansion method solution (CEM-EP) (i.e. $\frac{\Delta u_{max}}{s_{ud}} - ln\left(\frac{G_u}{s_{ud}}\right)$ *) against the factor* $1 - \frac{1}{S_t}$ *found in Chapter 12.7. Including the data from the sites with* $OCR \leq 2$ *and a trend line based on all the piles. Further description of the legend can be found above Figure 9.10.*

The y-axis in Figure 13.50 is the residual between the measured excess pore pressure and the predicted excess pore pressure based on the trend lines suggested by Karlsrud (2012) in Figure 9.11 (Equation 14.16). This indicates that the trend lines of Karlsrud (2012) capture the trend with sensitivity seen in Figure 13.46, without using S_t as input. This means that the OCR is probably the main reason for the increase, but we cannot say if the increase is also somewhat related to sensitivity. Since sensitivity and OCR are very correlated in our dataset (low sensitivity when OCR is high, and high sensitivity for low OCR) it is hard to separate the effects. This is discussed more thoroughly in Chapter 14.9. However, a decrease in excess pore pressure with increasing sensitivity is not seen in any of the plots.

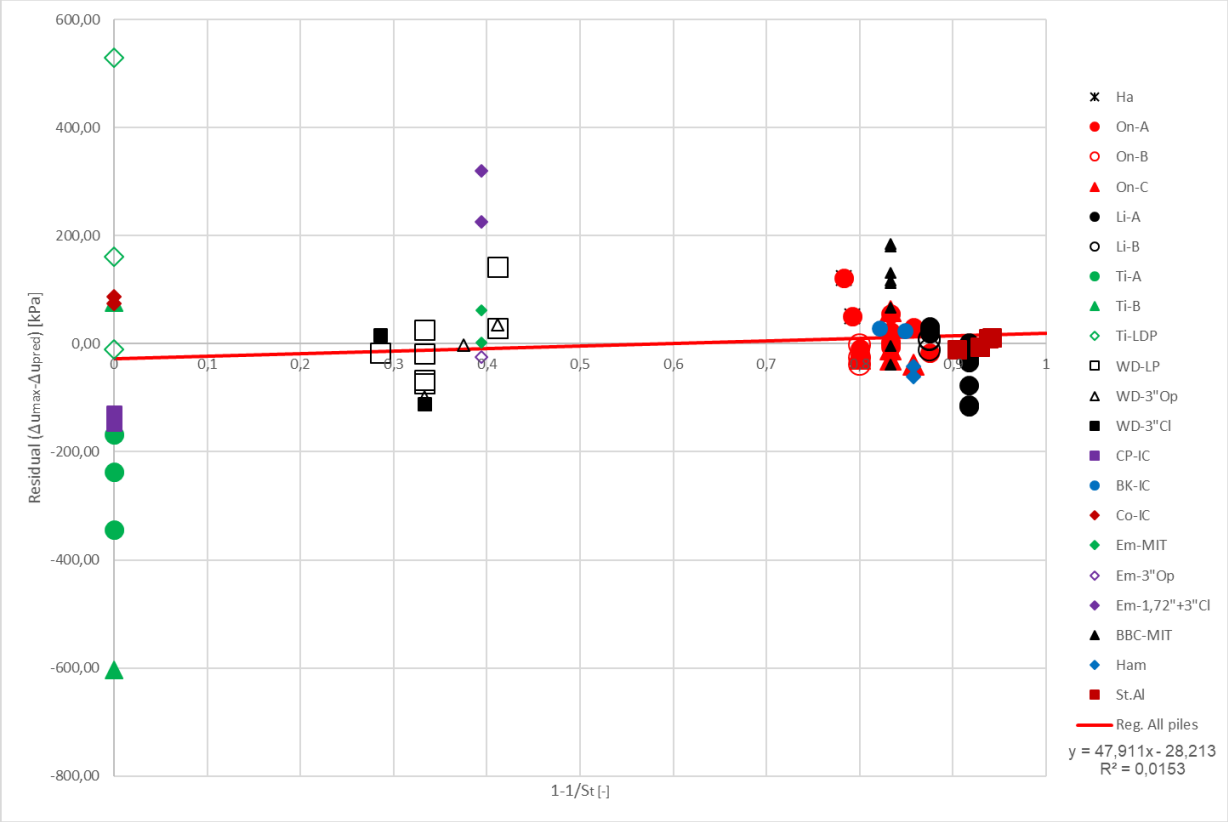

Figure 13.50: Measured excess pore pressure minus predicted excess pore pressure based on Equation 14.16 by Karlsrud (2012) against $1 - {}^{1}/_{S_t}$*. Including the data from all sites and a trend line based on all the piles. Further description of the legend can be found above Figure 9.10.*

13.5 Coefficient of lateral earth pressure for all the sites

The coefficient of lateral earth pressure (K_0) is very correlated to the OCR. Looking at the trend line based on all the sites we see a clear decrease in $\Delta u_{max}/s_{uD}$ for increasing K_0, as shown by Figure 13.51. This is solely due to OCR, and is actually the opposite trend of what we found when using CEM-MCC. In Chapter 12.6 we found that the Δu_{max} increase with $Bln(K_0)$ increasing. Where B is a factor which was found to be positive in the CEM-MCC analyses, and is assumed to depend on the stiffness and strength of the soil.

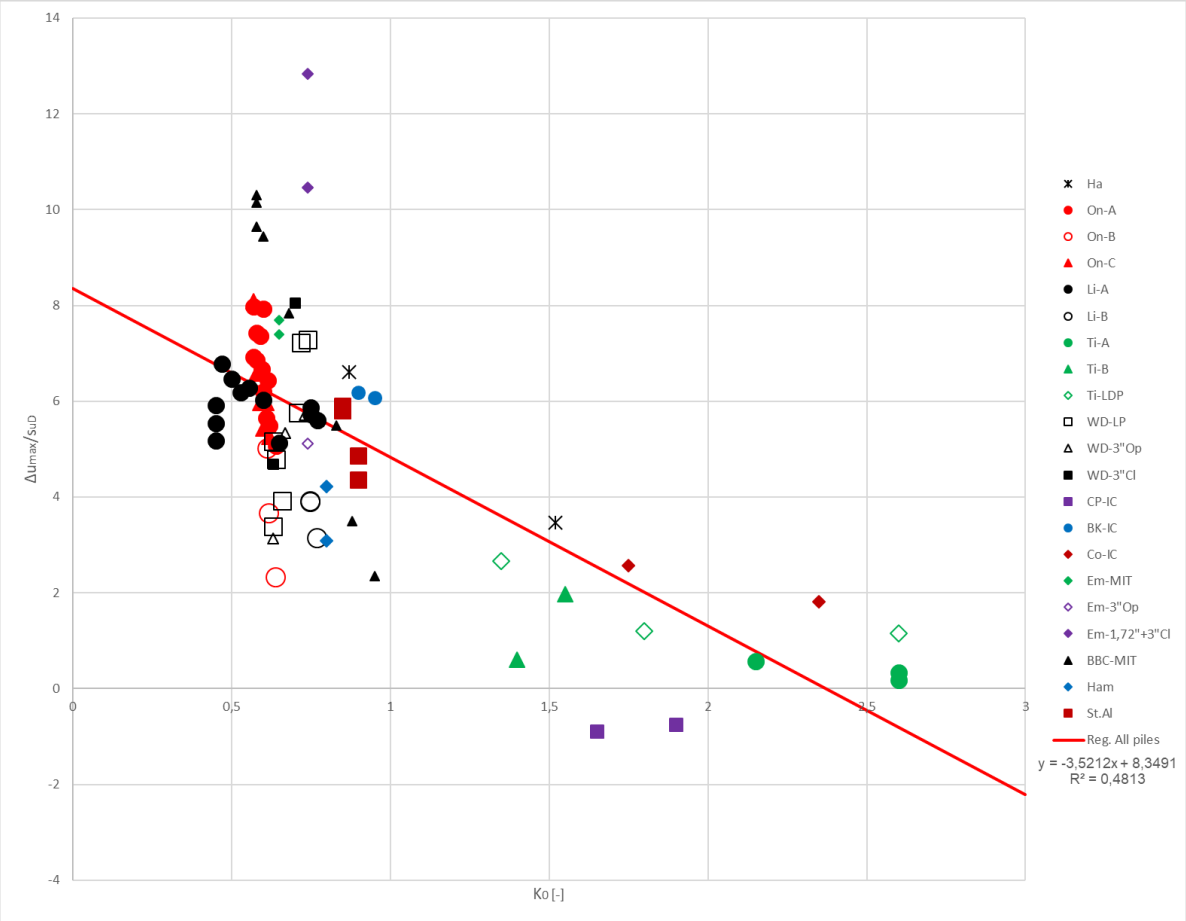

Figure 13.51: Normalized excess pore pressure ($\Delta u_{max}/s_{uD}$) versus the coefficient of lateral earth pressure (K_0) in a linear scale for all sites together with a trend line based on all the piles. Further description of the legend can be found above Figure 9.10.

If one use the trend lines proposed by Karlsrud (2012), and plot the residual (i.e. $\Delta u_{max} - \Delta u_{predicted}$) against K_0, as seen in Figure 13.52, the result is a much weaker, but still decreasing trend.

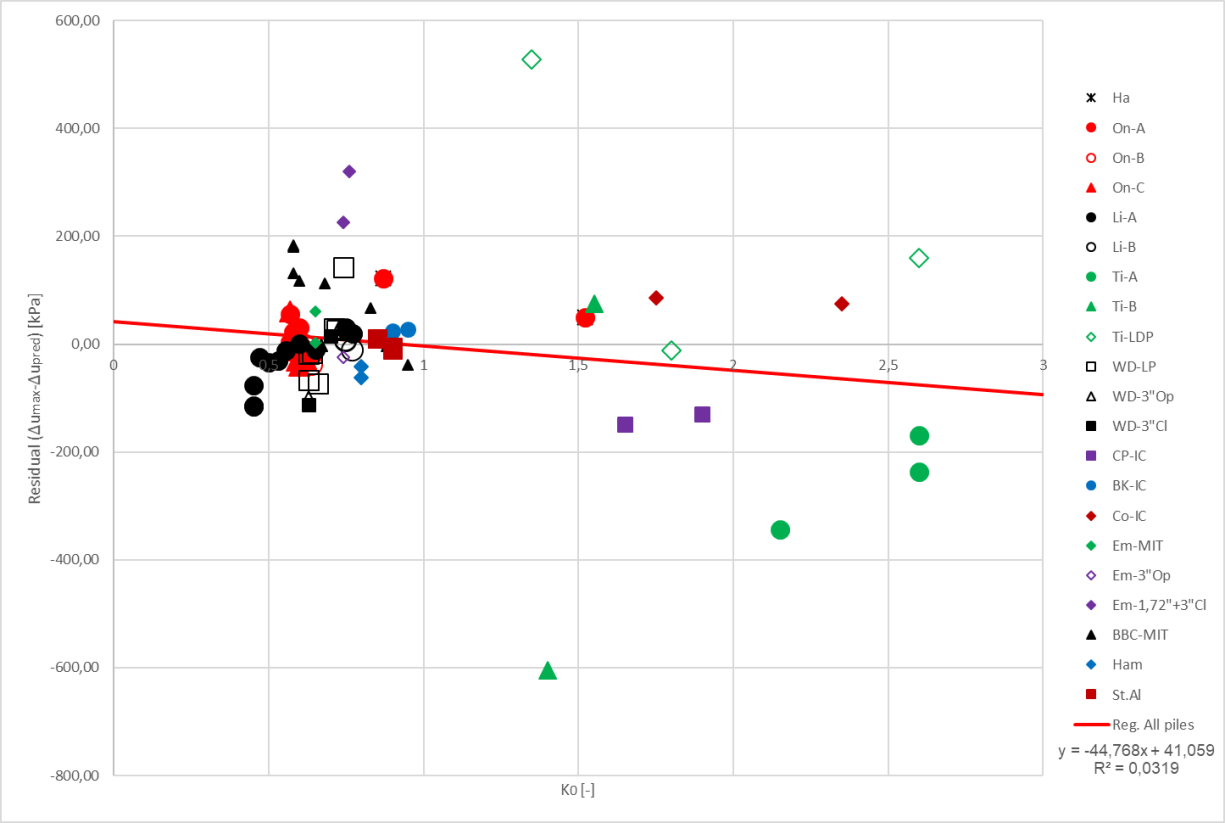

Figure 13.52: Measured excess pore pressure minus predicted excess pore pressure based on Equation 14.16 by Karlsrud (2012) against the coefficient of lateral earth pressure. Including the data from all sites and a trend line based on all the piles. Further description of the legend can be found above Figure 9.10.

Based on these results an increase in excess pore pressure due to an increase in the coefficient of lateral earth pressure seems very unlikely. The trend found in the CEM-MCC model cannot be seen in the empirical data. However, as for the sensitivity, K_0 is very correlated to the OCR. It could be that using CEM-MCC gives a larger decrease with increasing OCR than the trend lines of Karlsrud (2012), and that an increase due to high K_0 balance the prediction. This is however purely speculative and based on Figure 13.52 we see that using OCR alone capture the trend of the data.

13.6 Empirical data summarized in a table

Table 13.6: Summary of pile data, site conditions and measured excess pore pressure at the pile shaft for the different sites. Where the question mark (?) means the value have not been determined (also means it has been unnecessary to determine that parameter for our use for that specific site).

Test site	Pile name	Depth of measuring	Pile diameter	Pile wall tickness	Equivalent pile radius	Embedded length	Depth of pile tip	Jacked or driven	Sensitivity	Direct undrained shear strength	Initial pore pressure	Initival vertical effective stress
		z [m]	D [mm]	t [mm]	R_{eq} [mm]	L [m]	z_{tip} [m]	[-]	S_t [-]	s_{uD} [kPa]	u_0 [kPa]	sig'_{v0} [kPa]
Haga	B-piles	1,9	154	4,5	77	4,85	4,85	Jacked	4,8	41,5	5	39
		3,4	154	4,5	77	4,85	4,85	Jacked	4,6	41	-2	73
Onsøy	A1	7,5	219	8,2	109,5	10	15	Hammered	5	15	73,3	52
		10	219	8,2	109,5	10	15	Hammered	5	17,5	101,5	64
		12,5	219	8,2	109,5	10	15	Hammered	5	21	129,7	76
	A2	15	219	8,2	109,5	10	22,5	Hammered	5	23	157,9	88
		17,5	219	8,2	109,5	10	22,5	Hammered	8	26	186,1	100
		20	219	8,2	109,5	10	22,5	Hammered	7	28	214,3	112
	A3	22,5	219	8,2	109,5	10	30	Hammered	6	31,5	242,5	125
		25	219	8,2	109,5	10	30	Hammered	6	34,5	270,7	139
		27,5	219	8,2	109,5	10	30	Hammered	6	38	298,9	152
	A4	30	219	8,2	109,5	10	37,5	Hammered	6	42	327,1	166
		32,5	219	8,2	109,5	10	37,5	Hammered	6	45,5	355,3	180
		35	219	8,2	109,5	10	37,5	Hammered	6	49	383,5	195
	B1(open)	7,5	809	9,5	87,2	10	15	Hammered	5	15,5	73,3	52
		10	809	9,5	87,2	10	15	Hammered	5	17,5	101,5	64
		12,5	809	9,5	87,2	10	15	Hammered	5	21	129,7	76
	C1	10	219	8,2	109,5	30	35	Hammered	5	17,5	101,5	64
		15	219	8,2	109,5	30	35	Hammered	5	23	157,9	88
		20	219	8,2	109,5	30	35	Hammered	7	28	214,3	112
		25	219	8,2	109,5	30	35	Hammered	6	34,5	270,7	139
		30	219	8,2	109,5	30	35	Hammered	6	42	327,1	166
		35	219	8,2	109,5	30	35	Hammered	6	49	383,5	195
Lierstranda	A7	7,5	219	8,2	109,5	10	15	Hammered	8	25,2	83	61,1
		10	219	8,2	109,5	10	15	Hammered	8	30,8	112,6	70,5
		12,5	219	8,2	109,5	10	15	Hammered	8	33,3	142,2	86,5
	A8	15	219	8,2	109,5	10	22,5	Hammered	12	35,7	171,8	102,4
		17,5	219	8,2	109,5	10	22,5	Hammered	12	38,5	201,5	119,8
		20	219	8,2	109,5	10	22,5	Hammered	12	41,3	231,1	137,2
	A9	22,5	219	8,2	109,5	10	30	Hammered	12	44,5	260,7	154,9
		25	219	8,2	109,5	10	30	Hammered	12	47,6	290,3	172,5
		27,5	219	8,2	109,5	10	30	Hammered	12	50,4	320	191
	A10	30	219	8,2	109,5	10	37,5	Hammered	12	53,3	349,6	209,6
		32,5	219	8,2	109,5	10	37,5	Hammered	12	56,3	379,2	229
		35	219	8,2	109,5	10	37,5	Hammered	12	58,8	408,8	248,4
	B2(open)	7,5	809	9,5	87,2	10	15	Hammered	8	25,2	83	61,1
		10	809	9,5	87,2	10	15	Hammered	8	30,8	112,6	70,5
		12,5	809	9,5	87,2	10	15	Hammered	8	33,3	142,2	86,5
Tilbrooke Grange	NGI-A	5,1	219	16	109,5	9,5	12,5	Hammered	1	270	28	81
		7,6	219	16	109,5	9,5	12,5	Hammered	1	400	51	114
		10,1	219	20	109,5	9,5	12,5	Hammered	1	300	74	145
	NGI-B	22,5	219	16	109,5	10	27,5	Hammered	1	465	305	305
		25	219	16	109,5	10	27,5	Hammered	1	485	340	340
	LDP (open)	8	762	36	305,2	30,5	30,5	Hammered	1	365	55	118
		14,3	762	36	305,2	30,5	30,5	Hammered	1	350	112	200
		26,2	762	36	305,2	30,5	30,5	Hammered	1	460	210	360
Bothkennar	IC-pile	3,5	101,6	?	50,5	4,8	6,0	Jacked	5,6	18,1	27	32,9
		4,7	101,6	?	50,5	4,8	6,0	Jacked	6,6	20,2	38,5	39,7
Cowden	IC-pile	3,8	101,6	?	50,5	3,74	6,24	Jacked	1	138	25,2	56,5
		4,9	101,6	?	50,5	3,74	6,24	Jacked	1	101	38,6	71,2
Canons Park	IC-pile	2,8	101,6	?	50,5	4,06	6,06	Jacked	1	80	18	38
		4	101,6	?	50,5	4,06	6,06	Jacked	1	78	30	50
Empire	PLS	44,7	38,3	?	19	1,2	45,7	Pushed	1,65	66	475	296
		73,6	38,3	?	19	1,2	74,6	Pushed	1,65	116	775	538
	3"-Open	43,0	76,2	Assumed 3	14,8	4,28	45,9	Pushed	1,65	64	457	290
	3"-Closed	48,8	76,2	?	38	6,42	53,8	Pushed	1,65	72	526	328
	1,72"-Closed/x-pi	36,6	43,6	?	21,8	3	37,6	Pushed	1,65	56,5	384	240
Saugus	PLS	10,5	38	?	19	1,2	11,1	Pushed	6	45,9	90	75,1
		12	38	?	19	1,2	12,6	Pushed	6	45,3	105,3	86,5
		13,6	38	?	19	1,2	14,2	Pushed	6	44,7	120,7	98
		19,1	38	?	19	1,2	19,7	Pushed	6	44	175,4	140,5
		25,1	38	?	19	1,2	25,7	Pushed	6	42,4	237,1	185,1
		31,2	38	?	19	1,2	31,8	Pushed	6	49,7	296,9	230,9
		34,9	38	?	19	1,2	35,7	Pushed	6	55,8	333,5	259,3
		35,8	38	?	19	1,2	36,5	Pushed	6	57,1	342,7	265,3
West Delta	LP (open)	14	762	19,1	119,1	71,3	71,3	Hammered	1,5	14	330	51
		23,9	762	19,1	119,1	71,3	71,3	Hammered	1,4	23	450	97
		33,1	762	19,1	119,1	71,3	71,3	Hammered	1,5	29,5	575	137
		42,2	762	19,1	119,1	71,3	71,3	Hammered	1,5	37	700	162
		51,4	762	19,1	119,1	71,3	71,3	Hammered	1,5	46	830	195
		60,5	762	19,1	119,1	71,3	71,3	Hammered	1,7	57	970	223
		68,1	762	19,1	119,1	71,3	71,3	Hammered	1,7	66	1070	252
	3"-Closed	17,7	76,2	?	38	4,28	20,8	Pushed	1,4	17,5	380	67
		45,1	76,2	?	38	4,28	48,2	Pushed	1,5	39	750	178
	3"-Open	45,1	76,2	Assumed 3	21,1	4,28	48,2	Pushed	1,5	39	750	178
		54,3	76,2	Assumed 3	21,1	4,28	57,4	Pushed	1,6	48,5	885	203
		63,4	76,2	Assumed 3	21,1	4,28	66,5	Pushed	1,7	61	1015	235
Hamilton	TP1-JC	6,3	111,9	?	56	12,2	12,2	Jacked	7	18	51	47
	TP3-DC	6,2	111,9	?	56	12,2	12,2	Hammered	7	17,8	50	46
St. Alban	Pile B	2	219	8	109,5	6,1	7,6	Jacked	10,4	11	15,7	19,0
		3	219	8	109,5	6,1	7,6	Jacked	14	14,4	25,5	23,3
		4	219	8	109,5	6,1	7,6	Jacked	16	16	35,3	29,4
		5	219	8	109,5	6,1	7,6	Jacked	17	20	45,2	35,6
		6	219	8	109,5	6,1	7,6	Jacked	22	23,2	55,0	41,7

Test site	Pile name	Depth of measuring	Plasticity index	Water content	Overconsolidat-ion ratio	Coefficient of lateral earth pressure	Direct over active undrained shear strength	Active undrained shear strength	Stifness to strength ratio from Fig. 5.4	Undrained shear modulus from Fig. 5.4	Modulus number	Undrained shear modulus from Eq. 13.8	Excess pore pressure at the pile shaft
		z [m]	I_P [%]	w [%]	OCR [-]	K_0 [-]	s_{uD}/s_{uC} [-]	s_{uC} [kPa]	G_u/s_{uC} [-]	G_u [kPa]	m_0 [-]	G_u [kPa]	Δu_{max} [kPa]
Haga	B-piles	1,9	11	35	8,21	1,52	0,714	58,1	45	3236	16,0	1522	144
		3,4	15	40	3,7	0,87	0,714	57,4	130	3584	16,0	4100	271
Onsøy	A1	7,5	37	64	1,46	0,64	0,725	20,7	150	4459	7,0	3640	76
		10	40	68	1,3	0,62	0,725	24,1	165	5319	6,3	4032	96
		12,5	42,5	65,5	1,3	0,62	0,725	29	165	6222	6,6	5016	135
	A2	15	45	63	1,3	0,61	0,725	31,7	165	7168	6,8	5984	130
		17,5	46	62,5	1,3	0,60	0,725	35,9	165	8222	7,0	7000	161
		20	47	62	1,3	0,60	0,725	38,6	165	9452	7,2	8064	222
	A3	22,5	44,5	58	1,3	0,60	0,725	43,4	230	10674	7,4	9250	210
		25	42	54	1,3	0,59	0,725	47,6	230	12026	7,7	10634	254
		27,5	42	53,5	1,3	0,58	0,725	52,4	230	13440	7,9	12008	282
	A4	30	42	53	1,3	0,58	0,725	57,9	230	14993	8,2	13529	288
		32,5	41	52,2	1,3	0,57	0,725	62,8	230	3236	8,4	15120	315
		35	40	52	1,3	0,57	0,725	67,6	230	3584	8,7	16868	391
	B1(open)	7,5	37	64	1,46	0,64	0,725	21,4	150	4459	7,0	3640	36
		10	40	68	1,3	0,62	0,725	24,1	165	3584	6,3	4032	64
		12,5	42,5	65,5	1,3	0,62	0,725	29	165	5319	6,6	5016	105
	C1	10	40	68	1,3	0,62	0,725	24,1	165	7168	6,3	4032	92
		15	45	63	1,3	0,61	0,725	31,7	165	10070	6,8	5984	137
		20	47	62	1,3	0,60	0,725	38,6	165	12026	7,2	8064	152
		25	42	54	1,3	0,59	0,725	47,6	230	14993	8,2	11329	206
		30	42	53	1,3	0,58	0,725	57,9	230	6246	8,2	13529	276
		35	40	52	1,3	0,57	0,725	67,6	230	6580	8,7	16868	396
Lierstranda	A7	7,5	23	42	2,32	0,77	0,70	36	150	8612	11,5	7027	141
		10	25	43	2,3	0,75	0,70	44	150	10741	10,5	7403	181
		12,5	19	39	2,22	0,75	0,70	47,6	210	13844	11,2	9688	191
	A8	15	16	34	1,92	0,65	0,70	51	240	17074	11,8	12083	183
		17,5	15	33,5	1,62	0,60	0,70	55	280	19965	13,0	15574	232
		20	14	33	1,4	0,56	0,70	59	320	23000	14,0	19208	259
	A9	22,5	13	32,5	1,29	0,53	0,70	63,6	340	25467	14,5	22461	275
		25	12	32	1,2	0,50	0,70	68	360	27947	15,0	25875	308
		27,5	12	30	1,17	0,47	0,70	72	365	30533	15,0	28650	342
	A10	30	12	28	1,15	0,45	0,70	76,1	365	33120	15,0	31440	276
		32,5	12	27,5	1,17	0,45	0,70	80,4	365	6246	15,0	34350	333
		35	12	27	1,12	0,45	0,70	84	370	6580	15,0	37260	326
	B2(open)	7,5	23	42	2,32	0,77	0,70	36	150	8612	11,5	7027	79
		10	25	43	2,3	0,75	0,70	44	150	25920	10,5	7403	120
		12,5	19	39	2,22	0,75	0,70	47,6	220	31920	11,2	9688	130
Tilbrooke Grange	NGI-A	5,1	22	15	34	2,60	0,70	385,7	22	37378	36,0	29160	92
		7,6	22	15	50	2,60	0,70	571,4	18	77267	31,5	35910	69
		10,1	23	15	13	2,15	0,70	428,6	34	81600	29,0	42050	171
	NGI-B	22,5	35	17	12	1,55	0,70	664,3	36	34089	28,5	86925	913
		25	35	17	11,5	1,40	0,70	692,9	37	42667	27,0	91800	292
	LDP (open)	8	22	15	35	2,60	0,70	521,4	22	89600	32,5	38350	420
		14,3	26	15	14	1,80	0,70	500	33	5264	24,0	48000	420
		26,2	32	18	10	1,35	0,70	657,1	39	6352	28,0	100800	1222
Bothkennar	IC-pile	3,5	19	61	2,6	0,95	0,80	22,6	100	15067	18,0	5922	110
		4,7	21	68	2,22	0,90	0,80	25,3	110	18987	18,0	7146	125
Cowden	IC-pile	3,8	19	17	21,5	2,35	0,70	197,1	26	31667	Assumed 30	16950	250
		4,9	18	16	13	1,75	0,70	144,3	34	23333	Assumed 30	21360	260
Canons Park	IC-pile	2,8	54	28	41	1,90	0,75	107	30	21049	?	31667	-60
		4	40	30	32	1,65	0,75	104	36	38258	?	23333	-70
Empire	PLS	44,7	59	46	1,15	0,65	0,775	85,2	250	23324	8,0	23680	488
		73,6	50	38	1,2	0,65	0,775	149,7	360	23324	8,0	43040	893
	3"-Open	43,0	63	45	1,16	0,74	0,775	82,6	250	23324	8,0	23200	327
	3"-Closed	48,8	63	47	1,16	0,74	0,775	92,9	250	10948	8,0	26240	753
	1,72"-Closed/x-p	36,6	63	45	1,20	0,76	0,775	72,9	245	11380	8,0	19200	725
Saugus	PLS	10,5	17	33	4,6	0,95	0,75	61,2	100	11760	16,4	12316	108
		12	20	43	3,8	0,88	0,75	60,4	100	15112	14,8	12802	159
		13,6	26	42	3,2	0,83	0,75	59,6	110	15795	13,5	13230	245
		19,1	18,5	40	2,0	0,68	0,75	58,7	250	19293	12,1	17001	345
		25,1	19	45	1,35	0,60	0,75	56,5	220	21205	9,6	17770	400
		31,2	25	43	1,25	0,58	0,75	66,3	240	21696	9,4	21705	479
		34,9	22	41	1,25	0,58	0,75	74,4	240	3989	9,2	23856	575
		35,8	20	41	1,25	0,58	0,75	76,1	240	10347	9,2	24408	579
West Delta	LP (open)	14	53	70	1,2	0,72	0,75	18,7	180	17658	8,8	4488	101
		23,9	37	50	1,15	0,64	0,75	30,7	250	20880	12,0	11640	110
		33,1	33	42	1,1	0,63	0,75	39,3	260	18027	14,5	19865	100
		42,2	34	39,5	1,1	0,63	0,75	49,3	380	17245	14,5	23490	191
		51,4	47	48	1,15	0,66	0,75	61,3	250	15680	10,4	20280	180
		60,5	58	55,5	1,25	0,71	0,75	76	240	5658	8,7	19401	328
		68,1	65	56	1,3	0,74	0,75	88	230	20094	7,0	17640	481
	3"-Closed	17,7	49	65	1,2	0,70	0,75	23,3	180	20094	9,5	6365	141
		45,1	35	39	1,1	0,63	0,75	52	380	18044	12,7	22606	183
	3"-Open	45,1	35	39	1,1	0,63	0,75	52	380	17756	12,7	22606	122
		54,3	49	52	1,2	0,67	0,75	64,7	245	2089	10,0	20300	259
		63,4	65	57	1,3	0,73	0,75	81,3	230	2044	8,5	19975	348
Hamilton	TP1-JC	6,3	55	97	1,4	0,80	0,80	22,5	155	917	5,0	2350	76
	TP3-DC	6,2	55	97	1,4	0,80	0,80	22,3	155	1243	5,0	2300	55
St. Alban	Pile B	2	80	90	2,02	0,90	0,80	13,8	115	1568	6,0	1140	48
		3	60	80	2,02	0,90	0,80	18	115	2215	6,0	1398	70
		4	40	60	2,01	0,85	0,80	20	115	2595	6,0	1764	94
		5	35	60	2,01	0,85	0,80	25	115	2875	7,0	2492	116
		6	37	60	2,01	0,85	0,80	29	115	3335	7,0	2919	137

14 Regression based on the empirical data

When looking at Figure 9.13 one tries to see a trend based on the plasticity index (I_P) on one axis, and the normalized excess pore pressure ($\Delta u_{max}/s_{uD}$) on the other axis. The data shows no clear trend, however all the soil parameters change from site to site so there is more than just the I_P changing. In Figure 9.11 the overconsolidation ratio and normalized excess pore pressure are plotted. Here the data shows a clear trend, and the trend line proposed by Karlsrud (2012) based on that figure is looked at in Chapter 14.8. Knowing that the overconsolidation ratio (OCR) and the undrained shear strength (s_u) influence the excess pore pressure it is hard to make a two dimensional plot showing the effect of other variables for example I_P. Multivariate analysis is a tool to find patterns and relationships between several variables simultaneously.

14.1 Multivariate linear regression

We will in this chapter go through some basic statistical values and the basic principle of the linear multivariate analysis in an informal way. Equation 14.1 shows the mathematical expression assumed:

$$\hat{y}_i = \alpha_0 + \sum_{i=1}^{p} \alpha_i * x_i \tag{14.1}$$

where x_i is the regressors or input variables, α_i is the parameters and $\hat{y}_i$ is the dependent variable. The residual sum of squares (RSS) is the squared error between the prediction and the measured values summed together for all the data points in the dataset. This can be written mathematically as:

$$RSS = \sum_{i=1}^{n} (y_i - \hat{y}_i)^2 \tag{14.2}$$

where RSS is the residual sum of squares, y_i is the regressand or the measured variable, and $\hat{y}_i$ is the predicted variable found by using Equation 14.1.

The basic principle is to minimize RSS by changing the parameters (α_i). There are many ways to evaluate a regression. We will primarily use the coefficient of determination together with residual plots, maximum error, mean value and standard error. The coefficient of determination (R^2) is defined as:

$$R^2 = 1 - \frac{RSS}{TSS} = 1 - \frac{\sum_{i=1}^{n}(y_i - \hat{y}_i)^2}{\sum_{i=1}^{n}(y_i - \bar{y})^2} \tag{14.3}$$

where TSS is the total sum of squares, defined as the equation indicates, and $\bar{y}$ is the mean value of the measured variable. The R^2 is a number between one and minus infinity. When $R^2 = 1$ then the measured values are predicted perfectly with the regression (i.e. $y_i = \hat{y}_i$). If $R^2 = 0$ then $TSS = RSS$, meaning the mean value ($\bar{y}$) is an equally good prediction as $\hat{y}_i$. If R^2 is negative then the mean value ($\bar{y}$) gives a better prediction than the regression. TSS is closely related to the variance (s^2) as:

$$s^2 = \frac{1}{n}\sum_{i=1}^{n}(y_i - \bar{y})^2 = \frac{TSS}{n} \tag{14.4}$$

where n is the number of data points. Also the standard deviation of the sample (s), is simply the square of the variance. We will use the name standard error when RSS is used in Equation 14.4 instead of TSS. This then gives the difference between the predictions and the measured values on average.

If one adds a parameter then R^2 will always increase in a linear multivariate regression. If the amount of parameters equal the number of data points in the dataset then R^2 will always be equal to one. When comparing two regressions with a different number of parameters it is therefore common to use the adjusted coefficient of determination ($\bar{R}^2$). The RSS and TSS are so called biased estimates of the error and is replaced by unbiased versions (dividing with $n - p - 1$ and $n - 1$, respectively). The $\bar{R}^2$ is then only increasing when the increase in R^2 is more than what one would expect to see by chance.

Written mathematically this gives:

$$\bar{R}^2 = 1 - \frac{RSS}{TSS} * \frac{n-1}{n-p-1} = 1 - (1 - R^2)\frac{n-1}{n-p-1} \tag{14.5}$$

where p are the number of parameters (α_i) used in the regression. $\bar{R}^2$ can then be used to evaluate regressions with a different number of parameters. However, $\bar{R}^2$ can not be used to evaluate regressions where the number of data points (n) differ.

14.2 Statistics of the dataset

We will here present some boundaries and standard statistical values of the dataset presented in Table 13.6. The dataset contains $n = 84$ data points from 12 different sites. The dependent variable is the excess pore pressure at the pile shaft (Δu_{max}). There are 16 regressors. Six of these are related to the pile and contains little uncertainty. These are the measurement depth (z), the pile diameter (D), the pile wall thickness (t), the equivalent pile radius (R_{eq}), the embedded length (L) and the depth of the pile tip (z_{tip}).

The remaining 10 regressors are related to the soil conditions, and are more uncertain. Namely: the sensitivity (S_t), the direct undrained shear strength (s_{uD}), the initial pore pressure (u_0), the initial vertical effective stress (σ'_{v0}), the plasticity index (I_P), the water content (w), the overconsolidation ratio (OCR), the coefficient of lateral earth pressure (K_0), the ratio between direct and active undrained shear strength ($^{s_{uD}}/_{s_{uC}}$), and the undrained shear modulus (G_u) derived by Equation 13.8 as discussed in Chapter 13.2. Table 14.1 shows the range of the different regressors and the mean value in the dataset for the given regressor.

Table 14.1: Mean value and range (minimal-maximal value) of the regressor from the dataset.

Regressor	Mean	Range
z	$21{,}8m$	$1{,}9 \leftrightarrow 73{,}6m$
D	$278mm$	$38 \leftrightarrow 809mm$

t	$11{,}1mm$	$3 \leftrightarrow 36mm$
R_{eq}	$90{,}8mm$	$14{,}8 \leftrightarrow 305{,}2mm$
L	$15{,}0m$	$1{,}2 \leftrightarrow 71{,}3m$
z_{tip}	$28{,}7m$	$4{,}9 \leftrightarrow 74{,}6m$
S_t	$5{,}7$	$1 \leftrightarrow 22$
s_{uD}	$73{,}7kPa$	$11 \leftrightarrow 485kPa$
u_0	$267{,}2kPa$	$-2 \leftrightarrow 1070kPa$
σ'_{v0}	$139{,}5kPa$	$19 \leftrightarrow 538kPa$
I_P	$35{,}0\%$	$11 \leftrightarrow 80\%$
w	$46{,}6\%$	$15 \leftrightarrow 97\%$
OCR	$4{,}87$	$1{,}1 \leftrightarrow 50$
K_0	$0{,}869$	$0{,}45 \leftrightarrow 2{,}6$
s_{ud}/s_{uc}	$0{,}735$	$0{,}7 \leftrightarrow 0{,}8$
G_u	$18394kPa$	$1032 \leftrightarrow 100800kPa$

When using one of the regression lines proposed herein it is important that the regressors used are within the range of the regressors of the dataset. The mean value indicates where the

regression is most dependable, but the residual plot of the regression should also be used to see how well the regression does in the specific range.

Table 14.2 shows similar properties for the dependent variable (i.e. the excess pore pressure at the pile shaft) together with the standard deviation from the mean value.

Table 14.2: Mean value, range (minimal-maximal value) and standard deviation of the dependent variable.

Dependent variable	Mean value	Range	Standard deviation
Δu_{max}	$252{,}9kPa$	$-70 - 1222kPa$	$212{,}9kPa$

If the average direct undrained shear strength ($\bar{s}_{uD}$) and the average undrained shear modulus ($\bar{G}_u$) from Table 14.1 is used in the linear elastic-perfectly plastic (EP) analytical solution (i.e. Equation 5.15) one gets: $\Delta\bar{u}_{max} = \bar{s}_{uD} \ln\left(\frac{\bar{G}_u}{\bar{s}_{uD}}\right) = 73{,}7 * \ln\left(\frac{18394}{73{,}7}\right) = 406{,}8kPa$. The average excess pore pressure found from the dataset, as seen in Table 13.2, is $\Delta\bar{u}_{max} = 252{,}9$. The analytical solution is grossly over-predicting the data on average.

If the Modified Cam Clay (MCC) model is used the average parameters can, as an estimate, be based on $e_0 = 2{,}7w$, $\lambda = \frac{1+e_0}{m_0}$ and $\kappa = \frac{1+e_0}{m_{OC}} = \frac{1+e_0}{5m_0}$ according to Nordal (2018). Using the parameters from Table 14.1 we get: $\bar{w} = 46{,}6\%$, $\bar{e}_0 = 1{,}258$, $\bar{\lambda} = 0{,}182$ and $\bar{\kappa} = 0{,}0364$. Where the average modulus number ($\bar{m}_0$) is found from Table 13.6 to be equal to $12{,}4$. The model from Chapter 11 is then modified so that $u_0 = \bar{u}_0 = 267{,}2kPa$, and $\sigma'_{v0} = \bar{\sigma}'_{v0} = 139{,}5kPa$. Lastly, the inputted vertical overconsolidation ratio equals the average of Table 14.1 (i.e. $\overline{OCR} = 4{,}87$), and the slope of the critical state line (M) is modified so that $\tau_{mob} = \bar{s}_{ud} = 73{,}7kPa$.

This gave $\Delta u = 182{,}8kPa$ at the closest stress point (i.e. $r/r_0 = 1{,}15$). Extrapolating this to the pile surface gave $\Delta u_{max} \approx 195kPa$. Compared to the average excess pore pressure found from the dataset (i.e. $\Delta\bar{u}_{max} = 252{,}9$) this is surprisingly a bit low. However, using the mean values of the data is not the same as using site specific parameters as seen in Chapter 14.3 for the CEM-EP solution. Using site specific data for each case is however quite cumbersome so this is the best estimate of what the CEM-MCC model would give for our dataset.

Based on the information from Chapter 12.6 and Equation 12.7 this gives: $\frac{\Delta u_{max}}{s_{uD}} = \frac{195}{73,7} = \ln\left(\frac{G_u}{s_{uD}}\right) - Aln\left(\frac{OCR}{2}\right) = \ln\left(\frac{18394}{73,7}\right) - Aln\left(\frac{4,87}{2}\right)$. Solved for A one gets $A = 3,23$. This is then compared to the results of Chapter 14.4 and 14.5.

14.3 Comparison between CEM-EP and the empirical data

The excess pore pressure at the pile shaft can, according to the Cavity Expansion Method (CEM) in a linear elastic-perfectly plastic material (CEM-EP, see Chapter 5 and Equation 5.15), be expressed by:

$$\Delta\hat{u}_{max} = s_{uD} \ln\left(\frac{G_u}{s_{uD}}\right) \tag{14.6}$$

If Equation 14.6 is used to estimate the measured excess pore pressure with the soil parameters for the specific sites the mean value becomes $396,6kPa$. Which is higher than the mean found from the measured data (i.e. $252,9kPa$), meaning that the CEM-EP solution over-predicts the excess pore pressure on average. Notice that using the mean undrained shear strength and mean undrained shear modulus of the dataset (Table 14.1) does not give the same result ($\Delta\bar{u}_{max} = 406,8$).

The standard error between the prediction and the measured value is $485,9kPa$. The maximum error is $-2251kPa$ and comes from the Tilbrook Grange site, where the prediction is way too high as Figure 14.1 indicates. This is because of the high strength and stiffness of the soil at this site. As there are no parameters being optimized $p = 0$ and $R^2 = \bar{R}^2 = -4,21$. This means using the mean value of the data set (i.e. $252,9kPa$) for all the sites give a better prediction on average than Equation 14.6.

Figure 14.1 shows the residual plot of the prediction given by Equation 14.6. Residual plots are most commonly plotted with the error in the prediction (i.e. $\Delta u_{max,i} - \Delta\hat{u}_{max,i}$) on the y-axis and the measured dependent variable on the x-axis. It was however chosen to show the measured value ($\Delta u_{max,i}$) on the y-axis, and the predicted value ($\Delta\hat{u}_{max,i}$) on the x-axis. This does in principle not change the information obtained from the plot. If the data point lies on the $x = y$-line then the prediction equals the measured value.

If it lies above the $x = y$-line then the predicted value is too low, similarly if the data point is below the $x = y$-line then the predicted value is too high.

The residual plot should be used to check if there is a lot of data points in the predicted range and also if there is large errors in the predictions for the given range. By using the same system for the sites as previously explained, it is easy to check if the soil conditions at the site where the excess pore pressure is to be estimated are similar to the site defining the regression in a given range.

We see from Figure 14.1 that the Tilbrook Grange site is grossly over-predicted due to the high stiffness and strength. This is also the reason why the mean value of the predictions are too high. Figure 14.2 shows that if the predicted value lies between $0 - 300kPa$ then the predictions seem to correspond relatively well to the data. This also explains why there are discrepancies between reports on whether the linear-elastic perfectly plastic solution is a good or bad estimation.

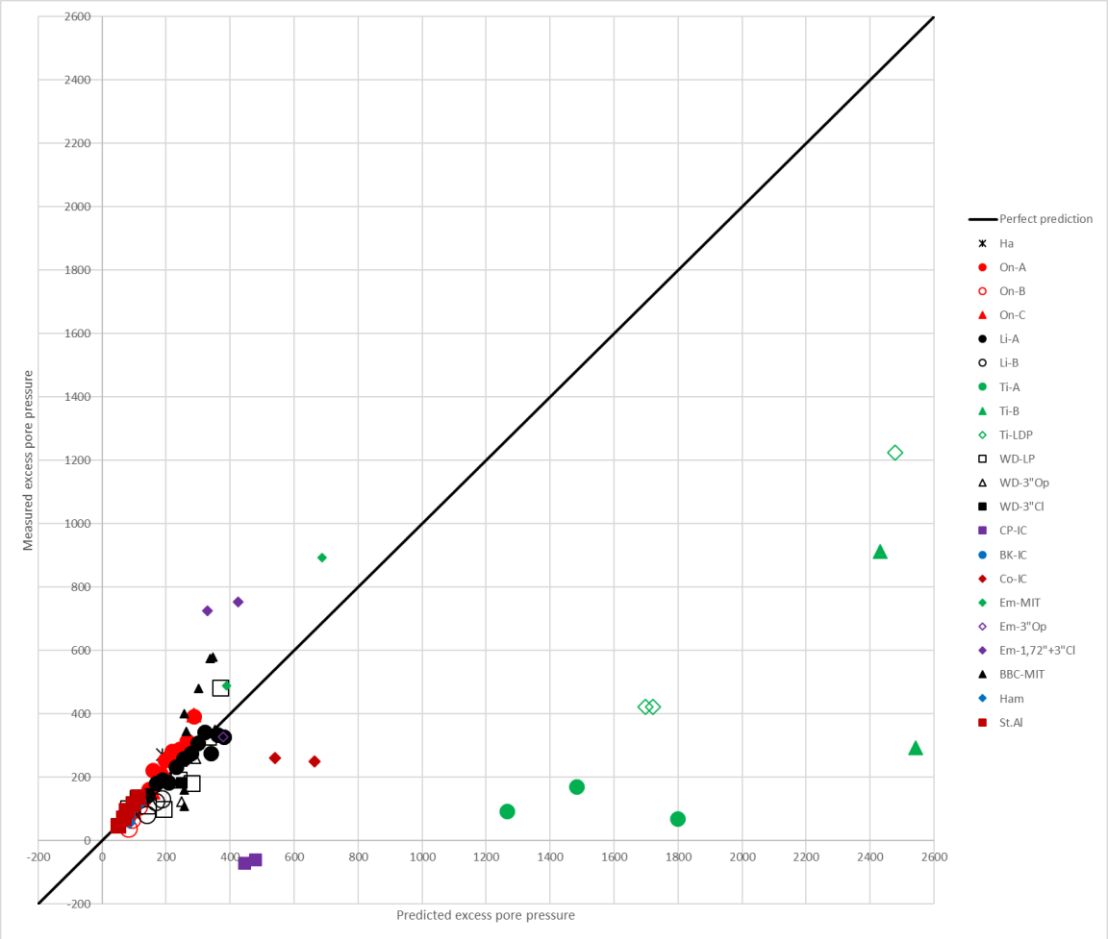

Figure 14.1: Residual plot of the prediction obtained by Equation 14.6 for all sites. Further description of the legend can be found above Figure 9.10.

Looking more closely at the sites in Figure 14.2, it was found that most of the sites (except the Haga site) had an OCR around or below two.

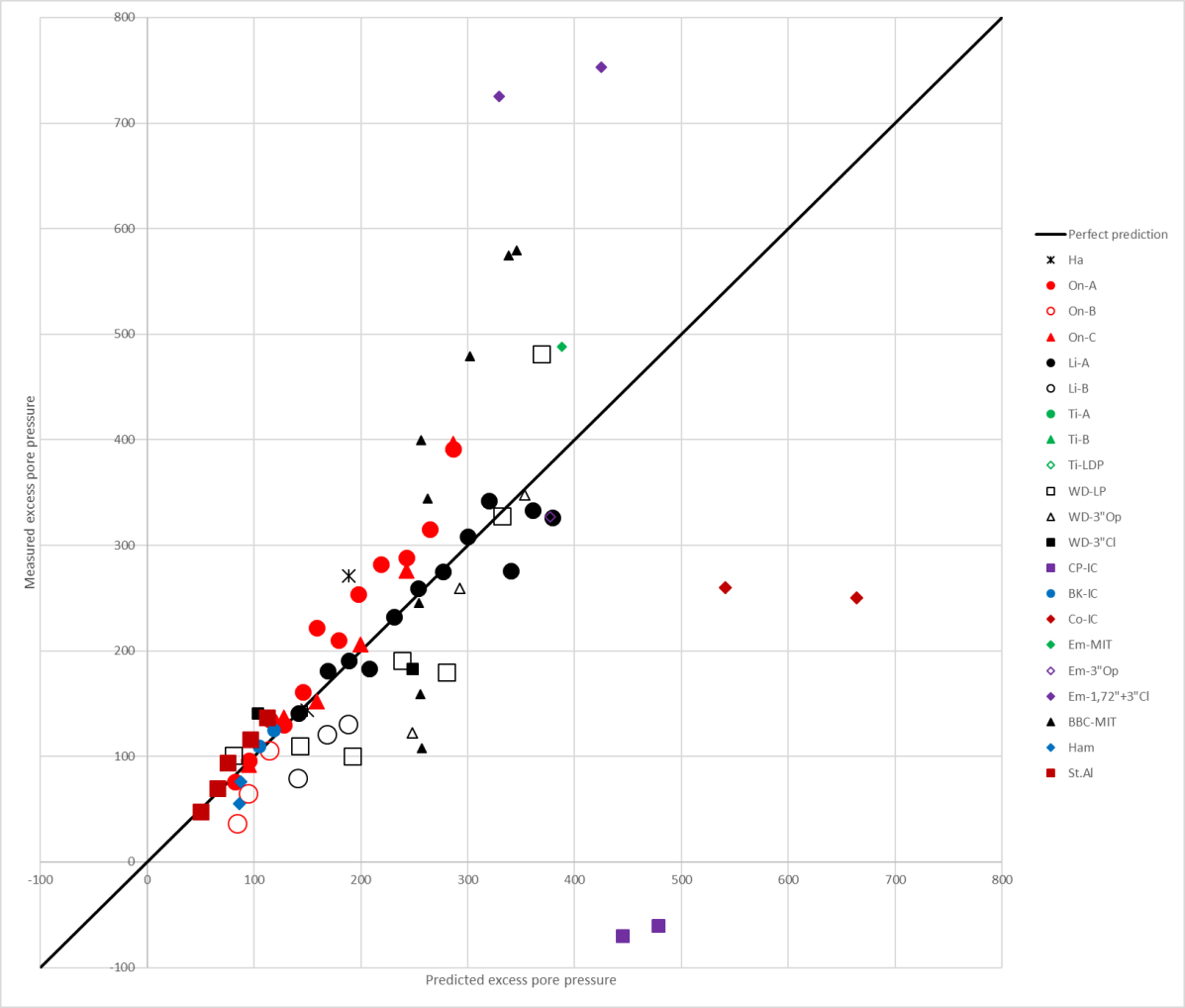

Figure 14.2: Residual plot of the prediction below 800kPa obtained by Equation 14.6. Further description of the legend can be found above Figure 9.10.

Figure 14.3 shows only the data for the sites with OCR less than or equal to two. The analytical solution seems to fit very well when $OCR \leq 2$, except to the measurements done with model sized piles at Empire (Em-1,72"+3"Cl) and Saugus (BBC-MIT).

The adjusted coefficient of determination is $\bar{R}^2 = 0{,}689$ when $OCR \leq 2$, which is a huge improvement. This is however not directly comparable as we have reduced the number of data points from $n = 84$ to $n = 59$, but the scatter plot shows that the fit has improved significantly. It is clear that high OCR affect the excess pore pressure, and that the analytical solution become insufficient. The mean value obtained for the sites with $OCR \leq 2$ is 258,7, while the predicted mean is 226,3. The maximum error is $+396kPa$ for the Empire site (Em-

1,72"+3"Cl). This means that the excess pore pressure is under-predicted on average for the sites with $OCR \leq 2$, and by quite a lot for the Empire site specifically.

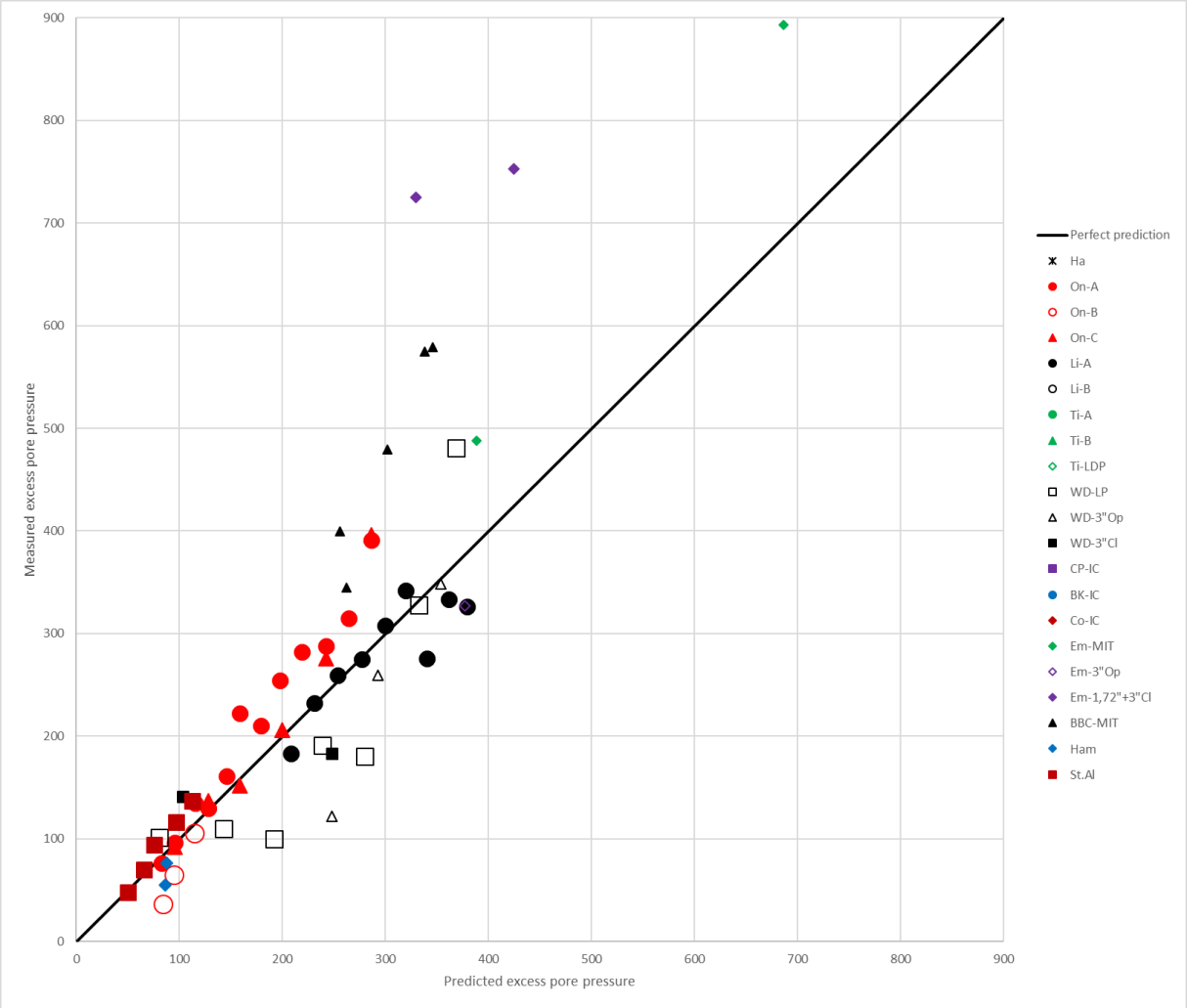

Figure 14.3: Residual plot of prediction obtained by Equation 14.6 for the sites with $OCR \leq 2$. Further description of the legend can be found above Figure 9.10.

The CEM-EP solution was also used with the undrained extension shear strength (s_{uE}) and the undrained compression shear strength (s_{uC}), to check if this gave a better fit. The s_{uE} was assumed to be given by: $s_{uE} = 0{,}5 s_{uD}$ as a crude approximation based on trends suggested by Nordal (2018), while the s_{uC} is given in Table 13.6. Using the entire dataset we got $\bar{R}^2 = -0{,}646$ when using s_{uE}, which is an approvement. This is however only because the high OCR sites are over-predicted. When only looking at the sites with $OCR \leq 2$, the adjusted coefficient of determination became $\bar{R}^2 = -0{,}0233$. This is much lower than that obtained when using the direct undrained shear strength (s_{uD}).

When using s_{uC} we got $\bar{R}^2 = -9{,}30$ which can be expected as using s_{uD} gave too high excess pore pressure on average. For the sites with $OCR \leq 2$ using s_{uC} gave $\bar{R}^2 = 0{,}712$, which is an approvement. However, Figure 14.4 shows that this is not a better fit for most of the sites. The increase in $\bar{R}^2$ is due to the large under-prediction for the Empire site (Em-1,72"+3"Cl). Based on the discussion from Chapter 5.3, the most theoretically correct value is to use the direct undrained shear strength when using the CEM-EP model. For low OCR clays it could be argued that using s_{uC} gives an equally good prediction. However, we see that for most of the sites using s_{uC} gives an over-prediction.

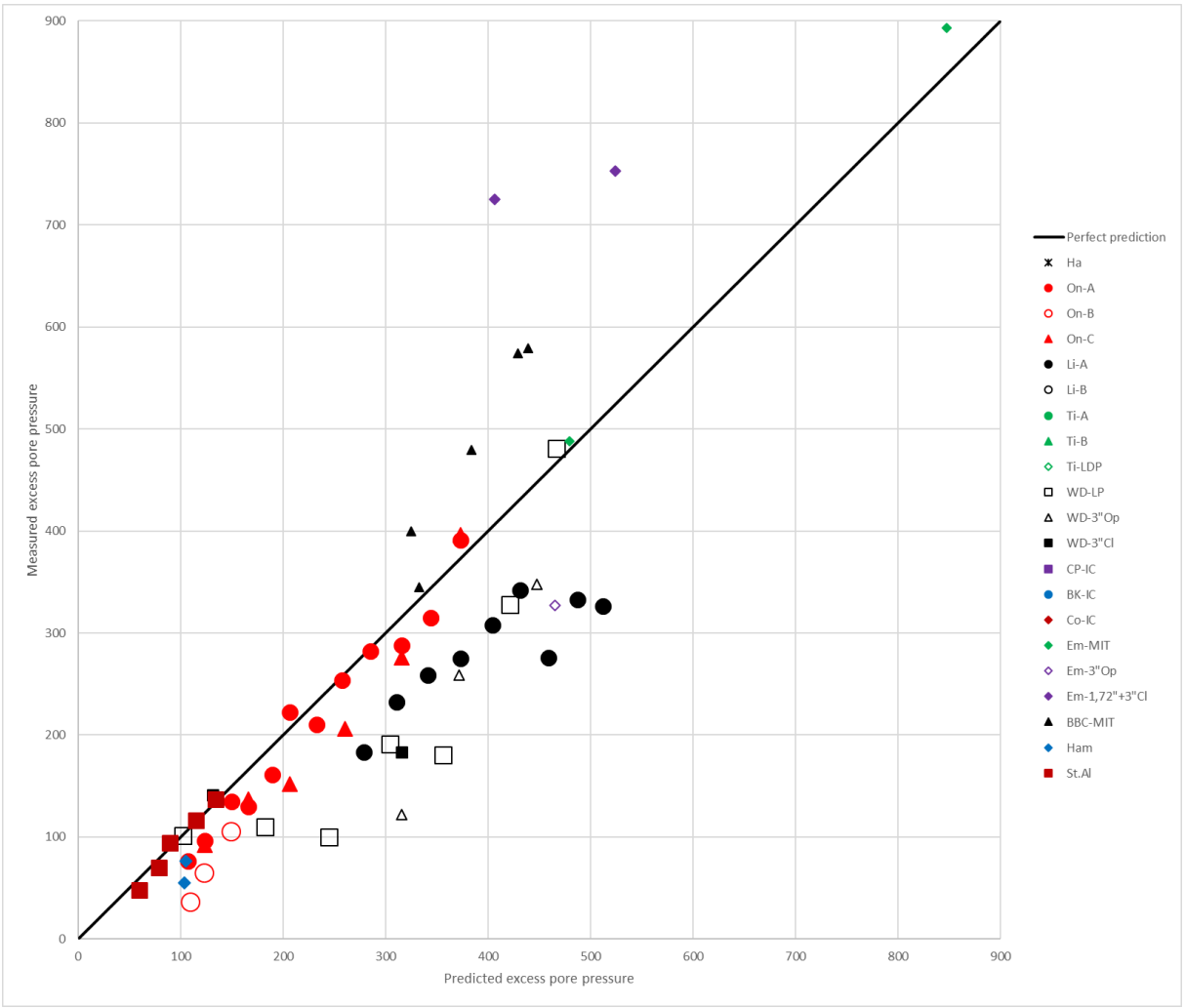

Figure 14.4: Residual plot of prediction obtained by Equation 14.6 with the compression undrained shear strength (s_{uC}) for the sites with $OCR \leq 2$. Further description of the legend can be found above Figure 9.10.

14.4 Regression based on the trend lines found in Chapter 12

Our analysis of the Modified Cam Clay (MCC) model, the linear elastic-perfectly plastic (EP) analytical solution and the effect of an inner remoulded zone in the Cavity Expansion Method (CEM) have led us to the conclusion that the maximum excess pore pressure can be expressed as an equation with s_{uD}, G_u, S_t, OCR and K_0 as input parameters.

The analytical solution simply give:

$$\frac{\Delta u_{max}}{s_{uD}} = \ln\left(\frac{G_u}{s_{uD}}\right) \tag{14.7}$$

The CEM-MCC model gives the exact same solution as the EP solution, given $OCR = 2$ and $K_0 = 1$, explaining the first term in Equation 14.8. The two last terms are based on the results of the numerical analysis in Chapter 12.6. The two factors A and B are positive according to the CEM-MCC model, but may very well depend on the stiffness (G_u) and strength (s_{uD}).

$$\frac{\Delta u_{max}}{s_{uD}} = \ln\left(\frac{G}{s_{uD}}\right) - A * \ln\left(\frac{OCR}{2}\right) + B * \ln(K_0) \tag{14.8}$$

From Chapter 12.7 we found that for a given remoulded limit (i.e. Equation 12.12):

$$\frac{\Delta u_{max}}{s_{uD}} = \ln\left(\frac{G_u}{s_{uD}}\right) - \left(1 - \frac{1}{S_t}\right)\beta \tag{14.9}$$

where β depends on the remoulded limit as seen in Equation 12.13 (see Chapter 12.7). This is however only the correct solution if the softening is modeled according to the model depicted in Figure 12.29. Based on this we might expect the maximum excess pore pressure to be represented by:

$$\Delta\hat{u}_{max} = s_{uD}\left(\ln\left(\frac{G_u}{s_{uD}}\right) - \alpha_1\left(1 - \frac{1}{S_t}\right) - \alpha_2 \ln\left(\frac{OCR}{2}\right) + \alpha_3 \ln(K_0)\right) \tag{14.10}$$

where the parameters (α_i) may be estimated by using multivariate analysis. The resulting factors are given in Table 14.3.

Table 14.3: Result of multivariate analysis of Equation 14.10 optimizing the α_i parameters so that RSS is minimized. The parameters are listed with three significant figures.

α_1	$-2{,}32$
α_2	$2{,}78$
α_3	$3{,}84$

It is worth noticing that $\alpha_1 = -2{,}32$ indicates ${}^{r_r}/_{r_0} = e^{\frac{\alpha_1+1}{2}} = 0{,}52$. Which is a little low according to the Haga site where Figure 2.1 shows a reduction of shear strength to about $0{,}9r_0$ and then an increase to the in-situ value at $3{,}6r_0$. However, this is only one site and the remoulded limit indicate a full reduction to the remoulded shear strength while the values from Haga is indicating also where the shear strength only reduced slightly.

α_2 has the same sign as we found in the numerical analysis, but using the CEM-MCC model we got $\alpha_2 = 4{,}75$ with $s_{uD} = 37kPa$ and $G_u = 7500kPa$. Using the empirical data which have a mean shear strength of $\bar{s}_{uD} = 73{,}7kPa$ and a mean undrained shear modulus of $\bar{G}_u = 18394kPa$, gave $\alpha_2 = 3{,}23$ as seen in Chapter 14.2. This compares quite well, the difference could very well be due to the fact that now the effect of K_0 and S_t is included as well.

α_3 found in the numerical analysis with $s_{uD} = 37kPa$ and $G_u = 7500kPa$ was $2{,}17$, compared to $3{,}84$ found from the empirical analysis. The difference here could very well come from the dependence of α_3 to s_{uD} and G_u, or the inclusion of S_t.

The regression line does show the same trends as the CEM-MCC model. The only factor that has a negative sign (i.e. shows the opposite effect than what we expected) is the α_1 factor and as already explained this could very well be correct due to a low ratio of ${}^{r_r}/_{r_0}$ giving an increase and not a decrease in excess pore pressure due to softening.

The analysis gave a predicted mean excess pore pressure of $267{,}1kPa$ and a standard error of $133{,}5kPa$. The maximum error is $-634kPa$, and comes from the Tilbrook Grange site, as

before. The adjusted coefficient of determination was $\bar{R}^2 = 0{,}592$, found by using Equation 14.5 with $p = 3$.

Figure 14.5 shows the residual plot between the predictions made by Equation 14.10 and the measured values. From the residual plot we see quite a lot of similarities to Figure 14.1. The major difference is that Equation 14.10 correspond much better to the measured values at the Canons Park (CP-IC) and the Cowden (Co-IC) sites. The measurements for the small scaled closed-ended pile at Empire (Em-3"Cl) is grossly under-predicted in both plots. This holds true for all the regression lines proposed herein.

The small scaled piles are driven at a faster rate than the real size piles and this could be the reason for the under-prediction, as mentioned in Chapter 9. However, the consolidation time is proportional to the square of the pile radius and this should counteract such an effect to some extent according to Karlsrud (2012).

In addition, the measurements done at the Tilbrook Grange site (Ti) is much better predicted, but there is still a very large scatter (as the maximum error suggests). The Tilbrook Grange site was found in Figure 14.1 to be the main reason for the over-prediction of the CEM-EP solution. By adding a term reducing the excess pore pressure due to dilation (high OCR) the prediction becomes better for the high OCR sites such as Canons Park, Cowden and Tilbrook Grange.

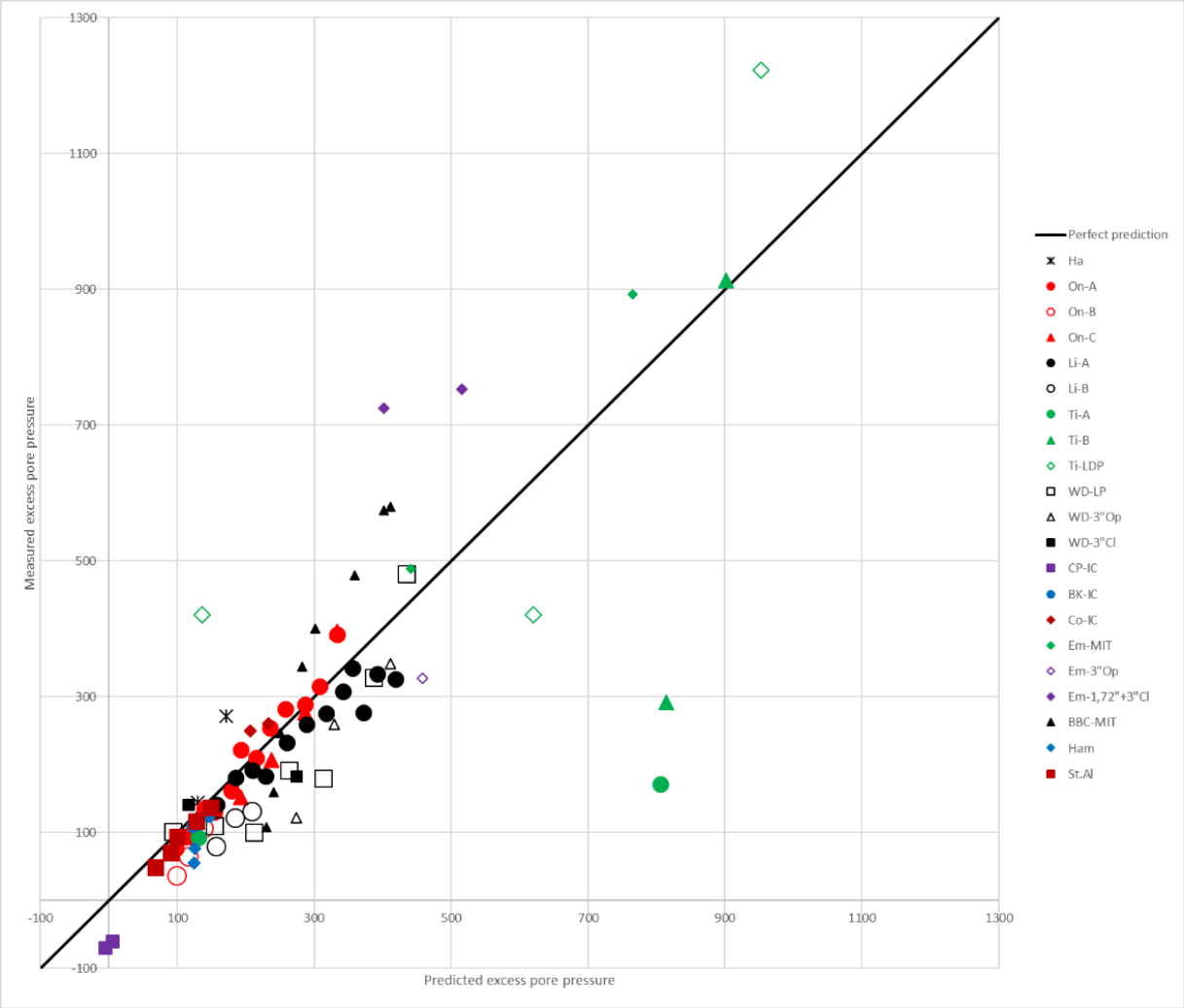

Figure 14.5: Residual plot of prediction made with Equation 14.10 with the parameters as stated in Table 14.3. Further description of the legend can be found above Figure 9.10.

14.5 Regression based on CEM, excluding the effect of K_0

Since the effect of the coefficient of lateral earth pressure on excess pore pressure is somewhat discussable (as discussed in Chapter 13.5), a regression without that term is presented. The prediction is based on Equation 14.11 and the parameters (α_i) is found by minimizing the RSS. The resulting parameters are presented in Table 14.4.

$$\Delta\hat{u}_{max} = s_{uD}\left(\ln\left(\frac{G_u}{s_{uD}}\right) - \alpha_1\left(1 - \frac{1}{S_t}\right) - \alpha_2 \ln\left(\frac{OCR}{2}\right)\right) \tag{14.11}$$

Table 14.4: Result of multivariate analysis of Equation 14.11 optimizing the α_i parameters so that RSS is minimized. The parameters are listed with three significant figures.

α_1	$-0{,}400$
α_2	$1{,}68$

The regression gives a mean excess pore pressure of $266{,}0kPa$, and a standard error of $149{,}0kPa$. The maximum error is $-826kPa$ and is obtained from the Tilbrook Grange site. The adjusted coefficient of determination is $\bar{R}^2 = 0{,}498$. That means there is a quite large drop in $\bar{R}^2$ when leaving out the coefficient of lateral earth pressure from Equation 14.10. In addition, α_2 becomes smaller deviating more from the value found in the numerical analysis in Chapter 14.2 of 3,23.

α_1 increase indicating a remoulded limit of ${}^{r_r}/_{r_0} = e^{\frac{\alpha_1+1}{2}} = 1{,}35$. The Haga site showed that the undrained shear strength was reduced from in-situ values to about $3{,}6r_0$ from the pile surface. Based on this the α_1 cannot be said to be more or less wrong than what we found previously.

Figure 14.6 shows the residual plot, and we see a quite similar picture as in Figure 14.5. The change between Figure 14.1 and Figure 14.5 previously presented was much greater as the $\bar{R}^2$-value indicates. The main change when removing the K_0 term in Equation 14.10 is seen in the high OCR sites. The predictions at Haga (Ha), Tilbrook Grange (Ti), Cowden (Co-IC) and Canons Park (CP-IC) are better when using Equation 14.10 (with the K_0 term) than when using Equation 14.11 (without the K_0 term). These are the sites that change the most between the different regressions proposed.

The K_0 term is also high when the OCR is high, so it makes sense that these sites are most influenced. However, the high OCR sites display large scatter, this will be discussed further in Chapter 14.9. However, having one more parameter to optimize is probably the main reason for the improved fit of the prediction to measurements.

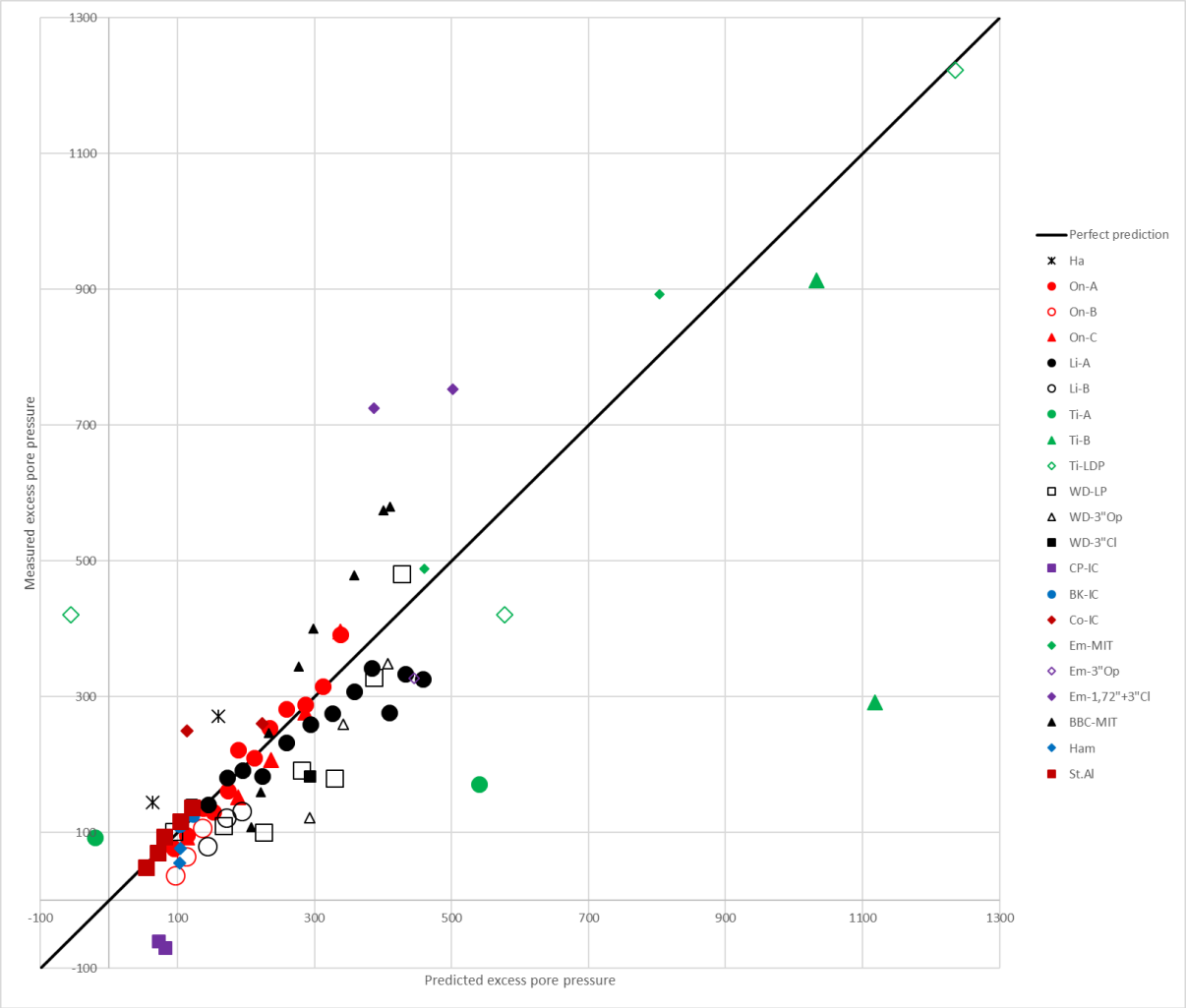

Figure 14.6: Residual plot of prediction made with Equation 14.11 with the parameters as stated in Table 14.4. Further description of the legend can be found above Figure 9.10.

14.6 Regression using the ten most influential regressors

By changing the regressors used in a multivariate linear regression, it was found that when using 10 regressors the highest $\bar{R}^2$-value was obtained when using the measurement depth (z), the equivalent pile radius (R_{eq}), the direct undrained shear strength (s_{uD}), the initial pore pressure (u_0), the initial vertical effective stress (σ'_{v0}), the plasticity index (I_P), the water content (w), the overconsolidation ratio (OCR), the coefficient of lateral earth pressure (K_0) and the undrained shear modulus (G_u) as regressors. Only linear dependence between the regressors and the dependent variable was tested.

This means the excess pore pressure is assumed to be predicted by:

$$\Delta\hat{u}_{max} = \alpha_0 + \alpha_1 * z + \alpha_2 * R_{eq} + \alpha_3 * s_{uD} + \alpha_4 * u_0 + \alpha_5 * \sigma'_{v0} + \alpha_6 * I_P + \alpha_7 * w + \alpha_8 * OCR + \alpha_9 * K_0 + \alpha_{10} * G_u \quad (14.12)$$

where the α_i parameters is found by minimizing the RSS and the result is listed in Table 14.5.

Table 14.5: Resulting parameters from multivariate linear regression of Equation 14.12 with three significant figures.

α_0	α_1	α_2	α_3	α_4	α_5	α_6	α_7	α_8	α_9	α_{10}
-225	10,2	0,454	$-0{,}360$	$-0{,}681$	1,37	$-0{,}128$	0,823	$-10{,}3$	206	0,00376

The predicted mean is equal to that of the dataset (i.e. $252{,}9kPa$) with a standard error of $96{,}6kPa$. The maximum error is $-371kPa$ again for the measurement done at $25m$ depth with the NGI-B pile type at the Tilbrook Grange site. The adjusted coefficient of determination is found to be $\bar{R}^2 = 0{,}762$.

The ten most "important" regressors are those one would expect, except for the fact that K_0 gives a higher correspondence to the data than when included than the sensitivity (S_t). If one use S_t instead of K_0, then the $\bar{R}^2$ reduce by 1,9%, which is quite substantial when having so many regressors and only changing a single one.

Figure 14.7 shows the residual plot of the prediction made by Equation 14.12. Comparing the predictions made by Equation 14.11 and Figure 14.6, to Figure 14.7 we see that the measurements from the Saugus site increase more with depth than what Equation 14.11 estimate. In Figure 14.6 it seems like Equation 14.11 over-predicts the open-ended piles compared to Equation 14.12. In addition we see that Equation 14.12 predicts better the Canons Park (CP-IC), Cowden (Co-IC) and Tilbrook (Ti) sites, which are high OCR sites. The St.Alban (St.Al) site seems, together with the open-ended pile at the Empire (Em-3"Op) site, to be the few places better predicted by Equation 14.11 than 14.12.

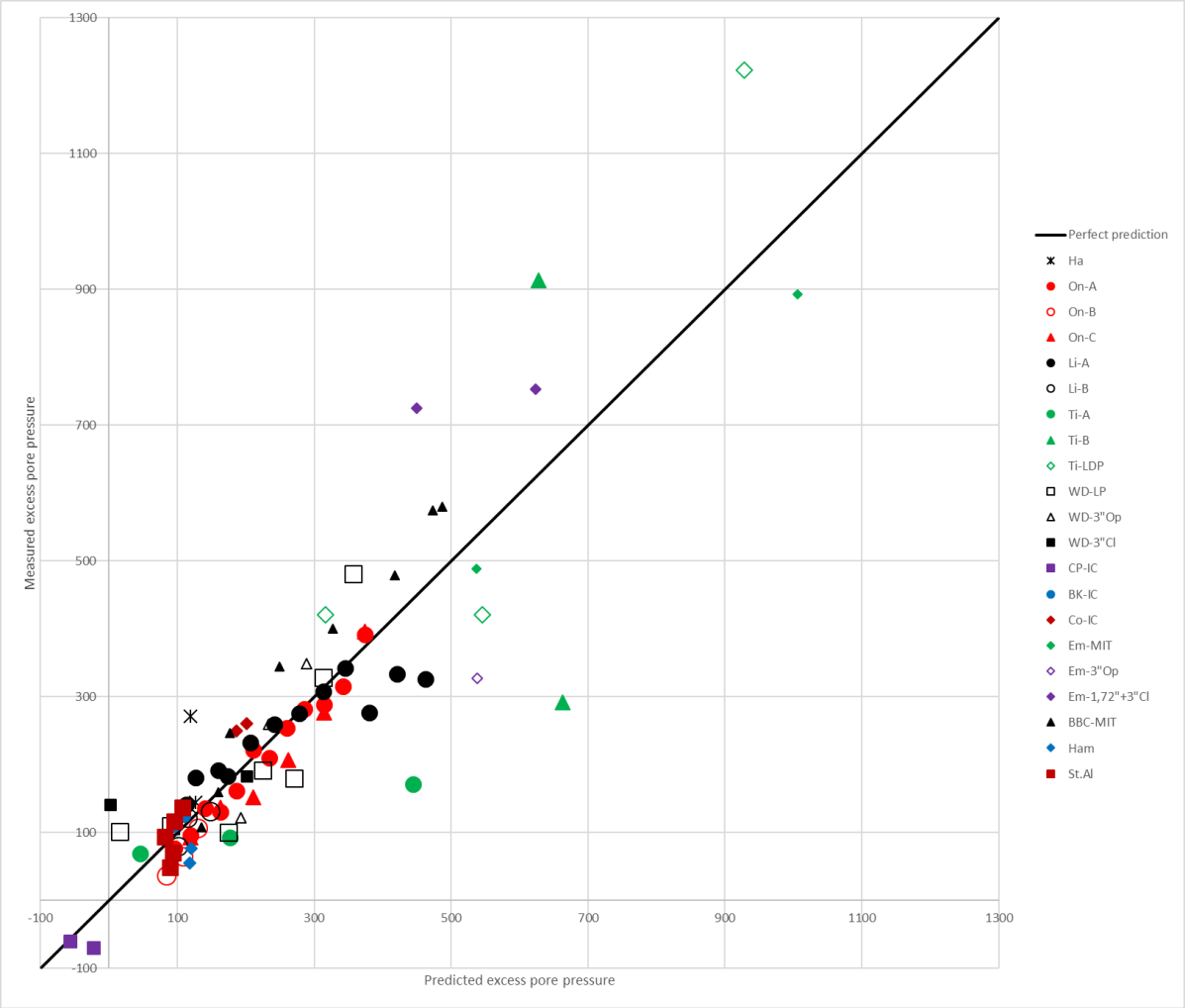

Figure 14.7: Residual plot of prediction made with Equation 14.12 with the parameters as stated in Table 14.5. Further description of the legend can be found above Figure 9.10.

14.7 Regression using the four, three and two most influential regressors

Following the same procedure as in Chapter 14.6, the number of regressors were reduced from then to four. The resulting prediction became:

$$\Delta\hat{u}_{max} = \alpha_0 + \alpha_1 * z + \alpha_2 * R_{eq} + \alpha_3 * \sigma'_{v0} + \alpha_4 * G_u \qquad (14.13)$$

where the α_i parameters is found by minimizing the RSS and the result is listed in Table 14.6.

Table 14.6: Resulting parameters from multivariate linear regression of Equation 14.13 with three significant figures.

α_0	α_1	α_2	α_3	α_4
$-48{,}5$	$-5{,}46$	$0{,}508$	$2{,}90$	$-0{,}00164$

The regression gave that the measurement depth (z), the equivalent radius (R_{eq}), the initial vertical effective stress (σ'_{v0}) and the undrained shear modulus (G_u) were the four most important regressors (of the 16 tabulated) to include in order for the $\bar{R}^2$ to be as high as possible given a linear relationship as shown in Equation 14.13.

Again the regressors one would expect to be of importance is in fact so, except the fact that OCR is not included. The linear-elastic solution gives us a maximum excess pore pressure at the pile shaft only given by the undrained strength and stiffness. However, the size of the excess pore pressure in the field and the extent (i.e. the plastic radius) depend on the pile radius. The fact that the equivalent pile radius trumps the pile diameter and the thickness, might be an indication that reducing the pile radius when a pile is open-ended is correct.

The fact that the initial vertical effective stress is deemed more important than the strength itself is not so troubling as there are multiple proposed relations between s_{uD} and σ'_{v0}. It could very well be that σ'_{v0} is determined more correctly and so the regression gives a higher $\bar{R}^2$ due to this, but it could just as likely be a coincidence or a mistake related to inaccurate measurements. OCR is not included, supprisingly, this might be due to the relations between s_{uD}, σ'_{v0}, G_u and OCR. This is however highly speculative, and based on the discussion of correlation between the regressors, it is just as likely that the regressors that are deemed to be most important are chosen quite randomely.

The depth (z) is not a factor in the analytical Cavity Expansion Method (CEM), but in reality there are many factors that change with depth. Close to the top of the pile there are ground heave due to the pile driving, which most likely cause a change in excess pore pressure. Close to the pile tip there are so called geometry effects. Karlsrud (2012) has removed the data which are closer than about four pile diameters to the pile tip. However, the geometry effect could be affecting the excess pore pressure further up than $4r_0$.

With parameters optimized the resulting mean prediction is still equal to the sample mean (i.e. $252{,}9kPa$), but the standard error increase to $104{,}8kPa$. The maximum error is $-414kPa$, and is from the measurement done at $25m$ depth with the NGI-B pile type at the Tilbrook Grange site, as before. The adjusted coefficient of determination only reduce to $\bar{R}^2 = 0{,}742$ (compared to that of Equation 14.12: $\bar{R}^2 = 0{,}762$). This means that reducing the number of regressors from ten to four only reduce the fit of the regression with 2%.

Figure 14.8 shows the residual plot of the prediction given by Equation 14.13. The figure is quite similar to that of Equation 14.12 (i.e. Figure 14.7). There are minor differences between many of the sites, but only the high OCR sites such as Haga (Ha), Tilbrook Grange (Ti), Cowden (Co-IC) and Canons Park (CP-IC) shows significant change.

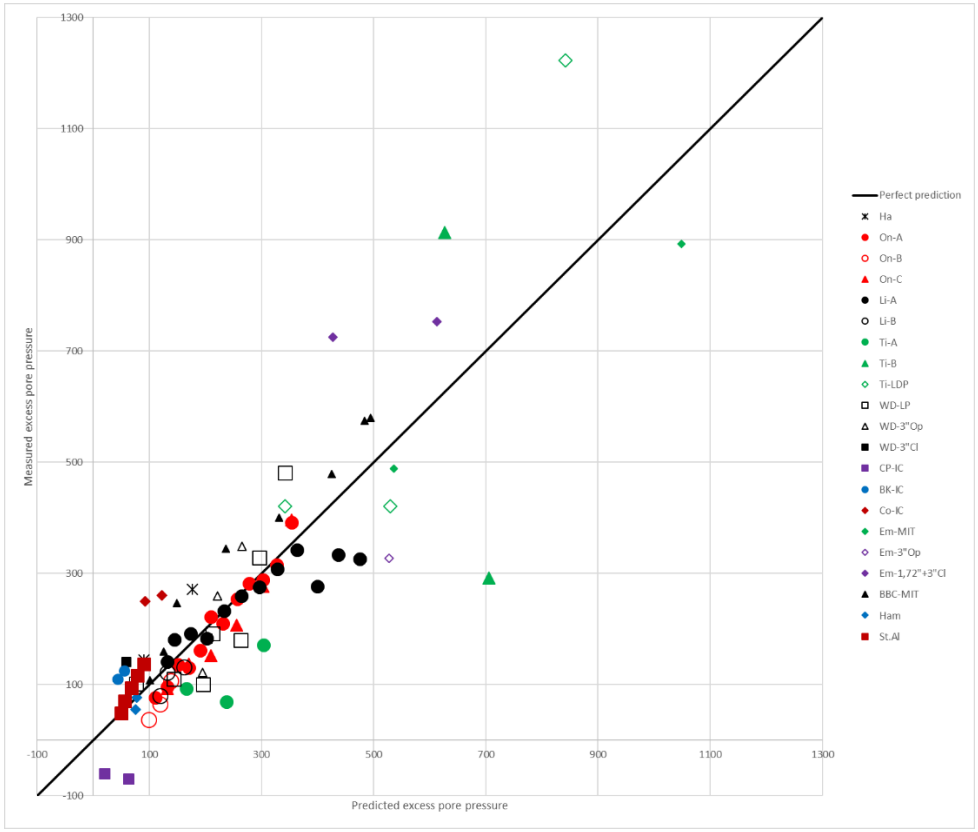

Figure 14.8: Residual plot of prediction made with Equation 14.13 with the parameters as stated in Table 14.6. Further description of the legend can be found above Figure 9.10.

Further reducing the number of regressors to three gave:

$$\Delta\hat{u}_{max} = -5{,}35z + 2{,}74\sigma'_{v0} - 0{,}000589G_u - 1{,}34 \tag{14.14}$$

with $\bar{R}^2 = 0{,}731$. Removing the depth (z) as well gives:

$$\Delta\hat{u}_{max} = 1{,}64\sigma'_{v0} + 0{,}00186G_u - 10{,}9 \tag{14.15}$$

with $\bar{R}^2 = 0{,}697$. If the initial effective vertical stress (σ'_{v0}) is replaced by the direct undrained shear strength (s_{uD}) in Equation 14.15 it is interesting to see that this reduces the $\bar{R}^2$ to 0,462. It could be that using s_{uD} instead of σ'_{v0} gives a lower $\bar{R}^2$-value because G_u and s_{uD} are very much influenced by OCR, while σ'_{v0} is unaffected by OCR. Combining σ'_{v0} and G_u then give more independence from OCR, and then more room to optimize the parameters to fit the data.

14.8 Trend line suggested by Karlsrud (2012)

Karlsrud (2012) suggested a trend line (as seen in Figure 9.11) based on the direct undrained shear strength (s_{uD}), the overconsolidation ratio (OCR) and wheter the pile is open- or closed-ended:

$$\Delta\hat{u}_{max} = \mu s_{ud} * OCR^{-0{,}6} \tag{14.16}$$

where $\mu = 6$ for open-ended, and $\mu = 8$ for closed-ended piles. It is a quite simple expression with essentially three input parameters or regressors. The fit of the expression is however relatively good. Karlsrud (2012) does not say why that exact expression was chosen, but based on Figure 9.11 it makes just as much sense as any other expression. The exponent and the μ factor are probably optimized to fit the data and the results is rather good.

The mean value of the prediction is $250{,}8kPa$ compared to the mean of the dataset of $252{,}9kPa$. The standard error in the prediction compared to the dataset is $126{,}3kPa$. The maximal error is $-604kPa$, and is obtained for the NGI-B pile type measured at $25m$ depth at the Tilbrook Grange site. The adjusted coefficient of determination becomes $\bar{R}^2 = 0{,}635$.

Figure 14.9 shows the residual plot of the expression proposed by Karlsrud (2012). Comparing this to Figure 14.6 shows us mainly two things. The open-ended piles at the West Delta (WD), Empire (Em-3”Op) and Onsøy (On-B) sites are better predicted with Equation 14.16 than Equation 14.11. In addition, the Tilbrook Grange (Ti) site shows a slightly better correspondence to Equation 14.16, but there is however very much scatter in the

measurements from this site. The predictions for the remaining sites compare quite well, but there are of course minor differences.

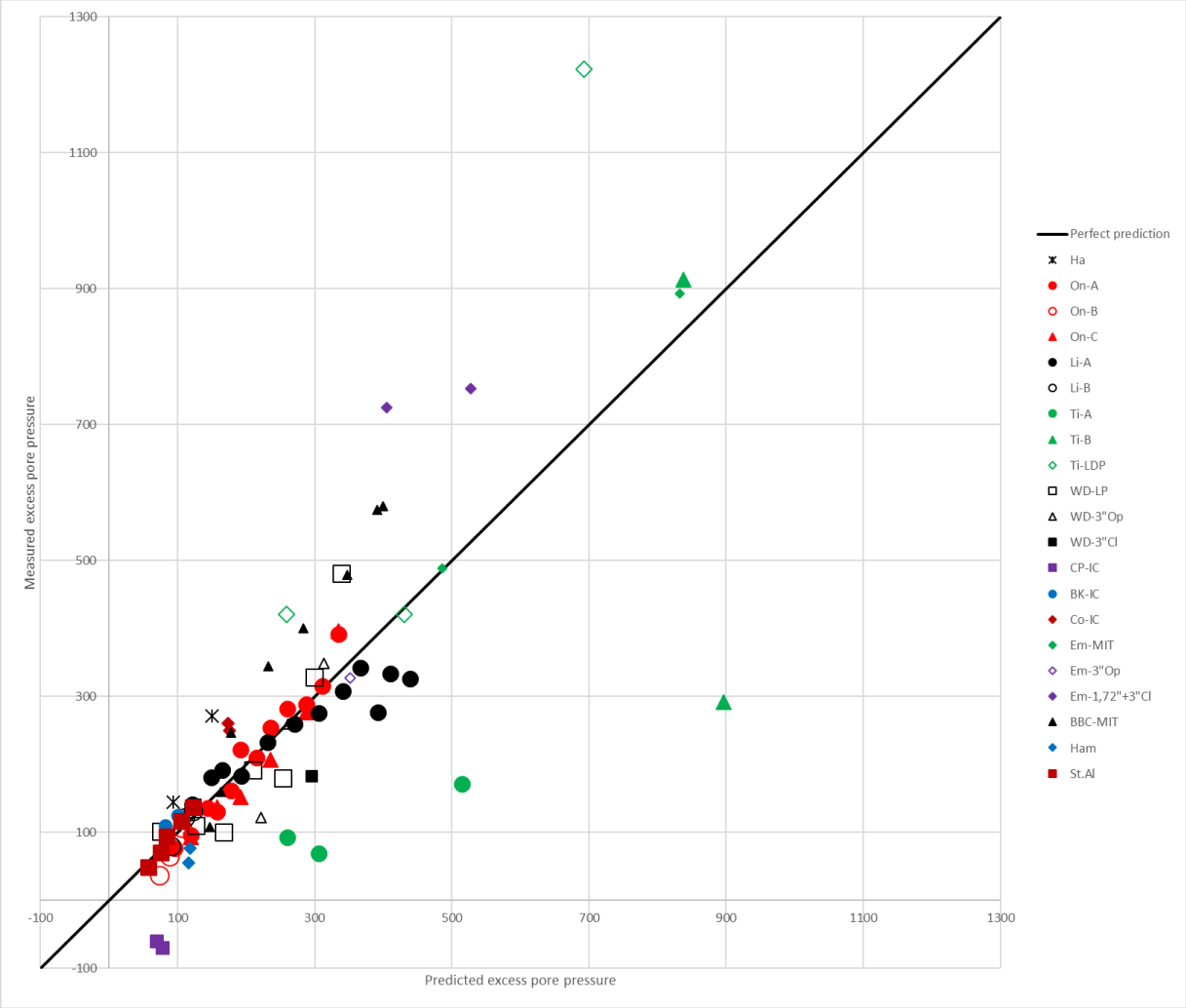

Figure 14.9: Residual plot of prediction made with Equation 14.16 suggested by Karlsrud (2012). Further description of the legend can be found above Figure 9.10.

Equation 14.16 includes the strength, the OCR and wheter the pile is open-ended or closed-ended. The stiffness is not directly included, but since the stiffness is related to the OCR and s_{uD} (as seen in Figure 5.6), one can argue that the stiffness is represented indirectly. Figure 14.10 shows the undrained shear modulus (G_u), against the residual between the measured excess pore pressure and the predicted excess pore pressure based on Equation 14.16 (i.e. the trend line suggested by Karlsrud (2012)), in the same manner as done for the sensitivity in Figure 13.50 in Chapter 13.4, and K_0 in Figure 13.52 in Chapter 13.5. It shows no significant trend, only larger scatter for the sites with high stiffness as we expect due to the correlation between high stiffness and high OCR.

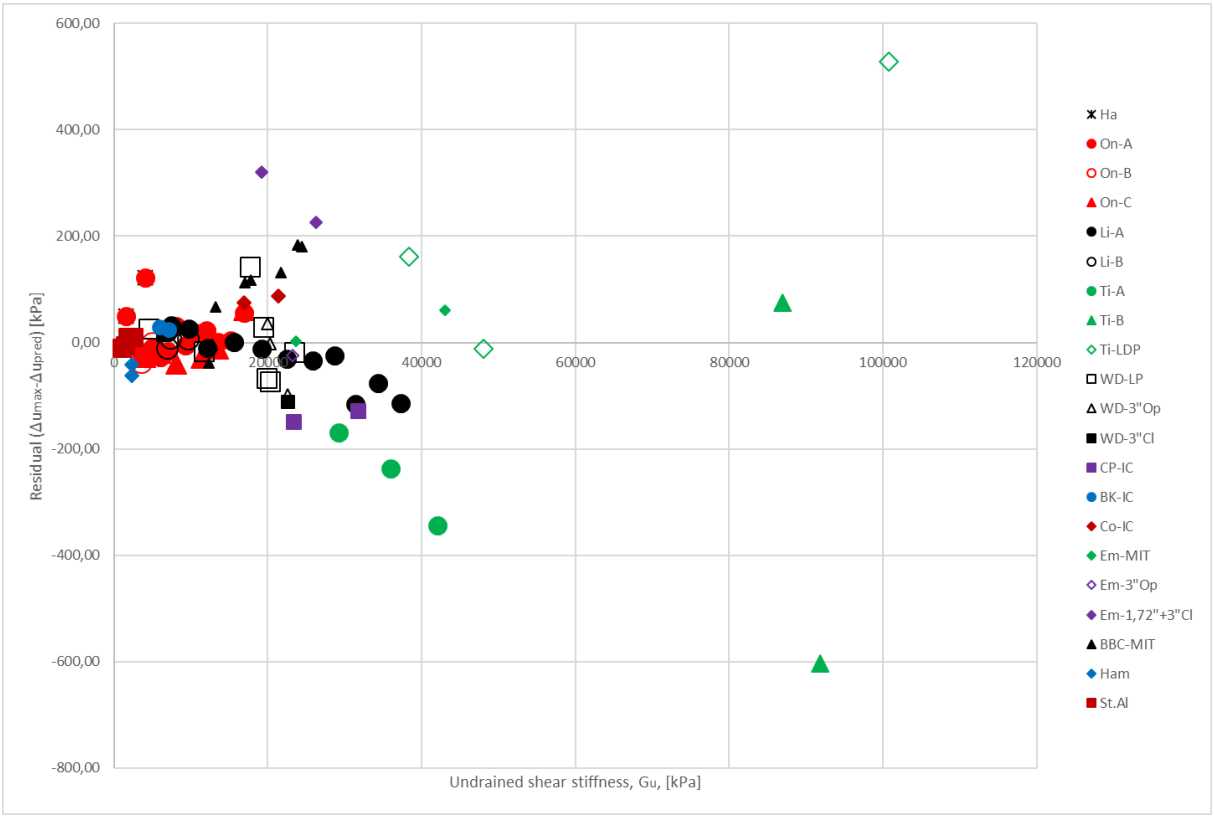

Figure 14.10: Measured excess pore pressure minus predicted excess pore pressure based on Equation 14.16 by Karlsrud (2012) against the undrained shear modulus (G_u). Further description of the legend can be found above Figure 9.10.

The size effect, plasticity index and geometry effect have also been checked for trends by plotting against the residual. In Figure 14.11 the pile diameter (D) is plotted on the x-axis to see if there is a trend with size of the pile. In Figure 14.12 the geometry effect have been checked by using the factor $\frac{z+L-z_{tip}}{L}$ where z is the measurement depth, L is the embedded length, and z_{tip} is the depth of the pile tip, all in meters. This factor is zero if the measurement is done at the top of the pile and one if the measurement is done at the tip of the pile.

Lastly the residual has been plotted against the plasticity index (I_P) in Figure 14.13. Just as Figure 13.50 show no trend with sensitivity Figure 14.11, 14.10 and 14.11 show no significant trend with D, $\frac{z+L-z_{tip}}{L}$ or I_P respectively. If one only includes the closed-ended piles the residual shows a decrease with increasing pile diameter (D). The $R^2 = 0{,}16$ so it could be said that there is a trend of decreasing excess pore pressure with increasing pile diameter for the closed-ended piles. As previously explained, this could be due to the fact that the small scale piles are driven at a faster rate than the full scale piles.

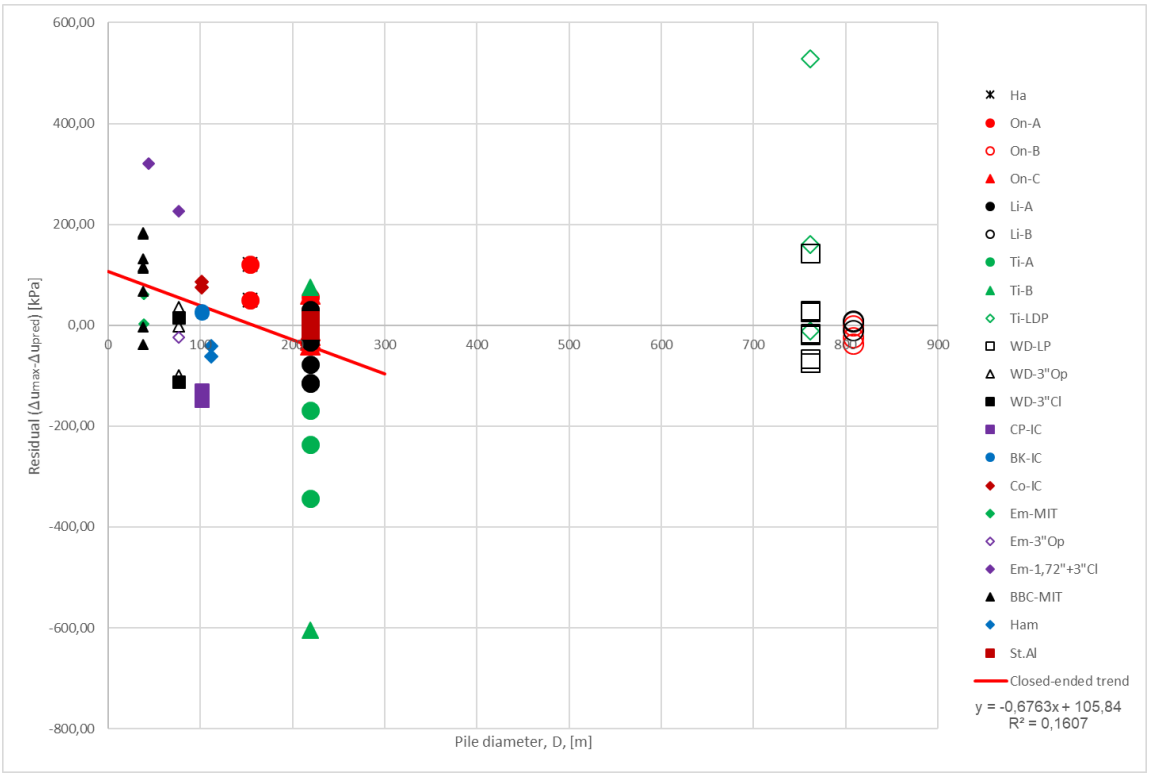

Figure 14.11: Measured excess pore pressure minus predicted excess pore pressure based on Equation 14.16 by Karlsrud (2012) against the pile diameter (D). Further description of the legend can be found above Figure 9.10.

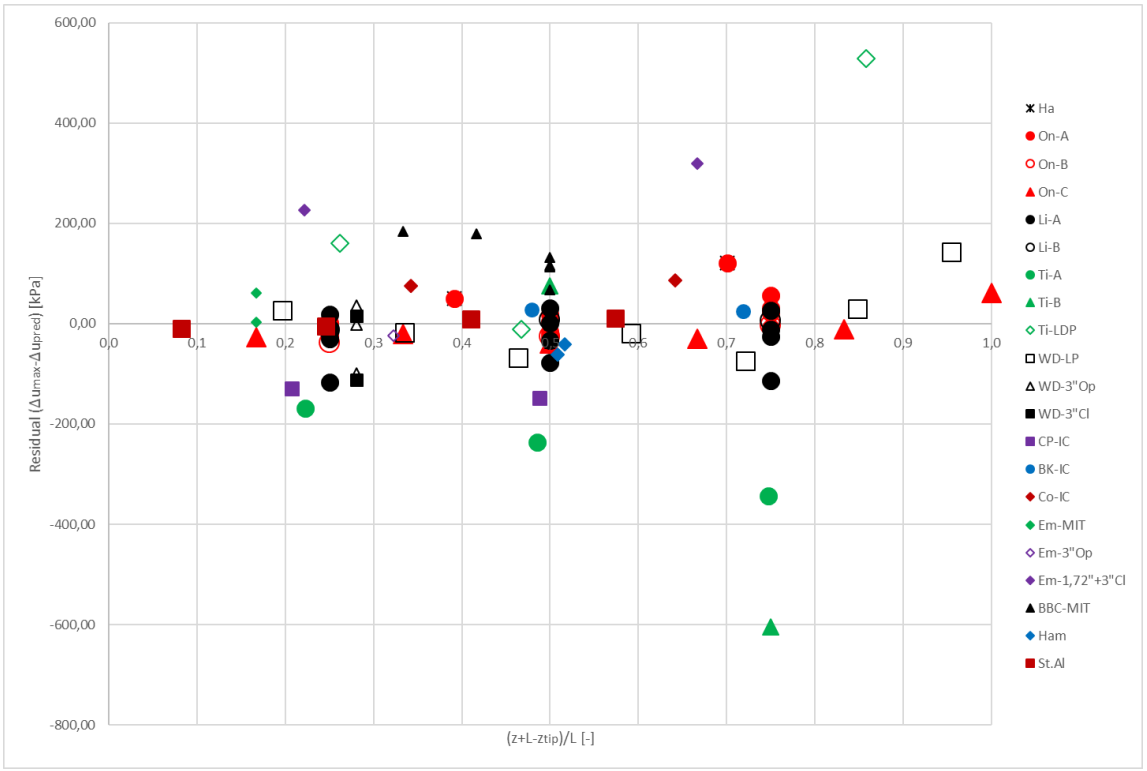

Figure 14.12: Measured excess pore pressure minus predicted excess pore pressure based on Equation 14.16 by Karlsrud (2012) against the factor $\frac{z+L-z_{tip}}{L}$ *where z is the measurement depth, L is the embedded length and* z_{tip} *is the depth of the pile tip. This factor is one if the measurement is done at the pile tip and zero if the measurement is done at the pile top. Further description of the legend can be found above Figure 9.10.*

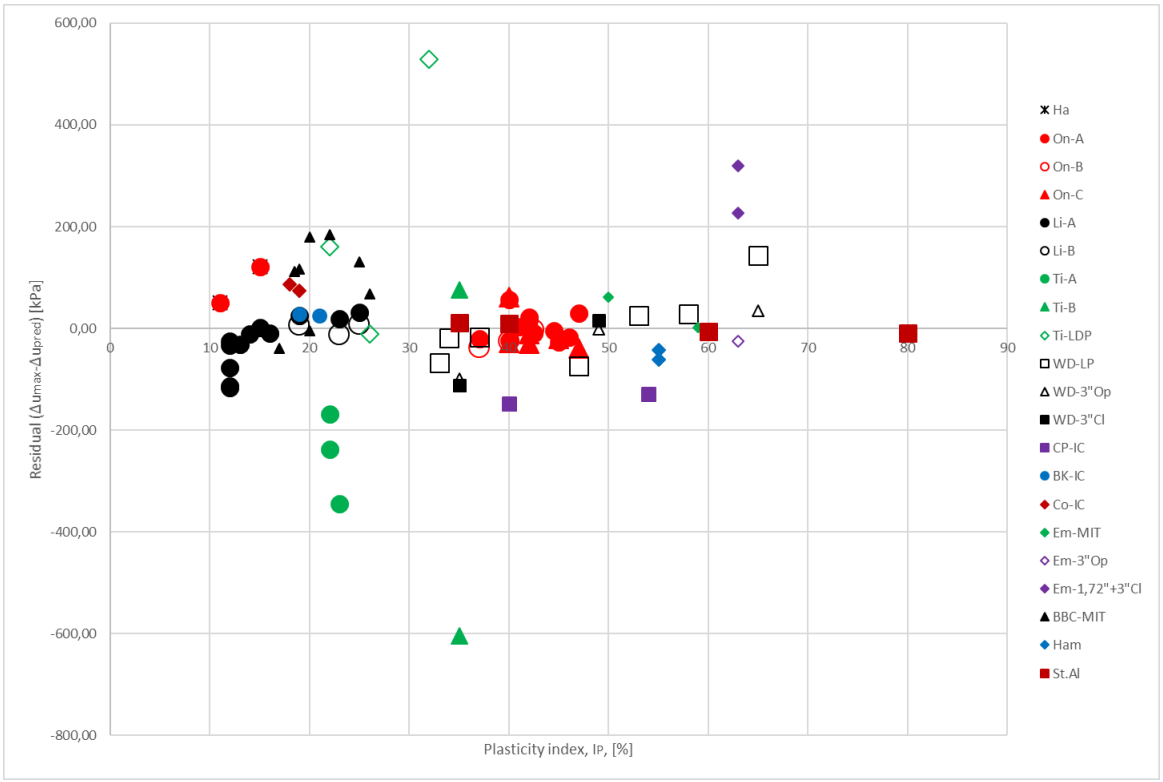

Figure 14.13: Measured excess pore pressure minus predicted excess pore pressure based on Equation 14.16 by Karlsrud (2012) against the plasticity index (I_P). Further description of the legend can be found above Figure 9.10.

Similar plots have been made with the remaining parameters from Table 13.6 on the x-axis. None showed a trend with a R^2-value above 6%. This means there is no parameter in Table 13.6 that if included would give a significant increase in the $\bar{R}^2$-value of Equation 14.16 other than the pile diameter (D). However, only direct relationships was checked, meaning there could be a relationship if different parameters was combined.

14.9 Correlation of the regressors and heteroscedasticity

Looking at the residual plots we see that all the prediction methods show so-called heteroscedasticity as illustrated in Figure 14.14. Heteroscedasticity is the opposite of homoscedasticity, and means that the variance is different for subpopulations. In our case we see that the variance, or standard deviation, between the predicted and the measured excess pore pressure increase as the predicted excess pore pressure increase. High excess pore pressure is mainly related to high strength and stiffness as the analytical solution suggests, and is then also related to high OCR.

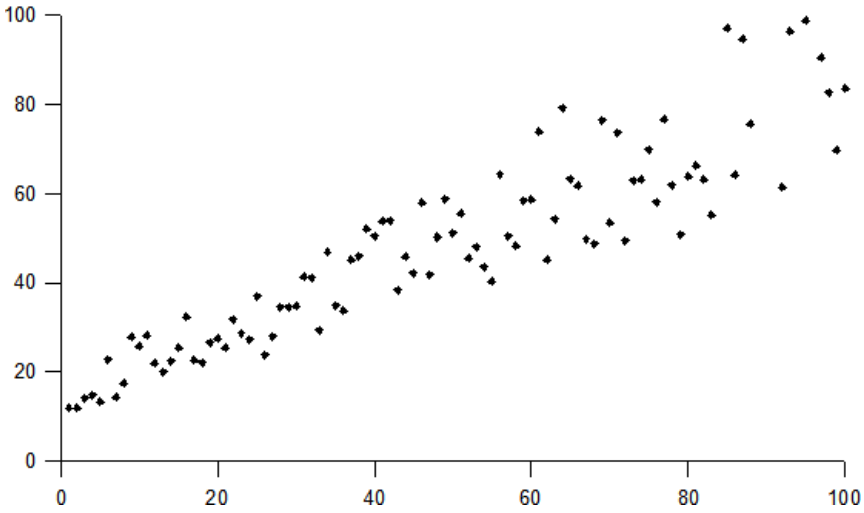

Figure 14.14: Plot of random data showing heteroscedasticity. (Wikipedia)

When doing regression analysis a basic assumption is that the modelling errors are uncorrelated and uniform. The presence of heteroscedasticity is then a concern as it invalidates many statistical tests and methods. The linear multivariate regression is based on this assumption, however the result of the analysis is not automatically wrong due to this. The method tries to minimize the error for all data points equally much, when the variance is actually higher for a certain subgroup. The results from this subgroup should however be given less weight when the error is minimized. How much less weight can be based on the increase in variance, but an assumption on how reliable the data is must be made. This has not been done herein.

In addition to the heteroscedasticity seen in the dataset, we have correlated regressors. We look for trends with the sensitivity (S_t), the coefficient of lateral earth pressure (K_0) and the overconsolidation ratio (OCR). These regressors are seen to be correlated. The sensitivity is seen in Figure 14.15 to be high when OCR is low. These are then negatively correlated, however they are not collinear.

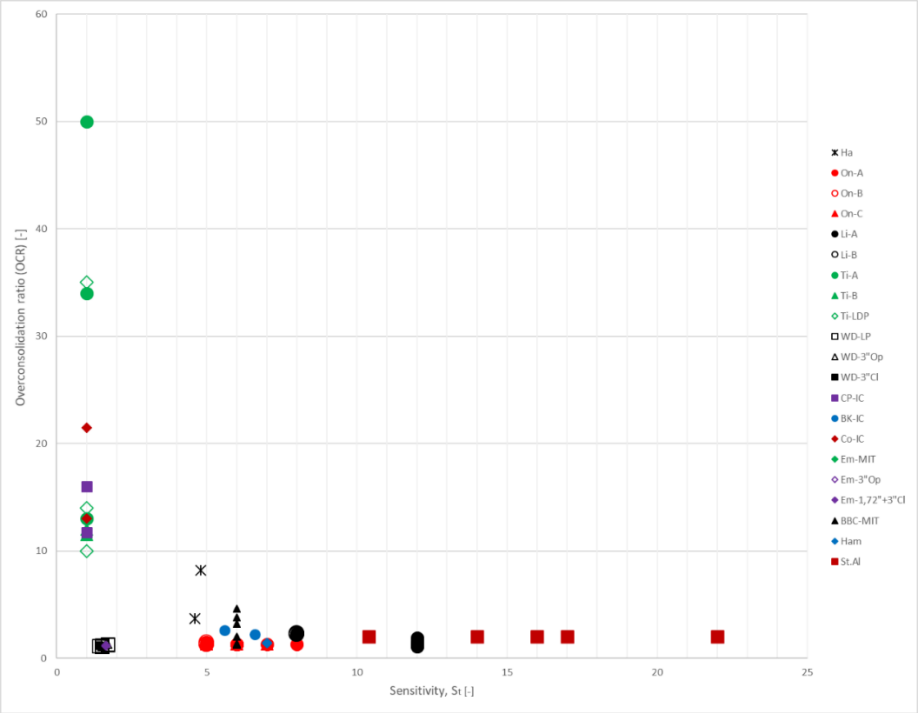

Figure 14.15: Correlation between the overconsolidation ratio (OCR) and the sensitivity (S_t). When OCR is low S_t is high and vice versa, meaning the regressors are negatively correlated. Further description of the legend can be found above Figure 9.10.

Figure 14.16 shows the correlation between the coefficient of lateral earth pressure, and the OCR. We see here a positive exponential correlation.

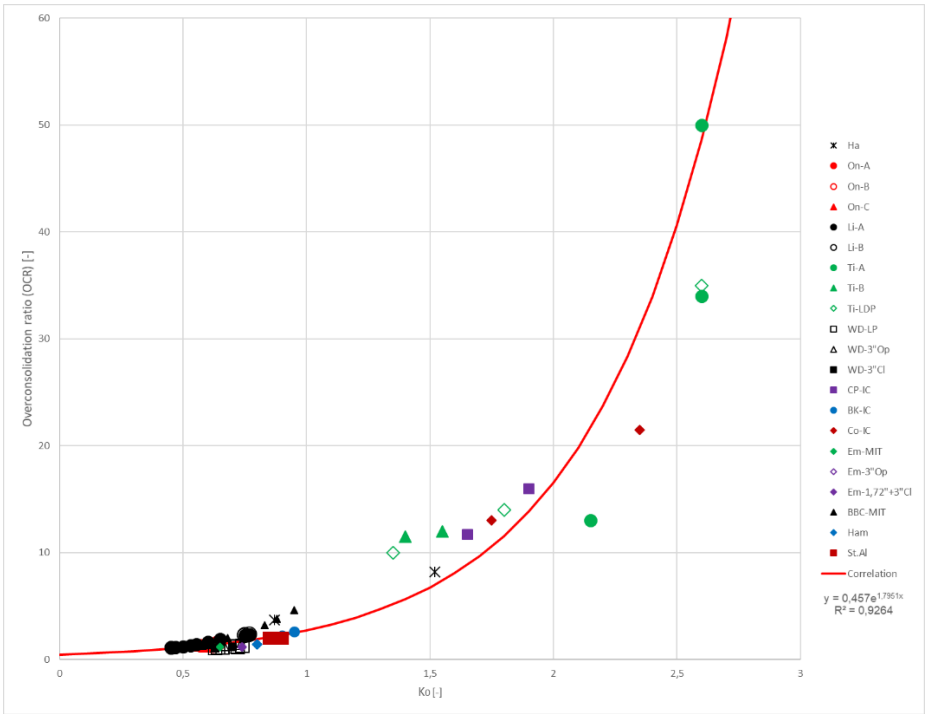

Figure 14.16: Correlation between the overconsolidation ratio (OCR) and the coefficient of lateral earth pressure (K_0). The correlation trend line suggest a positive exponential correlation and with a high coefficient of determination ($R^2 = 0{,}926$). Further description of the legend can be found above Figure 9.10.

Correlation of the regressors means that when optimizing the parameters the assumed effects merge. The parameters (α_i), found in Chapter 14.4 and 14.5, may then change erratically in response to small changes in the dataset, and separating the effect of S_t, K_0 and OCR becomes impossible.

The effect of correlation and heteroscedasticity means that even though Equation 14.11 shows a decrease in $\bar{R}^2$ when removing K_0 from Equation 14.10 we cannot conclude that K_0 is important when predicting the excess pore pressure. This is because the scatter for the high OCR sites give an increase in $\bar{R}^2$ when using more parameters to optimize the fit.

The correlation means that OCR could be used to explain the softening due to S_t, and the increase/decrease in mean stress due to K_0, alone. Due to the known effect of contraction/dilation on excess pore pressure, as seen in Janbu's pore pressure equation (Chapter 3.4, Equation 3.13), we know that OCR will influence the excess pore pressure generated. Due to the correlation, we cannot conclude that sensitivity nor K_0, actually affect the excess pore pressure. This is supported by Figure 13.50 and Figure 13.52 which shows no trend with S_t, and the opposite trend as to what we expect with K_0.

14.10 Conclusions based on the empirical data and the regressions

We have now proposed six different equations together with the trend lines suggested by Karlsrud (2012), and the analytical solution (CEM-EP), for estimating the excess pore pressure due to pile driving, at the pile shaft. The question remaining is then which estimation should be used, and this is also the hardest question to answer. The truth is that none of these methods seems to capture the data in such a way that we believe the equation itself to be accurate. The measured data seems to have too much spread in order for this to be possible to obtain. The spread in data combined with the correlation of the regressors means that drawing definitive conclusions becomes difficult and the results questionable. We will here however try to conclude as much as possible on the limited data.

Looking at all the residual plots presented in Chapter 14 there is a common denominator. The Cowden, Canons Park and Tilbrook Grange sites (i.e. sites of high OCR) change the most between the different prediction methods. At the same time these sites also deviate the most from the trend suggested by the other data. Especially the measurements from the Tilbrook Grange site is deviating.

Karlsrud (2012) reports that the measurement from $20m$ depth with the LDP pile at the Tilbrook Grange site showed an increasing pore pressure, before a peak value was reached 20 days after the pile was driven. At Cowden the delay lasted only a few minutes before the peak pore pressure was reached. Such delays could be an indication of poor filter saturation in the pore pressure measurement equipment.

According to Karlsrud (2012) the dilation of high OCR clays cause negative pore pressure that could desaturate the piezometer filter even if the filter was properly saturated before the pile driving began. This would lead to low values of the pore pressure immediately after pile driving. This could also explain the scatter (higher variance) seen in the data for the high OCR clays.

Some of the regression results have been checked and parameters have been re-optimized for only the sites with $OCR \leq 2$. When the change in parameters is large it could suggest that the scattered data from the high OCR clay sites disturb the regression. However, many of the trend lines suggested are trying to capture the effect of high OCR, and only using the sites with $OCR \leq 2$ will then of course change the optimized parameters. Nonetheless, it is

interesting to see how well the fit of the predictions are to the sites with low OCR clays, and how much the optimized parameters change when removing the sites with high OCR.

If one removes the data from the sites with $OCR > 2$ then the $\bar{R}^2$-values increase for all the estimations proposed herhein. However, all but Equation 14.11 and the trend line suggested by Karlsrud (2012) suggested large change in the optimized parameters. This is not unexpected for the regression lines proposed in Chapter 14.6 and 14.7 as these are only linear best fit, but the major change in parameters for Equation 14.10 was more surprising.

If the sites with $OCR > 2$ is neglected then Equation 14.11 give $\bar{R}^2 = 0{,}746$ without changing the parameters, and the CEM-EP solution give $\bar{R}^2 = 0{,}689$. Adjusting the parameters in Equation 14.11 to only fit the sites with $OCR \leq 2$, gave minor changes in the parameters compared to the other prediction methods ($\alpha_1 = -0{,}400 \rightarrow -0{,}618$ and $\alpha_2 = 1{,}68 \rightarrow 1{,}46$) and $\bar{R}^2 = 0{,}747$.

Including the K_0-term (Equation 14.10) give $\bar{R}^2 = 0{,}767$ without updating the parameters, and $\bar{R}^2 = 0{,}792$ when updating the parameters ($\alpha_1 = -2{,}32 \rightarrow -5{,}13, \alpha_2 = 2{,}78 \rightarrow 7{,}06$ and $\alpha_3 = 3{,}84 \rightarrow 11{,}3$). Based on this the K_0 cannot be said to influence the results substantially. The major decrease we saw in $\bar{R}^2$ (Chapter 14.5) when excluding K_0 was most likely related to removing a parameter that could be used to decrease the error for the high OCR clays. This is supported by the fact that OCR and K_0 is highely dependable, and changing the dataset then gives large changes of the optimized parameters.

The data from the high OCR sites are less dependable and the fact that Equation 14.11 did only change slightly when removing the high OCR clays makes the estimate more trustworthy. The trend line suggested by Karlsrud (2012) gave $\bar{R}^2 = 0{,}793$ without updating the parameters when only including the clays with $OCR \leq 2$. If the parameters were updated they gave $\bar{R}^2 = 0{,}811$ for an exponent of $-0{,}6$ and a factor $\mu = 8 \rightarrow 8{,}72$ for the closed-ended and $\mu = 6 \rightarrow 5{,}98$ for the open-ended piles.

I believe Equation 14.11 and the trend lines suggested by Karlsrud (2012) to give the best estimates as these are somewhat based on what we expect, and show the least change when excluding the data with $OCR > 2$. Equation 14.16 (the trend lines from Karlsrud (2012)) give the highest $\bar{R}^2$-value of the two. This means it is the best fit to the data, but the estimate is made by using three optimized parameters compared to Equation 14.11 which uses two.

Based on Chapter 13.4 it is however questionable if the sensitivity can be said to have an effect at all (see Figure 13.50). In Figure 14.15 we see that OCR and S_t are very correlated in our dataset. This means it is hard to separate the effects from each other. Equation 14.11 includes both, but do not give a higher $\bar{R}^2$-value than the trend lines suggested by Karlsrud (2012). This indicates that the low ratio of $\Delta u_{max}/_{S_{uD}}$ for the high OCR sites might solely be due to the OCR, and that the sensitivity have no effect.

As Figure 14.6 and Figure 14.9 indicates the scatter is large and one should be particularly careful using the estimates for heavily overconsolidated clays. The upside of Equation 14.11 is that it is more theoretically founded where the factors can be explained and represents physical quantities (i.e. the remoulded limit and dilation/contraction). The downside is that OCR and S_t is correlated and the parameters (α_i) may therefore interact during the optimization.

Based on Chapter 14.7 we see that the depth of the measurement (z), equivalent radius (R_{eq}), initial vertical effective stress (σ'_{v0}) and undrained shear modulus (G_u) is deemed the most important regressors in order for the $\bar{R}^2$-value to be as high as possible. The initial vertical effective stress combined with the undrained shear modulus can be used to estimate the undrained shear strength and the overconsolidation ratio. It can therefore be argued that the strength and dilation/contraction is represented. This is however an excuse, and not a reliable conclusion. The trend lines from Karlsrud (2012) also suggests that whether the piles are open- or closed-ended (i.e. equivalent radius) is important for the estimation.

The fact that the depth of the measurement is one of these factors could be due to ground heave or geometry effects due to closeness to the pile tip. However, the trend lines from Karlsrud (2012) do not show a significant trend with any of the parameters from Table 13.6 other than that the pile diameter (D) is seen to increase with decreasing excess pore pressure for the closed-ended piles. This is however probably due to higher driving rate for the small scale piles. Based on this, the main parameters are strength (s_{uD}), OCR and whether the piles are open- or closed-ended. The sensitivity is highly dependent on OCR in our dataset so whether sensitivity is affecting the excess pore pressure or not is questionable based on the empirical data.

Conclusion

In this report we have looked at the prediction of stresses after pile driving in clay, and focused on the excess pore pressure produced as this can be readily checked with measurements. The numerical methods reviewed herein are the Cavity Expansion Method (CEM) and the Strain Path Method (SPM). SPM has not been modeled, but results have been gathered from the literature.

Based on the results presented in Chapter 7 we see that SPM and CEM produce the same radial strains, when studied about $8r_0$ above the pile tip, and this is also seen to correspond well with measurements. SPM introduce the downward motion of installing a pile, giving vertical strains. This also gives an unloading procedure as the pile tip passes, leading to lower stresses than CEM, close to the pile wall (i.e. within about $10r_0$). Far away from the pile wall CEM and SPM is seen to produce quite similar stresses.

The radial effective stress after pile driving is grossly over-predicted by CEM, as seen when comparing Figure 9.12 and Figure 7.8, and SPM is seen to give a much better estimate due to the unloading procedure.

Johansson and Jendeby (1998) finds that the radial total stress decrease much faster than the excess pore pressure due to stress relaxation, as seen in Figure 2.14. This could explain the low radial effective stresses measured after pile driving. Karlsrud, Kalsnes et al. (1993) suggest that vertical silo effects and cylindrical arching may occur in lean clays during the reconsolidation phase. As discussed in Chapter 2.2 this would cause lower radial and vertical effective stress, close to the pile, inside the remoulded zone.

The vertical effective stress is seen to be reduced due to contraction and to increase due to dilation, when CEM is used. If neither dilation nor contraction is included in the material model then CEM will produce no change in vertical effective stress (see Chapter 12). SPM predicts a larger decrease of the vertical effective stress if a strain softening critical state material model is used, as seen in Figure 2.13. If the Modified Cam Clay model is used, SPM is seen to give larger vertical effective stress than CEM. If a strain softening material model is used in CEM, no further change in vertical effective stress is seen, other than that which comes from contraction/dilation.

It could be that the stress relaxation, observed in the radial total stress, also can occur in the vertical total stress. If either this or vertical silo effects do occur, it would lead to lower vertical effective stress. If piles are to be driven in a slope then the vertical effective stress after pile driving is of high importance, as shown in Chapter 2.6. In order to avoid failure it could be necessary to introduce the excess pore pressure without increasing the vertical total stress as a conservative estimate. The presence of permeable layers could drain the excess pore pressure to more critical parts of the slope, and in addition the permeable layers could lose its strength due to the excess pore pressure as well.

The excess pore pressure predicted at the pile shaft by SPM is lower than what CEM predicts. However, the empirical data, gathered by Karlsrud (2012), shows that the analytical linear elastic-perfectly plastic solution with a Tresca yield criterion in CEM (CEM-EP, Equation 5.15) under-predicts the excess pore pressure at the pile shaft on average when only the sites with an overconsolidation ratio (OCR) of less than two is included, as shown by Figure 14.3. Based on this, it could be argued that SPM predicts too low excess pore pressure when $OCR \leq 2$. The reason why SPM better fits the measurements of the radial effective stress, could then be due to stress relaxation or cylindrical arching, while the excess pore pressure is too low due to the unloading procedure introduzed.

Figure 6.13 shows that the measured excess pore pressure at the pile shaft normalized with the direct undrained shear strength ($\Delta u_{max}/s_{uD}$) reduce with increasing OCR. This is expected as G_u^{50}/s_{uD} reduce with increasing OCR (see Figure 5.4). However, the measurements show a steeper decrease with OCR than what Figure 5.4 suggests, as seen in Figure 9.11. This is supported by the fact that CEM-EP grossly over-predicts the excess pore pressure at the sites with $OCR > 2$, as shown by Figure 14.1. This is explained by Janbu's pore pressure equation (Equation 3.13), which shows that the excess pore pressure reduces when the material dilates, and overconsolidated clays are known to dilate.

By using the CEM model described in Chapter 11, strain softening has been modeled by introducing an inner remoulded zone with lower shear strength using the EP material model (see Chapter 12.7). The numerical simulations showed that an expression for the excess pore pressure at the pile shaft could quite easily be rendered for this way of modeling the strain softening (i.e. Equation 12.10). The results showed an increasing excess pore pressure when

the remoulded zone (r_r) over the initial pile radius (r_0) was ${r_r}/{r_0} < e^{1/2}$ regardless of soil sensitivity. If ${r_r}/{r_0} > e^{1/2}$ then the excess pore pressure at the pile shaft would decrease.

Randolph, Carter et al. (1979) and Castro and Karstunen (2010) used more advanced critical state strain softening soil models, and both got an increase in excess pore pressure due to softening. Even though the zone with reduced shear strength extended to ${r}/{r_0} \approx 6$ and ≈ 12, respectively. However, the shear strength was reduced gradually as seen in Figure 6.18 and Figure 12.27, and the models also included contraction when softening, which is known to give a higher excess pore pressure.

The empirical data show an increase in excess pore pressure with increasing sensitivity, as seen in Figure 13.46. The sensitivity is however very correlated to the OCR in our dataset (Table 13.6) as shown by Figure 14.15. This causes the increase in excess pore pressure due to sensitivity to be questionable, and if the residual between the measured excess pore pressure and the trend line proposed by Karlsrud (2012) is plotted against sensitivity (i.e. Figure 13.50) then there is no significant trend. The sensitivity could, however, be partly the reason for the increase, but due to the correlation with OCR in our dataset the two effects merge, and a definitive conclusion cannot be drawn. However, a decrease in excess pore pressure due to sensitivity is highly unlikely, and therefore one should be careful using softening material models that do not include contraction as the material soften.

The CEM-MCC model showed that the excess pore pressure increased logarithmically with the coefficient of lateral earth pressure (K_0), as seen in Figure 12.15. This is because the vertical stress goes towards the mean of the radial and the circumferential stress as described by Chen and Abousleiman (2012), and confirmed in Chapter 12.5. The empirical data did show a decrease in excess pore pressure with increasing K_0 as shown by Figure 13.51. Figure 14.16 shows that also K_0 is very correlated to the OCR. If the residual between the measured excess pore pressure and the trend line proposed by Karlsrud (2012) is plotted against K_0 (see Figure 13.52) we see a much weaker, but still decreasing trend. Based on this, the empirical data cannot be said to support any relation between K_0 and the excess pore pressure. Especially not an increasing excess pore pressure with increasing K_0, as the CEM-MCC model suggests.

If the excess pore pressure at the pile shaft is to be estimated, I would use the trend line proposed by Karlsrud (2012) (Equation 14.16), and then check with the residual plot (Figure 14.9), as this has shown a good fit to the empirical data. One could also go into the site specific data to see if one of the sites have similar soil conditions. Equation 14.11, has a slightly worse fit to the empirical data than Equation 14.16, but can be used as comparison as the equation is based on results from the CEM-MCC model and the results of CEM-EP with an inner remoulded zone, and is then not purely empirical.

CEM and SPM is seen to give a similar radial extent of the excess pore pressure, regardless of material model for low OCR. This extent is also shown to compare quite well with measurements. Equation 5.2 (CEM-EP) can therefore be used as an estimate, as long as the OCR is not very high.

The shape of the radial distribution of the excess pore pressure is seen to be captured quite well by the SPM model. The SPM model propose a near constant value before a log-linear decrease and this kind of shape is seen in Figure 9.2, 9.5, 9.6, 9.8 and 9.9. These figures do however only include measurements from sites with $OCR \leq 4$.

The excess pore pressure at the pile shaft can become negative according to the CEM-MCC model, and this is observed at the Canons Park site. Equation 14.11 can also predict negative excess pore pressure, while Equation 14.16 always give a positive prediction. There is not enough high OCR data in our dataset to conclude on this issue. The distribution and the radial extent of the excess pore pressure for high OCR clays is therefore also very uncertain. If Equation 14.11 gives a negative excess pore pressure at the pile shaft then either SPM or CEM should be used with site specific soil parameters to determine the radial distribution and extent. The empirical data herein does not give sufficient guidance if the OCR is very high, and other sources should be consulted.

Pile groups are seen to give a close to constant excess pore pressure inside the pile group (see Chapter 2.5). The radial extent of the excess pore pressure increase slightly. As a conservative estimate the prediction of the excess pore pressure at the pile shaft can be assumed constant within the pile group, and a slightly larger radial extent should be assumed as well.

Further work

There are quite a few things that can be further worked on. The dataset could be further supplemented and especially measurements of high OCR clays are lacking. More parameters could be determined. The driving rate could be of interest as this is seen to give higher excess pore pressure for some of the small scale piles than what the trend lines suggest. Since the strain rate during pile driving is shown by Baligh (1985) to be 14000 times higher than during an undrained triaxial test, one could use the empirical data suggesting an increase in peak strength, reduction in strain before peak strength, and increase in the softening behavior, to modify the soil parameters and see if this gives a better fit. One could also use the triaxial test results, which have been conducted at many of the sites, to give a better estimate of the undrained shear modulus.

The radial extent of the excess pore pressure could be more thoroughly checked with measurements as the fit of Equation 5.2 is based on limited data. Similarly, empirical data from pile groups can be used to check the assumption of a near constant excess pore pressure within a pile group. A 3D numerical simulation can be conducted expanding multiple cylindrical cavities and the results could be used to check the same assumption.

Most of the SPM simulations have been conducted using Boston Blue Clay (BBC) soil parameters. Especially results of high OCR clays are lacking. This is a cumbersome model to set up, however the results are seen to give a better fit to empirical data, so parametric studies and comparison between SPM and empirical data could be valuable. CEM-MCC could also be modeled with site specific data and then be compared with measurements from multiple sites. This has to the authors knowledge not been conducted, and could lead to a definitive conclusion on whether CEM-MCC gives a good estimate of the excess pore pressure or not.

The effect of pile driving on slope stability needs further work. The prediction of the vertical effective stress is uncertain and comparison between measurements and predictions are sorely needed. Empirical data, either from lab experiments or from the field, could show unknown mechanisms and could give valuable information. In addition, the presence of permeable layers could influence the slope stability as they could lose their strength, and drain the excess pore pressure to more critical parts of the slope. Experiments and modeling could be conducted to illuminate this and the effect on slope stability.

References

Ashour, M. and H. Ardalan (2012). "Analysis of pile stabilized slopes based on soil–pile interaction." Computers Geotechnics **39**: 85-97.

Audibert, J. M. E. and T. K. Hamilton (1998). West Delta 58A site selection and characterization. Offshore Technology Conference, Offshore Technology Conference.

Azzouz, A. S. and D. G. Lutz (1986). "Shaft behavior of a model pile in plastic Empire clays." Journal of Geotechnical Engineering **112**(4): 389-406.

Baligh, M. M. (1975). "Theory of deep site static cone penetration resistance." Massachusetts Inst. of Tech. Report.

Baligh, M. M. (1985). "Strain path method." Journal of Geotechnical Engineering **111**(9): 1108-1136.

Baligh, M. M. and J.-N. Levadoux (1980). Pore pressures dissipation after cone penetration, Massachusetts Institute of Technology, Department of Civil Engineering, Constructed Facilities Division.

Baligh, M. M., et al. (1979). "Exploration and evaluation of engineering properties for foundation design of offshore structures."

Berg-Knutsen, P. (1986). Poreovertrykk i leirige jordarter på grunn av peleramming. Geotechnical Division. Trondheim, University of Trondheim. **Master of Science**.

Bergset, K.-H. (2015). Radial Consolidation of Pore Pressure Induced by Pile Driving. Department of Civil and Transport Engineering. Trondheim, Norwegian University of Science and Technology. **Master of Science**.

Berre, T. (2013). "Test fill on soft plastic marine clay at Onsøy, Norway." Canadian Geotechnical Journal **51**(1): 30-50.

Bishop, A. W. (1954). "The use of pore-pressure coefficients in practice." Geotechnique **4**(4): 148-152.

Bishop, A. W. and D. J. Henkel (1957). The measurement of soil properties in the triaxial test, Edward Arnold (Publishers) Ltd; London.

Bishop, R. F., et al. (1945). "The theory of indentation and hardness tests." Proceedings of the Physical Society **57**(3): 147-159.

Bjerrum, L. (1954). "Geotechnical properties of Norwegian marine clays." Geotechnique **4**(2): 49-69.

Blanchet, R. (1976). Contribution au développement de la technique des pieux flottants foncés dans l'argile sensible. Quebec, Laval University. **Master of Science**.

Bond, A. J. and R. J. Jardine (1991). "Effects of installing displacement piles in a high OCR clay." Geotechnique **41**(3): 341-363.

Bozozuk, M., et al. (1978). "Soil disturbance from pile driving in sensitive clay." Canadian Geotechnical Journal **15**(3): 346-361.

Brinkgreve, R., et al. (2018). Plaxis 2D 2018 Manual, Delft University of Technology and Plaxis.

Budhu, M. (2008). Foundations and earth retaining structures, John Wiley & Sons.

Cao, L. F., et al. (2001). "Undrained cavity expansion in modified Cam clay." Geotechnique **51**(4): 323-334.

Carter, J. P., et al. (1979). "Stress and pore pressure changes in clay during and after the expansion of a cylindrical cavity." International journal for numerical analytical methods in geomechanics **3**(4): 305-322.

Carter, M. and S. P. Bentley (2016). Soil properties and their correlations, John Wiley & Sons.

Castro, J. and M. Karstunen (2010). "Numerical simulations of stone column installation." Canadian Geotechnical Journal **47**(10): 1127-1138.

Chen, S. L. and Y. N. Abousleiman (2012). "Exact undrained elasto-plastic solution for cylindrical cavity expansion in modified Cam Clay soil." Geotechnique **62**(5): 447.

Clark, J. I. and G. G. Meyerhof (1972). "The behavior of piles driven in clay. I. An investigation of soil stress and pore water pressure as related to soil properties." Canadian Geotechnical Journal **9**(4): 351-373.

Collins, I. F. and H.-S. Yu (1996). "Undrained cavity expansions in critical state soils." International journal for numerical analytical methods in geomechanics **20**(7): 489-516.

Coop, M. R. and C. P. Wroth (1989). Field studies of an instrumented model pile in clay, University of Oxford, Department of Engineering Science.

Croce, A., et al. (1973). "In situ investigation on pore pressures in soft clays." Proc., VIII ICSMFE: 53-60.

Dafalias, Y. F. (1987). An anisotropic critical state clay plasticity model. Proc. 2nd Int. Conf. on Constitutive Laws for Engineering Materials: Theory and Applications.

Emdal, A. (2014). Introduksjon til Geoteknikk. Trondheim, Norwegian University of Science and Technology Geotechnical Group.

Gibson, R. E. and W. F. Anderson (1961). "In-situ measurement of soil properties with the pressuremeter." Civil Engineering Public Works Reviews **56**: 615-618.

Group, N. G. (2016). Geoteknikk Beregningsmetoder. Trondheim, Norwegian University of Science and Technology Geotechnical Group.

Hagerty, D. J. and J. E. Garlanger (1972). Consolidation effects around driven piles. Performance of Earth and Earth-Supported Structures, ASCE.

Henkel, D. J. (1960). "The Relationships between the Effective Stresses and Water Content in Saturated Clays." Geotechnique **10**(2): 41-54.

Hight, D. W., et al. (2003). "The characterisation of the Bothkennar clay." Characterisation Engineering Properties of Natural Soils **1**: 543-597.

Hill, R. (1950). "The Mathematical Theory of Plasticity." Oxford University Press.

Hoem, O. (1975). Endring i poretrykk og stabilitet ved ramming av peler i skråninger. Geotechnical Division. Trondheim, University of Trondheim. **Master of Science**.

Janbu, N. (1976). Static bearing capacity of friction piles. Trondheim.

Jardine, R. J., et al. (1985). Field and laboratory measurements of soil stiffness. Proc. 11th International Conference on Soil Mechanics and Foundation Engineering. San Francisco.

Johansson, B. and L. Jendeby (1998). Portycksökningar till följd av pålslagning och dess betydelse för stabiliteten. NCC, Institutionen för Geoteknik Chalmers Tekniska Högskola. **4:** 55.

Jostad, H. P. (2018). Advanced Course in Computational Geotechincs NGI-ADP Model. Trondheim, NGI.

Karlsrud, K. (2012). Prediction of load-displacement behaviour and capacity of axially loaded piles in clay based on analyses and interpretation of pile load test results. Department of Civil and Transport Engineering. Trondheim, Norwegian University of Science and Technology, Faculty of Engineering Science and Technology. **2012:97**.

Karlsrud, K. and T. Haugen (1984). "Cyclic loading of piles and pile anchors-field model tests-Phase II. Final report. Summary and evaluation of test results and computational models." Norwegian Geotechnical Institute, Report **40018**(11): 1.

Karlsrud, K. and T. Haugen (1985). "Behaviour of piles in clay under cyclic axial loading." Results of field model tests. 4th Illt. COllf **11**: 589-600.

Karlsrud, K., et al. (1993). Response of piles in soft clay and silt deposits to static and cyclic axial loading based on recent instrumented pile load tests. Offshore Site Investigation and Foundation Behaviour, Springer**:** 549-583.

Karlsrud, K. and F. Nadim (1990). Axial capacity of offshore piles in clay. Offshore Technology Conference, Offshore Technology Conference.

Karstunen, M., et al. (2005). "Effect of anisotropy and destructuration on the behavior of Murro test embankment." International Journal of Geomechanics **5**(2): 87-97.

Kavvadas, M. (1982). Non-linear consolidation around driven piles in clays, Massachusetts Institute of Technology.

Konrad, J.-M. and M. Roy (1987). "Bearing capacity of friction piles in marine clay." Geotechnique **37**(2): 163-175.

Korhonen, K. H. and M. Lojander (1987). Yielding of Perno clay. Proceedings of the 2nd international conference on constitutive laws for engineering materials. NY: Tucson, Ariz. Elsevier.

Koskinen, M., et al. (2002). "Modelling destructuration and anisotropy of a soft natural clay."

Ladanyi, B. (1963). "Expansion of a cavity in a saturated clay medium." Journal of the Soil Mechanics Foundations Division **89**(4): 127-164.

Lehane, B. M. and R. J. Jardine (1994). "Displacement pile behaviour in glacial clay." Canadian Geotechnical Journal **31**(1): 79-90.

Lehane, B. M. and R. J. Jardine (1994). "Displacement-pile behaviour in a soft marine clay." Canadian Geotechnical Journal **31**(2): 181-191.

Lekhnitskii, S. G. (1963). "Theory of Elasticity of an Anisotropic Elastic Body." Holden-Day, Inc.

Leroueil, S. and P. R. Vaughan (1990). "The general and congruent effects of structure in natural soils and weak rocks." Geotechnique **40**(3): 467-488.

Lo, K. Y. and A. G. Stermac (1965). Induced pore pressures during pile-driving operations. Soil Mech & Fdn Eng Conf Proc/Canada/.

Lunne, T., et al. (2006). "Effects of sample disturbance and consolidation procedures on measured shear strength of soft marine Norwegian clays." Canadian Geotechnical Journal **43**(7): 726-750.

Lunne, T., et al. (2003). "Characterisation and engineering properties of Onsøy clay." Characterisationengineering properties of natural soils **1**: 395-427.

Massarsch, R. (1976). Soil movements caused by pile driving in clay. Stockholm, Ingenjörsvetenskapsakademien.

McCabe, B. A. and B. M. Lehane (2006). "Behavior of axially loaded pile groups driven in clayey silt." Journal of Geotechnical eoenvironmental Engineering **132**(3): 401-410.

Morrison, M. J. (1984). In situ measurements on a model pile in clay, Massachusetts Institute of Technology.

Nash, D. F. T., et al. (1992). "Initial investigations of the soft clay test site at Bothkennar." Geotechnique **42**(2): 163-181.

Nishida, Y. (1963). A basic calculation on the failure zone and the initial pore pressure around a driven pile in clay. Proc., 2nd Asian Conf. Soil Mech. Found. Engrg.

Nordal, S. (2018). TBA4116 Geotechnical engineering, advanced course, Lecture notes and background material. Trondheim, Norwegian University of Science and Technology Geotechnical Group.

Poulos, H. G. (1994). "Effect of pile driving on adjacent piles in clay." Canadian Geotechnical Journal **31**(6): 856-867.

Prévost, J. H. (1977). "Mathematical modelling of monotonic and cyclic undrained clay behaviour." International journal for numerical analytical methods in geomechanics **1**(2): 195-216.

Randolph, M. F., et al. (1979). "Driven piles in clay—the effects of installation and subsequent consolidation." Geotechnique **29**(4): 361-393.

Randolph, M. F., et al. (1979). The effect of pile type on design parameters for driven piles, Cambridge University Engineering Department.

Randolph, M. F. and C. P. Wroth (1979). "An analytical solution for the consolidation around a driven pile." International journal for numerical analytical methods in geomechanics **3**(3): 217-229.

Rochelle, P. L., et al. (1974). "Failure of a test embankment on a sensitive Champlain clay deposit." Canadian Geotechnical Journal **11**(1): 142-164.

Roscoe, K. H. and J. B. Burland (1968). "On the generalized stress strain behaviour of wet clay." Engineering Plasticity: 535-609.

Roscoe, K. H., et al. (1958). "On the yielding of soils." Geotechnique **8**(1): 22-53.

Roy, M., et al. (1981). "Behaviour of a sensitive clay during pile driving." Canadian Geotechnical Journal **18**(1): 67-85.

Roy, M. and M. Lemieux (1986). "Long-term behaviour of reconsolidated clay around a driven pile." Canadian Geotechnical Journal **23**(1): 23-29.

Sandven, R., et al. (2017). Geotechnics Fiels and Laboratory Investigations TBA4110. Trondheim, NTNU Geotechincal divison.

Schofield, A. N. and C. P. Wroth (1968). Critical state soil mechanics, McGraw-Hill London.

Skempton, A. W. (1954). "The pore-pressure coefficients A and B." Geotechnique **4**(4): 143-147.

Svanø, G. (1978). Poretrykksoppbygging rundt pel under ramming. Geotechincal Division. Trondheim, University of Trondheim. **Master of Science**.

Svanø, G. (1981). Undrained effective stress analyses, University of Trondheim.

Tavenas, F. and S. Leroueil (1977). Effects of stresses and time on the yielding of clay. Proceedings of the 9th ICSMFE.

Tavenas, F., et al. (1978). "Creep behaviour of an undisturbed lightly overconsolidated clay." Canadian Geotechnical Journal **15**(3): 402-423.

Terzaghi, K. and F. E. Richart, Jr. (1952). "Stresses in rock about cavities." Geotechnique **3**: 74-78.

Vesic, A. S. (1972). "Expansion of cavities in infinite soil mass." Journal of the Soil Mechanics and Foundations Division **98**: 265-290.

Wheeler, S. J., et al. (2003). "An anisotropic elastoplastic model for soft clays." Canadian Geotechnical Journal **40**(2): 403-418.

Whittle, A. J. (1987). A constitutive model for overconsolidated clays with application to the cyclic loading of friction piles, Massachusetts Institute of Technology.

Whittle, A. J. (1992). Assessment of an effective stress analysis for predicting the performance of driven piles in clays. Offshore site investigation and foundation behaviour, Springer**:** 607-643.

Wikipedia. "Heteroscedasticity." Retrieved 13.05, 2019, from https://en.wikipedia.org/wiki/Heteroscedasticity.

Wood, D. M. (1990). Soil behaviour and critical state soil mechanics, Cambridge university press.

Yu, H.-S. (2000). Cavity Expansion Methods in Geomechanics. Dordrecht, Springer Netherlands : Imprint: Springer.

Yu, H.-S. and G. T. Houlsby (1991). "Finite cavity expansion in dilatant soils: loading analysis." Geotechnique **41**(2): 173-183.

Appendix A

A.1 Stress paths from CEM-MCC varying the *OCR*

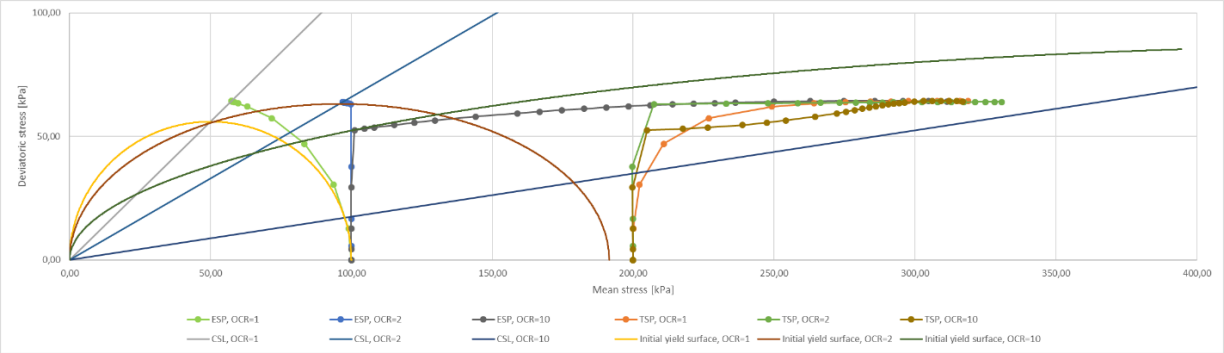

Figure A.1.1: Effective stress path (ESP) and total stress path (TSP) together with the critical state line (CSL) and the initial yield surface for different OCR, with the deviatoric stress (q) on the vertical axis and the mean stress (p', p) on the horizontal axis. Found by using the Cavity Expansion Method (CEM) and the Modified Cam Clay (MCC) model with parameters as in Table 12.2, but with M varying so that $s_u = 37kPa$ for the different values of OCR. The data is gathered from a stress point at $r/r_0 = 2$.

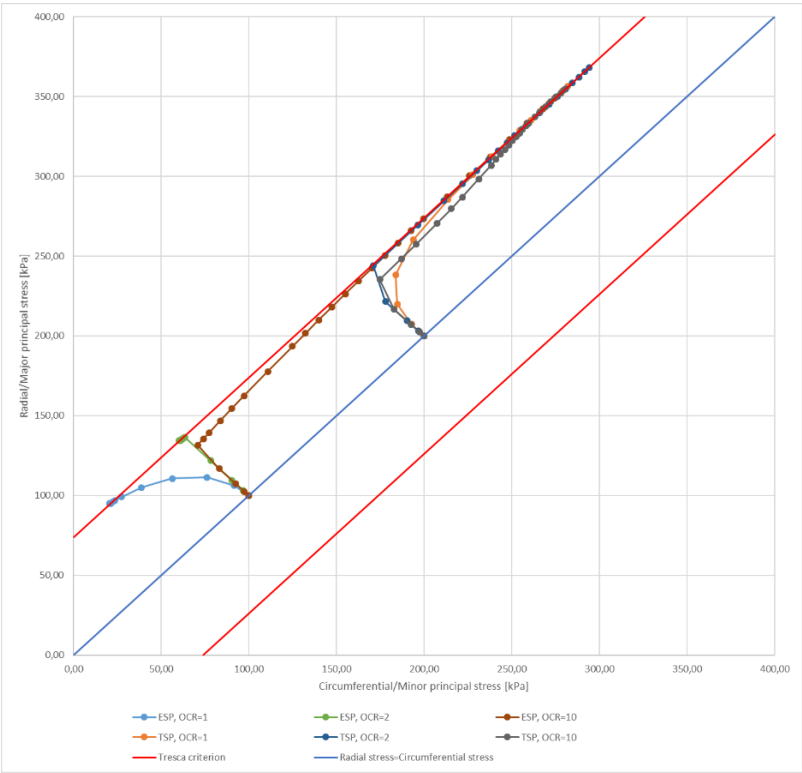

Figure A.1.2: Effective stress path (ESP) and total stress path (TSP) together with the Tresca yield criterion for different OCR, with the radial/major principal stress ($\sigma_r' = \sigma_1'$, $\sigma_r = \sigma_1$) on the vertical axis and the circumferential/minor principal stress ($\sigma_\theta' = \sigma_3'$, $\sigma_\theta = \sigma_3$) on the horizontal axis. Found by using the Cavity Expansion Method (CEM) and the Modified Cam Clay (MCC) model with parameters as in Table 12.2, but with M varying so that $s_u = 37kPa$ for the different values of OCR. The data is gathered from a stress point at $r/r_0 = 2$.

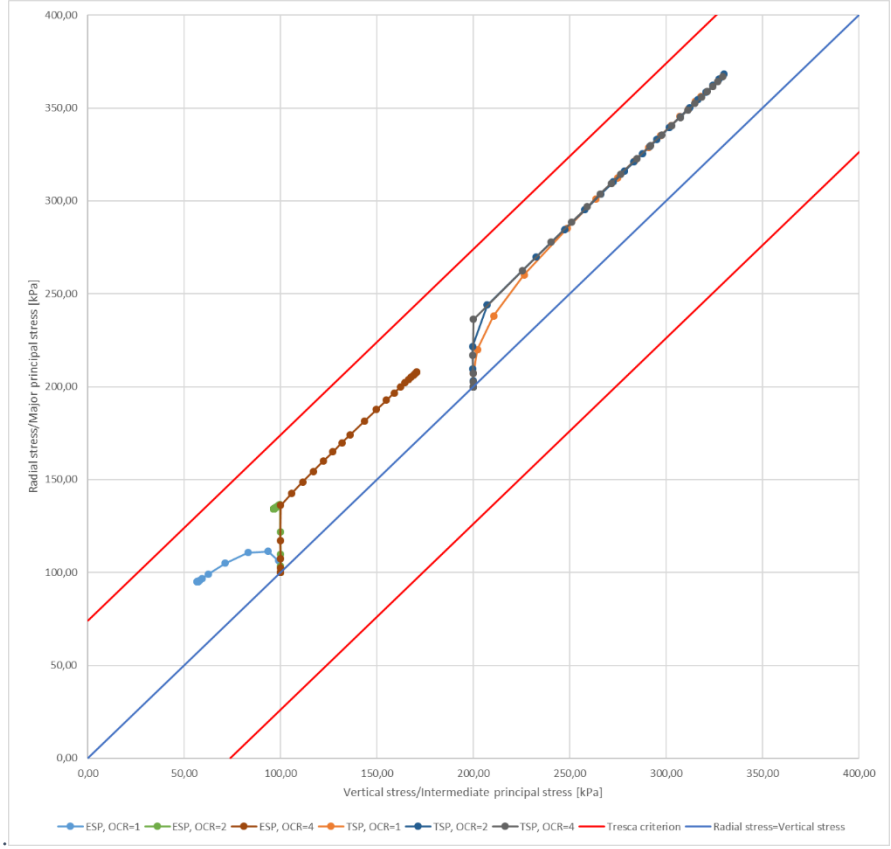

Figure A.1.3: Effective stress path (ESP) and total stress path (TSP) together with the Tresca yield criterion for different OCR, with the radial/major principal stress ($\sigma_r' = \sigma_1'$, $\sigma_r = \sigma_1$) on the vertical axis and the vertical/intermediate principal stress ($\sigma_z' = \sigma_2'$, $\sigma_z = \sigma_2$) on the horizontal axis. Found by using the Cavity Expansion Method (CEM) and the Modified Cam Clay (MCC) model with parameters as in Table 12.2, but with M varying so that $s_u = 37kPa$ for the different values of OCR. The data is gathered from a stress point at $r/r_0 = 2$.

A.2 Stress paths from CEM-EP varying the K_0

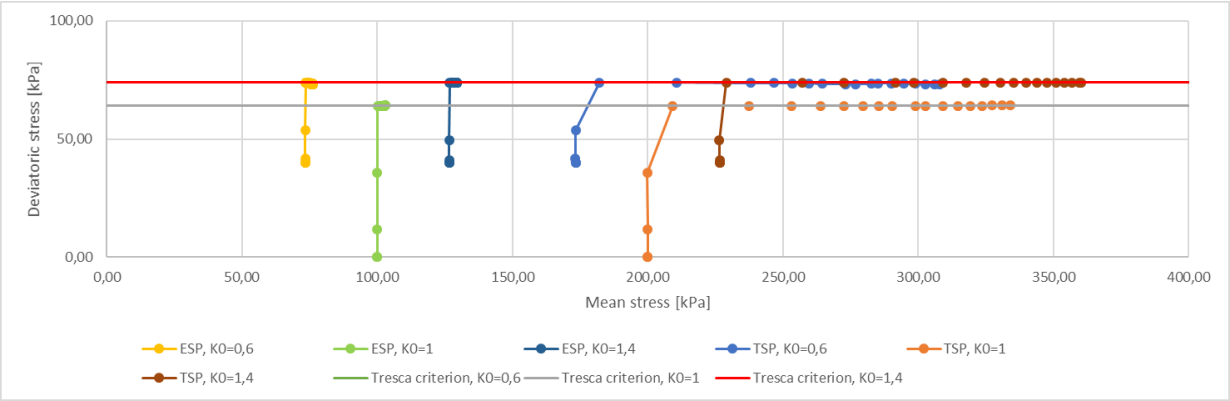

Figure A.2.1: Effective stress path (ESP) and total stress path (TSP) together with the Tresca yield criterion for different K_0, with the deviatoric stress (q) on the vertical axis and the mean stress (p', p) on the horizontal axis. Found by using the Cavity Expansion Method (CEM) and the linear elastic-perfectly plastic (EP) model with parameters as in Table 12.1, but with K_0 varying. The data is gathered from a stress point at $^{r}/_{r_0} = 2$.

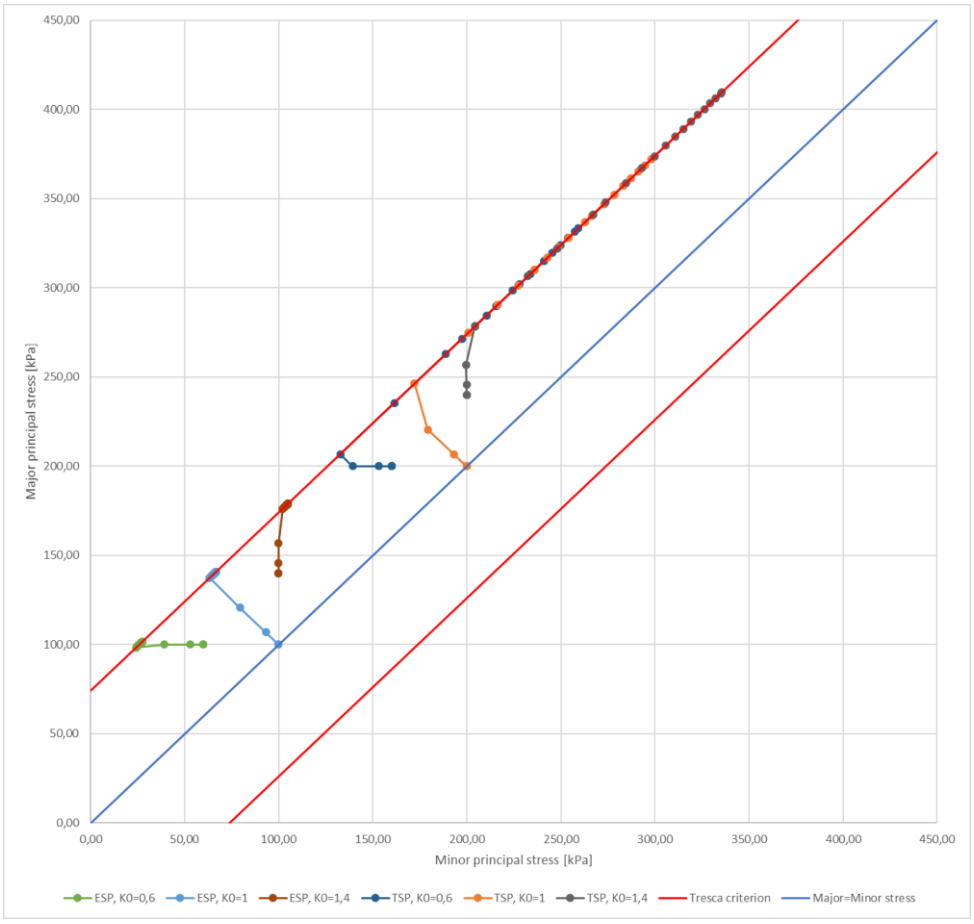

Figure A.2.2: Effective stress path (ESP) and total stress path (TSP) together with the Tresca yield criterion for different K_0, with the major principal stress (σ_1', σ_1) on the vertical axis and the minor principal stress (σ_3', σ_3) on the horizontal axis. Found by using the Cavity Expansion Method (CEM) and the linear elastic-perfectly plastic (EP) model with parameters as in Table 12.1, but with K_0 varying. The data is gathered from a stress point at $^{r}/_{r_0} = 2$.

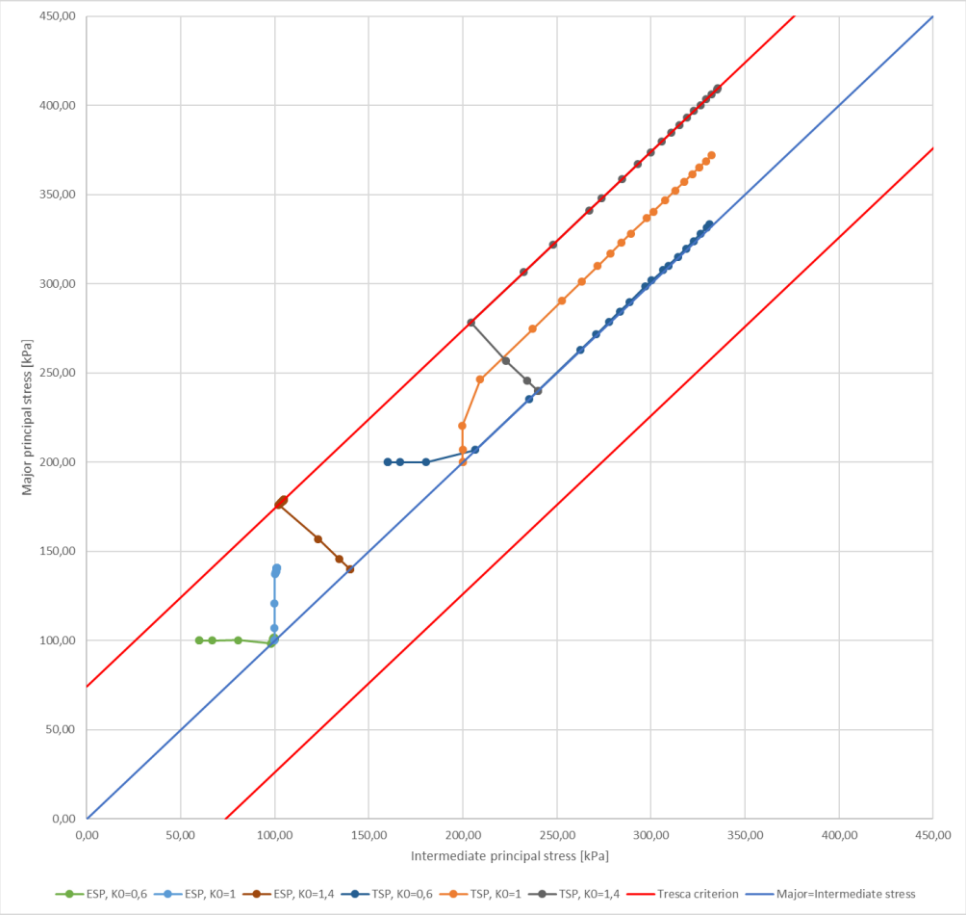

Figure A.2.3: Effective stress path (ESP) and total stress path (TSP) together with the Tresca yield criterion for different K_0, with the major principal stress (σ_1', σ_1) on the vertical axis and the intermediate principal stress (σ_2', σ_2) on the horizontal axis. Found by using the Cavity Expansion Method (CEM) and the linear elastic-perfectly plastic (EP) model with parameters as in Table 12.1, but with K_0 varying. The data is gathered from a stress point at $^{r}/_{r_0} = 2$.

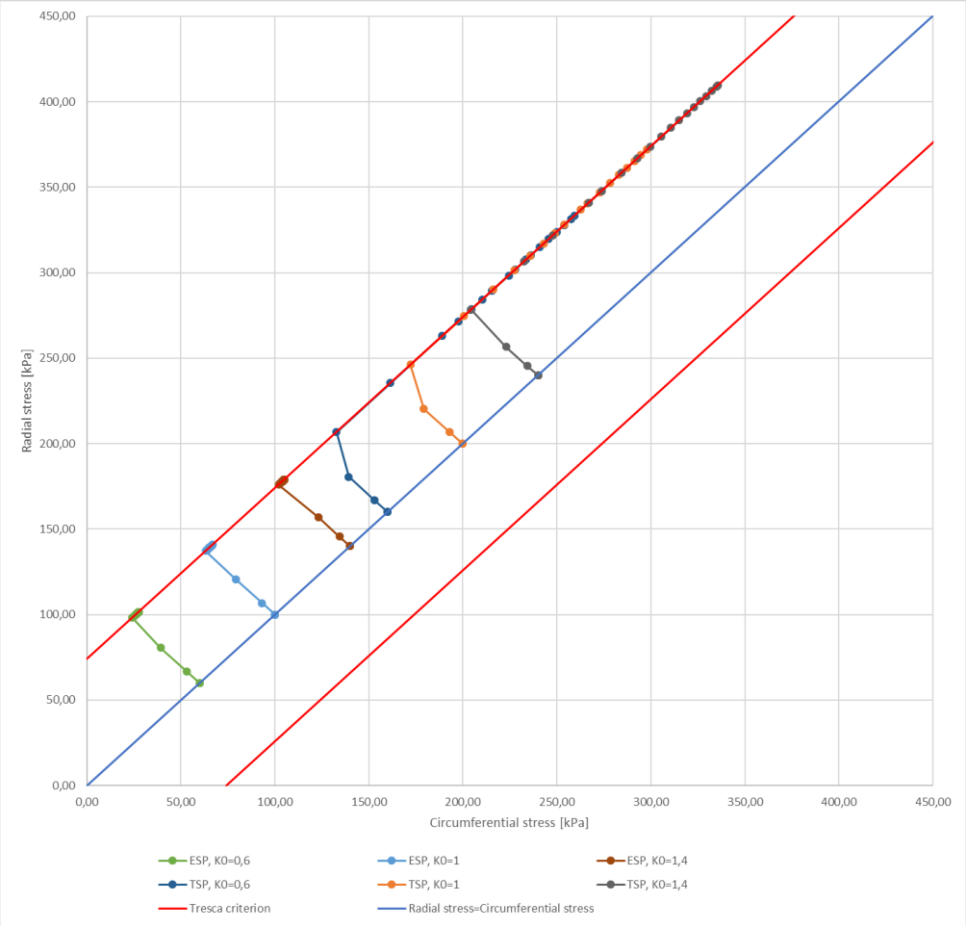

Figure A.2.4: Effective stress path (ESP) and total stress path (TSP) together with the Tresca yield criterion for different K_0, with the radial stress (σ_r', σ_r) on the vertical axis and the circumferential stress (σ_θ', σ_θ) on the horizontal axis. Found by using the Cavity Expansion Method (CEM) and the linear elastic-perfectly plastic (EP) model with parameters as in Table 12.1, but with K_0 varying. The data is gathered from a stress point at $^{r}/_{r_0} = 2$.

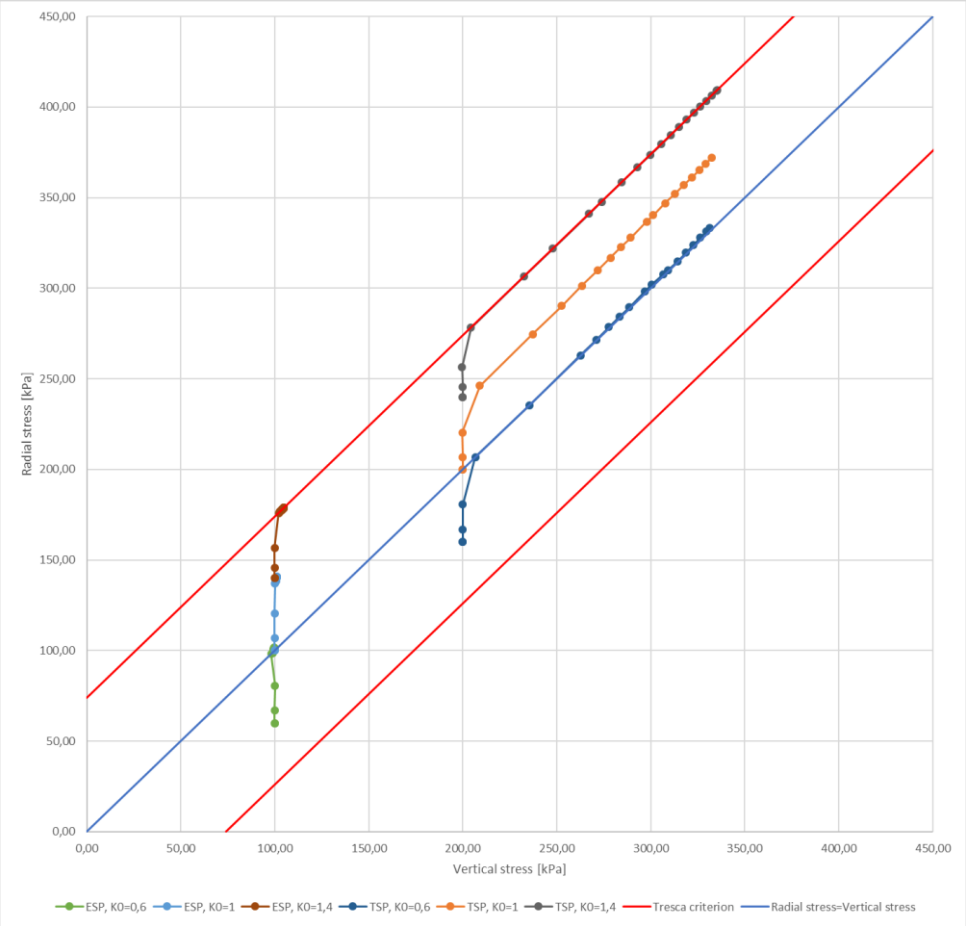

Figure A.2.5: Effective stress path (ESP) and total stress path (TSP) together with the Tresca yield criterion for different K_0, with the radial stress (σ_r', σ_r) on the vertical axis and the vertical stress (σ_z', σ_z) on the horizontal axis. Found by using the Cavity Expansion Method (CEM) and the linear elastic-perfectly plastic (EP) model with parameters as in Table 12.1, but with K_0 varying. The data is gathered from a stress point at $^{r}/_{r_0} = 2$.

A.3 Stress paths from CEM-MCC varying the K_0

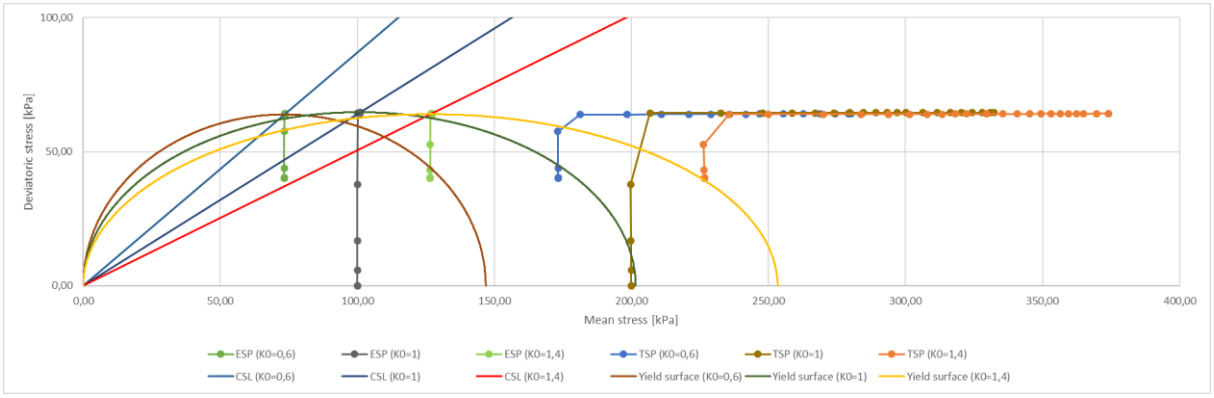

Figure A.3.1: Effective stress path (ESP) and total stress path (TSP) together with the critical state line (CSL) and the yield surface for different K_0, with the deviatoric stress (q) on the vertical axis and the mean stress (p', p) on the horizontal axis. Found by using the Cavity Expansion Method (CEM) and the Modified Cam Clay (MCC) model with parameters as in Table 12.2, but with OCR varying so that $\Delta p' = 0$ and M varying so that $s_u = 37kPa$ for the different values of K_0. The data is gathered from a stress point at $r/r_0 = 2$.

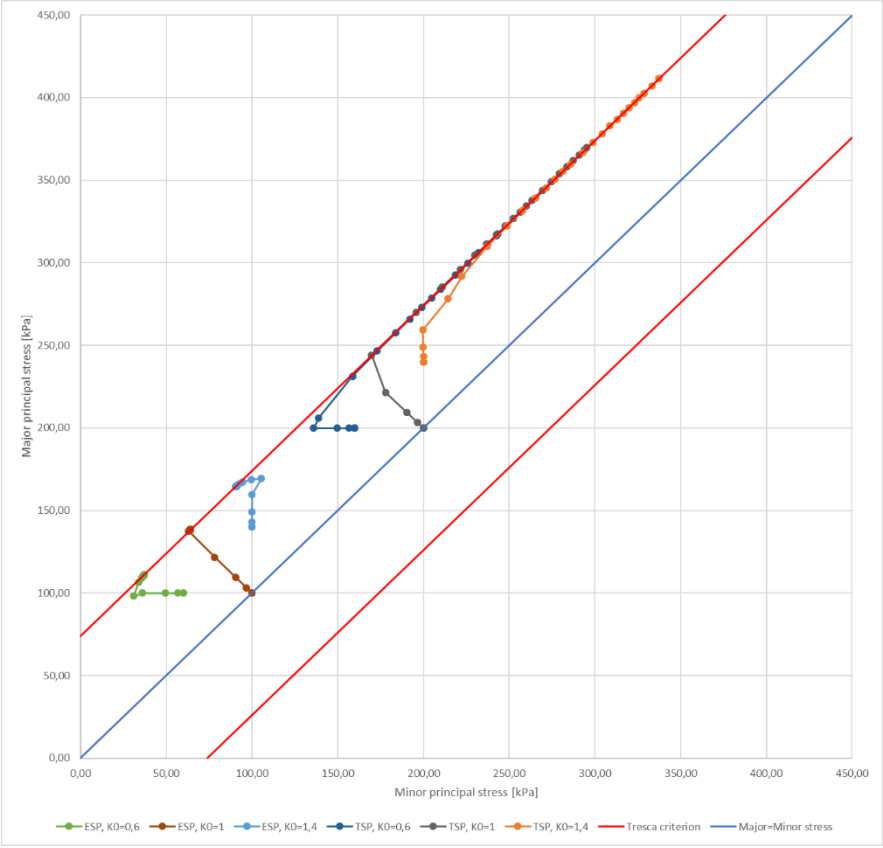

Figure A.3.2: Effective stress path (ESP) and total stress path (TSP) together with the Tresca yield criterion for different K_0, with the major principal stress (σ_1', σ_1) on the vertical axis and the minor principal stress (σ_3', σ_3) on the horizontal axis. Found by using the Cavity Expansion Method (CEM) and the Modified Cam Clay (MCC) model with parameters as in Table 12.2, but with OCR varying so that $\Delta p' = 0$ and M varying so that $s_u = 37kPa$ for the different values of K_0. The data is gathered from a stress point at $r/r_0 = 2$.

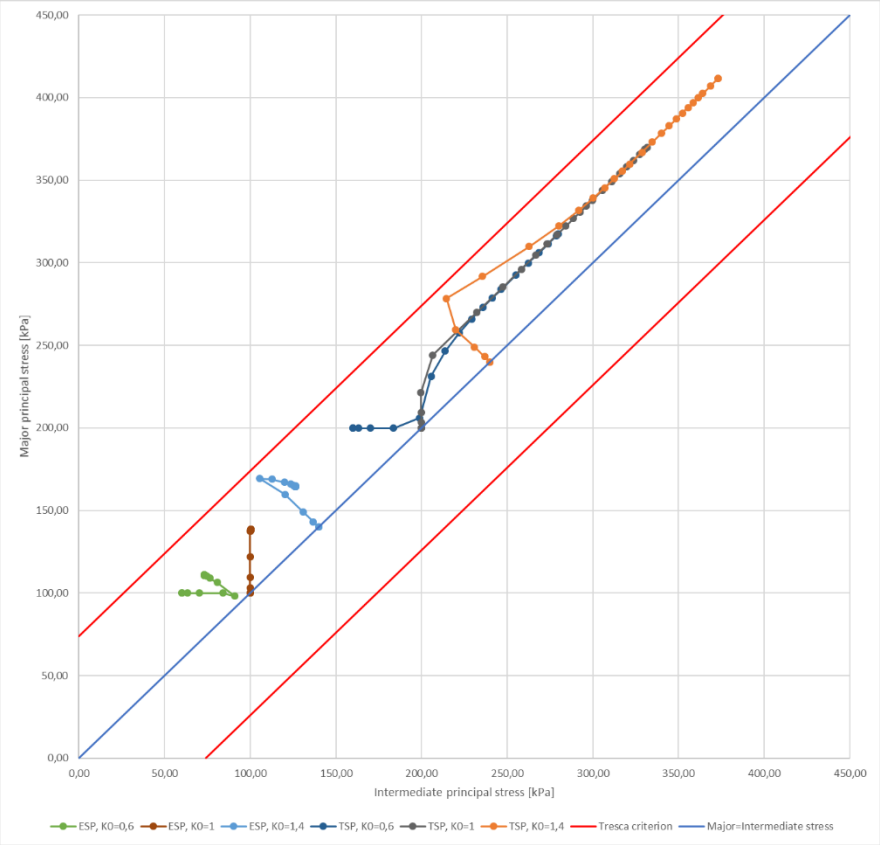

Figure A.3.3: Effective stress path (ESP) and total stress path (TSP) together with the Tresca yield criterion for different K_0, with the major principal stress (σ_1', σ_1) on the vertical axis and the intermediate principal stress (σ_2', σ_2) on the horizontal axis. Found by using the Cavity Expansion Method (CEM) and the Modified Cam Clay (MCC) model with parameters as in Table 12.2, but with OCR varying so that $\Delta p' = 0$ and M varying so that $s_u = 37kPa$ for the different values of K_0. The data is gathered from a stress point at ${}^{r}/_{r_0} = 2$.

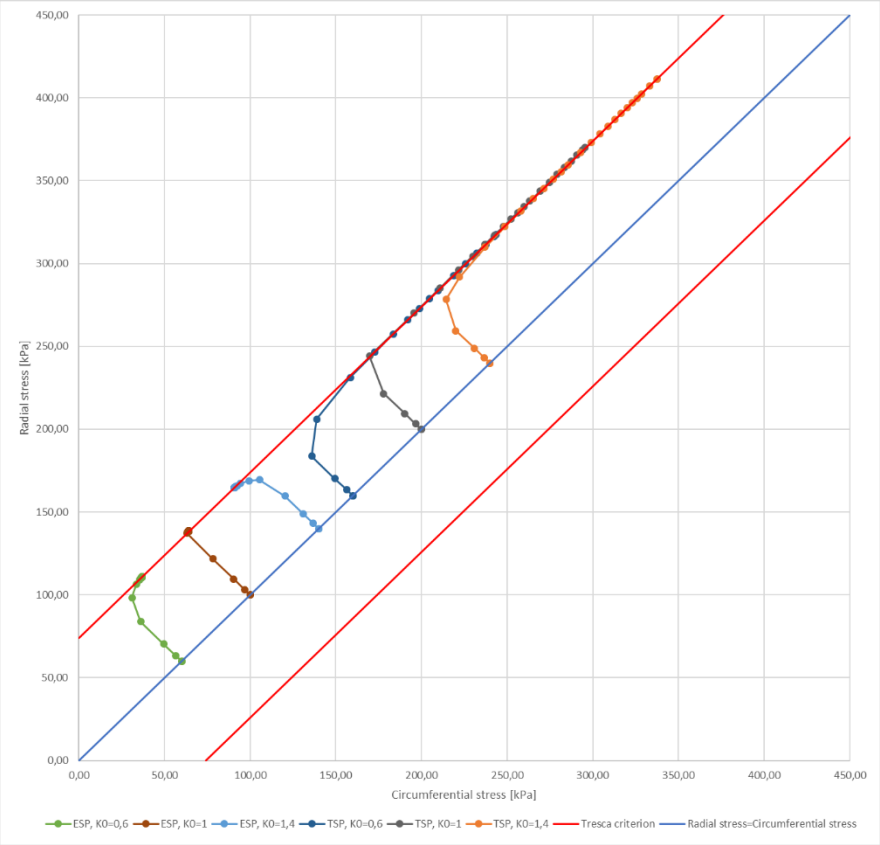

Figure A.3.4: Effective stress path (ESP) and total stress path (TSP) together with the Tresca yield criterion for different K_0, with the radial stress (σ_r', σ_r) on the vertical axis and the circumferential stress (σ_θ', σ_θ) on the horizontal axis. Found by using the Cavity Expansion Method (CEM) and the Modified Cam Clay (MCC) model with parameters as in Table 12.2, but with OCR varying so that $\Delta p' = 0$ and M varying so that $s_u = 37kPa$ for the different values of K_0. The data is gathered from a stress point at $^{r}/_{r_0} = 2$.

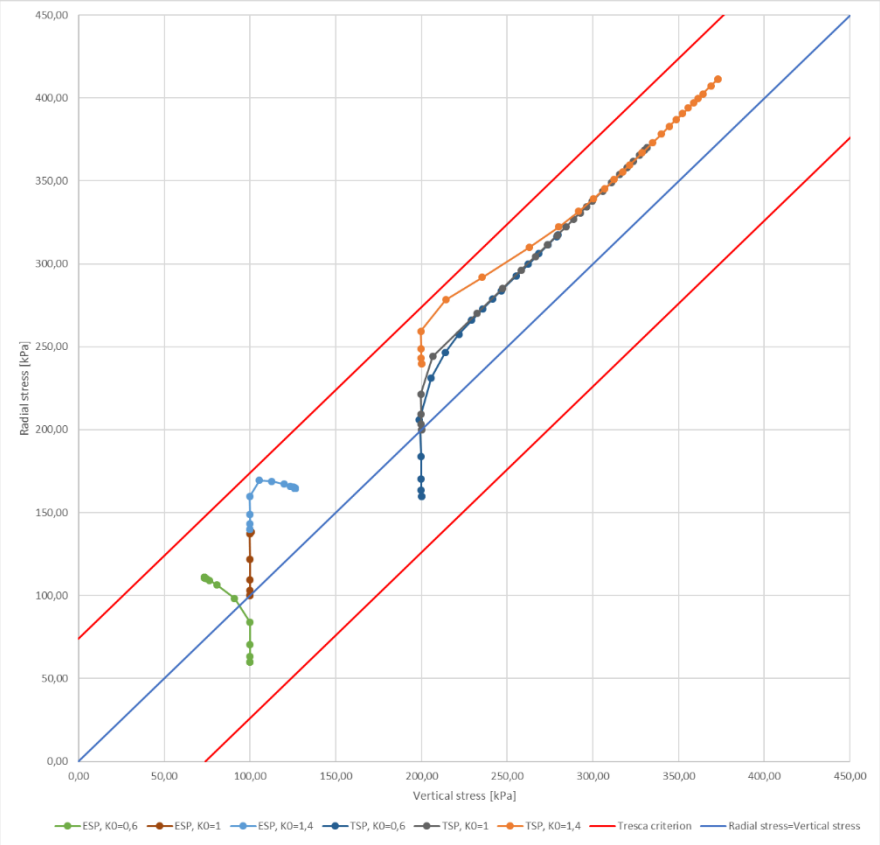

Figure A.3.5: Effective stress path (ESP) and total stress path (TSP) together with the Tresca yield criterion for different K_0, with the radial stress (σ_r', σ_r) on the vertical axis and the vertical stress (σ_z', σ_z) on the horizontal axis. Found by using the Cavity Expansion Method (CEM) and the Modified Cam Clay (MCC) model with parameters as in Table 12.2, but with OCR varying so that $\Delta p' = 0$ and M varying so that $s_u = 37kPa$ for the different values of K_0. The data is gathered from a stress point at $^{r}/_{r_0} = 2$.

A.4 Stress paths from CEM-EP with softening

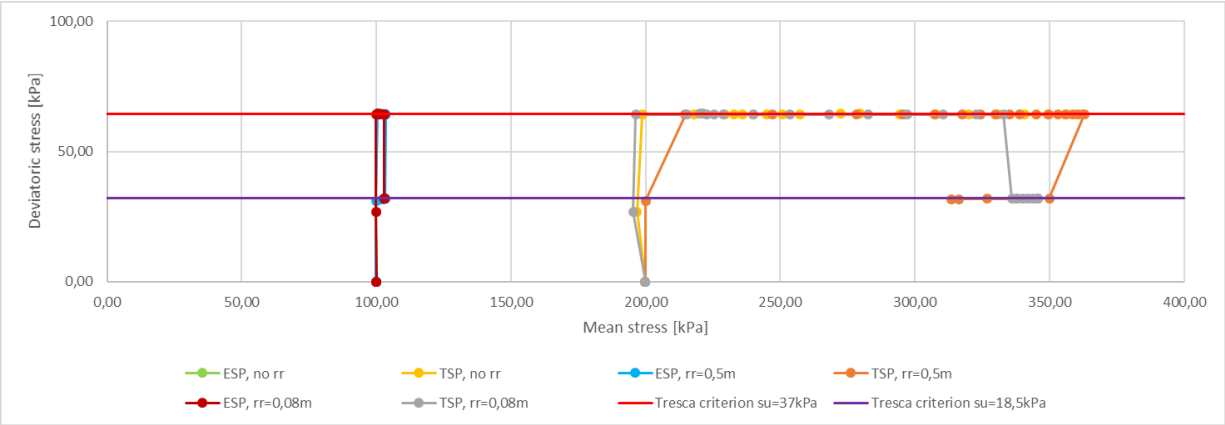

Figure A.4.1: Effective stress path (ESP) and total stress path (TSP) for a material with a sensitivity of $S_t = 2$ together with the Tresca yield criterion for both the intact undrained shear strength ($s_u = 37kPa$) amd the remoulded undrained shear strength ($s_{ur} = 18{,}5kPa$). With the remoulded limit (r_r) located at both ${}^{r_r}/_{r_0} = 1{,}58$ and ${}^{r_r}/_{r_0} = 9{,}90$, and without softening entirely. The deviatoric stress (q) is on the vertical axis and the mean stress (p', p) is on the horizontal axis. Found by using the Cavity Expansion Method (CEM) and the linear elastic-perfectly plastic (EP) model with parameters as in Table 12.1, but with softening as described in Chapter 12.7 included. The data is gathered from a stress point at ${}^{r}/_{r_0} = 1{,}27$.

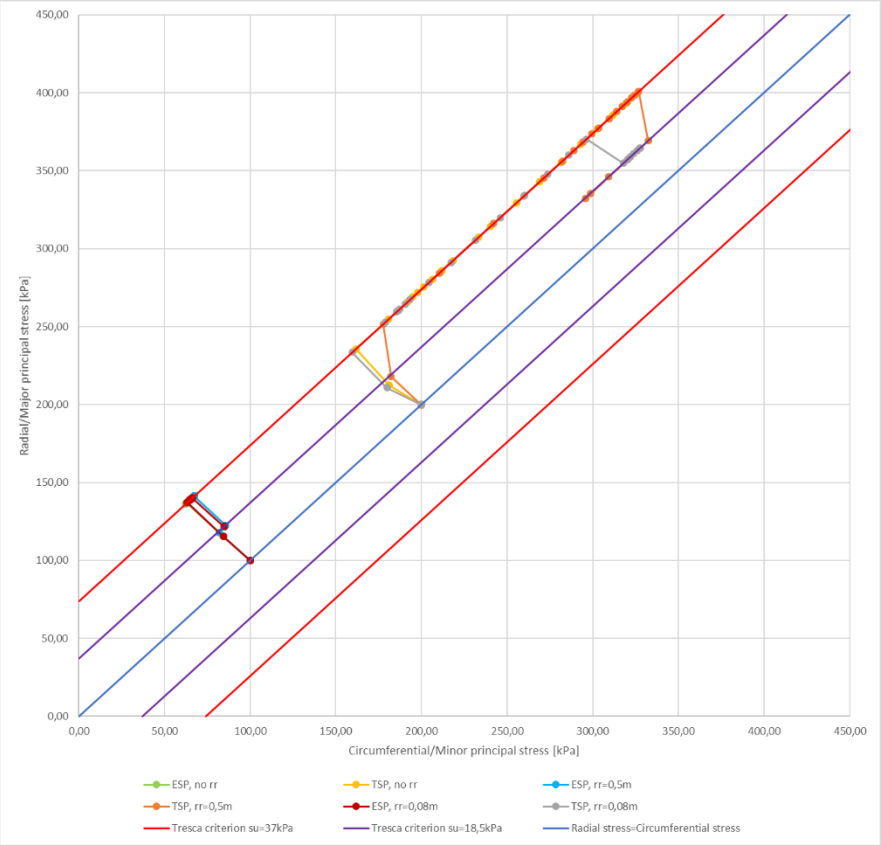

Figure A.4.2: Effective stress path (ESP) and total stress path (TSP) for a material with a sensitivity of $S_t = 2$ together with the Tresca yield criterion for both the intact undrained shear strength ($s_u = 37kPa$) amd the remoulded undrained shear strength ($s_{ur} = 18{,}5kPa$). With the remoulded limit (r_r) located at both ${}^{r_r}/_{r_0} = 1{,}58$ and ${}^{r_r}/_{r_0} = 9{,}90$, and without softening entirely. The radial/major principal stress ($\sigma_r' = \sigma_1'$, $\sigma_r = \sigma_1$) is on the vertical axis and the circumferential/minor principal stress ($\sigma_\theta' = \sigma_3'$, $\sigma_\theta = \sigma_3$) is on the horizontal axis. Found by using the Cavity Expansion Method (CEM) and the linear elastic-perfectly plastic (EP) model with parameters as in Table 12.1, but with softening as described in Chapter 12.7 included. The data is gathered from a stress point at ${}^{r}/_{r_0} = 1{,}27$.

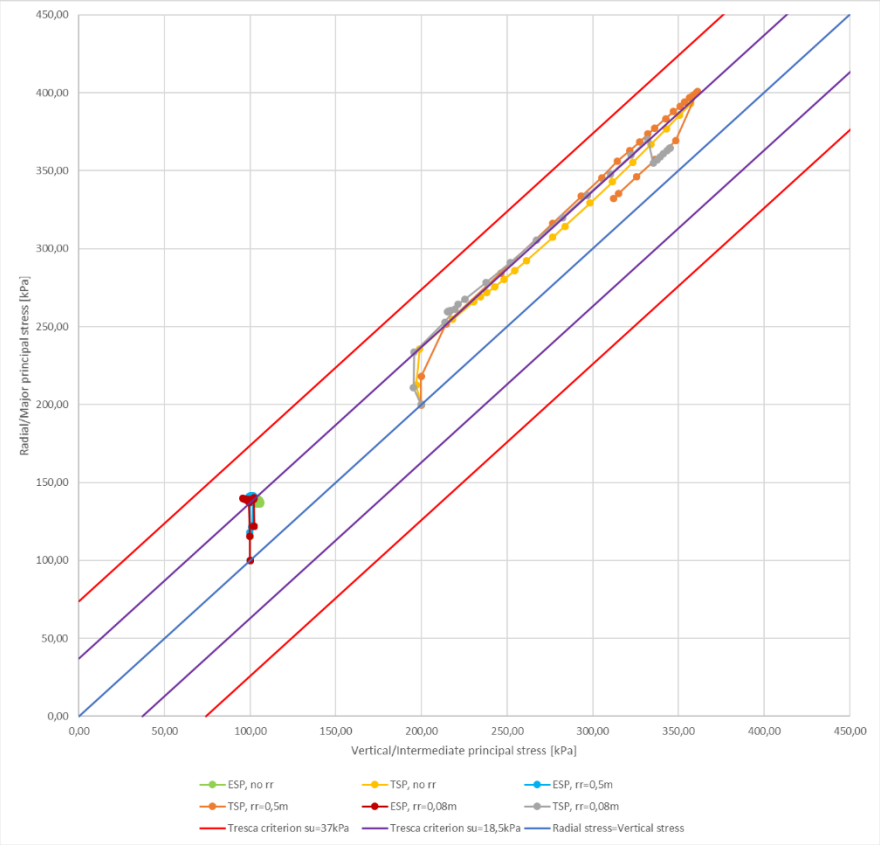

Figure A.4.3: Effective stress path (ESP) and total stress path (TSP) for a material with a sensitivity of $S_t = 2$ together with the Tresca yield criterion for both the intact undrained shear strength ($s_u = 37kPa$) amd the remoulded undrained shear strength ($s_{ur} = 18{,}5kPa$). With the remoulded limit (r_r) located at both ${}^{r_r}/_{r_0} = 1{,}58$ and ${}^{r_r}/_{r_0} = 9{,}90$, and without softening entirely. The radial/major principal stress ($\sigma_r' = \sigma_1'$, $\sigma_r = \sigma_1$) is on the vertical axis and the vertical/intermediate principal stress ($\sigma_z' = \sigma_2'$, $\sigma_z = \sigma_2$) is on the horizontal axis. Found by using the Cavity Expansion Method (CEM) and the linear elastic-perfectly plastic (EP) model with parameters as in Table 12.1, but with softening as described in Chapter 12.7 included. The data is gathered from a stress point at ${}^{r}/_{r_0} = 1{,}27$.

Appendix B

B.1 The method of Nishida (1963) compared to the data of Table 13.6

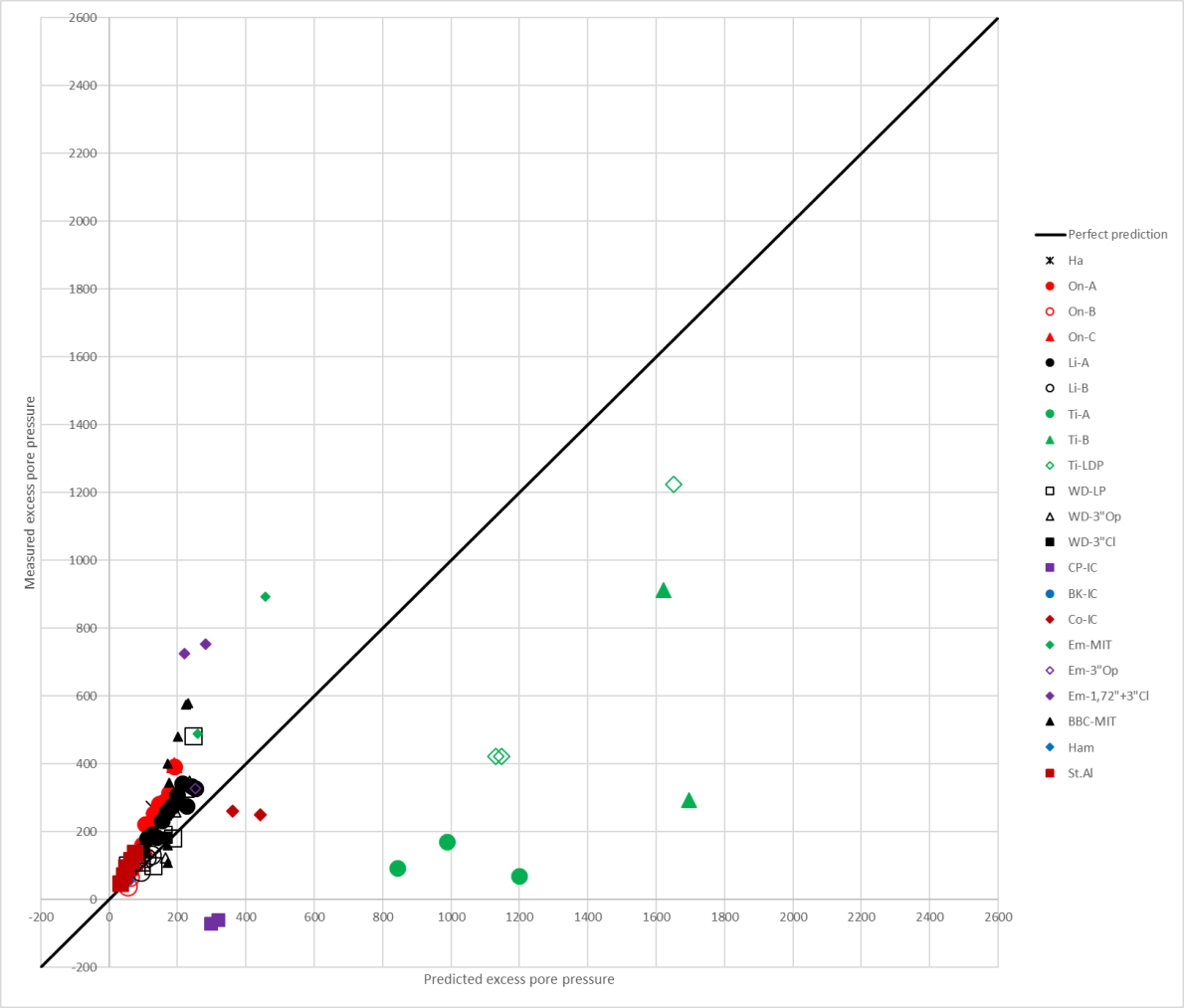

Figure B.1.1: Residual plot of the prediction obtained by Equation 8.3 for all sites. Further description of the legend can be found above Figure 9.10.

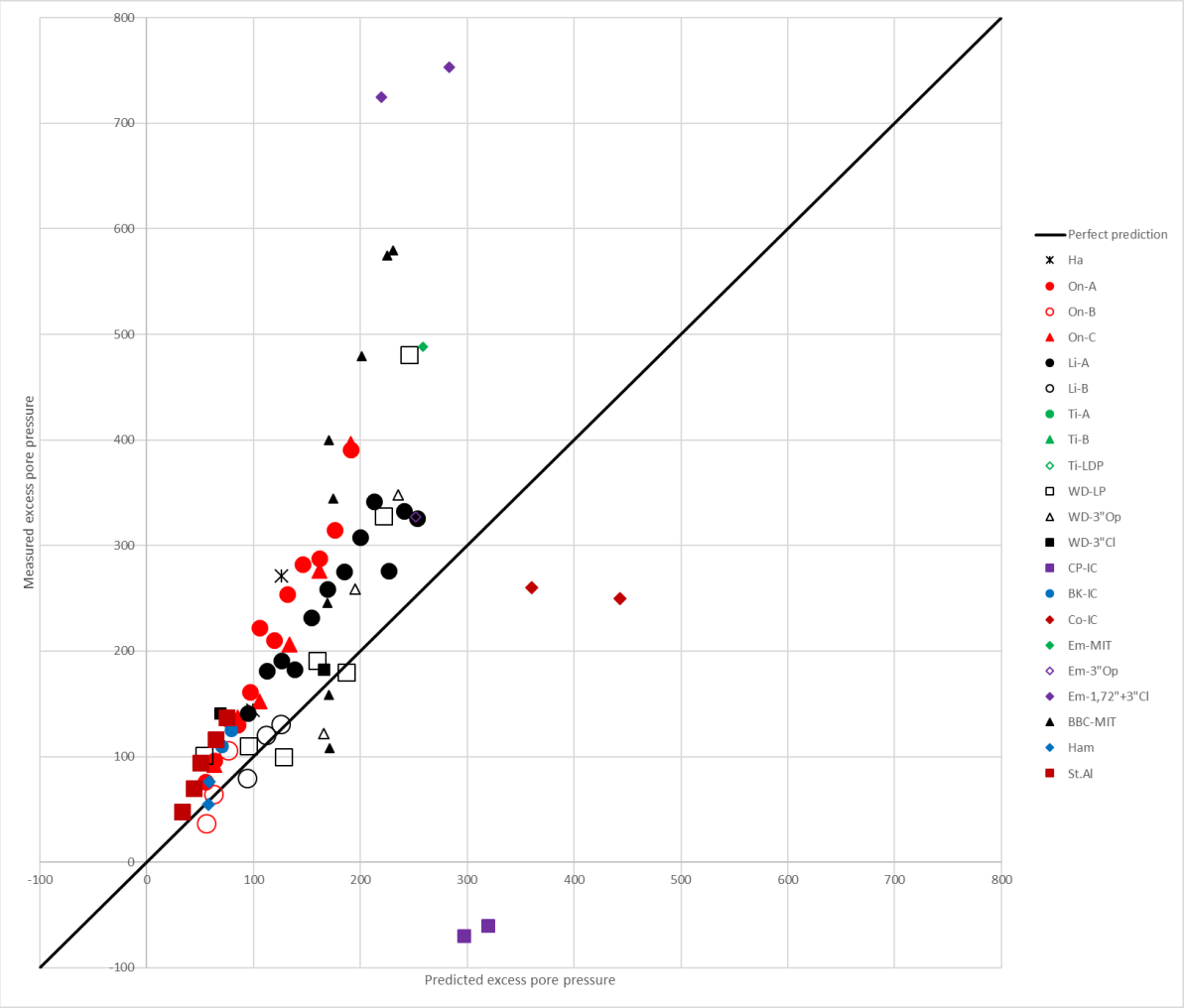

Figure B.1.2: Residual plot of the prediction below $800kPa$ *obtained by Equation 8.3. Further description of the legend can be found above Figure 9.10.*

B.2 The method of Svanø (1978) compared to the data of Table 13.6

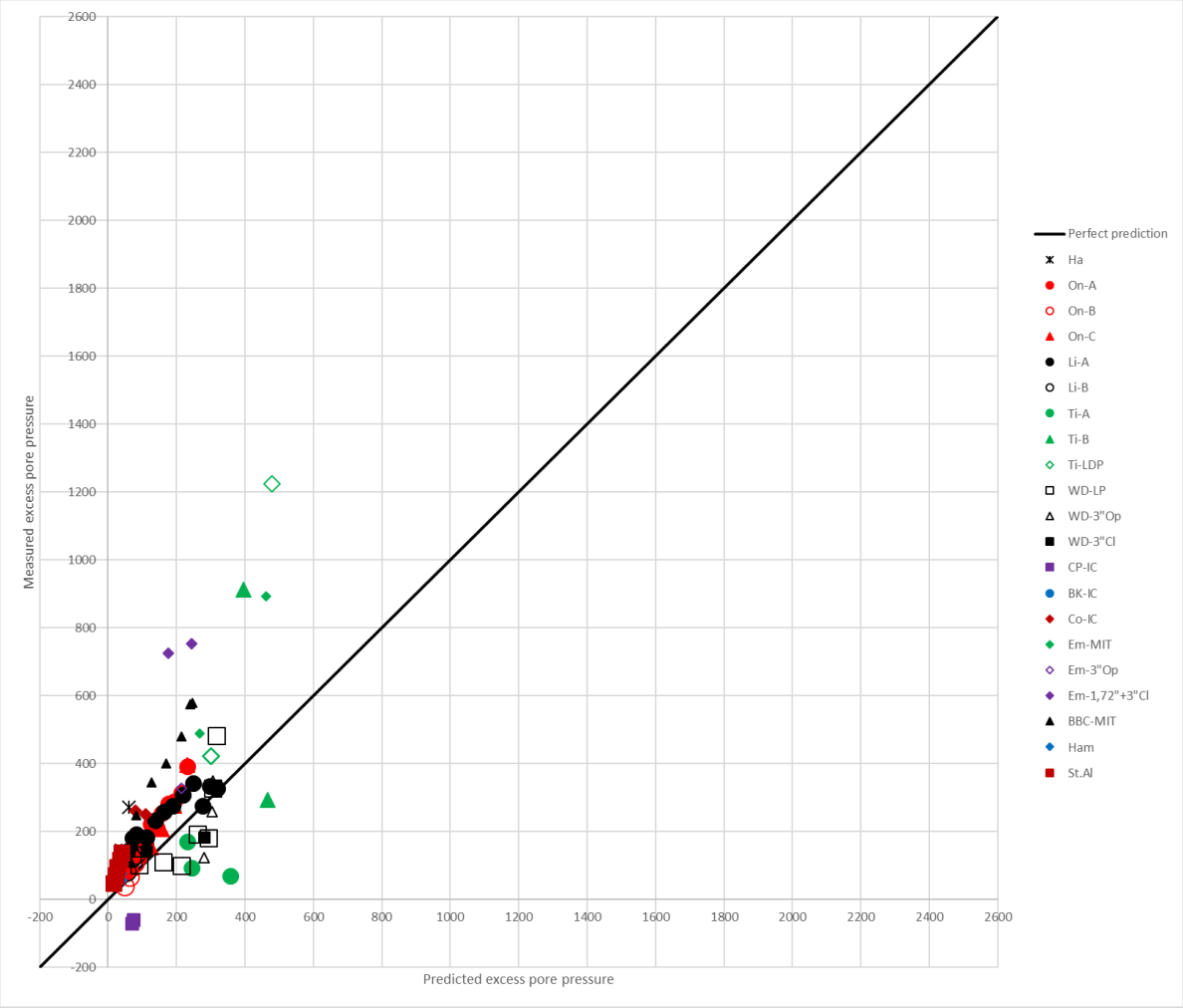

Figure B.2.1: Residual plot of the prediction obtained by Equation 8.8 for all sites. Further description of the legend can be found above Figure 9.10.

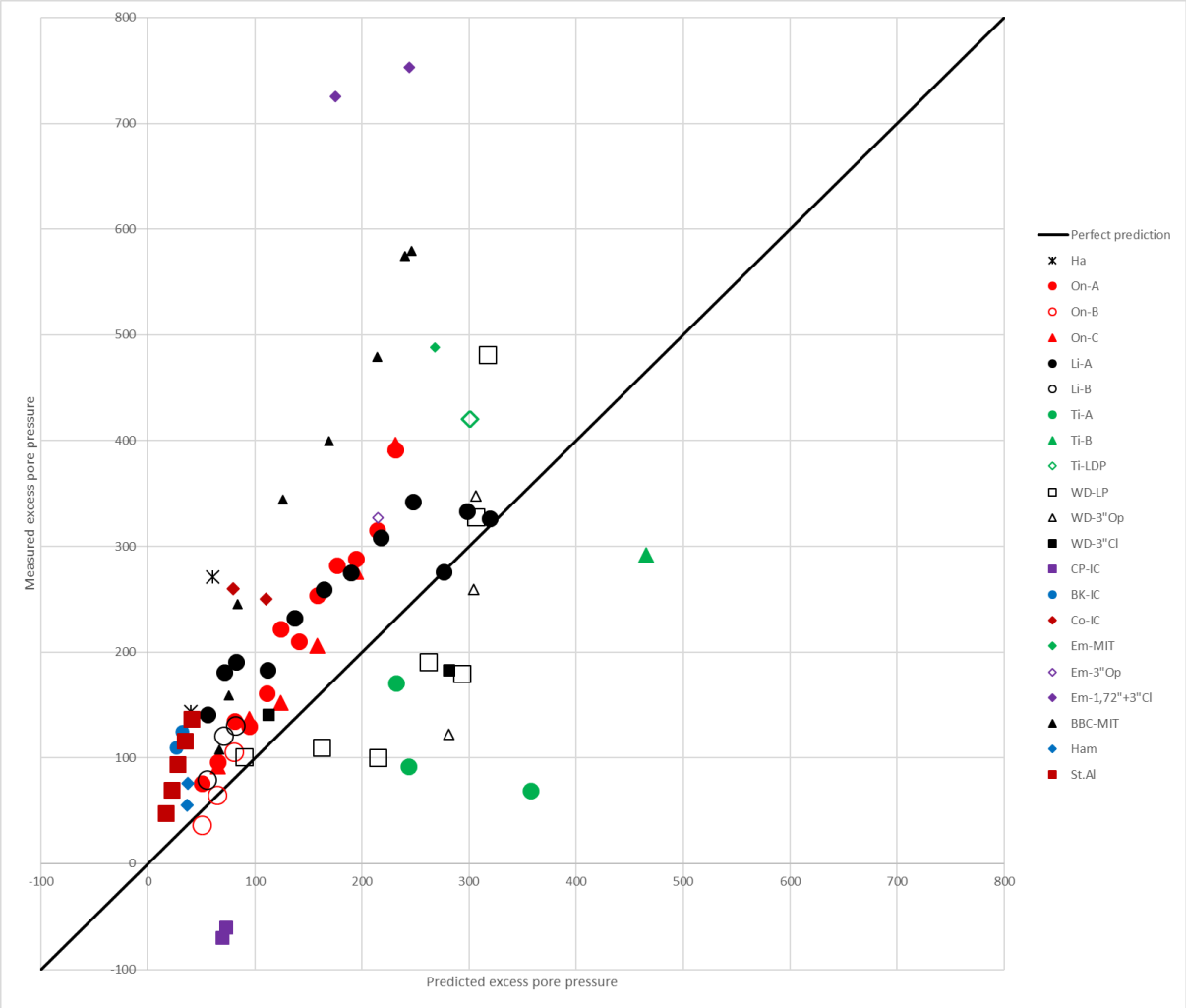

Figure B.2.2: Residual plot of the prediction below $800kPa$ obtained by Equation 8.8. Further description of the legend can be found above Figure 9.10.

B.3 The method of Broms and Massarch (1979) compared to the data of Table 13.6

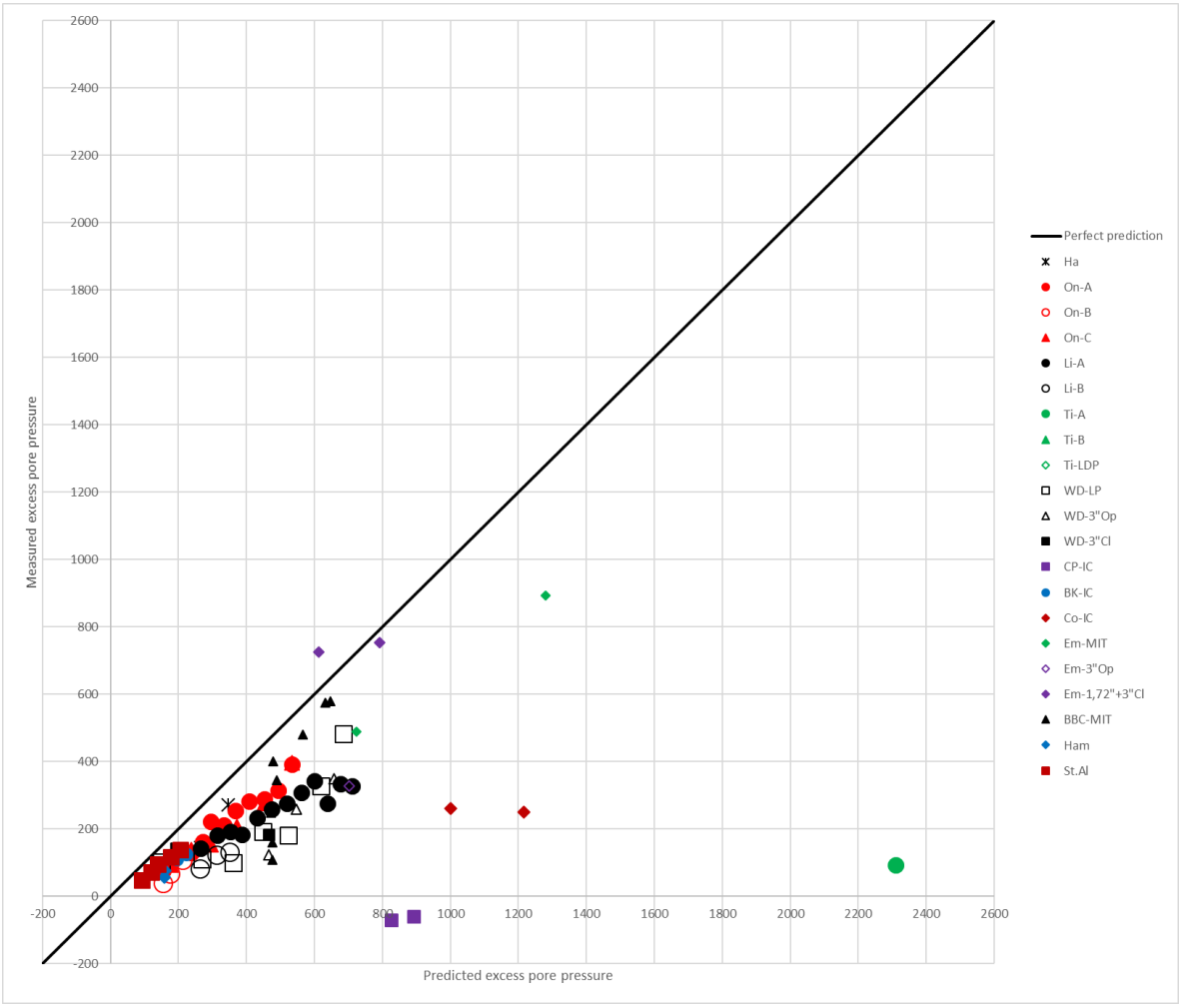

Figure B.3.1: Residual plot of the prediction obtained by Equation 8.10 for all sites. Further description of the legend can be found above Figure 9.10.

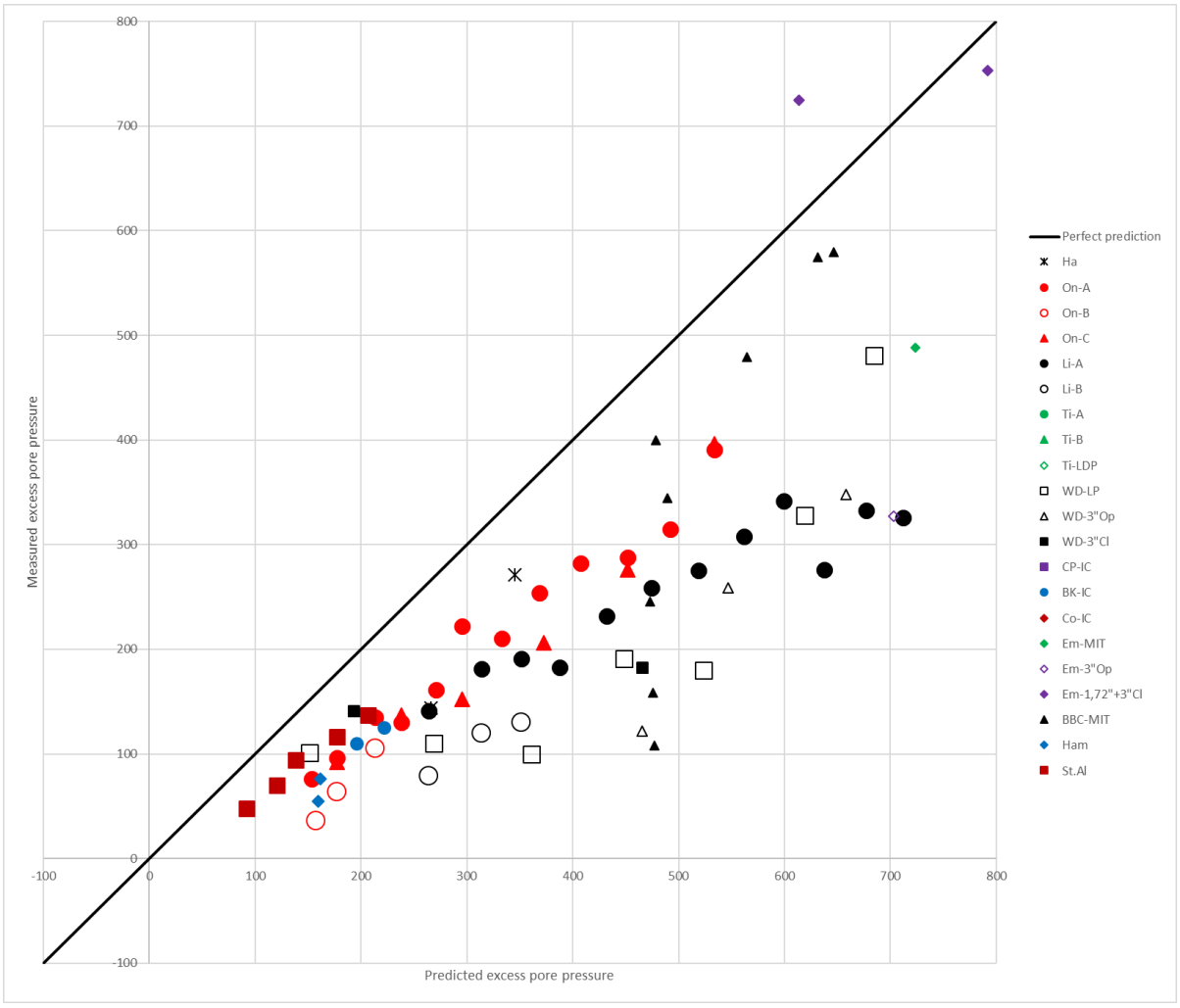

Figure B.3.2: Residual plot of the prediction below $800kPa$ *obtained by Equation 8.10. Further description of the legend can be found above Figure 9.10.*

Appendix C

C.1 Change in stress during expansion in CEM-MCC

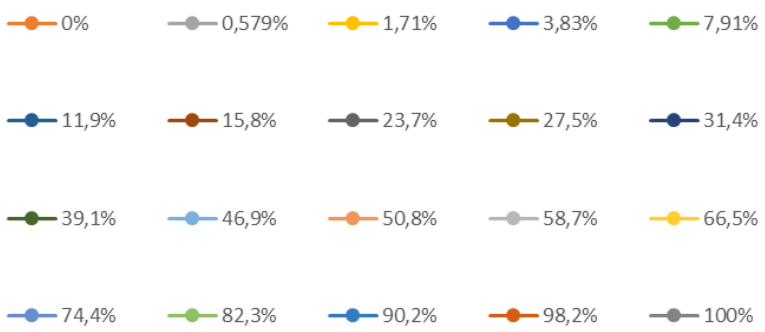

Figure C.1.1: Legend for the plots in Appendix C.1, showing the percentage of the applied displacement (i.e. the applied radial displacement over the final radial displacement) for each line.

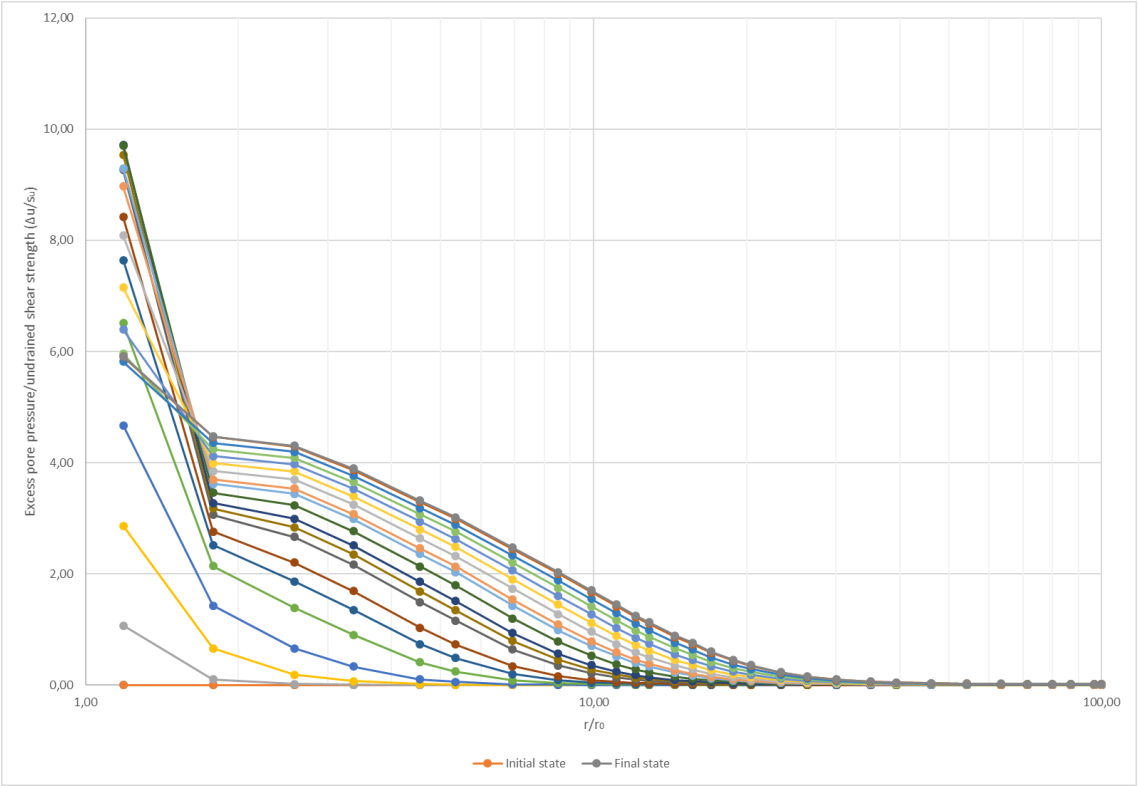

Figure C.1.2: Excess pore pressure normalized with the undrained shear strength from initial (i.e. before any displacement) to final (i.e. entire displacement applied) state against the normalized radial distance from the pile center in a logarithmic scale. Modeled in Plaxis with input parameters from Table 11.2.

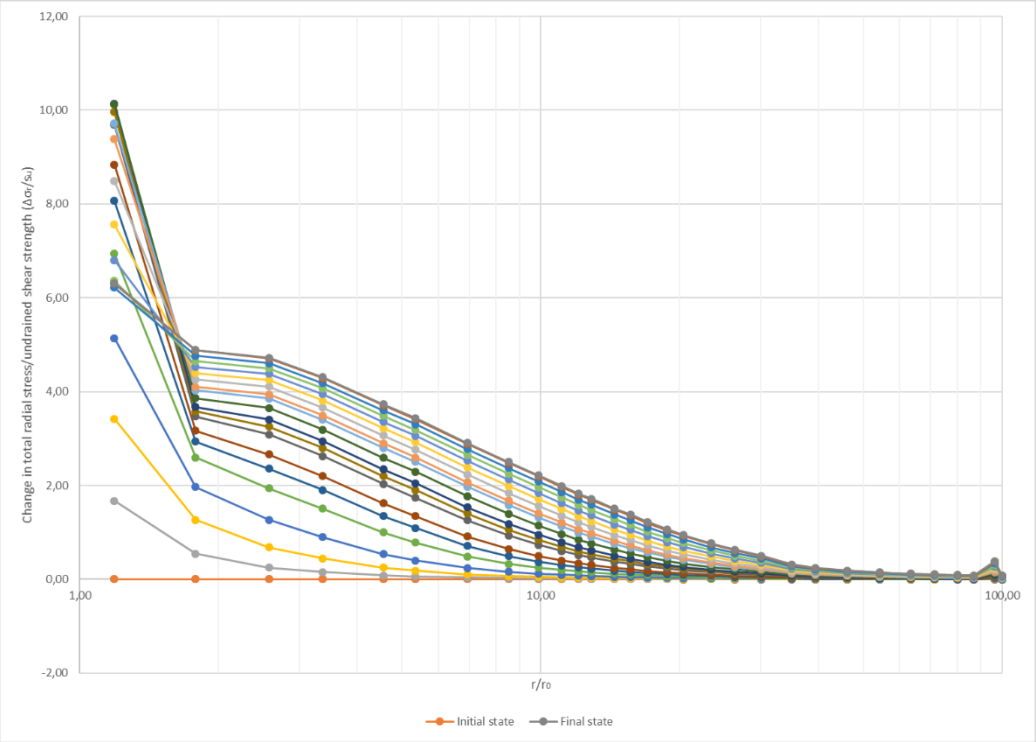

Figure C.1.3: Change in total radial stress normalized with the undrained shear strength from initial (i.e. before any displacement) to final (i.e. entire displacement applied) state against the normalized radial distance from the pile center in a logarithmic scale. Modeled in Plaxis with input parameters from Table 11.2.

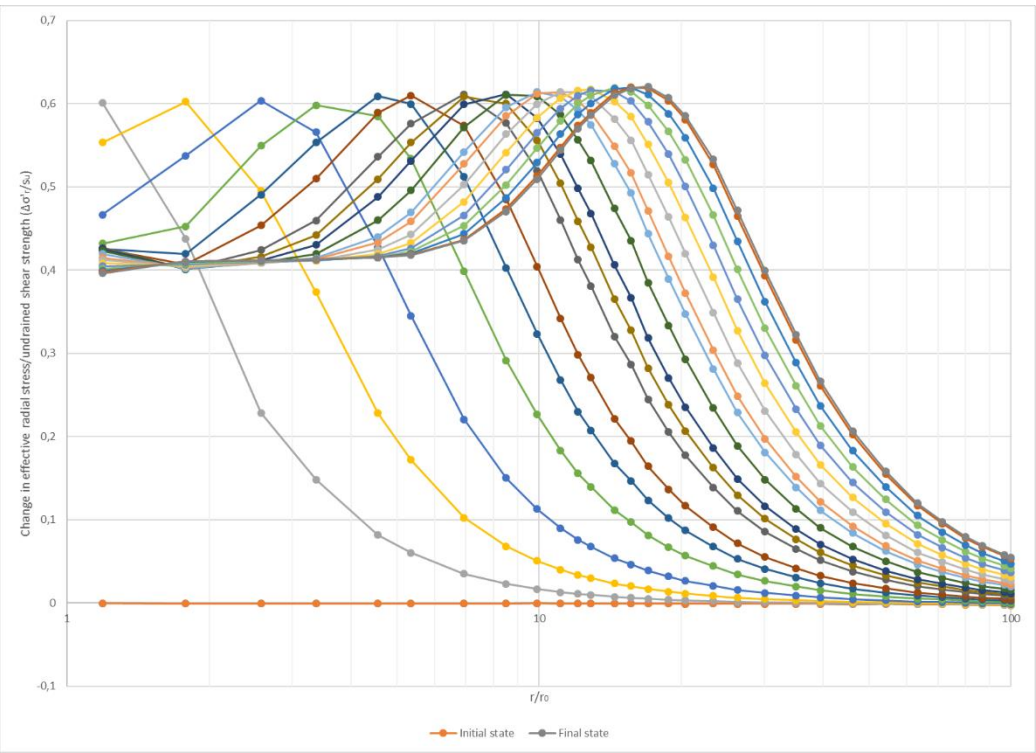

Figure C.1.4: Change in effective radial stress normalized with the undrained shear strength from initial (i.e. before any displacement) to final (i.e. entire displacement applied) state against the normalized radial distance from the pile center in a logarithmic scale. Modeled in Plaxis with input parameters from Table 11.2.

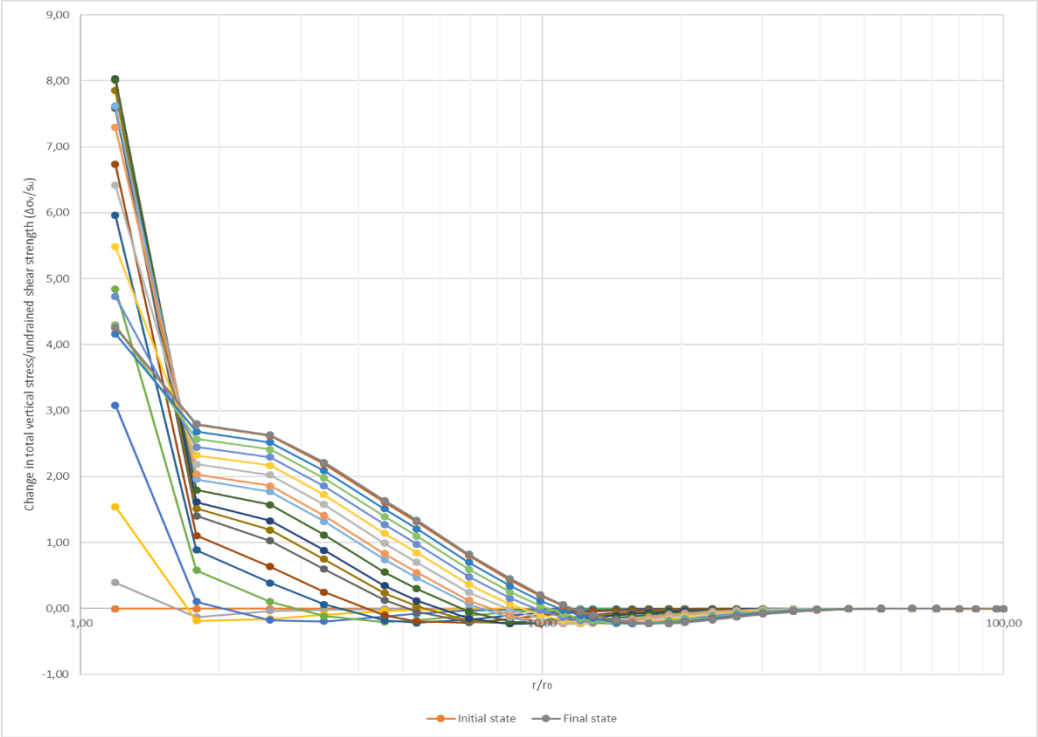

Figure C.1.5: Change in total vertical stress normalized with the undrained shear strength from initial (i.e. before any displacement) to final (i.e. entire displacement applied) state against the normalized radial distance from the pile center in a logarithmic scale. Modeled in Plaxis with input parameters from Table 11.2.

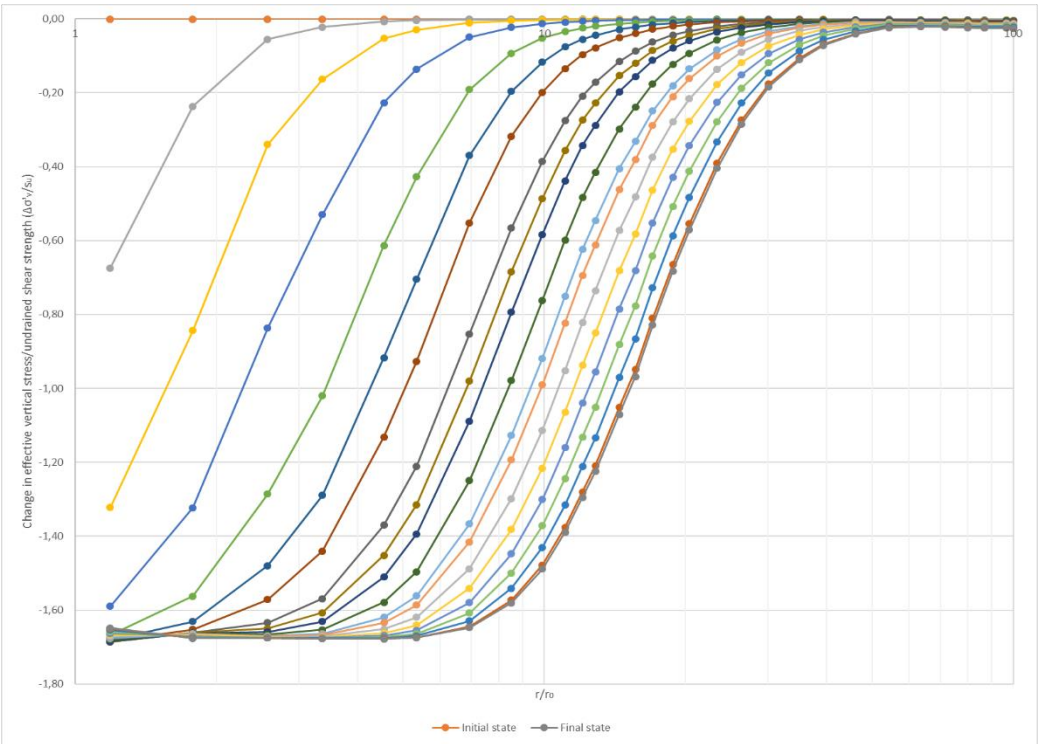

Figure C.1.6: Change in effective vertical stress normalized with the undrained shear strength from initial (i.e. before any displacement) to final (i.e. entire displacement applied) state against the normalized radial distance from the pile center in a logarithmic scale. Modeled in Plaxis with input parameters from Table 11.2.

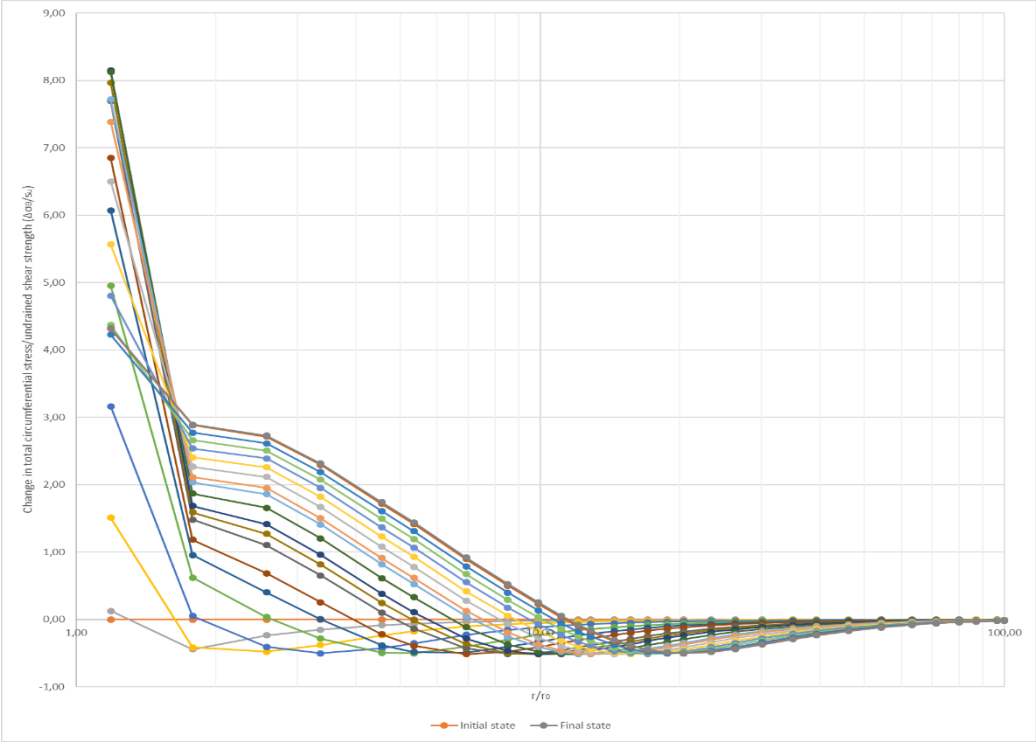

Figure C.1.7: Change in total circumferential stress normalized with the undrained shear strength from initial (i.e. before any displacement) to final (i.e. entire displacement applied) state against the normalized radial distance from the pile center in a logarithmic scale. Modeled in Plaxis with input parameters from Table 11.2.

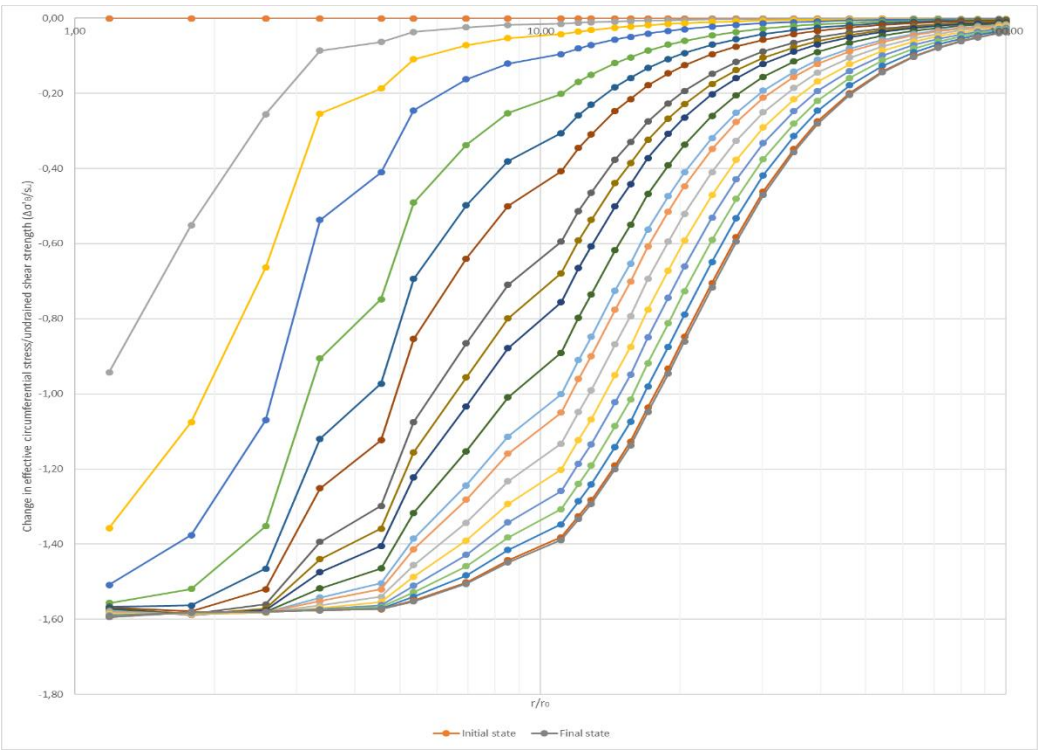

Figure C.1.8: Change in effective circumferential stress normalized with the undrained shear strength from initial (i.e. before any displacement) to final (i.e. entire displacement applied) state against the normalized radial distance from the pile center in a logarithmic scale. Modeled in Plaxis with input parameters from Table 11.2.

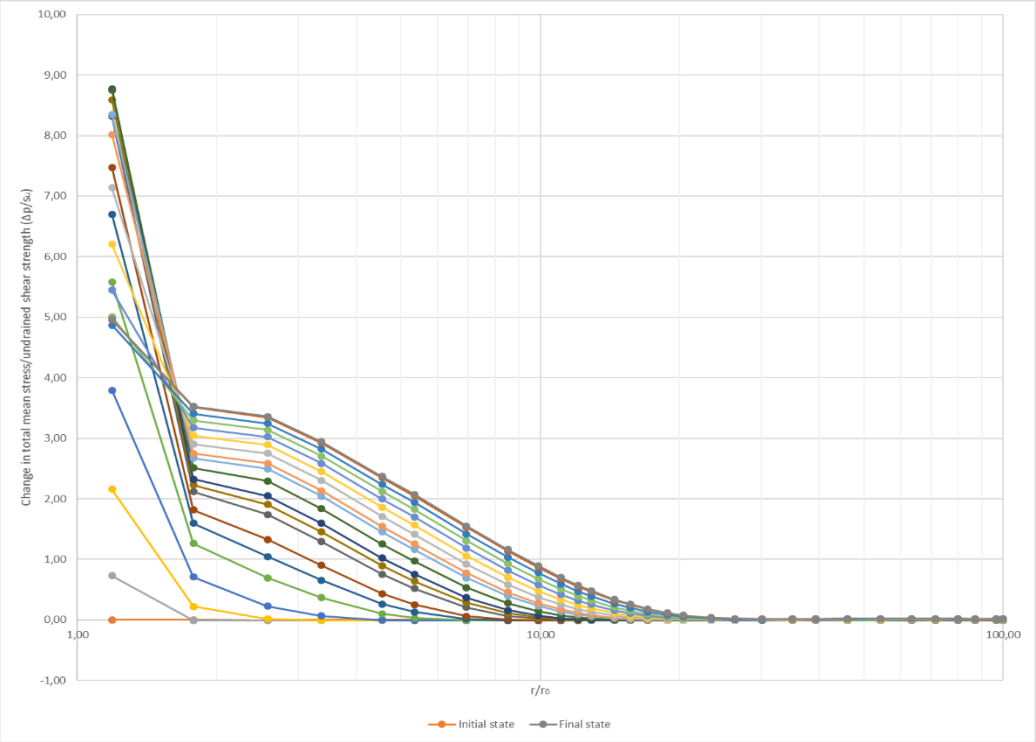

Figure C.1.9: Change in total mean stress normalized with the undrained shear strength from initial (i.e. before any displacement) to final (i.e. entire displacement applied) state against the normalized radial distance from the pile center in a logarithmic scale. Modeled in Plaxis with input parameters from Table 11.2.

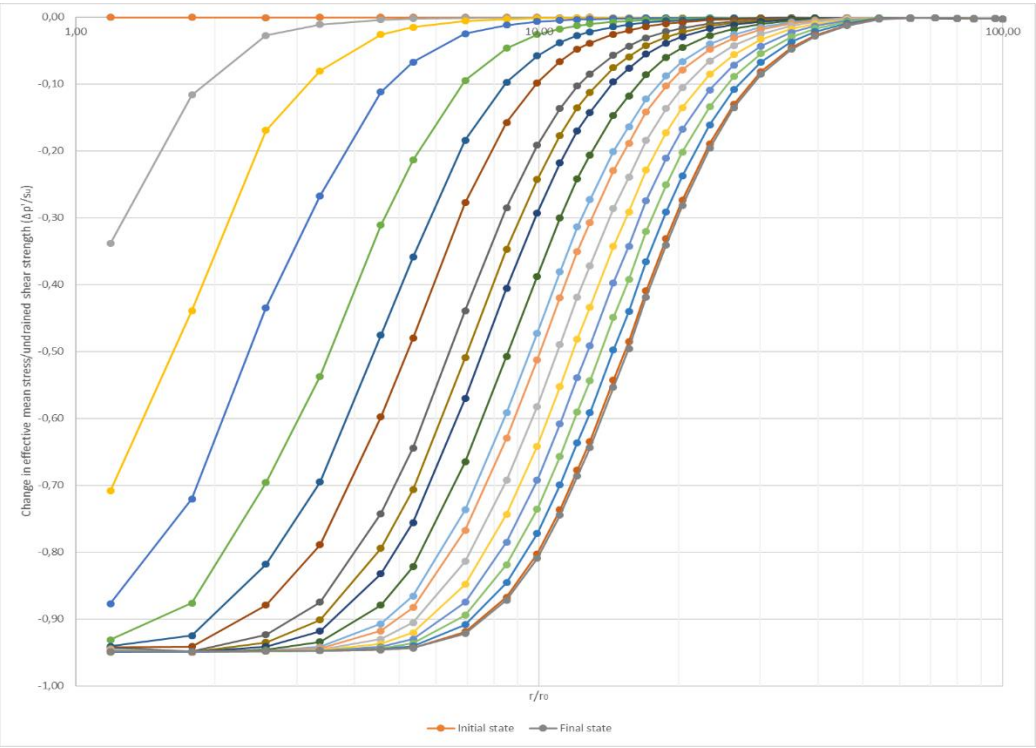

Figure C.1.10: Change in effective mean stress normalized with the undrained shear strength from initial (i.e. before any displacement) to final (i.e. entire displacement applied) state against the normalized radial distance from the pile center in a logarithmic scale. Modeled in Plaxis with input parameters from Table 11.2.

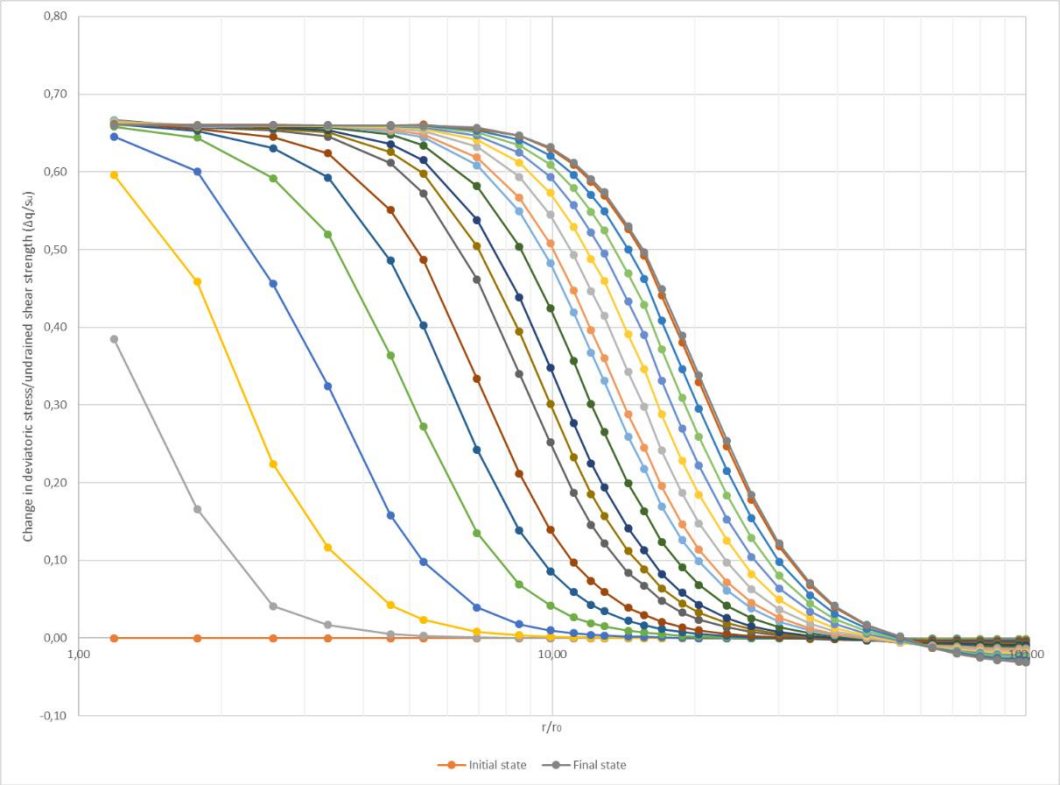

Figure C.1.11: Change in deviatoric stress normalized with the undrained shear strength from initial (i.e. before any displacement) to final (i.e. entire displacement applied) state against the normalized radial distance from the pile center in a logarithmic scale. Modeled in Plaxis with input parameters from Table 11.2.

C.2 Change in stress during dissipation in CEM-MCC

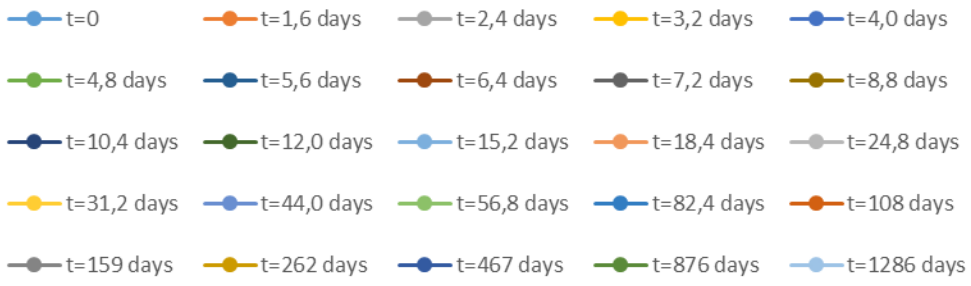

Figure C.2.1: Legend for the plots in Appendix C.2, showing the dissipation time for each line.

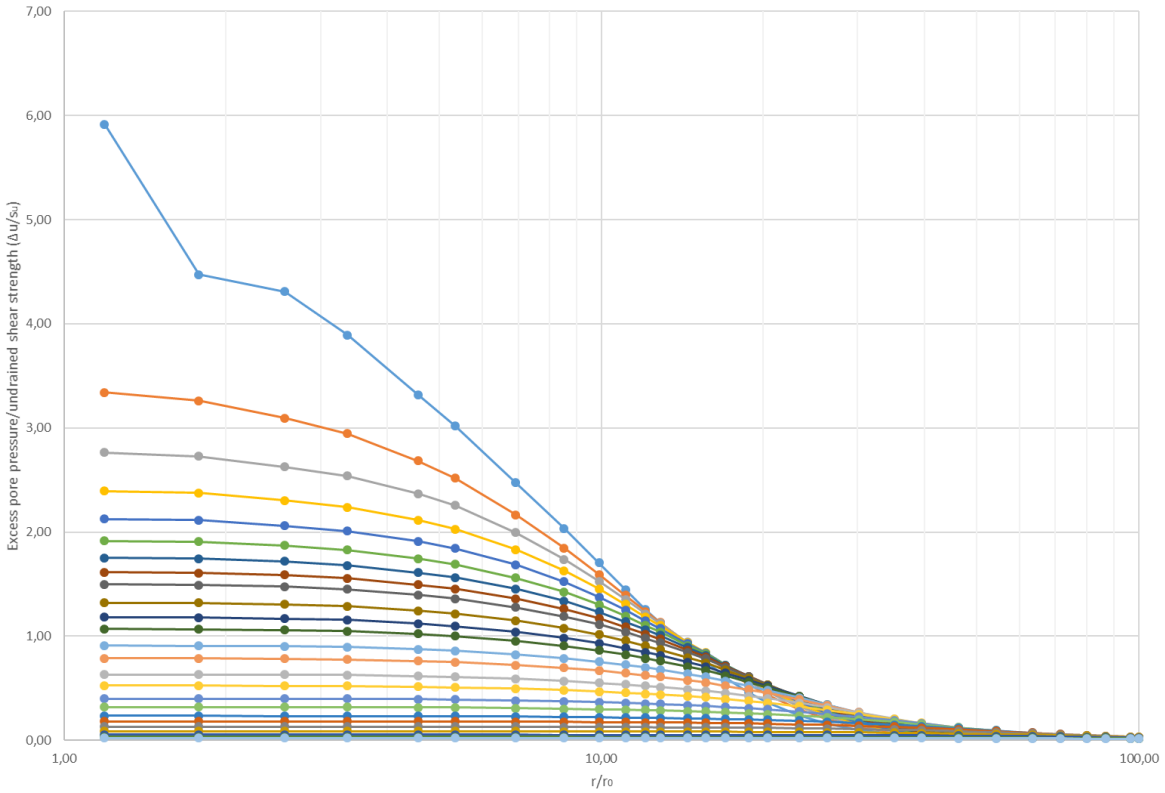

Figure C.2.2: Excess pore pressure normalized with the undrained shear strength from t=0, where the stress equals that of the final state from Appendix C.1, to t=1300days (i.e. $\Delta u \leq 1kPa$) against the normalized radial distance from the pile center in a logarithmic scale. Modeled in Plaxis with input parameters from Table 11.2.

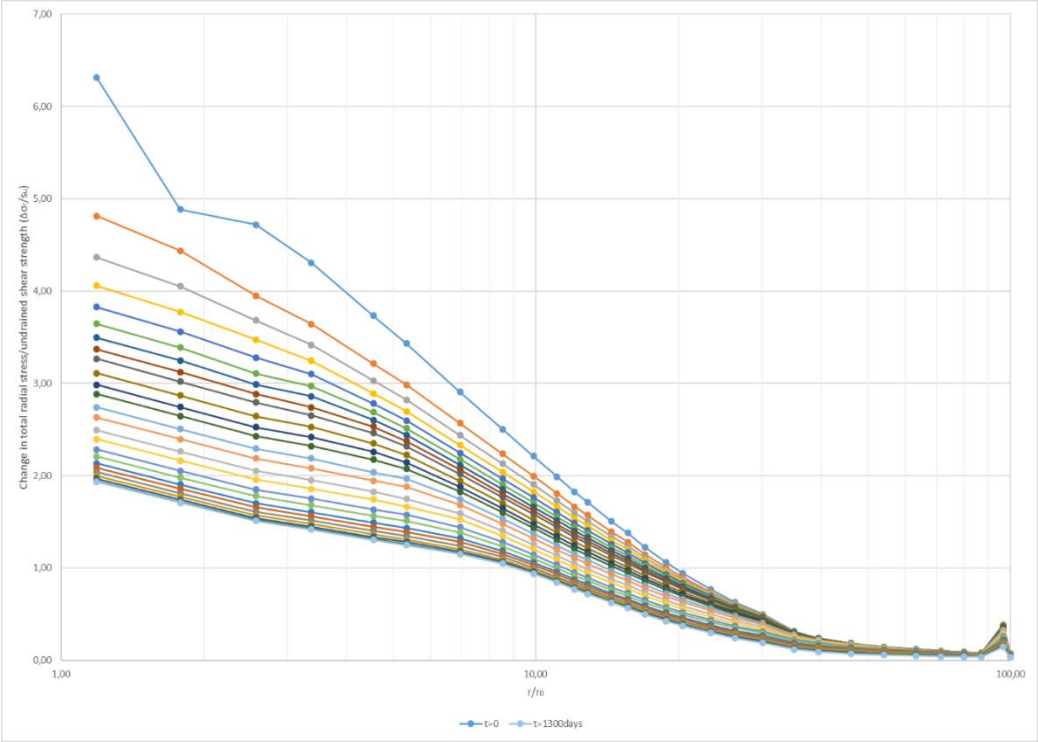

Figure C.2.3: Change in total radial stress normalized with the undrained shear strength from t=0, where the stress equals that of the final state from Appendix C.1, to t=1300days (i.e. $\Delta u \leq 1kPa$) against the normalized radial distance from the pile center in a logarithmic scale. Modeled in Plaxis with input parameters from Table 11.2.

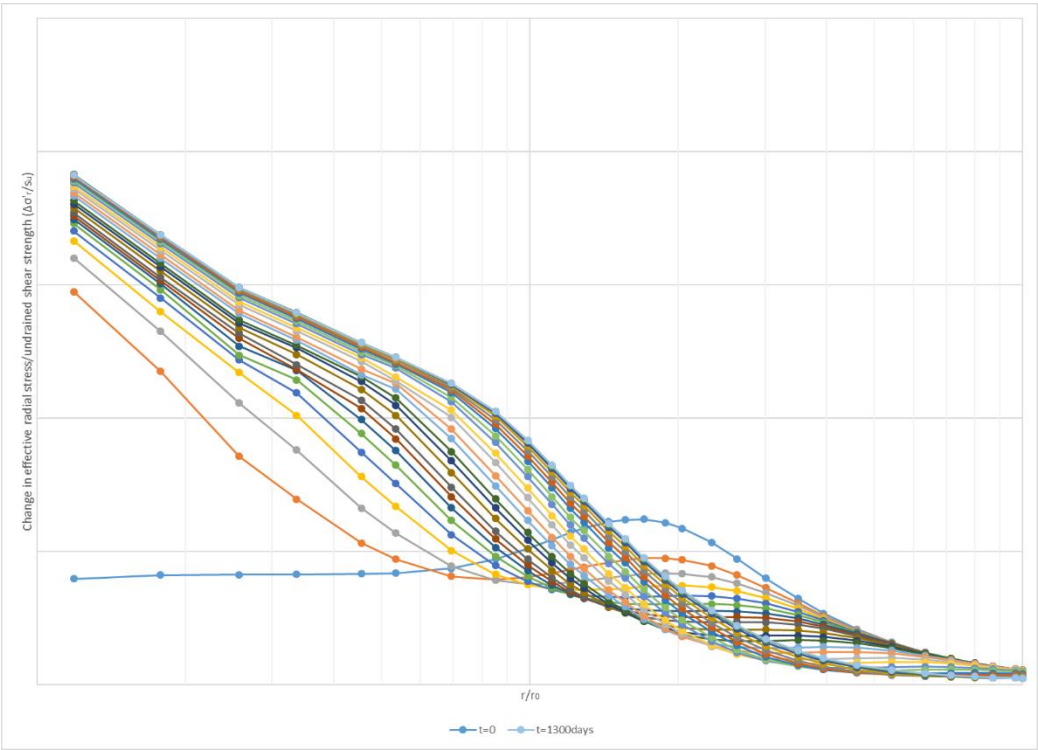

Figure C.2.4: Change in effective radial stress normalized with the undrained shear strength from t=0, where the stress equals that of the final state from Appendix C.1, to t=1300days (i.e. $\Delta u \leq 1kPa$) against the normalized radial distance from the pile center in a logarithmic scale. Modeled in Plaxis with input parameters from Table 11.2.

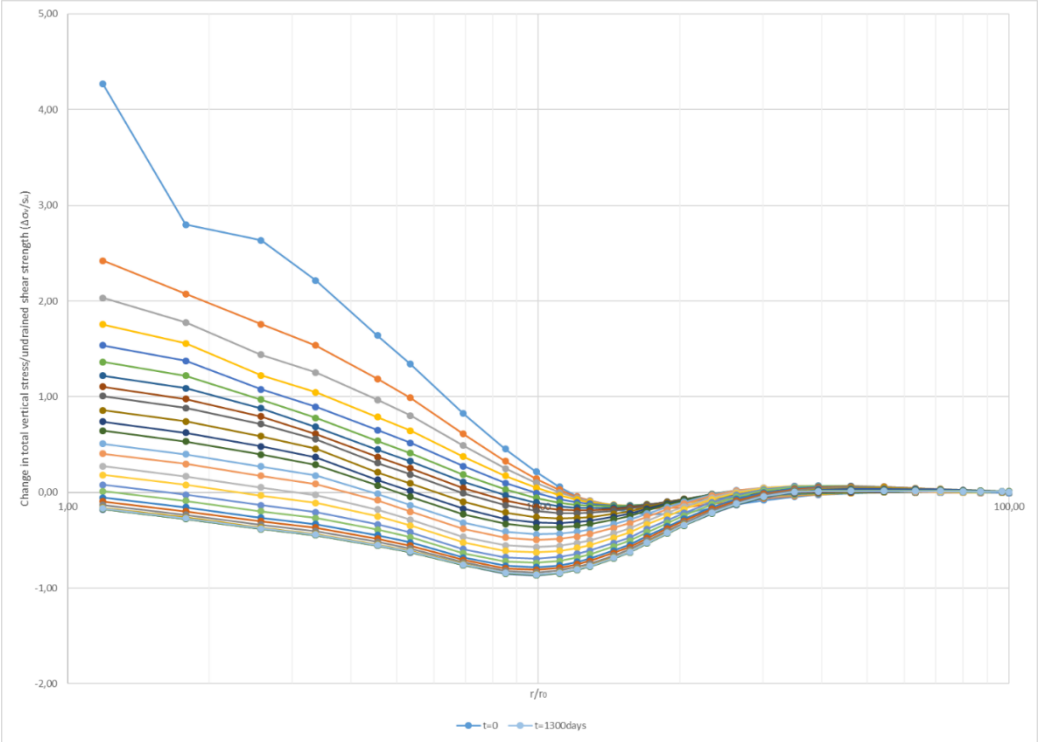

Figure C.2.5: Change in total vertical stress normalized with the undrained shear strength from t=0, where the stress equals that of the final state from Appendix C.1, to t=1300days (i.e. $\Delta u \leq 1kPa$) against the normalized radial distance from the pile center in a logarithmic scale. Modeled in Plaxis with input parameters from Table 11.2.

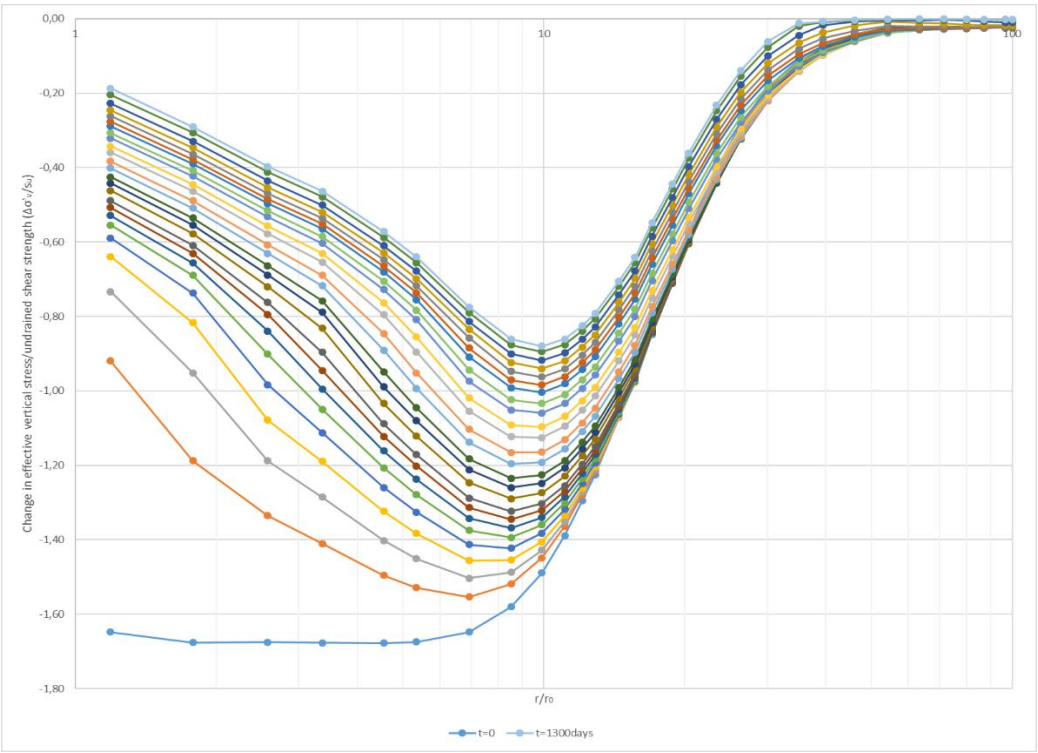

Figure C.2.6: Change in effective vertical stress normalized with the undrained shear strength from t=0, where the stress equals that of the final state from Appendix C.1, to t=1300days (i.e. $\Delta u \leq 1kPa$) against the normalized radial distance from the pile center in a logarithmic scale. Modeled in Plaxis with input parameters from Table 11.2.

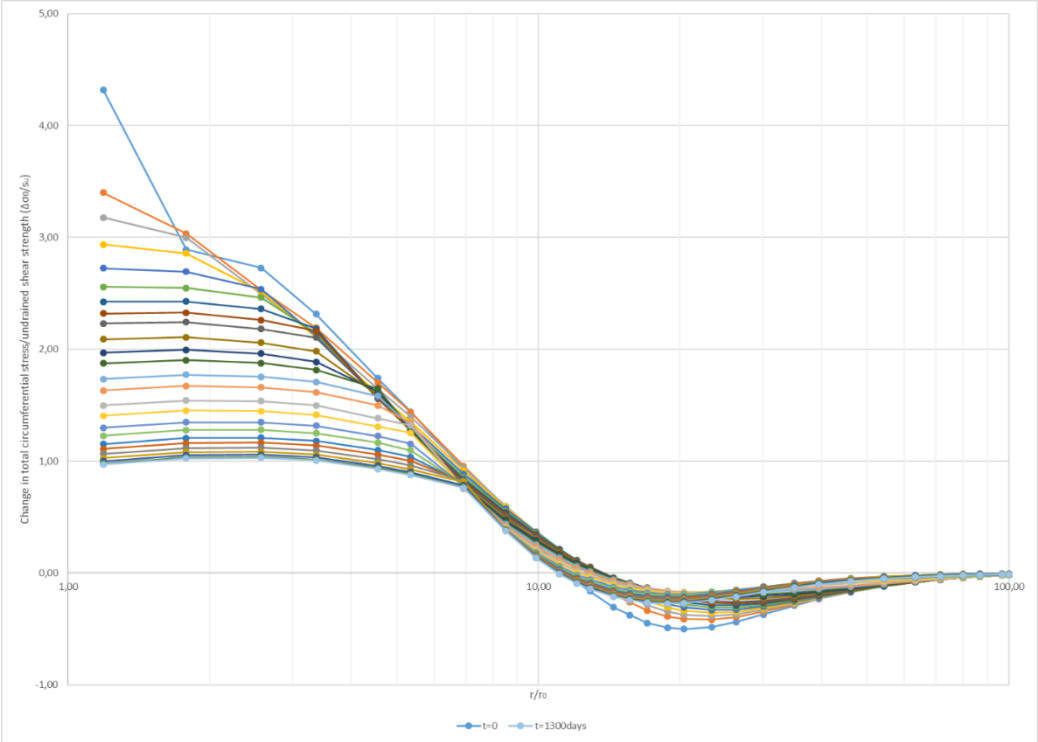

Figure C.2.7: Change in total circumferential stress normalized with the undrained shear strength from t=0, where the stress equals that of the final state from Appendix C.1, to t=1300days (i.e. $\Delta u \leq 1kPa$) against the normalized radial distance from the pile center in a logarithmic scale. Modeled in Plaxis with input parameters from Table 11.2.

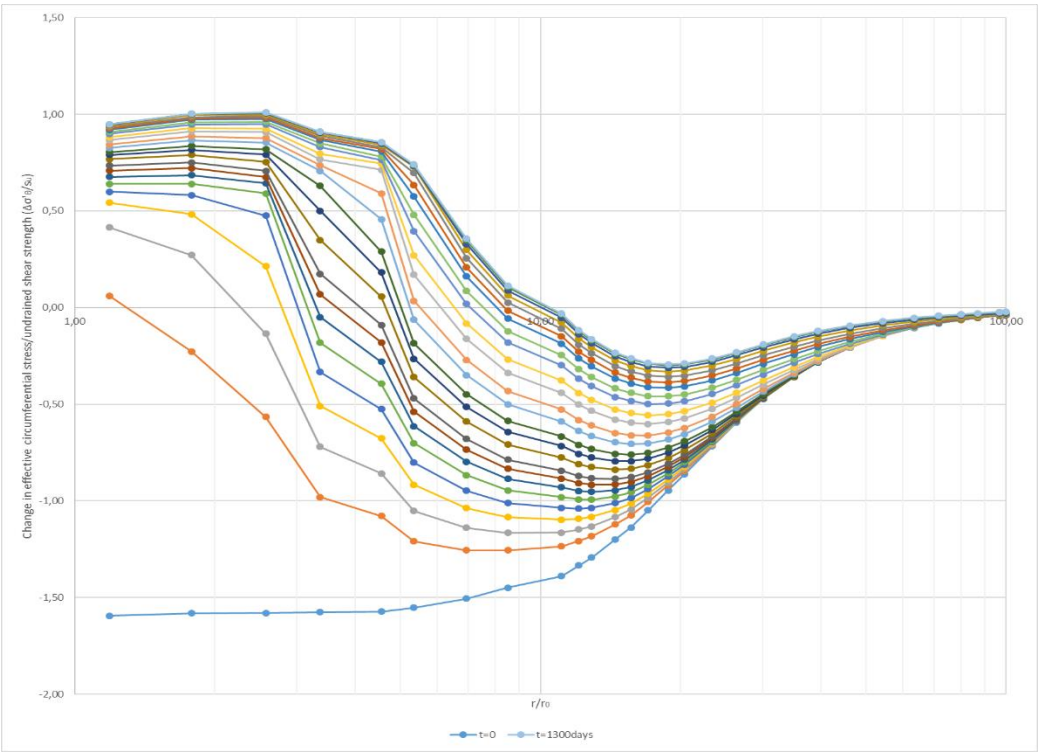

Figure C.2.8: Change in effective circumferential stress normalized with the undrained shear strength from t=0, where the stress equals that of the final state from Appendix C.1, to t=1300days (i.e. $\Delta u \leq 1kPa$) against the normalized radial distance from the pile center in a logarithmic scale. Modeled in Plaxis with input parameters from Table 11.2.

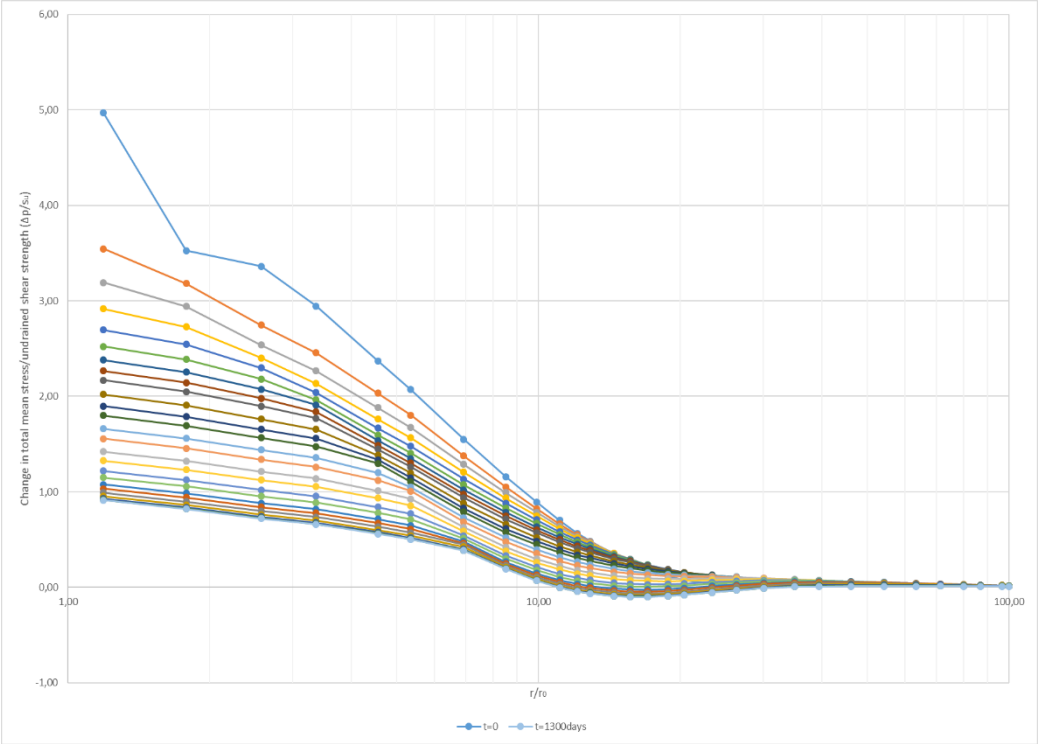

Figure C.2.9: Change in total mean stress normalized with the undrained shear strength from t=0, where the stress equals that of the final state from Appendix C.1, to t=1300days (i.e. $\Delta u \leq 1kPa$) against the normalized radial distance from the pile center in a logarithmic scale. Modeled in Plaxis with input parameters from Table 11.2.

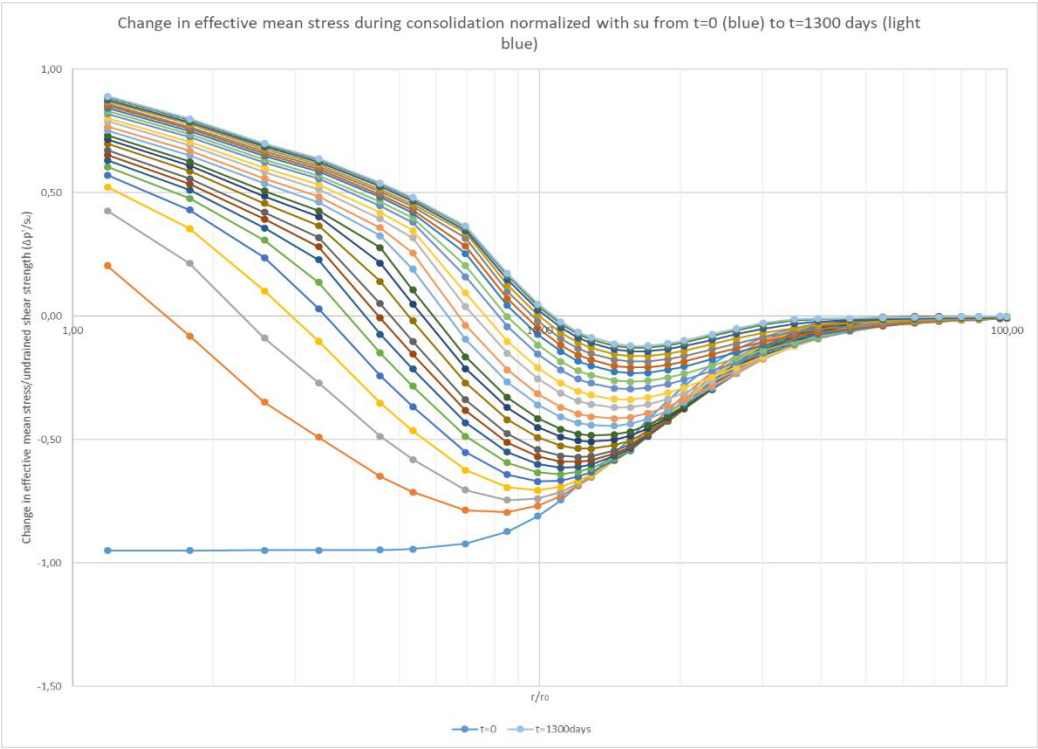

Figure C.2.10: Change in effective mean stress normalized with the undrained shear strength from t=0, where the stress equals that of the final state from Appendix C.1, to t=1300days (i.e. $\Delta u \leq 1kPa$) against the normalized radial distance from the pile center in a logarithmic scale. Modeled in Plaxis with input parameters from Table 11.2.

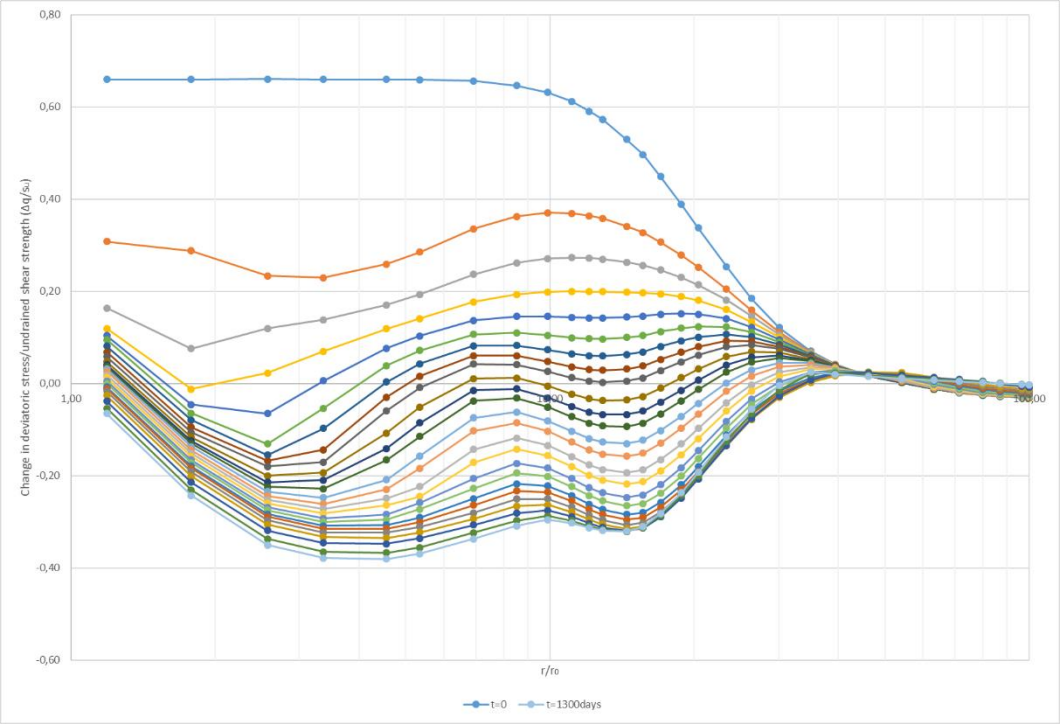

Figure C.2.11: Change in deviatoric stress normalized with the undrained shear strength from t=0, where the stress equals that of the final state from Appendix C.1, to t=1300days (i.e. $\Delta u \leq 1kPa$) against the normalized radial distance from the pile center in a logarithmic scale. Modeled in Plaxis with input parameters from Table 11.2.